INSIGHTS IN CELLULAR NEUROPHYSIOLOGY: 2021

EDITED BY: Enrico Cherubini, Daniela Tropea and Arianna Maffei
PUBLISHED IN: Frontiers in Cellular Neuroscience

frontiers Research Topics

ISSN 1664-8714
ISBN 978-2-83250-455-0
DOI 10.3389/978-2-83250-455-0

About Frontiers

Frontiers is more than just an open-access publisher of scholarly articles: it is a pioneering approach to the world of academia, radically improving the way scholarly research is managed. The grand vision of Frontiers is a world where all people have an equal opportunity to seek, share and generate knowledge. Frontiers provides immediate and permanent online open access to all its publications, but this alone is not enough to realize our grand goals.

Frontiers Journal Series

The Frontiers Journal Series is a multi-tier and interdisciplinary set of open-access, online journals, promising a paradigm shift from the current review, selection and dissemination processes in academic publishing. All Frontiers journals are driven by researchers for researchers; therefore, they constitute a service to the scholarly community. At the same time, the Frontiers Journal Series operates on a revolutionary invention, the tiered publishing system, initially addressing specific communities of scholars, and gradually climbing up to broader public understanding, thus serving the interests of the lay society, too.

Dedication to Quality

Each Frontiers article is a landmark of the highest quality, thanks to genuinely collaborative interactions between authors and review editors, who include some of the world's best academicians. Research must be certified by peers before entering a stream of knowledge that may eventually reach the public - and shape society; therefore, Frontiers only applies the most rigorous and unbiased reviews.
Frontiers revolutionizes research publishing by freely delivering the most outstanding research, evaluated with no bias from both the academic and social point of view. By applying the most advanced information technologies, Frontiers is catapulting scholarly publishing into a new generation.

What are Frontiers Research Topics?

Frontiers Research Topics are very popular trademarks of the Frontiers Journals Series: they are collections of at least ten articles, all centered on a particular subject. With their unique mix of varied contributions from Original Research to Review Articles, Frontiers Research Topics unify the most influential researchers, the latest key findings and historical advances in a hot research area! Find out more on how to host your own Frontiers Research Topic or contribute to one as an author by contacting the Frontiers Editorial Office: frontiersin.org/about/contact

INSIGHTS IN CELLULAR NEUROPHYSIOLOGY: 2021

Topic Editors:
Enrico Cherubini, European Brain Research Institute, Italy
Daniela Tropea, Trinity College Dublin, Ireland
Arianna Maffei, Stony Brook University, United States

Citation: Cherubini, E., Tropea, D., Maffei, A., eds. (2022). Insights in Cellular Neurophysiology: 2021. Lausanne: Frontiers Media SA.
doi: 10.3389/978-2-83250-455-0

Table of Contents

frontiers | Frontiers in Cellular Neuroscience

TYPE Editorial
PUBLISHED 27 September 2022
DOI 10.3389/fncel.2022.1037824

OPEN ACCESS

EDITED AND REVIEWED BY
Dirk Feldmeyer,
Julich Research Center (HZ), Germany

*CORRESPONDENCE
Enrico Cherubini
e.cherubini@ebri.it

SPECIALTY SECTION
This article was submitted to Cellular Neurophysiology, a section of the journal Frontiers in Cellular Neuroscience

RECEIVED 06 September 2022
ACCEPTED 15 September 2022
PUBLISHED 27 September 2022

CITATION
Cherubini E, Maffei A and Tropea D (2022) Editorial: Insights in cellular neurophysiology: 2021. *Front. Cell. Neurosci.* 16:1037824. doi: 10.3389/fncel.2022.1037824

Editorial: Insights in cellular neurophysiology: 2021

Enrico Cherubini[1]*, Arianna Maffei[2] and Daniela Tropea[3]

[1]European Brain Research Institute, Rome, Italy, [2]Department of Neurobiology and Behavior, Stony Brook University, Stony Brook, NY, United States, [3]Institute of Neuroscience, Trinity College, Dublin, Ireland

KEYWORDS

developing neocortex, electrical synapses, X-rays, hippocampus and striatum, spinal cord injury, dorsal raphe, circadian rhythms, olfaction

Editorial on the Research Topic
Insights in cellular neurophysiology: 2021

In the framework of Frontiers' initiative to highlight the latest advancements in Neuroscience, this Research Topic is focused on new insights, recent developments and major accomplishments achieved in the Cellular Neurophysiology field. The goal of this special edition is to shed light on the progress made in the past decade, and on future challenges, providing a thorough overview of the state of the art of this stimulating area of research.

This Research Topic gathers contributions (four reviews and twelve research articles) from editorial board members of the Cellular Neurophysiology Section of the Journal.

Reviews

Luhmann summarizes novel technologies used to explore the developing cerebral cortex in newborn rodents. In the past decade, high-density multi-electrode arrays and genetically encoded calcium indicators have been used to detect the activity of large neuronal ensembles, to characterize their connectivity and architectural layering which changes in an add-on daily basis process. Moreover, opto-chemogenetic approaches allowed the identification of transient cortical circuits, hub neurons and their role in generating spontaneous and sensory evoked activities. At early stages of development, network synchronization is facilitated by the early depolarizing action of GABA and by electrical synapses.

In mature neurons, electrical synapses are not only responsible for network synchronization but, as highlighted by Vaughn and Haas, they provide spike-dependent inhibition, acting as low-pass filters that can preferentially transfer the slow spike after-hyperpolarization. Furthermore, gap junctions are instrumental in processing a variety of neuronal signals. They have been shown to drive asynchronous firing, regulate excitation *via* shunting inhibition, and improve the signal to noise ratio. Computational modeling and imaging approaches will certainly contribute to a better understanding of how gap junctions integrate neuronal activity in a network.

The prefrontal cortex plays a key role in neuronal circuits responsible for social status, a major social determinant of health in primates (Wilkinson et al., 1998). This leads to hierarchical behavior, which represent a universal feature among animal species from insect to fishes, including rodents and primates. It is crucial for animals' survival, and is regulated by the interaction of neuroendocrine factors and neuronal circuits. The current "prefrontal-centric" view of social hierarchy behavior has been expanded in Ferreira-Fernandez and Peça's review, in which, on the basis of connectivity data, possible interactions at macro, micro and mesoscale levels of the prefrontal cortex with other brain regions are discussed.

The biological effects of X-rays, a form of high energy electromagnetic radiation that can penetrate tissues more readily than light thus affecting neuronal and behavioral functions in animals, have been reviewed by Mantraratnam et al. who have examined sensory effects of X-rays mediated by radiolysis of water and generation of reactive oxygen species in a variety of animals. The authors focused mainly on immediate appetitive and consummatory behaviors, radiotaxis (a locomotor movement toward the source of X-rays including flight in insects), arousal and olfactory responses.

Research articles

Interferon γ (IFN-γ) is a cytokine with neuromodulatory properties. In particular, IFN-γ enhances GABAergic transmission in the hippocampus (Flood et al., 2019). In view of the key role of GABA in shaping neuronal circuits early in development, Döhne et al. investigated whether IFN-γ affects miniature GABAergic currents in layer 5 pyramidal neurons of developing rat somatosensory cortex. IFN-γ enhanced the frequency and amplitude of spontaneous $GABA_A$-mediated events. While the increase in frequency was dependent on nitric oxide (NO) and guanylate cyclase, the amplitude relied on protein kinase C. In addition, IFN-γ shifted paired-pulse ratio toward facilitation in a NO-independent manner.

Piepgras et al. examined the effects *Clostridium botulinum* C3 transferase, C3BOT (an exoenzyme known to inhibit Rho-dependent signaling cascades) and the 26mer peptide derived from full length protein in regulating glutamate transporter EAAT3 in primary murine hippocampal neurons. Both proteins provide neuroprotection by promoting upregulation of glutamate uptake, an effect that is prevented by tyrosine kinase inhibitors. In pathological conditions, the C3-mediated increase of glutamate clearance would limit glutamate spillover and excitotoxicity.

Kamiya used the NEURON simulator to revise the model proposed by Alle and Geiger (2006) on excitatory presynaptic potentials (EPreSPs) at mossy fibers-CA3 synapses in the hippocampus. The model described by the author incorporated active axonal sodium, potassium and calcium conductance to affect transmitter release at axon terminals. In addition to their canonical mode of signaling, somato-dendritic depolarization can affect action potential amplitude and information transfer in neuronal circuits through passive propagation. Furthermore, he showed that activation of axonal $GABA_A$ receptors by EPreSPs generated by spillover of GABA from adjacent synapses reduced spike's amplitude *via* shunting inhibition.

Anandamide (AEA) and 2-arachidonylglycerol (2-AG), endogenous ligands of endocannabionoid receptors, regulate synaptic transmission in several brain areas. Recent evidence suggests that fatty acid-binding protein 5 (FABP5) controls synaptic 2-AG signaling at excitatory synapses in the dorsal raphe (Haj-Dahmane et al., 2018). Fauzan et al. investigated whether a similar effect occurs in the striatum, which expresses high levels of FABP5 mainly in astrocytes. They found that FABP5 deletion impairs tonic 2-AG and AEA signaling at medium spiny neurons synapses and alters short-term synaptic plasticity in the striatum.

Dysregulation of the activity of serotoninergic (5-HT) neurons in the dorsal raphe nucleus (DRN) is responsible for emotional disorders. The activity of 5-HT neurons is regulated by α1-adrenoreceptors activated by the noradrenergic input from locus coeruleus. In brain slice preparation, Wang et al. demonstrated that inhibition of K^+ currents from three K^+ channel families, A-type, Kv7/KCNQ and SK channels, contributes to spontaneous firing triggered in DRN 5-HT neurons by activation of α1-adrenoreceptors agonist phenylephrine.

Neurons in the rostral nucleus of the solitary tract (rNST), which receive taste information from the tongue, project to brainstem relay nuclei along the taste pathway. Park et al. used anterograde horseradish peroxidase labeling and post-embedding immunogold staining for glutamate to quantify, at the electron microscopic level, rNST terminals in parabrachial and medullary reticular formation nuclei, in order to examine how sensory information from rNST is processed.

Spinal cord injury (SCI) is one of the major causes of disability whose treatment is very limited. Among different neuronal populations, interneurons play a key role in circuit reorganization and partial recovery in less severe, anatomically incomplete SCI. Vargova et al. developed a new method, in rodents, aimed at enhancing the intrinsic regenerative properties of spinal cord interneurons, with the potential of expanding its use for SCI treatment.

Abbreviations: AEA, anandamide; 2-AG, 2-arachidonylglycerol; atVNS, auricular transcutaneous vagus nerve stimulation; C3BOT, *Clostrdium botulinum* C3 transferase; DRN, dorsal raphe nucleus; EA, evernic acid; EAAT3, excitatory amino acid transporter 3; EPreSPs, excitatory presynaptic potentials; FABP5, fatty acid-binding protein 5; IFN-γ, Interferon γ; NO, nitric oxide; OSNs, olfactory sensory neurons; rNST, rostral nucleus of the solitary tract; SCI, Spinal cord injury; UA, usnic acid.

In the spinal cord, substantia gelatinosa neurons of the dorsal horn are referred as "central gate" for transmission and regulation of nociceptive information. Zhu et al. demonstrated that a subset of these neurons, with particular morphological and electrophysiological characteristics, exhibit rebound depolarization (RD). RD is a transient membrane depolarization following hyperpolarizing pulses that is regulated by cyclic nucleotide and T-type calcium channels, and can transform inhibitory signals into excitatory ones. RD-expressing neurons receiving monosynaptic as well as polysynaptic inputs from Aδ and C fibers, differentially process somatosensory information along the pain pathway.

CLC-3-associated Cl^-/H^+ exchangers are expressed in multiple endosomal compartments, and regulate pH and $[Cl^-]$ *via* stoichiometrically coupled exchange of two Cl^- and one H^+. Downregulation of CLC-3 alters pain perception in mice (Pang et al., 2016), suggesting a role of Cl^-/H^+ exchangers in pain regulation. Sierra-Marquez et al. analyzed the involvement of CLC-3 Cl^-/H^+ transport in nociceptive pathways of the spinal cord. Genetic ablation of CLC-3-associated Cl^-/H^+ exchanger did not modify the excitability of DRG neurons, but enhanced microglia activation within spinal tissue, indicating that CLC-3 Cl^-/H^+ transport is needed for maintaining neuroglia homeostasis.

Brain stimulation devices are increasingly used to treat various forms of brain disorders. New insights into the mechanisms of bioelectronics in medicine have been provided by Brambilla-Pisoni et al. who used a non-invasive auricular transcutaneous vagus nerve stimulation (atVNS) to study its effects on cognitive processes in *naïve* CD-1 mice. Delivery of atVNS immediately, but not 3 h after the familiarization phase, induced a clear reorganization of the network leading to the enhancement of memory consolidation in a novel object recognition test and a re-distribution of the immediate early gene c-FOS.

In mammals, the circadian clock synchronizes physiological functions to day-night rhythms (Neumann et al., 2019). Disruption of circadian rhythms leads to chronic diseases including cardio-metabolic and neurodegenerative disorders, mainly *via* oxidative stress. Srimani et al., used three different cell lines and two circadian luminescence reporter systems to show that two lichen secondary metabolites, evernic and usnic acids (EA and UA), have marked neuroprotective and antioxidant effects. Both EA and UA significantly lower amplitudes and accelerate the dampening of cellular circadian rhythms.

In the last paper of this Research Topic, Miazzi et al. used functional imaging and analysis of calcium dynamics to detect how odors are processed in odorant receptors localized on olfactory sensory neurons (OSNs) in *Drosophila melanogaster*. Insects need chemoreception to identify food, mates, oviposition sites and, for their survival, to avoid exposure to harmful perils. In the fly, OSNs are expressed on two easily accessible organs: the antenna and the maxillary palps. To study odor-induced responses in OSNs under natural conditions, the authors used an *in vivo* and an *in vitro* preparation of isolated vital *Drosophila* OSNs from the antenna.

We hope that papers included in this Special Topic can stimulate further studies leading to new advances in the fast-growing field of Cellular Neuroscience.

Author contributions

All authors contributed to the article and approved the submitted version.

Funding

This research was funded by Fondo Ordinario Enti (FOE D.M 865/2019) to EC.

Acknowledgments

We wish to thank our colleagues who contributed to reviews and original studies reported in this topic.

Conflict of interest

The authors declare that the research was conducted in the absence of any commercial or financial relationships that could be construed as a potential conflict of interest.

Publisher's note

References

Alle, H., and Geiger, J. R. (2006). Combined analog and action potential coding in hippocampal mossy fibers. *Science* 311, 1290–1293. doi: 10.1126/science. 1119 055

Flood, L., Korol, S. V., Ekselius, L., Birnir, B., and Jin, Z. (2019). Interferonγ potentiates GABAA receptor-mediated inhibitory currents in rat hippocampal CA1 pyramidal neurons. *J. Neuroimmunol.* 337, 577050. doi: 10.1016/j.jneuroim. 2019.577050

Haj-Dahmane, S., Shen, R. Y., Elmes, M. W., Studholme, K., Kanjiya, M. P., and Bogdan, D., et al. (2018). Fatty-acid-binding protein 5 controls retrograde endocannabinoid signaling at central glutamate synapses. *Proc. Natl. Acad. Sci. U. S. A.* 115, 3482–3487. doi: 10.1073/pnas.1721339115

Neumann, A. M., Schmidt, C. X., Brockmann, R. M., and Oster, H. (2019). Circadian regulation of endocrine systems. *Auton. Neurosci.* 216, 1–8. doi: 10.1016/j.autneu.2018.10.001

Pang, R.-P., Xie, M.-X., Yang, J., Shen, K.-F., Chen, X., Su, Y.-X., et al. (2016). Downregulation of ClC-3 in dorsal root ganglia neurons contributes to mechanical hypersensitivity following peripheral nerve injury. *Neuropharmacology* 110, 181–189. doi: 10.1016/j.neuropharm.2016.07.023

Wilkinson, R. G., Marmot, M., World Health Organization, and Regional Office for Europe (1998). *The Solid Facts: Social Determinants of Health*. Copenhagen: WHO Regional Office for Europe. Available online at: https://apps.who.int/iris/handle/10665/108082

frontiers in Cellular Neuroscience

ORIGINAL RESEARCH
published: 21 September 2021
doi: 10.3389/fncel.2021.736879

Electrophysiological and Morphological Features of Rebound Depolarization Characterized Interneurons in Rat Superficial Spinal Dorsal Horn

Mengye Zhu[1,2†], Yi Yan[1,2†], Xuezhong Cao[1,2], Fei Zeng[1,2], Gang Xu[1,2], Wei Shen[1,2], Fan Li[1,2], Lingyun Luo[1,2], Zhijian Wang[1,2], Yong Zhang[1,2], Xuexue Zhang[1,2], Daying Zhang[1,2] and Tao Liu[3]**

[1] Department of Pain Medicine, The First Affiliated Hospital of Nanchang University, Nanchang, China, [2] Institute of Pain Medicine, Jiangxi Academy of Clinical and Medical Sciences, Nanchang, China, [3] Center for Experimental Medicine, The First Affiliated Hospital of Nanchang University, Nanchang, China

OPEN ACCESS

Edited by:
Arianna Maffei,
Stony Brook University, United States

Reviewed by:
Francesco Ferrini,
University of Turin, Italy
Brett A. Graham,
Independent Researcher, Newcastle, NSW, Australia

***Correspondence:**
Daying Zhang
zdysino@163.com
Tao Liu
liutao1241@ncu.edu.cn

[†] These authors have contributed equally to this work

Specialty section:
This article was submitted to Cellular Neurophysiology, a section of the journal Frontiers in Cellular Neuroscience

Received: 06 July 2021
Accepted: 25 August 2021
Published: 21 September 2021

Citation:
Zhu M, Yan Y, Cao X, Zeng F, Xu G, Shen W, Li F, Luo L, Wang Z, Zhang Y, Zhang X, Zhang D and Liu T (2021) Electrophysiological and Morphological Features of Rebound Depolarization Characterized Interneurons in Rat Superficial Spinal Dorsal Horn. Front. Cell. Neurosci. 15:736879. doi: 10.3389/fncel.2021.736879

Substantia gelatinosa (SG) neurons, which are located in the spinal dorsal horn (lamina II), have been identified as the "central gate" for the transmission and modulation of nociceptive information. Rebound depolarization (RD), a biophysical property mediated by membrane hyperpolarization that is frequently recorded in the central nervous system, contributes to shaping neuronal intrinsic excitability and, in turn, contributes to neuronal output and network function. However, the electrophysiological and morphological properties of SG neurons exhibiting RD remain unclarified. In this study, whole-cell patch-clamp recordings were performed on SG neurons from parasagittal spinal cord slices. RD was detected in 44.44% (84 out of 189) of the SG neurons recorded. We found that RD-expressing neurons had more depolarized resting membrane potentials, more hyperpolarized action potential (AP) thresholds, higher AP amplitudes, shorter AP durations, and higher spike frequencies in response to depolarizing current injection than neurons without RD. Based on their firing patterns and morphological characteristics, we propose that most of the SG neurons with RD mainly displayed tonic firing (69.05%) and corresponded to islet cell morphology (58.82%). Meanwhile, subthreshold currents, including the hyperpolarization-activated cation current (I_h) and T-type calcium current (I_T), were identified in SG neurons with RD. Blockage of I_h delayed the onset of the first spike in RD, while abolishment of I_T significantly blunted the amplitude of RD. Regarding synaptic inputs, SG neurons with RD showed lower frequencies in both spontaneous and miniature excitatory synaptic currents. Furthermore, RD-expressing neurons received either Aδ- or C-afferent-mediated monosynaptic and polysynaptic inputs. However, RD-lacking neurons received afferents from monosynaptic and polysynaptic Aδ fibers and predominantly polysynaptic C-fibers. These findings demonstrate that SG neurons with RD have a specific cell-type distribution, and may differentially process somatosensory information compared to those without RD.

Keywords: rebound depolarization, spinal dorsal horn, substantia gelatinosa neuron, morphology, electrophysiology, primary afferent input

INTRODUCTION

Rebound depolarization (RD) is a transient membrane depolarization (sometimes accompanied by a series of spikes) following hyperpolarizing pulses. It has been observed in various brain regions, which include the hippocampus (Surges et al., 2006), auditory midbrain (Sun et al., 2020), medial prefrontal cortex (Kurowski et al., 2018), thalamus (Wang et al., 2016; Zhu et al., 2018), and deep spinal dorsal horn (Rivera-Arconada and Lopez-Garcia, 2015), among others. RD substantially relies on channels with hyperpolarization-dependent activation or de-inactivation features. Hyperpolarization-activated cation current (I_h), a mixed inward current consisting of sodium and potassium ions, mediated by hyperpolarization-activated cyclic nucleotide-gated (HCN) channels has been confirmed to be able to regulate RD. In addition, T-type calcium channel-induced current (I_T) is another vital ionic conductance supporting RD generation (Sangrey and Jaeger, 2010; Engbers et al., 2011; Duan et al., 2018). Functionally, RD has been proposed as an inhibition-excitation converter transforming inhibitory inputs into excitatory signals (Sanchez-Vives and McCormick, 2000; Tadayonnejad et al., 2009; Pedroarena, 2010).

Lamina II of the spinal dorsal horn, namely substantia gelatinosa (SG), is an indisputably important component of the pain pathway. The SG is referred to as the "central gate" since it converses inputs from the primary afferents, local circuit interneurons, and endogenous descending tracts, and may therefore be essential in transmitting and modulating nociceptive information from the periphery (Todd, 2010; Duan et al., 2018). Alterations in SG neuronal excitability have been implicated as catalysts for the development and maintenance of pathological pain (Balasubramanyan et al., 2006; Kuner, 2010; Feng et al., 2019). The SG is composed of excitatory and inhibitory interneurons with substantial electrophysiological and morphological heterogeneity (Grudt and Perl, 2002; Maxwell et al., 2007; Yasaka et al., 2010; Graham and Hughes, 2020). RD is a striking biophysical property of SG neurons (Tadros et al., 2012; Hu et al., 2016). Nevertheless, whether SG neurons with RD display distinct morphological features, intrinsic electrophysiological properties, and input of afferent fibers has not yet been well studied. In addition, the ionic basis for RD in SG neurons also remains to be elucidated.

Here, we used the whole-cell patch-clamp technique to record passive and active membrane properties from SG neurons, which were further categorized to the neurons with RD and without RD. Interestingly, we found that a majority of the SG neurons with RD showed tonic firing, and a *post hoc* morphological study confirmed that most of the RD-expressing neurons exhibited islet morphology. Besides, RD neurons also presented significant differences in intrinsic neural excitability, as well as spontaneous, miniature, and evoked excitatory synaptic transmission. Additionally, we confirmed that I_h and I_T are vital ionic contributions to RD responses in SG neurons. Therefore, our results may provide new insights for unraveling the role of RD in pain processing.

MATERIALS AND METHODS

Animals

Sprague-Dawley (SD) rats (4–6 weeks old) of both sexes obtained from the Animal Center of Nanchang University were used. Rats were housed in same-sex groupings (4–5 animals per cage) in an air-conditioned room maintained at 24 ± 1°C and 50–60% humidity, under a 12:12 light/dark cycle (lights on at 7 a.m.). They had *ad libitum* access to food and water. All animal procedures were performed according to methods approved by the Institutional Animal Care and Use Committee of Nanchang University. Maximal efforts were made to minimize animal pain or discomfort and the number of animals used.

Spinal Cord Slice Preparation

Acute spinal cord slices were prepared as previously described (Wu et al., 2018; Zhu et al., 2019). Briefly, rats were deeply anesthetized with urethane (1.5 g/kg, i.p.), and were then transcardially perfused with an ice-cold sucrose-based artificial cerebrospinal fluid (sucrose-ACSF) containing (in mM): 204 sucrose, 2.5 KCl, 3.5 $MgCl_2$, 0.5 $CaCl_2$, 1.25 NaH_2PO_4, 0.4 ascorbic acid, 2 sodium pyruvate, 11 D-glucose, 25 $NaHCO_3$, and 1 kynurenic acid. The lumbosacral section of the vertebral column was quickly removed and placed into the same solution. After laminectomy and removal of the dura mater, the spinal cord was mounted on a vibratome (VT1000S, Leica, Nussloch, Germany) cutting stage. Sucrose-ACSF was preoxygenated with 95% O_2 and 5% CO_2 for at least 30 min before use. Parasagittal slices (400–600 μm) with or without dorsal root (DR) (8–12 mm long) attached were prepared and kept in an incubator at 32°C for at least 30 min before electrophysiological recording in carbonated standard ACSF. The standard ACSF consisted of (in mM) 117 NaCl, 3.6 KCl, 2.5 $CaCl_2$, 1.2 $MgCl_2$, 1.2 NaH_2PO_4, 25 $NaHCO_3$, 11 D-glucose, and 2 sodium pyruvate.

In vitro Electrophysiological Recordings

Spinal cord slices were transferred into a recording chamber and perfused continuously with carbogenated standard ACSF at a flow rate of 2–4 ml/min. Experiments were performed at room temperature (RT) under visual guidance using an Olympus microscope (BX51WI, Olympus Corp., Tokyo, Japan) and an IR-DIC camera (IR-1000, Dage-MTI, Michigan City, IN, United States). Patch-clamp recordings in the whole-cell configuration were made using an EPC-10 amplifier and Patchmaster software (HEKA Electronics, Lambrecht, Germany). Patch pipettes (3–6 MΩ) were pulled from borosilicate glass capillaries (1.5 mm OD, 1.12 mm ID, World Precision Instruments, Sarasota, FL, United States) with a Sutter P-97 puller (Sutter Instruments, Novato, CA, United States). The internal pipette solution contained (in mM) 130 K-gluconate, 5 KCl, 10 Na_2-phosphocreatine, 0.5 EGTA, 10 HEPES, 4 Mg-ATP, and 0.3 Li-GTP (pH 7.3 adjusted with KOH, 295 mOsm).

Only neurons with a resting membrane potential (RMP) more negative than −45 mV and showing overshooting action potentials (APs) (i.e., exceeding 0 mV) were included for this study. The series resistance was typically between 10 and 30 MΩ,

and cells in which the series resistance changed by more than 20% were discarded from further analysis. No correction for liquid junction potential (approximate 15 mV) was made in this study. All data analyses were performed using Clampfit (Molecular Devices, CA, United States) and Mini Analysis software (Synaptosoft Inc., GA, United States).

Membrane capacitance (Cm) was estimated from the area under the transient capacitive current evoked with a 5-mV depolarizing pulse by Patchmaster software in real-time automatically. Neuronal RMP was recorded within 20 s after the break-in. A hyperpolarizing voltage step was used to estimate the input resistance (Rin) of the tested SG neuron, while negative current pulses (−120 and −140 pA, 1 s) were applied to generate RD responses. The firing pattern of each neuron was determined with a series of depolarizing current pulses (20–140 pA in 20 pA increments) of 1-s duration in the current-clamp mode. The spike adaptation index was obtained by dividing the average of the first two interspike intervals (ISIs) by that of the last two ISIs (Ha et al., 2016). A subthreshold current was evoked by a series of hyperpolarizing voltage steps from −50 to −130 mV in 10 mV decrements (duration 1 s) at a −50 mV holding potential in the voltage-clamp mode.

To investigate the primary afferent inputs, neurons were voltage-clamped at −70 mV. DR-evoked excitatory postsynaptic currents (eEPSCs) were initiated by a constant current source of a pulse (duration 0.1 ms) at a frequency of 0.05 Hz delivered through a suction electrode. The stimulation intensities were set at 50 and 100 μA for the activation of Aδ fibers, 500 μA and 1 mA for the activation of C fibers using a stimulator (Master 8, AMP Instruments Ltd., Israel) and a stimulus isolator (ISO-Flex, AMP Instruments Ltd., Israel). Neurons without an evident monosynaptic response at 1 mA were subsequently stimulated at 3 and/or 5 mA. The Aδ or C-afferent-mediated responses evoked by DR stimulation were distinguished based on the stimulus intensity and the conduction velocity of afferent fibers (<0.8 m/s for C fibers and >1.0 m/s for Aδ fibers). Evoked-EPSCs were judged to be monosynaptic if there were no failures during subsequent repeated stimulation (20 times at 2 Hz for Aδ and 1 Hz for C fibers) and if their latency remained constant in repetitive trials as reported previously (Cui et al., 2016; Iwagaki et al., 2016).

Post hoc Morphological Identification

For morphological identification, an internal pipette solution containing 0.05% neurobiotin 488 was used. After maintaining the stable whole-cell patch-clamp configuration for at least 20 min, the electrode was gently withdrawn from the targeted neuron, and the slice was then fixed at RT for 1 h and then at 4°C overnight in 4% paraformaldehyde in 0.1 M PB (pH 7.4). Following fixation, slices were rinsed in PBS three times and treated with 50% ethanol for 30 min. After rinsing in PBS, the slices were mounted onto slides with a non-fluorescing mounting medium. Neurobiotin-filled neurons were identified and reconstructed under 20× magnification, 1.0–1.5 zoom, and 1.5 μm stack using a confocal microscope (LSM 700, Zeiss, Germany). Neurons were morphologically grouped on the basis of the following parameters regarding their dendritic arborizations (RC: rostro-caudal extent of dentrites, DV: dorsal-ventral expansion of dendrites, SR, SC, SD, SV: dendrites spread from center of the soma to rostral, caudal, dorsal and ventral limit, respectively) (Grudt and Perl, 2002; Yasaka et al., 2007). As long as the value of RC/DV exceeded 3.5, cells could be classified as an islet or a central cell. Within this group, islet cells exhibited abundant dendrites elongated in the RC dimension (>400 μm), whilst central neurons possessed strikingly shorter RC extents (<400 μm) of their dendric arbors. Neurons with RC/DV less than 3.5 were identified as vertical or radial cells. Vertical neurons generally had a predominantly ventrally oriented dendritic geometry with SV/SD > 3.5. If the ratio of SV/SD was less than 3.5, the neurons were defined as a radial neuron. Neurons differed from the four morphological categories were identified as unclassified cell.

Chemical Compounds

ZD7288 and tetrodotoxin (TTX) were purchased from Tocris Bioscience, 3,5-dichloro-*N*-[1-(2,2-dimethyl-tetrahydro-pyran-4-ylmethyl)-4-fluoro-piperidin-4-ylmethyl]-benzamide (TTA-P2) and neurobiotin 488 were obtained from Alomone Labs and Vector, respectively. All other reagents were obtained from Sigma-Aldrich. All chemicals were dissolved in distilled water except for TTA-P2, which was prepared in 0.1% DMSO. Chemical compounds were applied at final concentrations by dissolving them in standard ACSF to achieve the necessary final concentrations of antagonism established in previous studies (Peng et al., 2017; Wu et al., 2018).

Statistical Analysis

Statistical data analysis was conducted with GraphPad Prism 7 (GraphPad Software, La Jolla, CA, United States). For data displaying normal distribution and homogeneity of variance indicated by the Shapiro–Wilk normality test and Levene test respectively, ANOVA or *t*-test was used as appropriate. Numerical data are presented as mean ± SEM. Otherwise, the Mann Whitney Wilcoxon test or Wilcoxon matched-pairs signed-rank test was used for non-parametric statistical comparisons. Data of AP number were analyzed by two-way ANOVA followed by the Bonferroni *post hoc* test. The Chi-squared test or Fisher's exact test was applied to analyze the difference between groups regarding the proportions of the firing patterns, subthreshold currents, and morphological categories. Differences were considered significant when $p < 0.05$.

RESULTS

A total of 189 SG neurons were recorded from parasagittal spinal cord slices of SD rats. As shown in **Figure 1A**, RD exhibits a pronounced depolarization that often results in spikes at the end of a negative current pulse. According to their response to this current, SG neurons are divided into two groups: with RD (**Figure 1Aa**) and without RD (**Figure 1Ab**). The proportions were 44.44% (84/189) and 55.56% (105/189), respectively.

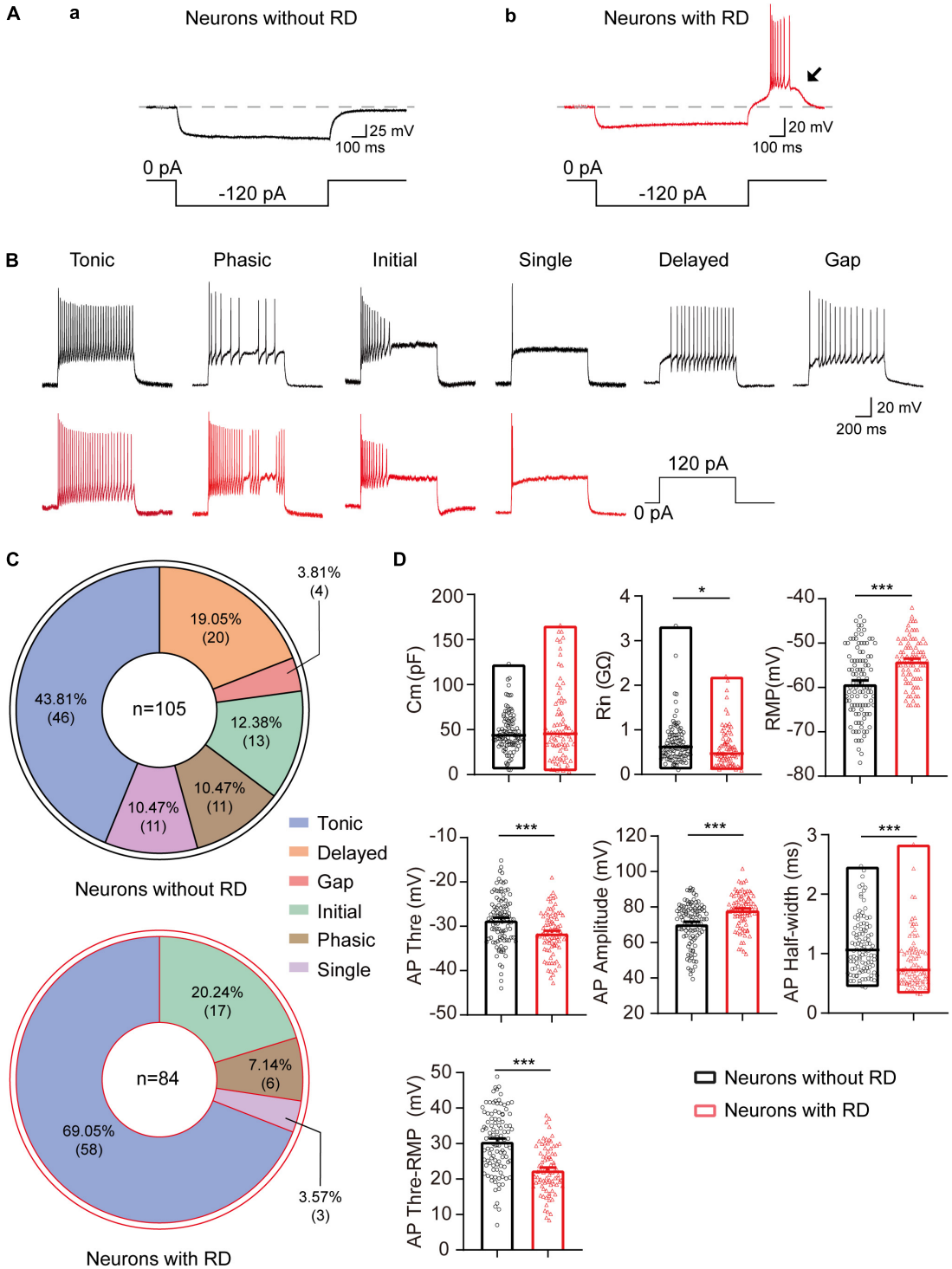

FIGURE 1 | Electrophysiological properties of SG neurons with or without RD from rats. **(A)** SG neurons without **(a)** or with RD **(b)** were classified by a hyperpolarizing current pulse (−120 pA, 1 s). The black arrow indicates the presence of RD. **(B)** Representative traces showing typical firing patterns recorded from SG neurons without (black) or with RD (red). **(C)** Pie graphs showing the proportion of the different firing patterns in SG neurons lacking RD and those expressing RD. In total, 105 and 84 cells were recorded in each group, respectively. **(D)** Summary of the passive and active membrane properties of RD-expressing SG neurons (red) and those lacking RD (black). RD, rebound depolarization; Cm, membrane capacitance; Rin, input resistance; RMP, resting membrane potential; AP, action potential. *$p < 0.05$, ***$p < 0.001$.

TABLE 1 | Comparison of intrinsic membrane properties of SG neurons with or without RD.

Parameter	Neurons without RD	Neurons with RD	*p* Value
Cm (pF)	47.24 ± 2.11	54.80 ± 4.60	0.948
Rin (GΩ)	0.71 ± 0.05	0.59 ± 0.05*	0.013
RMP (mV)	−59.18 ± 0.77	−54.05 ± 0.58***	<0.001
APThreshold (mV)	−28.59 ± 0.54	−31.53 ± 0.53***	<0.001
APAmplitude (mV)	70.52 ± 1.17	78.13 ± 1.09***	<0.001
APHalf-width (ms)	1.14 ± 0.05	0.87 ± 0.05***	<0.001
APThreshold - RMP (mV)	30.59 ± 0.84	22.52 ± 0.71***	<0.001

Values given as mean ± SEM. RD, rebound depolarization; Cm, membrane capacitance; Rin, input resistance; RMP, resting membrane potential; AP, action potential.
**$p < 0.05$.*
****$p < 0.001$.*

Intrinsic Passive and Active Membrane Properties

As shown previously, the discharge patterns of SG neurons were highly heterogeneous, including tonic firing, phasic firing, initial firing, single firing, delayed firing, and gap firing (Ruscheweyh and Sandkuhler, 2002; Zhu et al., 2019). We found that the distribution of the discharge patterns differed between the two groups ($p < 0.001$). All six firing categories were encountered in SG neurons lacking RD: tonic (43.81%), phasic (10.47%), initial (12.38%), single (10.47%), delayed (19.05%), and gap (3.81%) (**Figures 1B,C**). However, delayed firing and gap firing were not identified in SG neurons with RD, of which 69.05% displayed a tonic firing. The proportions of phasic, initial, and single firing in SG neurons with RD were 7.14, 20.24, and 3.57%, respectively (**Figures 1B,C**).

The results of the passive and active membrane properties of SG neurons with or without RD are summarized in **Figure 1D** and **Table 1**. There was no significant difference in Cm. However, the RMP, Rin, and properties of AP of the two populations were significantly different. Neurons with RD had a more depolarized RMP versus those without RD (−54.05 ± 0.58 mV vs −59.18 ± 0.77 mV, $p < 0.001$). In addition, RD-expressing neurons showed a smaller Rin (0.59 ± 0.05 GΩ vs 0.71 ± 0.05 GΩ, $p = 0.013$), a more hyperpolarized AP threshold (−31.53 ± 0.53 mV vs −28.59 ± 0.54 mV, $p < 0.001$), a shorter AP half-width (0.87 ± 0.05 ms vs 1.14 ± 0.05 ms, $p < 0.001$), a smaller potential difference between AP threshold and RMP (22.52 ± 0.71 mV vs 30.59 ± 0.84 mV, $p < 0.001$), and a larger AP amplitude (78.13 ± 1.09 mV vs 70.52 ± 1.17 mV, $p < 0.001$) compared to SG neurons without RD. These results suggest that RD-expressing SG neurons exhibit higher neuronal membrane excitability.

As tonic-firing neuron has repeated APs at relatively regular rates and is the highest proportion in both types of neurons, we next compared the responses of tonic-firing neurons to depolarized current injections (**Figure 2A**). Tonic-firing neurons from the group with RD showed significantly higher spike frequencies compared to those lacking RD (**Figure 2B**), suggesting that the former was more excitable. Furthermore, we found that the spike adaptation index was smaller in neurons with RD than those without RD (0.45 ± 0.03 vs 0.58 ± 0.05, $p = 0.015$) (**Figure 2C**).

Subthreshold Currents

Based on previous studies, three subthreshold currents, I_h, I_T, and A-type currents (I_A) were identified in SG neurons (**Figure 3Aa**; Tadros et al., 2012). In this study, we found that the expression and distribution of the subthreshold currents in RD-lacking SG neurons varied markedly from those in neurons with RD ($p < 0.001$) (**Figure 3Ab**). Overall, 76.00 and 71.11% of SG neurons with RD expressed I_h and I_T, respectively. I_A was rarely encountered (2.22%) in this population. However, in neurons without RD, the prevalence rates of I_h and I_T dropped to a relatively low level (30.61 and 20.41%, respectively), while I_A became the dominant subthreshold current accounting for 35.71%. Measurement of the amplitude and time constant of subthreshold currents showed that no significant differences were observed regarding the activation and inactivation time constants of I_T between RD-positive and RD-negative neurons. However, RD-expressing neurons possessed faster time constant of I_h, larger current amplitude and density of both I_h and I_T (**Supplementary Figure 3** and **Tables 1**, **2**).

Because I_h along with I_T has been proposed to be the major ionic basis responsible for RD in neurons of the deep cerebellar nuclei, periventricular preoptic area, etc. (Engbers et al., 2011; Zhang et al., 2013), we next studied the effects of I_h and I_T on RD in SG neurons. Bath application of ZD7288 (10 μM), a specific HCN channel blocker, increased RD latency from 42.64 ± 7.93 ms to 117.17 ± 20.11 ms ($p = 0.011$) but did not affect the number of spikes generated (3.63 ± 1.25 vs 3.13 ± 0.77, $p = 0.750$) (**Figure 3B**). In addition, the blockage of I_T by TTA-P2 (10 μM) markedly decreased RD spiking number from 4.90 ± 1.06 to 1.50 ± 0.27 ($p = 0.002$), and increased RD latency from 58.59 ± 10.07 ms to 97.79 ± 23.47 ms ($p = 0.034$) (**Figure 3C**).

In attempt to better addressing the influence of I_h or I_T on RD properties, TTX (0.5 μM) was applied to the bath solution to eliminate rebound discharge. In the presence of TTX, blockage of I_h led to a substantial delay in latency (66.71 ± 13.42 ms to 122.55 ± 14.38 ms, $p = 0.008$) without alterations of the RD amplitude (**Figure 3D**). In addition, the blocking effect of TTA-P2 almost eliminated RD. As illustrated in **Figure 3E**, the RD amplitude dropped by approximately 64.97% ± 8.03% ($p = 0.016$), and the RD latency raised from 64.67 ± 8.55 ms

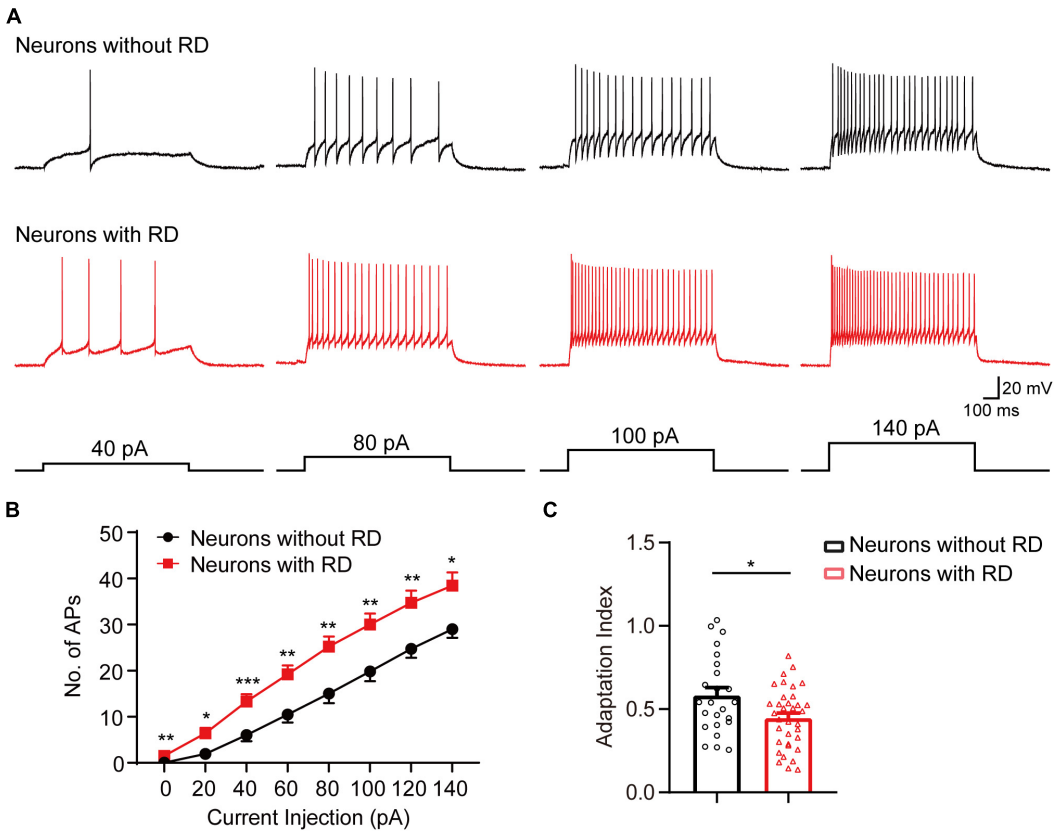

FIGURE 2 | SG neurons with RD that have a tonic-firing pattern exhibit elevated spike frequencies. **(A)** Representative current-clamp traces showing the responses of SG neurons without (black) or with (red) RD to the indicated depolarizing currents of 40, 80, 100, and 140 pA. **(B)** Population data showing the number of spikes of SG neurons expressing or lacking RD with a tonic-firing pattern. **(C)** Summary bar graphs showing that neurons with RD exhibited an elevated spike-frequency adaptation. RD, rebound depolarization; AP, action potential. *$p < 0.05$, **$p < 0.01$, ***$p < 0.001$.

TABLE 2 | Primary afferent input onto SG neurons with or without RD.

	Neurons without RD (n = 24)	Neurons with RD (n = 27)
Aδ-fiber monosynaptic	2 (8.33%)	10 (37.04%)
Aδ-fiber polysynaptic	13 (54.17%)	5 (18.52%)
C-fiber monosynaptic	0 (0.00%)	4 (14.81%)
C-fiber polysynaptic	20 (83.33%)	17 (62.96%)
Convergent Aδ- and C-fiber	11 (45.83%)	9 (33.33%)

RD, rebound depolarization.

to 90.05 ± 13.32 ms (p = 0.020) with bath application of TTA-P2(**Figure 3E**). Taken together, these results suggest that RD in SG neurons is mainly mediated by I_T, while I_h facilitate its onset.

Properties of Spontaneous and Miniature Excitatory Postsynaptic Currents

Next, we examined whether SG neurons with RD exhibited any difference in the excitatory synaptic communication compared to those lacking RD. As shown in **Figure 4**, the frequencies of sEPSCs recorded from neurons with RD tended to be approximately 56% of those without RD (2.89 ± 0.43 Hz vs 5.10 ± 0.60 Hz, p = 0.010), while the difference of amplitudes of sEPSCs was not significant (19.02 ± 1.57 pA vs 22.58 ± 1.91 pA, p = 0.182) (**Figures 4A–D**). SG neurons with and without RD did not differ in mEPSCs amplitudes (19.02 ± 1.91 pA vs 22.50 ± 1.56 pA, p = 0.169), but neurons with RD had considerably lower mEPSCs frequencies compared with neurons lacking RD (2.36 ± 0.37 Hz vs 3.91 ± 0.52 Hz, p = 0.032) (**Figures 4E–H**).

Excitatory Inputs From Both Aδ and C Primary Afferents

As SG neurons receive different inputs of Aδ and C primary afferents, we next examined the inputs onto SG neurons with

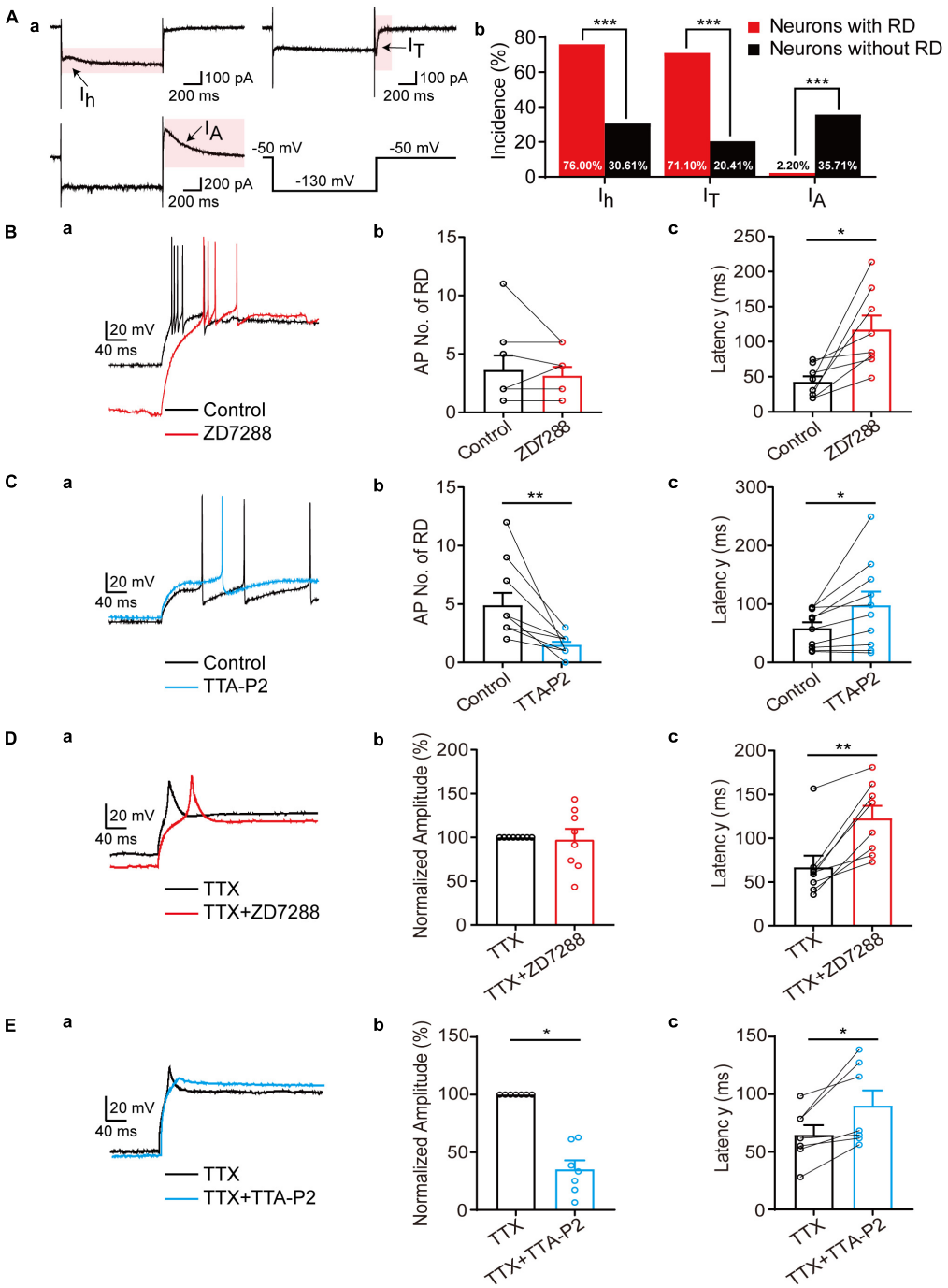

FIGURE 3 | Differential modulation of I_h and I_T to RD in SG neurons. **(A)** The subthreshold currents recorded from SG neurons. **(a)** Representative traces of the subthreshold currents (I_h, I_T, and I_A) recorded in SG neurons. **(b)** The subthreshold currents were differentially distributed among SG neurons with (red) or without (black). **(B)** RD in SG neurons was modulated by I_h. **(a)** Representative traces of RD elicited by a hyperpolarizing current pulse (−120 pA, 1 s) in control (black) and with 10 μM ZD7288 (red) in the absence of TTX. **(b,c)**. Summary of the blockage effect of ZD7288 on AP No. **(b)** and first spike latency of RD **(c)** in the absence of TTX. **(C)** RD in SG neurons was modulated by I_T. **(a)** Representative traces of RD in control (black) and with 10 μM TTA-P2 (blue) in the absence of TTX. **(b,c)** Summary of the blockage effect of TTA-P2 on AP No. **(b)** and first spike latency of RD **(c)** in the absence of TTX. **(D)** Effect of ZD7288 on RD of SG neurons in the presence of TTX. **(a)** Representative traces of RD response in TTX (black) and in TTX along with 10 μM ZD7288 (red) in the presence of TTX. **(b,c)** Summary of the blockage effect of ZD7288 on AP No. **(b)** and first spike latency of RD **(c)**. **(E)** Effect of TTA-P2 on RD of SG neurons in the presence of TTX. **(a)** Representative traces of RD response in TTX (black) and in TTX along with 10 μM TTA-P2 (blue) in the presence of TTX. **(b,c)** Summary of the blockage effect of TTA-P2 on AP No. **(b)** and first spike latency of RD **(c)**. RD, rebound depolarization; I_h, hyperpolarization-activated cation current; I_T, T-type calcium current; I_A, A-type current; AP, action potential; TTX, tetrodotoxin. *$p < 0.05$, **$p < 0.01$, ***$p < 0.001$.

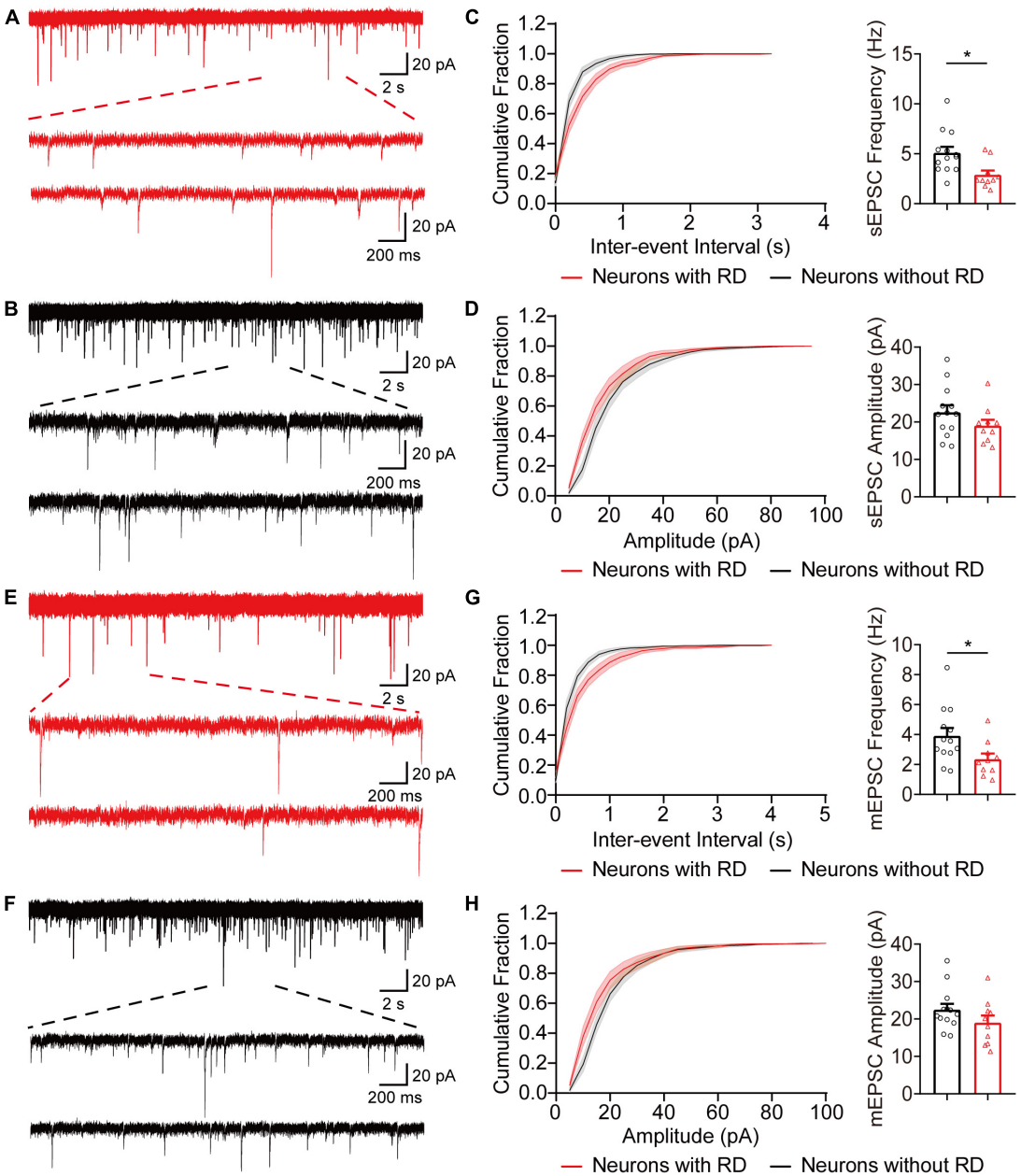

FIGURE 4 | Excitatory synaptic inputs differ in SG neurons with or without RD. **(A,B)** Exemplar traces of sEPSCs in SG neurons expressing **(A)** or lacking **(B)** RD. The bottom panels show the proportional enlargements corresponding to the upper traces. **(C,D)** Cumulative probability and summary bar graphs of the inter-event interval **(C)** as well as the amplitude **(D)** showing a lower frequency of sEPSCs in neurons with RD. **(E,F)** Typical traces of mEPSCs in RD-expressing **(E)** or RD-lacking **(F)** SG neurons. **(G,H)** Summarized data showing that RD-expressing neurons had a lower mEPSCs frequency compared to those lacking RD **(G)**, while mean amplitudes of mEPSCs from the two populations were comparable **(H)**. sEPSC, spontaneous excitatory postsynaptic current; mEPSC, miniature excitatory postsynaptic current. *$p < 0.05$.

or without RD (**Figure 5A**). DR stimulation resulted in eEPSCs in 27 (out of 39) RD-expressing and 24 (out of 34) RD-lacking neurons, respectively (**Figures 5B,C**). RD-expressing neurons received either mono- or polysynaptic inputs from Aδ- and/or C-fibers (**Figure 5C**). C-fiber-mediated EPSCs were observed in 77.78% (21/27) of the cells. Repetitive stimulation at 1 Hz revealed that in most cases, there was a polysynaptic component (80.95%, 17/21) (**Figures 5Ca,b,E**). In addition, 45.56% (15/27) of RD-expressing neurons exhibited eEPSCs produced by Aδ fibers, of which 66.67% (10/15) appeared to be monosynaptic (**Figures 5Cc,d,F**). Conversely, for neurons lacking RD, DR stimulation evoked polysynaptic but not monosynaptic C-fiber-induced EPSCs in 83.33% (20/24) of neurons (**Figures 5Ba,D,E**). In addition, we observed Aδ-fiber-mediated EPSCs in 62.50%

(15/24) of RD-lacking cells, with 13.33% (2/15) and 86.67% (13/15) of these Aδ-responsive cells displaying monosynaptic and polysynaptic responses, respectively (**Figures 5Bb,c,F**). The conduction velocity, rise time, decay time and mean amplitude of eEPSCs were comparable between neurons with or without RD except for the amplitude of Aδ-fiber-evoked responses (**Supplementary Tables 3**, **4**). RD-expressing neurons possessed larger Aδ-fiber-mediated EPSCs (235.04 ± 43.15 pA vs 86.86 ± 17.95 pA, $p = 0.003$) (**Supplementary Table 4**).

Morphological Characterization

It has been well established that SG neurons exhibit complex and diverse morphologies. In this study, 46 recordings were attempted to recover morphology among which 33 were finally morphologically identified, and examples were illustrated in **Figure 6A**. All five morphological categories (islet, radial, central, vertical, and unclassified) were observed in the examined neurons, and the morphology distributions between the two groups were statistically similar (**Figure 6B**) ($p = 0.332$). Islet cell was clearly the type with the highest prevalence encountered in both RD-expressing and -lacking SG neurons (58.82 and 43.75%, respectively). Given the crucial role of dendritic dimensions in morphological classification, we further conducted morphometric analysis by measuring the extents of the dendritic trees of neurons from the two groups. The mean rostro-caudal dendritic lengths for neurons with or without RD were 513.78 ± 56.95 μm and 361.88 ± 31.34 μm, respectively, and these were significantly different ($p = 0.029$). A similar comparison indicated that dendritic extents in the dorsal-ventral axis did not differ significantly between the two subpopulations (190.81 ± 24.12 μm vs 156.85 ± 21.62 μm, $p = 0.305$) (**Table 3**).

DISCUSSION

The aim of the present descriptive study is to define the electrophysiological and morphological characteristics of SG neurons with RD, and several key conclusions can be drawn from this study. First, compared to RD-lacking SG neurons, RD-expressing neurons showed distinctive electrophysiological signatures including more depolarized RMP, smaller Rin, more hyperpolarized AP thresholds, and increased spike frequencies, representing a higher membrane excitability. Meanwhile, SG neurons with RD predominantly exhibit a tonic firing pattern. Second, we found that I_T was a vital ionic mechanism basis responsible for the generation of RD in SG, while the onset of RD was regulated by I_h. Third, neurons with RD receive monosynaptic as well as polysynaptic excitatory inputs from both Aδ and C afferents, and they showed lower frequencies regarding sEPSCs together with mEPSCs than neurons without RD. Finally, we found anatomical diversity in RD-expressing neurons, with islet cells constituting half of the population.

SG Neurons With RD Exhibit Distinct Intrinsic Neuronal Characteristics

Recent studies have linked I_h/I_T to neuronal electrical properties. For instance, intracellular recording from primary sensory neurons found that I_h blockage by ZD7288 changed RMP toward the negative direction, prolonged AP duration, and resulted in diminished effects on AP frequency (Hogan and Poroli, 2008). In our prior investigations, we have noted that impeding I_h by using drugs interfering with the function of HCN channels robustly decreased firing rate, delayed RD latency, and lower post-hyperpolarization spike frequency in SG neurons, indicating an excitatory influence of I_h (Liu et al., 2015; Hu et al., 2016). Likewise, a number of groups have suggested the role of I_T in establishing intrinsic excitability. We have shown previously that there were remarkable differences in properties of SG neurons with or without I_T. For I_T-expressing neurons, they displayed a more hyperpolarized AP threshold, a smaller difference of AP threshold and RMP, as well as elevated firing frequency (Wu et al., 2018). Meanwhile, a recent study also showed that AP amplitude was decreased in Cav3.2-ablated SG neurons (Candelas et al., 2019). Thus, as suggested by identifying I_h/I_T in RD-expressing SG neurons, the intrinsic excitability of this population might involve a contribution from these two subthreshold currents.

Previous work on deep dorsal horn neurons, which are also of paramount importance for integrating somatosensory information, found that AP threshold was more hyperpolarized and the difference of AP threshold and RMP tended to be smaller in neurons with a high-amplitude RD; while RMP, Rin and AP amplitude in RD-expressing deep dorsal horn neurons were comparable to those lacking it (Rivera-Arconada and Lopez-Garcia, 2015). Here, marked differences in active and passive membrane properties were identified in SG neurons with or without RD. In line with the aforementioned study from the mouse deep dorsal horn, we found neurons with RD in superficial spinal dorsal horn exhibited significantly lower AP threshold and smaller difference of AP threshold and RMP. However, we also observed a significant difference in RMP, Rin, AP duration along with AP amplitude between the two groups. The differences in our observations raise the possibility that the intrinsic excitability of different spinal cord neurons may correlate with RD in unique ways. Besides, we found tonic-firing neurons with RD generated considerably increased spike frequencies in response to defined depolarizing currents. Together, these data indicate that SG neurons with RD display higher membrane excitability.

Additional support for the relationship between RD and neuron excitability came from the result of the spike adaption index. Diverse degrees of firing adaptation have been observed in SG neurons (Ruscheweyh and Sandkuhler, 2002; Olschewski et al., 2009; Melnick, 2011). An interesting study analyzed the major factors determining the appearance of spike frequency adaption in SG neurons and found that lower Na^+ conductance was critical for the generation of adapting firing (Melnick et al., 2004). Given that RD-expressing neurons exhibited stronger adaptation than RD-lacking neurons, the present study implies that the expression or function of Na^+ channels may differ between these two populations. Moreover, due to neurons with strong adaptation have been suggested to be nociceptive neurons with specific cutaneous afferent input (Lopez-Garcia and King, 1994), it is reasonable to assume

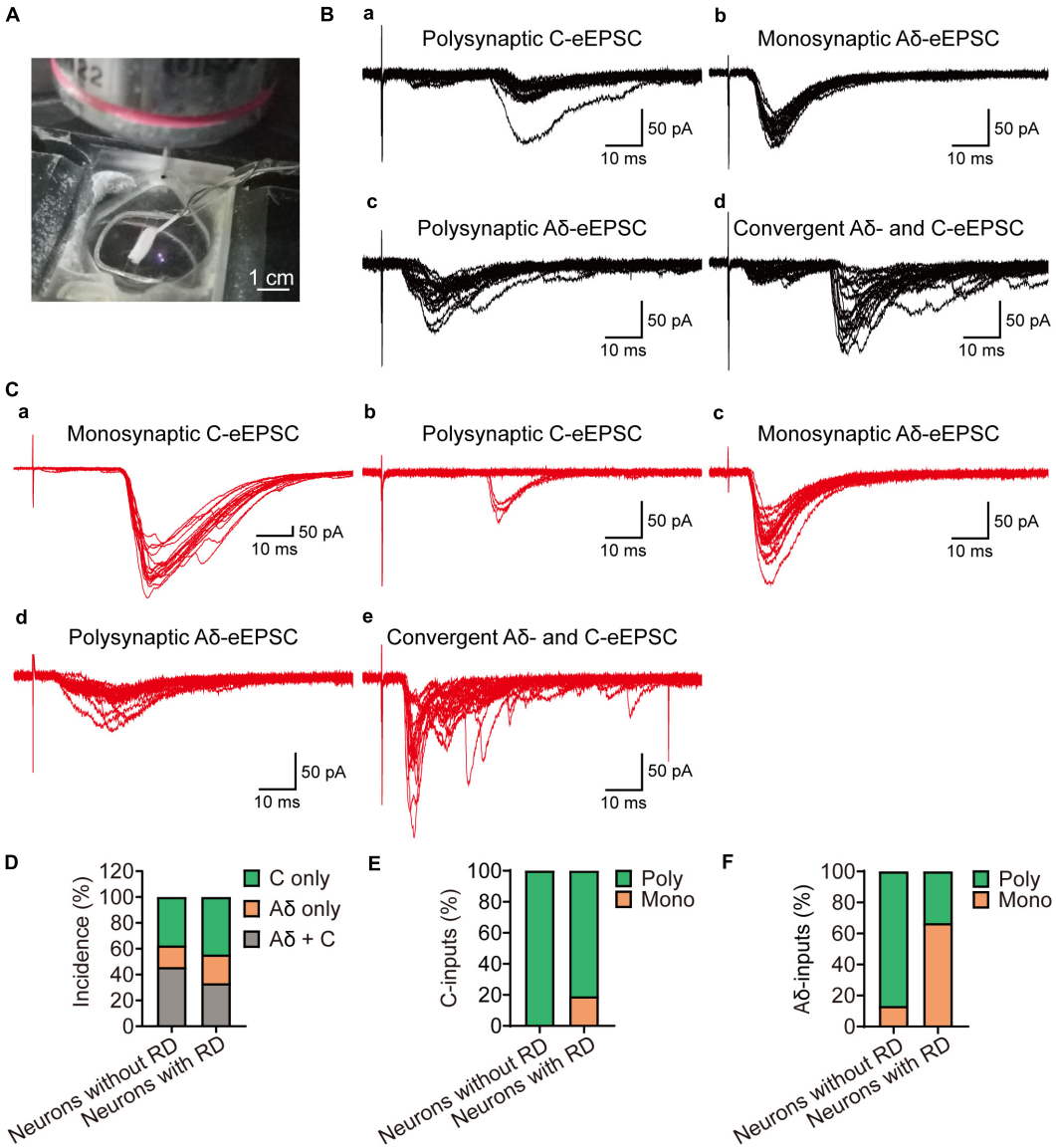

FIGURE 5 | Primary afferent innervation onto SG neurons with or without RD examined by dorsal root stimulation. **(A)** Exemplar image shows a customized suction electrode for the stimulation onto a DR that attached with a parasagittal spinal cord slice. **(B)** Representative traces of Aδ- and C-fiber induced EPSCs of SG neurons without RD, evoked by high-frequency stimulation. **(a)** Polysynaptic C-fiber evoked eEPSC, **(b)** Monosynaptic Aδ-fiber mediated eEPSC, **(c)** Polysynaptic Aδ-fiber mediated eEPSC, **(d)** Convergent Aδ- and C-fiber mediated inputs onto SG neurons without RD. **(C)** Representative traces of Aδ- and C-fiber-evoked EPSCs recorded from SG neurons with RD. **(a)** Monosynaptic C-fiber evoked eEPSC, **(b)** Polysynaptic C-fiber evoked eEPSC, **(c)** Monosynaptic Aδ-fiber mediated eEPSC, **(d)** Polysynaptic Aδ-fiber mediated eEPSC, **(e)** Convergent Aδ- and C-fiber mediated inputs onto SG neurons without RD. **(D)** Quantification of Aδ- and C-fiber-induced eEPSCs onto SG neurons with or without RD by electrical stimuli. **(E)** Quantification of mono- and polysynaptic C-fiber mediated responses in different groups upon DR stimulation. **(F)** Quantification of mono- and polysynaptic Aδ-fiber mediated responses in different groups upon DR stimulation. RD, rebound depolarization; DR, dorsal root; eEPSC, evoked excitatory postsynaptic current.

the importance of SG neurons with RD underpinning spinal sensory encoding.

SG Neurons With RD Show Specific Cellular Distributions

The prevalence of rebound spikes in randomly sampled mouse SG neurons was around 30% according to previous reports (Tadros et al., 2012; Candelas et al., 2019). However, the percentage of RD in SG neurons raised to 44.44% in this study. Reasons for this incidence discrepancy may attribute to the different species we used in our studies. Furthermore, recent literature segregating SG neurons in a genetically-defined approach found two-thirds of cholinergic interneurons in mouse dorsal horn displayed RD following hyperpolarization (Mesnage et al., 2011), whilst the fraction of RD in delayed

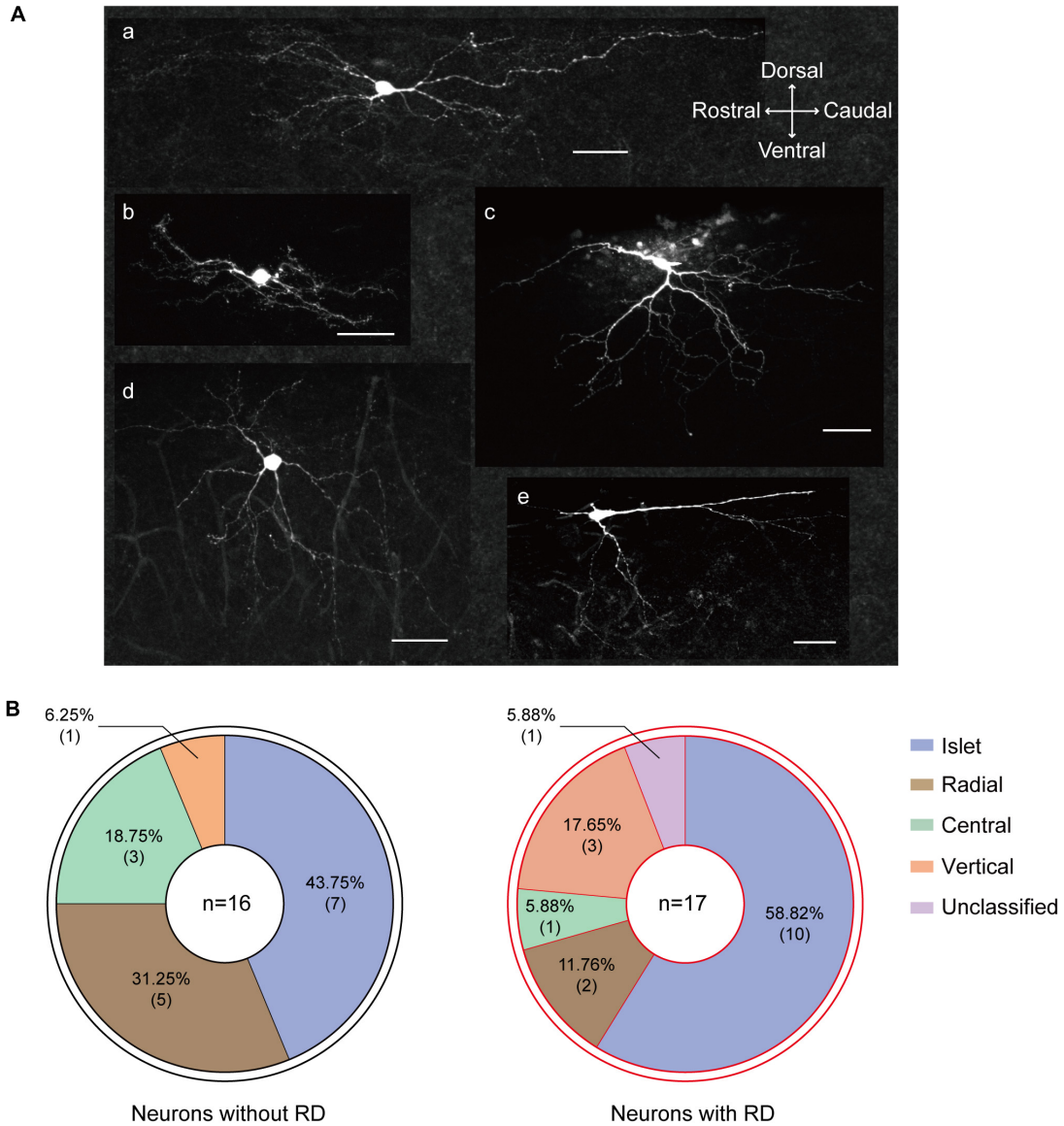

FIGURE 6 | Morphological heterogeneity of RD-expressing SG neurons. **(A)** Confocal images of SG neurons with RD labeled with biocytin. **(a)** islet, **(b)** central, **(c)** vertical, **(d)** radial, **(e)** unclassified. **(B)** Proportion of SG neurons with **(right)** or without **(left)** RD exhibiting different morphologies. RD, rebound depolarization.

TABLE 3 | Morphological dimensions of dendrites measured from SG neurons with or without RD.

Parameter	Neurons without RD (*n* = 16)	Neurons with RD (*n* = 17)	*p* Value
RC (μm)	361.88 ± 31.34	513.78 ± 56.95*	0.029
DV (μm)	156.85 ± 21.62	190.81 ± 24.12	0.305
SR (μm)	165.63 ± 17.51	269.00 ± 19.37***	<0.001
SC(μm)	196.25 ± 19.71	244.78 ± 45.39	0.736
SD (μm)	68.78 ± 11.25	71.35 ± 14.69	0.599
SV (μm)	88.07 ± 13.15	119.46 ± 12.93	0.099

Data reported as mean ± SEM. RC, rostro-caudal extent of dentrites; DV, dorsal-ventral expansion of dendrites; SR, SC, SD, SV, dendrites spread from center of the soma to rostral, caudal, dorsal, and ventral limit, respectively.
*$p < 0.05$.
***$p < 0.001$.

(short-latency) firing SG interneurons expressing neuropeptide Y (NPY) Y1 receptor from mice was 32% (Sinha et al., 2021). This quantitative difference suggests that RD might distribute in SG neurons in a specific cellular manner.

Substantia gelatinosa neurons are a very heterogeneous population of interneurons with varied electrophysiological features, morphologies, and molecular profiles (Lu et al., 2006; Todd, 2017; Peirs et al., 2020). SG neurons can be divided into five broad categories on structural grounds, namely islet, central, vertical, radial, and unclassified cells. A series of pioneering works well established that islet cells are predominantly inhibitory (Todd and Sullivan, 1990; Maxwell et al., 2007; Yasaka et al., 2010), while other morphologies have been proposed to be associated with both excitatory and inhibitory phenotypes in the literature (Hantman et al., 2004; Lu and Perl, 2005; Maxwell et al., 2007; Duan et al., 2014; Punnakkal et al., 2014; Smith et al., 2015; Boyle et al., 2019).

Given that the most common morphological type in our sample of SG neurons with RD was "islet," and that the majority of these cells discharged tonically when depolarized, a vital characteristic of inhibitory neurons (Lu and Perl, 2003; Zheng et al., 2010), a major finding of this study is that RD-expressing interneurons in SG have probably an inhibitory nature. However, a strict conclusion could finally be drawn based on future immunocytochemical studies. Furthermore, combined with transgenic technologies, recent publications have added greatly to our understanding of the functional heterogeneity of inhibitory interneurons in the superficial spinal dorsal horn. So far, several molecularly distinct inhibitory populations in the superficial region of the dorsal spinal cord have been described according to neurochemical classification scheme established based on the expression of NPY, nitric oxide synthase (nNOS), parvalbumin (PV), galanin, calretinin (CR), and receptor tyrosine kinase (Tiong et al., 2011; Polgár et al., 2013; Smith et al., 2015; Cui et al., 2016; Iwagaki et al., 2016). Future work that identifies the expression of molecular compounds in RD-expressing SG neurons will be required to elucidate their exact neurochemical subtype and hence be useful for addressing their functional role in-depth.

SG Neurons With RD Have Differential Excitatory Synaptic Inputs and Primary Afferent Innervations

Prior anatomical work on SG neurons from both rats and mice showed islet, central tonic, PV-positive, and CR-positive cells, which were identified with an inhibitory phenotype by morphology, electrophysiology, or the expression of particular molecular markers, received relatively weak excitatory inputs, as assessed by low-frequency sEPSCs (Grudt and Perl, 2002; Hughes et al., 2012; Smith et al., 2015; Graham, 2020). In keeping with these findings, our observation of excitatory synaptic inputs revealed that although the amplitudes of excitatory events (sEPSCs and mEPSCs) were comparable between the two clusters of SG neurons, neurons with RD presented lower frequencies of both sEPSCs and mEPSCs. Thus, our results mirror these recent reports indicating that inhibitory interneurons receive a lower excitatory drive. Because functional dendritic spines are recognized as sites of presynaptic inputs (Alvarez and Sabatini, 2007), it is tempting to speculate that a possible cause of the phenomenon reported here is RD-expressing SG neurons in our sample may exhibit less dendritic spine density in spite of larger dendritic areas. Another potential source of inconsistency regarding the EPSC frequency is that the presynaptic release probabilities for neurons with or without RD from local excitatory interneurons may differ. Nevertheless, these possible mechanisms need to be further confirmed by dendritic spine analysis along with a paired patch-clamp recording.

Numerous studies have investigated synaptic input onto inhibitory populations in dorsal horn superficial layers, and interpretations from these datasets suggest that discrete inhibitory SG interneurons have differing synaptic afferents. One of the previous studies from rats showed that islet cell normally received monosynaptic excitatory input from unmyelinated afferents (C afferents), this result was supported by an *in vitro* electrophysiological experiment using mice where NPY-expressing neurons displayed responses to monosynaptic inputs originated from C fibers (Grudt and Perl, 2002; Iwagaki et al., 2016). In contrast, immunolabelling work from Hughes et al. found that PV-immunoreactive cells, a subpopulation of islet neurons, were directly associated with VGLUT1-expressing terminals derived from myelinated afferent fibers, including both Aδ and Aβ fibers specifically (Hughes et al., 2012). Other inhibitory neurons belonging to the galanin or nNOS populations were likely to form contacts from both myelinated and unmyelinated classes of primary afferent either directly or indirectly, with many cells receiving convergent inputs (Hantman et al., 2004; Ganley et al., 2015). Although evidence from different groups showed disagreement about the primary innervations onto inhibitory SG neurons, the above evidence demonstrated that SG neurons with an inhibitory identity were likely recruited in gating innocuous as well as noxious information. In agreement with results reported by Ganley et al. and Hantman et al., we found that SG neurons with RD received both monosynaptic and polysynaptic inputs from Aδ and C fibers, the presumed nociceptive primary afferents. As we proposed that RD-expressing neurons were inhibitory interneurons based on their morphological and electrophysiological features, they may counterbalance excitatory drive through feedforward, feedback, or lateral inhibition in dorsal horn circuits, and hence contribute to nociceptive sensation and modulation.

RD in SG Neurons Is Regulated by I_h and I_T

Although several channels, for instance, inwardly-rectifying potassium channels (Wang et al., 2016), low-threshold TTX-resistant sodium channels (Kurowski et al., 2018), persistent sodium channels (Sangrey and Jaeger, 2010), and high-threshold calcium channels (Zheng and Raman, 2009) have been confirmed to be involved in regulating RD by hyperpolarizing RMP, decreasing neuronal input resistances, or enhancing synaptic inhibition that contributes to post-inhibitory depolarizations,

currents mediated by HCN channels and T-type calcium channels are recognized as pivotal ionic factors underlying RD (Boehme et al., 2011; Engbers et al., 2011). With respect to the role of I_T in RD, pharmacological blockade of T-type calcium channels by using blockers such as $NiCl_2$, mibefradil, or NNC 55-0396 could produce a significant block on the total number of spikes generated in RD (Alvina et al., 2009). In addition, in keeping with a recent study reporting that RD was barely detected in SG neurons without I_T (Wu et al., 2018), data from Candelas et al. also found that ablation of Cav3.2 but not Cav3.1 downregulated the proportion of RD in SG (Candelas et al., 2019). On the other hand, I_h has been proposed to be a key factor in determining the initiation of the first spike in RD, as both pharmacological blockade and genetic knockout of HCN2 could considerably delay RD latency (Zhu et al., 2018).

It has been demonstrated that various isoforms of T-type calcium channels along with HCN channels are present in SG (Peng et al., 2017; Candelas et al., 2019; Cheng et al., 2019). Alterations in the expression and function of these channels are responsible for the development and maintenance of chronic pain (Papp et al., 2010; Feng et al., 2019). Therefore, it is possible to assume a potential effect of RD on nociceptive processing. In the present work, we also found that abolishment of I_T significantly reduced the RD amplitude, while I_h blockade modulated the onset of the rebound firing. Our observations are in line with preceding reports showing the role of I_h and I_T in controlling rebound spike responses.

Functional Implications of RD in SG Neurons

It has been postulated that as an intrinsic biophysical property in the sensory system, RD may play a possible role in encoding stimulus intensity (Large and Crawford, 2002; Oswald et al., 2004; Rivera-Arconada and Lopez-Garcia, 2015). As indicated by pilot observations, different firing patterns were linked with distinct neuronal functions. For instance, neurons showing tonic firing are proposed to be involved in encoding both the strength and duration of input signals. In addition to tonic-firing, initial-firing neurons also contribute to encoding the intensity of afferent excitation (Ruscheweyh and Sandkuhler, 2002). Thus, as the tonic and initial firing were the top two patterns recorded in RD-expressing SG neurons, our results indicate that this group of cells plays a substantial role in coding the intensity of ascending impulses. Additionally, RD has also been speculated to be an inhibition-excitation converter that transforms an inhibitory input into excitatory output (Sanchez-Vives and McCormick, 2000; Surges et al., 2006). However, our results only provide information about excitatory inputs onto RD-expressing neurons; future studies addressing their presynaptic inhibitory circuits involving primary afferents may further constitute circumstantial evidence in favor of this possibility.

CONCLUSION

In summary, our study revealed that SG neurons with RD are not only electrophysiologically distinct from those lacking RD, but also differ in synaptic transmission and thus may play a unique physiological role in the nociception network.

DATA AVAILABILITY STATEMENT

The original contributions presented in the study are included in the article/**Supplementary Material**, further inquiries can be directed to the corresponding authors.

ETHICS STATEMENT

The animal study was reviewed and approved by Institutional Animal Care and Use Committee of Nanchang University.

AUTHOR CONTRIBUTIONS

TL and DZ interpreted the data and designed and supervised the study. MZ and TL drafted and edited the manuscript. MZ and YY performed the electrophysiological and morphological experiments. XC, FZ, GX, WS, FL, and LL assisted in analyzing and interpreting the data. ZW, YZ, and XZ provided discussion in study design and interpretation of data. All authors read and approved the final manuscript.

FUNDING

The study was supported by the National Natural Science Foundation of China (Nos. 81860216, 81560198 to DZ and 32060186 to TL).

SUPPLEMENTARY MATERIAL

The Supplementary Material for this article can be found online at: https://www.frontiersin.org/articles/10.3389/fncel.2021.736879/full#supplementary-material

REFERENCES

Alvarez, V. A., and Sabatini, B. L. (2007). Anatomical and physiological plasticity of dendritic spines. *Annu. Rev. Neurosci.* 30, 79–97. doi: 10.1146/annurev.neuro.30.051606.094222

Alvina, K., Ellis-Davies, G., and Khodakhah, K. (2009). T-type calcium channels mediate rebound firing in intact deep cerebellar neurons. *Neuroscience* 158, 635–641. doi: 10.1016/j.neuroscience.2008.09.052

Balasubramanyan, S., Stemkowski, P. L., Stebbing, M. J., and Smith, P. A. (2006). Sciatic chronic constriction injury produces cell-type-specific changes in the electrophysiological properties of rat substantia gelatinosa neurons. *J. Neurophysiol.* 96, 579–590. doi: 10.1152/jn.00087.2006

Boehme, R., Uebele, V. N., Renger, J. J., and Pedroarena, C. (2011). Rebound excitation triggered by synaptic inhibition in cerebellar nuclear neurons is suppressed by selective T-type calcium channel block. *J. Neurophysiol.* 106, 2653–2661. doi: 10.1152/jn.00612.2011

Boyle, K. A., Gradwell, M. A., Yasaka, T., Dickie, A. C., Polgár, E., Ganley, R. P., et al. (2019). Defining a spinal microcircuit that gates myelinated afferent input: implications for tactile allodynia. *Cell. Rep.* 28, 526–540. doi: 10.1016/j.celrep.2019.06.040

Candelas, M., Reynders, A., Arango-Lievano, M., Neumayer, C., Fruquiere, A., Demes, E., et al. (2019). Cav3.2 T-type calcium channels shape electrical firing in mouse Lamina II neurons. *Sci. Rep.* 9:3112. doi: 10.1038/s41598-019-39703-3

Cheng, X. E., Ma, L. X., Feng, X. J., Zhu, M. Y., Zhang, D. Y., Xu, L. L., et al. (2019). Antigen retrieval pre-treatment causes a different expression pattern of Cav3.2 in rat and mouse spinal dorsal horn. *Eur. J. Histochem.* 63:2988. doi: 10.4081/ejh.2019.2988

Cui, L., Miao, X., Liang, L., Abdus-Saboor, I., Olson, W., Fleming, M. S., et al. (2016). Identification of early RET+ deep dorsal spinal cord interneurons in gating pain. *Neuron* 91:1413. doi: 10.1016/j.neuron.2016.09.010

Duan, B., Cheng, L., Bourane, S., Britz, O., Padilla, C., Garcia-Campmany, L., et al. (2014). Identification of spinal circuits transmitting and gating mechanical pain. *Cell* 159, 1417–1432. doi: 10.1016/j.cell.2014.11.003

Duan, B., Cheng, L., and Ma, Q. (2018). Spinal circuits transmitting mechanical pain and itch. *Neurosci. Bull.* 34, 186–193. doi: 10.1007/s12264-017-0136-z

Engbers, J. D., Anderson, D., Tadayonnejad, R., Mehaffey, W. H., Molineux, M. L., and Turner, R. W. (2011). Distinct roles for I(T) and I(H) in controlling the frequency and timing of rebound spike responses. *J. Physiol.* 589, 5391–5413. doi: 10.1113/jphysiol.2011.215632

Feng, X. J., Ma, L. X., Jiao, C., Kuang, H. X., Zeng, F., Zhou, X. Y., et al. (2019). Nerve injury elevates functional Cav3.2 channels in superficial spinal dorsal horn. *Mol. Pain* 15:1744806919836569. doi: 10.1177/1744806919836569

Ganley, R. P., Iwagaki, N., del Rio, P., Baseer, N., Dickie, A. C., Boyle, K. A., et al. (2015). Inhibitory interneurons that express GFP in the PrP-GFP mouse spinal cord are morphologically heterogeneous, innervated by several classes of primary afferent and include Lamina I projection neurons among their postsynaptic targets. *J. Neurosci.* 35, 7626–7642. doi: 10.1523/jneurosci.0406-15.2015

Graham, B. A. (2020). Transgenic cross-referencing of inhibitory and excitatory interneuron populations to dissect neuronal heterogeneity in the dorsal horn. *Front. Mol. Neurosci.* 13:32. doi: 10.3389/fnmol.2020.00032

Graham, B. A., and Hughes, D. I. (2020). Defining populations of dorsal horn interneurons. *Pain* 161, 2434–2436. doi: 10.1097/j.pain.0000000000002067

Grudt, T. J., and Perl, E. R. (2002). Correlations between neuronal morphology and electrophysiological features in the rodent superficial dorsal horn. *J. Physiol.* 540, 189–207. doi: 10.1113/jphysiol.2001.012890

Ha, G. E., Lee, J., Kwak, H., Song, K., Kwon, J., Jung, S. Y., et al. (2016). The Ca(2+)-activated chloride channel anoctamin-2 mediates spike-frequency adaptation and regulates sensory transmission in thalamocortical neurons. *Nat. Commun.* 7:13791. doi: 10.1038/ncomms13791

Hantman, A. W., van den Pol, A. N., and Perl, E. R. (2004). Morphological and physiological features of a set of spinal substantia gelatinosa neurons defined by green fluorescent protein expression. *J. Neurosci.* 24, 836–842. doi: 10.1523/JNEUROSCI.4221-03.2004

Hogan, Q. H., and Poroli, M. (2008). Hyperpolarization-activated current (I(h)) contributes to excitability of primary sensory neurons in rats. *Brain Res.* 1207, 102–110. doi: 10.1016/j.brainres.2008.02.066

Hu, T., Liu, N. N., Lv, M. H., Ma, L. X., Peng, H. Z., Peng, S. C., et al. (2016). Lidocaine inhibits HCN currents in rat spinal substantia gelatinosa neurons. *Anesth. Analg.* 122, 1048–1059. doi: 10.1213/ANE.0000000000001140

Hughes, D. I., Sikander, S., Kinnon, C. M., Boyle, K. A., Watanabe, M., Callister, R. J., et al. (2012). Morphological, neurochemical and electrophysiological features of parvalbumin-expressing cells: a likely source of axo-axonic inputs in the mouse spinal dorsal horn. *J. Physiol.* 590, 3927–3951. doi: 10.1113/jphysiol.2012.235655

Iwagaki, N., Ganley, R. P., Dickie, A. C., Polgár, E., Hughes, D. I., Del Rio, P., et al. (2016). A combined electrophysiological and morphological study of neuropeptide Y-expressing inhibitory interneurons in the spinal dorsal horn of the mouse. *Pain* 157, 598–612. doi: 10.1097/j.pain.0000000000000407

Kuner, R. (2010). Central mechanisms of pathological pain. *Nat. Med.* 16, 1258–1266. doi: 10.1038/nm.2231

Kurowski, P., Grzelka, K., and Szulczyk, P. (2018). Ionic mechanism underlying rebound depolarization in medial prefrontal cortex pyramidal neurons. *Front. Cell. Neurosci.* 12:93. doi: 10.3389/fncel.2018.00093

Large, E. W., and Crawford, J. D. (2002). Auditory temporal computation: interval selectivity based on post-inhibitory rebound. *J. Comput. Neurosci.* 13, 125–142. doi: 10.1023/a:1020162207511

Liu, N. N., Zhang, D. Y., Zhu, M. Y., Luo, S. W., and Liu, T. (2015). Minocycline inhibits hyperpolarization-activated currents in rat substantia gelatinosa neurons. *Neuropharmacology* 95, 110–120. doi: 10.1016/j.neuropharm.2015.03.001

Lopez-Garcia, J. A., and King, A. E. (1994). Membrane properties of physiologically classified rat dorsal horn neurons in vitro: correlation with cutaneous sensory afferent input. *Eur. J. Neurosci.* 6, 998–1007. doi: 10.1111/j.1460-9568.1994.tb00594.x

Lu, V. B., Moran, T. D., Balasubramanyan, S., Alier, K. A., Dryden, W. F., Colmers, W. F., et al. (2006). Substantia Gelatinosa neurons in defined-medium organotypic slice culture are similar to those in acute slices from young adult rats. *Pain* 121, 261–275. doi: 10.1016/j.pain.2006.01.009

Lu, Y., and Perl, E. R. (2003). A specific inhibitory pathway between substantia gelatinosa neurons receiving direct C-fiber input. *J. Neurosci.* 23, 8752–8758. doi: 10.1523/jneurosci.23-25-08752.2003

Lu, Y., and Perl, E. R. (2005). Modular organization of excitatory circuits between neurons of the spinal superficial dorsal horn (laminae I and II). *J. Neurosci.* 25, 3900–3907. doi: 10.1523/jneurosci.0102-05.2005

Maxwell, D. J., Belle, M. D., Cheunsuang, O., Stewart, A., and Morris, R. (2007). Morphology of inhibitory and excitatory interneurons in superficial laminae of the rat dorsal horn. *J. Physiol.* 584, 521–533. doi: 10.1113/jphysiol.2007.140996

Melnick, I. V. (2011). A-type K+ current dominates somatic excitability of delayed firing neurons in rat substantia gelatinosa. *Synapse* 65, 601–607. doi: 10.1002/syn.20879

Melnick, I. V., Santos, S. F., and Safronov, B. V. (2004). Mechanism of spike frequency adaptation in substantia gelatinosa neurones of rat. *J. Physiol.* 559, 383–395. doi: 10.1113/jphysiol.2004.066415

Mesnage, B., Gaillard, S., Godin, A. G., Rodeau, J. L., Hammer, M., Von Engelhardt, J., et al. (2011). Morphological and functional characterization of cholinergic interneurons in the dorsal horn of the mouse spinal cord. *J. Comp. Neurol.* 519, 3139–3158. doi: 10.1002/cne.22668

Olschewski, A., Schnoebel-Ehehalt, R., Li, Y., Tang, B., Bräu, M. E., and Wolff, M. (2009). Mexiletine and lidocaine suppress the excitability of dorsal horn neurons. *Anesth. Analg.* 109, 258–264. doi: 10.1213/ane.0b013e3181a3d5d8

Oswald, A. M., Chacron, M. J., Doiron, B., Bastian, J., and Maler, L. (2004). Parallel processing of sensory input by bursts and isolated spikes. *J. Neurosci.* 24, 4351–4362. doi: 10.1523/JNEUROSCI.0459-04.2004

Papp, I., Holló, K., and Antal, M. (2010). Plasticity of hyperpolarization-activated and cyclic nucleotid-gated cation channel subunit 2 expression in the spinal dorsal horn in inflammatory pain. *Eur. J. Neurosci.* 32, 1193–1201. doi: 10.1111/j.1460-9568.2010.07370.x

Pedroarena, C. M. (2010). Mechanisms supporting transfer of inhibitory signals into the spike output of spontaneously firing cerebellar nuclear neurons in vitro. *Cerebellum* 9, 67–76. doi: 10.1007/s12311-009-0153-1

Peirs, C., Dallel, R., and Todd, A. J. (2020). Recent advances in our understanding of the organization of dorsal horn neuron populations and their contribution to cutaneous mechanical allodynia. *J. Neural. Transm. (Vienna)* 127, 505–525. doi: 10.1007/s00702-020-02159-1

Peng, S. C., Wu, J., Zhang, D. Y., Jiang, C. Y., Xie, C. N., and Liu, T. (2017). Contribution of presynaptic HCN channels to excitatory inputs of spinal substantia gelatinosa neurons. *Neuroscience* 358, 146–157. doi: 10.1016/j.neuroscience.2017.06.046

Polgár, E., Sardella, T. C. P., Tiong, S. Y. X., Locke, S., Watanabe, M., and Todd, A. J. (2013). Functional differences between neurochemically defined populations of inhibitory interneurons in the rat spinal dorsal horn. *Pain* 154, 2606–2615. doi: 10.1016/j.pain.2013.05.001

Punnakkal, P., von Schoultz, C., Haenraets, K., Wildner, H., and Zeilhofer, H. U. (2014). Morphological, biophysical and synaptic properties of glutamatergic neurons of the mouse spinal dorsal horn. *J. Physiol.* 592, 759–776. doi: 10.1113/jphysiol.2013.264937

Rivera-Arconada, I., and Lopez-Garcia, J. A. (2015). Characterisation of rebound depolarisation in mice deep dorsal horn neurons in vitro. *Pflugers Arch.* 467, 1985–1996. doi: 10.1007/s00424-014-1623-y

Ruscheweyh, R., and Sandkuhler, J. (2002). Lamina-specific membrane and discharge properties of rat spinal dorsal horn neurones in vitro. *J. Physiol.* 541, 231–244. doi: 10.1113/jphysiol.2002.017756

Sanchez-Vives, M. V., and McCormick, D. A. (2000). Cellular and network mechanisms of rhythmic recurrent activity in neocortex. *Nat. Neurosci.* 3, 1027–1034. doi: 10.1038/79848

Sangrey, T., and Jaeger, D. (2010). Analysis of distinct short and prolonged components in rebound spiking of deep cerebellar nucleus neurons. *Eur. J. Neurosci.* 32, 1646–1657. doi: 10.1111/j.1460-9568.2010.07408.x

Sinha, G. P., Prasoon, P., Smith, B. N., and Taylor, B. K. (2021). Fast A-type currents shape a rapidly adapting form of delayed short latency firing of excitatory superficial dorsal horn neurons that express the NPY Y1 receptor. *J. Physiol.* 599, 2723–2750. doi: 10.1113/jp281033

Smith, K. M., Boyle, K. A., Madden, J. F., Dickinson, S. A., Jobling, P., Callister, R. J., et al. (2015). Functional heterogeneity of calretinin-expressing neurons in the mouse superficial dorsal horn: implications for spinal pain processing. *J. Physiol.* 593, 4319–4339. doi: 10.1113/JP270855

Sun, H., Zhang, H., Ross, A., Wang, T. T., Al-Chami, A., and Wu, S. H. (2020). Developmentally regulated rebound depolarization enhances spike timing precision in auditory midbrain neurons. *Front. Cell. Neurosci.* 14:236. doi: 10.3389/fncel.2020.00236

Surges, R., Sarvari, M., Steffens, M., and Els, T. (2006). Characterization of rebound depolarization in hippocampal neurons. *Biochem. Biophys. Res. Commun.* 348, 1343–1349. doi: 10.1016/j.bbrc.2006.07.193

Tadayonnejad, R., Mehaffey, W. H., Anderson, D., and Turner, R. W. (2009). Reliability of triggering postinhibitory rebound bursts in deep cerebellar neurons. *Channels (Austin)* 3, 149–155. doi: 10.4161/chan.3.3.8872

Tadros, M. A., Harris, B. M., Anderson, W. B., Brichta, A. M., Graham, B. A., and Callister, R. J. (2012). Are all spinal segments equal: intrinsic membrane properties of superficial dorsal horn neurons in the developing and mature mouse spinal cord. *J. Physiol.* 590, 2409–2425. doi: 10.1113/jphysiol.2012.227389

Tiong, S. Y., Polgár, E., van Kralingen, J. C., Watanabe, M., and Todd, A. J. (2011). Galanin-immunoreactivity identifies a distinct population of inhibitory interneurons in laminae I-III of the rat spinal cord. *Mol. Pain* 7:36. doi: 10.1186/1744-8069-7-36

Todd, A. J. (2010). Neuronal circuitry for pain processing in the dorsal horn. *Nat. Rev. Neurosci.* 11, 823–836. doi: 10.1038/nrn2947

Todd, A. J. (2017). Identifying functional populations among the interneurons in laminae I-III of the spinal dorsal horn. *Mol. Pain* 13:1744806917693003. doi: 10.1177/1744806917693003

Todd, A. J., and Sullivan, A. C. (1990). Light microscope study of the coexistence of GABA-like and glycine-like immunoreactivities in the spinal cord of the rat. *J. Comp. Neurol.* 296, 496–505. doi: 10.1002/cne.902960312

Wang, X. X., Jin, Y., Sun, H., Ma, C., Zhang, J., Wang, M., et al. (2016). Characterization of rebound depolarization in neurons of the rat medial geniculate body in vitro. *Neurosci. Bull.* 32, 16–26. doi: 10.1007/s12264-015-0006-5

Wu, J., Peng, S. C., Xiao, L. H., Cheng, X. E., Kuang, H. X., Zhu, M. Y., et al. (2018). Cell-type specific distribution of T-Type calcium currents in Lamina II neurons of the rat spinal cord. *Front. Cell. Neurosci.* 12:370. doi: 10.3389/fncel.2018.00370

Yasaka, T., Kato, G., Furue, H., Rashid, M. H., Sonohata, M., Tamae, A., et al. (2007). Cell-type-specific excitatory and inhibitory circuits involving primary afferents in the rat spinal dorsal horn in vitro. *J. Physiol.* 581, 603–618. doi: 10.1113/jphysiol.2006.123919

Yasaka, T., Tiong, S. Y., Hughes, D. I., Riddell, J. S., and Todd, A. J. (2010). Populations of inhibitory and excitatory interneurons in lamina II of the adult rat spinal dorsal horn revealed by a combined electrophysiological and anatomical approach. *Pain* 151, 475–488. doi: 10.1016/j.pain.2010.08.008

Zhang, C., Tonsfeldt, K. J., Qiu, J., Bosch, M. A., Kobayashi, K., Steiner, R. A., et al. (2013). Molecular mechanisms that drive estradiol-dependent burst firing of Kiss1 neurons in the rostral periventricular preoptic area. *Am. J. Physiol. Endocrinol. Metab.* 305, E1384–E1397. doi: 10.1152/ajpendo.00406.2013

Zheng, J., Lu, Y., and Perl, E. R. (2010). Inhibitory neurones of the spinal substantia gelatinosa mediate interaction of signals from primary afferents. *J. Physiol.* 588, 2065–2075. doi: 10.1113/jphysiol.2010.188052

Zheng, N., and Raman, I. M. (2009). Ca currents activated by spontaneous firing and synaptic disinhibition in neurons of the cerebellar nuclei. *J. Neurosci.* 29, 9826–9838. doi: 10.1523/JNEUROSCI.2069-09.2009

Zhu, M. Y., Idikuda, V. K., Wang, J. B., Wei, F. S., Kumar, V., Shah, N., et al. (2018). Shank3-deficient thalamocortical neurons show HCN channelopathy and alterations in intrinsic electrical properties. *J. Physiol.* 596, 1259–1276. doi: 10.1113/jp275147

Zhu, M. Y., Zhang, D. Y., Peng, S. C., Liu, N. N., Wu, J., Kuang, H. X., et al. (2019). Preparation of acute spinal cord slices for whole-cell patch-clamp recording in substantia gelatinosa neurons. *J. Vis. Exp.* 143:e58479. doi: 10.3791/58479

Conflict of Interest: The authors declare that the research was conducted in the absence of any commercial or financial relationships that could be construed as a potential conflict of interest.

Publisher's Note: All claims expressed in this article are solely those of the authors and do not necessarily represent those of their affiliated organizations, or those of the publisher, the editors and the reviewers. Any product that may be evaluated in this article, or claim that may be made by its manufacturer, is not guaranteed or endorsed by the publisher.

frontiers in Cellular Neuroscience

REVIEW
published: 03 January 2022
doi: 10.3389/fncel.2021.814012

Neurophysiology of the Developing Cerebral Cortex: What We Have Learned and What We Need to Know

*Heiko J. Luhmann**

Institute of Physiology, University Medical Center Mainz, Mainz, Germany

This review article aims to give a brief summary on the novel technologies, the challenges, our current understanding, and the open questions in the field of the neurophysiology of the developing cerebral cortex in rodents. In the past, *in vitro* electrophysiological and calcium imaging studies on single neurons provided important insights into the function of cellular and subcellular mechanism during early postnatal development. In the past decade, neuronal activity in large cortical networks was recorded in pre- and neonatal rodents *in vivo* by the use of novel high-density multi-electrode arrays and genetically encoded calcium indicators. These studies demonstrated a surprisingly rich repertoire of spontaneous cortical and subcortical activity patterns, which are currently not completely understood in their functional roles in early development and their impact on cortical maturation. Technological progress in targeted genetic manipulations, optogenetics, and chemogenetics now allow the experimental manipulation of specific neuronal cell types to elucidate the function of early (transient) cortical circuits and their role in the generation of spontaneous and sensory evoked cortical activity patterns. Large-scale interactions between different cortical areas and subcortical regions, characterization of developmental shifts from synchronized to desynchronized activity patterns, identification of transient circuits and hub neurons, role of electrical activity in the control of glial cell differentiation and function are future key tasks to gain further insights into the neurophysiology of the developing cerebral cortex.

Keywords: cerebral cortex, neurophysiology, development, rodent, methods

OPEN ACCESS

Edited by:
Enrico Cherubini, European Brain Research Institute, Italy

Reviewed by:
Rustem Khazipov, Institut National de la Santé et de la Recherche Médicale (INSERM), France
Guillermina Lopez-Bendito, Miguel Hernández University of Elche, Spain

***Correspondence:**
Heiko J. Luhmann
luhmann@uni-mainz.de

Specialty section:
This article was submitted to Cellular Neurophysiology, a section of the journal Frontiers in Cellular Neuroscience

Received: *12 November 2021*
Accepted: *09 December 2021*
Published: *03 January 2022*

Citation:
Luhmann HJ (2022) Neurophysiology of the Developing Cerebral Cortex: What We Have Learned and What We Need to Know. Front. Cell. Neurosci. 15:814012. doi: 10.3389/fncel.2021.814012

INTRODUCTION—WHAT ARE OUR TOOLS?

In the last decade life sciences has shown a tremendous progress in developing and improving novel technologies. In cellular neurophysiology classical electrophysiological recording techniques and cellular imaging methods are very successfully combined with new tools in molecular biology and genetics to gain deeper insights into the function of single neurons and defined neuronal networks. Using the powerful Patch-seq technique, whole-cell patch-clamp recordings can be combined with morphological reconstructions, immunohistochemistry, and single-cell RNA-sequencing (scRNA-seq) to perform a multidimensional characterization of a single cell and to correlate the gene expression profile with its structural and functional properties (Cadwell et al., 2017; Scala et al., 2021). When combined with retrograde labeling, information on the projection patterns of single neurons can be added (Peng et al., 2021). Laser capture microdissection allows the transcriptomic characterization of subcellular compartments, such as soma vs. dendrite (Perez et al., 2021). Paired

recordings from synaptically connected neurons combined with precise 3D reconstructions of the cells' morphology provided very detailed information on the function of local neuronal networks, e.g., a cortical column (Feldmeyer et al., 2018). With the vitro multi-patch approach 10–15 neurons can be simultaneously patch-clamp recorded, intracellularly labeled and subsequently analyzed in their synaptic connectivity (Peng et al., 2019). Functional connectivity maps at a larger scale, but with less temporal and spatial precision, can be obtained in brain slices with caged glutamate laser-scanning photostimulation (Meng et al., 2020).

Beside these advances in *in vitro* neurophysiology, *in vivo* recording, and stimulation techniques became also very powerful. Two-photon microscopy can be used to accomplish whole-cell membrane potential recordings of fluorescently labeled and genetically defined neurons in awake head-fixed mice while performing specific behavioral tasks (Petersen, 2017). Juxtacellular stimulation and recording of single cells in head-fixed or freely moving rats allows to study the role of single neurons in cognition and behavior (Houweling and Brecht, 2008; Tang et al., 2014). The number of simultaneously recorded neurons increased over the last decade from a few hundreds to a few thousands (Steinmetz et al., 2019; Perez-Prieto and Delgado-Restituto, 2021) and we may soon approach the neurophysiologist's dream (or nightmare?) to "concurrently record electrical spikes from every neuron in a mammalian brain" (Kleinfeld et al., 2019). To reach this aim, close cooperations with other scientific fields are already on-going (Jun et al., 2017; Garcia-Etxarri and Yuste, 2021). Material sciences and electronic engineering will foster the development of biocompatible multi-electrode arrays with very high number of electrodes, which can be used for recordings of single units and focal electrical stimulation (Jun et al., 2017; Kleinfeld et al., 2019; Perez-Prieto and Delgado-Restituto, 2021). Recently, chronic single unit recordings could be obtained from freely moving rats over up to 4 months with Neuropixel electrodes (Luo et al., 2020). These technological developments will also have an impact on experimental and clinical approaches of deep brain stimulation and brain-machine interfaces.

In the last decade subcellular, cellular, meso-scale, and large-scale imaging methods also showed tremendous technological progress. Genetically encoded calcium indicators, mostly from the GCaMP family, are powerful tools to monitor neuronal activity in small networks up to large-scale dynamics in behaving animals (Cardin et al., 2020; Linden et al., 2021; Ren and Komiyama, 2021). The large majority of these *in vivo* studies are restricted to upper neocortical regions because of technical limitations (Yang and Yuste, 2017). However, red-shifted fluorescent calcium indicators (Tischbirek et al., 2017) and three-photon microscopy (Takasaki et al., 2019) now enables imaging of deep cortical layers with single-cell resolution. Longitudinal calcium imaging from cortical and also deep brain structures can be obtained in freely behaving mice with the (wireless) miniature fluorescence microscope (miniScope) technology (Barbera et al., 2019; Zhang et al., 2019), which also allows recording of neuronal activity at single-cell resolution. Recently high-resolution two-photon calcium imaging of both cortical hemispheres have been performed in awake head-fixed mice (Barson et al., 2020; Cardin et al., 2020). This powerful method allows for the first time the analysis of the entire cortical mantle with cellular resolution. However, calcium imaging still has a number of disadvantages when compared to cellular neurophysiology. Electrophysiological recordings with sub-millisecond resolution provides high temporal information on the spiking output of the neuron, whereas calcium imaging cannot directly monitor the output, but rather monitors the increase in $[Ca^{2+}]_i$ following (subthreshold) synaptic activation and internal state changes (West et al., 2001). A recent study in the visual cortex of awake mice using the genetically encoded calcium indicator GCaMP6f and extracellular recordings with silicon probes demonstrated the advantages and disadvantages of both methods (Siegle et al., 2021). While electrophysiological recordings showed a higher fraction of units with stimulus-driven activity, GCaMP6f calcium imaging revealed a higher selectivity (sharper tuning) among responsive neurons. Another *in vivo* study in the visual cortex of awake transgenic mice expressing GCaMP6s or GCaMP6f demonstrated that <10% and 20–30%, respectively, of isolated single spikes were detectable with calcium imaging (Huang et al., 2021). Critical assessment of calcium imaging data (Rupprecht et al., 2021) and the development of new calcium indicators with fast kinetics (such as jGCaMP8) may solve some of these problems (Zhang et al., 2021).

Subthreshold synaptic inputs are very difficult to detect with somatic calcium signals. Genetically encoded voltage indicators (GEVIs) can monitor subthreshold transmembrane potential dynamics *in vitro* and *in vivo* (Bando et al., 2019). The classical voltage-sensitive dyes developed over the last 30 years were most valuable in elucidating cortical function (Grinvald et al., 2016). The GEVIs have the advantage that they can be targeted to specific cell types and when combined with 2-photon excitation allows imaging of membrane potential dynamics with single-cell resolution in the cerebral cortex *in vivo* (Bando et al., 2019). GEVIs can be also used at the subcellular level, e.g., to study action potential generation at the axon initial segment or transmitter release at the presynaptic terminal (Panzera and Hoppa, 2019).

Beside this progress in cellular electrophysiological and imaging techniques a number of novel genetic and molecular biological methods became most valuable tools to manipulate gene expression and activity of defined single cells during distinct time points of development. Targeted gene delivery via *in vivo* (e.g., *in utero*) electroporation (De Vry et al., 2010), directed genetic manipulations by CRISPR-based technology (Kampmann, 2020), viral tools for specific cell and circuit manipulation (Vormstein-Schneider et al., 2020), Designer Receptors Exclusively Activated by Designer Drugs (DREADD)-based chemogenetic tools (Roth, 2016), and optogenetics (Deisseroth, 2015) are used to activate or silence specific neurons. Some of these methods, especially optogenetics, become even more powerful when combined with *in vivo* targeted whole-cell recordings in behaving animals (Gasselin et al., 2021) or with miniScope technology in freely moving mice (de Groot et al., 2020).

These impressive methodological developments offer the chance to booster interdisciplinary cooperations between experts in cellular electrophysiology, molecular biology, and biostatistics or biomathematicians, and as in the past, physicists are always welcome. Does that mean that the times, that a cellular neurophysiologist is sitting for 6–12 h alone at his/her *in vitro* or *in vivo* set-up, obtaining all relevant data on-line and analyzing the data with rather simple statistics and mathematics programs is over?

The next three sections will focus on the cellular neurophysiology of the developing cerebral cortex in rodents. Since the function of individual neurons is not only determined by its intrinsic properties, but also by its synaptic inputs, early cortical network activity will be also briefly discussed.

THE CHALLENGES OF STUDYING THE NEUROPHYSIOLOGY OF THE DEVELOPING CEREBRAL CORTEX IN RODENTS

Everybody who studies the cellular and network properties of the cerebral cortex in newborn rodents faces a number of challenges. In mice and rats (and in many other mammals such as ferrets), the cerebral cortex at birth has not yet reached its mature six-layered structure. Neurons are still migrating to their final location in layer (L) 2 and L3, perhaps even L4, and these layers are formed until postnatal day (P) 2–3. This migration process, as neuronal proliferation and differentiation (for review Uhlen et al., 2015), is controlled by spontaneous intracellular calcium transients (Bando et al., 2016). Thus, the neocortical network of a newborn rodent changes its layered architecture on a daily basis!

This add-on process in neocortical layering is accompanied by the reorganization of an early transient cortical network, which at birth consists of the marginal zone (later L1), the cortical plate (later L2–L6) and the subplate (for review Kanold and Luhmann, 2010; Hoerder-Suabedissen and Molnár, 2015). At late embryonic and early postnatal stage thalamocortical afferents form functional glutamatergic synapses with subplate neurons, which play important roles in synaptic plasticity and synchronized network activity of the developing cortical network (for review Colonnese and Phillips, 2018; López-Bendito, 2018; Luhmann et al., 2018; Molnár et al., 2020). Between P1 and P2, these thalamocortical fibers disconnect from the subplate and innervate their final targets in L4 and L5/6. Another transient thalamocortical circuit is assembled by infragranular somatostatin (SST) expressing interneurons which innervate parvalbumin (PV) and pyramidal neurons. This early thalamocortical-intracortical circuit disappears by the end of the first postnatal week and is important for the development of thalamic feedforward inhibition via PV interneurons (Tuncdemir et al., 2016). Using transgenic mouse lines Marques-Smith et al. identified in the neonatal mouse somatosensory a transient and activity-dependent early reciprocal circuit cortex between L5b SST-positive interneurons and L4 spiny stellate cells (Marques-Smith et al., 2016). Thus, the newborn rodent cortex exhibits a number of transient circuits and changes its thalamic activation pattern within 3–4 days.

Beside subplate cells, other neocortical neurons also fulfill important roles in early cortical development and are only transiently present during peri-/neonatal stages. Cajal-Retzius neurons in the marginal zone/L1 control a number of important developmental processes and mostly disappear by programmed cell death (apoptosis) during the first postnatal days after termination of neuronal migration (Causeret et al., 2021). Beside subplate and Cajal-Retzius neurons, glutamatergic and GABAergic neurons also die to a large extent by apoptosis during the first postnatal week (with a peak at ∼P7) (Causeret et al., 2018). Notably, this apoptosis process is strongly regulated by electrical activity (Blanquie et al., 2017; Riva et al., 2019). Beside the activity-dependent control in overall cell number, the axonal and dendritic morphology and synaptic connectivity of single cortical neurons is also regulated by early activity (Callaway and Borrell, 2011; Malyshevskaya et al., 2013; Grant et al., 2016) (for review Leighton and Lohmann, 2016). Defined subpopulations of GABAergic interneurons control spontaneous cortical activity patterns and play central roles in the early postnatal development of the cerebral cortex (Leighton et al., 2021). During the first two postnatal week, vasocative-intestinal-peptide and somatostatin interneurons undergo developmental transitions in their cortical function and their processing of sensory information (Kastli et al., 2020). Well-connected early generated interneurons with relatively mature electrophysiological and morphological properties exert a strong influence on cortical activity and ablation of these neurons disturbs spontaneous activity and inhibitory synapse formation (Wang et al., 2019). Using longitudinal *in vivo* calcium imaging of somatosensory cortical activity in non-anesthetized mouse pups, Duan et al. convincely demonstrated that developmental network patterns in interneurons and pyramidal cells are essential for the assembly of neocortical circuits and for the control of interneurons' cell death (Duan et al., 2020). Using *in vivo* imaging in the developing mouse barrel cortex, Modol et al. show that PV interneurons form transient periphery-driven and experience-dependent patches of correlated activity (Modol et al., 2020). Embryonic disturbances in interneuron generation and cortical network integration cause a transient dysfunction with long-term behavioral consequences (Magno et al., 2021). Thus, during the first two postnatal weeks the rodent cerebral cortex is characterized by the deconstruction of transient neuronal networks and simultaneously by the construction of its characteristic six-layered, columnar architecture, intracortical microcircuits, corticothalamic connections, and corticocortical connections.

Spontaneous and sensory evoked activity, monitored by calcium imaging *in vivo*, has been not only observed in neurons of the developing cerebral cortex (Rochefort et al., 2009; Yuryev et al., 2018), but also in astrocytes (Wang et al., 2006). In the embryonic ventricular zone spontaneous calcium waves propagate through radial glia cells and modulate proliferation (Weissman et al., 2004). Astrocytes in newborn mouse neocortical slices reveal spontaneous ultraslow (∼2 per hour) and very long (∼8 min) sodium fluctuations that are

largely restricted to the first postnatal week (Felix et al., 2019). The mechanisms underlying this slow activity and its functional role are currently unknown. Spontaneous activity controls myelination since oligodendrocytes preferentially myelinate electrically active axons via axo-glial interactions leading to local calcium rises in glial cell processes (Wake et al., 2015). *In vitro* data indicate that patterned neuronal activity promotes the survival of oligodendrocytes (Gary et al., 2012) and that GABA released from inhibitory neurons controls myelination and internode length thereby tuning the conduction velocity (Hamilton et al., 2017). Vice versa, oligodendrocyte precursor cells not only respond to, but also modulate neuronal network function, demonstrating a bidirectional glia-neuron cross-talk (Sakry et al., 2014).

This developmental reorganization in cortical structure is accompanied by four neurophysiological processes, which have a strong impact on early cortical function and development. As in the hippocampus (Ben-Ari, 2014), the cerebral cortex also shows a developmental shift in GABA action from depolarizing/excitatory to hyperpolarizing/inhibitory (for review Kirmse et al., 2018; Kilb, 2020). This shift in GABA action differs between *in vitro* and *in vivo* preparations as shown by optogenetic studies (Valeeva et al., 2016). Electrophysiological differences between *in vitro* and *in vivo* preparations have been further reported following the deletion of NKCC1, the primary chloride inward transporter (Graf et al., 2021). *In vivo* reports (Kirmse et al., 2015; Murata and Colonnese, 2020) and modeling studies (Lombardi et al., 2021) provide a more complex picture of the developmental shift in GABA action, especially when on-going spatiotemporal interactions between GABAergic and glutamatergic inputs are taken into account (for review Kilb, 2021). It is not the aim of this short review to summarize the current data on this topic, but it is well-accepted that the intracellular chloride concentration is regulated by development, various molecular factors, and neuronal activity (Kaila et al., 2014; Watanabe and Fukuda, 2015; Virtanen et al., 2020, 2021). Thus, the action and function of the important neurotransmitter GABA, and also glycine and taurine (for review Kilb and Fukuda, 2017), changes dramatically during the first postnatal week in rodent cortex!

The second developmental change in cortical function is the transition from electrical coupling via gap junctions to mostly chemical synaptic transmission (Valiullina et al., 2016; Yao et al., 2016). During embryonic and early postnatal development, gap junctions play important roles in various developmental processes (Allene and Cossart, 2010; Niculescu and Lohmann, 2014). Yu et al. found strong electrical coupling between clonally related excitatory neurons in columnar manner forming the functional template of ontogenetic columns (Yu et al., 2012). Lineage-related electrical coupling has been also demonstrated between interneurons of the same subtype over an extended period of time and across a range of distances (Zhang et al., 2017). At later stages electrical synapses may interact with chemical synapses (Pereda, 2014). Neonatal connexin 26 removal impairs neocortical development and leads to elevated anxiety (Su et al., 2017). With maturation intercellular communication via gap junctions largely disappears during the second postnatal week and remains restricted to specific cell types, mostly interneurons (Connors, 2017), or cell compartments as axo-axonal coupling (Traub et al., 2004). Thus, intercellular functional interactions shift from electrical coupling to chemical synaptic transmission!

The third developmental change in cortical function is the transition from highly synchronized network activity during the late prenatal/early postnatal period to a more desynchronized state at later stages. Using two-photon calcium imaging of the barrel cortex *in vivo*, Mizuno et al. demonstrated that during the first postnatal week L4 neurons within one barrel show synchronized spontaneous activity (Mizuno et al., 2018). This patchwork activity pattern disappeared during the second postnatal week when L4 neurons fired asynchronously within one barrel. Several spontaneous network activity patterns (cortical early network oscillations, spindle bursts/delta brushes, early gamma oscillations, cortical giant depolarizing potentials, spontaneous activity transients, and others) have been characterized in the neonatal cerebral cortex of various mammalian species, from mouse to human (Colonnese and Khazipov, 2012; Luhmann et al., 2016; Luhmann and Khazipov, 2018; Molnár et al., 2020). For some of these patterns, the subplate and other transient cortical circuits play a central role (Kanold and Luhmann, 2010; Colonnese and Phillips, 2018; Luhmann et al., 2018). Beside these developmental changes in the pattern of spontaneous activity, cortical processing of sensory evoked activity undergoes a similar transition from bursting in pre- and neonatal stages to continuous "adult-like" activity during further development (Colonnese et al., 2010). Thus, during early development the neocortex shifts from a highly synchronized to a more desynchronized state!

The fourth developmental change in cortical function is the gradual innervation of the cortical layers by ascending neuromodulatory systems, such as the cholinergic, serotonergic, dopaminergic, and the noradrenergic system. Although the subplate receives functional neuromodulatory inputs already at early stages (Hanganu and Luhmann, 2004; Dupont et al., 2006; Hanganu et al., 2009), cortical layers 2 to 6 are only gradually innervated in an inside first—out side last sequence (Calarco and Robertson, 1995; Mechawar and Descarries, 2001). The emergence of the neuromodulatory inputs accompanies the developmental switch from bursting to continuous desynchronized activity (Colonnese et al., 2010) and the developmental changes in vigilance states and active movements (Mukherjee et al., 2017; Dooley et al., 2020; Glanz et al., 2021). Thus, these neuromodulatory systems have a progressively stronger influence on spontaneous and sensory evoked cortical function during the early postnatal period.

These dramatic structural and functional changes in the rodent developing cortex represent a major problem for everybody studying early neocortical development in mice and rats, because one should not (or better cannot) merge data from different postnatal days. The neocortex of a P0 mouse is different from that of a P1 mouse, and that differs from a P2 mouse! In a careful and detailed study, one should either focus on one single postnatal day (Mojtahedi et al., 2021) or form groups that differ in age not more than 1–2 days (Yang et al., 2009; Shen and Colonnese, 2016).

NEUROPHYSIOLOGY OF THE DEVELOPING CEREBRAL CORTEX: WHAT WE HAVE LEARNED

Although recording techniques from freely moving rodents are important and become increasingly more powerful, such recordings from newborn rodents are only of limited value, because newborn mice and rats do not actively move so much during the first 10 postnatal days (van der Bourg et al., 2017). However, newborn rodents are exposed to a variety of sensory stimuli (e.g., from the proprioceptive and probably vestibular system) and from passive interactions with the mother and littermates. Sensory feedback from passive stimulation by littermates trigger cortical activity (Akhmetshina et al., 2016). Furthermore, spontaneous self-generated movements (myoclonic twitches) can be already observed very early and play an important role in the development of the sensorimotor system (Inacio et al., 2016; Dooley et al., 2020; Gomez et al., 2021). Head-fixation of newborn rodents allows simultaneous recordings of large-scale neuronal activity and spontaneous movements of the animal's snout including the whiskers, the forelimbs, hindlimbs, and the tail using electromyography (EMG) or multiple video camera monitoring (Dooley and Blumberg, 2018; Glanz et al., 2021; Gomez et al., 2021). Neuronal structures involved in the generation or modulation of spontaneous movements in newborns can be studied with imaging or multi-electrodes recording techniques. Central pattern generator (CPG) networks in spinal cord, brainstem, thalamus, motor cortex, and also cerebellum are of pivotal interest (Colonnese and Khazipov, 2012; Blumberg et al., 2013; Luhmann et al., 2016) and as many brain regions as possible should be recorded simultaneously in awake animals. CPGs and motor-related networks may trigger spontaneous movements, which subsequently activate the sensory system, thereby promoting the spatio-temporal binding of developing neuronal networks in the sensory-motor system. In the somatosensory and motor cortex of newborn rodents spindle burst and gamma oscillations mediate this binding process (Khazipov et al., 2004, 2013; Yang et al., 2009, 2013; Minlebaev et al., 2011; An et al., 2014; Luhmann and Khazipov, 2018; Dooley et al., 2020; Glanz et al., 2021).

Spindle burst and gamma oscillatory activity has been also demonstrated in the visual cortex of rodents before eye opening (Ackman and Crair, 2014; Colonnese and Phillips, 2018). Spindle bursts in the visual cortex are triggered by retinal bursts (Hanganu et al., 2006; Colonnese and Khazipov, 2010) and are modulated by the cholinergic system (Hanganu et al., 2006; Ackman et al., 2012). Spontaneous activity generated in the cochlea before hearing onset controls the development of central auditory pathways (Tritsch et al., 2007; Wang et al., 2015), but the function of spindle bursts and gamma oscillations in the auditory cortex of newborn rodents is less clear as compared to those in the visual and somatosensory system.

Nested gamma spindle bursts have been demonstrated in the prefrontal–hippocampal network of the neonatal rat (Brockmann et al., 2011; Bitzenhofer et al., 2015) and cholinergic projections facilitate this oscillatory coupling by activation of muscarinic acetylcholine receptors (Janiesch et al., 2011). In neonatal mice optogenetic activation of channelrhodopsin-expressing pyramidal neurons in L2/3, but not L5/6, of the prefrontal cortex boost oscillatory activity in beta–gamma frequency bands (Bitzenhofer et al., 2017).

In summary, spontaneous and sensory evoked activity pattern recorded in sensory, motor and prefrontal cortex of newborn rodents share many similarities and most likely fulfill similar functions. It is not surprising that these activity patterns also occur in the cerebral cortex of preterm human babies, when the cortex resembles in its structure and function the cortex of a newborn rodent (Colonnese et al., 2010; Luhmann and Fukuda, 2020). The activity patterns recorded in different cortical areas of preterm human babies are termed spindle bursts, delta brushes, *tracé discontinue, tracé alternant*, and spontaneous activity transients (SAT) (Vanhatalo and Kaila, 2006; Milh et al., 2007; Colonnese et al., 2010; Chipaux et al., 2013; Koolen et al., 2016) and serve as biomarkers for the cognitive and motor development of the child (Iyer et al., 2015; Tokariev et al., 2019; Moghadam et al., 2021).

Over the last decade we got deeper insights into the functional roles of these early cortical activity patterns. During embryonic stages spontaneous activity arising from the thalamus regulates coordinate cortical sensory area patterning and drives the emergence of functional cortical maps (Moreno-Juan et al., 2017; Anton-Bolanos et al., 2018, 2019; Martini et al., 2021). In newborn rodent cortex spontaneous and sensory evoked cortical activity often locally synchronizes column-like networks resembling early topographic cortical maps (Yang et al., 2013; Kummer et al., 2016). At perinatal stage this columnar cortical activity ("columnar burst," Colonnese et al., 2010) is mediated by the activation of a local network in the subplate (Dupont et al., 2006; Hanganu et al., 2009). Removal of the subplate in the neonatal rat barrel cortex reduces spindle burst activity and prevents the development of the thalamocortical barrel field patterning (Tolner et al., 2012). Li et al. have demonstrated that not only the development of barrel-related columns, but also the emergence of L4 depends on early activity, specifically on glutamate released from thalamocortical afferents (Li et al., 2013).

In a number of elegant studies Hanganu-Opatz and coworkers demonstrated how genetic or experimentally induced manipulations in the oscillatory network activity in neonatal prefrontal cortex results in long-term functional and behavioral deficits (Chini and Hanganu-Opatz, 2021). In a mouse model of mental disorders, Chini et al. demonstrated an early-emerging prefrontal network dysfunction that subsequently gives rise to cognitive deficits. They show that this deficiency can be rescued by minocycline administration, thus identifying a potential biomarker (Chini et al., 2020). Bitzenhofer et al. manipulated early activity in the prefrontal cortex of neonatal mice, resulting in disruption of coordinated patterns of electrical activity, excitation-inhibition imbalance, and impaired cognitive abilities at adult age. Thus, prefrontal activity during development is critical for adult network function and behavioral performance (Bitzenhofer et al., 2021).

THE OPEN QUESTIONS AND FUTURE TASKS

This last section provides a personal viewpoint on the open questions and tasks that should be addressed in the third decade of the 21st century to gain further insights into the neurophysiology of the developing cerebral cortex. If possible, these studies should be performed *in vivo* in non-anesthetized animals.

1) Study with cell resolution recording and imaging techniques the large-scale interactions between different cortical areas (sensory, association, prefrontal, motor) and subcortical regions in pre- and early postnatal development. What are the underlying mechanisms of local vs. global interactions and what are their functions? Define the relationship and the role of local vs. propagating activity.
2) Identify at different developmental stages the interactions between spontaneous, movement related and sensory evoked activity. Characterize the developmental shift from synchronized to desynchronized network activity in sensory, prefrontal, and motor system including subcortical regions.
3) What is the functional role of early cortical activity patterns in shaping the pre- and early postnatal cortex at micro- (e.g., spines), meso- (e.g., microcircuitry), and macroscale (e.g., cortico-cortical connections)?
4) Determine the dynamic spatio-temporal action of GABA and glycine during earliest (prenatal) stages of development under non-anesthetized *in vivo* conditions and by the use of non-invasive techniques?
5) Characterize the role of neuromodulators (e.g., acetylcholine, noradrenaline, serotonin) on cortical neurophysiology at different developmental stages.
6) Define and elucidate the emergence of cognitive functions, e.g., learning and memory, spatial navigation, social interactions.
7) Characterize the role of distinct populations of early generated GABAergic interneurons (Wang et al., 2019) and identify and manipulate hub neurons in developing neocortical networks (cf. hub neurons in immature hippocampal networks Bonifazi et al., 2009; Picardo et al., 2011; Bocchio et al., 2020).
8) In their seminal review article Connors and Gutnick described in the rodent cerebral cortex three distinct functional cell types based on their intrinsic firing pattern (Connors and Gutnick, 1990): regular spiking, fast spiking and bursting neurons. Over the last 30 years we learned that cortical neurons, especially interneurons, can be subdivided into many more cell type classes (DeFelipe et al., 2013). A recent single-cell transcriptomic analysis of the mouse primary motor cortex identified over 56 neuronal cell types (Yao et al., 2021). Kriegstein and coworkers recently characterized 138 neocortical cell type clusters throughout the second trimester of human development and demonstrated that "gene-expression patterns are highly dynamic across cortical regions" and "borders between clusters are fluid" (Bhaduri et al., 2021). Since it is well-established that the firing pattern of neocortical neurons *in vivo* is strongly regulated by the action of modulatory systems (Steriade, 2001a), cell classifications based on firing patterns may be also more "fluid" as estimated by experimental protocols used in mostly *in vitro* slice preparations. Thus, cell type classifications in (developing) cerebral cortex should take technical limitations (c.f. Steriade, 2001b) and dynamic changes into account.
9) Identify the mechanisms and the functional role of activity-dependent interactions between neurons and astrocytes, oligodendrocytes, radial glia, and microglia in perinatal cortex. How do certain spontaneous activity patterns promote myelination (for review Zuchero and Barres, 2013)? How does neuronal activity influence the development of the tri-partite synapse (for review Dallerac et al., 2018) and "quad-partite" synapse including microglia (for review Schafer et al., 2013)?
10) Characterize the neuro-glia-vessel communication in perinatal cortex (Segarra et al., 2018) and identify a potential role of early spontaneous and sensory evoked activity in cortical vascularization and development of the blood-brain barrier (Whiteus et al., 2013).
11) Critically evaluate the use of rodent models in understanding early cortical development in humans (Luhmann and Fukuda, 2020) and whether rodents fulfill criteria to study preclinical manifestations of human diseases (Al Dahhan et al., 2019).
12) Organoids may become most valuable models for early cortical development in humans (Trujillo et al., 2019; Chan et al., 2021). However, it needs to be studied whether important cortical circuits present in pre- and neonatal human cortex are also present in organoids (e.g., the fetal subplate circuits Kostovic, 2020; Kostovic et al., 2021). Further, it remains to be studied in more detail whether the spontaneous activity patterns present in pre- and neonatal human cortex (Stjerna et al., 2012; Omidvarnia et al., 2014; Koolen et al., 2016) can be also demonstrated in human organoids.
13) Complement experimental studies with computational modeling of neocortical circuit development (Richter and Gjorgjieva, 2017; Shenoy and Kao, 2021).
14) The Introduction gave a brief overview on the recent technological developments. However, as Frégnac stated in his review we may face "dangers of letting technology-driven—rather than concept-driven—strategies shape the future industrialization of neuroscience through the rapid emergence of very-large-scale data-mining initiatives" (Frégnac, 2017).

AUTHOR CONTRIBUTIONS

The author confirms being the sole contributor of this work and has approved it for publication.

FUNDING

HL was supported by the Deutsche Forschungsgemeinschaft.

REFERENCES

Ackman, J. B., Burbridge, T. J., and Crair, M. C. (2012). Retinal waves coordinate patterned activity throughout the developing visual system. *Nature*, 490, 219–225. doi: 10.1038/nature11529

Ackman, J. B., and Crair, M. C. (2014). Role of emergent neural activity in visual map development. *Curr. Opin. Neurobiol.* 24, 166–175. doi: 10.1016/j.conb.2013.11.011

Akhmetshina, D., Nasretdinov, A., Zakharov, A., Valeeva, G., and Khazipov, R. (2016). The nature of the sensory input to the neonatal rat barrel cortex. *J. Neurosci.* 36, 9922–9932. doi: 10.1523/JNEUROSCI.1781-16.2016

Al Dahhan, N. Z., De Felice, F. G., and Munoz, D. P. (2019). Potentials and pitfalls of cross-translational models of cognitive impairment. *Front. Behav. Neurosci.* 13:48. doi: 10.3389/fnbeh.2019.00048

Allene, C., and Cossart, R. (2010). Early NMDA receptor-driven waves of activity in the developing neocortex: physiological or pathological network oscillations? *J. Physiol.* 588, 83–91. doi: 10.1113/jphysiol.2009.178798

An, S., Kilb, W., and Luhmann, H. J. (2014). Sensory-evoked and spontaneous gamma and spindle bursts in neonatal rat motor cortex. *J. Neurosci.* 34, 10870–10883. doi: 10.1523/JNEUROSCI.4539-13.2014

Anton-Bolanos, N., Espinosa, A., and López-Bendito, G. (2018). Developmental interactions between thalamus and cortex: a true love reciprocal story. *Curr. Opin. Neurobiol.* 52, 33–41. doi: 10.1016/j.conb.2018.04.018

Anton-Bolanos, N., Sempere-Ferrandez, A., Guillamon-Vivancos, T., Martini, F. J., Perez-Saiz, L., Gezelius, H., et al. (2019). Prenatal activity from thalamic neurons governs the emergence of functional cortical maps in mice. *Science* 364, 987–990. doi: 10.1126/science.aav7617

Bando, Y., Irie, K., Shimomura, T., Umeshima, H., Kushida, Y., Kengaku, M., et al. (2016). Control of spontaneous Ca2+ transients is critical for neuronal maturation in the developing neocortex. *Cerebral Cortex* 26, 106–117. doi: 10.1093/cercor/bhu180

Bando, Y., Sakamoto, M., Kim, S., Ayzenshtat, I., and Yuste, R. (2019). Comparative evaluation of genetically encoded voltage indicators. *Cell Rep.* 26, 802–813 e804. doi: 10.1016/j.celrep.2018.12.088

Barbera, G., Liang, B., Zhang, L., Li, Y., and Lin, D. T. (2019). A wireless miniScope for deep brain imaging in freely moving mice. *J. Neurosci. Methods* 323, 56–60. doi: 10.1016/j.jneumeth.2019.05.008

Barson, D., Hamodi, A. S., Shen, X., Lur, G., Constable, R. T., Cardin, J. A., et al. (2020). Simultaneous mesoscopic and two-photon imaging of neuronal activity in cortical circuits. *Nat. Methods* 17, 107–113. doi: 10.1038/s41592-019-0625-2

Ben-Ari, Y. (2014). The GABA excitatory/inhibitory developmental sequence: a personal journey. *Neuroscience* 279, 187–219. doi: 10.1016/j.neuroscience.2014.08.001

Bhaduri, A., Sandoval-Espinosa, C., Otero-Garcia, M., Oh, I., Yin, R., Eze, U. C., et al. (2021). An atlas of cortical arealization identifies dynamic molecular signatures. *Nature* 598, 200–204. doi: 10.1038/s41586-021-03910-8

Bitzenhofer, S. H., Ahlbeck, J., Wolff, A., Wiegert, J. S., Gee, C. E., Oertner, T. G., et al. (2017). Layer-specific optogenetic activation of pyramidal neurons causes beta-gamma entrainment of neonatal networks. *Nat. Commun.* 8:14563. doi: 10.1038/ncomms14563

Bitzenhofer, S. H., Pöpplau, J. A., Chini, M., Marquardt, A., and Hanganu-Opatz, I. L. (2021). A transient developmental increase in prefrontal activity alters network maturation and causes cognitive dysfunction in adult mice. *Neuron* 109, 1350–1364 e1356. doi: 10.1016/j.neuron.2021.02.011

Bitzenhofer, S. H., Sieben, K., Siebert, K. D., Spehr, M., and Hanganu-Opatz, I. L. (2015). Oscillatory activity in developing prefrontal networks results from theta-gamma-modulated synaptic inputs. *Cell Rep.* 11, 486–497. doi: 10.1016/j.celrep.2015.03.031

Blanquie, O., Kilb, W., Sinning, A., and Luhmann, H. J. (2017). Homeostatic interplay between electrical activity and neuronal apoptosis in the developing neocortex. *Neuroscience* 358, 190–200. doi: 10.1016/j.neuroscience.2017.06.030

Blumberg, M. S., Marques, H. G., and Iida, F. (2013). Twitching in sensorimotor development from sleeping rats to robots. *Curr. Biol.* 23, R532–R537. doi: 10.1016/j.cub.2013.04.075

Bocchio, M., Gouny, C., Angulo-Garcia, D., Toulat, T., Tressard, T., Quiroli, E., et al. (2020). Hippocampal hub neurons maintain distinct connectivity throughout their lifetime. *Nat. Commun.* 11:4559. doi: 10.1038/s41467-020-18432-6

Bonifazi, P., Goldin, M., Picardo, M. A., Jorquera, I., Cattani, A., Bianconi, G., et al. (2009). GABAergic hub neurons orchestrate synchrony in developing hippocampal networks. *Science* 326, 1419–1424. doi: 10.1126/science.1175509

Brockmann, M. D., Poschel, B., Cichon, N., and Hanganu-Opatz, I. L. (2011). Coupled oscillations mediate directed interactions between prefrontal cortex and hippocampus of the neonatal rat. *Neuron* 71, 332–347. doi: 10.1016/j.neuron.2011.05.041

Cadwell, C. R., Scala, F., Li, S., Livrizzi, G., Shen, S., Sandberg, R., et al. (2017). Multimodal profiling of single-cell morphology, electrophysiology, and gene expression using Patch-seq. *Nat. Protoc.* 12, 2531–2553. doi: 10.1038/nprot.2017.120

Calarco, C. A., and Robertson, R. T. (1995). Development of basal forebrain projections to visual cortex: DiI studies in rat. *J. Comp. Neurol.* 354, 608–626. doi: 10.1002/cne.903540409

Callaway, E. M., and Borrell, V. (2011). Developmental sculpting of dendritic morphology of layer 4 neurons in visual cortex: influence of retinal input. *J. Neurosci.* 31, 7456–7470. doi: 10.1523/JNEUROSCI.5222-10.2011

Cardin, J. A., Crair, M. C., and Higley, M. J. (2020). Mesoscopic imaging: shining a wide light on large-scale neural dynamics. *Neuron* 108, 33–43. doi: 10.1016/j.neuron.2020.09.031

Causeret, F., Coppola, E., and Pierani, A. (2018). Cortical developmental death: selected to survive or fated to die. *Curr. Opin. Neurobiol.* 53, 35–42. doi: 10.1016/j.conb.2018.04.022

Causeret, F., Moreau, M. X., Pierani, A., and Blanquie, O. (2021). The multiple facets of Cajal-Retzius neurons. *Development* 148:dev199409. doi: 10.1242/dev.199409

Chan, W. K., Fetit, R., Griffiths, R., Marshall, H., Mason, J. O., and Price, D. J. (2021). Using organoids to study human brain development and evolution. *Dev. Neurobiol.* 81, 608–622. doi: 10.1002/dneu.22819

Chini, M., and Hanganu-Opatz, I. L. (2021). Prefrontal cortex development in health and disease: lessons from rodents and humans. *Trends Neurosci.* 44, 227–240. doi: 10.1016/j.tins.2020.10.017

Chini, M., Popplau, J. A., Lindemann, C., Carol-Perdiguer, L., Hnida, M., Oberlander, V., et al. (2020). Resolving and rescuing developmental miswiring in a mouse model of cognitive impairment. *Neuron* 105, 60–74 e67. doi: 10.1016/j.neuron.2019.09.042

Chipaux, M., Colonnese, M. T., Mauguen, A., Fellous, L., Mokhtari, M., Lezcano, O., et al. (2013). Auditory stimuli mimicking ambient sounds drive temporal "Delta-Brushes" in premature infants. *Plos ONE* 8:e79028. doi: 10.1371/journal.pone.0079028

Colonnese, M., and Khazipov, R. (2012). Spontaneous activity in developing sensory circuits: implications for resting state fMRI. *Neuroimage* 62, 2212–2221. doi: 10.1016/j.neuroimage.2012.02.046

Colonnese, M. T., Kaminska, A., Minlebaev, M., Milh, M., Bloem, B., Lescure, S., et al. (2010). A conserved switch in sensory processing prepares developing neocortex for vision. *Neuron* 67, 480–498. doi: 10.1016/j.neuron.2010.07.015

Colonnese, M. T., and Khazipov, R. (2010). "Slow activity transients" in infant rat visual cortex: a spreading synchronous oscillation patterned by retinal waves. *J. Neurosci.* 30, 4325–4337. doi: 10.1523/JNEUROSCI.4995-09.2010

Colonnese, M. T., and Phillips, M. A. (2018). Thalamocortical function in developing sensory circuits. *Curr. Opin. Neurobiol.* 52, 72–79. doi: 10.1016/j.conb.2018.04.019

Connors, B. W. (2017). Synchrony and so much more: diverse roles for electrical synapses in neural circuits. *Dev. Neurobiol.* 77, 610–624. doi: 10.1002/dneu.22493

Connors, B. W., and Gutnick, M. J. (1990). Intrinsic firing patterns of diverse neocortical neurons. *Trends Neurosci.* 13, 99–104. doi: 10.1016/0166-2236(90)90185-D

Dallerac, G., Zapata, J., and Rouach, N. (2018). Versatile control of synaptic circuits by astrocytes: where, when and how? *Nat. Rev. Neurosci.* 19, 729–743. doi: 10.1038/s41583-018-0080-6

de Groot, A., van den Boom, B. J., van Genderen, R. M., Coppens, J., van Veldhuijzen, J., Bos, J., et al. (2020). NINscope, a versatile miniscope for multi-region circuit investigations. *Elife* 9:e49987. doi: 10.7554/eLife.49987

De Vry, J., Martinez-Martinez, P., Losen, M., Temel, Y., Steckler, T., Steinbusch, H. W., et al. (2010). *In vivo* electroporation of the central nervous system: a non-viral approach for targeted gene delivery. *Prog. Neurobiol.* 92, 227–244. doi: 10.1016/j.pneurobio.2010.10.001

DeFelipe, J., Lopez-Cruz, P. L., Benavides-Piccione, R., Bielza, C., Larranaga, P., Anderson, S., et al. (2013). New insights into the classification and nomenclature of cortical GABAergic interneurons. *Nat. Rev. Neurosci.* 14, 202–216. doi: 10.1038/nrn3444

Deisseroth, K. (2015). Optogenetics: 10 years of microbial opsins in neuroscience. *Nat. Neurosci.* 18, 1213–1225. doi: 10.1038/nn.4091

Dooley, J. C., and Blumberg, M. S. (2018). Developmental 'awakening' of primary motor cortex to the sensory consequences of movement. *Elife* 7:e41841. doi: 10.7554/eLife.41841

Dooley, J. C., Glanz, R. M., Sokoloff, G., and Blumberg, M. S. (2020). Self-generated whisker movements drive state-dependent sensory input to developing barrel cortex. *Curr. Biol.* 30, 2404–2410 e2404. doi: 10.1016/j.cub.2020.04.045

Duan, Z. R. S., Che, A., Chu, P., Modol, L., Bollmann, Y., Babij, R., et al. (2020). GABAergic restriction of network dynamics regulates interneuron survival in the developing cortex. *Neuron* 105, 75–92 e75. doi: 10.1016/j.neuron.2019.10.008

Dupont, E., Hanganu, I. L., Kilb, W., Hirsch, S., and Luhmann, H. J. (2006). Rapid developmental switch in the mechanisms driving early cortical columnar networks. *Nature* 439, 79–83. doi: 10.1038/nature04264

Feldmeyer, D., Qi, G., Emmenegger, V., and Staiger, J. F. (2018). Inhibitory interneurons and their circuit motifs in the many layers of the barrel cortex. *Neuroscience* 368, 132–151. doi: 10.1016/j.neuroscience.2017.05.027

Felix, L., Ziemens, D., Seifert, G., and Rose, C. R. (2019). Spontaneous Ultraslow Na(+) fluctuations in the neonatal mouse brain. *Cells* 9:102. doi: 10.3390/cells9010102

Frégnac, Y. (2017). Big data and the industrialization of neuroscience: aa safe roadmap for understanding the brain? *Science* 358, 470–477. doi: 10.1126/science.aan8866

Garcia-Etxarri, A., and Yuste, R. (2021). Time for NanoNeuro. *Nat. Methods* 18, 1287–1293. doi: 10.1038/s41592-021-01270-9

Gary, D. S., Malone, M., Capestany, P., Houdayer, T., and McDonald, J. W. (2012). Electrical stimulation promotes the survival of oligodendrocytes in mixed cortical cultures. *J. Neurosci. Res.* 90, 72–83. doi: 10.1002/jnr.22717

Gasselin, C., Hohl, B., Vernet, A., Crochet, S., and Petersen, C. C. H. (2021). Cell-type-specific nicotinic input disinhibits mouse barrel cortex during active sensing. *Neuron* 109, 778–787 e773. doi: 10.1016/j.neuron.2020.12.018

Glanz, R. M., Dooley, J. C., Sokoloff, G., and Blumberg, M. S. (2021). Sensory coding of limb kinematics in motor cortex across a key developmental transition. *J Neurosci* 41, 6905–6918. doi: 10.1523/JNEUROSCI.0921-21.2021

Gomez, L. J., Dooley, J. C., Sokoloff, G., and Blumberg, M. S. (2021). Parallel and serial sensory processing in developing primary somatosensory and motor cortex. *J. Neurosci.* 41, 3418–3431. doi: 10.1523/JNEUROSCI.2614-20.2021

Graf, J., Zhang, C., Marguet, S. L., Herrmann, T., Flossmann, T., Hinsch, R., et al. (2021). A limited role of NKCC1 in telencephalic glutamatergic neurons for developing hippocampal network dynamics and behavior. *Proc. Natl. Acad. Sci. U.S.A.* 118:e2014784118. doi: 10.1073/pnas.2014784118

Grant, E., Hoerder-Suabedissen, A., and Molnár, Z. (2016). The regulation of corticofugal fiber targeting by retinal inputs. *Cereb. Cortex* 26, 1336–1348. doi: 10.1093/cercor/bhv315

Grinvald, A., Omer, D. B., Sharon, D., Vanzetta, I., and Hildesheim, R. (2016). Voltage-sensitive dye imaging of neocortical activity. *Cold Spring Harb. Protoc.* 2016 pdb.top089367 doi: 10.1101/pdb.top089367

Hamilton, N. B., Clarke, L. E., Arancibia-Carcamo, I. L., Kougioumtzidou, E., Matthey, M., Karadottir, R., et al. (2017). Endogenous GABA controls oligodendrocyte lineage cell number, myelination, and CNS internode length. *Glia* 65, 309–321. doi: 10.1002/glia.23093

Hanganu, I. L., Ben-Ari, Y., and Khazipov, R. (2006). Retinal waves trigger spindle bursts in the neonatal rat visual cortex. *J. Neurosci.* 26, 6728–6736. doi: 10.1523/JNEUROSCI.0752-06.2006

Hanganu, I. L., and Luhmann, H. J. (2004). Functional nicotinic acetylcholine receptors on subplate neurons in neonatal rat somatosensory cortex. *J. Neurophysiol.* 92, 189–198. doi: 10.1152/jn.00010.2004

Hanganu, I. L., Okabe, A., Lessmann, V., and Luhmann, H. J. (2009). Cellular mechanisms of subplate-driven and cholinergic input-dependent network activity in the neonatal rat somatosensory cortex. *Cereb. Cortex* 19, 89–105. doi: 10.1093/cercor/bhn061

Hoerder-Suabedissen, A., and Molnár, Z. (2015). Development, evolution and pathology of neocortical subplate neurons. *Nat. Rev. Neurosci.* 16, 133–146. doi: 10.1038/nrn3915

Houweling, A. R., and Brecht, M. (2008). Behavioural report of single neuron stimulation in somatosensory cortex. *Nature* 451, 65–68. doi: 10.1038/nature06447

Huang, L., Ledochowitsch, P., Knoblich, U., Lecoq, J., Murphy, G. J., Reid, R. C., et al. (2021). Relationship between simultaneously recorded spiking activity and fluorescence signal in GCaMP6 transgenic mice. *Elife* 10:e51675. doi: 10.7554/eLife.51675

Inacio, A. R., Nasretdinov, A., Lebedeva, J., and Khazipov, R. (2016). Sensory feedback synchronizes motor and sensory neuronal networks in the neonatal rat spinal cord. *Nat. Commun.* 7:13060. doi: 10.1038/ncomms13060

Iyer, K. K., Roberts, J. A., Hellstrom-Westas, L., Wikström, S., Hansen-Pupp, I., Ley, D., et al. (2015). Cortical burst dynamics predict clinical outcome early in extremely preterm infants. *Brain* 138, 2206–2218. doi: 10.1093/brain/awv129

Janiesch, P. C., Krüger, H. S., Pöschel, B., and Hanganu-Opatz, I. L. (2011). Cholinergic control in developing prefrontal-hippocampal networks. *J. Neurosci.* 31, 17955–17970. doi: 10.1523/JNEUROSCI.2644-11.2011

Jun, J. J., Steinmetz, N. A., Siegle, J. H., Denman, D. J., Bauza, M., Barbarits, B., et al. (2017). Fully integrated silicon probes for high-density recording of neural activity. *Nature* 551, 232–236. doi: 10.1038/nature24636

Kaila, K., Price, T. J., Payne, J. A., Puskarjov, M., and Voipio, J. (2014). Cation-chloride cotransporters in neuronal development, plasticity and disease. *Nat. Rev. Neurosci.* 15, 637–654. doi: 10.1038/nrn3819

Kampmann, M. (2020). CRISPR-based functional genomics for neurological disease. *Nat. Rev. Neurol.* 16, 465–480. doi: 10.1038/s41582-020-0373-z

Kanold, P. O., and Luhmann, H. J. (2010). The subplate and early cortical circuits. *Annu. Rev. Neurosci.* 33, 23–48. doi: 10.1146/annurev-neuro-060909-153244

Kastli, R., Vighagen, R., van der Bourg, A., Argunsah, A. O., Iqbal, A., Voigt, F. F., et al. (2020). Developmental divergence of sensory stimulus representation in cortical interneurons. *Nat. Commun.* 11:5729. doi: 10.1038/s41467-020-19427-z

Khazipov, R., Minlebaev, M., and Valeeva, G. (2013). Early gamma oscillations. *Neuroscience* 250, 240–252. doi: 10.1016/j.neuroscience.2013.07.019

Khazipov, R., Sirota, A., Leinekugel, X., Holmes, G. L., Ben-Ari, Y., and Buzsáki, G. (2004). Early motor activity drives spindle bursts in the developing somatosensory cortex. *Nature* 432, 758–761. doi: 10.1038/nature03132

Kilb, W. (2020). "The relation between neuronal chloride transporter activities, GABA inhibition, and neuronal activity," in *Neuronal Chloride Transporters in Health and Disease*, ed X. Tang (London: Elsevier), 43–57. doi: 10.1016/B978-0-12-815318-5.00003-0

Kilb, W. (2021). When are depolarizing GABAergic responses excitatory? *Front. Mol. Neurosci.* 14:747835. doi: 10.3389/fnmol.2021.747835

Kilb, W., and Fukuda, A. (2017). Taurine as an essential neuromodulator during perinatal cortical development. *Front. Cell. Neurosci.* 11:328. doi: 10.3389/fncel.2017.00328

Kirmse, K., Hübner, C. A., Isbrandt, D., Witte, O. W., and Holthoff, K. (2018). GABAergic transmission during brain development: multiple effects at multiple stages. *Neuroscientist* 24, 36–53. doi: 10.1177/1073858417701382

Kirmse, K., Kummer, M., Kovalchuk, Y., Witte, O. W., Garaschuk, O., and Holthoff, K. (2015). GABA depolarizes immature neurons and inhibits network activity in the neonatal neocortex *in vivo*. *Nat. Commun.* 6:7750. doi: 10.1038/ncomms8750

Kleinfeld, D., Luan, L., Mitra, P. P., Robinson, J. T., Sarpeshkar, R., Shepard, K., et al. (2019). Can one concurrently record electrical spikes from every neuron in a mammalian brain? *Neuron* 103, 1005–1015. doi: 10.1016/j.neuron.2019.08.011

Koolen, N., Dereymaeker, A., Räsänen, O., Jansen, K., Vervisch, J., Matic, V., et al. (2016). Early development of synchrony in cortical activations in the human. *Neuroscience* 322, 298–307. doi: 10.1016/j.neuroscience.2016.02.017

Kostovic, I. (2020). The enigmatic fetal subplate compartment forms an early tangential cortical nexus and provides the framework for construction of cortical connectivity. *Prog. Neurobiol.* 194:101883. doi: 10.1016/j.pneurobio.2020.101883

Kostovic, I., Rados, M., Kostovic-Srzentic, M., and Krsnik, Z. (2021). Fundamentals of the development of connectivity in the human fetal

brain in late gestation: from 24 weeks gestational age to term. *J. Neuropathol. Exp. Neurol.* 80, 393–414. doi: 10.1093/jnen/nlab024

Kummer, M., Kirmse, K., Zhang, C., Haueisen, J., Witte, O. W., and Holthoff, K. (2016). Column-like Ca(2+) clusters in the mouse neonatal neocortex revealed by three-dimensional two-photon Ca(2+) imaging *in vivo*. *Neuroimage* 138, 64–75. doi: 10.1016/j.neuroimage.2016.05.050

Leighton, A. H., Cheyne, J. E., Houwen, G. J., Maldonado, P. P., De Winter, F., Levelt, C. N., et al. (2021). Somatostatin interneurons restrict cell recruitment to retinally driven spontaneous activity in the developing cortex. *Cell Rep.* 36:109316. doi: 10.1016/j.celrep.2021.109316

Leighton, A. H., and Lohmann, C. (2016). The wiring of developing sensory circuits-from patterned spontaneous activity to synaptic plasticity mechanisms. *Front. Neural Circuits* 10:71. doi: 10.3389/fncir.2016.00071

Li, H., Fertuzinhos, S., Mohns, E., Hnasko, T. S., Verhage, M., Edwards, R., et al. (2013). Laminar and columnar development of barrel cortex relies on thalamocortical neurotransmission. *Neuron* 79, 970–986. doi: 10.1016/j.neuron.2013.06.043

Linden, N. J., Tabuena, D. R., Steinmetz, N. A., Moody, W. J., Brunton, S. L., and Brunton, B. W. (2021). Go with the FLOW: visualizing spatiotemporal dynamics in optical widefield calcium imaging. *J. R. Soc. Interface* 18:20210523. doi: 10.1098/rsif.2021.0523

Lombardi, A., Jedlicka, P., Luhmann, H. J., and Kilb, W. (2021). Coincident glutamatergic depolarizations enhance GABAA receptor-dependent Cl- influx in mature and suppress Cl- efflux in immature neurons. *PLoS Comput. Biol.* 17:e1008573. doi: 10.1371/journal.pcbi.1008573

López-Bendito, G. (2018). Development of the thalamocortical interactions: past, present and future. *Neuroscience* 385, 67–74. doi: 10.1016/j.neuroscience.2018.06.020

Luhmann, H. J., and Fukuda, A. (2020). Can we understand human brain development from experimental studies in rodents? *Pediatr. Int.* 62, 1139–1144. doi: 10.1111/ped.14339

Luhmann, H. J., and Khazipov, R. (2018). Neuronal activity patterns in the developing barrel cortex. *Neuroscience* 368, 256–267. doi: 10.1016/j.neuroscience.2017.05.025

Luhmann, H. J., Kirischuk, S., and Kilb, W. (2018). The superior function of the subplate in early neocortical development. *Front. Neuroanat.* 12:97. doi: 10.3389/fnana.2018.00097

Luhmann, H. J., Sinning, A., Yang, J. W., Reyes-Puerta, V., Stüttgen, M. C., Kirischuk, S., et al. (2016). Spontaneous neuronal activity in developing neocortical networks: from single cells to large-scale interactions. *Front. Neural Circuits* 10:40. doi: 10.3389/fncir.2016.00040

Luo, T. Z., Bondy, A. G., Gupta, D., Elliott, V. A., Kopec, C. D., and Brody, C. D. (2020). An approach for long-term, multi-probe Neuropixels recordings in unrestrained rats. *Elife* 9:e59716. doi: 10.7554/eLife.59716

Magno, L., Asgarian, Z., Pendolino, V., Velona, T., Mackintosh, A., Lee, F., et al. (2021). Transient developmental imbalance of cortical interneuron subtypes presages long-term changes in behavior. *Cell Rep.* 35:109249. doi: 10.1016/j.celrep.2021.109249

Malyshevskaya, O., Shiraishi, Y., Kimura, F., and Yamamoto, N. (2013). Role of electrical activity in horizontal axon growth in the developing cortex: a time-lapse study using optogenetic stimulation. *PLoS ONE* 8:e82954. doi: 10.1371/journal.pone.0082954

Marques-Smith, A., Lyngholm, D., Kaufmann, A. K., Stacey, J. A., Hoerder-Suabedissen, A., Becker, E. B. E., et al. (2016). A transient translaminar GABAergic interneuron circuit connects thalamocortical recipient layers in neonatal somatosensory cortex. *Neuron* 89, 536–549. doi: 10.1016/j.neuron.2016.01.015

Martini, F. J., Guillamon-Vivancos, T., Moreno-Juan, V., Valdeolmillos, M., and López-Bendito, G. (2021). Spontaneous activity in developing thalamic and cortical sensory networks. *Neuron* 109, 2519–2534. doi: 10.1016/j.neuron.2021.06.026

Mechawar, N., and Descarries, L. (2001). The cholinergic innervation develops early and rapidly in the rat cerebral cortex: a quantitative immunocytochemical study. *Neuroscience* 108, 555–567. doi: 10.1016/S0306-4522(01)00389-X

Meng, X., Solarana, K., Bowen, Z., Liu, J., Nagode, D. A., Sheikh, A., et al. (2020). Transient subgranular hyperconnectivity to L2/3 and enhanced pairwise correlations during the critical period in the mouse auditory cortex. *Cereb. Cortex* 30, 1914–1930. doi: 10.1093/cercor/bhz213

Milh, M., Kaminska, A., Huon, C., Lapillonne, A., Ben-Ari, Y., and Khazipov, R. (2007). Rapid cortical oscillations and early motor activity in premature human neonate. *Cereb. Cortex* 17, 1582–1594. doi: 10.1093/cercor/bhl069

Minlebaev, M., Colonnese, M., Tsintsadze, T., Sirota, A., and Khazipov, R. (2011). Early gamma oscillations synchronize developing thalamus and cortex. *Science* 334, 226–229. doi: 10.1126/science.1210574

Mizuno, H., Ikezoe, K., Nakazawa, S., Sato, T., Kitamura, K., and Iwasato, T. (2018). Patchwork-type spontaneous activity in neonatal barrel cortex layer 4 transmitted via thalamocortical projections. *Cell Rep.* 22, 123–135. doi: 10.1016/j.celrep.2017.12.012

Modol, L., Bollmann, Y., Tressard, T., Baude, A., Che, A., Duan, Z. R. S., et al. (2020). Assemblies of perisomatic GABAergic neurons in the developing barrel cortex. *Neuron* 105, 93–105e104. doi: 10.1016/j.neuron.2019.10.007

Moghadam, S. M., Pinchefsky, E., Tse, I., Marchi, V., Kohonen, J., Kauppila, M., et al. (2021). Building an open source classifier for the neonatal EEG background: a systematic feature-based approach from expert scoring to clinical visualization. *Front. Hum. Neurosci.* 15:675154. doi: 10.3389/fnhum.2021.675154

Mojtahedi, N., Kovalchuk, Y., Bottcher, A., and Garaschuk, O. (2021). Stable behavioral state-specific large scale activity patterns in the developing cortex of neonates. *Cell Calcium* 98:102448. doi: 10.1016/j.ceca.2021.102448

Molnár, Z., Luhmann, H. J., and Kanold, P. O. (2020). Transient cortical circuits match spontaneous and sensory-driven activity during development. *Science* 370:eabb2153. doi: 10.1126/science.abb2153

Moreno-Juan, V., Filipchuk, A., Anton-Bolanos, N., Mezzera, C., Gezelius, H., Andres, B., et al. (2017). Prenatal thalamic waves regulate cortical area size prior to sensory processing. *Nat. Commun.* 8:14172. doi: 10.1038/ncomms14172

Mukherjee, D., Yonk, A. J., Sokoloff, G., and Blumberg, M. S. (2017). Wakefulness suppresses retinal wave-related neural activity in visual cortex. *J. Neurophysiol.* 118, 1190–1197. doi: 10.1152/jn.00264.2017

Murata, Y., and Colonnese, M. T. (2020). GABAergic interneurons excite neonatal hippocampus *in vivo*. *Sci. Adv.* 6:eaba1430. doi: 10.1126/sciadv.aba1430

Niculescu, D., and Lohmann, C. (2014). Gap junctions in developing thalamic and neocortical neuronal networks. *Cereb. Cortex* 24, 3097–3106. doi: 10.1093/cercor/bht175

Omidvarnia, A., Fransson, P., Metsaranta, M., and Vanhatalo, S. (2014). Functional bimodality in the brain networks of preterm and term human newborns. *Cereb. Cortex* 24, 2657–2668. doi: 10.1093/cercor/bht120

Panzera, L. C., and Hoppa, M. B. (2019). Genetically encoded voltage indicators are illuminating subcellular physiology of the axon. *Front. Cell. Neurosci.* 13:52. doi: 10.3389/fncel.2019.00052

Peng, H., Xie, P., Liu, L., Kuang, X., Wang, Y., Qu, L., et al. (2021). Morphological diversity of single neurons in molecularly defined cell types. *Nature* 598, 174–181. doi: 10.1038/s41586-021-03941-1

Peng, Y., Mittermaier, F. X., Planert, H., Schneider, U. C., Alle, H., and Geiger, J. R. P. (2019). High-throughput microcircuit analysis of individual human brains through next-generation multineuron patch-clamp. *Elife* 8:e48178. doi: 10.7554/eLife.48178

Pereda, A. E. (2014). Electrical synapses and their functional interactions with chemical synapses. *Nat. Rev. Neurosci.* 15, 250–263. doi: 10.1038/nrn3708

Perez, J. D., Dieck, S. T., Alvarez-Castelao, B., Tushev, G., Chan, I. C., and Schuman, E. M. (2021). Subcellular sequencing of single neurons reveals the dendritic transcriptome of GABAergic interneurons. *Elife* 10:e63092. doi: 10.7554/eLife.63092

Perez-Prieto, N., and Delgado-Restituto, M. (2021). Recording strategies for high channel count, densely spaced microelectrode arrays. *Front. Neurosci.* 15:681085. doi: 10.3389/fnins.2021.681085

Petersen, C. C. H. (2017). Whole-cell recording of neuronal membrane potential during behavior. *Neuron* 95, 1266–1281. doi: 10.1016/j.neuron.2017.06.049

Picardo, M. A., Guigue, P., Bonifazi, P., Batista-Brito, R., Allene, C., Ribas, A., et al. (2011). Pioneer GABA cells comprise a subpopulation of hub neurons in the developing hippocampus. *Neuron* 71, 695–709. doi: 10.1016/j.neuron.2011.06.018

Ren, C., and Komiyama, T. (2021). Characterizing cortex-wide dynamics with wide-field calcium imaging. *J. Neurosci.* 41, 4160–4168. doi: 10.1523/JNEUROSCI.3003-20.2021

Richter, L. M., and Gjorgjieva, J. (2017). Understanding neural circuit development through theory and models. *Curr. Opin. Neurobiol.* 46, 39–47. doi: 10.1016/j.conb.2017.07.004

Riva, M., Genescu, I., Habermacher, C., Orduz, D., Ledonne, F., Rijli, F. M., et al. (2019). Activity-dependent death of transient Cajal-Retzius neurons is required for functional cortical wiring. *Elife* 8:e50503. doi: 10.7554/eLife.50503

Rochefort, N. L., Garaschuk, O., Milos, R. I., Narushima, M., Marandi, N., Pichler, B., et al. (2009). Sparsification of neuronal activity in the visual cortex at eye-opening. *Proc. Natl. Acad. Sci. U.S.A.* 106, 15049–15054. doi: 10.1073/pnas.0907660106

Roth, B. L. (2016). DREADDs for neuroscientists. *Neuron* 89, 683–694. doi: 10.1016/j.neuron.2016.01.040

Rupprecht, P., Carta, S., Hoffmann, A., Echizen, M., Blot, A., Kwan, A. C., et al. (2021). A database and deep learning toolbox for noise-optimized, generalized spike inference from calcium imaging. *Nat. Neurosci.* 24, 1324–1337. doi: 10.1101/2020.08.31.272450

Sakry, D., Neitz, A., Singh, J., Frischknecht, R., Marongiu, D., Biname, F., et al. (2014). Oligodendrocyte precursor cells modulate the neuronal network by activity-dependent ectodomain cleavage of glial NG2. *PLoS Biol.* 12:e1001993. doi: 10.1371/journal.pbio.1001993

Scala, F., Kobak, D., Bernabucci, M., Bernaerts, Y., Cadwell, C. R., Castro, J. R., et al. (2021). Phenotypic variation of transcriptomic cell types in mouse motor cortex. *Nature* 598, 144–150. doi: 10.1038/s41586-020-2907-3

Schafer, D. P., Lehrman, E. K., and Stevens, B. (2013). The "quad-partite" synapse: microglia-synapse interactions in the developing and mature CNS. *Glia* 61, 24–36. doi: 10.1002/glia.22389

Segarra, M., Aburto, M. R., Cop, F., Llao-Cid, C., Hartl, R., Damm, M., et al. (2018). Endothelial Dab1 signaling orchestrates neuro-glia-vessel communication in the central nervous system. *Science* 361:eaao2861. doi: 10.1126/science.aao2861

Shen, J., and Colonnese, M. T. (2016). Development of activity in the mouse visual cortex. *J. Neurosci.* 36, 12259–12275. doi: 10.1523/JNEUROSCI.1903-16.2016

Shenoy, K. V., and Kao, J. C. (2021). Measurement, manipulation and modeling of brain-wide neural population dynamics. *Nat. Commun.* 12:633. doi: 10.1038/s41467-020-20371-1

Siegle, J. H., Ledochowitsch, P., Jia, X., Millman, D. J., Ocker, G. K., Caldejon, S., et al. (2021). Reconciling functional differences in populations of neurons recorded with two-photon imaging and electrophysiology. *Elife* 10:e69068. doi: 10.7554/eLife.69068

Steinmetz, N. A., Zatka-Haas, P., Carandini, M., and Harris, K. D. (2019). Distributed coding of choice, action and engagement across the mouse brain. *Nature* 576, 266–273. doi: 10.1038/s41586-019-1787-x

Steriade, M. (2001a). Impact of network activities on neuronal properties in corticothalamic systems. *J. Neurophysiol.* 86, 1–39. doi: 10.1152/jn.2001.86.1.1

Steriade, M. (2001b). *The Intact and Sliced Brain*. Cambridge: MIT Press. doi: 10.7551/mitpress/3822.001.0001

Stjerna, S., Voipio, J., Metsaranta, M., Kaila, K., and Vanhatalo, S. (2012). Preterm EEG: a multimodal neurophysiological protocol. *J. Visual. Exp.* 18:3774. doi: 10.3791/3774

Su, X., Chen, J. J., Liu, L. Y., Huang, Q., Zhang, L. Z., Li, X. Y., et al. (2017). Neonatal CX26 removal impairs neocortical development and leads to elevated anxiety. *Proc. Natl. Acad. Sci. U.S.A.* 114, 3228–3233. doi: 10.1073/pnas.1613237114

Takasaki, K. T., Tsyboulski, D., and Waters, J. (2019). Dual-plane 3-photon microscopy with remote focusing. *Biomed. Opt. Express* 10, 5585–5599. doi: 10.1364/BOE.10.005585

Tang, Q. S., Brecht, M., and Burgalossi, A. (2014). Juxtacellular recording and morphological identification of single neurons in freely moving rats. *Nat. Protoc.* 9, 2369–2381. doi: 10.1038/nprot.2014.161

Tischbirek, C. H., Birkner, A., and Konnerth, A. (2017). *In vivo* deep two-photon imaging of neural circuits with the fluorescent Ca2+ indicator Cal-590. *J. Physiol.* 595, 3097–3105. doi: 10.1113/JP272790

Tokariev, A., Roberts, J. A., Zalesky, A., Zhao, X., Vanhatalo, S., Breakspear, M., et al. (2019). Large-scale brain modes reorganize between infant sleep states and carry prognostic information for preterms. *Nat. Commun.* 10:2619. doi: 10.1038/s41467-019-10467-8

Tolner, E. A., Sheikh, A., Yukin, A. Y., Kaila, K., and Kanold, P. O. (2012). Subplate neurons promote spindle bursts and thalamocortical patterning in the neonatal rat somatosensory cortex. *J. Neurosci.* 32, 692–702. doi: 10.1523/JNEUROSCI.1538-11.2012

Traub, R. D., Bibbig, A., LeBeau, F. E., Buhl, E. H., and Whittington, M. A. (2004). Cellular mechanisms of neuronal population oscillations in the hippocampus *in vitro*. *Annu. Rev. Neurosci.* 27, 247–278. doi: 10.1146/annurev.neuro.27.070203.144303

Tritsch, N. X., Yi, E., Gale, J. E., Glowatzki, E., and Bergles, D. E. (2007). The origin of spontaneous activity in the developing auditory system. *Nature* 450, 50–55. doi: 10.1038/nature06233

Trujillo, C. A., Gao, R., Negraes, P. D., Gu, J., Buchanan, J., Preissl, S., et al. (2019). Complex oscillatory waves emerging from cortical organoids model early human brain network development. *Cell Stem Cell* 25, 558–569 e557. doi: 10.1016/j.stem.2019.08.002

Tuncdemir, S. N., Wamsley, B., Stam, F. J., Osakada, F., Goulding, M., Callaway, E. M., et al. (2016). Early somatostatin interneuron connectivity mediates the maturation of deep layer cortical circuits. *Neuron* 89, 521–535. doi: 10.1016/j.neuron.2015.11.020

Uhlen, P., Fritz, N., Smedler, E., Malmersjo, S., and Kanatani, S. (2015). Calcium signaling in neocortical development. *Dev. Neurobiol.* 75, 360–368. doi: 10.1002/dneu.22273

Valeeva, G., Tressard, T., Mukhtarov, M., Baude, A., and Khazipov, R. (2016). An optogenetic approach for investigation of excitatory and inhibitory network GABA actions in mice expressing Channelrhodopsin-2 in GABAergic neurons. *J. Neurosci.* 36, 5961–5973. doi: 10.1523/JNEUROSCI.3482-15.2016

Valiullina, F., Akhmetshina, D., Nasretdinov, A., Mukhtarov, M., Valeeva, G., Khazipov, R., et al. (2016). Developmental changes in electrophysiological properties and a transition from electrical to chemical coupling between excitatory layer 4 neurons in the rat barrel cortex. *Front. Neural Circuits* 10:1. doi: 10.3389/fncir.2016.00001

van der Bourg, A., Yang, J. W., Reyes-Puerta, V., Laurenczy, B., Wieckhorst, M., Stüttgen, M. C., et al. (2017). Layer-specific refinement of sensory coding in developing mouse barrel cortex. *Cereb. Cortex* 27, 4835–4850. doi: 10.1093/cercor/bhw280

Vanhatalo, S., and Kaila, K. (2006). Development of neonatal EEG activity: from phenomenology to physiology. *Semin. Fetal Neonatal Med.* 11, 471–478. doi: 10.1016/j.siny.2006.07.008

Virtanen, M. A., Uvarov, P., Hübner, C. A., and Kaila, K. (2020). NKCC1, an elusive molecular target in brain development: making sense of the existing data. *Cells* 9:2607. doi: 10.3390/cells9122607

Virtanen, M. A., Uvarov, P., Mavrovic, M., Poncer, J. C., and Kaila, K. (2021). The multifaceted roles of KCC2 in cortical development. *Trends Neurosci.* 44, 378–392. doi: 10.1016/j.tins.2021.01.004

Vormstein-Schneider, D., Lin, J. D., Pelkey, K. A., Chittajallu, R., Guo, B., Arias-Garcia, M. A., et al. (2020). Viral manipulation of functionally distinct interneurons in mice, non-human primates and humans. *Nat. Neurosci.* 23, 1629–1636. doi: 10.1101/808170

Wake, H., Ortiz, F. C., Woo, D. H., Lee, P. R., Angulo, M. C., and Fields, R. D. (2015). Nonsynaptic junctions on myelinating glia promote preferential myelination of electrically active axons. *Nature Commun.* 6:7844. doi: 10.1038/ncomms8844

Wang, C. Z., Ma, J., Xu, Y. Q., Jiang, S. N., Chen, T. Q., Yuan, Z. L., et al. (2019). Early-generated interneurons regulate neuronal circuit formation during early postnatal development. *Elife* 8:e44649. doi: 10.7554/eLife.44649

Wang, H. C., Lin, C. C., Cheung, R., Zhang-Hooks, Y., Agarwal, A., Ellis-Davies, G., et al. (2015). Spontaneous activity of cochlear hair cells triggered by fluid secretion mechanism in adjacent support cells. *Cell* 163, 1348–1359. doi: 10.1016/j.cell.2015.10.070

Wang, X., Lou, N., Xu, Q., Tian, G. F., Peng, W. G., Han, X., et al. (2006). Astrocytic Ca2+ signaling evoked by sensory stimulation *in vivo*. *Nat. Neurosci.* 9, 816–823. doi: 10.1038/nn1703

Watanabe, M., and Fukuda, A. (2015). Development and regulation of chloride homeostasis in the central nervous system. *Front. Cell. Neurosci.* 9:371. doi: 10.3389/fncel.2015.00371

Weissman, T. A., Riquelme, P. A., Ivic, L., Flint, A. C., and Kriegstein, A. R. (2004). Calcium waves propagate through radial glial cells and modulate proliferation in the developing neocortex. *Neuron* 43, 647–661. doi: 10.1016/j.neuron.2004.08.015

West, A. E., Chen, W. G., Dalva, M. B., Dolmetsch, R. E., Kornhauser, J. M., Shaywitz, A. J., et al. (2001). Calcium regulation of neuronal gene expression. *Proc. Natl. Acad. Sci. U.S.A.* 98, 11024–11031. doi: 10.1073/pnas.191352298

Whiteus, C., Freitas, C., and Grutzendler, J. (2013). Perturbed neural activity disrupts cerebral angiogenesis during a postnatal critical period. *Nature* 505, 407–411. doi: 10.1038/nature12821

Yang, J. W., An, S., Sun, J. J., Reyes-Puerta, V., Kindler, J., Berger, T., et al. (2013). Thalamic network oscillations synchronize ontogenetic columns in the newborn rat barrel cortex. *Cereb. Cortex* 23, 1299–1316. doi: 10.1093/cercor/bhs103

Yang, J. W., Hanganu-Opatz, I. L., Sun, J. J., and Luhmann, H. J. (2009). Three patterns of oscillatory activity differentially synchronize developing neocortical networks *in vivo*. *J. Neurosci.* 29, 9011–9025. doi: 10.1523/JNEUROSCI.5646-08.2009

Yang, W., and Yuste, R. (2017). *In vivo* imaging of neural activity. *Nat. Methods* 14, 349–359. doi: 10.1038/nmeth.4230

Yao, X. H., Wang, M., He, X. N., He, F., Zhang, S. Q., Lu, W., et al. (2016). Electrical coupling regulates layer 1 interneuron microcircuit formation in the neocortex. *Nat. Commun.* 7:12229. doi: 10.1038/ncomms12229

Yao, Z., Liu, H., Xie, F., Fischer, S., Adkins, R. S., Aldridge, A. I., et al. (2021). A transcriptomic and epigenomic cell atlas of the mouse primary motor cortex. *Nature* 598, 103–110. doi: 10.1038/s41586-021-03500-8

Yu, Y. C., He, S. J., Chen, S., Fu, Y. H., Brown, K. N., Yao, X. H., et al. (2012). Preferential electrical coupling regulates neocortical lineage-dependent microcircuit assembly. *Nature* 486, 113–U139. doi: 10.1038/nature10958

Yuryev, M., Andriichuk, L., Leiwe, M., Jokinen, V., Carabalona, A., and Rivera, C. (2018). *In vivo* two-photon imaging of the embryonic cortex reveals spontaneous ketamine-sensitive calcium activity. *Sci. Rep.* 8:16059. doi: 10.1038/s41598-018-34410-x

Zhang, L., Liang, B., Barbera, G., Hawes, S., Zhang, Y., Stump, K., et al. (2019). Miniscope GRIN lens system for calcium imaging of neuronal activity from deep brain structures in behaving animals. *Curr. Protoc. Neurosci.* 86:e56. doi: 10.1002/cpns.56

Zhang, X. J., Li, Z., Han, Z., Sultan, K. T., Huang, K., and Shi, S. H. (2017). Precise inhibitory microcircuit assembly of developmentally related neocortical interneurons in clusters. *Nat. Commun.* 8:16091. doi: 10.1038/ncomms16091

Zhang, Y., Rózsa, M., Liang, Y., Bushey, D., Wei, Z., Zheng, J., et al. (2021). Fast and sensitive GCaMP calcium indicators for imaging neural populations. *BioRxiv* PPR417430. doi: 10.1101/2021.11.08.467793

Zuchero, J. B., and Barres, B. A. (2013). Intrinsic and extrinsic control of oligodendrocyte development. *Curr. Opin. Neurobiol.* 23, 914–920. doi: 10.1016/j.conb.2013.06.005

Conflict of Interest: The author declares that the research was conducted in the absence of any commercial or financial relationships that could be construed as a potential conflict of interest.

Publisher's Note: All claims expressed in this article are solely those of the authors and do not necessarily represent those of their affiliated organizations, or those of the publisher, the editors and the reviewers. Any product that may be evaluated in this article, or claim that may be made by its manufacturer, is not guaranteed or endorsed by the publisher.

frontiers in Cellular Neuroscience

ORIGINAL RESEARCH
published: 07 February 2022
doi: 10.3389/fncel.2022.827628

Long-Term Cultures of Spinal Cord Interneurons

*Ingrid Vargova[1,2], Jan Kriska[3], Jessica C. F. Kwok[4,5], James W. Fawcett[4,6] and Pavla Jendelova[1,2]**

[1] Department of Neuroregeneration, Institute of Experimental Medicine, Czech Academy of Sciences, Prague, Czechia, [2] Second Faculty of Medicine, Charles University, Prague, Czechia, [3] Department of Cellular Neurophysiology, Institute of Experimental Medicine, Czech Academy of Sciences, Prague, Czechia, [4] The Center for Reconstructive Neuroscience, Institute of Experimental Medicine, Czech Academy of Sciences, Prague, Czechia, [5] Faculty of Biological Sciences, University of Leeds, Leeds, United Kingdom, [6] John van Geest Centre for Brain Repair, Department of Clinical Neurosciences, University of Cambridge, Cambridge, United Kingdom

Spinal cord interneurons (SpINs) are highly diverse population of neurons that play a significant role in circuit reorganization and spontaneous recovery after spinal cord injury. Regeneration of SpIN axons across rodent spinal injuries has been demonstrated after modification of the environment and neurotrophin treatment, but development of methods to enhance the intrinsic regenerative ability of SpINs is needed. There is a lack of described *in vitro* models of spinal cord neurons in which to develop new regeneration treatments. For this reason, we developed a new model of mouse primary spinal cord neuronal culture in which to analyze maturation, morphology, physiology, connectivity and regeneration of identified interneurons. Isolated from E14 mice, the neurons mature over 15 days *in vitro*, demonstrated by expression of maturity markers, electrophysiological patch-clamp recordings, and formation of synapses. The neurons express markers of SpINs, including Tlx3, Lmx1b, Lbx1, Chx10, and Pax2. The neurons demonstrate distinct morphologies and some form perineuronal nets in long-term cultivation. Live neurons in various maturation stages were axotomized, using a 900 nm multiphoton laser and their fate was observed overnight. The percentage of axons that regenerated declined with neuronal maturity. This model of SpINs will be a valuable tool in future regenerative, developmental, and functional studies alongside existing models using cortical or hippocampal neurons.

Keywords: spinal interneurons, culture, maturation, axon regeneration, laser axotomy

OPEN ACCESS

Edited by:
Daniela Tropea,
Trinity College Dublin, Ireland

Reviewed by:
Kai Liu,
Hong Kong University of Science and Technology, Hong Kong SAR, China
Kirsten Haastert-Talini,
Hannover Medical School, Germany

****Correspondence:***
Pavla Jendelova
pavla.jendelova@iem.cas.cz

Specialty section:
This article was submitted to Cellular Neurophysiology, a section of the journal Frontiers in Cellular Neuroscience

Received: *02 December 2021*
Accepted: *12 January 2022*
Published: *07 February 2022*

Citation:
Vargova I, Kriska J, Kwok JCF, Fawcett JW and Jendelova P (2022) Long-Term Cultures of Spinal Cord Interneurons. Front. Cell. Neurosci. 16:827628. doi: 10.3389/fncel.2022.827628

INTRODUCTION

The intrinsic regeneration capacity of mature mammalian central nervous system (CNS) is poor. This makes spinal cord injury (SCI) a detrimental condition that represents one of the major causes of disability, and treatment possibilities are limited. However, continued research in the field has led to an increased understanding of the causes of the regeneration failure, which if appropriately modulated, can be used for treatment of the SCI. The extracellular environment of the CNS is not favorable for axon outgrowth due to production of growth-inhibiting molecules such as NogoA and CSPGs from glial scars surrounding the damaged tissue (Shen et al., 2009; Schwab and Strittmatter, 2014; Uyeda and Muramatsu, 2020), and there is a lack of some necessary growth factors that provide trophic support for neurons and act as chemoattractants for axons (Blesch et al., 2012; Anderson et al., 2018). Another important limiting factor is the intrinsic loss of regenerative ability

in CNS neurons that comes with neuronal maturation. Various factors contribute to this loss of regeneration, including failure of CNS neurons to activate appropriate transcriptional, translational and epigenetic programs at appropriate subcellular locations that would enable axon growth after injury (van Niekerk et al., 2016; Petrova et al., 2021), changes in axonal transport that exclude growth-related molecules from mature axons and decreased signaling in some pathways. A high level of intrinsic regeneration ability is present in immature neurons but ceases abruptly with maturation (Nicholls and Saunders, 1996; Lu et al., 2014; Koseki et al., 2017).

Maturation and aging in the CNS involve complex and numerous pathways, so it is challenging to study their effect on the regeneration ability of neurons *in vivo*. *In vitro* models, on the other hand, can offer a wide variety of tools to study individual neuronal cell types, to regulate and describe neuronal behavior, and to uncover molecular pathways relating to development and regeneration of neurons (Abu-Rub et al., 2010; Franssen et al., 2015). Therefore, describing axon growth inhibition mechanisms *in vitro* is a valuable approach that could lead to further comprehension of the limits of CNS regeneration and subsequently to discovery of new therapeutic avenues. Various *in vitro* models have been established to explore CNS axon regeneration. These include primary cell cultures created by dissociating neural tissue from animals at various ages (Donaldson and Höke, 2014). Dorsal root ganglia (DRGs) (Cheah et al., 2016), hippocampal (Kaech and Banker, 2006; Moore et al., 2009), and cortical cultures (Koseki et al., 2017) are among the most commonly used models. Primary spinal cord cultures have been described as well (Thomson et al., 2008; Eldeiry et al., 2017), but their application in axon regeneration studies has so far been limited. Investigation of the regenerative capacity of spinal interneurons (SpINs) is of particular interest, as it was shown, that less severe, anatomically incomplete SCI can result in partial recovery that follows after spontaneous reorganization of neural circuits (Bareyre et al., 2004; Martinez et al., 2012), and growth of spinal interneuron neurites across mouse spinal injuries can be stimulated by treatments to enhance neuronal regenerative ability, astrocyte permissiveness and axonal chemoattraction (Anderson et al., 2016). Key components of neuroplasticity in these incomplete lesions are SpINs, as they form alternative routes to convey information between cells above and below the lesion (Courtine et al., 2008; May et al., 2017).

Here, we describe a robust model of long-term dissociated embryonic spinal cord cultures. During cultivation, neurons in these cultures form synapses, acquire mature electrical properties and markers of mature neurons, lose regenerative capacity, and express markers of SpINs. The culture model will be valuable for future developmental, functional as well as axonal regeneration studies.

MATERIALS AND METHODS

Cell Culture

The method of generating mature spinal cord neurons was based on previously published methods for culturing spinal cord (Thomson et al., 2008), hippocampal and cortical neurons (Barbati et al., 2013; Koseki et al., 2017; Petrova et al., 2020), with modifications. Spinal neurons were isolated from E13.5-E14.5 embryos of the C57BL/6J mice. Spinal cords were dissected from embryos immersed in a cold Hibernate-E medium (Gibco, Thermo Fisher). The meninges were removed, and tissue was stored over ice in Hibernate-E (Gibco, Thermo Fisher). The collected tissue was washed with 1 ml of HBSS without Ca^{2+} or Mg^{2+} (Gibco, Thermo Fisher) two times. Next, the tissue was digested in papain-based Neuron Isolation Enzyme (Thermo Scientific^{TM} Pierce) by adding 30 μl of enzyme solution per 1 spinal cord for 9 min at 37°C. After digestion, the enzyme was carefully removed, and the tissue was placed in disruption medium 1 (DM1) (**Table 1**). Tissue was disrupted by trituration with P1000 tip and left to settle for 2 min. The supernatant was transferred to a new tube, while the tissue pellet was triturated again in disruption medium 2 (DM2) (**Table 1**). This step was repeated once more if any tissue fragments remained after the second disruption. Supernatant containing disrupted tissue was transferred by a polished Pasteur pipette into a new falcon tube through a 40 μm cell strainer to remove undisrupted tissue fragments. Plating medium (PM) (**Table 1**) was added in a 1:1 ratio to the filtered solution containing the cells. The cell suspension was centrifuged for 5 min at 90 *g* at 37°C, the supernatant was removed, and the pellet was resuspended in 2 ml of PM. Then, the cells were counted (approximate expected amount is 1.2 million cells per spinal cord) and plated on glass coated with 100 μg/ml poly-D-lysine (Thermo Fisher) dissolved in pH 8.6 borate buffer. The cells were cultured either in a 24-well plate on sterilized 12 mm borosilicate glass coverslips (Karl Hecht), or glass-bottom 10-well CELLview^{TM} Cell Culture Slides (Greiner). The optimal plating density of dissociated spinal cord cells in our cultures was around 93,000 cells/cm^2. The best plating method that resulted in evenly distributed cells on the coverslips, was to dilute the dissociated cells in PM to a final concentration of 500,000 cells/ml and then add 350 μl of cell suspension into 24-well plate, or 80 μl into 10-well cell culture slide. After 1 h, most of the cells adhered to the coverslips, and cultivation medium (CM) was added to the PM in 1:1 proportion, but not before some of the PM was discarded. Final media volume used for cultivation in the 24-well plate was 500 μl and in the 10-well cell culture slide, it was 150 μl. Cultures were maintained by exchanging 1/2 of the media volume every 2 days. To limit the proliferation of glia, CM with the ITS+ supplement was replaced with CM without ITS+ after 7 days of culture. Importantly, we were able to maintain the cultures for 72 days.

Plasmid Transfection

Cultures were transfected with CAG-GFP plasmid using NeuroMag magnetofection (OZ Biosciences) at DIV3. The CM was removed from the wells, stored, and replaced with 80% of regular cultivation volume of unsupplemented MACS Neuro Medium (Miltenyi Biotech). An appropriate amount of DNA plasmid was mixed with magnetic beads in OptiMEM medium (Gibco, Thermo Fisher) and incubated for 15 min at room temperature (RT), facilitating the binding reaction. The amount of reagents used for the transfection depended on the

TABLE 1 | Media compositions used for preparation and maintaining spinal cord cultures.

Medium	Composition	Approximate total volume needed
Disruption medium 1 (DM1)	Hibernate-E (Gibco, Thermo Fisher), 0.8% BSA (Sigma-Aldrich) 100 μg/ml DNase (Sigma-Aldrich)	1 ml
Disruption medium 2 (DM2)	Hibernate-E, 0.4% BSA 20 μg/ml DNase	2 ml
Plating medium (PM)	50% DMEM, low glucose (Gibco, Thermo Fisher) 25% Horse serum (Gibco, Thermo Fisher) 25% HBSS without Ca^{2+} or Mg^{2+} (Gibco, Thermo Fisher) 1% Penicillin-Streptomycin (10,000 U/mL) (Gibco, Thermo Fisher)	30 ml
Cultivation medium (CM)	MACS Neuro Medium (Miltenyi Biotech) 2% NeuroBrew 21 (Miltenyi Biotech) 1% Glutamax (Thermo Fisher) *1% ITS+ (Sigma-Aldrich) 1% Penicillin-Streptomycin	50 ml

**ITS+ was excluded from cultivation media in cultures cultivated for more than 7 days.*

cultivation volume of the particular plate used in experiment. The proportions were calculated according to an optimized 24-well plate protocol, where 0.2 μg of DNA, 0.8 μl of magnetic beads, and 100 μl of OptiMEM were added per well. OptiMEM volume represented 20% of the regular cultivation volume. After the incubation, the mixture was added dropwise into wells with cells and unsupplemented medium. Plates were incubated on top of a strong magnet, purchased along with NeuroMag Starting Kit (OZ Biosciences), for 20 min at 37°C. The magnetic plate was removed and cells were incubated for another 40 min, after which original CM was returned to the wells. GFP was expressed in the culture 24 h after transfection. The conditions of transfection were optimized to attain low-efficacy transfection so that only a few of the cells in the culture expressed GFP and their morphology could be observed.

Immunocytochemistry

Cells were fixed using 4% paraformaldehyde in phosphate-buffered saline (PBS) for 15 min at RT, washed twice, and kept in PBS at 4°C until further use. The staining protocol was started with permeabilization and blocking of the sample using solution containing 10% goat or donkey serum (according to secondary antibodies used) and 0.4% Triton-X in PBS for 1 h at RT with shaking. Next, primary antibodies were diluted in 2% goat serum and 0.1% Triton-X in PBS according to concentrations indicated in **Table 2**. Primary antibodies were incubated with the cells overnight at 4°C with gentle shaking, after which the solution was aspirated and the coverslips were washed twice with PBS. Secondary antibodies, diluted in the same solution as primary antibodies, were incubated with the samples for 1 h at RT. Next, nuclei were stained with DAPI (1/3,000 in PBS) for 5 min. Coverslips were then washed two times with PBS and mounted on microscopy slides with Aqua-Poly/Mount (Polysciences) and kept in the dark at 4°C until imaging.

Microscopy and Image Analysis

Brightfield images of live cultures were captured on a Zeiss Axio Vert.A1 inverted microscope equipped with AxioCam ERc 5s camera.

Fluorescence microscopy of the cultures was done on a LEICA CTR 6500 microscope. Analysis of neuronal and non-neuronal composition of the culture during cultivation was done by counting DAPI+ nuclei and DAPI+ nuclei colocalized with βIII-tubulin-positive cells with Fiji software (Schindelin et al., 2012). Expression of doublecortin (DBC) and neurofilament 70 kDa (NF70) during cultivation was analyzed by measuring the average gray value of captured fluorophore of a random region on coverslips using Fiji software. To define the background signal, the mean gray value was also measured in three random, smaller areas of the analyzed region without apparent signal. Morphological analysis of GFP-transfected neurons was performed using Fiji SNT plugin (Arshadi et al., 2020). Analyzed morphological metrics were: average length of branches, cable length, number of branches, axonal length, number of axonal branch points, length of axonal branches, average dendrite length, cable length of dendrites, and number of dendrites. Axons and dendrites were identified by morphologic norms established by Kaech and Banker (2006).

Confocal microscopy images were captured on a Zeiss LSM 880 Airyscan inverted microscope. Confocal images were used for presynaptic and postsynaptic marker colocalization analysis as well as spinal cord neuronal markers visualization. A Z-stack of images with 0.5 μm thickness increment was captured in random regions of the coverslip. Maximum frontal orthogonal projection of the Z-stack made in ZEN 3.1 (blue edition) was used for colocalization analysis. Synapses were counted using Puncta Analyzer v2.0, a Fiji plugin written by Bary Wark[1].

Laser Axotomy

Cells cultured on Greiner Bio-One CELLview^{TM} Cell Culture Slides, transfected with GFP plasmid at DIV3, were kept in the microscope incubation chamber at 37°C and 5% CO_2. After finding regions of interest, cells were captured before cutting using Carl Zeiss AxioObserver.Z1 microscope with confocal module LSM 880 NLO. Objective LD LCI Plan-Apochromat 25x/0.8 Imm Corr DIC M27 with oil immersion was used in the experiment. Next, axotomy was performed using a Ti: Sapphire femtosecond laser Chameleon Ultra II (Coherent), set at 900 nm. The cut was achieved by scanning a 3.4 μm long line across the axon, approximately 250 μm (253.8 ± 75.160 μm) from the cell body, in line-scan mode repeatedly 100–200 times, using 80–100% of the laser power. Axons were identified by morphologic norms established by Kaech and Banker (2006). Cells were then scanned every 30 min for 14 h to observe the post-axotomy response. Images were analyzed using ZEN 3.1 (blue edition) (Carl Zeiss Microscopy GmbH) and Fiji.

[1]https://github.com/physion/puncta-analyzer

Electrophysiological Recordings

The patch-clamp technique in the whole-cell configuration was used to evaluate the cell membrane properties of neurons. Micropipettes with a tip resistance of approximately 10 MΩ were made of borosilicate glass using a P-97 Flaming/Brown micropipette puller (Sutter Instruments) and filled with intracellular solution (0.5 mM $CaCl_2$, 130 mM KCl, 2 mM $MgCl_2$, 3 mM ATP, 5 mM EGTA, and 10 mM HEPES with pH 7.2). Coverslips with the cultures were placed on the recording chamber of an upright Axioskop microscope (Zeiss), equipped with a high-resolution AxioCam HR digital camera (Zeiss) and electronic micromanipulators (Luigs and Neumann). Electrophysiological data were recorded on cells perfused in artificial cerebrospinal fluid (2.7 mM KCl, 135 mM NaCl, 1 mM $MgCl_2$, 2.5 mM $CaCl_2$, 10 mM glucose, 1 mM Na_2HPO_4 and 10 mM HEPES with osmolality 312.5 ± 2.5 mOsmol/kg and pH 7.4). The signals were measured with a 10 kHz sample frequency and amplified with an EPC9 amplifier, controlled by the PatchMaster software (HEKA Elektronik), and filtered using a Bessel filter. Resting membrane potential (E_m) was recorded by switching the EPC9 amplifier to the current-clamp mode. Raw data were processed with the FitMaster software (HEKA Elektronik). Input resistance (IR) was assessed from the current value at 40 ms after the onset of the 50 ms depolarizing pulse from the holding potential of −70 mV to −60 mV. Membrane capacitance (C_m) was determined by Lock-in protocol in the PatchMaster software. To measure the sodium currents (I_{Na+}), neurons were depolarized, and amplitude of the current was recorded at voltage step with the maximal current activation. In order to isolate the Na^+ component only, the time- and voltage-independent currents were subtracted, and the peak value was considered the I_{Na+}. Action potentials (AP) were recorded in the current-clamp mode. The current varied from 50 pA to 1 nA, in 50 pA increments; the pulse duration was 300 ms. Cells that produced at least one AP were considered capable of generating AP.

Statistics

Statistically significant differences between multiple time points during culture cultivation groups were determined by Mann–Whitney test, one-way or two-way ANOVA, followed by Tukey's multiple comparisons *post hoc* test (GraphPad Prism 9 software). Differences were regarded as significant at $p < 0.05$. Graphs were drawn using GraphPad Prism 9 software as means ± standard error of the mean (SEM), while the level of statistical significance was marked as follows: $^*p < 0.05$, $^{**}p < 0.01$, $^{***}p < 0.001$.

RESULTS

The study aimed to establish culture conditions that would enable stable cultivation, maturation, and characterization of spinal cord interneurons isolated from E14 mice embryos. The composition of the culture during cultivation was analyzed using immunocytochemistry; maturity of the neurons was analyzed by immunocytochemistry and patch-clamp, and regenerative capacity of neurons was established by laser axotomy.

Cellular Composition Changes During Cultivation

At day *in vitro* (DIV) 1, cells were attached and started to grow processes (**Figure 1**). Cells formed processes at DIV1, which extended during DIV3 and DIV10. Formation of complex network of processes over the whole culture surface could be seen at DIV17, and more robustly in older cultures at DIV41 and DIV70.

The total number of neurons in spinal cord culture was assessed by counting βIII-tubulin-positive cells per unit area of the fluorescence microscopy images (**Figure 2**). Although the total number of neurons remained stable (**Figure 2E**), the total number of cells, assessed by counting DAPI-stained nuclei in the culture, continued to rise during cultivation (**Figure 2F**). Due to the proliferation of glia, the neuronal fraction of the culture steadily, but significantly, declined from the average of 60.6% at DIV3 to 29.5% at DIV20 (**Figure 2G**). Despite the glial proliferation, long-term cultivation was achieved, with the longest maintained culture surviving past DIV72.

Electrophysiological Properties of Neurons Mature by DIV16

To describe the maturation process of embryonic spinal cord culture on the functional level, electrophysiological properties of neurons were recorded using patch-clamp technique in the whole-cell configuration at four timepoints: DIV2, DIV9, DIV16, and DIV24.

The E_m is considered a general characteristic of mature neurons (Sun et al., 2018). Average E_m of neurons significantly decreased from −55 ± 12.2 mV and −51.1 ± 10 mV at DIV2 and DIV9, respectively, to −59.6 ± 8.8 mV at DIV16 ($p = 0.01$ and $p = 0.006$) and to −59.9 ± 7.1 mV at DIV24 ($p = 0.009$ and $p < 0.001$) (**Figure 3A**), a figure consistent with mature interneurons. No further significant shift in E_m was observed between the neurons cultured for 16 and 24 days.

The IR is inversely proportional to the number of open ion channels and the size of the cell. A decrease in IR has been routinely used as an indicator of maturation of neurons in previous studies (Takazawa et al., 2012; Kopach et al., 2020). The average IR of studied neurons dropped significantly from 1,832 ± 591.7 MΩ at DIV2 to 817 ± 224.7 MΩ at DIV9 ($p = 0.021$) (**Figure 3B**). At later timepoints, IR values of 392.7 ± 111.1 MΩ at DIV16 and 387.3 ± 79.39 MΩ at DIV 24 were not significantly decreased, compared to IR at DIV9.

Cell size increased during development due to growth of the cells, which is why total C_m, a physical quantity directly proportional to the membrane surface area, is a useful tool to assess changes in neuronal maturation in culture (Golowasch et al., 2009). We found that a statistically significant shift in C_m value occurred between DIV2 and DIV9, after which no significant changes ensued (**Figure 3C**). At DIV2, the average C_m was 6.63 ± 0.13 pF while at DIV9, it was 14.77 ± 5.09 pF ($p = 0.042$).

The I_{Na+} plays a significant role in the action potential amplitude and has been reported to change during differentiation of embryonic and human-induced pluripotent stem cells into

TABLE 2 | List of antibodies used for immunocytochemistry.

Primary antibodies			
Immunogen	**Dilution**	**Manufacturer**	**Cat. #**
Chx10	1/100	Santa Cruz	sc-365519
Doublecortin	1/200	Santa Cruz	sc-271390
GDNF Receptor alpha 1	1/100	Abcam	ab8026
Gephyrin	1/500	Synaptic systems	147111
GFP	1/1,000	Thermo Fisher	A10262
Homer 1	1/500	Synaptic systems	160003
Lbx1	1/10,000	Prof. Dr. Carmen Birchmeier-Kohler's lab	
Lmx1b (guinea pig)	1/10,000	Prof. Dr. Carmen Birchmeier-Kohler's lab	
Lmx1b (rabbit)	1/10,000	Prof. Dr. Carmen Birchmeier-Kohler's lab	
Neurofilament 70 kDa	1/400	Sigma-Aldrich	MAB1615
Parvalbumin	1/500	Synaptic systems	195002
PAX2	1/200	Thermo Fisher	71–6,000
PKC γ	1/100	Santa Cruz	sc-166385
Tlx3 (guinea pig)	1/20,000	Prof. Dr. Carmen Birchmeier-Kohler's lab	
Tlx3 (rabbit)	1/10,000	Prof. Dr. Carmen Birchmeier-Kohler's lab	
VGAT	1/500	Synaptic systems	131008
VGLUT 1	1/500	Synaptic systems	135011
WFA	1/500	Sigma-Aldrich	L1516
βIII tubulin	1/1,000	Abcam	ab78078
βIII tubulin	1/1,200	Abcam	ab68193

Secondary antibodies				
Immunogen	**Fluorophore**	**Dilution**	**Manufacturer**	**Cat. #**
Chicken IgY	Alexa Fluor 488	1/200	Thermo Fisher	A-11039
Guinea Pig IgG (H + L)	Alexa Fluor 546	1/200	Thermo Fisher	A-11074
Mouse IgG (H + L)	Alexa Fluor 633	1/200	Thermo Fisher	A-21052
Mouse IgG (H + L)	Alexa Fluor 594	1/200	Thermo Fisher	A-11032
Mouse IgG (H + L)	Alexa Fluor 488	1/200	Thermo Fisher	A-11001
Rabbit IgG (H + L)	Alexa Fluor 594	1/200	Thermo Fisher	A-11012
Rabbit IgG (H + L)	Alexa Fluor 546	1/200	Thermo Fisher	A-11035
Rabbit IgG (H + L)	Alexa Fluor 488	1/200	Thermo Fisher	A-11034
Rabbit IgG (H + L)	Alexa Fluor 405	1/200	Thermo Fisher	A-31556

neuronal cells (Song et al., 2013). At DIV9, neurons in our culture exhibited an average I_{Na+} of −785.4 ± 387.5 pA, which was significantly lower compared to DIV24 I_{Na+} of −1,248 ± 684.3 pA ($p = 0.031$) (**Figure 3D**).

Neurons in primary cultures were reported to have little spontaneous activity in the initial stages of cultivation, however, they exhibit it in later stages during cultivation, corresponding with synapse formation (Norris et al., 2006). The fraction of neurons generating AP increased significantly between DIV2 and DIV9 ($p = 0.003$) (**Figure 3E**) and did not change significantly in more mature cultures.

Maturity Markers of Primary Cortical Cultures Are Regulated in Primary Spinal Cord Cultures

Koseki et al. (2017) identified maturity markers in embryonic cortical neuron *in vitro* model by RNA sequencing and confirmed by immunocytochemistry. NF70 is upregulated, while DBC is downregulated during maturation of these cultures. To assess the maturation process of spinal cord cultures, we analyzed expression of above-mentioned markers using immunocytochemistry (**Figure 4**). We found that the greatest downregulation of DBC expression in our cultures was between DIV6 and DIV13 ($p = 0.011$). NF70 immunoreactivity increased most significantly at DIV20, compared to DIV3 ($p = 0.025$) and DIV6 ($p = 0.029$).

Cells in the Spinal Cord Culture Form Inhibitory and Excitatory Synapses

To investigate neuronal connectivity and network development in the culture, we investigated colocalization of pre-synaptic and post-synaptic markers using immunocytochemistry (**Figure 5**). The excitatory pre-synaptic marker, vesicular glutamate transporter 1 (VGLUT1), was colocalized with Homer1, a post-synaptic density protein, that has a role in directing glutamate receptors. The largest shift in colocalization of these two markers was detected between DIV7 and DIV15

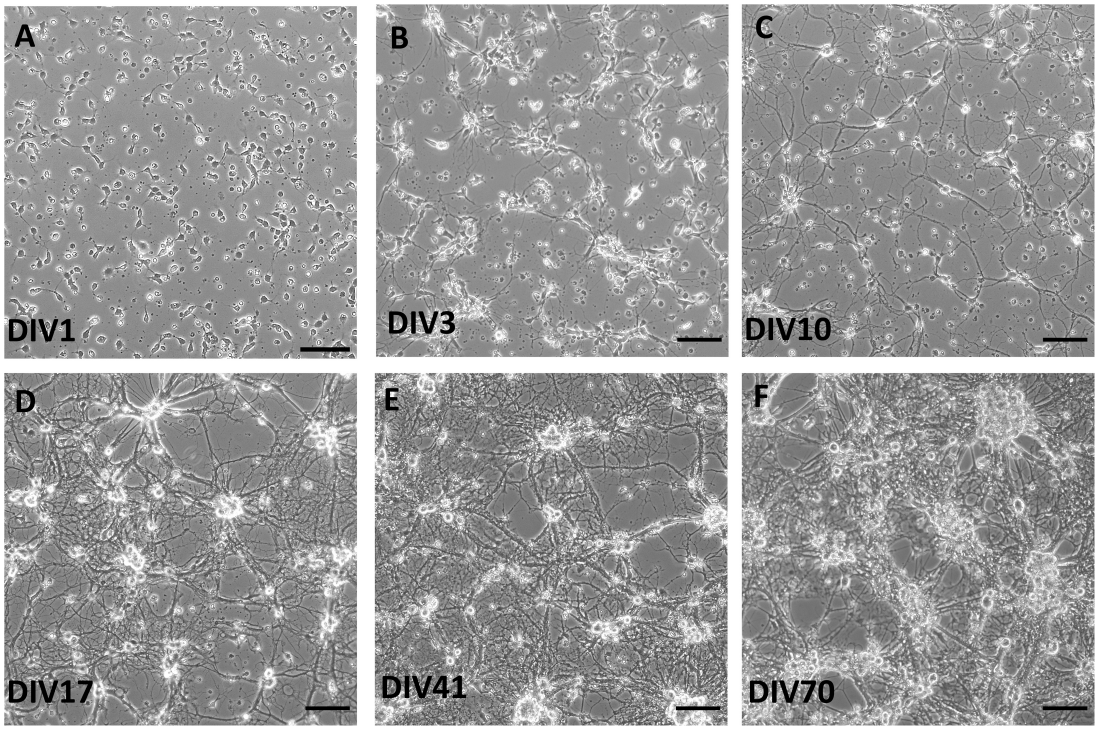

FIGURE 1 | Brightfield images of live spinal cord culture in day *in vitro* (DIV) 1 **(A)**, DIV3 **(B)**, DIV10 **(C)**, DIV17 **(D)**, DIV41 **(E)**, and DIV70 **(F)**. Growth of processes was observed already at DIV3, while more complex network occurred in older cultures, after DIV17. Scale bars: 50 μm.

(p = 0.003) (**Figure 5C**). After DIV15, we saw no significant increase in the colocalization of excitatory synapse markers. Regarding inhibitory synapses, colocalization of vesicular GABA transporter (VGAT) and gephyrin, a scaffold protein responsible for shaping the inhibitory postsynaptic density, was analyzed (**Figure 5E**). Similar to excitatory synapses, inhibitory synaptic marker colocalization increased significantly between DIV7 and DIV15 (p = 0.043). However, we also detected a significant increase in inhibitory synapse numbers between DIV15 and DIV28 (p = 0.029).

To assess whether the individual synaptic markers colocalize to differing extents during maturation, we analyzed the average ratio of co-localized synaptic puncta compared to total puncta counted for each individual synaptic marker (**Figures 5D,F**). We found that during cultivation, VGLUT1, Homer1, and VGAT colocalized in similar ratios, meaning that in immature and mature cultures, the same fraction of these synaptic markers did not colocalize with their counterpart synaptic marker. On the other hand, the gephyrin co-localized fraction was not as stable (**Figure 5F**). We detected an increase in the colocalized gephyrin fraction between DIV7 and DIV15 (p = 0.005).

Diverse Neuronal Markers Are Expressed in Primary Spinal Cord Culture

Utilizing immunocytochemistry in mature cultures, we confirmed that neurons express transcription factors associated with particular types of spinal interneuron. Lbx1 (**Figure 6A**), Lmbx1 (**Figure 6B**), Chx10 (**Figure 6C**), Tlx3, and Pax2 (**Figure 6I**) were expressed in differing proportions of neurons in our *in vitro* model. These transcription factors have been used as markers of neuronal classes in developing spinal cord (Alaynick et al., 2011; Lu et al., 2015). Counting the number of neurons stained by these markers, the most frequent markers in the culture were Pax2 and Tlx3. By counting Tlx3+ and Pax2+ nuclei of neurons identified by βIIItubulin staining, we observed that Pax2 is expressed by approximately 28.5% of neurons and Tlx3+ by 24.3% of neurons in the culture on average and these values did not change significantly during cultivation (**Figure 6H**). Coexpression of both markers by the same cell was almost non-existent and the ratio of expression of both markers did not change significantly during maturation. Similarly, we estimated that 5.8% of neurons were Lbx1+ and 35.3% of neurons were Lmx1b+ at DIV17. Chx10+ neurons were sparsely present in the culture at DIV20, on average 30 cells per coverslip. Some motoneurons identified by ChAT staining were present in the culture in the first few days of the culture (data not shown), however, none of them survived during long-term cultivation. Next, we confirmed that subsets of neurons in the culture expressed protein kinase C gamma (PKCγ) (**Figure 6D**), parvalbumin (PV) (**Figure 6F**) at DIV20, and GDNF family receptor alpha-1 (GFRα1) at DIV 17 (**Figure 6E**). These three proteins were expressed by the majority of neurons in the culture. *Wisteria floribunda* agglutinin (WFA) staining around neuronal cell bodies and dendrites identifies perineuronal nets (PNNs).

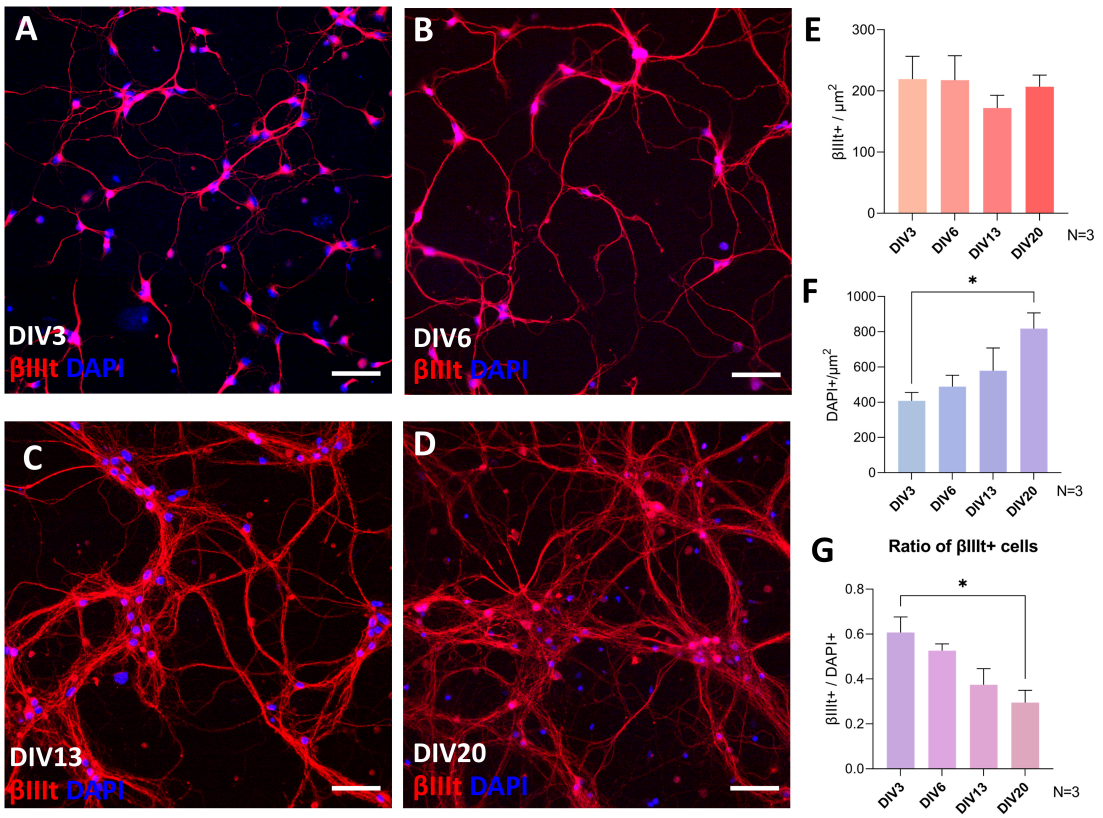

FIGURE 2 | βIII tubulin and DAPI immunocytochemistry analysis of the cultures during day *in vitro* (DIV) 3 **(A)**, DIV6 **(B)**, DIV13 **(C)**, and DIV20 **(D)**. The number of neurons was stable during cultivation **(E)**, but the number of cells assessed by DAPI increased continuously **(F)**, which led to a decrease in the ratio of neuronal population in the culture **(G)**. Scale bars: 50 μm. Data are shown as means + SEM of $N = 3$ biological replicate cultures; $^*p < 0.05$.

Neurons expressing perineuronal nets were only observed in exceptionally aged cultures (**Figure 6G**). At DIV72, we observed on average 23.5 WFA+ neurons per coverslip.

Neurons in Primary Culture Have Distinct Morphologies

To investigate the morphology of neurons present in the culture, we transfected the cultures with GFP at DIV3 using a low transfection efficiency protocol. This resulted in expression of GFP by only a few cells on the coverslip, whose morphology could then be studied. The number and length of processes and their branches were analyzed with the SNT plugin in Fiji. DIV7-8 cells were sorted into three groups, simple, intermediate, and branched, based on the number of processes (**Figure 7A** and **Table 3**). Successful separation of the groups was confirmed by significant differences of multiple morphological parameters between the groups. In older cultures, at DIV14-15 (**Figure 7B**), DIV21-22 (**Figure 7C**), and DIV28-29 (**Figure 7D**), cable length (sum length of all analyzed processes) was identified as a better parameter for segregating morphologies. Morphologies identified in these timepoints were named small, medium, and large, but in all three DIVs, the range of cable length in each group was slightly different (**Table 3**).

In an effort to identify neuronal subtypes that these distinct morphologies belong to, we costained the GFP expressing neuronal cultures for Pax2 and Tlx3 (data not shown). We chose these markers because they were expressed by a large portion of neurons in the culture and because they allowed us to identify two different types of interneurons. We found that there were no clear differences between the morphologies of Pax2+ and Tlx3+ neurons at any of the analyzed time points of cultivation.

Comparison of morphological parameters of all neurons at different maturation stages revealed marked changes in the morphology of the neurons between DIV7-8 and DIV14-15 (**Figure 8**). The majority of the studied parameters did not significantly change after DIV15, except for the sum of all processes (cable length) and the sum of axonal branches. This indicates that even in older cultures, neuronal processes continue to grow.

Regenerative Capacity of Axons Decreases With Maturity

To characterize the regenerative capacity of neurons in the cultures, axons of individual cells at DIV7, 16, and 23 were cut using a 900 nm laser and observed over 14 h. Individual cells and their processes were visualized utilizing low-efficiency GFP transfection at DIV3. After the cut, cells either died or managed

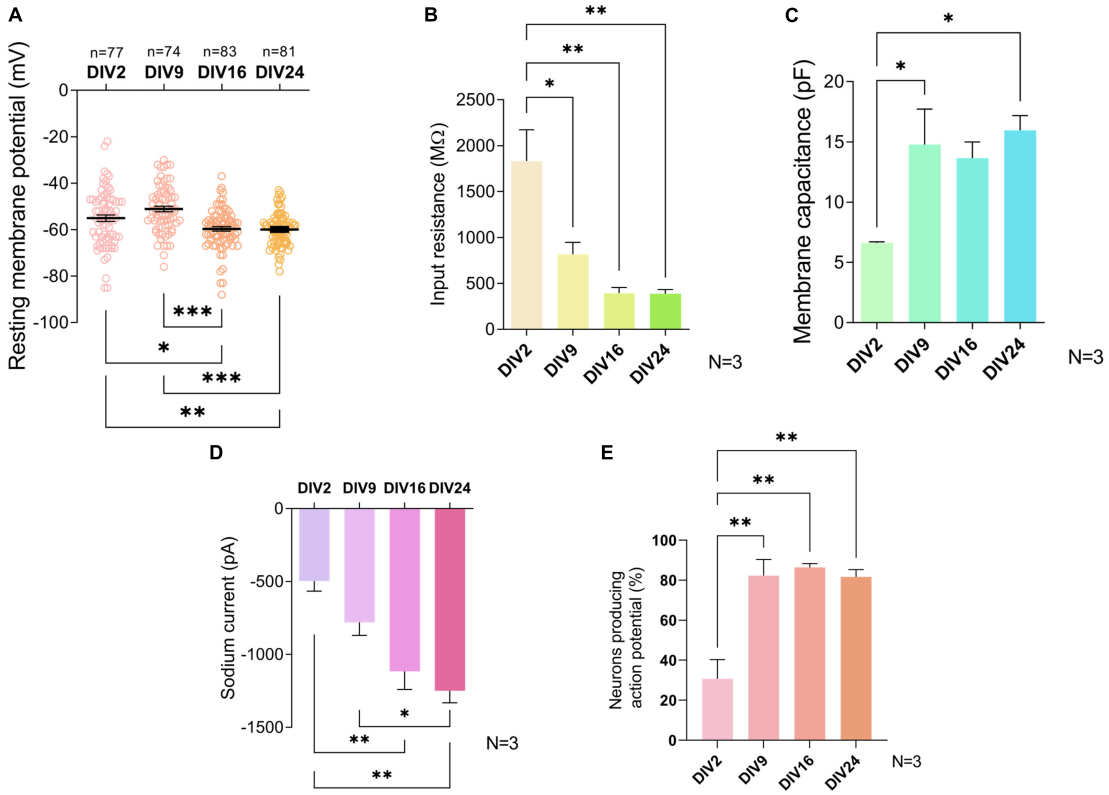

FIGURE 3 | Electrophysiological properties of cultured neurons during maturation. Resting membrane potential **(A)** and sodium current **(D)** did not change significantly after day *in vitro* (DIV) 16. Input resistance **(B)**, membrane capacitance **(C)**, and the percentage of neurons producing action potentials **(E)** did not change significantly after DIV9. Data are presented as means ± SEM of $N = 3$ biological replicate cultures and n number of cells; $^{*}p < 0.05$, $^{**}p < 0.01$, $^{***}p < 0.001$.

to close the damaged area and form a characteristic retraction bulb—a swollen structure at the tip of the axon still attached to the cell (**Figure 9A**). The maturity of neurons did not affect the percentage of dead cells following the injury, which varied between 6–25% across individual experiments.

Formation of the retraction bulb sometimes occurred right next to the site of injury, or there was more retraction, and the retraction bulb formed further up the axons (**Figure 9F**). The time needed for formation of the retraction bulb was also variable. These two parameters—retraction distance and bulb formation time—were found to be significantly different in young neurons at DIV7, compared to DIV16 and DIV23 neurons (**Figures 9B,C**). In DIV7 neurons retraction distance was 31 ± 16.81 μm, while the bulb formation time was on average 1.7 ± 1.6 h. At DIV16, retraction distance was longer, at 40.6 ± 28.1 μm, while bulb formation time of 3.8 ± 2.7 h was prolonged significantly ($p = 0.004$). DIV23 neurons had both significantly longer retraction distance (56.1 ± 43.5 μm) and bulb formation time (4 ± 2.2 h), compared to DIV7 ($p = 0.02$ and $p = 0.002$). Correlation analysis of all cells at all time points revealed a positive correlation between retraction distance and bulb formation time ($p < 0.001$) (**Figure 9D**), which indicates that longer retraction leads to slower sealing of the axon tip.

After successful bulb formation, the axons either initiated regeneration by forming a growth cone or failed to regenerate. Failure of regeneration increased with maturity of the culture (**Figure 9E**). While at DIV7, 59.3% of axotomized neurons regenerated, only 25% regenerated at DIV16; no regenerating axons were observed at DIV23. In regenerating axons, initiation time, the time between retraction bulb and growth cone formation, was also evaluated (**Figure 9F**). We observed that regenerating DIV16 cells had longer initiation time compared to DIV7 neurons ($p = 0.02$). The speed of regeneration (length of newly synthesized axon in 2 h after initiation time) was lower at DIV7, although not significantly (**Figure 9G**).

DISCUSSION

In the present study, we optimized a method of culturing primary spinal cord neurons, investigated their growth and maturation, and tested their regenerative ability. The cultures are robust, able to survive long term (>2 months), and are maintained in defined, simple serum-free medium. With increasing time in culture, we observed proliferation of glia. The use of anti-mitotic agents, such as 5-Fluoro-2′-deoxyuridine (FdU) and arabinosylcytosine C (AraC) has been routinely used previously in primary neuronal cultures to eradicate dividing cells (Stahl et al., 2007; Roppongi et al., 2017). However, their use in long-term cultivation has been reported to be problematic. It can lead

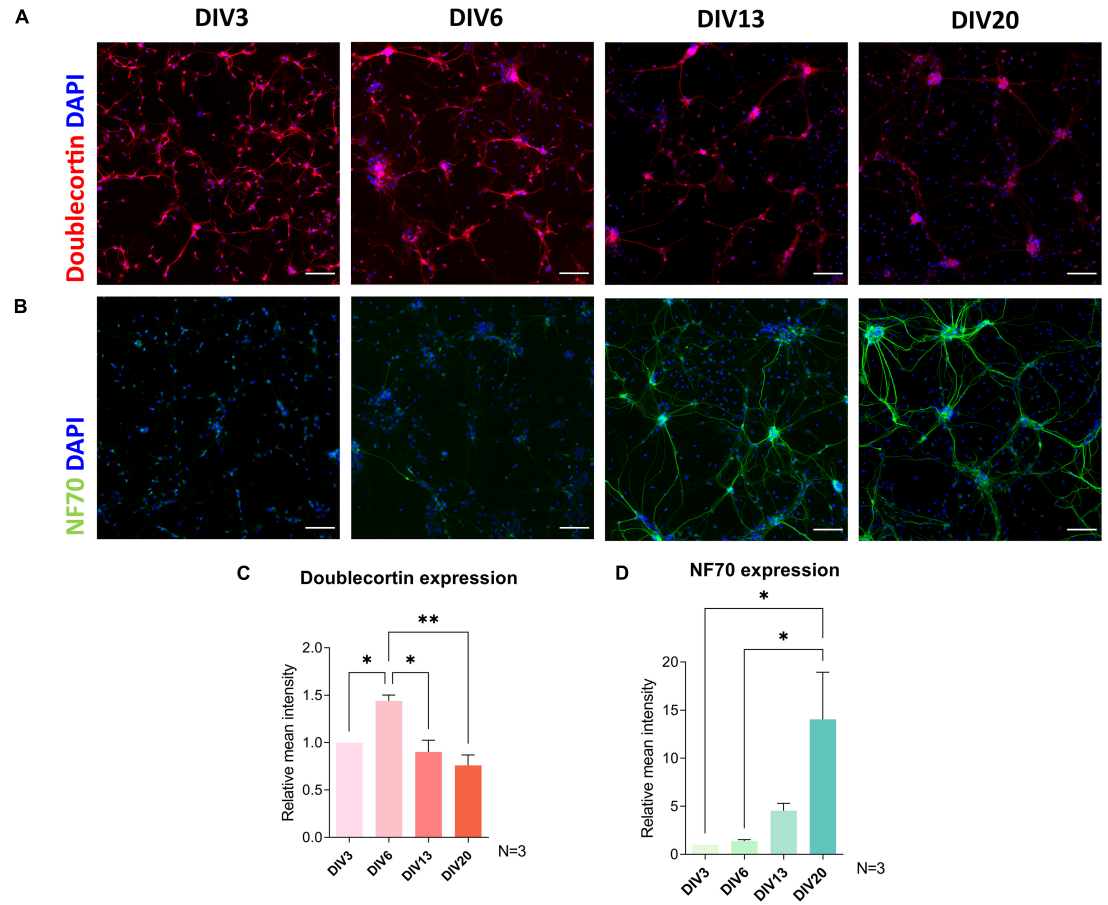

FIGURE 4 | Immunocytochemical analysis of maturity markers doublecortin **(A,C)** and neurofilament 70 kDa (NF70) **(B,D)** expression during cultivation. Doublecortin expression was downregulated after DIV6, while a significant increase in NF70 signal was observed after DIV13. Scale bars: 100 μm. Data are presented as means + SEM of $N = 3$ biological replicate cultures; $^{*}p < 0.05$, $^{**}p < 0.01$.

to death of neurons through glutamate excitotoxicity (Ahlemeyer et al., 2003), oxidative stress (Geller et al., 2001), or neurotrophic factor deprivation (Martin et al., 1990). On top of that, glial cells have been shown to be a crucial factor in synaptogenesis and in recreating complex functionality of the CNS in an *in vitro* system (Allen and Barres, 2005; Hui et al., 2016; Enright et al., 2020). For these reasons, we excluded the use of anti-mitotic agents in our culture, which led to proliferation of glia but did not affect the survival of neurons and probably encouraged neuronal maturation (**Figure 2**).

Our goal was to create a culture of spinal cord neurons that models the maturing and mature CNS and which is suitable for future experiments designed to enhance the ability of the neurons to regenerate. The viability of embryonic neuronal cultures is a great advantage in culture preparation, but the immaturity of the neurons after seeding is a problem as they display entirely different properties compared to mature neurons that have lost their intrinsic ability to regenerate (LaBarbera et al., 2021). To evaluate the maturity of our cultures, we investigated the expression of DBC, NF70, synaptic development, and electrophysiological properties of neurons during cultivation.

The alterations in the electrophysiological properties are hallmarks of neurodevelopment of spinal cord neurons (Durand et al., 2015) and have been used to stage neuronal maturation in cortical cultures (Koseki et al., 2017). The electrophysiological properties of neurons in our culture showed the typical changes associated with maturation until DIV16 after which there was no further change (**Figure 3**). In more detail, the major shift in most parameters in our functional studies already transpired before DIV9. Comparing these parameters to the electrical activity of neurons in P6-10 spinal cord slices recorded in a previous study by Sun and Harrington (2019), it can be argued that our neuronal culture is composed solely of interneurons. Interneurons in the cited study had high IR (305 ± 33 MΩ), E_m of −54.2 ± 1 mV, and 65% of them exhibited spontaneous activity, which helped in distinguishing interneurons from motoneurons. Actual postnatal maturity of the neurons in the culture is difficult to assess using electrophysiological properties. We compared the properties in our cells with spinal cord slice recordings of P6-14 mice (Wilson et al., 2005; Sun and Harrington, 2019) and P0-3 whole cord recordings (Zhong et al., 2006). While some parameters, such

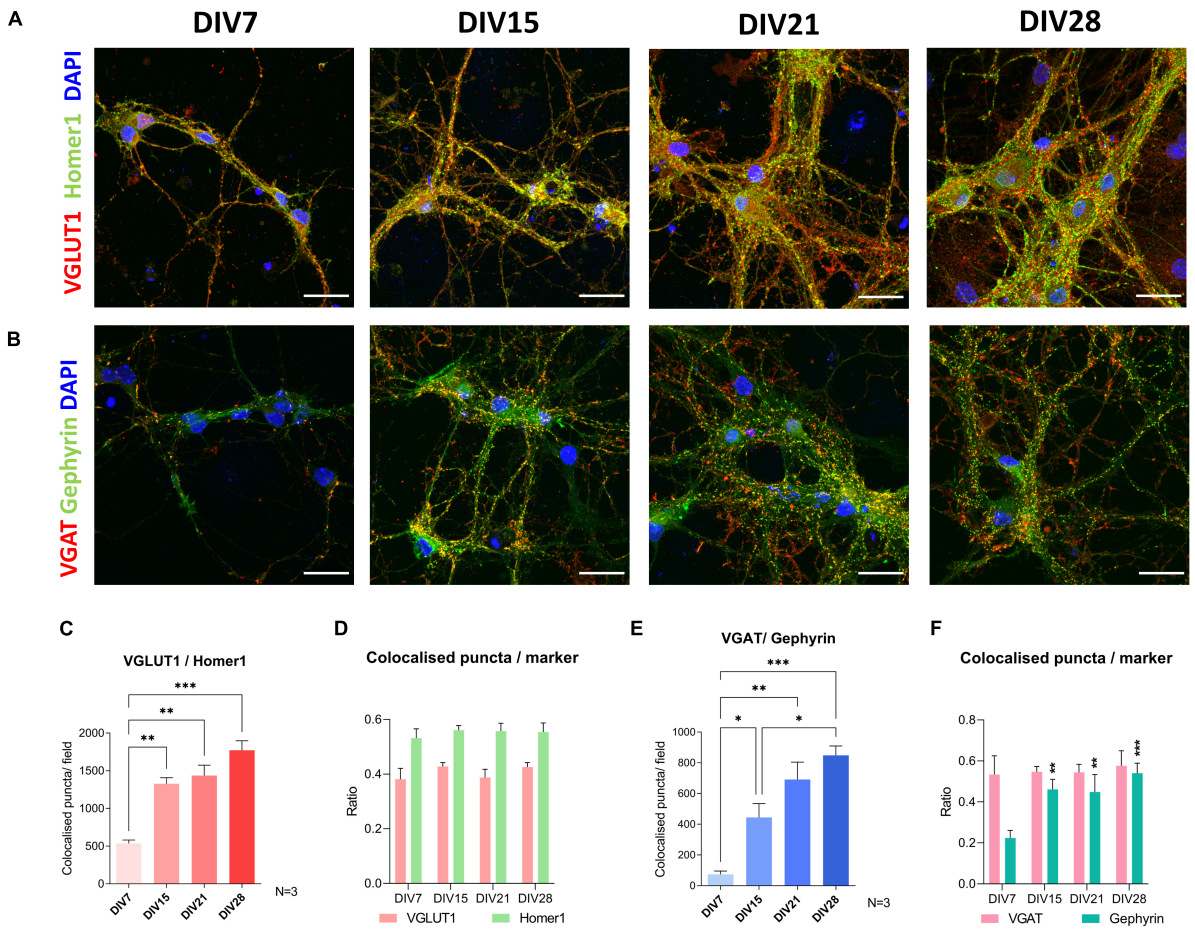

FIGURE 5 | Immunocytochemical analysis of synapse formation during cultivation of spinal cord culture. For excitatory synapse analysis, colocalization of VGLUT1 and Homer1 was examined **(A,C,D)**, while colocalization of synaptic markers VGAT and Gephyrin was used for analysis of inhibitory synapses **(B,E,F)**. Formation of new excitatory synapses was the most prominent between day *in vitro* (DIV) 7 and 15 **(C)**. A similar pattern was observed in colocalization analysis of inhibitory synapses **(E)**. VGLUT1, Homer1, and VGAT colocalization ratios were stable during cultivation **(D,F)**, while an increase of ratio of Gephyrin marked synapses that colocalized with VGAT occurred between DIV7 and DIV15 **(F)**. Scale bars: 25 μm. Data are presented as means + SEM of $N = 3$ biological replicate cultures; $^{*}p < 0.05$, $^{**}p < 0.01$, $^{***}p < 0.001$.

as E_m, were comparable to neurons of P0-3 spinal cord, other properties such as IR and percentage of spontaneously firing neurons indicated that our neurons were more mature at DIV16 than those of the P4-16 spinal cords. These results suggest that our cultures at around DIV16 exhibit electrical properties of early to late postnatal neurons.

DBC is a microtubule-associated protein expressed by migrating neurons during development. It has been used as a marker of neuronal precursors (Ayanlaja et al., 2017), while its downregulation has been reported in mature neurons (Brown et al., 2003). Developmental regulation of DBC was also observed *in vivo*. In mouse embryonic extracts, DBC expression is absent at E10.5, but present from E12.5 to newborn. Although DBC expression is still present in neonatal mouse brain, it is absent in adult mice (Francis et al., 1999). We observed a significant decrease in DBC immunoreactivity after DIV6 of culture (**Figure 4**). NF70 has been previously used as a mature axonal marker (Lu et al., 2017). NF70 mRNA analysis in embryonic and early postnatal mouse spinal cords shows, that this transcript is present already in E13. The expression is downregulated until E18 and then starts to increase until postnatal day 21 (Pernas-Alonso et al., 1996). In our cultures, there was a sharp upregulation of this marker at DIV20. Maturity of the culture was also confirmed by observing the formation of neural networks (**Figure 5**). The number of excitatory and inhibitory synapses was increasing during the first 2 weeks of culture, after which they plateaued, which was previously observed to occur in cultures of primary cortical and striatal neurons between DIV14 and DIV21 (Moutaux et al., 2018).

Although there is no consensus of neuronal subtypes classification in adult spinal cord, there have been several recent studies that tackled this problem in various approaches (Zeng and Sanes, 2017; Hayashi et al., 2018; Dobrott et al., 2019). The most efficient way is to classify cell types by molecular markers- proteins expressed by only specific cell groups. Transcription factors have been used to classify spinal neurons,

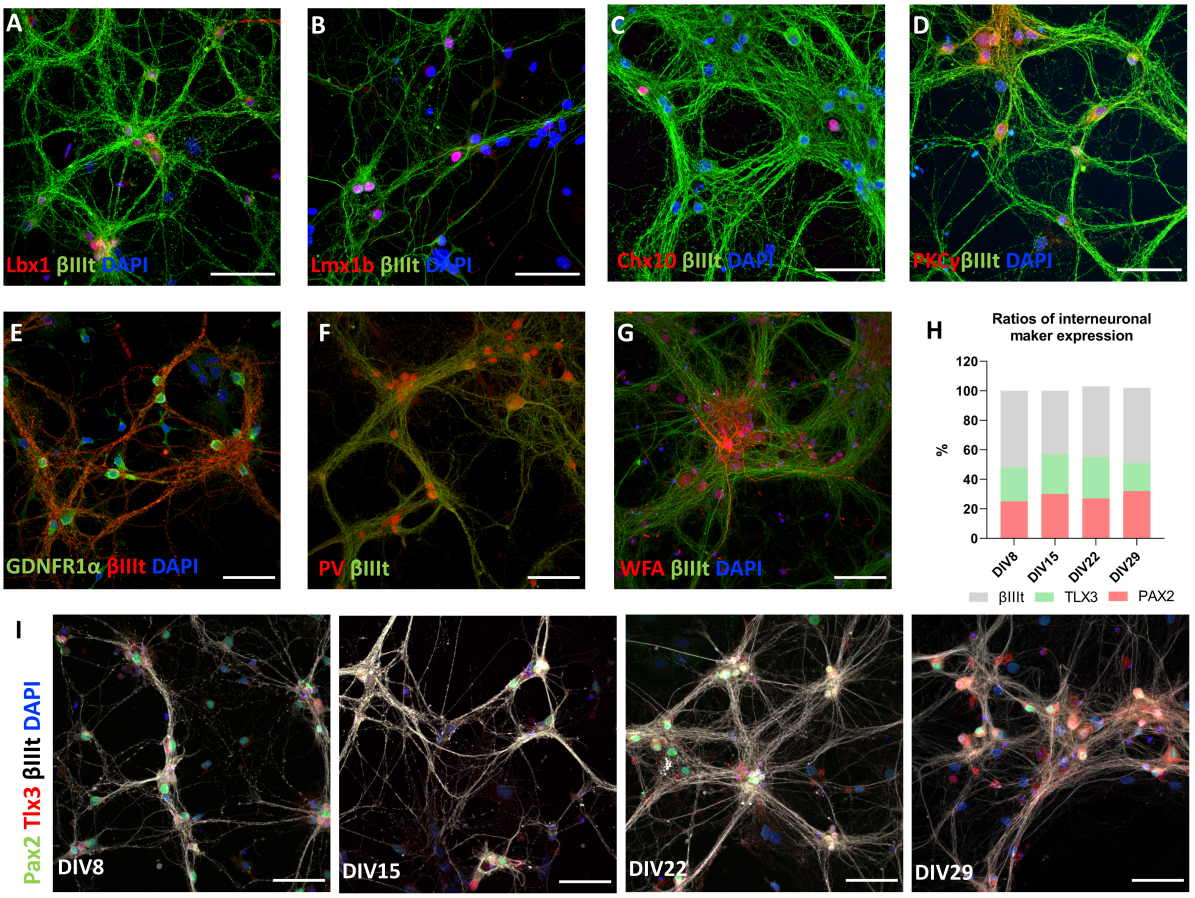

FIGURE 6 | Markers of spinal interneurons Lbx1 **(A)**, Lmx1b **(B)**, Chx10 **(C)**, Pax2, and Tlx3 **(I)** are present in primary spinal cord cultures. Pax2+ and Tlx3+ cells represent approximately half of neurons in the culture **(H)**. Neurons also expressed PKCγ **(D)**, GDNFR1α **(E)**, parvalbumin (PV) **(F)**, and *Wisteria floribunda* agglutinin (WFA) **(G)**. Scale bars: 50 μm.

as they control neuronal specialization during development (Lu et al., 2015; Russ et al., 2021). Although the expression of the transcription factors can be transient- their expression is decreased after differentiation (Gosgnach et al., 2017), some continue to be expressed during adulthood (Del Barrio et al., 2013). We identified expression of several of these transcription factors in our cultures, namely Lbx1, Lmx1b, Chx10, Pax2, and Tlx3 (**Figure 6**). Lbx1 transcription factor participates in differentiation of dorsal horn neurons (Müller et al., 2002), it is expressed by laminae III-IV neurons of adult spinal cord, which are mostly excitatory, but not exclusively. Lmx1b+ neurons also express Lbx1, but they are only excitatory and expressed at high levels in laminae I-III (Del Barrio et al., 2013). Lmx1b+ neurons in our cultures were colocalized with majority of Tlx3 neurons (data not shown), which was also previously confirmed *in vivo* (Dai et al., 2008). Tlx3 transcription factor, present mostly in laminae I-II, has been identified to have direct control in specifying excitatory neurons in the dorsal horn (Monteiro et al., 2021). Apart from the previously mentioned, mostly excitatory, interneurons, we have also observed a large population of Pax2+ neurons in our cultures. Pax2 is essential for the differentiation of GABAergic neurons and its expression has been used as a marker of inhibitory neurons in the mouse dorsal horn (Larsson, 2017). The presence of ventral interneurons was also confirmed using Chx10 staining. Chx10 has been used as a marker of V2a excitatory interneurons in the ventral spinal cord, which participate in control of the limbs (Hayashi et al., 2018). In addition to transcription factors, other proteins have also been used to classify neurons in adult spinal cord. PKCγ is one such protein that is expressed by excitatory interneurons in lamina II that participate in mechanical and thermal allodynia (Neumann et al., 2008). Parvalbumin, on the other hand, is a marker of inhibitory interneurons, both GABAergic and glycinergic, located between the lamina II and III, which act as filters of low-threshold mechanoreceptive inputs (Petitjean et al., 2015; Häring et al., 2018). Both PKCγ and PV were expressed by our neuronal cultures. We found that ChAT positive cells do not survive long in the described culture. Motor neurons are known to be particularly vulnerable and rely heavily on trophic support of peripherally connected cells, such as muscle cells and Schwann cells for survival (Bucchia et al., 2018). The loss of trophic support after dissection could have eventually led to death

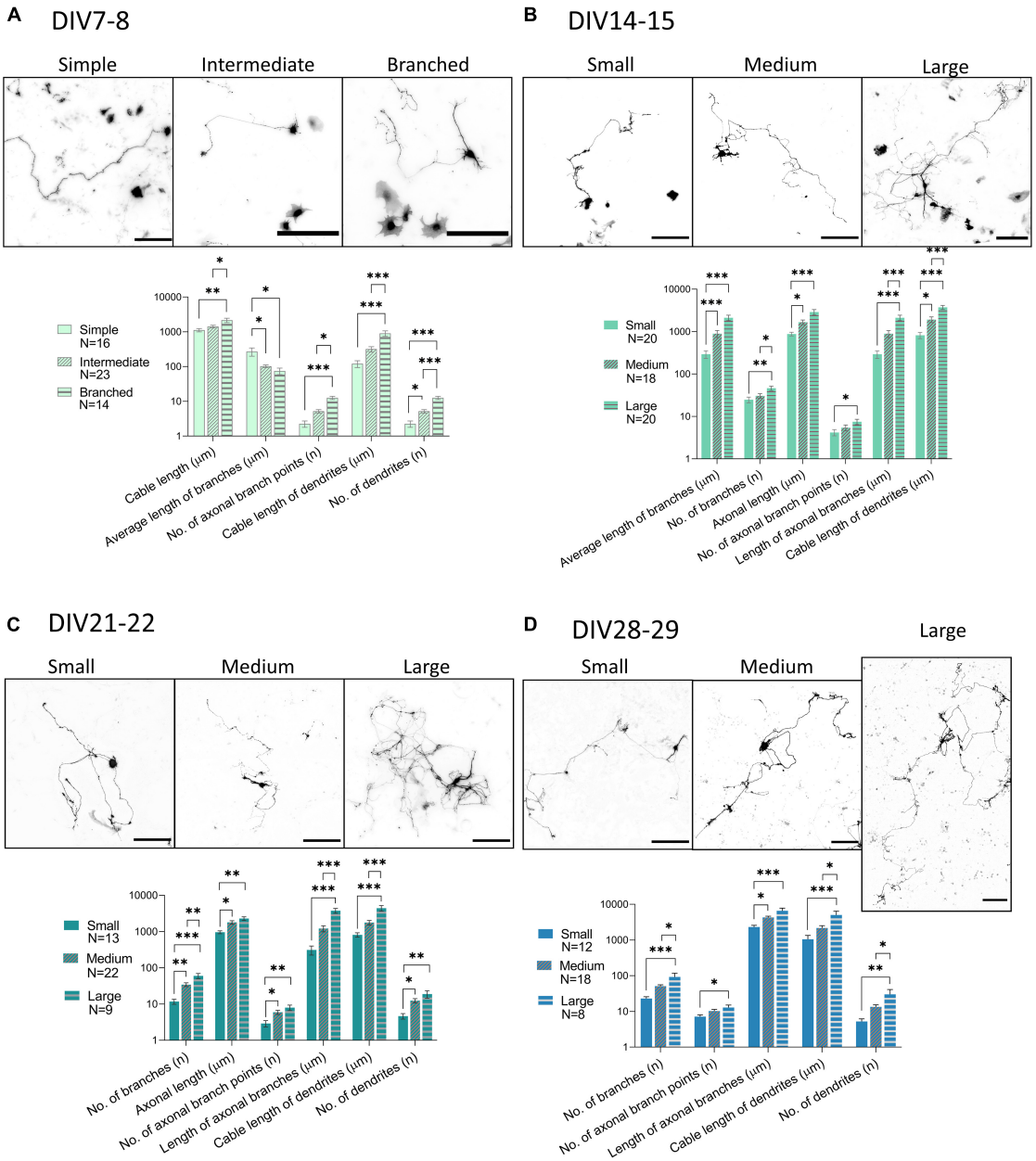

FIGURE 7 | Morphological groups of neurons transfected with GFP (black) during various days *in vitro* (DIV), DIV7-8 **(A)**, DIV14-15 **(B)**, DIV21-22 **(C)**, DIV28-29 **(D)**. While DIV7 neurons were successfully categorized according to the number of processes into simple, intermediate, and branched, from DIV14 onward, the length of processes was found to be a better parameter for segregating morphologies into small, medium, and large. Scale bars: 200 µm. One-way ANOVA with Turkey's *post hoc* test was used for analyzing the difference between morphological groups. Data are presented as means + SEM of N number of cells from 3 biological replicates; $*p < 0.05$, $**p < 0.01$, $***p < 0.001$.

of motor neurons in our cultures. Due to the lack of specific markers, we can only speculate if projection neurons shared the same fate. Projection neurons represent a very small portion (<1%) of neurons of the dorsal horn. They are located in lamina I and dispersed throughout lamina III–VI (Abraira and Ginty, 2013). The majority of projection neurons retrogradely traced by cholera toxin B subunit (CTb) were found to express neurokinin 1 receptor (NK1r) (Spike et al., 2003; Cameron et al., 2015), but a big portion of lamina I, IV, V and VI neurons, therefore mostly interneurons, express this receptor as well (Todd et al., 1998). NK1r immunostaining alone is therefore not sufficient to prove the presence of projection neurons.

To analyze the morphology of neurons during maturation and to attempt to classify them into characteristic groups, we measured the length and number of their processes. Previous studies classified the spinal cord neuron morphology according

TABLE 3 | Morphological groups of neurons identified during cultivation of spinal cord cultures.

	Morphological group	Range	*N*	*N* total
DIV7-8	Simple	1–9 b	16	53
	Intermediate	10–19 b	23	
	Branched	20–58 b	14	
DIV15-16	Small	300–3,000 μm	20	58
	Medium	3,000–6,000 μm	18	
	Large	6,000–13,000 μm	20	
DIV21-22	Small	900–3,000 μm	13	44
	Medium	3,000–7,500 μm	22	
	Large	7,500–14,000 μm	9	
DIV28-29	Small	1,700–4,500 μm	12	38
	Medium	4,500–8,000 μm	18	
	Large	8,000–20,000 μm	8	

DIV7-8 neurons were separated according to the number of branches (b), while older neurons were grouped according to the sum length of their processes.

to laminar location, particular geometry, and neurite orientation (Grudt and Perl, 2002; Hantman et al., 2004), which is not possible *in vitro*. Gertz et al. (2010) reported increasing length and number of neurites of spinal cord motoneurons during cultivation, but 48 h. We analyzed the morphology parameters in the course of 4 weeks *in vitro*, during which we distinguished individual morphologies and observed growth of processes even in older cultures. The morphological groups that were identified were not characteristic of either Tlx3+ or Pax2+ cells, which are markers of two different interneuronal subtypes. Electrophysiological characteristics of the morphological groups were not assessed. Additionally, we observed that even in older cultures, neuronal processes continue to grow (**Figure 8**). Electrophysiological parameters IR and C_m correlate with cell size (Sun et al., 2018), but we did not see changes in these parameters after DIV9 (**Figures 3B,C**). It is important to note, that the morphological changes in older cultures were identified at DIV28, while the oldest cultures recorded by patch-clamp were at DIV24, which could be the reason for this inconsistency. On the other hand, we observed an increase in the number of synapses at DIV28 (**Figure 5**), which could indicate that elongation of the processes observed at the same timepoint in morphology analysis is due to formation of new connections between neurons in the culture.

By following events that occurred after axotomy of spinal cord neurons, we observed that more mature cells react more slowly to laser-induced injury and retract further from the injury site compared to younger cells (**Figure 9**). By DIV23, neurons lost all regenerative capacity and even at DIV16, the axon regeneration was slower. These results indicate that spinal neurons lose their regenerative capacity during maturation *in vitro*, similarly to cortical cultures, as was shown before (Koseki et al., 2017). We observed a similar transition in neuronal properties in other experiments around

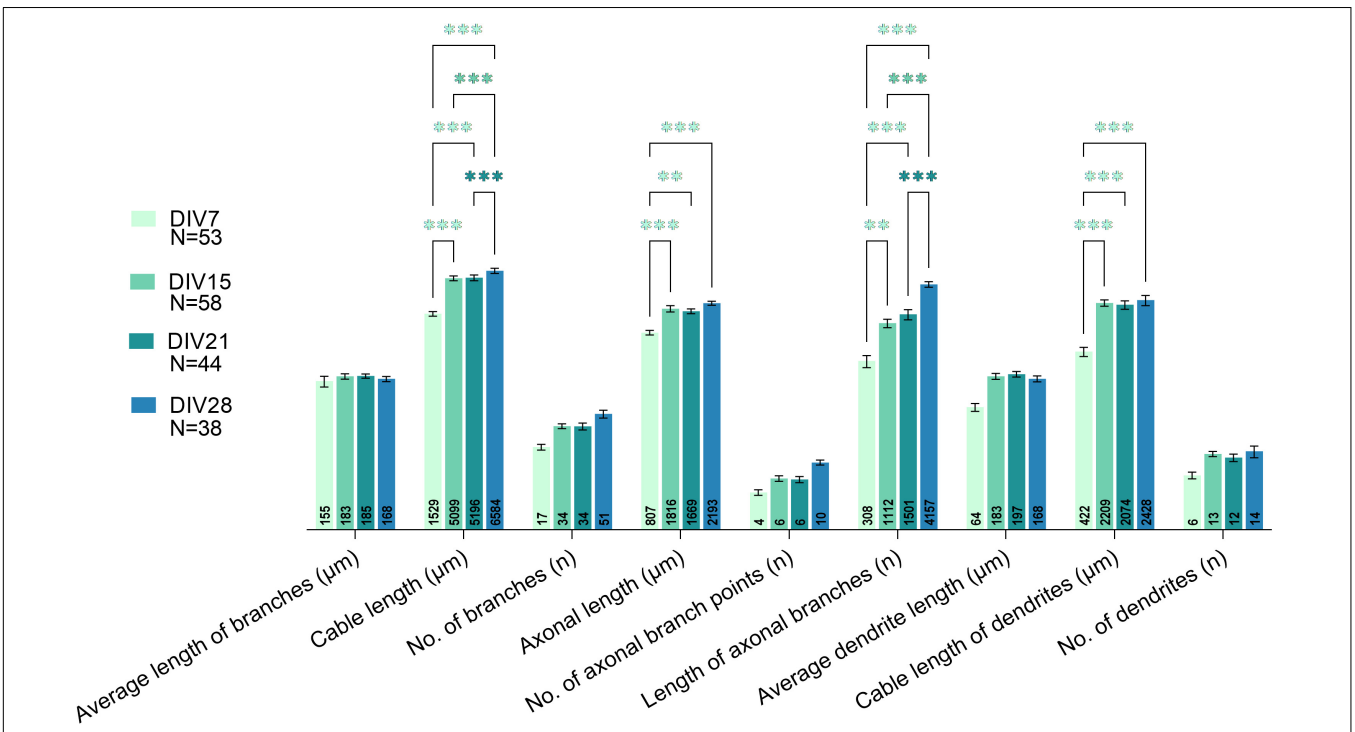

FIGURE 8 | Comparison of all studied morphological parameters between various days *in vitro* (DIVs). A major shift in morphological properties was observed between DIV7 and DIV15. Growth of processes was observed even in prolonged cultivation periods, as parameters related to length of processes increased significantly at DIV28. Two-way ANOVA followed by Turkey's *post hoc* test was used for analyzing the difference between DIVs. Data are presented as means ± SEM, means of plotted values are annotated in each bar; $^{**}p < 0.01$, $^{***}p < 0.001$ of N number of cells from 3 biological replicates.

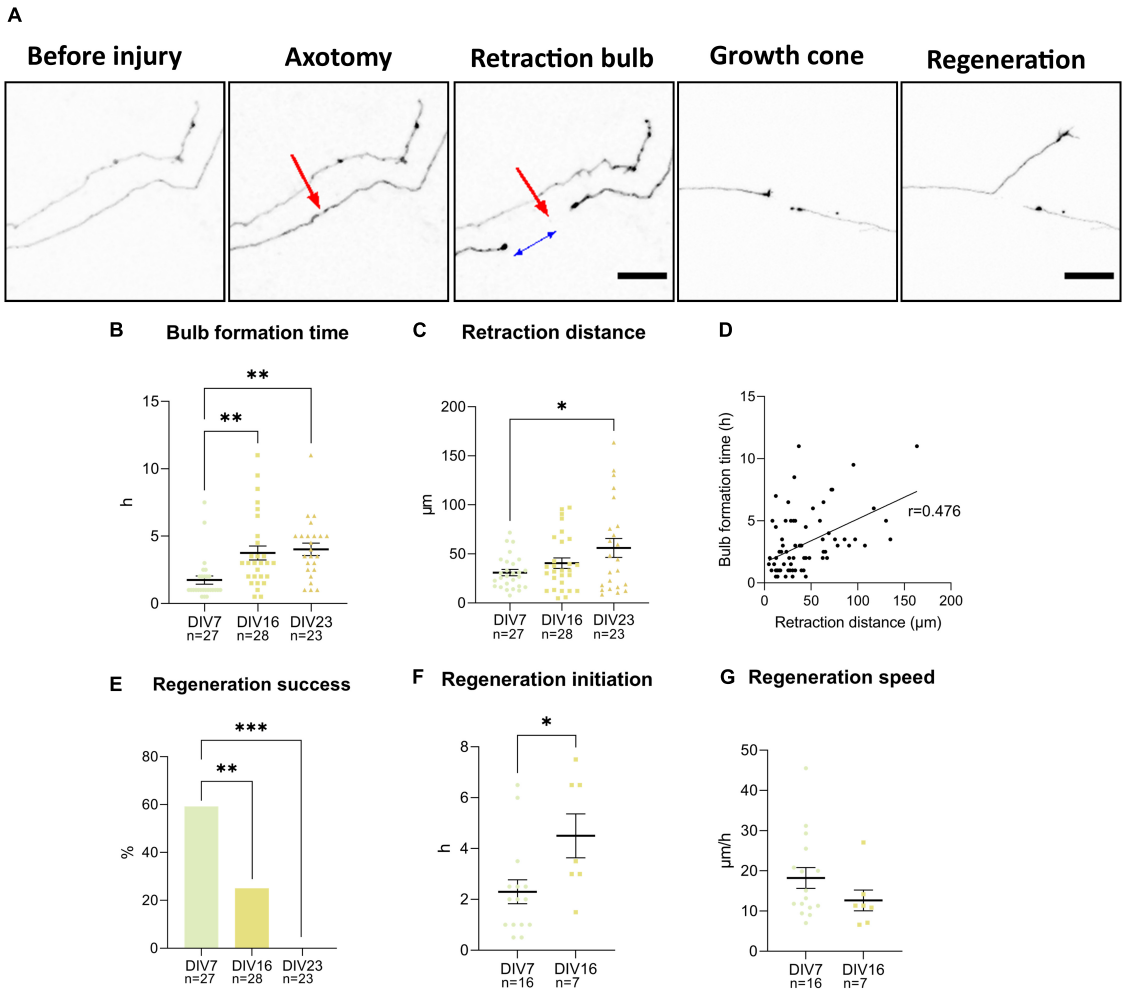

FIGURE 9 | Axotomy of the GFP (black) transfected neurons was achieved using a 900 nm laser **(A)**. Red arrow points at the location of the cut. Retraction bulb formed at certain distance from the injury site as indicated by the blue arrow. Bulb formation time **(B)** and retraction distance **(C)** were lower in DIV7 neurons. These two parameters have a positive linear relationship demonstrated by Pearson's correlation coefficient **(D)**. Percentage of regenerating axons decreased significantly between DIV7 and DIV16 **(E)**. Time between retraction bulb formation and growth cone formation increased significantly at DIV16 **(F)**, while speed of regeneration decreased marginally **(G)**. Scale bars: 25 µm. Data are presented as means ± SEM of n number of cells from 3 biological replicates; $^{*}p < 0.05$, $^{**}p < 0.01$, $^{***}p < 0.001$.

this time point as well. The major shift in morphology during *in vitro* maturation was observed between DIV7 and DIV15 (**Figure 8**). The same cultivation period was critical in changes of maturity marker expressions, synaptic connectivity, and most of the electrophysiological properties. These results indicate that major intrinsic maturation events are occurring at this time point in the cultured neurons. Loss of plasticity and regenerative ability in CNS neurons during development *in vivo* is well established (Fawcett, 2020). Apart from the inhibitory environment that is created at the injury site, mature neurons themselves lack intrinsic regenerative properties. During the loss of regenerative ability, neurons show changes in expression of growth-related molecules, and they also become polarized into somatodendritic and axonal domains. Axons alone lack molecules such as growth-related receptors, as well as mechanisms deemed vital for regeneration (Kappagantula et al., 2014; Franssen et al., 2015; Cheah et al., 2016). Apart from non-regenerating axons, CNS neurons do not express the regenerative program that is seen with the upregulation of many genes that is initiated after injury of peripheral nerves (Ben-Yaakov et al., 2012).

In conclusion, we developed, validated, and described a new culture of spinal cord neurons. We believe that the described culture efficiently models the biology of the spinal cord, which makes it a valuable tool for future studies.

DATA AVAILABILITY STATEMENT

The original contributions presented in the study are included in the article/supplementary material, further inquiries can be directed to the corresponding author/s.

ETHICS STATEMENT

All cell isolations from mice embryos were performed in accordance with the European Communities Council Directive of 22.09.2010 (2010/63/EU) regarding the use of animals in research and were approved by the Ethics Committee of the Institute of Experimental Medicine ASCR, Prague, Czechia under no. 54/2017 (approved 14.10.2017 and valid till 31.07.2022).

AUTHOR CONTRIBUTIONS

IV drafted the manuscript, performed and analyzed all experiments, except patch-clamp recordings, which were performed by JK. JCK, JF, and PJ conceived of the project and supervised the experiments. All authors contributed to editing the manuscript.

FUNDING

This work was supported by Operational Program Research, Development, and Education in the framework of the project "Center of Reconstructive Neuroscience," registration number CZ.02.1.01/0.0./0.0/15_003/0000419. We acknowledge the core facility IMCF BIOCEV, supported by the MEYS CR (LM2018129 Czech-BioImaging) for their support with obtaining scientific data presented in this manuscript.

ACKNOWLEDGMENTS

We would like to thank Carmen Birchmeier-Kohler and Thomas Müller from Max-Delbrueck Center for Molecular Medicine, Berlin, Germany for proving us with antibodies against Tlx3, Lbx1, and Lmx1b.

REFERENCES

Abraira, V. E., and Ginty, D. D. (2013). The sensory neurons of touch. *Neuron* 79, 618–639. doi: 10.1016/j.neuron.2013.07.051

Abu-Rub, M., McMahon, S., Zeugolis, D. I., Windebank, A., and Pandit, A. (2010). Spinal cord injury in vitro: modelling axon growth inhibition. *Drug Discov. Today* 15, 436–443. doi: 10.1016/j.drudis.2010.03.008

Ahlemeyer, B., Kölker, S., Zhu, Y., Hoffmann, G. F., and Krieglstein, J. (2003). Cytosine arabinofuranoside-induced activation of astrocytes increases the susceptibility of neurons to glutamate due to the release of soluble factors. *Neurochem. Int.* 42, 567–581. doi: 10.1016/s0197-0186(02)00164-x

Alaynick, W. A., Jessell, T. M., and Pfaff, S. L. (2011). SnapShot: spinal cord development. *Cell* 146, 178.e–178.e. doi: 10.1016/j.cell.2011.06.038

Allen, N. J., and Barres, B. A. (2005). Signaling between glia and neurons: focus on synaptic plasticity. *Curr. Opin. Neurobiol.* 15, 542–548. doi: 10.1016/j.conb.2005.08.006

Anderson, M. A., Burda, J. E., Ren, Y., Ao, Y., O'Shea, T. M., Kawaguchi, R., et al. (2016). Astrocyte scar formation aids central nervous system axon regeneration. *Nature* 532, 195–200. doi: 10.1038/nature17623

Anderson, M. A., O'Shea, T. M., Burda, J. E., Ao, Y., Barlatey, S. L., Bernstein, A. M., et al. (2018). Required growth facilitators propel axon regeneration across complete spinal cord injury. *Nature* 561, 396–400. doi: 10.1038/s41586-018-0467-6

Arshadi, C., Günther, U., Eddison, M., Harrington, K. I. S., and Ferreira, T. A. (2020). SNT: A Unifying Toolbox for Quantification of Neuronal Anatomy. Neuroscience. *Nat. Methods* 18, 374–377. doi: 10.1101/2020.07.13.179325

Ayanlaja, A. A., Xiong, Y., Gao, Y., Ji, G., Tang, C., Abdikani Abdullah, Z., et al. (2017). Distinct Features of Doublecortin as a Marker of Neuronal Migration and Its Implications in Cancer Cell Mobility. *Front. Mol. Neurosci.* 10:199. doi: 10.3389/fnmol.2017.00199

Barbati, A. C., Fang, C., Banker, G. A., and Kirby, B. J. (2013). Culture of primary rat hippocampal neurons: design, analysis, and optimization of a microfluidic device for cell seeding, coherent growth, and solute delivery. *Biomed. Microdevices* 15, 97–108. doi: 10.1007/s10544-012-9691-2

Bareyre, F. M., Kerschensteiner, M., Raineteau, O., Mettenleiter, T. C., Weinmann, O., and Schwab, M. E. (2004). The injured spinal cord spontaneously forms a new intraspinal circuit in adult rats. *Nat. Neurosci.* 7, 269–277. doi: 10.1038/nn1195

Ben-Yaakov, K., Dagan, S. Y., Segal-Ruder, Y., Shalem, O., Vuppalanchi, D., Willis, D. E., et al. (2012). Axonal transcription factors signal retrogradely in lesioned peripheral nerve. *EMBO J.* 31, 1350–1363. doi: 10.1038/emboj.2011.494

Blesch, A., Fischer, I., and Tuszynski, M. H. (2012). Gene therapy, neurotrophic factors and spinal cord regeneration. *Handb. Clin. Neurol.* 109, 563–574. doi: 10.1016/B978-0-444-52137-8.00035-8

Brown, J. P., Couillard-Després, S., Cooper-Kuhn, C. M., Winkler, J., Aigner, L., and Kuhn, H. G. (2003). Transient expression of doublecortin during adult neurogenesis. *J. Comp. Neurol.* 467, 1–10. doi: 10.1002/cne.10874

Bucchia, M., Merwin, S. J., Re, D. B., and Kariya, S. (2018). Limitations and Challenges in Modeling Diseases Involving Spinal Motor Neuron Degeneration in Vitro. *Front. Cell. Neurosci.* 12:61. doi: 10.3389/fncel.2018.00061

Cameron, D., Polgár, E., Gutierrez-Mecinas, M., Gomez-Lima, M., Watanabe, M., and Todd, A. J. (2015). The organisation of spinoparabrachial neurons in the mouse. *Pain* 156, 2061–2071. doi: 10.1097/j.pain.0000000000000270

Cheah, M., Andrews, M. R., Chew, D. J., Moloney, E. B., Verhaagen, J., Fässler, R., et al. (2016). Expression of an Activated Integrin Promotes Long-Distance Sensory Axon Regeneration in the Spinal Cord. *J. Neurosci.* 36, 7283–7297. doi: 10.1523/JNEUROSCI.0901-16.2016

Courtine, G., Song, B., Roy, R. R., Zhong, H., Herrmann, J. E., Ao, Y., et al. (2008). Recovery of supraspinal control of stepping via indirect propriospinal relay connections after spinal cord injury. *Nat Med* 14, 69–74. doi: 10.1038/nm1682

Dai, J.-X., Hu, Z.-L., Shi, M., Guo, C., and Ding, Y.-Q. (2008). Postnatal ontogeny of the transcription factor Lmx1b in the mouse central nervous system. *Journal of Comparative Neurology* 509, 341–355. doi: 10.1002/cne.21759

Del Barrio, M. G., Bourane, S., Grossmann, K., Schüle, R., Britsch, S., O'Leary, D. D. M., et al. (2013). A transcription factor code defines nine sensory interneuron subtypes in the mechanosensory area of the spinal cord. *PLoS ONE* 8:e77928. doi: 10.1371/journal.pone.0077928

Dobrott, C. I., Sathyamurthy, A., and Levine, A. J. (2019). Decoding cell type diversity within the spinal cord. *Curr. Opin. Physiol.* 8, 1–6. doi: 10.1016/j.cophys.2018.11.006

Donaldson, K., and Höke, A. (2014). Studying axonal degeneration and regeneration using in vitro and in vivo models: the translational potential. *Fut. Neurol.* 9, 461–473. doi: 10.2217/fnl.14.29

Durand, J., Filipchuk, A., Pambo-Pambo, A., Amendola, J., Borisovna Kulagina, I., and Guéritaud, J.-P. (2015). Developing electrical properties of postnatal mouse lumbar motoneurons. *Front. Cell. Neurosci.* 9:349. doi: 10.3389/fncel.2015.00349

Eldeiry, M., Yamanaka, K., Reece, T. B., and Aftab, M. (2017). Spinal cord neurons isolation and culture from neonatal mice. *J. Vis. Exp.* 11:55856. doi: 10.3791/55856

Enright, H. A., Lam, D., Sebastian, A., Sales, A. P., Cadena, J., Hum, N. R., et al. (2020). Functional and transcriptional characterization of complex neuronal co-cultures. *Sci. Rep.* 10:11007. doi: 10.1038/s41598-020-67691-2

Fawcett, J. W. (2020). The Struggle to Make CNS Axons Regenerate: Why Has It Been so Difficult? *Neurochem. Res.* 45, 144–158. doi: 10.1007/s11064-019-02844-y

Francis, F., Koulakoff, A., Boucher, D., Chafey, P., Schaar, B., Vinet, M.-C., et al. (1999). Doublecortin is a developmentally regulated, microtubule-associated protein expressed in migrating and differentiating neurons. *Neuron* 23, 247–256. doi: 10.1016/S0896-6273(00)80777-1

Franssen, E. H. P., Zhao, R.-R., Koseki, H., Kanamarlapudi, V., Hoogenraad, C. C., Eva, R., et al. (2015). Exclusion of integrins from CNS axons is regulated by Arf6 activation and the AIS. *J. Neurosci.* 35, 8359–8375. doi: 10.1523/JNEUROSCI.2850-14.2015

Geller, H. M., Cheng, K. Y., Goldsmith, N. K., Romero, A. A., Zhang, A. L., Morris, E. J., et al. (2001). Oxidative stress mediates neuronal DNA damage and apoptosis in response to cytosine arabinoside. *J. Neurochem.* 78, 265–275. doi: 10.1046/j.1471-4159.2001.00395.x

Gertz, C. C., Leach, M. K., Birrell, L. K., Martin, D. C., Feldman, E. L., and Corey, J. M. (2010). Accelerated neuritogenesis and maturation of primary spinal motor neurons in response to nanofibers. *Dev Neurobiol* 70, 589–603. doi: 10.1002/dneu.20792

Golowasch, J., Thomas, G., Taylor, A. L., Patel, A., Pineda, A., Khalil, C., et al. (2009). Membrane capacitance measurements revisited: dependence of capacitance value on measurement method in nonisopotential neurons. *J. Neurophysiol.* 102, 2161–2175. doi: 10.1152/jn.00160.2009

Gosgnach, S., Bikoff, J. B., Dougherty, K. J., Manira, A. E., Lanuza, G. M., and Zhang, Y. (2017). Delineating the Diversity of Spinal Interneurons in Locomotor Circuits. *J. Neurosci.* 37, 10835–10841. doi: 10.1523/JNEUROSCI.1829-17.2017

Grudt, T. J., and Perl, E. R. (2002). Correlations between neuronal morphology and electrophysiological features in the rodent superficial dorsal horn. *J. Physiol.* 540, 189–207. doi: 10.1113/jphysiol.2001.012890

Hantman, A. W., van den Pol, A. N., and Perl, E. R. (2004). Morphological and physiological features of a set of spinal substantia gelatinosa neurons defined by green fluorescent protein expression. *J. Neurosci.* 24, 836–842. doi: 10.1523/JNEUROSCI.4221-03.2004

Häring, M., Zeisel, A., Hochgerner, H., Rinwa, P., Jakobsson, J. E. T., Lönnerberg, P., et al. (2018). Neuronal atlas of the dorsal horn defines its architecture and links sensory input to transcriptional cell types. *Nat. Neurosci.* 21, 869–880. doi: 10.1038/s41593-018-0141-1

Hayashi, M., Hinckley, C. A., Driscoll, S. P., Moore, N. J., Levine, A. J., Hilde, K. L., et al. (2018). Graded Arrays of Spinal and Supraspinal V2a Interneuron Subtypes Underlie Forelimb and Hindlimb Motor Control. *Neuron* 97, 869-884.e5. doi: 10.1016/j.neuron.2018.01.023

Hui, C. W., Zhang, Y., and Herrup, K. (2016). Non-Neuronal Cells Are Required to Mediate the Effects of Neuroinflammation: Results from a Neuron-Enriched Culture System. *PLoS One* 11:e0147134. doi: 10.1371/journal.pone.0147134

Kaech, S., and Banker, G. (2006). Culturing hippocampal neurons. *Nat. Protoc.* 1, 2406–2415. doi: 10.1038/nprot.2006.356

Kappagantula, S., Andrews, M. R., Cheah, M., Abad-Rodriguez, J., Dotti, C. G., and Fawcett, J. W. (2014). Neu3 Sialidase-Mediated Ganglioside Conversion Is Necessary for Axon Regeneration and Is Blocked in CNS Axons. *J. Neurosci.* 34, 2477–2492. doi: 10.1523/JNEUROSCI.4432-13.2014

Kopach, O., Esteras, N., Wray, S., Rusakov, D. A., and Abramov, A. Y. (2020). Maturation and phenotype of pathophysiological neuronal excitability of human cells in tau-related dementia. *J. Cell. Sci.* 133, jcs241687. doi: 10.1242/jcs.241687

Koseki, H., Donegá, M., Lam, B. Y., Petrova, V., van Erp, S., Yeo, G. S., et al. (2017). Selective rab11 transport and the intrinsic regenerative ability of CNS axons. *Elife* 6:e26956. doi: 10.7554/eLife.26956

LaBarbera, K. M., Limegrover, C., Rehak, C., Yurko, R., Izzo, N. J., Knezovich, N., et al. (2021). Modeling the mature CNS: A predictive screening platform for neurodegenerative disease drug discovery. *J. Neurosci. Methods* 358:109180. doi: 10.1016/j.jneumeth.2021.109180

Larsson, M. (2017). Pax2 is persistently expressed by GABAergic neurons throughout the adult rat dorsal horn. *Neurosci. Lett.* 638, 96–101. doi: 10.1016/j.neulet.2016.12.015

Lu, D. C., Niu, T., and Alaynick, W. A. (2015). Molecular and cellular development of spinal cord locomotor circuitry. *Front. Mol. Neurosci.* 8:25. doi: 10.3389/fnmol.2015.00025

Lu, P., Ceto, S., Wang, Y., Graham, L., Wu, D., Kumamaru, H., et al. (2017). Prolonged human neural stem cell maturation supports recovery in injured rodent CNS. *J. Clin. Invest.* 127, 3287–3299. doi: 10.1172/JCI92955

Lu, P., Kadoya, K., and Tuszynski, M. H. (2014). Axonal growth and connectivity from neural stem cell grafts in models of spinal cord injury. *Curr. Opin. Neurobiol.* 27, 103–109. doi: 10.1016/j.conb.2014.03.010

Martin, D., Wallace, T., and Johnson, E. (1990). Cytosine arabinoside kills postmitotic neurons in a fashion resembling trophic factor deprivation: evidence that a deoxycytidine-dependent process may be required for nerve growth factor signal transduction. *J. Neurosci.* 10, 184–193. doi: 10.1523/JNEUROSCI.10-01-00184.1990

Martinez, M., Delivet-Mongrain, H., Leblond, H., and Rossignol, S. (2012). Incomplete spinal cord injury promotes durable functional changes within the spinal locomotor circuitry. *J. Neurophysiol.* 108, 124–134. doi: 10.1152/jn.00073.2012

May, Z., Fenrich, K. K., Dahlby, J., Batty, N. J., Torres-Espín, A., and Fouad, K. (2017). Following Spinal Cord Injury Transected Reticulospinal Tract Axons Develop New Collateral Inputs to Spinal Interneurons in Parallel with Locomotor Recovery. *Neural Plasticity* 2017:1932875. doi: 10.1155/2017/1932875

Monteiro, F. A., Miranda, R. M., Samina, M. C., Dias, A. F., Raposo, A. A. S. F., Oliveira, P., et al. (2021). Tlx3 Exerts Direct Control in Specifying Excitatory Over Inhibitory Neurons in the Dorsal Spinal Cord. *Front. Cell. Dev. Biol.* 9:642697. doi: 10.3389/fcell.2021.642697

Moore, D. L., Blackmore, M. G., Hu, Y., Kaestner, K. H., Bixby, J. L., Lemmon, V. P., et al. (2009). KLF family members regulate intrinsic axon regeneration ability. *Science* 326, 298–301. doi: 10.1126/science.1175737

Moutaux, E., Christaller, W., Scaramuzzino, C., Genoux, A., Charlot, B., Cazorla, M., et al. (2018). Neuronal network maturation differently affects secretory vesicles and mitochondria transport in axons. *Sci. Rep.* 8:13429. doi: 10.1038/s41598-018-31759-x

Müller, T., Brohmann, H., Pierani, A., Heppenstall, P. A., Lewin, G. R., Jessell, T. M., et al. (2002). The homeodomain factor lbx1 distinguishes two major programs of neuronal differentiation in the dorsal spinal cord. *Neuron* 34, 551–562. doi: 10.1016/s0896-6273(02)00689-x

Neumann, S., Braz, J. M., Skinner, K., Llewellyn-Smith, I. J., and Basbaum, A. I. (2008). Innocuous, not noxious, input activates PKCgamma interneurons of the spinal dorsal horn via myelinated afferent fibers. *J. Neurosci.* 28, 7936–7944. doi: 10.1523/JNEUROSCI.1259-08.2008

Nicholls, J., and Saunders, N. (1996). Regeneration of immature mammalian spinal cord after injury. *Trends Neurosci.* 19, 229–234. doi: 10.1016/0166-2236(96)10021-7

Norris, C. M., Blalock, E. M., Thibault, O., Brewer, L. D., Clodfelter, G. V., Porter, N. M., et al. (2006). Electrophysiological mechanisms of delayed excitotoxicity: positive feedback loop between nmda receptor current and depolarization-mediated glutamate release. *J. Neurophysiol.* 96, 2488–2500. doi: 10.1152/jn.00593.2005

Pernas-Alonso, R., Schaffner, A. E., Perrone-Capano, C., Orlando, A., Morelli, F., Hansen, C. T., et al. (1996). Early upregulation of medium neurofilament gene expression in developing spinal cord of the wobbler mouse mutant. *Brain Res. Mol. Brain Res.* 38, 267–275. doi: 10.1016/0169-328x(95)00344-r

Petitjean, H., Pawlowski, S. A., Fraine, S. L., Sharif, B., Hamad, D., Fatima, T., et al. (2015). Dorsal Horn Parvalbumin Neurons Are Gate-Keepers of Touch-Evoked Pain after Nerve Injury. *Cell. Rep.* 13, 1246–1257. doi: 10.1016/j.celrep.2015.09.080

Petrova, V., Nieuwenhuis, B., Fawcett, J. W., and Eva, R. (2021). Axonal Organelles as Molecular Platforms for Axon Growth and Regeneration after Injury. *Int. J. Mol. Sci.* 22:1798. doi: 10.3390/ijms22041798

Petrova, V., Pearson, C. S., Ching, J., Tribble, J. R., Solano, A. G., Yang, Y., et al. (2020). Protrudin functions from the endoplasmic reticulum to support axon regeneration in the adult CNS. *Nat. Commun.* 11, 5614. doi: 10.1038/s41467-020-19436-y

Roppongi, R. T., Champagne-Jorgensen, K. P., and Siddiqui, T. J. (2017). Low-Density Primary Hippocampal Neuron Culture. *J. Vis. Exp.* 122:55000. doi: 10.3791/55000

Russ, D. E., Cross, R. B. P., Li, L., Koch, S. C., Matson, K. J. E., Yadav, A., et al. (2021). A harmonized atlas of mouse spinal cord cell types and their spatial organization. *Nat. Commun.* 12:5722. doi: 10.1038/s41467-021-25125-1

Schindelin, J., Arganda-Carreras, I., Frise, E., Kaynig, V., Longair, M., Pietzsch, T., et al. (2012). Fiji: an open-source platform for biological-image analysis. *Nat. Methods* 9, 676–682. doi: 10.1038/nmeth.2019

Schwab, M. E., and Strittmatter, S. M. (2014). Nogo limits neural plasticity and recovery from injury. *Curr. Opin. Neurobiol.* 27, 53–60. doi: 10.1016/j.conb.2014.02.011

Shen, Y., Tenney, A. P., Busch, S. A., Horn, K. P., Cuascut, F. X., Liu, K., et al. (2009). PTPsigma is a receptor for chondroitin sulfate proteoglycan, an inhibitor of neural regeneration. *Science* 326, 592–596. doi: 10.1126/science.1178310

Song, M., Mohamad, O., Chen, D., and Yu, S. P. (2013). Coordinated Development of Voltage-Gated Na+ and K+ Currents Regulates Functional Maturation of Forebrain Neurons Derived from Human Induced Pluripotent Stem Cells. *Stem. Cells Dev.* 22, 1551–1563. doi: 10.1089/scd.2012.0556

Spike, R. C., Puskar, Z., Andrew, D., and Todd, A. J. (2003). A quantitative and morphological study of projection neurons in lamina I of the rat lumbar spinal cord. *Eur. J. Neurosci.* 18, 2433–2448. doi: 10.1046/j.1460-9568.2003.02981.x

Stahl, A. M., Ruthel, G., Torres-Melendez, E., Kenny, T. A., Panchal, R. G., and Bavari, S. (2007). Primary cultures of embryonic chicken neurons for sensitive cell-based assay of botulinum neurotoxin: implications for therapeutic discovery. *J. Biomol. Screen* 12, 370–377. doi: 10.1177/1087057106299163

Sun, J., and Harrington, M. A. (2019). The Alteration of Intrinsic Excitability and Synaptic Transmission in Lumbar Spinal Motor Neurons and Interneurons of Severe Spinal Muscular Atrophy Mice. *Front. Cell. Neurosci.* 13:15. doi: 10.3389/fncel.2019.00015

Sun, Z., Williams, D. J., Xu, B., and Gogos, J. A. (2018). Altered function and maturation of primary cortical neurons from a 22q11.2 deletion mouse model of schizophrenia. *Trans. Psychiat.* 8:85. doi: 10.1038/s41398-018-0132-8

Takazawa, T., Croft, G. F., Amoroso, M. W., Studer, L., Wichterle, H., and MacDermott, A. B. (2012). Maturation of Spinal Motor Neurons Derived from Human Embryonic Stem Cells. *PLoS ONE* 7:e40154. doi: 10.1371/journal.pone.0040154

Thomson, C. E., McCulloch, M., Sorenson, A., Barnett, S. C., Seed, B. V., Griffiths, I. R., et al. (2008). Myelinated, synapsing cultures of murine spinal cord – validation as an in vitro model of the central nervous system. *Eur. J. Neurosci.* 28, 1518–1535. doi: 10.1111/j.1460-9568.2008.06415.x

Todd, A. J., Spike, R. C., and Polgár, E. (1998). A quantitative study of neurons which express neurokinin-1 or somatostatin sst2a receptor in rat spinal dorsal horn. *Neuroscience* 85, 459–473. doi: 10.1016/S0306-4522(97)00669-6

Uyeda, A., and Muramatsu, R. (2020). Molecular Mechanisms of Central Nervous System Axonal Regeneration and Remyelination: A Review. *Int. J. Mol. Sci.* 21:8116. doi: 10.3390/ijms21218116

van Niekerk, E. A., Tuszynski, M. H., Lu, P., and Dulin, J. N. (2016). Molecular and Cellular Mechanisms of Axonal Regeneration After Spinal Cord Injury. *Mol. Cell. Proteomics* 15, 394–408. doi: 10.1074/mcp.R115.053751

Wilson, J. M., Hartley, R., Maxwell, D. J., Todd, A. J., Lieberam, I., Kaltschmidt, J. A., et al. (2005). Conditional Rhythmicity of Ventral Spinal Interneurons Defined by Expression of the Hb9 Homeodomain Protein. *J. Neurosci.* 25, 5710–5719. doi: 10.1523/JNEUROSCI.0274-05.2005

Zeng, H., and Sanes, J. R. (2017). Neuronal cell-type classification: challenges, opportunities and the path forward. *Nat. Rev. Neurosci.* 18, 530–546. doi: 10.1038/nrn.2017.85

Zhong, G., Díaz-Ríos, M., and Harris-Warrick, R. M. (2006). Intrinsic and Functional Differences among Commissural Interneurons during Fictive Locomotion and Serotonergic Modulation in the Neonatal Mouse. *J. Neurosci.* 26, 6509–6517. doi: 10.1523/JNEUROSCI.1410-06.2006

Conflict of Interest: The authors declare that the research was conducted in the absence of any commercial or financial relationships that could be construed as a potential conflict of interest.

Publisher's Note: All claims expressed in this article are solely those of the authors and do not necessarily represent those of their affiliated organizations, or those of the publisher, the editors and the reviewers. Any product that may be evaluated in this article, or claim that may be made by its manufacturer, is not guaranteed or endorsed by the publisher.

frontiers in Cellular Neuroscience

ORIGINAL RESEARCH
published: 24 February 2022
doi: 10.3389/fncel.2022.839811

Targeting Insect Olfaction *in vivo* and *in vitro* Using Functional Imaging

Fabio Miazzi[1], Kalpana Jain[1], Sabine Kaltofen[1], Jan E. Bello[2], Bill S. Hansson[1†] and Dieter Wicher[1†]*

[1] Department of Evolutionary Neuroethology, Max Planck Institute for Chemical Ecology, Jena, Germany, [2] Department of Entomology, University of California, Riverside, Riverside, CA, United States

Insects decode volatile chemical signals from its surrounding environment with the help of its olfactory system, in a fast and reliable manner for its survival. In order to accomplish this task, odorant receptors (ORs) expressed in olfactory sensory neurons (OSNs) in the fly's antenna process such odor information. In order to study such a sophisticated process, we require access to the sensory neurons to perform functional imaging. In this article, we present different preparations to monitor odor information processing in *Drosophila melanogaster* OSNs using functional imaging of their Ca^{2+} dynamics. First, we established an *in vivo* preparation to image specific OSN population expressing the fluorescent Ca^{2+} reporter GCaMP3 during OR activation with airborne odors. Next, we developed a method to extract and to embed OSNs in a silica hydrogel with OR activation by dissolved odors. The odor response dynamics under these different conditions was qualitatively similar which indicates that the reduction of complexity did not affect the concentration dependence of odor responses at OSN level.

Keywords: insect olfaction, *Drosophila melanogaster*, olfactory sensory neuron, calcium imaging, silica hydrogel, waterglass

OPEN ACCESS

Edited by:
Daniela Tropea, Trinity College Dublin, Ireland

Reviewed by:
Hiro Matsunami, Duke University, United States
Merid Negash Getahun, International Centre of Insect Physiology and Ecology (ICIPE), Kenya

***Correspondence:**
Dieter Wicher
dwicher@ice.mpg.de

†These authors shared supervision

Specialty section:
This article was submitted to Cellular Neurophysiology, a section of the journal Frontiers in Cellular Neuroscience

Received: *20 December 2021*
Accepted: *03 February 2022*
Published: *24 February 2022*

Citation:
Miazzi F, Jain K, Kaltofen S, Bello JE, Hansson BS and Wicher D (2022) Targeting Insect Olfaction in vivo and in vitro Using Functional Imaging. Front. Cell. Neurosci. 16:839811. doi: 10.3389/fncel.2022.839811

INTRODUCTION

In order to build their representation of the external world, animals must acquire and integrate a plethora of different visual, auditory, tactile, magnetic and chemical stimuli. Chemoreception, i.e., the detection of volatile and non-volatile compounds by olfaction and taste, respectively, plays a pivotal role in the ecology for example of nematodes, vertebrates and insects. With the use of genetic tools such as the GAL4-UAS system, it became possible to study molecular mechanisms in insect physiology (Brand and Perrimon, 1993). Especially in the vinegar fly *Drosophila melanogaster* the GAL4-UAS system is extensively used to study tissue specific gene expression and function due to advantages such as short life cycle and complete availability of genomic sequence (Jennings, 2011). For *Drosophila*, olfaction – as for other insects – is the main sense to assess food, mates, oviposition sites and to avoid perils (Hansson and Stensmyr, 2011; Mansourian and Stensmyr, 2015). Volatile compounds in particular are detected by the two main olfactory organs of the fly: the antennae and the maxillary palps. They are covered by porous hair-like structures called sensilla, each one housing the dendrites of up to four olfactory sensory neurons (OSNs). They possess three main classes of olfactory receptors: the odorant receptors (ORs), the ionotropic receptors (IRs), related to the ionotropic glutamate receptors and specific gustatory receptors (GRs), which in the antennae detect, e.g., carbon dioxide (Touhara and Vosshall, 2009; Joseph and Carlson, 2015). ORs are used to perceive a variety of compounds, from food odors and harmful bacterial contaminations to

pheromones (Mansourian and Stensmyr, 2015). These receptors are heteromers composed of a ubiquitous odorant co-receptors (Orco) and a neuron-specific receptor (OrX) (Larsson et al., 2004; Neuhaus et al., 2005; Benton et al., 2006). They share a seven transmembrane-domain topology, but unlike canonic G protein-coupled receptors they show an inverted topology with an intracellular N-terminus (Benton et al., 2006; Lundin et al., 2007; Smart et al., 2008; Tsitoura et al., 2010). ORs form ligand-gated cationic channels (Sato et al., 2008; Wicher et al., 2008), which are regulated by multiple metabotropic cascades influencing for example the receptor sensitivity (Nakagawa and Vosshall, 2009; Wicher, 2015).

In vivo studies on insect olfaction have greatly benefited from the position of these organs, which are extrovert and easily accessible in the fly's head, in comparison to the mammalian olfactory epithelium, which is deeply buried inside the nasal cavity. This allowed researchers to perform comprehensive odor-response profile screenings from antennal and palp sensilla using extracellular electrophysiological recordings (de Bruyne et al., 2001; Dobritsa et al., 2003; Hallem et al., 2004; Dweck et al., 2016). On the other hand, imaging experiments from these organs suffer from a limited space resolution, particularly using epifluorescence microscopy, due to the light scattering induced by the cuticle and the sensory hairs. Reports on cellular, functional imaging and patch clamp from OSNs are based on antennal preparations and involved in slicing the antenna and fixing it on a support via silicon-based media and delivering stimuli in water solutions (Mukunda et al., 2014, 2016; Cao et al., 2016). Such approaches are certainly limited due to the invasive techniques used to prepare the samples, but their success clearly shows their potential and urges for further improvements to refine them to and expand the range of biological questions that is possible to address. Insect ORs are also heterologously expressed in *in vitro* and *in vivo* systems to study functional properties and identify specific ligands (Fleischer et al., 2018). For example, the *in vivo* expression system "*Drosophila* empty neuron" allows the ectopic expression of ORs in *Drosophila* OSNs by removing the native OrX protein (Dobritsa et al., 2003; Kurtovic et al., 2007; Gonzalez et al., 2016). Insect OR function is also studied in *in vitro* expression systems as Human Embryonic Kidney (HEK) 293 cells (Große-Wilde et al., 2007; Sato et al., 2008; Wicher et al., 2008; Corcoran et al., 2014). Mammalian HeLa cells (Sato et al., 2008), *Spodoptera frugiperda* Sf9 cells (Kiely et al., 2007), and also *Xenopus laevis* oocytes (Wagner et al., 2000). However, such systems also bear the risk of a low expression level, inadequate protein translation or impaired OR trafficking to the plasma membrane.

In this study, we present preparations of different complexity to study the function of *D. melanogaster* OSNs. We first present an *in vivo* preparation that allows the OSN stimulation with airborne odors, i.e., to study odor-induced responses elicited under natural conditions. We then developed a technique to isolate vital *Drosophila* OSNs from antennal tissue. To allow further functional studies on these isolated cells we established a new embedding method based on sodium silicate (also called waterglass) (Avnir et al., 2006; Pierre and Rigacci, 2011) without any need of greasy or silicon media, which may affect the odor delivery and the response temporal properties. Finally, we offer proof of principle of the effectiveness of such preparations and we discuss their potential to advance our knowledge about olfactory transduction mechanisms in insects.

MATERIALS AND METHODS

Insect Rearing

Drosophila melanogaster with genotype (*w, UAS-GCaMP3.0; +; Or22a-Gal4*), (*w; UAS-GCaMP6f; Orco-Gal4*), (*w; UAS-GCaMP6f; Or22a-Gal4*), and (*+; Orco-Gal4/CyO; UAS-Syn21-GFP-p10/TM6B*) were reared on conventional cornmeal agar medium under a 12 h light: 12 h dark cycle at 25°C. UAS-GCamP3.0; Orco-Gal4; UAS-GCaMP6f parental line was obtained from Bloomington Stock Center (#32234), (#42747), (#26818), and Or22a-Gal4 line was kindly provided by Dr. Leslie Vosshall, The Rockefeller University.

Chemicals

VUAA1 (N-(4-ethylphenyl)-2-((4-ethyl-5-(3-pyridinyl)-4H-1,2,4-triazol-3-yl)thio)acetamide) was synthesized by the group "Mass Spectrometry/Proteomics" of the Max Planck Institute for Chemical Ecology (Jena, Germany). Ethyl hexanoate (99%, Sigma-Aldrich), L-Cysteine hydrochloride (Cat. Nr. C1276, Sigma-Aldrich), Papain (Cat. Nr. 5125, Calbiochem, San Diego, CA, United States), cOmplete protease inhibitor cocktail (Cat. Nr. 04693116001, Roche, Basel, Switzerland), methanol (≥99.5%, Roth) HCl (≥32%, Sigma-Aldrich), H_2SO_4 (95∼97%, Sigma-Aldrich), sodium metasilicate solution (Cat. Nr. 13729, Sigma-Aldrich), low Ca^{2+}-Schneider's medium (Cat. Nr. S9895, Sigma-Aldrich), Benzaldehyde (Acros Organics, NJ, United States) were used in following experiments.

Functional Calcium Imaging From an *in vivo* Antennal Preparation

Flies with the genotype (*w, UAS-GCaMP3.0; +; Or22a-Gal4*) were anesthetized in ice for 30 min, and then placed into a truncated 1 ml pipette tip, leaving the head out of the tip and fixed using odor-free glue. The truncated tip was fixed using modeling clay on a custom Plexiglas mounting block (Strutz et al., 2012). Next, a custom holder to fix the antenna in vertical position was produced (**Figures 1A–C** and **Supplementary Figure 1**). A piece of aluminum foil (5 mm × 5 mm) with a slit (0.5 mm) for inserting the antenna and a small plastic ring (cut from an Eppendorf Microloader^{TM}) were glued on a glass coverslip (18 mm × 24 mm, #0 thickness, Menzel-Gläser, Braunschweig, Germany). The arista was then glued on the top of the glass coverslip with odor-free glue and the funiculus was manually cut at around half of its length with a scalpel blade #22 (Fine Science Tools, Heidelberg, Germany). Immediately after cutting the antenna, a small glass coverslip (15 mm × 15 mm, #00 thickness, Menzel-Gläser) moistened with a very thin layer of halocarbon oil 700 (Sigma-Aldrich) was laid on the open funiculus to seal it. Both coverslips were fixed to each other and to the Plexiglas holder with odor-free

glue to prevent movement artifacts. Imaging was performed using a BX51W1 wide field fluorescence microscope (Olympus, Hamburg, Germany) equipped with a DCLP490 dichroic mirror and a 60x/0.90 water immersion LUMPFL objective (Olympus). The objective was immersed in a drop of distilled water put on top of the coverslip sealing the funiculus. GCaMP3.0 stimulation with a 475 nm light and an exposition time of 50 ms was performed using a monochromator (Polychrome V, TILL Photonics, Gräfelfing, Germany). Emitted light was filtered with a LP515 filter and acquired at a 4 Hz frequency using a cooled CCD camera (Sensicam, PCO Imaging, Kelheim, Germany) controlled by TILLVision 4.5 software (TILL Photonics). Odor stimuli were sampled from the headspace of a 50 ml volume glass bottle (Schott, Jena, Germany) containing 2 ml of ethyl hexanoate (99% purity, Sigma-Aldrich) diluted in mineral oil to a 10^{-2} dilution. A stimulus controller (Syntech, Kirchzarten, Germany) was used to deliver for 2 s the bottle headspace into a charcoal-filtered and humidified constant air flow (0.5 m/s) in a Teflon tube, where inlet was positioned 5–10 mm from the recorded antenna. The stimulus was delivered at 10 s from the start of the recording; the total duration of the experiment was 35 s. The response magnitude was calculated for each frame as the average $\Delta F/F_0$ and expressed in percentage after background subtraction. Regions of interest (ROIs) were selected using the built-in tools of TILLVision 4.5 and F_0 was estimated as the mean fluorescence level calculated for each selected region of interest as the average intensity from 3 to 5.25 s of the recording and paired *t*-tests were performed using Prism 4 software (GraphPad Software Inc., La Jolla, CA, United States).

Functional Calcium Imaging From an *ex vivo* Antenna Preparation

Four to eight old female flies of the genotype (*w; UAS-GCaMP6f; Orco-Gal4*), (*w; UAS-GCaMP6f; Or22a-Gal4*) were decapitated, then the antennae were excised and fixed on a Sylgard-coated support using the two-component silicon curing medium and immersed in *Drosophila* Ringer solution (130 mM NaCl, 5 mM KCl, 4 mM $MgCl_2 \times 6H_2O$, 2 mM $CaCl_2$, 36 mM sucrose, 5 mM Hepes, pH = 7.3, osmolality = 312 mOsm/kg). Samples were immersed in *Drosophila* Ringer solution and imaged using the imaging setup described above with a LUMPFL 60x/0.90 water immersion objective (Olympus, Hamburg, Germany). Emitted light was separated by a 490 nm dichroic mirror and filtered with a 515 nm long-pass filter. GCaMP6f was excited with a 475 nm light for 50 ms per frame and a temporal resolution of 0.2 Hz. Stimuli consisted of 100 μl of ethyl hexanoate (99%, Sigma-Aldrich) or VUAA1 (N-(4-ethylphenyl)-2-((4-ethyl-5-(3-pyridinyl)-4H- 1,2,4-triazol-3-yl)thio)acetamide, synthesized by the working group "Mass Spectrometry/Proteomics" of the Max Planck Institute for Chemical Ecology, Jena) at the required concentration. Ethyl hexanoate and VUAA1 working solutions were freshly prepared from 100 mM (or 500 mM, for final concentrations >100 μM) stocks in DMSO, kept at −20°C. DMSO at a 1:1000 dilution in *Drosophila* Ringer was used as control.

Calcium Imaging and Data Analysis From *D. melanogaster* Olfactory Neurons

Females between 4 and 8 days old were decapitated, the antennae were excised and fixed on a Sylgard-coated support (Sylgard 184, Dow Corning Corp., Midland, MI, United States) using a two-component silicon curing medium (Kwik-Sil, World Precision Instruments, Sarasota, FL, United States). The antennae were immersed in dissecting solution (Au – Sicaeros et al., 2007) (Solution A: 137 mM NaCl, 5.4 mM KCl, 0.17 mM Na_2HPO_4, 0.22 mM KH_2PO_4. Solution B: 9.9 mM HEPES). For 500 ml of dissecting solution: 400 ml ultra-filtered water, 25 ml of Solution A, 14 ml of Solution B, 3.0 g (33.3 mM) D(+)-Glucose, 7.5 g (43.8 mM) Sucrose. Brought to pH 6.7 with 1 N NaOH and to the final volume of 500 ml with ultra-filtered water supplemented with 1 mM EDTA, 5 mM L-Cysteine hydrochloride (Cat. Nr. C1276, Sigma-Aldrich), and after equilibrating the pH to 6.7 with 1 N NaOH, 0.5 mg/ml Papain (Cat. Nr. 5125, Calbiochem, San Diego, CA, United States). Funiculi were cut between one third and one-half of their length and incubated at 27°C for 30 min. After incubation, the dissecting solution was removed and the antennae were rinsed twice for 5 min at 27°C with Ca^{2+}-free Ringer (130 mM NaCl, 4 mM $MgCl_2 \times 6H_2O$, 36 mM sucrose, 5 mM HEPES, 5 mM KCl. Osmolality = 312 mOsm/kg, pH = 6.7 adjusted with 1 N NaOH) supplemented with 1:75 cOmplete protease inhibitor cocktail (Cat. Nr. 04693116001, Roche, Basel, Switzerland) dissolved in a 100 mM PBS solution (50.93 mM Na_2HPO_4, 60.22 mM KH_2PO_4, 80.42 mM NaCl; pH = 6.7 adjusted with 1 N NaOH). A stock of Protease inhibitory solution was prepared by dissolving one tablet of cOmplete Protease Inhibitor Cocktail in 2 ml of 100 mM PBS. The solution was aliquoted and stored at −20°C for max 3 months. As an excessive concentration of cOmplete protease may cause cell permeabilization, the protease solution was added to the Ca^{2+}-free Ringer in a 1:75 dilution, as suggested by the manufacturer.

Glass Coverslip Preparation

Round glass coverslips (12 mm diameter, Cat. Nr. P231.1, Carl Roth, Karlsruhe, Germany) were cleaned by immersion in methanol (≥99.5%, Roth) and HCl (≥32%, Sigma-Aldrich) 1:1 for 30 min and after rinsing in double distilled water, by immersion in H_2SO_4 (95∼97%, Sigma-Aldrich) for 30 min (Cras et al., 1999). Coverslips were then thoroughly rinsed and kept in methanol under N_2; immediately before use, they were thoroughly washed in double distilled water and dried under N_2.

Glass Capillaries and Dissociated Antennal Tissue Preparation

Borosilicate glass capillaries (0.86 mm × 150 mm × 80 mm, Cat. Nr. GB150-8P, Science Products, Hofheim, Germany) were pulled using a P-97 Micropipette puller (Sutter Instrument, Novato, CA, United States) and their tip was cut and fire polished in order to obtain holding micropipettes with an internal diameter ∼0.4 mm. The capillary tip size was found to be critical in order to extract viable neurons. The inner diameter of the tip should be slightly larger than the width

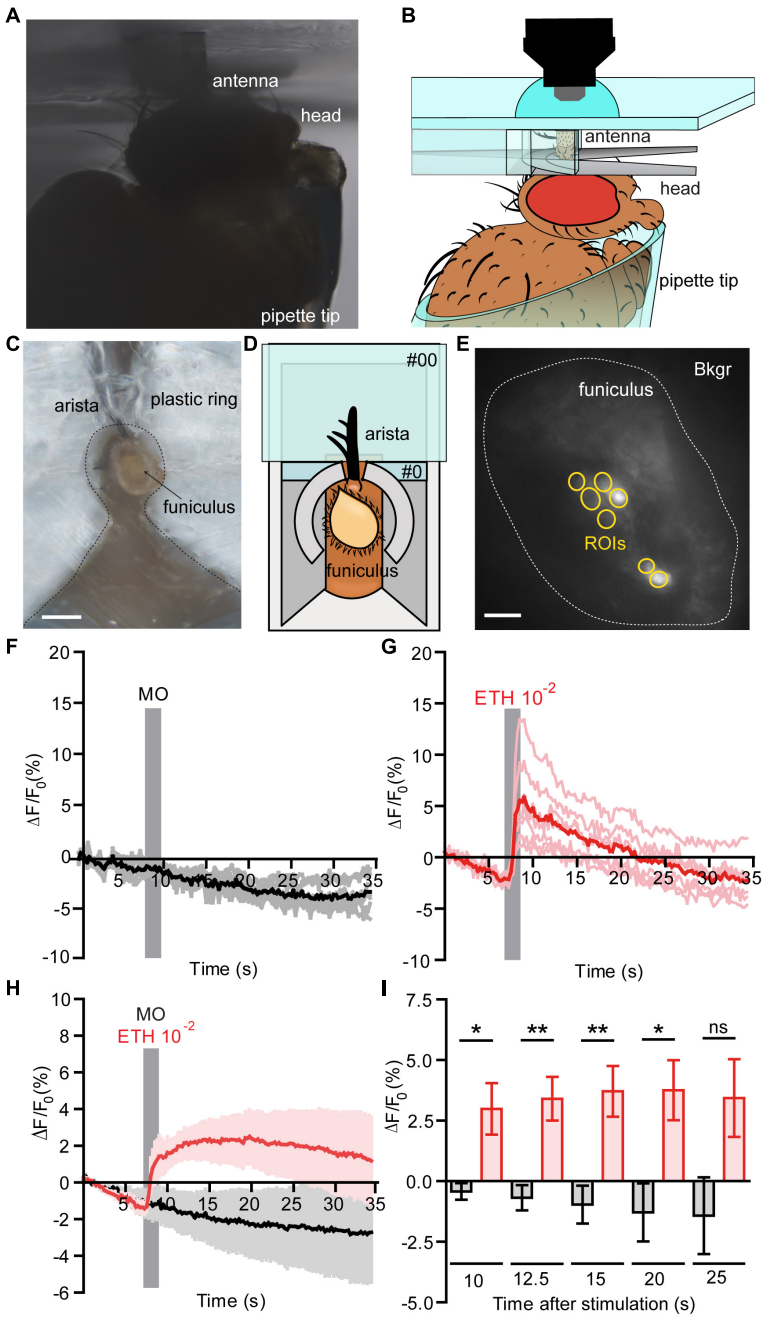

FIGURE 1 | Functional calcium imaging from an *in vivo* antennal preparation. **(A)** Image of the *in vivo* preparation from the side view. **(B)** Schematic representation of the fly placed in a pipette tip with it's excised antenna held in vertical position on a custom holder, for the detailed information see **Supplementary Figure 1**. **(C)** Image of the *in vivo* preparation from a top view, Scale bar = 0.5 mm. **(D)** Representation of the *in vivo* preparation from a top view, where open antenna is held within a #0 glass coverslip with support of an aluminum foil holder and a plastic ring around the antenna. A posterior slit on the plastic ring allowed fixing the arista directly on the #0 coverslip with odor-free glue. **(E)** Normalized fluorescence base level intensity from a fly preparation expressing GCaMP3.0 in Or22a olfactory neurons. The regions of interest (ROIs) are marked in yellow and the area used for the background subtraction (Bkgr) are marked in white, Scale bar = 10 μm. **(F,G)** Example of the recorded fluorescence intensity (expressed in ΔF/F0) over time from the same preparation as shown in **(D)**. **(F)** The fly was first stimulated with mineral oil (MO, negative control); the stimulus duration is marked with a vertical gray bar, each ROI as in **(E)** is represented in gray and the mean value in black. **(G)** The fly was then stimulated with ethyl hexanoate (EH) at a 10^{-2} dilution in mineral oil; the stimulus duration is marked with a vertical gray bar, each ROI as in **(E)** is represented in light red and the mean value in red. **(H)** Pooled responses from $n = 5$ antennae to MO (black) and EH 10^{-2} (red). Traces represents mean ± SEM. **(I)** Intensity of the responses to MO (black) and EH 10^{-2} (red) calculated subtracting the fluorescence value at the moment of stimulation (7 s) from the fluorescence intensity at a given time expressed in seconds after stimulation. The response to EH is long lasting and is statistically significant until 20 s after stimulation [correspondent to time = 27 s plotted in **(G)**]. Paired *t*-tests, without multiple comparison correction, $^{*}p < 0.05$, $^{**}p < 0.01$, ns, not significant. Graphs represent mean ± SEM. Statistics for each test is reported in the **Supplementary Table 4**.

of the cut antenna when fixed in a vertical position. The capillaries were subsequently silanized by immersion for 10–15 s in 5% dimethyldichlorosilane in toluene (Cat. Nr. 33065, Supelco, Sigma-Aldrich) and rinsed twice in toluene (≥99.5%, Sigma-Aldrich) and three times in methanol (≥99.5%, Sigma-Aldrich). The capillaries were then dried under N_2 and heated at 200°C for 2 h.

To embed the dissociated antennal tissue, we first used 0.01% sterile filtered poly-L-lysine (Sigma-Aldrich, article no. P4707), Concanavalin A/laminin (Sigma-Aldrich: article no. C2010, L2020) or Collagenase Clostridium (Sigma-Aldrich, article no. C9891) on the coverslips to adhere cells but *Drosophila* OSNs did not attach to the cover slip. We next used a sodium metasilicate solution (Avnir et al., 2006; Pierre and Rigacci, 2011) to adhere the cells, for that, this solution was prepared immediately before use by mixing 2.71 μl of HCl 0.05 M, 2.43 μl of sodium metasilicate solution (Cat. Nr. 13729, Sigma-Aldrich) diluted 1:10 in double distilled water and 13.86 μl of low Ca^{2+}-Schneider's medium [Cat. Nr. S9895, Sigma-Aldrich, modified with 0.4 g EGTA (1 mM), 22.2 mg $CaCl_2$ (free Ca^{2+} = 500 nM), 0.4 g $NaHCO_3$, total volume: 1 L, pH = 6.7 adjusted with 1 N NaOH; sterile filtered and kept at 4°C]. After a 1 μl drop of Ca^{2+}-free Ringer was deposited on a cleaned coverslip, the content of the treated antennae was gently sucked using a silanized capillary attached to a 2 μl micropipette. Usually ∼0.5/1 μl of liquid was sucked together with each antenna. Within 10 min from mixing, the complete volume of the silicate gel solution was added to the coverslip and distributed uniformly. The total volume of liquid on a coverslip should be ∼ 25 μl, for a final Na_2SiO_3 concentration equal to 0.972% of the Na_2SiO_3 (≥27% SiO_2 basis) stock solution. Coverslips were incubated for 1 h at 26°C in a high humidity environment, to avoid desiccation.

Data Analysis

Imaging data were exported as uncompressed tiff files and analyzed using custom scripts in Fiji-ImageJ2 (Schindelin et al., 2012; Rueden et al., 2017) where the regions of interest were selected using a semi-automatic procedure and the $\Delta F/F_0$ values were calculated after background, flat-field and movement correction. Statistical analysis was performed in R (R Core Team, 2017) using custom scripts including add-on packages (Chang, 2014; Ritz et al., 2015; Wickham, 2016; Arnold, 2017; Auguie, 2017). Parametric statistics for data analysis of the standard deviation of base level $\Delta F/F_0$ values for GCaMP6f (**Figure 3I**) was used after evaluation of the pooled $\Delta F/F_0$ values distribution of all analyzed cells (ROIs) (**Supplementary Figure 5** and see section "Statistical Methods" below). In all preparation types we occasionally observed a reduction in base level fluorescence (e.g., **Figure 1** and **Supplementary Figure 5**). Such artifacts, e.g., due to fluophore bleaching were compensated during data analysis.

Statistical Methods

The appropriate statistics for data analysis on **Supplementary Figures 2D,E** and **Figure 3I** was evaluated after assessment of the data distributions. For GCaMP6f $\Delta F/F_0$ data relative frequency distributions — including all regions of interest (ROIs) selected for each treatment— were evaluated for the basal intracellular free Ca^{2+} concentration ($[Ca^{2+}]_i$) at time t = 0 s (**Supplementary Figure 4**). Moreover, the standard deviation of $\Delta F/F_0$ values before stimulus application was calculated for each ROI and the relative frequency distribution of values for each treatment was assessed (**Supplementary Figure 5**). In this case, none of the treatments showed a terminal long tail, meaning that the number of ROIs with skewed high values — and consequently with the chance to skew the mean — was negligible. Consequently, the mean value between all ROIs was selected for each independent measure and the difference between groups was evaluated using two-tailed Welch's t-tests.

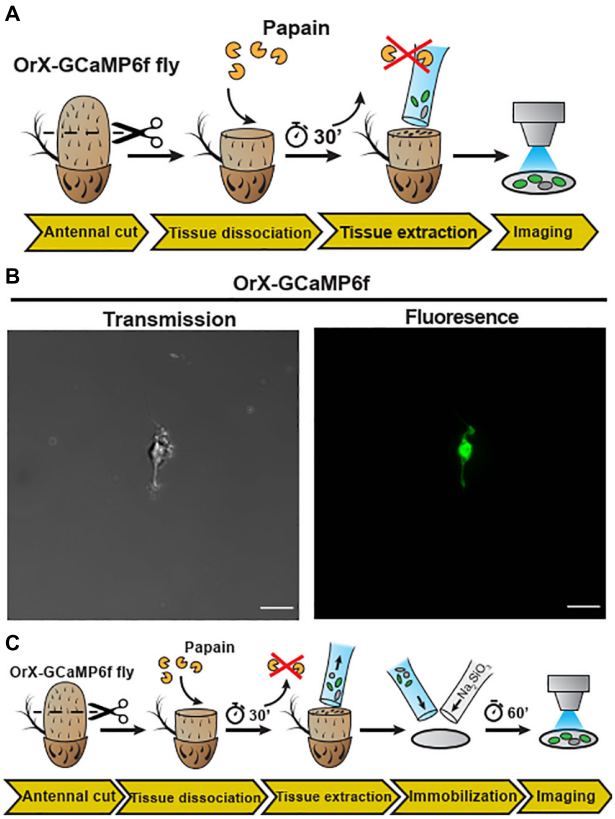

FIGURE 2 | Embedding of dissociated *D. melanogaster* antennal tissue in a sodium metasilicate gel. **(A)** Schematic procedure for dissociation and embedding of vinegar fly antennal tissue (see section "Materials and Methods"). After fixing the antenna with a silicon-based curing medium, the funiculus was cut and incubated with a papain solution for 30 min. Then, the dissociated tissue was extracted with a silanized glass capillary and then single neuron was extracted from this fly (*+; Orco-Gal4/CyO; UAS-Syn21-GFP-p10/TM6B*), using this preparation. **(B)** Confocal image of single cell as shown in transmission (gray) and fluorescence (green) signals, Scale bar = 8 μm. In the next illustration **(C)**, after tissue extraction, the sample was mixed with a modified *Drosophila* Schneider's medium containing 0.972% of a Na_2SiO_3 stock solution (≥27% SiO_2 basis) on a methanol treated cover slip. Ca^{2+} imaging was performed after a 60 min incubation time, to allow the Na_2SiO_3 gelation.

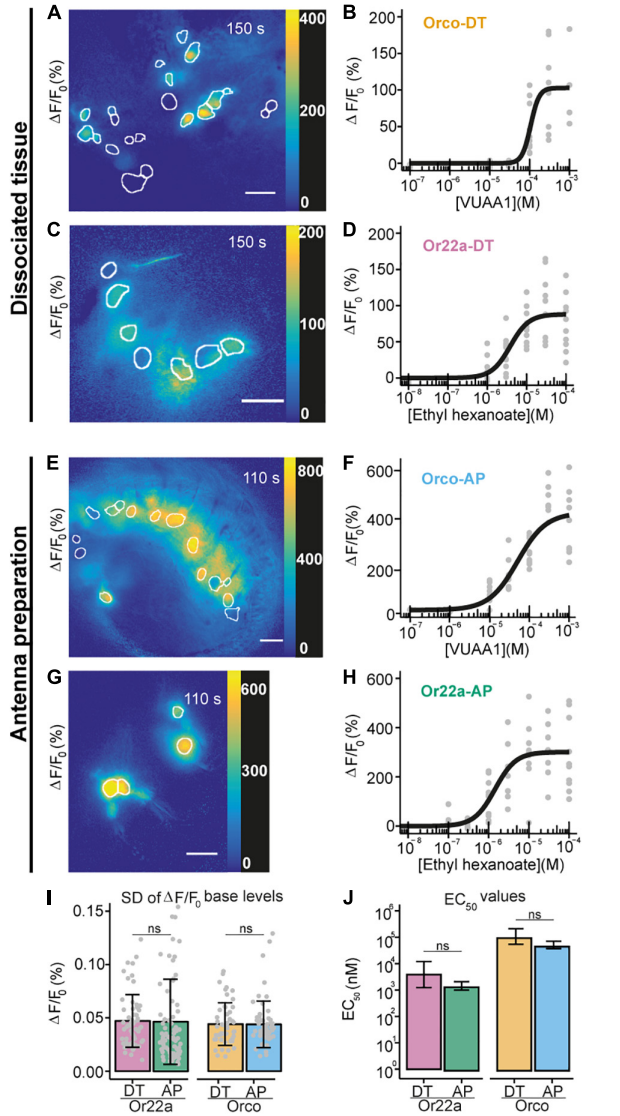

FIGURE 3 | Comparison between Ca^{2+} imaging from OSNs in sodium metasilicate-embedded and undissociated antennal tissue. **(A–D)** $\Delta F/F_0$ (%) from antennal dissociated tissue with **(A)** Orco expressing neurons and **(C)** Or22a OSNs following the application of ethyl hexanoate (EH) and VUAA1, respectively, at dose-dependent concentration. White boundaries indicate regions of interest (ROIs) for quantitative analysis. Gray lines show the $\Delta F/F_0$ (%) of each ROI shown in the corresponding left panel; the black line represents the average taken for subsequent analysis ($n = 1$). Scale bar = 8 μm. **(B,D)** Concentration-response curves for Na_2SiO_3-embedded dissociated antennal tissue with Orco (**B**, Orco-DT) and Or22a OSNs (**D**, Or22a-DT) stimulated with VUAA1 ($4 \leq n \leq 11$ for each concentration, 49 total data points) and ethyl hexanoate ($8 \leq n \leq 10$ for each concentration, 60 total data points), respectively. Examples of Ca^{2+} imaging from Orco **(E)** and Or22a-expressing **(G)** OSNs from undissociated antennal tissue with the ROIs highlighted in white. **(F,H)** Concentration-response curves from Orco **(F)** and Or22a-expressing OSNs **(H)** from undissociated antennal tissue after stimulation with increasing concentrations of VUAA1 (Orco-AP) **(F)** and ethyl hexanoate (Or22a-AP) **(H)**. $5 \leq n \leq 11$ **(F)** and $6 \leq n \leq 11$ **(H)** for each concentration, 60 and 71 total data points, respectively. Parameters for curve fits are reported in **Supplementary Table 5**. **(I,J)** Comparison between the $\Delta F/F_0$ standard deviation (SD) before stimulus application **(I)** and the half maximal effective concentrations (EC_{50}) **(J)** of the OSNs from the

(Continued)

FIGURE 3 | undissociated antennal preparation (AP) and the dissociated tissue (DT) after stimulation of Or22a OSNs with ethyl hexanoate and Orco OSNs with VUAA1. **(I)** Or22a-AP: $n = 71$, Or22a-DN: $n = 60$, Or22a AP vs. DT: $p = 0.9036$. Orco-AP: $n = 60$, Orco-DN: $n = 49$, Orco AP vs. DT: $p = 0.9816$. Two-tailed Welch two-sample t-tests. Graphs represent mean ± SD. Test statistic values, confidence intervals and degrees of freedom are given in **Supplementary Table 6**. **(J)** Or22a AP vs. DT: $p = 0.1313$. Orco AP vs. DT: $p = 0.06676$. Parameter comparison using the compParm function of the R (R Core Team, 2017) drc (Ritz et al., 2015) package. Statistic values are given in **Supplementary Table 7**. Graphs represent mean ± 95% CI.

RESULTS

In vivo Cellular-Resolution Calcium Imaging From Antennal Olfactory Sensory Neurons

The isolated antenna preparation according to Mukunda et al. (2014) allows to study OR activation in the OSNs. This approach, however, requires dissolved OR activators. To overcome this limitation we developed a whole animal preparation that allows to stimulate OSNs with airborne odorants. To access the antennal olfactory neurons in a living fly, we first immobilized the animal in a custom Plexiglas holder inside a pipette tip and we fixed the antenna in vertical position using a custom holder without disrupting the antennal sensilla (**Figures 1A,B** and **Supplementary Figure 1**). After that, we made a transversal cut of the funiculus, stimulated the animal with airborne odorants, and recorded their neuronal activity (**Figures 1C–E**). The transversal cut did not induce disruption of the antennal tissue sufficient to impair the ability of olfactory neurons to respond to odors. Using a fly line expressing GCaMP3.0 in Or22a olfactory neurons we checked for the viability of these cells by recording their responses first to mineral oil (solvent) and comparing them to the responses elicited by ethyl hexanoate at a 10^{-2} dilution in mineral oil. We could show the viability of this preparation as cells were responding to a 10^{-2} dilution of the odor, but not to the solvent alone (**Figures 1F,G**). Moreover, the response was sustained and lasted up to 20 s after stimulation (**Figures 1H,I** and **Supplementary Table 4**).

In vitro Cellular-Resolution Calcium Imaging From Dissociated Antennal Tissue

With the whole animal preparation and open antenna preparation, calcium imaging on *Drosophila* OSNs can be studied under *in situ* conditions. However, to apply high-resolution techniques such as cryogenic electron microscopy (Cryo-EM) or direct stochastic optical reconstruction microscopy (dSTORM; Heilemann et al., 2008) imaging requires single *Drosophila* OSNs. We thus established a protocol to mildly digest *Drosophila* antennal tissue and then isolate OSNs. In detail, after funiculi from excised antennae were transversally cut, the antennal tissue was partially digested with papain – allowing the extraction of the digested content using silanized glass capillary (see schematic diagram **Figure 2A**). A drop of low Ca^{2+} Schneider's medium

containing *Drosophila* OSNs from (+; *Orco-Gal4/CyO; UAS-Syn21-GFP-p10/TM6B*) fly line were kept on a glass slide, covered with a cover slip and then single cell was immediately captured using laser scanning microscopy [**Figure 2B**, transmission (left), fluorescence (right)]. Next, in order to perform physiological recordings from dissociated tissue, it was necessary to adhere the cells. Initially, we used standard histology procedures to adhere the isolated OSNs on to the coverslip by coating it with Poly-L-lysine, Collagenase Clostridium, or Concanavalin A/Laminin but we failed to attach the cells using this approach.

We thus established a sodium metasilicate hydrogel system to embed biological tissue in hope to successfully apply this embedding system for the isolated *Drosophila* OSNs. First we started by assessing the effects of the gelation process on the properties of pH-buffered solutions. We found that Na_2SiO_3 had significantly smaller effects on the buffer osmolality than other embedding media as agarose and sodium alginate (**Supplementary Figure 2B**) and this parameter was not affected by the silicate polymerization process (**Supplementary Figures 2C**, **3**), making sodium silicate hydrogels suitable for functional studies. In particular, sodium metasilicate (Na_2SiO_3)-based aqueous solutions constitute an interesting case as they polymerize through a pH-driven condensation reaction (Pierre and Rigacci, 2011) with salts and water as the only byproducts. Partial neutralization of basic Na_2SiO_3 solutions (pH $\sim$ 12.5) to physiological (pH $\sim$ 6.7–7.4) pH levels induce the gelation of colloidal silica particles through a chain of condensation reactions (Rao et al., 2011; **Supplementary Figure 2A**).

$$Na_2SiO_3 + 2HCl + (x-1)\,H_2O \rightarrow SiO_2 \cdot xH_2O + 2NaCl$$

We then explored the effects of Na_2SiO_3 on the dynamics of the morphology and the free intracellular calcium concentration ($[Ca^{2+}]_i$) of adherent HEK293 cells (**Supplementary Figures 2D–F**). Calcium imaging using the dye Fura2-AM demonstrated that Na_2SiO_3 did not affect the cell basal $[Ca^{2+}]_i$ (**Supplementary Figure 2D**) and did not induce variations of the $[Ca^{2+}]_i$ over time (**Supplementary Figure 2E**). Moreover, we observed changes in the cell morphology due to Na_2SiO_3 only at high concentrations ($>$1.5% of a $\geq$27% SiO_2 basis stock solution, see section "Materials and Methods"), where cells tended to aggregate in clusters (**Supplementary Figure 2F**). We can conclude that Na_2SiO_3 hydrogels are compatible with the embedding of living cells for functional studies. Therefore, we now dissociated *Drosophila* antennal tissue and then embedded on a clean glass coverslip using a modified Schneider's medium containing 0.972% Na_2SiO_3 stock solution (see schematic diagram **Figure 2C**). This concentration of Na_2SiO_3 allowed us to reliably embed the tissue samples while having minimal effects on the cell physiology (**Supplementary Figure 3**). Following this procedure, we obtained OSNs that retained their morphology, including the ciliated outer dendritic segment (**Figures 3A,C**). The density of isolated OSNs was about 20 OSNs/100 μ m^2.

We then asked whether the embedded neurons also retained their functional properties. We performed Ca^{2+} imaging from OSNs expressing the calcium indicator GCaMP6f (Chen et al., 2013) under the co-receptor Orco or the odorant receptor Or22a promoters and stimulated OSNs expressing Orco or Or22a with their respective agonists, the synthetic compound VUAA1 (Jones et al., 2011; **Figure 3A**) and ethyl hexanoate (Münch and Galizia, 2016; **Figure 3C** and **Supplementary Video 1**). After extraction of regions of interest (see section "Materials and Methods"), we calculated the changes in GCaMP6f fluorescence intensity with respect to the base level expressed in percent (% $\Delta F/F_0$). In both cases, OR agonists induced calcium responses in a concentration-dependent manner (**Figures 3B,D**). In order to determine if the OSN response profile was affected by the tissue dissociation process or Na_2SiO_3, we performed calcium imaging from excised antennae immediately after the funiculus cut (**Figures 3E–H**), and we compared the response profiles of Orco and Or22a-expressing OSNs from dissociated and undigested antennal tissue (**Figures 3I,J**). The response profiles between the OSNs in dissociated and undigested tissues showed differences in the maximal intensity and time course of Ca^{2+} responses (**Supplementary Figure 5**). Nevertheless, we did not find significant differences in the fluctuation of the basal fluorescence levels (**Figure 3I**) and in the EC_{50} of concentration-response curves for Or22a neurons stimulated with ethyl hexanoate and Orco expressing neurons stimulated with VUAA1 (**Figure 3J**). In addition to the excitatory ethyl hexanoate, we tested the inhibitory benzaldehyde. At 10^{-3} dilution we observed a decrease in GCaMP6f fluorescence intensity $\Delta F/F_0$ by 7 $\pm$ 4% (n = 6) (**Supplementary Figure 7**). This illustrates that after cell isolation and embedding the inhibitory response remained conserved, as observed upon heterologous expression of Or22a (Wicher et al., 2008). OSN isolation removes the direct contact of these neurons to their support cells. Ablation of thecogen cells which directly envelop OSNs did not affect the odor selectivity of tested cells (Prelic et al., 2022).

This suggests that the tissue dissociation and embedding procedures, at the Na_2SiO_3 concentration used, did not significantly affect the viability of OSNs as well as the diffusion of the OR agonists through the embedding medium.

DISCUSSION

We here report the development and the validation of new preparations to access antennal OSNs and to perform functional imaging experiments in *in vivo and* dissociated tissue conditions. As olfactory stimuli are usually carried by air, studies of olfactory function using water-borne stimuli may lead to artifacts, due to the much higher time scale in which these experiments are usually carried and the irreversible change of the sensillum and antennal fluids to a standard Ringer solution. Therefore, we designed an *in vivo* preparation to study the activity of antennal OSNs at cellular resolution under more natural conditions. We could obtain Ca^{2+} imaging responses from olfactory neurons expressing the Or22a receptor, after stimulation with the agonist ethyl hexanoate, but not with the mineral oil solvent (**Figure 1**). This preparation is most suited for experiments, which require delivering odors through

an airstream with higher temporal resolution, or where it is important to keep unaltered the composition of the antennal and sensillum fluids. By combining it with the genetic tools available in *Drosophila*, e.g., RNA interference, such technique can be of great help to investigate signal transduction mechanisms of insect olfactory neurons in their native environment. Thus, this *in vivo* preparation fills the gap between techniques that allow odor stimulation via air but getting no spatially resolved output like single sensillum recordings and those allowing to observe odor response on OSN level but with stimuli provided via solution. Our finding that the odor responses observed with the *in vivo* preparation do not qualitatively differ from those obtained in the previous open antenna preparation supports the view that both approaches provide consistent results.

We next isolated *Drosophila* OSNs and embedded them in a permeable watery-based medium sufficiently rigid to allow the fixation of the preparation, but at the same time allowing the stimulus to penetrate through it. Remarkably, such medium did not require any sort of heating making it more suitable than low temperature-melting agarose media, which tended to damage the neurons and compromise functional imaging experiments (**Figure 3** and **Supplementary Figure 2B**). Here, the gelation process is driven by a series of hydrolysis and condensation reactions happening at room temperature and with the fastest kinetics at pH $\sim$ 7 (Pierre and Rigacci, 2011), making this method extremely attractive for applications in physiology and neuroscience. Moreover, the use of silica aero- and hydro-gels is already established in biotechnology to build reactors for the encapsulation of DNA molecules, enzymes and bacteria to accelerate biochemical reactions (Gill and Ballesteros, 2000; Depagne et al., 2011) or to design ceramics for medical applications (Vallet-Regí, 2001). We here demonstrated for the first time — to our knowledge — that sodium metasilicate hydrogels are excellent cell and tissue embedding agents for imaging experiments as they stabilize samples on uncoated glass surfaces, while retaining the function of neural cells without appreciable signs of cellular stress. The absence of toxic byproducts, the ability to form the gel at room temperature, together with the colloidal organization of silicate particles, which does not interfere with the osmolality of saline solutions during the gelation process, and its complete transparency make Na_2SiO_3 hydrogels an attractive choice, when embedding neural cell and tissue samples for physiological investigations.

This preparation maintains the native cellular environment of the ORs which is in contrast to a heterologous expression system or even in an empty neuron system (Fleischer et al., 2018). In the latter one, although the ORs are expressed in OSNs, the sensillar composition might be less compatible with the OR (Fleischer et al., 2018). On the other hand, the isolated OSN preparation lacks the surrounding support cells present in the native tissue. As shown in Prelic et al. (2022), these support cells contribute to the management of ion homeostasis. This might be one reason that we observe differences in the odor response size and time course between isolated OSNs and OSNs in the antenna preparation (**Supplementary Figure 5**).

As the isolated OSN preparation is an acute procedure, there are no changes in the protein expression level which can be observed in long term cell cultures. In cockroach neurons occurred, for example, a neosynthesis of Na^+ channels after 24 h culture (Tribut et al., 1991).

CONCLUSION

These two new preparations described here form the basis for the development of new tools to access and to investigate OSNs under controlled conditions. This is much of a necessity in order to validate studies based on the expression of insect proteins in heterologous systems and to advance our knowledge of olfactory signal transduction in insects.

DATA AVAILABILITY STATEMENT

The original contributions presented in the study are included in the article/**Supplementary Material**, further inquiries can be directed to the corresponding author.

AUTHOR CONTRIBUTIONS

DW, FM, and BH formulated the ideas for the study. FM and DW designed the study. JB contributed to study design. KJ contributed to **Figure 2B** and **Supplementary Figure 7**. FM and SK performed the experiments. FM analyzed the data. FM, KJ, and DW wrote the manuscript. All authors contributed to the final version of the manuscript.

FUNDING

This project received funding from the International Max Planck Research School (FM), the European Union's Horizon 2020 Research and Innovation Program under the Grant Agreement No. 662629 (FM), Alexander von Humboldt Foundation (JB), and Max Planck Society (DW, SK, and BH).

ACKNOWLEDGMENTS

We thank Silke Trautheim for help rearing the fly lines and Aleš Svatoš and Jerrit Weißflog for the synthesis of VUAA1.

SUPPLEMENTARY MATERIAL

The Supplementary Material for this article can be found online at: https://www.frontiersin.org/articles/10.3389/fncel.2022.839811/full#supplementary-material

REFERENCES

Arnold, J. B. (2017). *ggthemes: Extra Themes, Scales and Geoms for "ggplot2"*. Available online at: https://CRAN.R-project.org/package=ggthemes

Auguie, B. (2017). *gridExtra: Miscellaneous Functions for "Grid" Graphics*. Available online at: https://CRAN.R-project.org/package=gridExtra

Avnir, D., Coradin, T., Lev, O., and Livage, J. (2006). Recent bio-applications of sol–gel materials. *J. Mater. Chem.* 16, 1013–1030. doi: 10.3390/pharmaceutics12050449

Benton, R., Sachse, S., Michnick, S. W., and Vosshall, L. B. (2006). Atypical membrane topology and heteromeric function of *Drosophila* odorant receptors in vivo. *PLoS Biol.* 4:e20. doi: 10.1371/journal.pbio.0040020

Brand, A. H., and Perrimon, N. (1993). Targeted gene expression as a means of altering cell fates and generating dominant phenotypes. *Development* 118, 401–415.

Cao, L. H., Jing, B. Y., Yang, D., Zeng, X., Shen, Y., Tu, Y., et al. (2016). Distinct signaling of *Drosophila* chemoreceptors in olfactory sensory neurons. *Proc. Natl. Acad. Sci. U.S.A.* 113, E902–E911. doi: 10.1073/pnas.1518329113

Chang, W. (2014). *extrafont: Tools for Using Fonts*. Available online at: https://CRAN.R-project.org/package=extrafont

Chen, T. W., Wardill, T. J., Sun, Y., Pulver, S. R., Renninger, S. L., Baohan, A., et al. (2013). Ultrasensitive fluorescent proteins for imaging neuronal activity. *Nature* 499, 295–300. doi: 10.1038/nature12354

Corcoran, J. A., Jordan, M. D., Carraher, C., and Newcomb, R. D. (2014). A novel method to study insect olfactory receptor function using HEK293 cells. *Insect Biochem. Mol. Biol.* 54, 22–32. doi: 10.1016/j.ibmb.2014.08.005

Cras, J. J., Rowe-Taitt, C. A., Nivens, D. A., and Ligler, F. S. (1999). Comparison of chemical cleaning methods of glass in preparation for silanization. *Biosens. Bioelectron.* 14, 683–688. doi: 10.1016/s0956-5663(99)00043-3

de Bruyne, M., Foster, K., and Carlson, J. R. (2001). Odor coding in the *Drosophila* antenna. *Neuron* 30, 537–552. doi: 10.1016/s0896-6273(01)00289-6

Depagne, C., Roux, C., and Coradin, T. (2011). How to design cell-based biosensors using the sol-gel process. *Anal. Bioanal. Chem.* 400, 965–976. doi: 10.1007/s00216-010-4351-y

Dobritsa, A. A., Van Der Goes Van Naters, W., Warr, C. G., Steinbrecht, R. A., and Carlson, J. R. (2003). integrating the molecular and cellular basis of odor coding in the *Drosophila* antenna. *Neuron* 37, 827–841.

Dweck, H. K., Ebrahim, S. A., Khallaf, M. A., Koenig, C., Farhan, A., Stieber, R., et al. (2016). Olfactory channels associated with the *Drosophila* maxillary palp mediate short- and long-range attraction. *Elife* 5:e14925. doi: 10.7554/eLife.14925

Fleischer, J., Pregitzer, P., Breer, H., and Krieger, J. (2018). Access to the odor world: olfactory receptors and their role for signal transduction in insects. *Cell. Mol. Life Sci.* 75, 485–508. doi: 10.1007/s00018-017-2627-5

Gill, I., and Ballesteros, A. (2000). Bioencapsulation within synthetic polymers (Part 1): sol-gel encapsulated biologicals. *Trends Biotechnol.* 18, 282–296. doi: 10.1016/s0167-7799(00)01457-8

Gonzalez, F., Witzgall, P., and Walker, W. B. (2016). Protocol for heterologous expression of insect odourant receptors in *Drosophila*. *Front. Ecol. Evol.* 4:24. doi: 10.3389/fevo.2016.00024

Große-Wilde, E., Gohl, T., Bouché, E., Breer, H., and Krieger, J. (2007). Candidate pheromone receptors provide the basis for the response of distinct antennal neurons to pheromonal compounds. *Eur. J. Neurosci.* 25, 2364–2373. doi: 10.1111/j.1460-9568.2007.05512.x

Hallem, E. A., Ho, M. G., and Carlson, J. R. (2004). The molecular basis of odor coding in the *Drosophila* antenna. *Cell* 117, 965–979. doi: 10.1016/j.cell.2004.05.012

Hansson, B. S., and Stensmyr, M. C. (2011). Evolution of insect olfaction. *Neuron* 72, 698–711. doi: 10.1016/j.neuron.2011.11.003

Heilemann, M., Van De Linde, S., Schüttpelz, M., Kasper, R., Seefeldt, B., Mukherjee, A., et al. (2008). Subdiffraction-resolution fluorescence imaging with conventional fluorescent probes. *Angew. Chem. Int. Ed.* 47, 6172–6176. doi: 10.1002/anie.200802376

Jennings, B. H. (2011). *Drosophila* – a versatile model in biology & medicine. *Mater. Today* 14, 190–195. doi: 10.1016/s1369-7021(11)70113-4

Jones, P. L., Pask, G. M., Rinker, D. C., and Zwiebel, L. J. (2011). Functional agonism of insect odorant receptor ion channels. *Proc. Natl. Acad. Sci. U.S.A.* 108:8821. doi: 10.1073/pnas.1102425108

Joseph, R. M., and Carlson, J. R. (2015). *Drosophila* chemoreceptors: a molecular interface between the chemical world and the brain. *Trends Genet.* 31, 683–695. doi: 10.1016/j.tig.2015.09.005

Kiely, A., Authier, A., Kralicek, A. V., Warr, C. G., and Newcomb, R. D. (2007). Functional analysis of a *Drosophila* melanogaster olfactory receptor expressed in Sf9 cells. *J. Neurosci. Methods* 159, 189–194.

Kurtovic, A., Widmer, A., and Dickson, B. J. (2007). A single class of olfactory neurons mediates behavioural responses to a *Drosophila* sex pheromone. *Nature* 446, 542–546. doi: 10.1038/nature05672

Larsson, M. C., Domingos, A. I., Jones, W. D., Chiappe, M. E., Amrein, H., and Vosshall, L. B. (2004). Or83b encodes a broadly expressed odorant receptor essential for *Drosophila* olfaction. *Neuron* 43, 703–714. doi: 10.1016/j.neuron.2004.08.019

Lundin, C., Käll, L., Kreher, S. A., Kapp, K., Sonnhammer, E. L., Carlson, J. R., et al. (2007). Membrane topology of the *Drosophila* OR83b odorant receptor. *FEBS Lett.* 581, 5601–5604.

Mansourian, S., and Stensmyr, M. C. (2015). The chemical ecology of the fly. *Curr. Opin. Neurobiol.* 34, 95–102. doi: 10.1016/j.conb.2015.02.006

Mukunda, L., Miazzi, F., Kaltofen, S., Hansson, B. S., and Wicher, D. (2014). Calmodulin modulates insect odorant receptor function. *Cell Calcium* 55, 191–199. doi: 10.1016/j.ceca.2014.02.013

Mukunda, L., Miazzi, F., Sargsyan, V., Hansson, B. S., and Wicher, D. (2016). Calmodulin affects sensitization of *Drosophila* melanogaster odorant receptors. *Front. Cell. Neurosci.* 10:28. doi: 10.3389/fncel.2016.00028

Münch, D., and Galizia, C. G. (2016). DoOR 2.0 - Comprehensive mapping of *Drosophila* melanogaster odorant responses. *Sci. Rep.* 6:21841. doi: 10.1038/srep21841

Nakagawa, T., and Vosshall, L. B. (2009). Controversy and consensus: noncanonical signaling mechanisms in the insect olfactory system. *Curr. Opin. Neurobiol.* 19, 284–292. doi: 10.1016/j.conb.2009.07.015

Neuhaus, E. M., Gisselmann, G., Zhang, W., Dooley, R., Störtkuhl, K., and Hatt, H. (2005). Odorant receptor heterodimerization in the olfactory system of *Drosophila melanogaster*. *Nat. Neurosci.* 8, 15–17. doi: 10.1038/nn1371

Pierre, A. C., and Rigacci, A. (2011). "SiO2 aerogels," in *Aerogels Handbook*, eds M. A. Aegerter, N. Leventis, and M. M. Koebel (New York, NY: Springer New York), 21–45.

Prelic, S., Pal Mahadevan, V., Venkateswaran, V., Lavista-Llanos, S., Hansson, B. S., and Wicher, D. (2022). Functional interaction between *Drosophila* olfactory sensory neurons and their Support Cells. *Front. Cell. Neurosci.* 15:789086. doi: 10.3389/fncel.2021.789086

R Core Team (2017). *R: A Language and Environment for Statistical Computing*. Vienna: R Foundation for Statistical Computing.

Rao, A. V., Pajonk, G. M., Bangi, U. K. H., Rao, A. P., and Koebel, M. M. (2011). "Sodium silicate based aerogels via ambient pressure drying," in *Aerogels Handbook*, eds M. A. Aegerter, N. Leventis, and M. M. Koebel (New York, NY: Springer New York), 103–124. doi: 10.1088/1468-6996/9/3/035006

Ritz, C., Baty, F., Streibig, J. C., and Gerhard, D. (2015). Dose-response analysis using R. *PLoS One* 10:e0146021. doi: 10.1371/journal.pone.0146021

Rueden, C. T., Schindelin, J., Hiner, M. C., Dezonia, B. E., Walter, A. E., Arena, E. T., et al. (2017). ImageJ2: ImageJ for the next generation of scientific image data. *BMC Bioinformatics* 18:529. doi: 10.1186/s12859-017-1934-z

Sato, K., Pellegrino, M., Nakagawa, T., Nakagawa, T., Vosshall, L. B., and Touhara, K. (2008). Insect olfactory receptors are heteromeric ligand-gated ion channels. *Nature* 452, 1002–1006.

Schindelin, J., Arganda-Carreras, I., Frise, E., Kaynig, V., Longair, M., Pietzsch, T., et al. (2012). Fiji: an open-source platform for biological-image analysis. *Nat. Methods* 9, 676–682. doi: 10.1038/nmeth.2019

Sicaeros, B., Campusano, J. M., and O'Dowd, D. K. (2007). Primary neuronal cultures from the brains of late stage *Drosophila* pupae. *J. Vis. Exp.* 4:e200. doi: 10.3791/200

Smart, R., Kiely, A., Beale, M., Vargas, E., Carraher, C., Kralicek, A. V., et al. (2008). *Drosophila* odorant receptors are novel seven transmembrane domain proteins that can signal independently of heterotrimeric G proteins. *Insect Biochem. Mol. Biol.* 38, 770–780. doi: 10.1016/j.ibmb.2008.05.002

Strutz, A., Völler, T., Riemensperger, T., Fiala, A., and Sachse, S. (2012). "Calcium imaging of neural activity in the olfactory system of *Drosophila*," in *Genetically Encoded Functional Indicators*, ed. J.-R. Martin (Totowa, NJ: Humana Press), 43–70. doi: 10.1007/978-1-62703-014-4_3

Touhara, K., and Vosshall, L. B. (2009). Sensing odorants and pheromones with chemosensory receptors. *Annu. Rev. Physiol.* 71, 307–332. doi: 10.1146/annurev.physiol.010908.163209

Tribut, F., Lapied, B., Duval, A., and Pelhate, M. (1991). A neosynthesis of sodium channels is involved in the evolution of the sodium current in isolated adult DUM neurons. *Pflügers Arch.* 419, 665–667. doi: 10.1007/BF00370313

Tsitoura, P., Andronopoulou, E., Tsikou, D., Agalou, A., Papakonstantinou, M. P., Kotzia, G. A., et al. (2010). Expression and membrane topology of *Anopheles gambiae* odorant receptors in Lepidopteran insect cells. *PLoS One* 5:e15428. doi: 10.1371/journal.pone.0015428

Vallet-Regí, M. (2001). Ceramics for medical applications. *J. Chem. Soc. Dalton Trans.* 2, 97–108.

Wagner, C. A., Friedrich, B., Setiawan, I., Lang, F., and Bröer, S. (2000). The use of *Xenopus laevis* oocytes for the functional characterization of heterologously expressed membrane proteins. *Cell. Physiol. Biochem.* 10, 1–12. doi: 10.1159/000016341

Wicher, D. (2015). Olfactory signaling in insects. *Prog. Mol. Biol. Transl. Sci.* 130, 37–54. doi: 10.1016/bs.pmbts.2014.11.002

Wicher, D., Schäfer, R., Bauernfeind, R., Stensmyr, M. C., Heller, R., Heinemann, S. H., et al. (2008). *Drosophila* odorant receptors are both ligand-gated and cyclic-nucleotide-activated cation channels. *Nature* 452, 1007–1011. doi: 10.1038/nature06861

Wickham, H. (2016). *Ggplot2: Elegant Graphics for Data Analysis, Use R!*. Cham: Springer International Publishing.

Conflict of Interest: The authors declare that the research was conducted in the absence of any commercial or financial relationships that could be construed as a potential conflict of interest.

Publisher's Note: All claims expressed in this article are solely those of the authors and do not necessarily represent those of their affiliated organizations, or those of the publisher, the editors and the reviewers. Any product that may be evaluated in this article, or claim that may be made by its manufacturer, is not guaranteed or endorsed by the publisher.

frontiers in Cellular Neuroscience

BRIEF RESEARCH REPORT
published: 17 March 2022
doi: 10.3389/fncel.2022.858617

Ultrastructure of Rat Rostral Nucleus of the Solitary Tract Terminals in the Parabrachial Nucleus and Medullary Reticular Formation

*Sook Kyung Park†, Yi Sul Cho†, Jong Ho Kim†, Yun Sook Kim and Yong Chul Bae**

Department of Anatomy and Neurobiology, School of Dentistry, Kyungpook National University, Daegu, South Korea

Neurons in the rostral nucleus of the solitary tract (rNST) receive taste information from the tongue and relay it mainly to the parabrachial nucleus (PBN) and the medullary reticular formation (RF) through two functionally different neural circuits. To help understand how the information from the rNST neurons is transmitted within these brainstem relay nuclei in the taste pathway, we examined the terminals of the rNST neurons in the PBN and RF by use of anterograde horseradish peroxidase (HRP) labeling, postembedding immunogold staining for glutamate, serial section electron microscopy, and quantitative analysis. Most of the anterogradely labeled, glutamate-immunopositive axon terminals made a synaptic contact with only a single postsynaptic element in PBN and RF, suggesting that the sensory information from rNST neurons, at the individual terminal level, is not passed to multiple target cells. Labeled terminals were usually presynaptic to distal dendritic shafts in both target nuclei. However, the frequency of labeled terminals that contacted dendritic spines was significantly higher in the PBN than in the RF, and the frequency of labeled terminals that contacted somata or proximal dendrites was significantly higher in the RF than in the PBN. Labeled terminals receiving axoaxonic synapses, which are a morphological substrate for presynaptic modulation frequently found in primary sensory afferents, were not observed. These findings suggest that the sensory information from rNST neurons is processed in a relatively simple manner in both PBN and RF, but in a distinctly different manner in the PBN as opposed to the RF.

Keywords: gustatory, rNST neurons, synapse, central connectivity, ultrastructure

OPEN ACCESS

Edited by:
Se-Young Choi,
Seoul National University,
South Korea

Reviewed by:
Paul J. May,
University of Mississippi Medical Center, United States
Jessica Fawley,
Oregon Health and Science University, United States

****Correspondence:***
Yong Chul Bae
ycbae@knu.ac.kr

† These authors have contributed equally to this work and share first authorship

Specialty section:
This article was submitted to Cellular Neurophysiology, a section of the journal Frontiers in Cellular Neuroscience

Received: *20 January 2022*
Accepted: *18 February 2022*
Published: *17 March 2022*

Citation:
Park SK, Cho YS, Kim JH, Kim YS and Bae YC (2022) Ultrastructure of Rat Rostral Nucleus of the Solitary Tract Terminals in the Parabrachial Nucleus and Medullary Reticular Formation. Front. Cell. Neurosci. 16:858617. doi: 10.3389/fncel.2022.858617

INTRODUCTION

Information on the central connectivity of axon terminals of specific neurons can help understand how the neuronal signals are transmitted and processed by the targeted brain areas. We and others have shown that the pattern of central connectivity of primary sensory afferents differs among individual fiber types (Alvarez et al., 1992, 1993; Bae et al., 2005a; Yeo et al., 2010; Kim et al., 2014). The central connectivity of the primary sensory afferents of a single type also differs with respect to their target nucleus in which they are associated with functionally different neural circuits (Alvarez, 1998). For example, the connectivity of the terminals of a single Aβ low-threshold mechanoreceptive afferent in the trigeminal principal nucleus is different from that found in

the trigeminal oral nucleus. These differences may relate to the fact that the principal nucleus is involved in the discriminative aspect of orofacial mechanosensation, while the oral nucleus is involved in reflexive jaw movement (Bae et al., 1994, 2000).

Neurons in the rostral nucleus of the solitary tract (rNST) relay gustatory information from the tongue to the parabrachial nucleus (PBN) and the medullary reticular formation (RF). These two second-order relay nuclei in the taste pathways are involved in the discriminative aspect of taste perception and reflexive orofacial movements, respectively (Travers and Hu, 2000; King, 2006; Zaidi et al., 2008; Jarvie et al., 2021). Electrophysiological studies and immunohistochemical studies with retrograde neural tracing have shown that rNST neurons that project to PBN and RF are mainly glutamatergic (Gill et al., 1999; Nasse et al., 2008).

Recently, we showed that the terminals of chorda tympani afferents, primarily an Aδ fiber, convey gustatory information from the anterior part of the tongue and make simple synaptic connections in the first relay nucleus, the rNST. This organization differs from that of the complex synaptic connections made by non-gustatory Aδ fibers in the trigeminal nuclei (Alvarez et al., 1992; Park et al., 2016). However, less is yet known about the central connectivity of the glutamatergic rNST neurons in the PBN and RF. More detailed study of these structures may help us understand how sensory information from rNST neurons is processed at these secondary relay nuclei in the taste pathway.

To address this issue, we investigated the synaptic connectivity of rNST neurons in the PBN and RF by anterograde tracing with horseradish peroxidase (HRP), postembedding immunogold staining for glutamate, serial section electron microscopy, and quantitative analysis.

MATERIALS AND METHODS

Anterograde Labeling of Axon Terminals of the Rostral Nucleus of the Solitary Tract Neurons

All animal procedures were performed according to the National Institute of Health guidelines and were approved by the Kyungpook National University Intramural Animal Care and Use Committee. Seven 9–10-week-old male Sprague-Dawley rats weighing 300–320 g were used for this study. Animals were anesthetized with an i.p. injection of a mixture of ketamine (40 mg/kg) and xylazine (4 mg/kg) and fixed on a stereotaxic frame (Narishige, Tokyo, Japan). A glass micropipette (internal tip diameter, 20–30 μm) was filled with HRP (5% HRP in 5% DMSO, TOYOBO Co., Osaka, Japan) and inserted stereotaxically into rNST (AP: 2.6–2.65 mm caudal to the interaural line, L: 1.7 mm to the midline, and H: 8.0 mm below the bone surface; Paxinos and Watson, 2005). The tracer was injected iontophoretically (1.2–2 μA, 7 s on/off cycle, for 8 min), and the micropipette was kept in position for another 6 min after the injection.

Tissue Preparation

After 24–27 h, the rats were deeply anesthetized with a mixture of ketamine (80 mg/kg) and xylazine (10 mg/kg, i.p.) and were perfused transcardially with freshly prepared fixative containing 2.5% glutaraldehyde, 1% paraformaldehyde, and 0.1% picric acid in 0.1 M phosphate buffer (PB, pH 7.4). The brainstem was removed and postfixed in the same fixative for 2 h at 4°C. Then, sections were cut coronally on a vibratome at 60 μm. Anterogradely transported HRP was revealed using a tungstate/tetramethylbenzidine protocol (Weinberg and van Eyck, 1991) and stabilized with diaminobenzidine in PB (pH 6.0). Wet sections were examined on a light microscope, and further studies were performed only on the material in which the tracer was concentrated in the rNST, including its rostral central subdivision. Sections of three rats showing that HRP is confined to rNST, among seven rats that HRP was injected iontophoretically, were used for electron microscopy. Sections containing HRP-labeled puncta in the PBN and RF were selected, postfixed in 0.5% osmium tetroxide in PB for 25 min, dehydrated in the graded alcohols, flat-embedded in Durcupan ACM (Fluka, Buchs, Switzerland) between strips of Aclar plastic film (EMS, Hatfield, PA, United States), and cured for 48 h at 60°C. Chips containing numerous HRP-labeled puncta in the central medial subdivision of the PBN or in the RF were cut and glued onto blank resin with cyanoacrylate. Serial thin sections were collected on formvar-coated single slot nickel grids. Grids were stained with uranyl acetate and lead citrate and examined on a Hitachi H-7500 electron microscope (Hitachi, Tokyo, Japan) at 80 kV accelerating voltage. Electron micrographs at a final magnification of 30,000× were taken from every other section through the HRP-labeled boutons with a Digital Micrograph software driving a cooled CCD camera (SC1000; Orius; Gatan, Pleasanton, CA, United States), attached to the microscope, and saved as TIFF files. The brightness and contrast of the images were adjusted using Adobe Photoshop CS5.1 (Adobe Systems Inc., San Jose, CA, United States).

Postembedding Immunogold Staining for Glutamate

One in every 5–6 grids containing serial thin sections were selected for immunogold staining for glutamate, which was performed as described previously from our laboratory (Park et al., 2019; Paik et al., 2021). In brief, grids were treated in 1% periodic acid for 6 min to etch the resin, followed by 9% sodium periodate for 10 min to remove the osmium tetroxide, and then washed in distilled water. After incubation in 2% human serum albumin (HSA) in Tris-buffered saline containing 0.1% Triton X-100 (TBST; pH 7.4) for 10 min, the grids were incubated with rabbit antiserum against glutamate (1:30,000; G6642; Sigma-Aldrich, St. Louis, MO, United States) in TBST containing 2% HSA for 3.5 h at room temperature. To eliminate cross-reactivity, the diluted antiserum was preadsorbed with glutaraldehyde (G)-conjugated amino acids, namely, 300 μM glutamine-G, 100 μM aspartate-G, and 200 μM β-alanine-G. After rinsing in TBST, the grids were incubated for 1.5 h in goat anti-rabbit IgG coupled to 15 nm gold particles (1:25 in TBST containing 0.05% polyethylene glycol; BioCell Co., Cardiff, United Kingdom). After washing in distilled water, the grids were counterstained with uranyl acetate and lead citrate and then examined on a Hitachi H-7500 electron microscope at

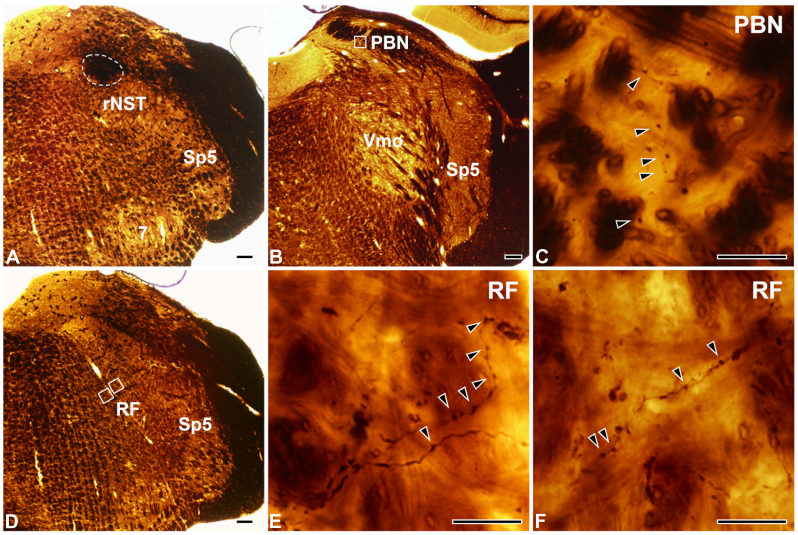

FIGURE 1 | Light micrographs showing the tracer injection site in the rostral part of the nucleus of the solitary tract (rNST; **A**) and anterogradely labeled axon terminals in the parabrachial nucleus (PBN; **B,C**) and the reticular formation (RF; **D–F**). **(A)** The horseradish peroxidase (HRP) injection, outlined with a dashed line, is confined to the rNST. **(B–F)** Dark HRP-labeled axons and terminals (arrowheads) are observed in the central medial subnucleus of the PBN **(B,C)** and the medullary RF **(D–F)**. Panel **(C)** is the enlargement of the square in panel **(B)**. Panels **(E,F)** are enlargements of the medial and lateral squares, respectively, in panel **(D)**. Sp5, spinal trigeminal nucleus; Vmo, trigeminal motor nucleus; 7, facial nucleus. Scale bars, 200 μm in panels **(A,B,D)** and 20 μm in panels **(C,E,F)**.

80 kV accelerating voltage. To assess the immunoreactivity for glutamate, the gold particle density of HRP-labeled boutons was compared with the average tissue density in 10–15 randomly selected areas (2 μm^2 each, a total area of 20–30 μm^2 per section). Boutons containing gold particles at a density greater than the average tissue density + 2.576 SD (significant difference at 99% confidence level) were considered glutamate-immunopositive (Paik et al., 2019, 2021); immunogold labeling over mitochondrial profiles was excluded from the analysis. Measurements were performed on electron micrographs using a digitizing tablet and Image J software. We analyzed synaptic connectivity of 50 and 43 labeled boutons that are Glut+ in the PBN and RF, respectively, from three rats (15–18 boutons per rat in the PBN and 13–16 boutons per rat in the RF).

The specificity of the glutamate antiserum was confirmed on test thin sections of "sandwiches" of rat brain macromolecule-glutaraldehyde fixed complexes of different amino acids, such as GABA, glutamate, taurine, glycine, aspartate, and glutamine (Ottersen, 1987; Bae et al., 2000). Test sections were also incubated in the same drops of glutamate antiserum as the tissue sections, and the respective conjugate in the test sections was selectively labeled. Omission or replacement of the primary antisera with normal goat serum abolished the immunostaining. Consistency of immunostaining was also confirmed in consecutive thin sections of the same boutons.

RESULTS

At the light microscopic level, the injected HRP was confined to the rNST (**Figure 1A**). Dark HRP-labeled puncta, which is how labeled axon terminals appear at that level of magnification, were dense in the medial PBN (**Figures 1B,C**) and in the medullary RF (**Figures 1D–F**), ipsilateral to the tracer injection. At the electron microscopic level, HRP-labeled axon terminals (boutons) were identified by the presence of HRP reaction product (arrows, **Figure 2**), appearing as electron-dense rods or amorphous deposits within the axoplasm. Most labeled boutons had dome or ellipsoid shape, whereas scalloped or glomerular shape, typical of the primary somatosensory afferent terminals, was not observed. In glutamate-immunopositive (Glut+) boutons, the gold particles labeling for glutamate were dense over regions containing synaptic vesicles and over mitochondria (**Figure 2**): the gold particle density for Glut was 1.2–19.5 times higher than the average tissue density + 2.576 SD. Boutons labeled with anterogradely transported HRP were mostly Glut+ and established synaptic contacts (arrowheads, **Figure 2**) of asymmetrical type with postsynaptic dendrites or somata. Glut immunoreactivity was consistent in the adjacent serial sections of the labeled boutons, confirming their glutamatergic nature (**Figure 2**). Most of the profiles postsynaptic to the anterogradely labeled terminals were also Glut+ (**Figures 2A–D,G,H**), although the number of gold particles over others did not reach the level of Glut+ (**Figures 2E,F**). By EM observation, postsynaptic targets of Glut+ labeled boutons differed in the PBN compared with the RF, which led to statistical analysis on the serial sections of the Glut+ labeled boutons.

We analyzed 50 anterogradely labeled boutons that were Glut+ in the centromedial nucleus of the PBN and 43 anterogradely labeled boutons that were Glut+ in the parvocellular and intermediate regions of the RF. The large majority of the labeled boutons (94.0% in the PBN and 97.7% in the RF) established a synaptic contact with a single postsynaptic element, and the remaining with two postsynaptic elements

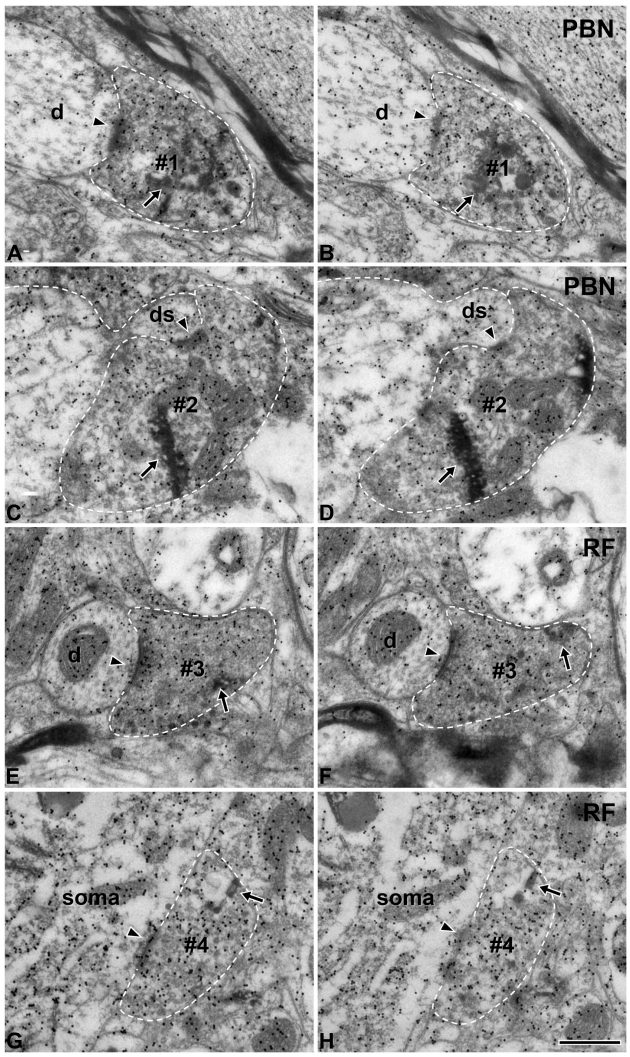

FIGURE 2 | Electron micrographs of immunogold staining for glutamate in adjacent thin sections through anterogradely labeled Glut+ terminals (#1–#4) in the parabrachial nucleus (PBN, **A–D**) and medullary reticular formation (RF, **E–H**) after tracer injection in the rNST. Postsynaptic targets of Glut+ labeled terminals (boutons) are different in the PBN and RF. Glut+ labeled terminals are presynaptic to the dendritic spine more frequently in the PBN than in the RF, while they are presynaptic to soma or proximal dendrite more frequently in the RF than in the PBN. **(A–D)** The labeled terminals (#1, #2) in the PBN establish synaptic contacts (arrowheads) with a dendritic shaft (d; **A,B**) and a dendritic spine (ds; **C,D**). **(E–H)** The labeled terminals in the RF (#3, #4) establish synaptic contacts (arrowheads) with a small dendritic shaft (d; **E,F**) and a cell body (soma; **G,H**). The labeled terminals can be identified by the presence of the HRP reaction product (arrows) within the axoplasm. Labeled terminals that are Glut+ were analyzed in this study: note the high density of gold particles coding for glutamate over the areas of the axoplasm containing synaptic vesicles. Glut immunoreactivity is consistent in the pairs of serial sections of the labeled terminal, confirming their glutamatergic nature. The labeled terminals and the postsynaptic dendritic spine are outlined with a dashed line for clarity. Scale bar, 500 nm.

(we did not observe any boutons that established synaptic contacts with more than two postsynaptic elements, **Table 1**). Most postsynaptic elements in both PBN and RF were dendritic

TABLE 1 | Frequency (%) of occurrence of terminals of the rostral nucleus of the solitary tract (rNST) neurons in the parabrachial nucleus (PBN) and medullary reticular formation (RF), according to the number of their postsynaptic profiles.

Region	Number of terminals examined	No. of postsynaptic profiles	
		1	2
PBN	50	94.0 (47/50)	6.0 (3/50)
RF	43	97.7 (42/43)	2.3 (1/43)

n in parentheses indicates the number of terminals/total number of terminals examined.

shafts. Glut+ labeled boutons in the PBN frequently established synapses with dendritic spines (14.0% vs. 2.3% in the PBN vs. RF, respectively), whereas Glut+ labeled boutons in the RF frequently established synapses with soma or proximal dendrites that contained rough endoplasmic reticulum, suggesting their proximity to the cell body (4.0% vs. 27.9% in the PBN and RF, respectively). The frequency of synaptic contacts between labeled boutons and dendritic spines was significantly higher in the PBN than in the RF, whereas the frequency of synaptic contacts between labeled boutons and soma or proximal dendrites was significantly higher in the RF than in the PBN (**Table 2**). None of the labeled boutons established axoaxonic synapses.

DISCUSSION

The main finding of this study is that most Glut+ terminals from the rNST contact a single dendrite in both PB and RF, suggesting that sensory signals from the rNST are processed in a relatively simple manner in both these nuclei. In contrast, we observed that the frequency with which these labeled terminals established contacts on somata and proximal dendrites vs. dendritic spines differed between the PBN and RF target nuclei. This suggests that there are distinct differences in how the sensory information from the rNST is handled by the PB and RF.

Rostral Nucleus of the Solitary Tract Afferent Terminals Establish Simple Synaptic Connections in the Parabrachial Nucleus and Reticular Formation

In both PBN and RF, most Glut+ axon terminals of rNST neurons synapsed with a single postsynaptic dendrite or cell body, suggesting that, at the single bouton level, the afferent signal is transmitted to a specific group of target neurons with less synaptic divergence. This type of synaptic connectivity is analogous to that of axon terminals of the second-order neurons receiving primary sensory input and involved in the reflexive jaw movement, such as the neurons in the supratrigeminal nucleus, that receive proprioceptive input from jaw-closing muscle spindle afferents and project to trigeminal motor nucleus (Paik et al., 2009). However, it is very different from the synaptic connectivity of the chorda tympani afferents conveying gustatory input from the anterior tongue to the rNST. In this nucleus,

TABLE 2 | Frequency of occurrence (mean ± SD) of different types of synaptic contacts per labeled terminal of rNST neurons in the PBN and medullary RF.

Region	Number of terminals examined	Type of postsynaptic profile			Total number of contacts
		Soma/proximal dendrite	Dendritic shaft	Dendritic spine	
PBN	50	0.04 ± 0.20* (*n* = 2)	0.88 ± 0.44 (*n* = 44)	0.14 ± 0.35* (*n* = 7)	1.06 ± 0.24 (*n* = 53)
RF	43	0.28 ± 0.45* (*n* = 12)	0.72 ± 0.45 (*n* = 31)	0.02 ± 0.15* (*n* = 1)	1.02 ± 0.15 (*n* = 44)

"n" is the total number of synaptic contacts for all examined boutons.
**Indicates statistically significant differences between PBN and RF (unpaired t-test, $p < 0.05$).*

the large majority of their axon terminals contact two or more dendrites (Park et al., 2016). Similarly, the organization of the rNST projections is also simpler than that of the somatosensory primary afferents in the spinal dorsal horn and trigeminal sensory nuclei, where the terminals usually contact multiple (2–13) dendrites (Alvarez et al., 1992; Bae et al., 2003, 2005a; Kim et al., 2008; Yeo et al., 2010; Park et al., 2019). Thus, the axon terminals of second-order neurons that receive gustatory or proprioceptive input from primary sensory afferents contact few postsynaptic neurons in the second-order relay nuclei, in contrast with the axon terminals of primary sensory afferents, which usually contact multiple dendrites in the first-order relay nuclei, suggesting the spread of sensory information to multiple postsynaptic neurons.

In some cases, axoaxonic synapses in the dorsal horn and trigeminal nuclei provide the basis for presynaptic modulation of the primary afferent input and are implicated in the sharpening of the sensory signal (Gray, 1962; Rudomin and Schmidt, 1999). For example, the primary somatosensory afferents, including Aβ and Aδ afferents, frequently receive axoaxonic synapses from GABAergic terminals (Alvarez et al., 1992; Bae et al., 2005b; Moon et al., 2008; Park et al., 2019). Chorda tympani afferents also frequently receive axoaxonic synapses from GABAergic axon terminals in the rNST, suggesting presynaptic modulation of the gustatory signal before it is relayed to the postsynaptic neurons in the first-order relay nuclei (Park et al., 2016). In this study, however, none of the rNST afferents in PBN and RF were involved in axoaxonic synapses, suggesting that, in contrast to the primary sensory afferents, rNST neurons relay taste information to their postsynaptic neurons without presynaptic modulation.

Afferents of Rostral Nucleus of the Solitary Tract Neurons Have Different Somatodendritic Targets in the Parabrachial Nucleus and Reticular Formation

The spatial distribution of excitatory input along the soma-dendritic tree of the postsynaptic neuron plays a role in determining its influence, so that the input onto the soma/proximal dendrite compartment exerts a more powerful effect on the excitability of the postsynaptic neurons, and that onto the distal dendrites exerts a weaker effect (Burke, 2004). The frequency of labeled boutons of rNST axons establishing synapses within the soma/proximal dendrite was seven times higher in the RF, a center for reflexive orofacial motor control, than in the PBN, a center for taste perception (Bradley and Kim, 2006; King, 2006). This arrangement is analogous to the primary somatosensory afferents that show more frequent contact with the soma/proximal dendrite compartment of the postsynaptic neurons in the trigeminal oral nucleus, which controls reflexive oral motor behavior, than in the trigeminal principal nucleus, which is involved in the somatosensory perception (Bae et al., 2000). Axon terminals of premotor neurons also very frequently form synapses with the soma/proximal dendrite compartment of the postsynaptic neurons in the trigeminal motor nucleus (Shigenaga et al., 2000; Paik et al., 2009). All of the above suggests that the terminals of excitatory neurons that mediate motor reflexes may exert a stronger influence on the activity of the postsynaptic neurons than those that mediate sensory perception.

We observed far more contacts between rNST terminals and spines in the PBN. Dendritic spines undergo activity-dependent plasticity with respect to their profile diameter, number, and the size of their postsynaptic densities, all resulting in changes in the strength of the synaptic transmission (Harms and Dunaevsky, 2007; Baczynska et al., 2021). Many studies have shown that synaptic plasticity is common in the brain regions involved in gustatory perception (Hill, 2004; Dekkers et al., 2021; Martin et al., 2021). rNST afferent terminals established synaptic contacts with dendritic spines much more frequently in the PBN than in the RF, and the number of dendritic spines receiving synaptic contact from an rNST afferent terminal was six times higher in the PBN than in the RF. Thus, the plasticity of dendritic spines and the changes in the postsynaptic neuron excitability due to alteration of the input from rNST neurons under pathological or experimental conditions, such as sodium restriction or gustatory nerve section, may be more extensive in the PBN than in the RF.

Many postsynaptic dendrites of the Glut+ labeled boutons in the PBN and RF showed dense gold particles for glutamate, suggesting that they are Glut+, whereas some postsynaptic dendrites showed few gold particles for glutamate, suggesting Glut-immunonegative. Considering that GAD+ or tyrosine hydroxylase+ neurons exist in the PBN and RF (Guthmann et al., 1998; Weihe et al., 2006; Travers et al., 2007), the Glut-immunonegative postsynaptic neurons might be either GABAergic or dopaminergic neurons. Activation of various types of postsynaptic neurons by Glut+ labeled boutons of rNST

neurons in the PBN and RF may be involved in the precise modulation of taste perception and reflexive jaw movement.

In summary, our findings suggest that sensory information from rNST neurons in the second-order relay nuclei of taste pathways is processed in a distinct manner that is different from gustatory information from the tongue in the first relay nucleus, rNST, and that it is processed differently between in the PBN and in the RF.

DATA AVAILABILITY STATEMENT

The original contributions presented in the study are included in the article/supplementary material, further inquiries can be directed to the corresponding author.

ETHICS STATEMENT

The animal study was reviewed and approved by Research and Ethics Committee of Kyungpook National University.

AUTHOR CONTRIBUTIONS

YB designed the study. SP, YC, and JK contributed to tracing, postembedding staining, and electron microscopy. SP and YB wrote the manuscript. All authors contributed to analysis and interpretation of the data and have full access to all the data in this study and take responsibility for the integrity of the data and the accuracy of the data analysis.

FUNDING

This study was supported by the National Research Foundation of Korea (NRF) grant funded by the Korea government (MSIT, NRF-2017R1A5A2015391, and NRF-2021R1A2C1007061).

ACKNOWLEDGMENTS

We sincerely thank Juli Valtschanoff for helpful discussion and careful reading of the manuscript.

REFERENCES

Alvarez, F. J. (1998). "Anatomical basis of presynaptic inhibition of primary afferent fibers," in *Presynaptic Inhibition and Neural Control*, eds P. Rudomin, R. Romo, and L. M. Mendell (New York, NY: Oxford University Press), 13–49. doi: 10.1016/s0306-4522(00)00269-4

Alvarez, F. J., Kavookjian, A. M., and Light, A. R. (1992). Synaptic interactions between GABA-immunoreactive profiles and the terminals of functionally defined myelinated nociceptors in the monkey and cat spinal cord. *J. Neurosci.* 12, 2901–2917. doi: 10.1523/JNEUROSCI.12-08-02901.1992

Alvarez, F. J., Kavookjian, A. M., and Light, A. R. (1993). Ultrastructural morphology, synaptic relationships, and CGRP immunoreactivity of physiologically identified C-fiber terminals in the monkey spinal cord. *J. Comp. Neurol.* 329, 472–490. doi: 10.1002/cne.903290405

Baczynska, E., Pels, K. K., Basu, S., Wlodarczyk, J., and Ruszczycki, B. (2021). Quantification of dendritic spines remodeling under physiological stimuli and in pathological conditions. *Int. J. Mol. Sci.* 22:4053. doi: 10.3390/ijms22084053

Bae, Y. C., Ahn, H. J., Park, K. P., Kim, H. N., Paik, S. K., Bae, J. Y., et al. (2005a). The synaptic microcircuitry associated with primary afferent terminals in the interpolaris and caudalis of trigeminal sensory nuclear complex. *Brain Res.* 1060, 118–125. doi: 10.1016/j.brainres.2005.08.042

Bae, Y. C., Park, K. S., Bae, J. Y., Paik, S. K., Ahn, D. K., Moritani, M., et al. (2005b). GABA and glycine in synaptic microcircuits associated with physiologically characterized primary afferents of cat trigeminal principal nucleus. *Exp. Brain Res.* 162, 449–457. doi: 10.1007/s00221-004-2022-y

Bae, Y. C., Ihn, H. J., Park, M. J., Ottersen, O. P., Moritani, M., Yoshida, A., et al. (2000). Identification of signal substances in synapses made between primary afferents and their associated axon terminals in the rat trigeminal sensory nuclei. *J. Comp. Neurol.* 418, 299–309.

Bae, Y. C., Kim, J. P., Choi, B. J., Park, K. P., Choi, M. K., Moritani, M., et al. (2003). Synaptic organization of tooth pulp afferent terminals in the rat trigeminal sensory nuclei. *J. Comp. Neurol.* 463, 13–24. doi: 10.1002/cne.10741

Bae, Y. C., Nakagawa, S., Yoshida, A., Nagase, Y., Takemura, M., and Shigenaga, Y. (1994). Morphology and synaptic connections of slowly adapting periodontal afferent terminals in the trigeminal subnuclei principalis and oralis of the cat. *J. Comp. Neurol.* 348, 121–132. doi: 10.1002/cne.903480107

Bradley, R. M., and Kim, M. (2006). "Reflex connections," in *The Role of the Nucleus of the Solitary Tract in Gustatory Processing*, ed. R. M. Bradley (Boca Raton, FL: CRC Press), 67–82.

Burke, R. E. (2004). "Spinal cord: ventral horn," in *The Synaptic Organization of the Brain*, 5th Edn, ed. G. M. Shepherd (Oxford: Oxford University Press), 79–124.

Dekkers, M. P. J., Salfelder, F., Sanders, T., Umuerri, O., Cohen, N., and Jansen, G. (2021). Plasticity in gustatory and nociceptive neurons controls decision making in *C. elegans* salt navigation. *Commun. Biol.* 4:1053. doi: 10.1038/s42003-021-02561-9

Gill, C. F., Madden, J. M., Roberts, B. P., Evans, L. D., and King, M. S. (1999). A subpopulation of neurons in the rat rostral nucleus of the solitary tract that project to the parabrachial nucleus express glutamate-like immunoreactivity. *Brain Res.* 821, 251–262. doi: 10.1016/s0006-8993(98)01270-0

Gray, E. G. (1962). A morphological basis for pre-synaptic inhibition? *Nature* 193, 82–83. doi: 10.1038/193082a0

Guthmann, A., Fritschy, J. M., Ottersen, O. P., Torp, R., and Herbert, H. (1998). GABA, GABA transporters, GABA(A) receptor subunits, and GAD mRNAs in the rat parabrachial and Kolliker-Fuse nuclei. *J. Comp. Neurol.* 400, 229–243.

Harms, K. J., and Dunaevsky, A. (2007). Dendritic spine plasticity: looking beyond development. *Brain Res.* 1184, 65–71. doi: 10.1016/j.brainres.2006.02.094

Hill, D. L. (2004). Neural plasticity in the gustatory system. *Nutr. Rev.* 62, S208-S217; discussion S224-S241. doi: 10.1111/j.1753-4887.2004.tb00101.x

Jarvie, B. C., Chen, J. Y., King, H. O., and Palmiter, R. D. (2021). Satb2 neurons in the parabrachial nucleus mediate taste perception. *Nat. Commun.* 12:224. doi: 10.1038/s41467-020-20100-8

Kim, Y. S., Paik, S. K., Cho, Y. S., Shin, H. S., Bae, J. Y., Moritani, M., et al. (2008). Expression of P2X3 receptor in the trigeminal sensory nuclei of the rat. *J. Comp. Neurol.* 506, 627–639. doi: 10.1002/cne.21544

Kim, Y. S., Park, J. H., Choi, S. J., Bae, J. Y., Ahn, D. K., McKemy, D. D., et al. (2014). Central connectivity of transient receptor potential melastatin 8-expressing axons in the brain stem and spinal dorsal horn. *PLoS One* 9:e94080. doi: 10.1371/journal.pone.0094080

King, M. S. (2006). "Anatomy of the rostral nucleus of the solitary tract," in *The Role of the Nucleus of the Solitary Tract in Gustatory Processing*, ed. R. M. Bradley (Boca Raton, FL: CRC Press), 17–39.

Martin, L. J., Breza, J. M., and Sollars, S. I. (2021). Taste activity in the parabrachial region in adult rats following neonatal chorda tympani transection. *J. Neurophysiol.* 125, 2178–2190. doi: 10.1152/jn.00552.2020

Moon, Y. S., Paik, S. K., Seo, J. H., Yi, H. W., Cho, Y. S., Moritani, M., et al. (2008). GABA- and glycine-like immunoreactivity in axonal endings presynaptic to the vibrissa afferents in the cat trigeminal interpolar nucleus. *Neuroscience* 152, 138–145. doi: 10.1016/j.neuroscience.2007.11.033

Nasse, J., Terman, D., Venugopal, S., Hermann, G., Rogers, R., and Travers, J. B. (2008). Local circuit input to the medullary reticular formation from the rostral nucleus of the solitary tract. *Am. J. Physiol. Regul. Integr. Comp. Physiol.* 295, R1391–R1408. doi: 10.1152/ajpregu.90457.2008

Ottersen, O. P. (1987). Postembedding light- and electron microscopic immunocytochemistry of amino acids: description of a new model system allowing identical conditions for specificity testing and tissue processing. *Exp. Brain Res.* 69, 167–174. doi: 10.1007/BF00247039

Paik, S. K., Lee, H. J., Choi, M. K., Cho, Y. S., Park, M. J., Moritani, M., et al. (2009). Ultrastructural analysis of glutamate-, GABA-, and glycine-immunopositive boutons from supratrigeminal premotoneurons in the rat trigeminal motor nucleus. *J. Neurosci. Res.* 87, 1115–1122. doi: 10.1002/jnr.21929

Paik, S. K., Yoo, H. I., Choi, S. K., Bae, J. Y., Park, S. K., and Bae, Y. C. (2019). Distribution of excitatory and inhibitory axon terminals on the rat hypoglossal motoneurons. *Brain Struct. Funct.* 224, 1767–1779. doi: 10.1007/s00429-019-01874-0

Paik, S. K., Yoshida, A., and Bae, Y. C. (2021). Development of gamma-aminobutyric acid-, glycine-, and glutamate-immunopositive boutons on the rat genioglossal motoneurons. *Brain Struct. Funct.* 226, 889–900. doi: 10.1007/s00429-021-02216-9

Park, S. K., Devi, A. P., Bae, J. Y., Cho, Y. S., Ko, H. G., Kim, D. Y., et al. (2019). Synaptic connectivity of urinary bladder afferents in the rat superficial dorsal horn and spinal parasympathetic nucleus. *J. Comp. Neurol.* 527, 3002–3013. doi: 10.1002/cne.24725

Park, S. K., Lee, D. S., Bae, J. Y., and Bae, Y. C. (2016). Central connectivity of the chorda tympani afferent terminals in the rat rostral nucleus of the solitary tract. *Brain Struct. Funct.* 221, 1125–1137. doi: 10.1007/s00429-014-0959-6

Paxinos, G., and Watson, C. (2005). *The Rat Brain in Stereotaxic Coordinates*. San Diego, CA: Elsevier Academic.

Rudomin, P., and Schmidt, R. F. (1999). Presynaptic inhibition in the vertebrate spinal cord revisited. *Exp. Brain Res.* 129, 1–37. doi: 10.1007/s002210050933

Shigenaga, Y., Hirose, Y., Yoshida, A., Fukami, H., Honma, S., and Bae, Y. C. (2000). Quantitative ultrastructure of physiologically identified premotoneuron terminals in the trigeminal motor nucleus in the cat. *J. Comp. Neurol.* 426, 13–30.

Travers, J. B., Herman, K., Yoo, J., and Travers, S. P. (2007). Taste reactivity and Fos expression in GAD1-EGFP transgenic mice. *Chem. Senses* 32, 129–137. doi: 10.1093/chemse/bjl038

Travers, S. P., and Hu, H. (2000). Extranuclear projections of rNST neurons expressing gustatory-elicited Fos. *J. Comp. Neurol.* 427, 124–138.

Weihe, E., Depboylu, C., Schutz, B., Schafer, M. K., and Eiden, L. E. (2006). Three types of tyrosine hydroxylase-positive CNS neurons distinguished by dopa decarboxylase and VMAT2 co-expression. *Cell. Mol. Neurobiol.* 26, 659–678. doi: 10.1007/s10571-006-9053-9

Weinberg, R. J., and van Eyck, S. L. (1991). A tetramethylbenzidine/tungstate reaction for horseradish peroxidase histochemistry. *J. Histochem. Cytochem.* 39, 1143–1148. doi: 10.1177/39.8.1906909

Yeo, E. J., Cho, Y. S., Paik, S. K., Yoshida, A., Park, M. J., Ahn, D. K., et al. (2010). Ultrastructural analysis of the synaptic connectivity of TRPV1-expressing primary afferent terminals in the rat trigeminal caudal nucleus. *J. Comp. Neurol.* 518, 4134–4146. doi: 10.1002/cne.22369

Zaidi, F. N., Todd, K., Enquist, L., and Whitehead, M. C. (2008). Types of taste circuits synaptically linked to a few geniculate ganglion neurons. *J. Comp. Neurol.* 511, 753–772. doi: 10.1002/cne.21869

Conflict of Interest: The authors declare that the research was conducted in the absence of any commercial or financial relationships that could be construed as a potential conflict of interest.

Publisher's Note: All claims expressed in this article are solely those of the authors and do not necessarily represent those of their affiliated organizations, or those of the publisher, the editors and the reviewers. Any product that may be evaluated in this article, or claim that may be made by its manufacturer, is not guaranteed or endorsed by the publisher.

frontiers | Frontiers in Cellular Neuroscience

BRIEF RESEARCH REPORT
published: 25 April 2022
doi: 10.3389/fncel.2022.856855

Auricular Transcutaneous Vagus Nerve Stimulation Acutely Modulates Brain Connectivity in Mice

Cecilia Brambilla-Pisoni[1], *Emma Muñoz-Moreno*[2], *Ianire Gallego-Amaro*[1], *Rafael Maldonado*[1,3], *Antoni Ivorra*[4,5], *Guadalupe Soria*[2,6] *and Andrés Ozaita*[1,3]*

[1] *Laboratory of Neuropharmacology, Department of Medicine and Life Sciences, Universitat Pompeu Fabra, Barcelona, Spain,* [2] *Experimental 7T MRI Unit, Magnetic Resonance Imaging Core Facility, Institut d'Investigacions Biomediques August Pi i Sunyer, Barcelona, Spain,* [3] *Institut Hospital del Mar d'Investigacions Mèdiques (IMIM), Barcelona, Spain,* [4] *Department of Information and Communication Technologies, Universitat Pompeu Fabra, Barcelona, Spain,* [5] *Serra Húnter Fellow Programme, Universitat Pompeu Fabra, Barcelona, Spain,* [6] *Laboratory of Surgical Neuroanatomy, Faculty of Medicine and Health Sciences, Institute of Neurosciences, University of Barcelona, Barcelona, Spain*

Brain electrical stimulation techniques take advantage of the intrinsic plasticity of the nervous system, opening a wide range of therapeutic applications. Vagus nerve stimulation (VNS) is an approved adjuvant for drug-resistant epilepsy and depression. Its non-invasive form, auricular transcutaneous VNS (atVNS), is under investigation for applications, including cognitive improvement. We aimed to study the effects of atVNS on brain connectivity, under conditions that improved memory persistence in CD-1 male mice. Acute atVNS in the *cymba conchae* of the left ear was performed using a standard stimulation protocol under light isoflurane anesthesia, immediately or 3 h after the training/familiarization phase of the novel object-recognition memory test (NORT). Another cohort of mice was used for bilateral c-Fos analysis after atVNS administration. Spearman correlation of c-Fos density between each pair of the thirty brain regions analyzed allowed obtaining the network of significant functional connections in stimulated and non-stimulated control brains. NORT performance was enhanced when atVNS was delivered just after, but not 3 h after, the familiarization phase of the task. No alterations in c-Fos density were associated with electrostimulation, but a significant effect of atVNS was observed on c-Fos-based functional connectivity. atVNS induced a clear reorganization of the network, increasing the inter-hemisphere connections and the connectivity of locus coeruleus. Our results provide new insights into the effects of atVNS on memory performance and brain connectivity extending our knowledge of the biological mechanisms of bioelectronics in medicine.

Keywords: auricular transcutaneous vagus nerve stimulation, memory persistence, brain connectivity, electrostimulation, c-Fos functional networks

OPEN ACCESS

Edited by:
Federico Bermudez-Rattoni, National Autonomous University of Mexico, Mexico

Reviewed by:
Matthias Prigge, Leibniz Institute for Neurobiology (LG), Germany
Luis A. Tellez, National Autonomous University of Mexico, Mexico

***Correspondence:**
Andrés Ozaita
andres.ozaita@upf.edu

Specialty section:
This article was submitted to Cellular Neurophysiology, a section of the journal Frontiers in Cellular Neuroscience

Received: *17 January 2022*
Accepted: *09 March 2022*
Published: *25 April 2022*

Citation:
Brambilla-Pisoni C, Muñoz-Moreno E, Gallego-Amaro I, Maldonado R, Ivorra A, Soria G and Ozaita A (2022) Auricular Transcutaneous Vagus Nerve Stimulation Acutely Modulates Brain Connectivity in Mice. Front. Cell. Neurosci. 16:856855. doi: 10.3389/fncel.2022.856855

INTRODUCTION

Nowadays, brain stimulation devices have gained significant interest in the scientific community and have received European Medicine Agency (EMA) and US Food and Drug Administration (FDA) approvals for different therapeutic purposes. An approach to achieve brain stimulation is through vagus nerve afferents. Indeed, vagus nerve stimulation (VNS) has become an interesting

strategy to help handle drug-resistant epilepsy and depression (Yuan and Silberstein, 2015). In this context, transcutaneous VNS (tVNS), given its non-invasiveness, has received substantial attention. tVNS can be applied to different locations, such as in the neck (Brock et al., 2017) or in the *cymba conchae* of the external ear (Peuker and Filler, 2002), and, similar to the invasive form of VNS, has already been approved as an adjuvant in the clinical applications, such as for the treatment of drug-resistant epilepsy and depression (Hein et al., 2013; Bauer et al., 2016). Surprisingly, the direct effect of tVNS over brain function is far from understood. Renewed attention to this electrostimulation technique derives from its neuromodulatory effect on cognitive processes. The vagus nerve afferent fibers in the brainstem end in the nucleus of the solitary tract (NTS) (Ruffoli et al., 2011), a relevant relay area for visceral information. From there, afferent information is distributed to many brain regions, including the *locus coeruleus* (LC) (Grimonprez et al., 2015). The LC provides a widespread innervation to the hippocampus, amygdala, and prefrontal cortex, among other regions (Ruffoli et al., 2011). In this regard, it has been postulated that the LC could regulate cognition through the release of norepinephrine and dopamine in memory processing areas (Ruffoli et al., 2011; Duszkiewicz et al., 2019), mimicking those physiological processes involved in attention-driven cognition (Mello-Carpes and Izquierdo, 2013; Mather and Harley, 2016; Zerbi et al., 2019), but whether such interaction results in the modulation of brain networks is not completely understood. Among those brain networks supporting brain activity, the default mode network (DMN), a brain network predominantly active when the brain is not engaged in an attention-driven task (Raichle et al., 2001; Stafford et al., 2014), has received much consideration due to the reproducibility in its detection in the clinical and preclinical settings (Stafford et al., 2014). The DMN is therefore disengaged during periods of active brain function, as during attention-associated periods, and it has been described to be modulated by tVNS in patients with mild or moderate depressive symptoms (Fang et al., 2016). Focusing on the cognitive functions associated with memory, our group already reported that auricular tVNS (atVNS) enhanced novel object-recognition (NOR) memory persistence in *naïve* CD-1 mice (Vázquez Oliver et al., 2020). The brain mechanisms recruited by atVNS to enhance memory performance have not been described, so we further explored the cellular outcome of atVNS under conditions that potentiate object-recognition memory persistence. First, we assessed whether a critical time window for atVNS efficacy may limit its effect on favoring object-recognition memory. Second, we analyzed the expression of an immediate early gene c-Fos as an approach to study brain activity in discrete brain regions (Guzowski et al., 2005). In line with the current view proposing that specific cognitive functions are supported by a network of functionally connected brain regions, rather than isolated areas, together with the region-specific analysis of c-Fos, we also evaluated the c-Fos-based functional network (Vetere et al., 2017). We focused our analysis on areas of the brainstem, hippocampus, amygdala, thalamus, and frontal/dorsal cortex, some of which are components of the DMN. Starting from these c-Fos data, we analyzed and estimated the functional connectivity network based on c-Fos density for both stimulated and non-stimulated brains to find significant changes in network connectivity patterns in atVNS condition.

MATERIALS AND METHODS

Animals

Young adult male CD-1 mice (10 weeks old) were purchased from the Charles River Laboratories (France). All the experimental mice were bred at the Barcelona Biomedical Research Park (PRBB) Animal Facility. All animal procedures were conducted in accordance with the standard ethical guidelines (European Communities Directive 2010/63/EU). Mice were housed in a temperature-controlled (21 ± 1°C) and humidity-controlled (55 ± 10%) environment. Lighting was maintained at 12 h' cycles (on at 8 a.m. and off at 8 p.m.). Food and water were available *ad libitum*. Mice were handled for 1 week before starting the experiment and were randomly distributed among experimental groups. All the procedures were performed by experimenters blind to the experimental conditions.

Experimental Design—Behavioral and Electrostimulation Procedures

The electrostimulation was performed at the time points indicated later after the familiarization/training phase in the novel object-recognition test (NORT), following a similar approach to that described earlier (Vázquez Oliver et al., 2020). Briefly, on the habituation phase performed on day 1, mice were habituated to an empty V-shape maze (V-maze) for 9 min. The next day, on the training phase performed on day 2, mice were presented in the V-maze to two identical objects for 9 min, each object at the end of the maze corridors. Immediately after the familiarization phase [atVNS (0 h), $n = 11$] or 3 h after the familiarization phase [atVNS (3 h), $n = 12$] mice were anesthetized with isoflurane (1.5%) in 0.8 L/min O_2 during 30 min, and subjected or not to atVNS. Normothermic conditions were maintained during anesthesia with a heating pad. For atVNS (0 h) and atVNS (3 h) conditions, a newly custom-designed bipolar electrode (described in Vázquez Oliver et al., 2020) was placed in the *cymbae concha* of the left ear. Rectangular biphasic pulses were delivered with a Beurer EM49 stimulator (Beurer, Germany). The stimulation parameters were: 1 mA, 20 Hz, 30 s ON and 5 min OFF, the total length of 30 min, with a 320 μs pulse width. For the No stimulation condition ($n = 12$), mice were anesthetized for 30 min immediately after the NORT familiarization, but no electrical stimulation was delivered. Forty eight h after the NORT familiarization phase and the atVNS or No stimulation procedures, mice were tested for 9 min in the V-maze, substituting one of the familiar objects for a new one, to assess memory performance.

Tissue Preparation for Immunofluorescence

In another batch of animals, the exact same NORT + atVNS or NORT + No stimulation protocols described earlier were followed, returning the mice to their home-cage afterward. atVNS nomenclature corresponds to atVNS (0 h) when not

otherwise specified. Ninety minutes following the completion of the NORT + atVNS [similar to atVNS (0 h) condition, $n = 8$] or the NORT + No stimulation (No stimulation condition, $n = 8$), mice were deeply anesthetized by intraperitoneal injection (0.2 ml/10 g of the body weight) of a mixture of ketamine (100 mg/kg) and xylazine (20 mg/kg) prior to intracardiac perfusion with 4% paraformaldehyde in 0.1 M Na_2HPO_4/0.1 M NaH_2PO_4 buffer (PB), pH 7.5, delivered with a peristaltic pump at 19 ml/min flow for 3 min. Subsequently, the brain was extracted and post-fixed in the same fixative solution for 24 h and transferred to a solution of 30% sucrose in PB overnight at 4°C. After postfixation, the brains were marked in the right hemisphere to preserve laterality in the subsequent measures. Coronal sections of 30 μm were obtained on a freezing microtome and stored in a solution of 5% sucrose at 4°C until used.

Immunofluorescence

Sections from the No stimulation and the atVNS groups were processed in parallel for immunofluorescence. Briefly, free-floating brain slices were rinsed in PB, blocked in a solution containing 3% normal goat serum (GS) (S-1000-20, Vector Laboratories Incorporation, California, USA) and 0.3% Triton X-100 (T) in PB (GS-T-PB) at room temperature for 2 h, and incubated overnight in the same solution with the primary antibody to c-Fos (sc-7202, 1:1,000, rabbit, Santa Cruz Biotechnology) and, only for LC slices, with tyrosine hydroxylase (T1299, 1:1,000, mouse, Sigma-Aldrich) at 4°C. The next day, after 3 rinses in PB, sections were incubated at room temperature with the secondary antibody AlexaFluor-555 goat anti-rabbit (ab150078, 1:1,000, Abcam) and, only for LC slices, with AlexaFluor-488 goat anti-mouse (115-545-003, 1:1,000, Jackson ImmunoResearch Laboratories Incorporation) for 2 h. After incubation, sections were rinsed and mounted immediately after onto glass slides coated with gelatin in Fluoromont-G with 4',6-diamidino-2-phenylindole (DAPI) (00-4959-52, Invitrogen, Thermo Fisher Scientific, Massachusetts, USA) as counterstaining.

c-Fos Quantification

c-Fos density was analyzed in thirty brain regions (fifteen per hemisphere), taking into account brain laterality. Analyzed brain regions included (from frontal to caudal): cingulate cortex (Cg), prelimbic cortex (PrL), infralimbic cortex (IL) (coordinates relative to Bregma: 1.94–1.54 mm), dentate gyrus (DG), CA1 and CA3 areas of the hippocampus (from Bregma: −1.46 to −1.82 mm), basolateral amygdala (BLA), lateral amygdala (LA) and central amygdala (CeA) (from Bregma: −1.46 to −1.82 mm), paraventricular nucleus of the thalamus (PVT) (from Bregma: −1.46 to −1.82 mm), anterior and posterior retrosplenial cortex (RSP, pRSP) (from Bregma: −1.46 to −2.92 mm), *locus coeruleus* (LC) (from Bregma: −5.34 to −5.68 mm), the nucleus of the solitary tract (NTS), and dorsal vagal nucleus (DMX) (from Bregma: −7.32 to −7.64) (**Supplementary Figure 1**). The immunostained brain sections were analyzed with a 10X objective using a Leica DMR microscope (DM6000B, Leica Microsystems, Wetzlar, Germany) equipped with a digital camera Leica DFX 3000FX (Leica Microsystems). The borders of all the regions were defined manually according to the mouse brain atlas (Paxinos and Franklin, 2019). For prelimbic, infralimbic, and cingulate cortexes analysis, a 430-μm-sided square region of interest (ROI) was delimited for quantification. For amygdala and dorsal hippocampus analysis, the DAPI signal was used for the delimitation of the areas in each image for quantification. For the LC, the tyrosine hydroxylase signal was used for the delimitation of the area in each image for quantification. The images were processed using ImageJ software (Rasband, 1997-2018). c-Fos-positive cells in each brain area were quantified manually using the cell counter plugin of ImageJ software. The average number of c-Fos-positive cells on four determinations for each brain area on each hemisphere were calculated for each mouse. The c-Fos density for each region was quantified by dividing the number of c-Fos-positive cells to the area considered for each region (c-Fos+/mm^2) (see **Supplementary Figure 1** for representative examples).

Generation of Functional Connectivity Network

The functional network was estimated for each condition based on the correlation between regional c-Fos density, considering that a functional connection exists between the two regions if their activity covaries (Park and Friston, 2013; Vetere et al., 2017). Therefore, within each experimental group (No stimulation and atVNS), the pair-wise Spearman's correlation coefficient between each pair of regional c-Fos density was calculated. In this way, a correlation matrix was obtained from each condition representing the correlation coefficients between all thirty brain regions analyzed, taking into account the brain laterality. By considering only significant correlations ($p < 0.05$), both the positive and negative, we obtained the condition-related functional network for atVNS and No stimulation protocols. These networks were represented by circos plots, using a custom R-code (R version 4.0.4) (R Core Team, 2020). Finally, we computed the z-Fisher transform of significant positive correlation coefficients, as a measure of connectivity strength between nodes (z-score), for both conditions and displayed them by Kamada-Kawai graphs using NetworkX graph python package (NetworkX version 2.5.1) (Hagberg et al., 2008) to visualize network organization.

Network Analysis

First, the total functional connectivity strengths for all the possible connections were compared between atVNS and No stimulation conditions, considering z-score. Likewise, for the LC region, we compared its connectivity strength with all the other evaluated regions between atVNS and non-stimulated networks.

To have a global characterization of the condition-related functional connectivity, we also computed graph metrics on the network of significant positive connectivity strengths using Brain Connectivity Toolbox (BCT) (Rubinov and Sporns, 2010). In particular, global efficiency, average clustering, average strength, and average degree of the network were estimated. In addition, regional network metrics such as nodal strength and nodal

degree coefficients were also computed. To compare network organization and the relevance of each region in the functional network, regional metrics were normalized to the maximum in the network and ordered from higher to lower value to identify network hubs (Wheeler et al., 2013).

Statistical Analysis

Data were analyzed with STATISTICA (StatSoft) software using the one-way ANOVA for multiple comparisons of parametric variables. The Kruskal–Wallis test was used for non-parametric variables. Subsequent *post-hoc* analysis (Newman–Keuls test) was

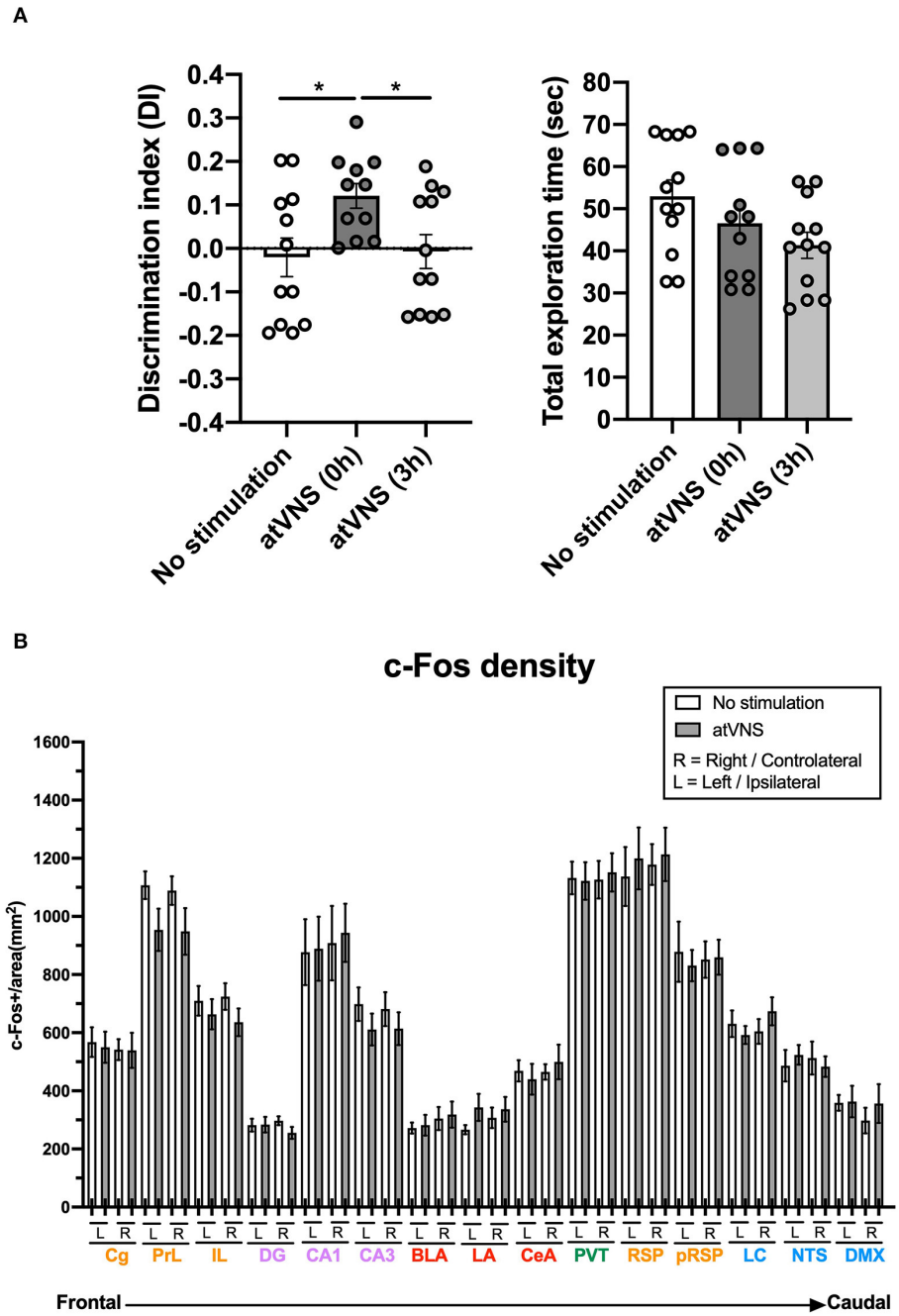

FIGURE 1 | (A) atVNS improves object-recognition memory persistence in naïve mice when administered immediately after the familiarization phase of the novel object-recognition test (NORT). Discrimination index and total exploration time in NORT for atVNS (0 h), atVNS (3 h), and No stimulation conditions in naïve CD-1 mice [atVNS (0 h) condition, $n = 11$; atVNS (3 h) condition, $n = 12$; No stimulation condition, $n = 12$]. $^*p < 0.05$ by the one-way ANOVA. **(B)** c-Fos density in No stimulation and atVNS (0 h) conditions, separating contralateral (right, R) and ipsilateral (left, L) sides according to the site of the stimulation. The brain regions analyzed are organized from frontal to caudal and grouped in the cortical (orange), hippocampal (purple), amygdalar (red), thalamic (green), and brainstem (blue) groups.

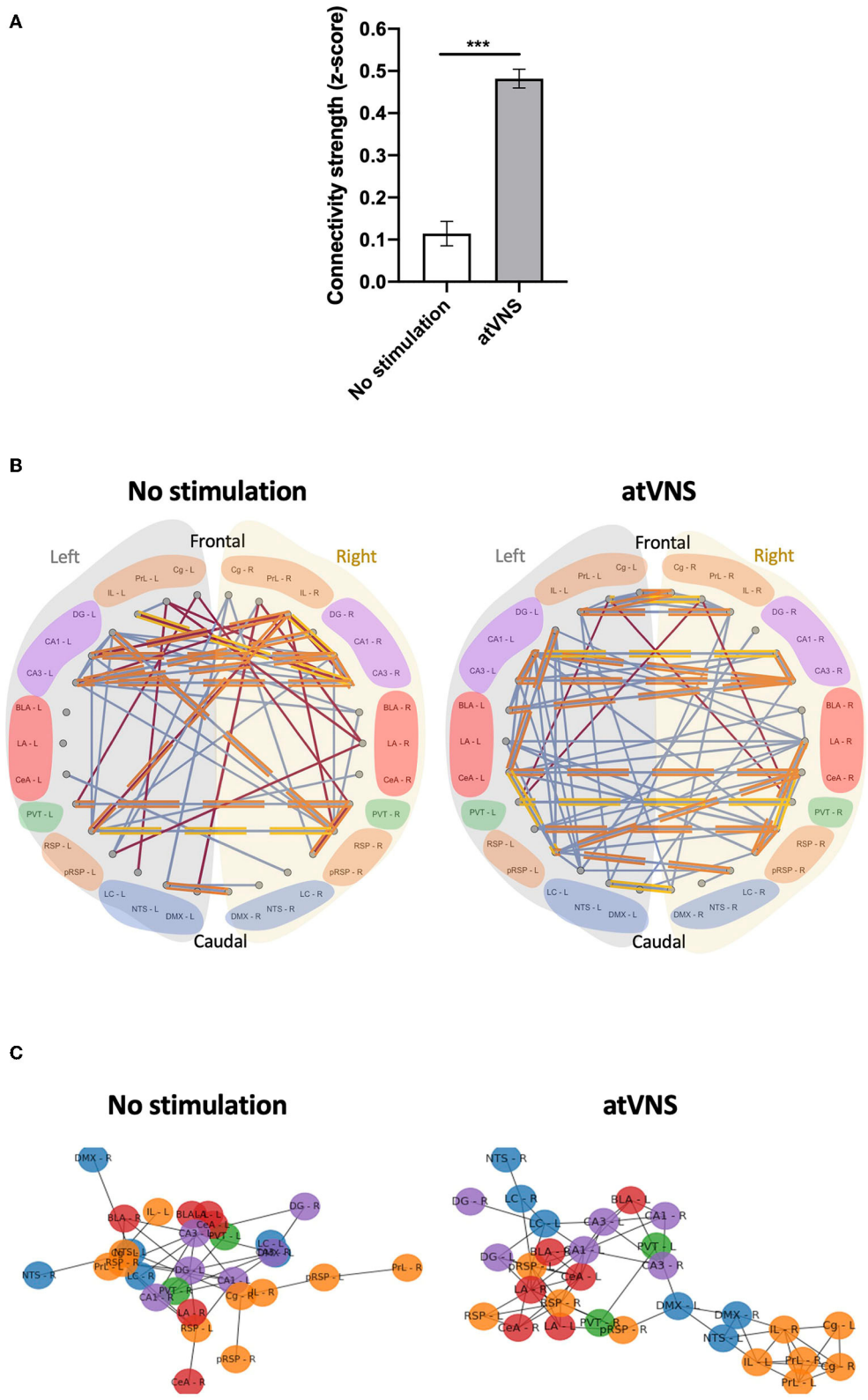

FIGURE 2 | (A) Effects of atVNS on global network connectivity. Total connectivity presented as z-score, comparing No stimulation and atVNS (0 h) conditions. ***$p <$ 0.001 by the Kruskal–Wallis test. **(B)** Network connectivity graphs displaying only the significant correlations ($p < 0.05$). Connecting lines represent Spearman

(Continued)

FIGURE 2 | correlation (positive correlation in blue, negative correlation in red). Strongest significant correlations are highlighted in orange ($p < 0.01$) and yellow ($p < 0.001$). Regions are presented from frontal to caudal and separating left (light gray) and right (light yellow) sides. Regions are grouped into the cortical (orange), hippocampal (purple), amygdalar (red), thalamic (green), and brainstem (blue) groups. **(C)** Network connectivity Kamada–Kawai plots displaying only positive significant z-score for No stimulation and atVNS (0 h) conditions. Colors represent the cortical (orange), hippocampal (purple), amygdalar (red), thalamic (green), and brainstem (blue) groups. Regions are grouped based on the connectivity strength between them.

used when required to reveal a significant interaction between factors. The artwork was designed using GraphPad Prism version 7. Comparisons were considered statistically significant when $p < 0.05$. Data are represented as mean ± SEM.

RESULTS

Object-Recognition Memory Enhancement by Acute Auricular Transcutaneous Vagus Nerve Stimulation Depends on the Time of Administration

Auricular transcutaneous vagus nerve stimulation was administered after the familiarization phase of the NORT at two different time points, immediately after [atVNS (0 h) group] or 3 h after [atVNS (3 h) group]. As control, we intermingled another batch of animals that were similarly handled but did not receive the electrostimulation procedure (No stimulation group). We found that an acute session of atVNS, delivered immediately after the NORT familiarization phase, significantly improved object-recognition memory performance at 48 h (**Figure 1A**) compared with atVNS (3 h) and No stimulation conditions which showed similar results with no enhancement in memory persistence. This result indicates that the modulation of object-recognition memory persistence depends on the time of application after familiarization/training, with a critical time window for effective action of atVNS.

c-Fos Density Is Not Significantly Modified in Various Brain Regions After atVNS

Brain samples from NORT + No stimulation and NORT + atVNS (0 h) [atVNS (0 h) was termed atVNS for the rest of the study] conditions were obtained 90 min after sham or atVNS handling to match the peak of expression of c-Fos. We focused on the analysis of c-Fos density in areas involved in novel object-recognition memory processing. Laterality was considered in the analysis.

Notably, c-Fos density analysis did not reveal significant differences between experimental conditions in any of the areas considered, although prelimbic and infralimbic regions and CA3 area showed a non-significant trend to reduce the density of c-Fos positive cells after atVNS (**Figure 1B**). This result showed that atVNS is not associated with localized regional changes, and therefore, we investigated whether its effects are related to a network reorganization of brain functioning.

Inferred Brain Connectivity Is Relevantly Modulated by atVNS

To gain deeper insights into the functional connections within the set of brain regions in our analysis, we computed the connectivity matrices for each experimental group (**Supplementary Figure 2**). Comparing both connectivity matrices, an overall effect of atVNS on the relation of c-Fos density among different brain areas was observed, with a higher percentage of positive correlations under atVNS condition. To investigate deeper into this difference, we calculated the z-Fisher transform of correlations coefficients in both the conditions. The z-scores we obtained for each correlation coefficient represent the connectivity strength. When we statistically compared the strengths of all the connections between both conditions, we observed a significant increase in the total connectivity [No stimulation: 0.11 ± 0.029; atVNS: 0.48 ± 0.022; $t_{(868)} = 10.05$; $p < 0.0001$] induced by atVNS (**Figure 2A**).

Subsequently, we also focused on the networks created by significant correlations ($p < 0.05$). To disclose intra- and interhemispheric correlated activities for the network associated with each condition, we generated representative circos plots (**Figure 2B**). This analysis revealed that atVNS coupled the activity of left and right LC, also increasing its correlated activity with the dentate gyrus. Furthermore, the electrostimulation reinforced the relation in activity of all subregions of the hippocampus (DG, CA1, and CA3). Moreover, atVNS produced a marked enhancement in the correlated activity between hemispheres, especially in the frontal and amygdalar areas. A summary of intra- and interhemispheric significant correlations for each condition is shown in **Table 1**.

Notably, while there was an overall increase in connectivity after atVNS, the prefrontal-retrosplenial axis, characteristic of the default mode network, was not observed in control conditions, and atVNS did not have any marked effects on engaging this axis (**Supplementary Figure 3**).

In order to highlight the brain regions relevant in the network for each condition, we used the force-directed Kamada–Kawai plots. This representation revealed a re-organization of

TABLE 1 | Intrahemisphere and interhemisphere number of significant correlations in No stimulation and atVNS (0 h) conditions for frontal (Cg, PrL, and IL), hippocampal (DG, CA1, and CA3), amygdalar (BLA, LA, and CeA), and brainstem (LC, NTS, and DMX) areas.

Areas	Intra-hemisphere				Inter-hemisphere	
	No stimulation		atVNS		No stimulation	atVNS
	Left	Right	Left	Right		
Frontal cortex	3	5	4	5	7	10
Hippocampus	5	3	11	1	10	8
Amygdala	0	1	5	4	5	11
Brainstem	1	0	6	2	3	5

the network due to atVNS with a more evident cross-talk between the brainstem areas and frontal and hippocampal regions (**Figure 2C**). Indeed, atVNS produced a clear segregation of Cg, IL, and PrL cortices with left NTS and DMX as connection nodes to the remaining structures. Also, the amygdaloid nuclei and the RSP cortex took a central role that was occupied by the hippocampal nuclei under No stimulation conditions.

Global brain network metrics were used to account for the segregation and integration properties in each condition. We found a marked increase in all the evaluated properties in atVNS brains (global efficiency: No stimulation = 0.346, atVNS = 0.500; average clustering: No stimulation = 0.478, atVNS = 0.734; average strength: No stimulation = 4.037; atVNS = 5.956; average degree: No stimulation = 3.266; atVNS = 4.933).

We further assessed the relative importance of the brain regions analyzed in the overall brain network based on the regional network metrics. An increase in the relative importance of frontal areas in atVNS condition is observed, compared with No stimulation condition in which hippocampal regions showed a more relevant role. Furthermore, we found that brainstem regions, especially left LC, had a more relevant role in the atVNS network than in the No stimulation network, with a relatively higher value of both nodal strength and nodal degree coefficients (**Figure 3A**), since the brainstem regions constitute a passage between the vagus nerve afferents and superior brain regions. Indeed, if we compare the overall connectivity for the LC region, we observe a significant increase in the connectivity of both left and right LC (**Figure 3B**).

DISCUSSION

Invasive and non-invasive vagus nerve stimulations (VNSs) have been shown to modulate memory functions, both in animal (Clark et al., 1995, 1998; Vázquez Oliver et al., 2020) and human studies (Clark et al., 1999; Ghacibeh et al., 2006; Jacobs et al., 2015). However, the presence of an effective time window for atVNS effectiveness has not been explored before. In addition, the brain activity outcome of atVNS under memory retention facilitated conditions is still under study.

Therefore, first we aimed to determine whether there was a critical time window for effective enhancement of object-recognition memory persistence through an acute session of atVNS. We found that atVNS in the *concha* of the left external ear of naïve CD-1 male mice, improved memory persistence, when the electrostimulation protocol was delivered immediately after the familiarization phase of the NORT. Conversely, atVNS delivered 3 h after the training of the NORT did not show any sign of effect on recognition memory at 48 h. This evidence points out the presence of an effective time window for atVNS efficacy in modulating memory persistence. This result is in agreement with a previous clinical report describing that the stimulation, in this case through an invasive approach, was effective when given around the learning phase of a Hopkins Verbal Learning Test, and not during the recall phase (Ghacibeh et al., 2006). Therefore, both invasive and non-invasive forms of VNS, would principally enhance memory consolidation, leading to a better retention power when the electrical stimulus is delivered immediately after the familiarization or learning process.

Second, we investigated atVNS effects on neuronal and network activity, taking into consideration brainstem regions associated with vagal afferences, brain areas important for memory processes, and brain regions implicated in the DMN. It is well established that memory is not stored in a single brain area, but in a network composed of multiple regions (Tanimizu et al., 2017). In the case of recognition memory, the hippocampal formation comprises the main brain region involved (Brown and Aggleton, 2001), although cortical and subcortical areas are also engaged (Frankland and Bontempi, 2005). It has been postulated that memories are initially retained in the hippocampus, and then the information is transferred into the neocortex where it can be consolidated and stored for longer periods (Frankland and Bontempi, 2005; Insel and Takehara-Nischiuchi, 2013). Furthermore, the amygdala complex plays an important role in memory processes, especially under emotionally arousing experiences (Richter-Levin, 2004). These brain regions are contacted by brainstem regions which are relevant for setting the stage concerning the responsiveness associated with the arousal state (Roozendaal and McCaugh, 2011). In this regard, the LC can convey the information from vagal afferents arriving into the NTS (Grimonprez et al., 2015) and affecting the memory-related regions. Hence, we wondered whether the consolidation of new object-recognition memories, facilitated by atVNS, could be mediated by a change in the neuronal activation or a re-distribution of the activity relation between the brain areas.

Neuronal activation and functional connectivity were analyzed by computing the c-Fos density and interregional correlations across animals that received or not the electrostimulation procedure immediately after the familiarization phase of the NORT. We first bilaterally calculated the c-Fos density in a set of cortical, hippocampal, amygdalar, thalamic, and brainstem regions for No stimulation and atVNS conditions. Notably, atVNS did not promote significant changes in c-Fos density in any of the thirty (fifteen per hemisphere) brain regions studied. Other previous reports found changes in c-Fos density after the electrostimulation, particularly an increase in the number of c-Fos+ cells, in areas of the brainstem (Huffman et al., 2019; Jiang et al., 2019; Katagiri et al., 2019). However, all these studies used percutaneous or invasive VNS approaches, or applied the stimulation longer times. Our atVNS protocol instead is completely non-invasive, involves the auricular branch of the vagus nerve and the stimulation period is limited to 30 min, producing a significant effect in memory performance. Thus, the fact that no significant differences could be observed in the number of c-Fos+ cells in brain areas where other studies have found VNS-associated modulations, are probably due to the non-invasiveness and short stimulation protocol of atVNS procedure. Furthermore, several studies have been conducted using functional MRI (fMRI) and atVNS, especially in humans, to shed some light on the possible mechanisms and brain networks involved during

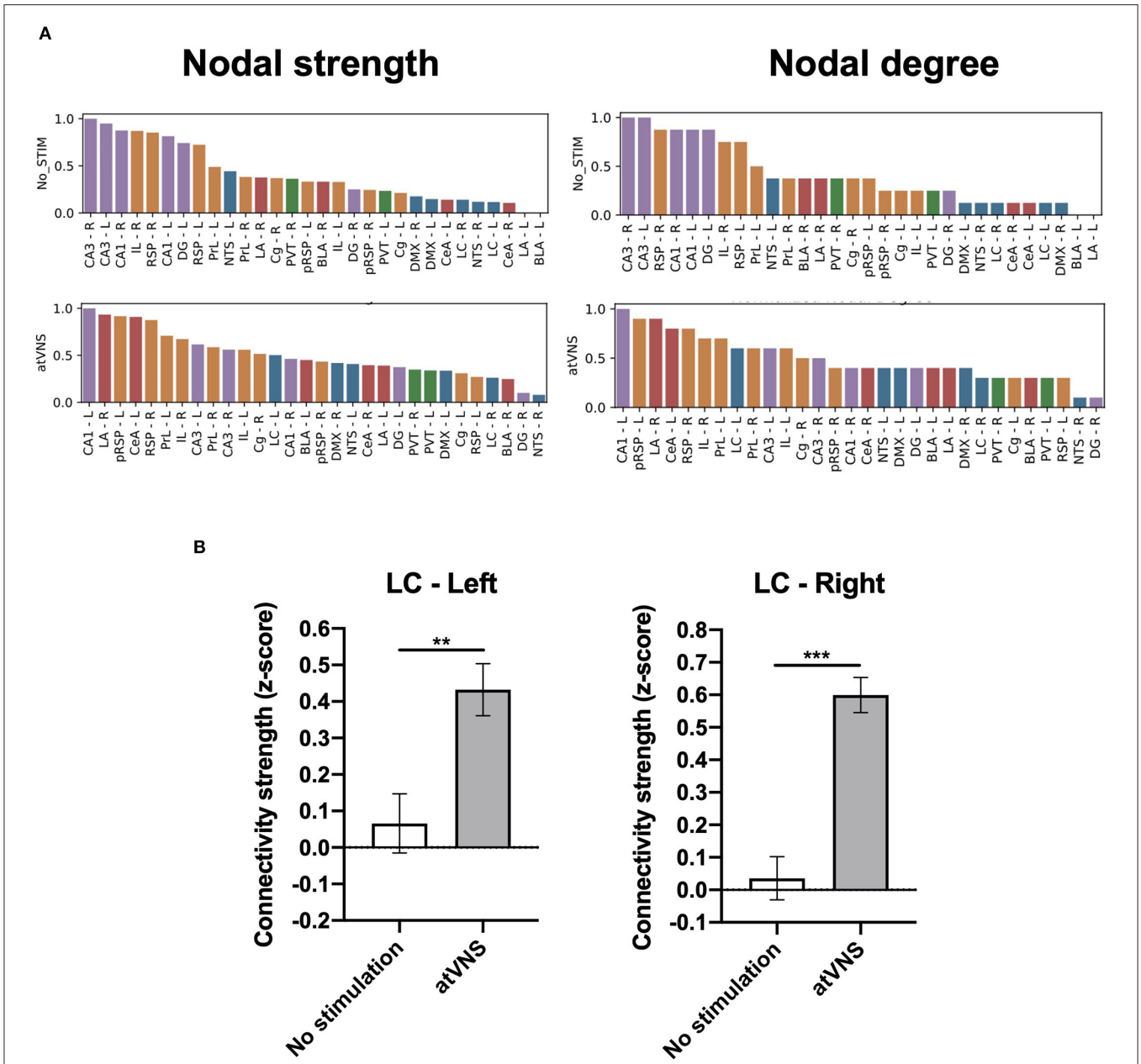

FIGURE 3 | (A) Brain regions ranked in descending order based on nodal strength and nodal degree coefficients for No stimulation and atVNS (0 h) conditions. Regions are displayed with color coding: cortex (orange), hippocampus (purple), amygdala (red), thalamus (green), and brainstem (blue). **(B)** Difference in the total connectivity of right and left *locus coeruleus* (LC) regions with the rest of the brain areas analyzed, presented as z-score and comparing No stimulation and atVNS (0 h) conditions. $^{**}p < 0.01$; $^{***}p < 0.001$ by the Kruskal–Wallis test.

atVNS. In general, left atVNS produced a significant activation in the ipsilateral NTS, LC and prefrontal and cingulate cortices, while bilateral deactivation was found in the hippocampus and hypothalamus, and controversial results were described in the amygdala (Kraus et al., 2007; Dietrich et al., 2008; Frangos et al., 2015; Butt et al., 2020). In contrast to fMRI procedure, we used c-Fos as a proxy for cellular activity; the main advantage of this approach is the cellular resolution mapping, although the poor temporal resolution is the principal limitation (McReynolds et al., 2018). Indeed, higher temporal resolution techniques would likely show distinct inter and intra-hemisphere differences that should be addressed in future studies. Additionally, all the animals were actively handled before sampling collections. This process could influence some of the results presented in the analysis, although extreme care was taken to make sure all animals were similarly handled, in order for the groups to

only differ in the stimulation procedure. Notably, when we investigated c-Fos functional network, we found a significant reorganization, due to the electrostimulation procedure. atVNS resulted in an enhanced number of significant inter-hemisphere correlations compared to those observed in the No stimulation condition, especially in frontal and amygdalar areas. Moreover, significant correlations were found for sub-networks in the hippocampus (DG, CA1, and CA3) and frontal areas (PrL, IL, and Cg), with a specific increase in the correlation between the left LC and the dentate gyrus after atVNS. The distribution of the network differed between stimulation conditions. Under atVNS prefrontal cortices were segregated and linked to the remaining structures through DMX and left NTS, compared to No stimulation conditions, suggesting the ability of atVNS to dynamically reconfigure large-scale organization. In addition, a reorganization of the amygdala nuclei was observed pointing to a key role of this structure in the atVNS-mediated memory enhancement.

We also explored the effect of atVNS on selected DMN regions. This network has been also described in the mouse brain and involves the pRSP, RSP, Cg, PrL, and IL areas as components of the network (Stafford et al., 2014). By studying these areas in both hemispheres separately, we found that atVNS does not favor the connectivity of the DMN areas, as there is an absence of communication of the DMN anterior–posterior axis between frontal areas and retrosplenial cortex. This is in agreement with the idea that the DMN is mostly disengaged during task performance, and atVNS does not facilitate its engagement, and it may favor its disengagement.

Previous studies, using a combination of c-Fos expression and network analysis, found that long-term contextual fear memories are stored in a brain network composed by thalamic, hippocampal, and cortical regions (Wheeler et al., 2013), while the brain network composed by hippocampus, medial prefrontal cortex, anterior cingulate cortex, and amygdala was found required for the consolidation of social recognition memory (Tanimizu et al., 2017). These studies suggest that distinct types of memory are supported by exclusive functional memory networks that can be revealed by c-Fos analysis. Our findings in this study suggest that enhanced object-recognition memory consolidation is not prompted by an increase in neuronal activation by acute atVNS. Instead, we found a redistribution of the activity, and identified the correlation between brainstem nuclei and hippocampus and frontal areas as the privileged communication that may support the enhancement in memory persistence. Therefore, future studies should also focus on the real-time assessment of changes in neuronal activity induced by atVNS, to better understand its potential in modulating memory processes.

DATA AVAILABILITY STATEMENT

The raw data supporting the conclusions of this article will be made available by the authors, without undue reservation.

ETHICS STATEMENT

The procedures involving experimentation on animals were reviewed and approved by the Barcelona Biomedical Research Park Experimentation Animal Ethical Committee and the local competent authorities.

AUTHOR CONTRIBUTIONS

CB-P participated in experimental design, conducted and analyzed experiments, and wrote the manuscript. EM-M produced network analysis and revised the manuscript. IG-A conducted and analyzed experiments. RM participated in the supervision and experimental design, funded the project, and revised the manuscript. AI participated in the supervision and stimulator design and generation, funded the project, and revised the manuscript. GS participated in the supervision and analysis of network data and revised the manuscript. AO conceptualized, participated in experimental design, supervised, funded the project, and wrote the manuscript. All authors reviewed and approved the final version of the manuscript.

FUNDING

The project that gave rise to these results received the support of a fellowship from la Caixa Foundation (ID 100010434). The fellowship code is LCF/BQ/IN18/11660012 (CB-P). This project has received funding from the European Union's Horizon 2020 research and innovation program under the Marie Slodowska-Curie grant agreement No. 713673. This work was supported by the Ministerio de Economía, Innovación y Competitividad (MINECO) (#RTI2018-099282-B-I00 to AO and PID2020-120029GB-I00/MICIN/AEI/10.13039/501100011033 to RM); the Instituto de Salud Carlos III (#RD16/0017/0020 to RM and PI18/00893 cofunded by ERDF A way to make Europe to GS); the Generalitat de Catalunya (2017SGR-669 to RM); the ICREA (Institució Catalana de Recerca i Estudis Avançats) Academia to AO, AI, and RM; Grant Unidad de Excelencia María de Maeztu, funded by the MINECO (#MDM-2014-0370); and PLAN E (Plan Español para el Estímulo de la Economía y el Empleo). FEDER funding is also acknowledged.

ACKNOWLEDGMENTS

We thank Dulce Real and Francisco Porrón for expert technical assistance and the Laboratory of Neuropharmacology-NeuroPhar for helpful discussion.

SUPPLEMENTARY MATERIAL

The Supplementary Material for this article can be found online at: https://www.frontiersin.org/articles/10.3389/fncel.2022.856855/full#supplementary-material

REFERENCES

Bauer, S., Baier, H., Baumgartner, C., Bohlmann, K., Fauser, S., Graf, W., et al. (2016). Transcutaneous vagus nerve stimulation (tVNS) for treatment of drug-resistant epilepsy: a randomized, double-bind clinical trial (cMPsE02). *Brain Stimul.* 9, 356–363. doi: 10.1016/j.brs.2015.11.003

Brock, C., Brock, B., Aziz, Q., Moller, H. J., Pfeiffer Jensen, M., Drewes, A. M., et al. (2017). Trascutaneous cervical vagal nerve stimulation modulates cardiac vagal tone and tumor necrosis factor-alpha. *Neurogastroenterol. Motil.* 29, el12999. doi: 10.1111/nmo.12999

Brown, M. W., and Aggleton, J. P. (2001). Recognition memory: what are the roles of the perirhinal cortex and the hippocampus? *Nat. Rev. Neurosci.* 2, 51–61. doi: 10.1038/35049064

Butt, M. F., Albusoda, A., Farmer, A. D., and Aziz, Q. (2020). The anatomical basis for transcutaneous auricular vagus nerve stimulation. *J. Anat.* 236, 588–611. doi: 10.1111/joa.13122

Clark, K. B., Krahl, S. E., Smith, D. C., and Jensen, R. A. (1995). Post-training unilateral vagal stimulation enhances retention performance in the rat. *Neurobiol. Learn. Mem.* 63, 213–216. doi: 10.1006/nlme.1995.1024

Clark, K. B., Naritoku, D. K., Smith, D. C., Browning, R. A., and Jensen, R. A. (1999). Enhanced recognition memory following vagus nerve stimulation in human subjects. *Nat. Neurosci.* 2, 94–98. doi: 10.1038/4600

Clark, K. B., Smith, D. C., Hassert, D. L., Browning, R. A., Naritoku, D. K., and Jensen, R. A. (1998). Posttraining electrical stimulation of vagal afferents with concomitant vagal efferent inactivation enhances memory storage processes in the rat. *Neurobiol. Learn. Mem.* 70, 364–373. doi: 10.1006/nlme.1998.3863

Dietrich, S., Smith, J., Scherzinger, C., Hofmann-Preib, K., Freitag, T., Eisenkolb, A., et al. (2008). A novel transcutaneous vagus nerve stimulation leads to brainstem and cerebral activations measures by functional MRI. *Biomed. Tech.* 53, 104–111. doi: 10.1515/BMT.2008.022

Duszkiewicz, A. J., McNamara, C. G., Takeuchi, T., and Genzel, L. (2019). Novelty and dopaminergic modulation of memory persistence: a tale of two systems. *Trends Neurosci.* 42, 102–114. doi: 10.1016/j.tins.2018.10.002

Fang, J., Rong, P., Hong, Y., Fan, Y., Liu, J., Wang, H., et al. (2016). Transcutaneous vagus nerve stimulation modulates default mode network in major depressive disorder. *Biol. Psychiatry* 79, 266–273. doi: 10.1016/j.biopsych.2015.03.025

Frangos, E., Ellirch, J., and Komisaruk, B. R. (2015). Non-invasive access to the vagus nerve central projections via electrical stimulation of the external ear: fMRI evidence in humans. *Brain Stim* 8, 624–636. doi: 10.1016/j.brs.2014.11.018

Frankland, P. W., and Bontempi, B. (2005). The organization of recent and remote memories. *Nat. Rev. Neurosci.* 6, 119–130. doi: 10.1038/nrn1607

Ghacibeh, G. A., Shenker, J. I., Shenal, B., Uthman, B. M., Kenneth, M., and Heilman, M. (2006). The influence of vagus nerve stimulation on memory. *Cogn. Behav. Neurol.* 19, 119–122. doi: 10.1097/01.wnn.0000213908.34278.7d

Grimonprez, A., Raedt, R., Portelli, J., Dauwe, I., Larsen, L. E., Bouckaert, C., et al. (2015). The antidepressant-like effect of vagus nerve stimulation is mediated through the locus coeruleus. *J. Psychiatr. Res.* 68, 1–7. doi: 10.1016/j.jpsychires.2015.05.002

Guzowski, J. F., Timlin, J. A., Roysam, B., McNaughton, B. L., Worley, P. F., and Barnes, C. A. (2005). Mapping behaviorally relevant neural circuits with immediate-early gene expression. *Curr. Opin. Neurobiol.* 15, 599–606. doi: 10.1016/j.conb.2005.08.018

Hagberg, A., Swart, P., and Shult, D. (2008). "Exploring network structure, dynamics, and function using networkx," in *Proceedings of the 7th Python in Science Conference*. Availalbe online at: https://permalink.lanl.gov/object/tr?what=info:lanl-repo/lareport/LA-UR-08-05495

Hein, E., Nowak, M., Kiess, O., Biermann, T., Bayerlein, K., Kornhuber, J., et al. (2013). Auricular transcutaneous electrical nerve stimulation in depressed patients: a randomized controlled pilot study. *J. Neural Transm.* 120, 821–827. doi: 10.1007/s00702-012-0908-6

Huffman, W. J., Subramaniyan, S., Rodriguiz, R. M., Wetsel, W. C., Grill, W. M., and Terrando, N. (2019). Modulation of neuroinflammation and memory dysfunction using percutaneous vagus nerve stimulation in mice. *Brain Stim.* 12, 19–29. doi: 10.1016/j.brs.2018.10.005

Insel, N., and Takehara-Nischiuchi, K. (2013). The cortical structure of consolidated memory: a hypothesis on the role of the cingulate-entorhinal cortical connection. *Neurobiol. Learn. Mem.* 106, 343–350. doi: 10.1016/j.nlm.2013.07.019

Jacobs, H. I. L., Riphagen, J. M., Razat, C. M., Wiese, S., and Sack, A. T. (2015). Transcutaneous vagus nerve stimulation boosts associative memory in older individuals. *Neurobiol. Aging* 36, 1860–1867. doi: 10.1016/j.neurobiolaging.2015.02.023

Jiang, M-N., Zhou, Y-Y., Hua, D-H., Yang, J-Y., Hu, M-L., and Xing, Y-Q. (2019). Vagal nerve stimulation attenuates ischemia-reperfusion induced retina dysfunction in acute ocular hypertension. *Front. Neurosci.* 13, 87. doi: 10.3389/fnins.2019.00087

Katagiri, M., Iida, K., Ishihara, K., Nair, D., Harada, K., Kagawa, K., et al. (2019). Anti-seizure effect and neuronal activity change in the genetic-epileptic model rat with acute and chronic vagus nerve stimulation. *Epilepsy Res.* 155, 106159. doi: 10.1016/j.eplepsyres.2019.106159

Kraus, T., Hosl, K., Kiess, O., Schanze, A., Kornhuber, J., and Forster, C. (2007). BOLD fMRI deactivation of limbic and temporal brain structures and mood enhancing effect by transcutaneous vagus nerve stimulation. *J. Neural Transm.* 114, 1486–1493. doi: 10.1007/s00702-007-0755-z

Mather, M., and Harley, C. W. (2016). The locus coeruleus: essential for maintaining cognitive functioning and the aging brain. *Trends Cogn. Sci.* 20, 214–226. doi: 10.1016/j.tics.2016.01.001

McReynolds, J. R., Christianson, J. P., Blacktop, J. M., and Mantsch, J. R. (2018). What does the Fos say? Using Fos-based approaches to understand the contribution of stress to substance use disorders. *Neurobiol. Stress* 9, 271–285. doi: 10.1016/j.ynstr.2018.05.004

Mello-Carpes, P. B., and Izquierdo, I. (2013). The nucleus of the solitary tract > nucleus paragigantocellularis > locus coeruleus > CA1 region of the dorsal hippocampus pathway is important for consolidation of object recognition memory. *Neurobiol. Learn. Mem.* 100, 56–63. doi: 10.1016/j.nlm.2012.12.002

Park, H.-J., and Friston, K. (2013). Structural and functional brain networks: from connections to cognition. *Science* 342, 1238411. doi: 10.1126/science.1238411

Paxinos, G., and Franklin, K. B. J. (2019). *Paxinos and Franklin's The Mouse Brain in Stereotaxis Coordinates*, 5th Edn. San Diego: Elsevier Academic Press.

Peuker, E. T., and Filler, T. J. (2002). The nerve supply of the human auricle. *Clin. Anat.* 15, 35–37. doi: 10.1002/ca.1089

R Core Team (2020). *R: A Language and Environment for Statistical Computing*. Vienna: R Foundation for Statistical Computing. Available online at: https://R-project.org/ (accessed January 15, 2022).

Raichle, M. E., MacLeod, A. M., Snyder, A. Z., Powers, W. J., Gusnard, D. A., and Shulman, G. L. (2001). A default mode of brain function. *PNAS* 98, 676–682. doi: 10.1073/pnas.98.2.676

Rasband, W. S. (1997-2018). *ImageJ*. Bethesda, MA: U. S. National Institutes of Health. Available online at: https://imagej.nih.gov/ij/ (accessed January 15, 2022).

Richter-Levin, G. (2004). The amygdala, the hippocampus and emotional modulation of memory. *Neuroscientist* 10, 31–39. doi: 10.1177/1073858403259955

Roozendaal, B., and McCaugh, J. (2011). Memory modulation. *Behav. Neurosci.* 125, 797–824. doi: 10.1037/a0026187

Rubinov, M., and Sporns, O. (2010). Complex network measures of brain connectivity: uses and interpretations. *Neuroimage* 52, 1059–1069. doi: 10.1016/j.neuroimage.2009.10.003

Ruffoli, R., Giorgi, F. S., Pizzanelli, C., Murri, L., Paparelli, A., and Fornai, F. (2011). The chemical neuroanatomy of vagus nerve stimulation. *J. Chem. Neuroanat.* 42, 288–296. doi: 10.1016/j.jchemneu.2010.12.002

Stafford, J. M., Jarrett, B. R., Miranda-Dominguez, O., Mills, B. D., Cain, N., Mihalas, S., et al. (2014). Large-scale topology and the default mode network in the mouse connectome. *PNAS* 111, 18745–18750. doi: 10.1073/pnas.1404346111

Tanimizu, T., Kenney, J. W., Okano, E., Kadoma, K., Frankland, P. W., and Kida, S. (2017). Functional connectivity of multiple brain regions required for the consolidation of social recognition memory. *J. Neurosci.* 37, 4103–4116. doi: 10.1523/JNEUROSCI.3451-16.2017

Vázquez Oliver, A., Brambilla Pisoni, C., Domingo Gainza, M., Maldonado, R., Ivorra, A., and Ozaita, A. (2020). Auricular trascutaneous vagus nerve stimulation improves memory persistence in naive mice and

in an intellectual disability mouse model. *Brain Stimul.* 13, 494–498. doi: 10.1016/j.brs.2019.12.024

Vetere, G., Kenney, J. W., Tran, L. M., Xia, F., Steadman, P. E., Parkinson, J., et al. (2017). Chemogenetic interrogation of a brain-wide fear memory network in mice. *Neuron* 94, 363–374. doi: 10.1016/j.neuron.2017.03.037

Wheeler, A. L., Teixeira, C. M., Wang, A. H., Xiong, X., Kovacevic, N., Lerch, J. P., et al. (2013). Identification of a functional connectome for long-term fear memory in mice. *PLoS Comput. Biol.* 9, e1002853. doi: 10.1371/journal.pcbi.1002853

Yuan, H., and Silberstein, S. D. (2015). Vagus nerve and vagus nerve stimulation, a comprehensive review: part II. *Headache* 56, 259–266. doi: 10.1111/head.12650

Zerbi, V., Floriou-Servou, A., Markicevic, M., Vermeiren, Y., Sturman, O., Privitera, M., et al. (2019). Rapid reconfiguration of the function connectome after chemogenic locus coeruleus activation. *Neuron* 103, 702–718. doi: 10.1016/j.neuron.2019.05.034

Conflict of Interest: The authors declare that the research was conducted in the absence of any commercial or financial relationships that could be construed as a potential conflict of interest.

Publisher's Note: All claims expressed in this article are solely those of the authors and do not necessarily represent those of their affiliated organizations, or those of the publisher, the editors and the reviewers. Any product that may be evaluated in this article, or claim that may be made by its manufacturer, is not guaranteed or endorsed by the publisher.

frontiers | Frontiers in Cellular Neuroscience

REVIEW
published: 12 May 2022
doi: 10.3389/fncel.2022.874310

The Neural Circuit Architecture of Social Hierarchy in Rodents and Primates

Emanuel Ferreira-Fernandes[1,2] *and João Peça*[1,3]*

[1]CNC—Center for Neuroscience and Cell Biology, University of Coimbra, Coimbra, Portugal, [2]Institute of Interdisciplinary Research (IIIUC), University of Coimbra, Coimbra, Portugal, [3]Department of Life Sciences, University of Coimbra, Coimbra, Portugal

Social status is recognized as a major determinant of social behavior and health among animals; however, the neural circuits supporting the formation and navigation of social hierarchies remain under extensive research. Available evidence suggests the prefrontal cortex is a keystone in this circuit, but upstream and downstream candidates are progressively emerging. In this review, we compare and integrate findings from rodent and primate studies to create a model of the neural and cellular networks supporting social hierarchies, both from a macro (i.e., circuits) to a micro-scale perspective (microcircuits and synapses). We start by summarizing the literature on the prefrontal cortex and other relevant brain regions to expand the current "prefrontal-centric" view of social hierarchy behaviors. Based on connectivity data we also discuss candidate regions that might inspire further investigation, as well as the caveats and strategies that have been used to further our understanding of the biological substrates underpinning social hierarchy and dominance.

Keywords: social hierarchies, neuronal circuits, dominance, status syndrome, microcircuitry, social status

OPEN ACCESS

Edited by:
Heiko J. Luhmann, Johannes Gutenberg University Mainz, Germany

Reviewed by:
Srikanth Ramaswamy, Newcastle University, United Kingdom
Shimpei Ishiyama, Johannes Gutenberg University Mainz, Germany

***Correspondence:**
João Peça
jpeca@cnc.uc.pt

Specialty section:
This article was submitted to Cellular Neurophysiology, a section of the journal Frontiers in Cellular Neuroscience

Received: *11 February 2022*
Accepted: *29 March 2022*
Published: *12 May 2022*

Citation:
Ferreira-Fernandes E and Peça J (2022) The Neural Circuit Architecture of Social Hierarchy in Rodents and Primates. Front. Cell. Neurosci. 16:874310. doi: 10.3389/fncel.2022.874310

INTRODUCTION

Social status is recognized as a major social determinant of health (Wilkinson and Marmot, 1998). Seminal studies by Marmot and Sapolsky provided evidence that social hierarchies in primates, both human and non-human, lead to social gradients in health, whereby lower rank individuals exhibit progressively higher morbidity and mortality rates (Marmot, 2004; Marmot and Sapolsky, 2014). Examples of this can be found broadly in human societies, for example, in the Scottish city of Glasgow, there is a 28-year difference in life expectancy between the wealthiest and poorest

Abbreviations: ACC, Anterior cingulate cortex; aHIPP, Anterior hippocampus; AMY, Amygdala; BA, Basal amygdala; BF, Basal forebrain; BLA, Basolateral amygdala; CeL, Centrolateral amygdala; CeM, Centromedial amygdala; dlPFC, Dorsolateral prefrontal cortex; EC, Entorhinal cortex; fMRI, Functional magnetic resonance imaging; HIPP, Hippocampus; IL, Infralimbic cortex; IPC, Inferior parietal cortex; ITC, Inferior temporal cortex; LA, Lateral amygdala; LHb, Lateral habenula; LS, Lateral septum; MDT, Mediodorsal thalamus; mPFC, Medial prefrontal cortex; MRI, Magnetic resonance imaging; MSN, Medium spiny neurons; NAc, Nucleus accumbens; NDB, Nucleus of the diagonal band; OFC, Orbitofrontal cortex; PAG, Periaqueductal gray; PCC, Posterior cingulate cortex; PFC, Prefrontal cortex; pHIPP, Posterior hippocampus; PrL, Prelimbic cortex; PV, Parvalbumin; RN, Raphe nucleus; rPFC, Rostral prefrontal cortex; SLM, Stratum lacunosum-moleculare; SO, Stratum oriens; SP, Stratum pyramidale; SR, Stratum radiatum;STR, Striatum; STS, Superior temporal sulcus; SWR, Sharp wave ripples; vCA1, Ventral CA1; VIP, Vasoactive intestinal polypeptide; vlPFC, Ventrolateral prefrontal cortex;vmPFC, Ventromedial prefrontal cortex; vSTR, Ventral striatum; VTA, Ventral tegmental area.

suburbs (Hanlon et al., 2006), and in the poorer neighborhoods of Washington DC, life expectancy decreases by 16 years compared to wealthier areas (Murray et al., 2006). Similar correlations are reported in all rich, poor, and intermediate countries surveyed (Victora et al., 2003; Hurt et al., 2004; Marmot, 2004). Socioeconomic status is, therefore, the single strongest predictor of life expectancy and disease risk in humans (Sapolsky, 2004, 2005). It seems obvious that low-status individuals have limited access to essential resources, partially explaining their health conditions, however, the social gradient in health persists in human populations free from extreme poverty, suggesting that other factors might underlie this phenomenon. In this regard, Marmot and Sapolsky proposed a novel perspective, whereby gradients in psychosocial stressors would contribute to the observed gradient in health, even in the absence of substantial deprivation (Marmot and Sapolsky, 2014). Since their studies focused on humans or troops of baboons, the gradient of stress, due to the respective organization of these societies, tends to increase in subordinates.

Subordinate baboons displayed basal hypercortisolism in the range known to adversely impact blood pressure, insulin sensitivity, and immunity (Sapolsky et al., 2000). This gradient of stress is, however, not universal, and depends on the stability of the hierarchy and the mechanisms used for rank maintenance (Sapolsky, 2005). For example, in highly stable, despotic societies where rank is maintained through intimidation, which is prominent among humans and baboons, subordinate individuals are under pressure. However, in unstable, despotic societies that require frequent physical reassertion of dominance, dominant individuals experience the highest levels of stress. Even though Marmot's and Sapolsky's hypothesis is under debate, it calls attention to the relevance of social hierarchies for stress gradients and health in animal societies (Marmot and Sapolsky, 2014).

Since hierarchies inevitably produce inequalities, it is legitimate to ask why natural selection has favored them. Under naturalistic settings, animals have to compete for limited resources, including food, mating opportunities, and nesting sites. To mitigate the risk of constant fighting for limited resources, animals adopted basic, albeit not mutually exclusive strategies, such as territoriality and the formation of social hierarchies (Chase, 1974; Wilson, 1975). When groups of conspecifics are confined to the same territory, hierarchies dictate an individual's priority in accessing the resources (Wilson, 1975). Dominant individuals have higher reproductive success (Samuels et al., 1984; Ostner et al., 2008; Rodriguez-Llanes et al., 2009) and increased access to food (Whitten, 1983; Isbell et al., 1999) at the expense of sustaining a higher metabolic rate (Røskaft et al., 1986; Martin and Salvador, 1993) and higher propensity for injuries (Røskaft et al., 1986), whereas subordinate individuals save energy and avoid injuries at the expense of lower reproductive success (Martin and Salvador, 1993; Ellis, 1995) and lower access to food resources (Dittus, 1977; Owens and Owens, 1996). Still, subordinate individuals might have ecological value presumably because dominant animals eventually need replacement (Darling, 2008) and because they might abandon their current group to form new groups (Christian, 1970; Esser, 1971). Therefore, territoriality and social hierarchies ensure efficient sharing of resources and regulate aggression. However, there is considerable plasticity in these social strategies, as illustrated by the adaptation of rodents to their population density (Singleton and Krebs, 2007). Under low population densities, as seen in the remaining groups of wild rodents, their territoriality is reinforced, whereas under high population densities, as seen in rodents living alongside human settlements and in lab cages, social hierarchies are reinforced (Singleton and Krebs, 2007).

Natural selection favored a strategy that ensures the fitness of the population at the expense of the individual well-being, so it might be tempting to dismiss social hierarchies in favor of fully egalitarian systems. However, disturbing hierarchies may have a devastating effect on the population, as illustrated by the famous experiments carried out by John B. Calhoun (for a complete historical review, see Ramsden and Adams, 2009). While addressing Malthusian concerns of overpopulation, Calhoun conducted a series of behavioral studies where rats (Calhoun, 1970) and mice (Calhoun, 1973) were bred in a closed environment free from predators and deprivation. Notably, these "Rodent Utopias" resulted in population collapse catalyzed by unconstrained growth, which drastically changed the rodents' natural behaviors, rendering these societies and the remaining individuals unviable. This catastrophic change in behavior was named "behavioral sink" (Bliss, 1962; Calhoun, 1970). Focusing on Universe 25 (Calhoun, 1973)—Calhoun's most famous experiment—social collapse was preceded by a profound perturbation of the social hierarchy, noticeable on the 315th experimental day. Omega males, spurned by females and devoid of social duties, wandered apart from the larger groups in a solitary existence, losing social skills (Calhoun, 1973). Alpha males, on the other hand, became highly aggressive, spontaneously attacking other individuals regardless of their gender (Calhoun, 1973). Notably, as dominant males abandoned their traditional roles, generalized aggressiveness was reported to escalate among females in the attempt to defend their nests, resulting also in violence towards their own pups (Calhoun, 1973). These findings were essentially recapitulated in all Universe experiments (Calhoun, 1966, 1970). When raised in such conditions of severe early-life stress, upon reaching maturity, several animals would disregard most social activities and focus only on feeding and grooming (Calhoun, 1977). These so-called "Beautiful ones" could no longer form new societies when placed in a novel enclosure, eventually leading to population extinction in the Universe experiments, well before the maximal putative limit in terms of space, food, and water availability (Calhoun, 1977). This overwhelming experiment was used to illustrate the putative consequences of unconstrained population growth, however, it also showed that the breakdown of social behaviors and hierarchies was the precipitating step in the downward spiral within the enclosed environments. The relevance of social hierarchies becomes even more expressive if one realizes that maladaptive behavior and population dysfunction started significantly before the theoretical maximal population level.

In light of the critical impact of social hierarchies on individual health and ecological balance, efforts have been

made to uncover their supporting mechanisms. This question was tackled using neuroendocrine studies, but a fundamental goal in the field has been the delineation of the neural network subserving the encoding, inference, and use of the social rank to inform actions. In this review, we compare and integrate findings from primate (human and non-human), fish, and rodent studies to create a model of the neural network supporting hierarchical behavior. We start with a macroscale (i.e., brain regions) description of that network and further highlight mesoscale (i.e., circuits) and microscale mechanisms (micro-circuits and synapses) that serve the organism in its navigation of social hierarchical behavior. We also discuss the major emerging candidates in these social brain networks.

THE DETERMINANTS OF SOCIAL HIERARCHIES

Since the description of *pecking orders* in domestic fowls by Schjelderup-Ebbe (Schjelderup-Ebbe, 1922), social hierarchies have been recognized as a near-universal phenomenon among social animals, from insects and fishes to rodents and primates (**Figure 1A**; Wilson, 1975). Regardless of the species, social hierarchies require contests between conspecifics where several factors, both intrinsic and extrinsic, play a combined and non-linear role in influencing the outcome (Wilson, 1975; Chase et al., 2002). Intrinsic traits include size, age, kinship, gender, and personality traits (Wilson, 1975). Extrinsic factors, on the other hand, are more difficult to isolate and include fatigue, fighting skills, environmental aspects, prior experience, and stochastic events (Wilson, 1975). In rodents, like in many other simple species relying on physical contests, higher ranks are reserved for bigger and less timid males. Size is, therefore, one of the strongest single predictors of outcome in confrontations, where dominant rodents seem to control the space shared by the group (Wilson, 1975). More complex animals, such as primates, have more complex rules. In fact, high-rank primates tend to be descendants of high-rank mothers, bigger, older, and display extroverted behavior (Wilson, 1975). Other critical aspects of understanding of the behavioral and physiological determinants of social hierarchies have also emerged from fish studies, where this field of research is considerably developed (Oliveira, 2005; Hsu et al., 2006; Gonçalves et al., 2017).

Cichlids and other fish species used in social behavior research readily engage in dyadic contests and form social hierarchies. Behavioral studies have focused mostly on fish size and prior experience to explain social rank (Beaugrand et al., 1991). Not surprisingly, bigger fish tend to conquer higher ranks (**Figure 1B-1**; but see Beaugrand et al., 1991). Prior experience, on the other hand, has proven to exert a more complex effect on future dyadic contests. In general terms, past victories increase the probability of winning ("winner effect"; Hsu and Wolf, 1999), whereas past losses increase the probability of losing future contests ("loser effect"; **Figure 1B-2**; Hsu and Wolf, 1999). The detailed analysis of past dyadic encounters and their effect in future contests further isolated: spatial context (**Figure 1B-3**; Zayan, 1975a; Beaugrand and Zayan, 1985); the opponent's identity (Zayan, 1974, 1975b; Beaugrand and Zayan, 1985; Madeira and Oliveira, 2017); and past experience (**Figure 1B-4**; Beaugrand and Zayan, 1985; Beaugrand et al., 1991; Hsu and Wolf, 1999; wining, losing or the absence of fighting experience), as variables with significant meaning. Even though these data were obtained exclusively through dyadic confrontations, winner and loser effects impact the formation of social hierarchies in fish, since randomly chosen winners (and losers) in pairwise contests were more likely to emerge as high ranked (and low ranked) individuals when grouped with conspecifics (Dugatkin and Druen, 2004). Curiously, the effect of prior experience does not necessarily imply overt confrontation. Interestingly, bystanders, who do not engage in overt confrontation but simply observe a contest, also change their winning and losing probabilities in future contests (**Figure 1B-5**; Johnsson and Åkerman, 1998; Silk, 1999; Oliveira et al., 2001; for review on the "bystander effect" and bystander-related phenomena, see Oliveira, 2005). Similar effects have been described in rodents (Van de Poll et al., 1982; Fuxjager and Marler, 2010), humans (Page and Coates, 2017), and invertebrates (Van Wilgenburg et al., 2010; Stevenson and Schildberger, 2013; Benelli et al., 2015). Efforts have been made to uncover the mechanisms supporting these behavioral observations. A major hypothesis in the field suggests that hierarchical behavior is regulated by the interaction between neuroendocrine factors and neural circuits. While neuroendocrine mechanisms have been thoroughly explored in many animal models (for review, see Oliveira, 2005), the neural circuits supporting social hierarchies are less understood and have been the focus of recent research efforts.

THE MACROSCALE NETWORKS SUPPORTING SOCIAL HIERARCHIES

Social animals do not just navigate the physical world to survive; they also navigate complex social worlds, where they have to respect hierarchies to maximize benefits, avoid injury and exclusion (Schafer and Schiller, 2018). While neuroendocrine mechanisms certainly shape these behaviors, there is growing interest in uncovering the neural circuits subserving social navigation within hierarchies. In this sense, rodents and primate studies (human and non-human) during hierarchy-related behaviors have been providing a growing list of candidate regions that are modulated and/or necessary for the encoding, inference, and expression of social rank. Although rodent and primate findings do not perfectly overlap, there is considerable evidence toward the existence of a critical network of neural substrates supporting hierarchical behavior (**Figure 2**).

Large screenings in rodents were performed mostly through the evaluation of a c-fos expression in dominant and submissive mice after performing the tube test (Fan et al., 2019). Compared to submissive mice, dominant animals display significant activity differences in ventromedial hypothalamus, lateral habenula (LHb), anterior cingulate cortex (ACC), medial preoptic area, and mediodorsal thalamus (MDT; Nelson et al., 2019).

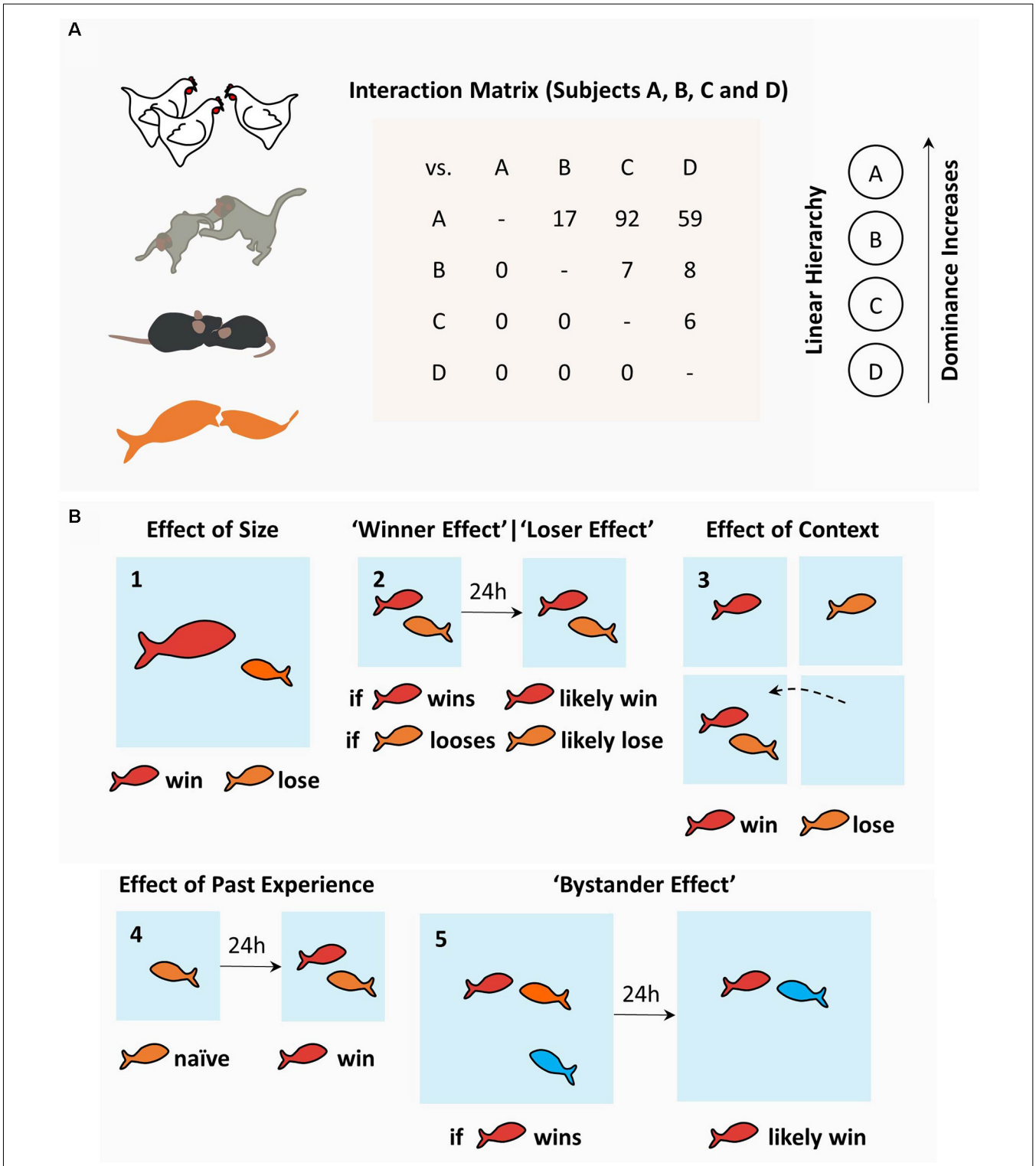

FIGURE 1 | The sociobiology of hierarchies: determinants and consequences. **(A)** Social hierarchies, or pecking orders, emerge in diverse animal species and can be characterized using interaction matrices as used by Schjelderup-Ebbe, depicting the number of attacks (or victories) of one individual over others, which may lead to social hierarchies in a variety of topographies (linear hierarchy displayed from the matrix data). **(B)** Determinants of social hierarchies in fish models include: **(1)** effect of size; **(2)** effect of past winning ("winner effect") and past losing ("loser effect"); **(3)** the effect of familiar vs. novel context ("homefield"); **(4)** effect of past experience; and **(5)** the bystander effect. Among fish, dominance is attained by bigger fish and winning experience when fighting familiar opponents in a familiar context. Rodents share most of these rules. More complex species, such as primates, have additional, more complex determinants (see text).

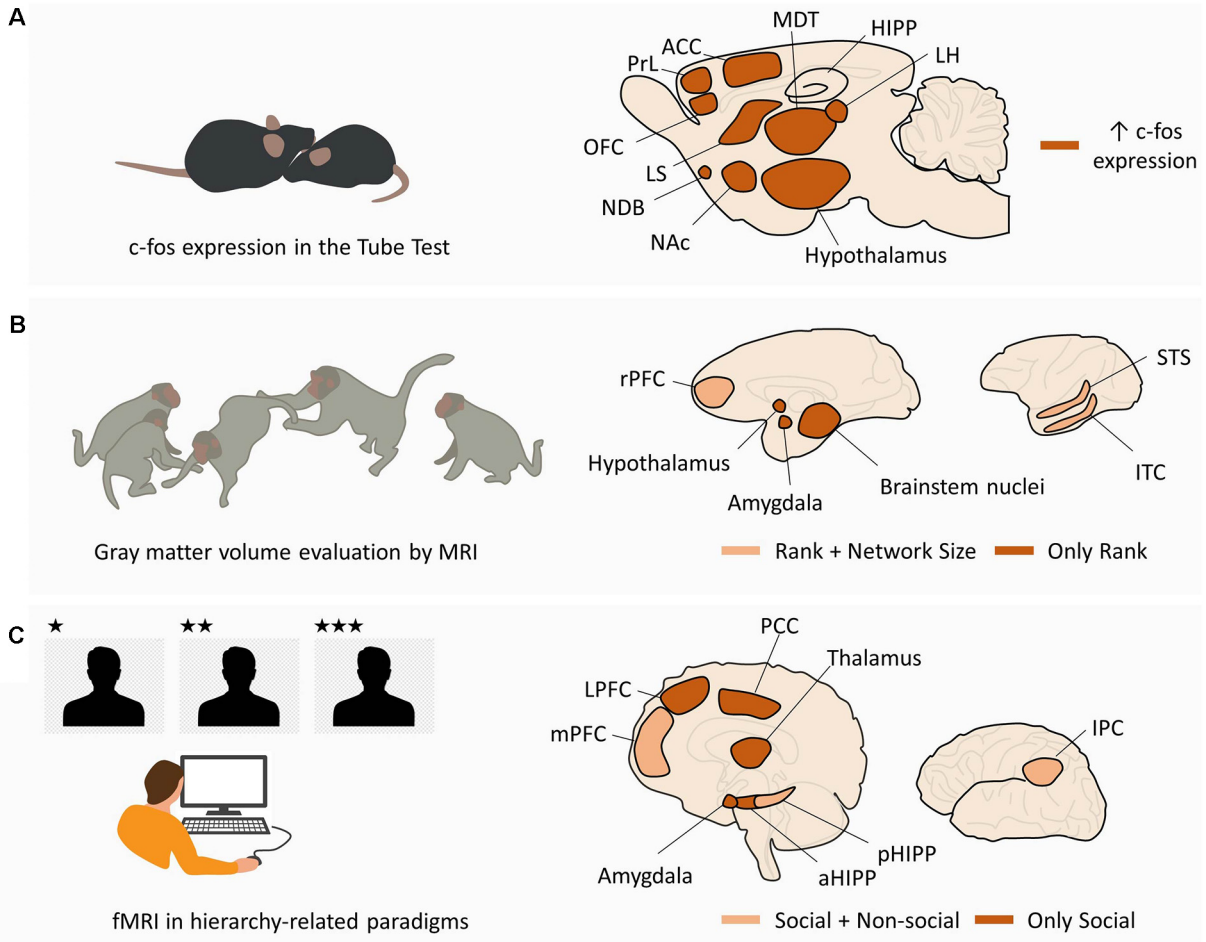

FIGURE 2 | Macroscale networks supporting social hierarchies. **(A)** Macroscale network in rodents. In mice performing tube tests for social hierarchy, c-fos expression in dominant animals is increased in the ventromedial hypothalamus, LH, ACC, medial preoptic area (hypothalamus), and MDT. In addition, pairwise correlations were found between MDT-PrL, MDT-OFC, MDT-ACC, MDT-CA2, ACC-MDT, ACC-LH, ACC-NDB, ACC-LS, and ACC-NAc. **(B)** Macroscale network in non-human primates. MRI studies in non-human primates from different social statuses and living in groups of different sizes have shown a correlation between social rank and gray matter volume in the hypothalamus, amygdale, and brainstem nuclei ("Only Rank"). Gray matter volume in rPFC, STS, and ITC was correlated with both social rank and group size ("Rank + Network Size"). **(C)** Macroscale network in humans. fMRI studies in human subjects performing hierarchy-related tasks have shown selective activation of LPFC, amygdala, aHIPP, thalamus, and PCC by the social component of the task ("Only Social"). The mPFC, pHIPP, and IPC were activated in the social and non-social conditions, suggesting a domain-general function ("Social + Non-social"). See text for other domain-general regions in human literature not depicted in the figure. Abbreviations: LH, lateral habenula; ACC, anterior cingulate cortex; MDT, medial preoptic area (hypothalamus), and mediodorsal thalamus; PrL, prelimbic cortex; OFC, orbitofrontal cortex; NDB, nucleus of the diagonal band; LS, lateral septum; NAc, nucleus accumbens; rPFC, rostral prefrontal cortex; STS, superior temporal sulcus; ITC, inferior temporal cortex; LPFC, lateral prefrontal cortex; aHIPP, anterior hippocampus; pHIPP, posterior hippocampus; PCC, posterior cingulate cortex; mPFC, medial prefrontal cortex; IPC, inferior parietal cortex.

In addition, nine pairwise correlations significantly differed between dominant and submissive mice, specifically MDT-Prelimbic cortex (PrL), MDT-Orbitofrontal cortex (OFC), MDT-ACC, MDT-CA2, ACC-MDT, ACC-LHb, ACC-Nucleus of the Diagonal Band, ACC-Lateral Septum (LS), and ACC-Nucleus Accumbens (NAc; Nelson et al., 2019; **Figure 2A**).

There are, however, considerable differences in social behavior between rodents and primates, which raises the question of whether neural substrates differ between species. To tackle this, several structural and functional studies have also been performed in human and non-human primates during hierarchy-related behaviors. Monkeys from different ranks, living in groups of different sizes, exhibit brain structural adaptations observable using structural Magnetic Resonance Imaging (MRI). Specifically, gray matter volume in the amygdala (AMY), brainstem [from the medulla to the midbrain, including parts of the raphe nucleus (RN)], hypothalamus, and basal ganglia (posterior putamen and caudate) were found to be correlated with social rank (Noonan et al., 2014). On the other hand, gray matter volume in the superior temporal sulcus and rostral prefrontal cortex (PFC) was found to be correlated with both social rank and social network size (Sallet et al., 2011; Noonan et al., 2014). Similar structural correlations between

gray matter and social network size were also observed in humans, particularly for the AMY (Bickart et al., 2011), OFC (Powell et al., 2012), ventromedial prefrontal cortex (vmPFC; Lewis et al., 2011), superior temporal sulcus (Kanai et al., 2012), and temporal cortex (Kanai et al., 2012; **Figure 2B**). On a functional domain, human research using hierarchy-related paradigms and functional Magnetic Resonance Imaging (fMRI) has provided compelling evidence of the neural dynamics subserving the encoding, inference, and expression of social rank (**Figure 2C**). Regarding rank coding, it was found that human subjects generate dissociable neural responses when playing a computer game against (simulated) higher-ranked and lower-ranked players. Individuals playing against a higher rank player displayed increased activity in bilateral occipital/parietal cortex, ventral striatum (vSTR), parahippocampal cortex, and dorsolateral prefrontal cortex (dlPFC), compared to when they faced a lower rank player (Zink et al., 2008). These results were observed in stable hierarchies, where participants were unable to change their rank irrespective of the outcome of the game, and in unstable hierarchies, where the outcome of the game allowed moving up or down in the hierarchy. In the unstable condition, additional brain regions displayed increased activity when participants faced higher rank opponents, including the AMY, medial prefrontal cortex (mPFC), posterior cingulate, bilateral thalamus, primary motor cortex, somatosensory cortex, and supplementary motor area (Zink et al., 2008). However, when individuals repeated the task but were informed that they were playing against computers, dlPFC, AMY, thalamus, posterior cingulate, and mPFC were not significantly activated, suggesting that these brain regions were sensitive to the social component of the task (Zink et al., 2008). In a related work involving the observation of higher and lower ranked individuals, test subjects perceived and gauged the social rank of others. This task engaged the inferior parietal cortex (Chiao et al., 2009).

However, contrary to the paradigms in which ranks are explicitly known *a priori*, in natural conditions, social rank is often inferred from another's behavior, and demeanor and social hierarchies are progressively assimilated through experience. Functional studies have shed light on the neural substrates supporting rank inference by showing the recruitment of occipitotemporal regions, including the superior temporal, fusiform, and lingual gyri as subjects classified individuals as dominant or submissive based on their facial expressions (Chiao et al., 2008). Moreover, dominance-related signals (brow position, posture, gaze, and gesture) increase the activity in dlPFC and ventrolateral PFC (vlPFC; Marsh et al., 2009). Rank coding and inference presumably allow individuals to acquire knowledge about social hierarchies in order to guide behavior and navigate their social world. The acquisition and use of hierarchy-related information seems to depend upon the AMY, hippocampus (HIPP), and vmPFC (Kumaran et al., 2012). Notably, the AMY and anterior HIPP are specifically engaged when subjects learn and apply knowledge about social hierarchies, compatible with social specificity, whereas the posterior HIPP and vmPFC are engaged in tasks involving the acquisition and use of knowledge about social and non-social hierarchies, compatible with a domain-general role (Kumaran et al., 2012). A parsimonious hypothesis is that social-specific areas (AMY and anterior HIPP) are modulated by rank-related information, further introducing this information in pre-existing domain-general mechanisms subserving domain-general learning, cognitive control, and goal-directed behavior. Spatial navigation can be, however, either egocentric (self-referenced) or allocentric (using distal cues). Interestingly, the acquisition and use of hierarchy-related information seem to show some differences depending on whether one is part of the hierarchy (Self hierarchy) or not (Other hierarchy). Human studies showed that learning Self hierarchies was correlated with the activity in the mPFC, whereas learning both hierarchies (Self and Other) was correlated with the activity in the AMY and HIPP (Kumaran et al., 2016). Curiously, during these studies using Self hierarchies, subjects performed a categorization task where they had to assign pictures of individuals to a pre-learned Self hierarchy and Other hierarchy (Kumaran et al., 2016). Even though this task did not require the explicit retrieval of rank-related information, rank-related activity was detected in the AMY and anterior HIPP when categorizing the pictures and lower-ranked stimuli elicited higher activity (Kumaran et al., 2016). This suggests that social rank becomes an integral trait of each individual in the social network and is spontaneously and implicitly retrieved during social interactions. Rank-related activity was also detected in the mPFC but only when categorizing stimuli from the Self hierarchy (Kumaran et al., 2016).

Despite the value of these findings, the level of variability in the anatomical definition of each region, methodologies, behavioral tasks and results, hinder our ability to fully conciliate all the observations. Still, they provided a preliminary mapping that can now be used to direct more detailed inquiry at the level of circuits, microcircuits, and synapses.

MESOSCALE AND MICROSCALE MECHANISMS SUPPORTING SOCIAL HIERARCHIES

Prefrontal Cortex: A Major Hub in Social Hierarchies

The PFC has been consistently suggested as a neural substrate supporting social and hierarchy-related behaviors (**Figure 3A**), but the mechanisms underlying its role remained unknown until recently. A pioneering study by Hailan Hu and colleagues, found that layer 5 pyramidal neurons in the mPFC play a pivotal role in dominance and submissive behaviors in mice (Wang et al., 2011; **Figure 3B-1**). Miniature excitatory postsynaptic currents mediated by AMPA receptors in these neurons display increased amplitude, but not frequency, in dominant mice (**Figure 3B-1**). Moreover, increasing the strengths of these synapses through viral overexpression of AMPA-receptor subunit GluA4 led to dominance behavior, whereas decreasing the strengths of synapses through a viral expression of GluA4 C-tail led to subordinate behavior (Wang et al., 2011). This

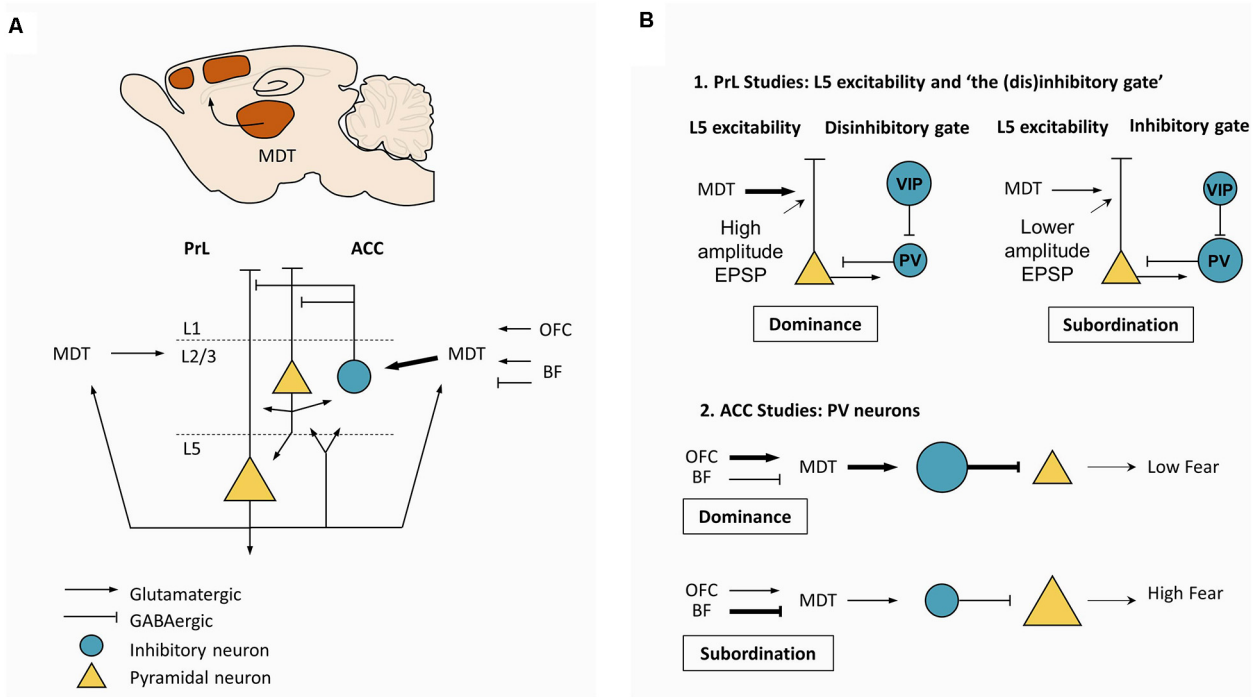

FIGURE 3 | Mesoscale mechanisms supporting dominance. **(A)** Canonical circuit in PrL and ACC. Glutamatergic neurons from MDT project strongly to L2/3 PV neurons in ACC, with a less dense projection to L2/3 in PrL. Depolarization of MDT neurons is determined by excitatory projections from OFC, L5 pyramidal neurons from PrL and ACC, and from excitatory and inhibitory projections from the BF. **(B)** Two major types of studies to explain dominance. **(B-1)** Studies in the PrL support the central role of MDT. Strong excitatory drive coming from MDT is thought to favor effortful, persistent behavior by increasing the excitability in L5 pyramidal neurons. Potentiation of MDT-PrL synapses by repeated winning and activation is thought to increase the probability of winning, triggering a "winner effect". In addition, a disinhibitory gate may also contribute to regulating the excitability of L5 pyramidal neurons. Specifically, increased activity in the VIP interneurons would open the gate by inhibiting PV interneurons, leading to increased excitability in L5 pyramidal neurons, favoring dominance. On the other hand, increased activity in PV interneurons would close the gate, leading to decreased excitability in L5 pyramidal neurons, favoring subordination. **(B-2)** Studies in the ACC suggest that high MDT excitability and firing due to a strong excitatory drive coming from the OFC would lead to increased depolarization of PV neurons, decreasing fear expression. These hypotheses suggest that differences in synaptic plasticity and neuronal excitability *per se* could explain dominance among rodents. Plasticity and excitability are prone to genetic influences and environmental effects, including hormones and degree of behavioral training. Abbreviations: PrL, prelimbic cortex; ACC, anterior cingulate cortex; MDT, mediodorsal thalamus; PV, parvalbumin; OFC, orbitofrontal cortex; BF, basal forebrain; VIP, vasoactive intestinal peptide.

work stimulated the search for neural pathways capable of acting as molecular switches between dominance and subordinate behaviors. Extending these findings, neuronal populations in mouse mPFC were found to display increased firing rate during effortful behaviors, such as pushing and resistance in the Tube test, but not during retreat, suggesting that mPFC might mediate the behavioral persistence to win the social contest (Zhou et al., 2017). In fact, optogenetic activation (mediated by channelrhodopsin-2, ChR2) and chemogenetic inhibition (mediated by hM4D muscarinic receptors) of mPFC, induced instantaneous winning and losing, respectively, but only when the manipulations were performed in the PL and in rostral ACC (Zhou et al., 2017). In addition, optogenetic stimulation delivered to the mPFC caused the maintenance of dominance behavior and repeated winning in animals experiencing more than six photoinduced wins (Zhou et al., 2017). This effect was inhibited upon treatment with MK801, an antagonist of NMDA receptors, suggesting this effect was due to NMDA-dependent plasticity mechanisms (Zhou et al., 2017). Notably, cingulate parvalbumin-positive interneurons seem to be required for hierarchical behavior as well, since the chemogenetic inhibition of this inhibitory population leads to a pronounced decline in competitive performance among dominant mice, whereas chemogenetic excitation causes a striking increase in competitive performance among subordinate mice (Nelson et al., 2019). More recently, an interneuron-based gating mechanism was described in PFC capable of acting as a switch between dominance and subordination (Zhang et al., 2022; **Figure 3B-1**). Increased activity of local vasoactive intestinal polypeptide (VIP) interneurons in PFC leads to direct inhibition of local parvalbumin (PV) interneurons, generating a window of opportunity for increased excitability in L5 pyramidal neurons, resulting in dominance. Contrarily, increased activity of local PV interneurons, preceding the activity of VIP interneurons, decreases the excitability of L5 pyramidal neurons, working as a gate and resulting in subordinate behavior, expressed by losing in social confrontations. This work supports previous observations that mice subjected to early life stress develop strong subordinate behavior, which was correlated with morphological alterations in pyramidal neurons in PFC and increased inhibitory postsynaptic

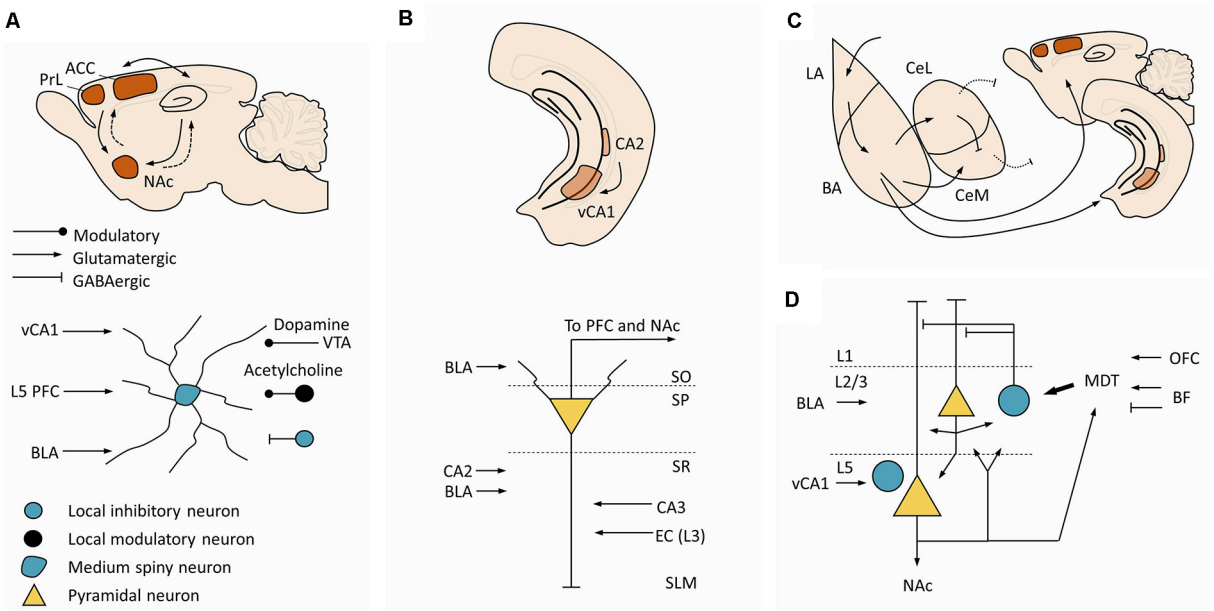

FIGURE 4 | Additional circuits to interrogate in future dominance studies. **(A)** Circuit of the NAc. *Top.* Macroscale circuit. The NAc receives monosynaptic projections (arrows) from PrL, ACC, and ventral hippocampus, projecting back to these regions through indirect connections (dashed arrows). *Bottom.* Canonical microcircuit in the NAc. Medium spiny neurons in NAc are the major targets of L5 pyramidal neurons from PrL and ACC, pointing to striatal circuits as a logical downstream target to expand current ACC and PrL hypotheses for social dominance. **(B)** Circuit in vCA1. *Top.* Macroscale circuit. Hippocampus anatomy highlighting the location of CA2 and vCA1. *Bottom*. Canonical microcircuit in ventral CA1, pyramidal neurons in vCA1 receive inputs from CA2, CA3 and EC, and project to the PFC and NAc. This microcircuit suggests an interplay between dominance mechanisms and the circuits regulating social memory. **(C)** Macroscale circuit in the amygdala. Amygdala anatomy highlighting the connectivity between LA, BA, CeL, and CeM, and the PFC and ventral hippocampus. Arrows represent excitatory projections, blunt lines represent inhibitory projections, and dashed lines represent inhibitory projections to brainstem regions responsible for aggression. **(D)** Microcircuit in the PFC. Panel **(D)** is similar to **Figure 3A** but here are included afferent projections from vCA1, which target mostly L5 prelimbic neurons (including L5 parvalbumin interneurons), afferent projections from the BLA, which target mostly L2 prelimbic neurons, and efferent projections to the NAc. Other prefrontal subareas receive vCA1 and BLA projections with different laminar distributions compared with the prelimbic region (not illustrated here). This panel summarizes candidate regions upstream and downstream to the prefrontal cortex that may be considered in future studies aiming at unraveling the circuitry supporting hierarchical behavior. Abbreviation: NAc, nucleus accumbens; PrL, prelimbic cortex; ACC, anterior cingulate cortex; PFC, prefrontal cortex; VTA, ventral tegmental area; vCA1, ventral CA1; EC, entorhinal cortex; SO, stratum oriens; SP, stratum pyramidale; SR, stratum radiatum; SLM, stratum lacunosum-moleculare; LA, lateral amygdala; BA, basal amygdala; BLA, basolateral amygdala; CeL, centrolateral amygdala; CeM, centromedial amygdala.

current amplitude (Franco et al., 2020). An elegant hypothesis to explain this observation is that early life stress alters the local wiring of PFC, creating conditions to exacerbate the gating mechanism described above (Franco et al., 2020).

Thalamus: A Driver of the Prefrontal Cortex

Even though there is considerable evidence suggesting the PFC is a central hub in social and hierarchy-related behaviors, the PFC function depends upon the activity of its upstream and downstream regions. This raises the question of which partners interact with the PFC during hierarchical behavior. Since the mPFC receives dense projections from MDT (Hoover and Vertes, 2007; **Figure 3A**) and since repeated defeat-induced social avoidance leads to depression of MDT-mPFC synapses (Franklin et al., 2017), strengthening of MDT-mPFC synapses could contribute to attaining a high social rank. Indeed, repeated winning in a tube test led to a sustained increase in the field excitatory postsynaptic potentials in MDT-mPFC synapses *in vivo* (**Figure 3B-1**), and long-term potentiation of MDT-mPFC synapses using ChR2 *in vivo* elicited dominance (Zhou et al., 2017).

Expanding these findings regarding the MDT-mPFC projection, which focused mostly on PrL-targeting axons, the MDT-ACC projection was also found to trigger dominant and subordinate behavior (**Figure 3B-2**). Chemogenetic excitation of glutamatergic MDT neurons increased competitive performance in subordinate mice, without affecting dominant animals (Nelson et al., 2019). Notably, this glutamatergic population received monosynaptic input from the deep layers of ACC, PrL, and OFC, while projecting to layer 2/3 of ACC, PrL, and OFC, and to the NAc (Nelson et al., 2019). Their major output area was, however, the ACC, where glutamatergic MDT neurons target parvalbumin-positive neurons (Nelson et al., 2019). Whole-cell recordings in these MDT neurons revealed two functional clusters, one with a low firing rate and the other with a high firing rate (Nelson et al., 2019). Dominant mice had an approximately five-fold higher ratio of high vs. low firing rate neurons, suggesting that MDT neurons might have two excitability states according to the animal's rank. Focusing on the inputs to MDT neurons, dominant mice had a higher frequency and amplitude of spontaneous excitatory postsynaptic currents, whereas submissive animals showed

a higher frequency of spontaneous inhibitory postsynaptic currents (Nelson et al., 2019). Notably, OFC was shown to make excitatory synapses in these MDT neurons, while the basal forebrain (BF) makes excitatory and inhibitory synapses (Nelson et al., 2019). ChR2-based paired-pulse stimulation of OFC-MDT synapses produced facilitation in submissive mice and depression in dominant mice, compatible with increased release probability in the latter (Nelson et al., 2019). When the same strategy was applied to BF-MDT synapses, which include inhibitory and excitatory synapses, submissive animals showed paired-pulse depression in inhibitory synapses, compatible with increased release probability, and no changes were seen in dominant mice (Nelson et al., 2019). Excitatory synapses showed depression in both groups. Together, these data converge to a model (**Figure 3B-2**) where dominant behavior is linked to strengthened excitatory OFC-MDT synapses and increased excitatory drive onto parvalbumin-positive cingulate neurons. Submissive behavior, on the other hand, is linked to strengthened inhibitory BF-MDT synapses and less excitatory drive onto parvalbumin-positive cingulate neurons.

In summary, circuit-based research in hierarchy-related behavior suggests that the PFC contributes to hierarchical behavior, with emphasis on layer 5 pyramidal neurons, and the MDT^{Glut}-PrL, OFC-MDT^{Glut}-ACC^{PV}, and BF-MDT^{Glut}-ACC^{PV} are pathways whose modulation can bidirectionally switch between dominance and subordination. In addition to these long-range modulators, a local interneuron-based gate, possibly targeted by these modulatory long-range projections, would create windows of increased (VIP neurons) and decreased (PV neurons) excitability in L5 pyramidal neurons, increasing the tendency for dominant and subordinate-related actions, respectively. mPFC could regulate dominance due to its effect on behavioral persistence or, alternatively, the excitatory drive to parvalbumin-positive cingulate neurons could decrease fear expression, prompting mice to exhibit dominant behavior. These pathways should play a substantial role in the networks outlined in **Figure 2**. Future detailed mesoscale and microscale studies similar to these will allow the molecular and circuit understanding of other hubs which have not received as wide attention.

NEW DIRECTIONS: EMERGING CANDIDATES IN SOCIAL HIERARCHIES

Ventral Striatum: The Major Downstream Target of the Prefrontal Cortex

The successful manipulation of social hierarchies upon modulation of PrL and ACC might have ultimately implied changes in striatal circuits (Zhou et al., 2017; Nelson et al., 2019). PrL and ACC display monosynaptic projections to the striatum (STR), whereas the STR communicates indirectly with the cortex *via* polysynaptic projections (Ferino et al., 1987; Wilson, 1987; Levesque et al., 1996; Smith et al., 2014; **Figure 4A**-*top*). The monosynaptic projections follow a structural gradient, whereby infralimbic (IL) and ventral PrL project to ventromedial STR, the NAc shell, and the remaining PrL and ACC project to the NAc core, further extending to the dorsomedial caudate-putamen complex (Groenewegen et al., 1997). Furthermore, the STR is particularly active during socially rewarding events (Bault et al., 2011), social status information triggers ventral striatal responses that are modulated by one's own subjective social status (Ly et al., 2011), and vSTR shows increased activity when participants face higher rank individuals (Zink et al., 2008). Despite this evidence, mechanistic research in striatal circuits in hierarchical behavior has been scarce and fragmented. Socially-housed dominant cynomolgus monkeys display significantly higher expression of D2/D3 receptors in the STR compared to socially-housed subordinate and single-housed individuals (Morgan et al., 2002). No significant changes are seen in subordinate individuals (Morgan et al., 2002). Complementing these data, rodent studies have shown specific metabolic signatures in the NAc of dominant and subordinate mice, with dominant mice exhibiting higher levels of energy-related metabolites under basal conditions (Larrieu et al., 2017). Accordingly, accumbal administration of mitochondrial complex I and II inhibitors prompted subordination (Hollis et al., 2015). Within the NAc, the population of dopamine D1 receptor-containing neurons emerged as a targetable candidate to modulate hierarchical behavior, as these neurons were activated by social competition in dominant animals (Hollis et al., 2015; van der Kooij et al., 2018), D1 receptors blockade decreased dominance (van der Kooij et al., 2018), and dominance was improved upon downregulation of the expression of glucocorticoid receptors in that neural population (Papilloud et al., 2020). Together, these data suggest that the mechanistic studies in prefrontal and thalamic loops should be extended to include striatal circuits and accumbal medium spiny neurons (MSN), at least the D1 receptor-containing population (**Figure 4A**-*bottom*). While NAc is a major target from PrL and ACC, prefrontal (and amygdalar) action potentials alone may be sufficient to reliably trigger spiking activity in the accumbal MSN, which may require concurrent hippocampal action potentials exerting a gating effect on MSNs (O'Donnell and Grace, 1995; French and Totterdell, 2002). From this observation, functional studies devoted to clarifying the role of the mPFC-NAc or AMY-NAc projections in hierarchical behavior should also include the HIPP (**Figure 4A**-*bottom*). As a final note, the available evidence strongly supports the NAc as an emerging hub in hierarchical behavior, but other striatal divisions might be implied as well. In fact, studies in monkeys found a negative correlation between gray matter volume in the posterior putamen and caudate and social rank (Noonan et al., 2014), suggesting a wider approach to striatal circuits in social and hierarchy-related behaviors.

Hippocampus: The Social Memory Hub

Our current understanding of hippocampal function results from two major lines of research. Human studies found marked anterograde amnesia for episodic events in patients harboring hippocampal lesions, leading to the conclusion that HIPP is necessary for episodic memory (Scoville and Milner, 1957; Penfield and Milner, 1958; Squire, 2009). On the other hand, rodent research described hippocampal neurons whose firing rate is modulated by the animal's spatial position, the

so-called place cells (O'Keefe and Dostrovsky, 1971; O'Keefe, 1976; O'Keefe and Conway, 1978; O'Keefe, 1979). By firing at particular places, place cells presumably contribute to an internal representation of the environment, a cognitive map (Tolman, 1948; O'Keefe and Dostrovsky, 1971; O'Keefe, 1991). Accordingly, hippocampal inactivation impairs allocentric navigation in rodents (Morris et al., 1982) and these findings were also reproduced in humans (Ekstrom et al., 2003; Parslow et al., 2005), implying that HIPP is necessary for spatial navigation and goal-directed behavior. While efforts were made to conciliate these perspectives (see Eichenbaum and Cohen, 2014), many studies described hippocampal modulation by non-spatial variables, including objects (Manns and Eichenbaum, 2009), time (Eichenbaum, 2014), and social variables (Tavares et al., 2015), providing evidence against a purely spatial theory of the HIPP. Since the observation that conspecifics and other social variables modulate hippocampal neurons (Danjo et al., 2018; Omer et al., 2018), the HIPP has been hypothesized as a hub in social behavior, presumably mapping the animal's social space (Tavares et al., 2015), and studies showed that the HIPP is necessary for social recognition memory (Okuyama et al., 2016).

Anatomical studies described prominent direct and indirect prefrontal-hippocampal loops (Eichenbaum, 2017). Furthermore, stress prior to a social encounter leads the stressed animal to a long-term subordinate behavior, presumably due to amplification of memory for the hierarchy (Cordero and Sandi, 2007). This effect is blocked by protein synthesis inhibitors and is not evoked by stress alone or, crucially, when the stressed animal faces a novel male, suggesting a superimposed role for recognition memory, for which the HIPP is necessary (Cordero and Sandi, 2007). Curiously, social memory depends upon CA2 (Hitti and Siegelbaum, 2014) and ventral CA1 (Okuyama et al., 2016), and there is a correlation between c-fos expression in MDT and CA2 that changes according to the mouse rank in the Tube test (Nelson et al., 2019). Together, these findings suggest a putative role for hippocampal circuits not only in social behavior but specifically in hierarchy-related behavior.

Siegelbaum and colleagues pioneered the mechanistic study of CA2 in social memory. Indeed, CA2 inactivation produces striking deficits in social memory in a transgenic mouse model (Hitti and Siegelbaum, 2014). Since this publication, CA2 was found to contain a high proportion of social-sensitive cells and CA2 inactivation during social tasks inhibited the formation of social memories (Azahara et al., 2020). As CA2 has restricted output regions (Cui et al., 2013), ventral CA1 (vCA1) has been hypothesized as an intermediate region supporting most of the CA2 communication with cortical and subcortical targets (Meira et al., 2018). Accordingly, studies reported social memory deficits upon inactivation of ventral CA1 (Okuyama et al., 2016) and ventral CA1 projections targeting the NAc (Okuyama et al., 2016) and the PFC (Phillips et al., 2019; Sun et al., 2020). In addition, CA2 inactivation decreases aggressive behavior, illustrated by a marked decrease in the tendency of a resident mouse to engage in social contests with never-met intruders, due to CA2 projections to the LS (Leroy et al., 2018). In light of these, CA2-vCA1-PFC and CA2-vCA1-NAc pathways should be investigated in hierarchical behavior (**Figure 4B**). Interestingly, hippocampal circuits produce sharp wave ripples (SWR) under native conditions (Buzsáki, 2015) and these were shown to naturally induce plasticity changes (Sadowski et al., 2016), participating in memory consolidation (Ego-Stengel and Wilson, 2010). It would be relevant to assess if SWR could evoke plasticity changes in prefrontal layer 5 pyramidal neurons by strengthening the vCA1-PFC synapses and whether this mechanism would impact the social rank and hierarchical behavior. In light of the recent findings of an interneuron-based gating mechanism for dominance and subordination in PFC (Zhang et al., 2022), it would be also relevant to test whether vCA1 can modulate the gate since there is a well-known projection from vCA1 to the PV interneurons in PFC, whose inhibition produces deficits in social memory (Sun et al., 2020). It would be expected that excitation of PV interneurons in PFC by the same pathway would modulate hierarchical behavior, specifically leading to subordination, establishing a definitive link between hierarchical behavior and social memory, thus explaining the former observation that stress prior to a social encounter leads to long-term subordinate behavior, due to amplification of memory, or, more specifically, due to a putative increase in vCA1-triggered excitation of PV interneurons in PFC.

Amygdala: An Understudied Area With Diverse Roles in Hierarchy-Related Behavior

The AMY is a classical hub that is broadly implicated in social behavior (Adolphs, 2010). Also, the studies reviewed above have provided strong evidence supporting its specific role in hierarchical behavior in human and non-human primates. In brief, correlational studies found AMY differential activation in human participants during hierarchy-related paradigms, particularly when hierarchies had a social component (Zink et al., 2008; Kumaran et al., 2012, 2016), firing rate modulation of AMY ensembles in monkeys according to the social status of the observed conspecifics (Munuera et al., 2018), and a positive correlation between gray matter volume in the AMY and social status in monkeys, independently of social network size (Noonan et al., 2014). These correlative studies were complemented by lesion studies, but the results are hard to conciliate. In fact, previously dominant monkeys were shown to lose social status and acquire subordinate behavior upon lesions in the AMY (Rosvold et al., 1954), and rats harboring AMY damage lose 85% of the encounters when competing for food against controls (Lukaszewska et al., 1984), suggesting that AMY lesions decrease dominance. Contrary to these, selective ablation of the AMY was found to increase confidence in social interactions (Emery et al., 2001) and increase dominant posture in rhesus monkeys (Machado and Bachevalier, 2006). This heterogeneity might result from variability across lesions and from functional differences between individual AMY subnuclei, but, most importantly, highlights our need for refined mechanistic studies. Surprisingly, this gap remains unexplored, contrasting with the overwhelming progress achieved in the last years regarding AMY research, particularly in classical conditioning

(Ehrlich et al., 2009; Orsini and Maren, 2012; Duvarci and Pare, 2014; Tovote et al., 2015). Among the few molecular studies in hierarchical behavior, one group found a positive correlation between social rank and the expression of corticotropin releasing factor mRNA in the AMY of mice (So et al., 2015). Notably, no differences were found when the c-fos expression was compared across dominant and submissive mice after performing the tube test, although c-fos expression was increased in both groups compared to controls, which traversed the tube, but that did not perform the tube test nor engaged in social interactions inside the tube (Nelson et al., 2019). Additional mechanistic studies are clearly needed and two candidate pathways would be a rational starting point, namely the basolateral amygdala (BLA)-mPFC and the BLA-vCA1 synapse (**Figures 4C,D**). In fact, modulation of the BLA-mPFC projection bidirectionally modulates social behavior in a resident-intruder paradigm (Felix-Ortiz et al., 2016). However, this study used juvenile intruders to avoid aggression, hindering our ability to clearly translate their findings to hierarchical behavior. Nonetheless, optogenetic stimulation of BLA-mPFC projections decreased social behavior, including chasing and contact, and had an anxiogenic effect, whereas inhibition produced the opposite results (Felix-Ortiz et al., 2016). Similar results in terms of social and anxiety-related behaviors were obtained when the same experiments were carried out in BLA-vCA1 projections (Felix-Ortiz et al., 2013). The antisocial and anxiogenic effect of BLA stimulation would suggest a role in subordinate behavior. An alternative explanation was put forward by a growing body of literature which has correlated AMY divisions and aggression (reviewed in Haller, 2018). Still, a putative role for the AMY in aggression does not fully explain its role in hierarchical behavior because dominance does not strictly imply aggression (see Wang et al., 2014). This is clearly illustrated in two studies showing that dominant mice in the tube test do not appear to be more aggressive (Benton et al., 1980), and treatment with cannabinoids decreased aggression and increased winning in the tube test (Masur et al., 1971).

Subcortical Nuclei and Brainstem Nuclei: The Aggression Circuit

Contrasting with the human studies reviewed above, studies in non-human primates (Noonan et al., 2014) and rodents (Nelson et al., 2019) found a strong engagement of additional subcortical and brainstem nuclei during hierarchical behavior, particularly the hypothalamus, periaqueductal gray (PAG), LHb, LS, and RN.

Among these brain areas, the hypothalamus, PAG, LHb, and LS were mostly studied in the context of aggressive behavior. Their modulation in hierarchical behavior thus suggests a putative overlap between the circuits supporting aggressive behavior and those supporting social hierarchies. The neural substrates of aggression have been reviewed elsewhere (Aleyasin et al., 2018; Flanigan and Russo, 2019) and a considerable amount of data highlighted the hypothalamus as a major hub in aggressive behavior (Hashikawa et al., 2017). In fact, stimulation of its mediobasal aspects, including the mediobasal hypothalamus in cats, the attack area in rats, and the ventrolateral region of the ventromedial hypothalamus in mice, triggered intraspecific aggression in different animal models (Kruk, 1991; Siegel et al., 1999; Lin et al., 2011). Despite the central relevance of the hypothalamus, research on aggression moved beyond the hypothalamus to identify its downstream and upstream partners. The PAG represents the most likely relay between the hypothalamus and the spinal cord (Beart et al., 1988; Chung et al., 1990; Canteras et al., 1994), and has been implicated in social and non-social behavior, including in defense-related behavior like immobility, flight, and escape jump (Wang et al., 2015; Motta et al., 2017). Since aggression must be under efficient control, the hypothalamus and PAG are modulated by upstream brain areas. To illustrate this, the electrical stimulation of AMY divisions was shown to modulate the efficacy of stimulations directly delivered to the mediobasal hypothalamus and PAG to trigger defensive rage in cats. More specifically, stimulation of the basal and medial AMY positively modulated defensive rage, whereas stimulation of the central AMY negatively modulated defensive rage (Shaikh and Siegel, 1994; Shaikh et al., 1994; Siegel et al., 1999). While no such studies were carried out in rodents, rivalry-aggression in the resident-intruder test reliably increased c-fos expression in medial AMY, BLA, and cortical AMY, with mild to no effect in central AMY (Halász et al., 2002; Veening et al., 2005; Duncan et al., 2009; Konoshenko et al., 2013). Although the hypothalamus-PAG circuit is a canonical hub in aggressive behavior, efforts have been made to find additional partners and new ones are emerging, specifically LHb, LS, RN, and even the mPFC (see Aleyasin et al., 2018). Aggressive, but not non-aggressive, mice develop conditioned place preference toward a context where they confronted a subordinate intruder (Golden et al., 2016). Optogenetic inhibition of GABAergic BF-LHb projections in aggressive males abolishes conditioned place preference, whereas its stimulation in non-aggressive males induced conditioned place preference (Golden et al., 2016). These manipulations did not affect the initiation of aggressive behavior, suggesting that GABAergic BF-LHb projections bidirectionally control the valence of aggression. On the other hand, optogenetic stimulation of the mPFC and LS decreased inter-male aggression (Takahashi et al., 2014), but stimulation of LS-projecting CA2 neurons increased inter-male aggression in mice (Leroy et al., 2018). The studies reviewed in this section can hardly illustrate all the exciting advances in the field of aggressive behavior but clearly show that hierarchical and aggressive behavior are indissociable, albeit distinct, and it is crucial to address the channels supporting the cross-talk between the two networks.

Focusing on the RN, MRI studies showed a positive correlation between gray matter volume in the RN, the major source of serotonin in the brain, and social dominance in monkeys (Noonan et al., 2014). Strengthening these data, fluoxetine treatment enhances serotonergic signaling in vervet monkeys, leading to decreased aggression, more affiliative behavior, and better social skills, resulting in higher social rank (Raleigh et al., 1991). On the other hand, monkeys with low serotonergic signaling display impulsive aggression and lower social rank (Raleigh et al., 1991). This association between low serotonergic signaling, impulsive behavior, and aggression was recapitulated in other species, including rodents (Caramaschi et al., 2007; Audero et al., 2013)

and fish (Winberg and Nilsson, 1993; Cubitt et al., 2008). While these studies suggest a reproducible negative association between serotonin levels and aggression, the relation between serotonergic signaling and dominance is more complex, probably due to the skills needed to attain high social ranks, which vary from species to species depending on their social complexity and the role played by aggression in the hierarchy. In this sense, increasing the serotonin levels in vervet monkeys resulted in higher social ranks probably because it enhanced the social skills necessary to navigate their hierarchies and invest in affiliative interactions. While human studies supporting a role for serotonin in social dominance are still sparse, treatment with antidepressant medications or serotonin precursors, which increase serotonin levels, also increased the frequency of dominant behaviors (Moskowitz et al., 2001). However, for simpler animals whose social ranks strongly depend upon their agonistic behavior, a similar increase in serotonergic signaling and decreased aggression would be a disadvantage. To illustrate this, pharmacological inhibition of serotonergic activity caused a shift from subordination to dominance in rats competing for water, whereas stimulation of the serotonergic system had the opposite effect (Kostowski et al., 1984). In addition, subordinate fish consistently show high serotonergic activity, in association with decreased locomotor activity, decreased aggression, and lower food intake (Winberg and Nilsson, 1993; Cubitt et al., 2008). Curiously, serotonergic signaling in rodents also showed a sex-dependent effect on dominance, since hypothalamic injection of 8-OH-DPAT, a serotonin 1A agonist, decreased aggression in male hamsters, but increased the aggression level in female hamsters (Terranova et al., 2016). Together, these findings suggest that the PFC-RN loop would be an interesting candidate pathway to target in hierarchical behavior. Effortful behavior has been studied in the rat using a forced swim test, where animals display epochs of resilient behavior in attempting to escape the water tank, interchanged with epochs of immobility in which they stop struggling (Warden et al., 2012). Notably, optogenetic stimulation of RN-targeting mPFC axons triggers resilient escaping behavior, whereas direct stimulation of the RN only increases general locomotor activity (Warden et al., 2012). It is tempting to speculate that PFC-RN projections would be implicated in resilience during stress and that serotonergic activity contributes to coping mechanisms within social settings (for a more detailed review on neuromodulation and social hierarchies, see Watanabe and Yamamoto, 2015; Qu et al., 2017).

CURRENT CAVEATS AND FUTURE STRATEGIES TO INVESTIGATE HIERARCHICAL BEHAVIOR

The combination of different animal models and technologies has provided a considerable understanding of the neural substrates supporting social hierarchies, from the identification of macroscale regions engaged to the mechanistic dissection of some prominent cell-specific hubs. Despite the evidence reviewed here, the core questions in the field remain largely unanswered. Finding neural correlates (structural or functional) during hierarchical behavior is an important exploratory strategy to quickly identify candidate regions, including a dissection of what brain areas are necessary and sufficient for a given behavior. However, this is still distant from a complete dissection of the neural basis and computations underlying the phenomenon. To complement this strategy the following strategies could prove beneficial:

Investing in *In vivo* Recordings in Freely-Behaving Animals to Understand Intraregional and Interregional Mechanisms

To understand the neural mechanisms supporting social hierarchies it is essential to record neural activity in multiple brain regions, while animals perform hierarchical behaviors. This will provide access to the populational dynamics, allowing the study of the neural ensembles engaged during hierarchical behavior, their relations in upstream and downstream brain areas, and their relation with the brain rhythms that organize populational activity (Buzsáki, 2010; Buzsáki and Watson, 2012). *In vivo* recordings can be complemented by modern genetic models with conditional expression of neuronal markers to identify neural ensembles active during hierarchical behavior (Reijmers et al., 2007; Liu et al., 2012; Kim and Cho, 2017), characterize them in terms of cell types, and tag neurons during *in vivo* recordings (Tanaka et al., 2018). Besides fostering an understanding of neural mechanisms, this will provide an integrative approach whereby neural mechanisms underlying hierarchical behavior might be integrated with domain-general mechanisms common to other social and non-social behaviors (Schafer and Schiller, 2018; Ramsey and Ward, 2020).

Improve Manipulation Studies

Modern optogenetic (Fenno et al., 2011; Lee et al., 2020) and pharmacogenetic (Roth, 2016) tools revolutionized neurosciences by allowing the reversible manipulation of genetically defined neural populations. However, direct application of these tools to stimulate and inhibit brain regions during behavior can identify regions of potential interest, but fails to provide mechanistic insight and may even lead to epiphenomena that occlude naturalistic behavior. Efforts should be made to combine manipulations with *in vivo* recordings to monitor the changes produced in the populational dynamics. Furthermore, optogenetic- and pharmacogenetic-based stimulation (unlike inhibition) should be interpreted with caution as these methods do not preserve native brain dynamics. This may be mitigated by adopting new tools that increase neuronal excitability without triggering action potentials.

In vivo Recordings and Manipulations in Non-human Primates

When studying social behavior and social hierarchies, there are considerable differences in the intrinsic and extrinsic factors governing social rank in rodents and primates. In addition, major substrates of hierarchical behavior as the PFC, specifically its lateral division, do not have a rodent homolog so they can only be properly studied using non-human primates (Carlén, 2017). In

this sense, efforts should be made to translate rodent protocols to non-human primates. Notably, small non-human primates are emerging models in Neurosciences that have the potential to open new avenues in the study of the neural substrates of social behavior and associated disorders (Miller et al., 2016; Feng et al., 2020).

CONCLUSION

Social hierarchies have profound implications for species' survival and individual health, but the neural mechanisms subserving hierarchical behavior remain elusive, hindering our ability to signal dominance- or subordination-prone individuals and to design strategies to mitigate hierarchy-related effects on health. Correlative and manipulation studies in human and non-human primates and rodents led to the identification of distributed brain networks underpinning hierarchical behavior, as well as mechanisms whose modulation bidirectionally switches between dominant and subordinate phenotypes in animal models. In this review, we synthesized the available knowledge and models of networks supporting social hierarchies. However, additional *in vivo* monitoring of neural activity across multiple brain regions is needed to foster the understanding and integration of how information flow across candidate regions acts in the service of social hierarchy behavior.

AUTHOR CONTRIBUTIONS

EF-F and JP wrote the manuscript. JP directed the bibliography search and defined the scope of the review. All authors contributed to the article and approved the submitted version.

FUNDING

This work was financed by the European Regional Development Fund (ERDF), through the Centro 2020 Regional Operational Programme, under project CENTRO-01-0145-FEDER-000008 (BrainHealth 2020), the COMPETE 2020—Operational Programme for Competitiveness and Internationalization and Portuguese national funds *via* FCT—Fundação para a Ciência e Tecnologia, under projects POCI-01-0145-FEDER-007440, UIBD/04539/2020, PTDC/NEU-SCC/3247/2014. This work was supported by Bial Foundation Grants #266/2016 and #074/2020, 2019 Pfizer Prize in Basic Sciences and a 2020 IBRO Early Career Award.

REFERENCES

Adolphs, R. (2010). What does the amygdala contribute to social cognition. *Ann. N Y Acad. Sci.* 1191, 42–61. doi: 10.1111/j.1749-6632.2010.05445.x

Aleyasin, H., Flanigan, M., and Russo, S. J. (2018). Neurocircuitry of aggression and aggression seeking behavior: nose poking into brain circuitry controlling aggression. *Curr. Opin. Neurobiol.* 49, 184–191. doi: 10.1016/j.conb.2018.02.013

Audero, E., Mlinar, B., Baccini, G., Skachokova, Z. K., Corradetti, R., and Gross, C. (2013). Suppression of serotonin neuron firing increases aggression in mice. *J. Neurosci.* 33, 8678–8688. doi: 10.1523/JNEUROSCI.2067-12.2013

Azahara, O., Antonio, F.-R., Felix, L., and Steven, S. A. (2020). Hippocampal CA2 sharp-wave ripples reactivate and promote social memory. *Nature* 587, 264–269. doi: 10.1038/s41586-020-2758-y

Bault, N., Joffily, M., Rustichini, A., and Coricelli, G. (2011). Medial prefrontal cortex and striatum mediate the influence of social comparison on the decision process. *Proc. Natl. Acad. Sci. U S A* 108, 16044–16049. doi: 10.1073/pnas.1100892108

Beart, P. M., Nicolopoulos, L. S., West, D. C., and Headley, P. M. (1988). An excitatory amino acid projection from ventromedial hypothalamus to periaqueductal gray in the rat: autoradiographic and electrophysiological evidence. *Neurosci. Lett.* 85, 205–211. doi: 10.1016/0304-3940(88)90352-7

Beaugrand, J., Goulet, C., and Payette, D. (1991). Outcome of dyadic conflict in male green swordtail fish, *Xiphophorus helleri*: effects of body size and prior dominance. *Anim. Behav.* 41, 417–424. doi: 10.1016/s0003-3472(05)80842-5

Beaugrand, J. P., and Zayan, R. (1985). An experimental model of aggressive dominance in *Xiphophorus helleri* (pisces, poeciliidae). *Behav. Processes* 10, 1–52. doi: 10.1016/0376-6357(85)90116-0

Benelli, G., Desneux, N., Romano, D., Conte, G., Messing, R. H., and Canale, A. (2015). Contest experience enhances aggressive behaviour in a fly: when losers learn to win. *Sci. Rep.* 5:9347. doi: 10.1038/srep09347

Benton, D., Dalrymple-Alford, J. C., and Brain, P. F. (1980). Comparisons of measures of dominance in the laboratory mouse. *Anim. Behav.* 28, 1274–1279. doi: 10.1016/s0003-3472(80)80115-1

Bickart, K. C., Wright, C. I., Dautoff, R. J., Dickerson, B. C., and Barrett, L. F. (2011). Amygdala volume and social network size in humans. *Nat. Neurosci.* 14, 163–164. doi: 10.1038/nn.2724

Bliss, E. L. (1962). *Roots of Behavior, Genetics, Instinct and Socialization in Animal Behavior.* New York: Harper.

Buzsáki, G. (2010). Neural syntax: cell assemblies, synapsembles and readers. *Neuron* 68, 362–385. doi: 10.1016/j.neuron.2010.09.023

Buzsáki, G. (2015). Hippocampal sharp wave-ripple: a cognitive biomarker for episodic memory and planning. *Hippocampus* 25, 1073–1188. doi: 10.1002/hipo.22488

Buzsáki, G., and Watson, B. O. (2012). Brain rhythms and neural syntax: implications for efficient coding of cognitive content and neuropsychiatric disease. *Dialogues Clin. Neurosci.* 14, 345–367. doi: 10.31887/DCNS.2012.14.4/gbuzsaki

Calhoun, J. B. (1966). The role of space in animal sociology. *J. Soc. Issues* 22, 46–58. doi: 10.1111/j.1540-4560.1966.tb00548.x

Calhoun, J. B. (1970). Population density and social pathology. *Calif. Med.* 113:54. doi: 10.1177/107808747501100205

Calhoun, J. B. (1973). Death squared: the explosive growth and demise of a mouse population. *Proc. R Soc. Med.* 66, 80–88.

Calhoun, J. B. (1977). *Looking Backward From "The Beautiful Ones"*. U.S. Department of Health, Education, and Welfare, National Institutes of Health.

Canteras, N. S., Simerly, R. B., and Swanson, L. W. (1994). Organization of projections from the ventromedial nucleus of the hypothalamus: a Phaseolus vulgaris-leucoagglutinin study in the rat. *J. Comp. Neurol.* 348, 41–79. doi: 10.1002/cne.903480103

Caramaschi, D., de Boer, S. F., and Koolhaas, J. M. (2007). Differential role of the 5-HT1A receptor in aggressive and non-aggressive mice: an across-strain comparison. *Physiol. Behav.* 90, 590–601. doi: 10.1016/j.physbeh.2006.11.010

Carlén, M. (2017). What constitutes the prefrontal cortex. *Science* 358, 478–482. doi: 10.1126/science.aan8868

Chase, I. D. (1974). Models of hierarchy formation in animal societies. *Behav. Sci.* 19, 374–382. doi: 10.1002/bs.3830190604

Chase, I. D., Tovey, C., Spangler-Martin, D., and Manfredonia, M. (2002). Individual differences versus social dynamics in the formation of animal dominance hierarchies. *Proc Natl Acad Sci. U S A* 99, 5744–5749. doi: 10.1073/pnas.082104199

Chiao, J. Y., Adams, R. B., Tse, P. U., Lowenthal, L., Richeson, J. A., and Ambady, N. (2008). Knowing who's boss: fMRI and ERP investigations of social

dominance perception. *Group Processes & Intergroup Relations* 11, 201–214. doi: 10.1177/1368430207088038

Chiao, J. Y., Harada, T., Oby, E. R., Li, Z., Parrish, T., and Bridge, D. J. (2009). Neural representations of social status hierarchy in human inferior parietal cortex. *Neuropsychologia* 47, 354–363. doi: 10.1016/j.neuropsychologia.2008.09.023

Christian, J. J. (1970). Social subordination, population density and mammalian evolution. *Science* 168, 84–90. doi: 10.1126/science.168.3927.84

Chung, S. K., Pfaff, D. W., and Cohen, R. S. (1990). Projections of ventromedial hypothalamic neurons to the midbrain central gray: an ultrastructural study. *Neuroscience* 38, 395–407. doi: 10.1016/0306-4522(90)90037-5

Cordero, M. I., and Sandi, C. (2007). Stress amplifies memory for social hierarchy. *Front. Neurosci.* 1, 175–184. doi: 10.3389/neuro.01.1.1.013.2007

Cubitt, K. F., Winberg, S., Huntingford, F. A., Kadri, S., Crampton, V. O., and verli, O. (2008). Social hierarchies, growth and brain serotonin metabolism in Atlantic salmon (*Salmo salar*) kept under commercial rearing conditions. *Physiol. Behav.* 94, 529–535. doi: 10.1016/j.physbeh.2008.03.009

Cui, Z., Gerfen, C. R., and Young, W. S. (2013). Hypothalamic and other connections with the dorsal CA2 area of the mouse hippocampus. *J. Comp. Neurol.* 521, 1844–1866. doi: 10.1002/cne.23263

Danjo, T., Toyoizumi, T., and Fujisawa, S. (2018). Spatial representations of self and other in the hippocampus. *Science* 359, 213–218. doi: 10.1126/science.aao3898

Darling, F. F. (2008). *A Herd of Red Deer: A Study in Animal Behaviour*. New York: Luath Press

Dittus, W. P. J. (1977). The social regulation of population density and age-sex distribution in the toque monkey. *Behaviour* 63, 281–322. doi: 10.1163/156853977x00450

Dugatkin, L. A., and Druen, M. (2004). The social implications of winner and loser effects. *Proc. Biol. Sci.* 271, S488–S489. doi: 10.1098/rsbl.2004.0235

Duncan, G. E., Inada, K., Farrington, J. S., Koller, B. H., and Moy, S. S. (2009). Neural activation deficits in a mouse genetic model of NMDA receptor hypofunction in tests of social aggression and swim stress. *Brain Res.* 1265, 186–195. doi: 10.1016/j.brainres.2009.02.002

Duvarci, S., and Pare, D. (2014). Amygdala microcircuits controlling learned fear. *Neuron* 82, 966–980. doi: 10.1016/j.neuron.2014.04.042

Ego-Stengel, V., and Wilson, M. A. (2010). Disruption of ripple-associated hippocampal activity during rest impairs spatial learning in the rat. *Hippocampus* 20, 1–10. doi: 10.1002/hipo.20707

Ehrlich, I., Humeau, Y., Grenier, F., Ciocchi, S., Herry, C., and Lüthi, A. (2009). Amygdala inhibitory circuits and the control of fear memory. *Neuron* 62, 757–771. doi: 10.1016/j.neuron.2009.05.026

Eichenbaum, H. (2014). Time cells in the hippocampus: a new dimension for mapping memories. *Nat. Rev. Neurosci.* 15, 732–744. doi: 10.1038/nrn3827

Eichenbaum, H. (2017). Prefrontal-hippocampal interactions in episodic memory. *Nat. Rev. Neurosci.* 18, 547–558. doi: 10.1038/nrn.2017.74

Eichenbaum, H., and Cohen, N. J. (2014). Can we reconcile the declarative memory and spatial navigation views on hippocampal function. *Neuron* 83, 764–770. doi: 10.1016/j.neuron.2014.07.032

Ekstrom, A. D., Kahana, M. J., Caplan, J. B., Fields, T. A., Isham, E. A., Newman, E. L., et al. (2003). Cellular networks underlying human spatial navigation. *Nature* 425, 184–188. doi: 10.1038/nature01964

Ellis, L. (1995). Dominance and reproductive success among nonhuman animals: a cross-species comparison. *Ethol. Sociobiol.* 16, 257–333. doi: 10.1016/0162-3095(95)00050-u

Emery, N. J., Capitanio, J. P., Mason, W. A., Machado, C. J., Mendoza, S. P., and Amaral, D. G. (2001). The effects of bilateral lesions of the amygdala on dyadic social interactions in rhesus monkeys (*Macaca mulatta*). *Behav. Neurosci.* 115, 515–544. doi: 10.1037/0735-7044.115.3.515

Esser, A. (1971). *Behavior and Environment: The Use of Space by Animals and Men*, New York: Springer. Available online at: https://www.springer.com/gp/book/9781468418958.

Fan, Z., Zhu, H., Zhou, T., Wang, S., Wu, Y., and Hu, H. (2019). Using the tube test to measure social hierarchy in mice. *Nat. Protoc.* 14, 819–831. doi: 10.1038/s41596-018-0116-4

Felix-Ortiz, A. C., Burgos-Robles, A., Bhagat, N. D., Leppla, C. A., and Tye, K. M. (2016). Bidirectional modulation of anxiety-related and social behaviors by amygdala projections to the medial prefrontal cortex. *Neuroscience* 321, 197–209. doi: 10.1016/j.neuroscience.2015.07.041

Felix-Ortiz, A. C., Beyeler, A., Seo, C., Leppla, C. A., Wildes, C. P., and Tye, K. M. (2013). BLA to vHPC inputs modulate anxiety-related behaviors. *Neuron* 79, 658–664. doi: 10.1016/j.neuron.2013.06.016

Feng, G., Jensen, F. E., Greely, H. T., Okano, H., Treue, S., Roberts, A. C., et al. (2020). Opportunities and limitations of genetically modified nonhuman primate models for neuroscience research. *Proc. Natl. Acad. Sci. U S A* 117, 24022–24031. doi: 10.1073/pnas.2006515117

Fenno, L., Yizhar, O., and Deisseroth, K. (2011). The development and application of optogenetics. *Annu. Rev. Neurosci.* 34, 389–412. doi: 10.1146/annurev-neuro-061010-113817

Ferino, F., Thierry, A. M., Saffroy, M., and Glowinski, J. (1987). Interhemispheric and subcortical collaterals of medial prefrontal cortical neurons in the rat. *Brain Res.* 417, 257–266. doi: 10.1016/0006-8993(87)90450-1

Flanigan, M. E., and Russo, S. J. (2019). Recent advances in the study of aggression. *Neuropsychopharmacology* 44, 241–244. doi: 10.1038/s41386-018-0226-2

Franco, L. O., Carvalho, M. J., Costa, J., Ferreira, P. A., Guedes, J. R., Sousa, R., et al. (2020). Social subordination induced by early life adversity rewires inhibitory control of the prefrontal cortex via enhanced Npy1r signaling. *Neuropsychopharmacology* 45, 1438–1447. doi: 10.1038/s41386-020-0727-7

Franklin, T. B., Silva, B. A., Perova, Z., Marrone, L., Masferrer, M. E., Zhan, Y., et al. (2017). Prefrontal cortical control of a brainstem social behavior circuit. *Nat. Neurosci.* 20, 260–270. doi: 10.1038/nn.4470

French, S. J., and Totterdell, S. (2002). Hippocampal and prefrontal cortical inputs monosynaptically converge with individual projection neurons of the nucleus accumbens. *J. Comp. Neurol.* 446, 151–165. doi: 10.1002/cne.10191

Fuxjager, M. J., and Marler, C. A. (2010). How and why the winner effect forms: influences of contest environment and species differences. *Behav. Ecol.* 21, 37–45. doi: 10.1093/beheco/arp148

Golden, S. A., Heshmati, M., Flanigan, M., Christoffel, D. J., Guise, K., Pfau, M. L., et al. (2016). Basal forebrain projections to the lateral habenula modulate aggression reward. *Nature* 534, 688–692. doi: 10.1038/nature18601

Gonçalves, D., Félix, A. S., and Oliveira, R. F. (2017). "Neuroendocrinology of social behavior in teleost fish," in *Hormones, Brain, and Behavior*, 3rd Edn., Vol. 2, D. W. Pfaff and M. Joëls (editors-in-chief), (Oxford: Academic Press), 3–18.

Groenewegen, H. J., Wright, C. I., and Uylings, H. B. (1997). The anatomical relationships of the prefrontal cortex with limbic structures and the basal ganglia. *J. Psychopharmacol. Oxf. Engl.* 11, 99–106. doi: 10.1177/026988119701100202

Halász, J., Liposits, Z., Kruk, M. R., and Haller, J. (2002). Neural background of glucocorticoid dysfunction-induced abnormal aggression in rats: involvement of fear- and stress-related structures. *Eur. J. Neurosci.* 15, 561–569. doi: 10.3389/fnut.2022.790157

Haller, J. (2018). The role of central and medial amygdala in normal and abnormal aggression: a review of classical approaches. *Neurosci. Biobehav. Rev.* 85, 34–43. doi: 10.1016/j.neubiorev.2017.09.017

Hanlon, P., Walsh, D., and Whyte, B. (2006). *Let Glasgow Flourish | Glasgow Centre for Population Health*. Available online at: https://www.gcph.co.uk/publications/86_let_glasgow_flourish.

Hashikawa, Y., Hashikawa, K., Falkner, A. L., and Lin, D. (2017). Ventromedial hypothalamus and the generation of aggression. *Front. Syst. Neurosci.* 11:94. doi: 10.3389/fnsys.2017.00094

Hitti, F. L., and Siegelbaum, S. A. (2014). The hippocampal CA2 region is essential for social memory. *Nature* 508, 88–92. doi: 10.1038/nature13028

Hollis, F., van der Kooij, M. A., Zanoletti, O., Lozano, L., Cantó, C., and Sandi, C. (2015). Mitochondrial function in the brain links anxiety with social subordination. *Proc. Natl. Acad. Sci. U S A* 112, 15486–15491. doi: 10.1073/pnas.1512653112

Hoover, W. B., and Vertes, R. P. (2007). Anatomical analysis of afferent projections to the medial prefrontal cortex in the rat. *Brain Struct. Funct.* 212, 149–179. doi: 10.1007/s00429-007-0150-4

Hsu, Y., Earley, R. L., and Wolf, L. L. (2006). Modulation of aggressive behaviour by fighting experience: mechanisms and contest outcomes. *Biol. Rev. Camb. Philos. Soc.* 81, 33–74. doi: 10.1017/S146479310500686X

Hsu, Y., and Wolf, L. L. (1999). The winner and loser effect: integrating multiple experiences. *Anim. Behav.* 57, 903–910. doi: 10.1006/anbe.1998.1049

Hurt, L. S., Ronsmans, C., and Saha, S. (2004). Effects of education and other socioeconomic factors on middle age mortality in rural bangladesh. *J. Epidemiol. Commun. Health* 58, 315–320. doi: 10.1136/jech.2003.007351

Isbell, L. A., Pruetz, J. D., Lewis, M., and Young, T. P. (1999). Rank differences in ecological behavior: a comparative study of patas monkeys (*Erythrocebus patas*) and vervets (*Cercopithecus aethiops*). *Int. J. Primatol.* 20, 257–272. doi: 10.1002/ajp.1350130307

Johnsson, J. I., and Åkerman, A. (1998). Watch and learn: preview of the fighting ability of opponents alters contest behaviour in rainbow trout. *Anim. Behav.* 56, 771–776. doi: 10.1006/anbe.1998.0824

Kanai, R., Bahrami, B., Roylance, R., and Rees, G. (2012). Online social network size is reflected in human brain structure. *Proc. Biol. Sci.* 279, 1327–1334. doi: 10.1098/rspb.2011.1959

Kim, W. B., and Cho, J.-H. (2017). Encoding of discriminative fear memory by input-specific LTP in the amygdala. *Neuron* 95, 1129–1146.e5. doi: 10.1016/j.neuron.2017.08.004

Konoshenko, M. Y., Timoshenko, T. V., and Plyusnina, I. Z. (2013). c-Fos activation and intermale aggression in rats selected for behavior toward humans. *Behav. Brain Res.* 237, 103–106. doi: 10.1016/j.bbr.2012.09.022

Kostowski, W., Plewako, M., and Bidzinski, A. (1984). Brain serotonergic neurons: their role in a form of dominance-subordination behavior in rats. *Physiol. Behav.* 33, 365–371. doi: 10.1016/0031-9384(84)90155-0

Kruk, M. R. (1991). Ethology and pharmacology of hypothalamic aggression in the rat. *Neurosci. Biobehav. Rev.* 15, 527–538. doi: 10.1016/s0149-7634(05)80144-7

Kumaran, D., Banino, A., Blundell, C., Hassabis, D., and Dayan, P. (2016). Computations underlying social hierarchy learning: distinct neural mechanisms for updating and representing self-relevant information. *Neuron* 92, 1135–1147. doi: 10.1016/j.neuron.2016.10.052

Kumaran, D., Melo, H. L., and Duzel, E. (2012). The emergence and representation of knowledge about social and nonsocial hierarchies. *Neuron* 76, 653–666. doi: 10.1016/j.neuron.2012.09.035

Larrieu, T., Cherix, A., Duque, A., Rodrigues, J., Lei, H., Gruetter, R., et al. (2017). Hierarchical status predicts behavioral vulnerability and nucleus accumbens metabolic profile following chronic social defeat stress. *Curr. Biol.* 27, 2202–2210.e4. doi: 10.1016/j.cub.2017.06.027

Lee, C., Lavoie, A., Liu, J., Chen, S. X., and Liu, B. (2020). Light up the brain: the application of optogenetics in cell-type specific dissection of mouse brain circuits. *Front. Neural Circuits* 14:18. doi: 10.3389/fncir.2020.00018

Leroy, F., Park, J., Asok, A., Brann, D. H., Meira, T., Boyle, L. M., et al. (2018). A circuit from hippocampal CA2 to lateral septum disinhibits social aggression. *Nature* 564, 213–218. doi: 10.1038/s41586-018-0772-0

Levesque, M., Charara, A., Gagnon, S., Parent, A., and Deschenes, M. (1996). Corticostriatal projections from layer V cells in rat are collaterals of long-range corticofugal axons. *Brain Res.* 709, 311–315. doi: 10.1016/0006-8993(95)01333-4

Lewis, P. A., Rezaie, R., Brown, R., Roberts, N., and Dunbar, R. I. M. (2011). Ventromedial prefrontal volume predicts understanding of others and social network size. *Neuroimage* 57, 1624–1629. doi: 10.1016/j.neuroimage.2011.05.030

Lin, D., Boyle, M. P., Dollar, P., Lee, H., Lein, E. S., Perona, P., et al. (2011). Functional identification of an aggression locus in the mouse hypothalamus. *Nature* 470, 221–226. doi: 10.1038/nature09736

Liu, X., Ramirez, S., Pang, P. T., Puryear, C. B., Govindarajan, A., Deisseroth, K., et al. (2012). Optogenetic stimulation of a hippocampal engram activates fear memory recall. *Nature* 484, 381–385. doi: 10.1038/nature11028

Lukaszewska, I., Korczynski, R., Kostarczyk, E., and Fonberg, E. (1984). Food-motivated behavior in rats with cortico-basomedial amygdala damage. *Behav. Neurosci.* 98, 441–451. doi: 10.1037//0735-7044.98.3.441

Ly, M., Haynes, M. R., Barter, J. W., Weinberger, D. R., and Zink, C. F. (2011). Subjective socioeconomic status predicts human ventral striatal responses to social status information. *Curr. Biol.* 21, 794–797. doi: 10.1016/j.cub.2011.03.050

Machado, C. J., and Bachevalier, J. (2006). The impact of selective amygdala, orbital frontal cortex, or hippocampal formation lesions on established social relationships in rhesus monkeys (*Macaca mulatta*). *Behav. Neurosci.* 120, 761–786.

Madeira, N., and Oliveira, R. F. (2017). Long-term social recognition memory in zebrafish. *Zebrafish* 14, 305–310. doi: 10.1089/zeb.2017.1430

Manns, J. R., and Eichenbaum, H. (2009). A cognitive map for object memory in the hippocampus. *Learn. Mem.* 16, 616–624. doi: 10.1101/lm.1484509

Marmot, M. G. (2004). *Status Syndrome: How Your Social Standing Directly Affects Your Health and Life Expectancy*. London: Bloomsbury Publishing PLC.

Marmot, M. G., and Sapolsky, R. (2014). "Of Baboons and Men: social circumstances, biology and the social gradient in health," in *Sociality, Hierarchy, Health: Comparative Biodemography: A Collection of Papers*, eds M. Weinstein and M. A. Lane (Washington, DC: National Academies Press (US)), 365–388. Available online at: https://www.ncbi.nlm.nih.gov/books/NBK242456/.

Marsh, A. A., Blair, K. S., Jones, M. M., Soliman, N., and Blair, R. J. R. (2009). Dominance and submission: the ventrolateral prefrontal cortex and responses to status cues. *J. Cogn. Neurosci.* 21, 713–724. doi: 10.1162/jocn.2009.21052

Martin, J., and Salvador, A. (1993). Tail loss reduces mating success in the Iberian rock-lizard, Lacerta monticola. *Behav. Ecol. Sociobiol.* 32, 185–189. doi: 10.1007/BF00173776

Masur, J., Martz, R. M., Bieniek, D., and Korte, F. (1971). Influence of (-) 9 -trans-tetrahydrocannabinol and mescaline on the behavior of rats submitted to food competition situations. *Psychopharmacologia* 22, 187–194. doi: 10.1007/BF00403627

Meira, T., Leroy, F., Buss, E. W., Oliva, A., Park, J., and Siegelbaum, S. A. (2018). A hippocampal circuit linking dorsal CA2 to ventral CA1 critical for social memory dynamics. *Nat. Commun.* 9:4163. doi: 10.1038/s41467-018-06501-w

Miller, C. T., Freiwald, W. A., Leopold, D. A., Mitchell, J. F., Silva, A. C., and Wang, X. (2016). Marmosets: a neuroscientific model of human social behavior. *Neuron* 90, 219–233. doi: 10.1016/j.neuron.2016.03.018

Morgan, D., Grant, K. A., Gage, H. D., Mach, R. H., Kaplan, J. R., Prioleau, O., et al. (2002). Social dominance in monkeys: dopamine D2 receptors and cocaine self-administration. *Nat. Neurosci.* 5, 169–174. doi: 10.1038/nn798

Morris, R. G., Garrud, P., Rawlins, J. N., and O'Keefe, J. (1982). Place navigation impaired in rats with hippocampal lesions. *Nature* 297, 681–683. doi: 10.1038/297681a0

Moskowitz, D. S., Pinard, G., Zuroff, D. C., Annable, L., and Young, S. N. (2001). The effect of tryptophan on social interaction in everyday life: a placebo-controlled study. *Neuropsychopharmacology* 25, 277–289. doi: 10.1016/S0893-133X(01)00219-6

Motta, S. C., Carobrez, A. P., and Canteras, N. S. (2017). The periaqueductal gray and primal emotional processing critical to influence complex defensive responses, fear learning and reward seeking. *Neurosci. Biobehav. Rev.* 76, 39–47. doi: 10.1016/j.neubiorev.2016.10.012

Munuera, J., Rigotti, M., and Salzman, C. D. (2018). Shared neural coding for social hierarchy and reward value in primate amygdala. *Nat. Neurosci.* 21, 415–423. doi: 10.1038/s41593-018-0082-8

Murray, C. J. L., Kulkarni, S. C., Michaud, C., Tomijima, N., Bulzacchelli, M. T., Iandiorio, T. J., et al. (2006). Eight Americas: investigating mortality disparities across races, counties and race-counties in the United States. *PLoS Med.* 3:e260. doi: 10.1371/journal.pmed.0030260

Nelson, A. C., Kapoor, V., Vaughn, E., Gnanasegaram, J. A., Rubinstein, N. D., Murthy, V. N., et al. (2019). Molecular and circuit architecture of social hierarchy. *bioRxiv* [Preprint]. 838664. doi: 10.1101/838664

Noonan, M. P., Sallet, J., Mars, R. B., Neubert, F. X., O'Reilly, J. X., Andersson, J. L., et al. (2014). A neural circuit covarying with social hierarchy in macaques. *PLoS Biol.* 12:e1001940. doi: 10.1371/journal.pbio.1001940

O'Donnell, P., and Grace, A. A. (1995). Synaptic interactions among excitatory afferents to nucleus accumbens neurons: hippocampal gating of prefrontal cortical input. *J. Neurosci.* 15, 3622–3639. doi: 10.1523/JNEUROSCI.15-05-03622.1995

O'Keefe, J. (1976). Place units in the hippocampus of the freely moving rat. *Exp. Neurol.* 51, 78–109. doi: 10.1016/0014-4886(76)90055-8

O'Keefe, J. (1979). A review of the hippocampal place cells. *Prog. Neurobiol.* 13, 419–439. doi: 10.1016/0301-0082(79)90005-4

O'Keefe, J. (1991). An allocentric spatial model for the hippocampal cognitive map. *Hippocampus* 1, 230–235. doi: 10.1002/hipo.450010303

O'Keefe, J., and Conway, D. H. (1978). Hippocampal place units in the freely moving rat: why they fire where they fire. *Exp. Brain Res.* 31, 573–590. doi: 10.1007/BF00239813

O'Keefe, J., and Dostrovsky, J. (1971). The hippocampus as a spatial map. Preliminary evidence from unit activity in the freely-moving rat. *Brain Res.* 34, 171–175. doi: 10.1016/0006-8993(71)90358-1

Okuyama, T., Kitamura, T., Roy, D. S., Itohara, S., and Tonegawa, S. (2016). Ventral CA1 neurons store social memory. *Science* 353, 1536–1541. doi: 10.1126/science.aaf7003

Oliveira, R. (2005). "Hormones, social context and animal communication," in *Animal Communication Networks*, ed P. McGregor (Cambridge: Cambridge University Press), 481–520. doi: 10.1017/CBO9780511610363.026

Oliveira, R. F., Lopes, M., Carneiro, L. A., and Canário, A. V. M. (2001). Watching fights raises fish hormone levels. *Nature* 409:475. doi: 10.1038/35054128

Omer, D. B., Maimon, S. R., Las, L., and Ulanovsky, N. (2018). Social place-cells in the bat hippocampus. *Science* 359, 218–224. doi: 10.1126/science.aao3474

Orsini, C. A., and Maren, S. (2012). Neural and cellular mechanisms of fear and extinction memory formation. *Neurosci. Biobehav. Rev.* 36, 1773–1802. doi: 10.1016/j.neubiorev.2011.12.014

Ostner, J., Nunn, C. L., and Schülke, O. (2008). Female reproductive synchrony predicts skewed paternity across primates. *Behav. Ecol.* 19, 1150–1158. doi: 10.1093/beheco/arn093

Owens, D., and Owens, M. (1996). Social dominance and reproductive patterns in brown hyaenas, *Hyaena brunnea*, of the central Kalahari desert. *Anim. Behav.* 51, 535–551. doi: 10.1006/anbe.1996.0058

Page, L., and Coates, J. (2017). Winner and loser effects in human competitions. Evidence from equally matched tennis players. *Evol. Hum. Behav.* 38, 530–535. doi: 10.1016/j.evolhumbehav.2017.02.003

Papilloud, A., Weger, M., Bacq, A., Zalachoras, I., Hollis, F., Larrieu, T., et al. (2020). The glucocorticoid receptor in the nucleus accumbens plays a crucial role in social rank attainment in rodents. *Psychoneuroendocrinology* 112:104538. doi: 10.1016/j.psyneuen.2019.104538

Parslow, D. M., Morris, R. G., Fleminger, S., Rahman, Q., Abrahams, S., and Recce, M. (2005). Allocentric spatial memory in humans with hippocampal lesions. *Acta Psychol. (Amst)* 118, 123–147. doi: 10.1016/j.actpsy.2004.10.006

Penfield, W., and Milner, B. (1958). Memory deficit produced by bilateral lesions in the hippocampal zone. *AMA Arch. Neurol. Psychiatry* 79, 475–497. doi: 10.1001/archneurpsyc.1958.02340050003001

Phillips, M. L., Robinson, H. A., and Pozzo-Miller, L. (2019). Ventral hippocampal projections to the medial prefrontal cortex regulate social memory. *eLife* 8:e44182. doi: 10.7554/eLife.44182

Powell, J., Lewis, P. A., Roberts, N., García-Fiñana, M., and Dunbar, R. I. M. (2012). Orbital prefrontal cortex volume predicts social network size: an imaging study of individual differences in humans. *Proc. Biol. Sci.* 279, 2157–2162. doi: 10.1098/rspb.2011.2574

Qu, C., Ligneul, R., der Henst, J.-B. V., and Dreher, J.-C. (2017). An integrative interdisciplinary perspective on social dominance hierarchies. *Trends Cogn. Sci.* 21, 893–908. doi: 10.1016/j.tics.2017.08.004

Røskaft, E., Järvi, T., Bakken, M., Bech, C., and Reinertsen, R. E. (1986). The relationship between social status and resting metabolic rate in great tits (*Parus major*) and pied flycatchers (*Ficedula hypoleuca*). *Anim. Behav.* 34, 838–842. doi: 10.1016/S0003-3472(86)80069-0

Raleigh, M. J., McGuire, M. T., Brammer, G. L., Pollack, D. B., and Yuwiler, A. (1991). Serotonergic mechanisms promote dominance acquisition in adult male vervet monkeys. *Brain Res.* 559, 181–190. doi: 10.1016/0006-8993(91)90001-c

Ramsden, E., and Adams, J. (2009). Escaping the laboratory: the rodent experiments of John B. Calhoun & their cultural influence. *J. Soc. Hist.* 42, 761–792. doi: 10.1353/jsh.0.0156

Ramsey, R., and Ward, R. (2020). Putting the nonsocial into social neuroscience: a role for domain-general priority maps during social interactions. *Perspect. Psychol. Sci.* 15, 1076–1094. doi: 10.1177/1745691620904972

Reijmers, L. G., Perkins, B. L., Matsuo, N., and Mayford, M. (2007). Localization of a stable neural correlate of associative memory. *Science* 317, 1230–1233. doi: 10.1126/science.1143839

Rodriguez-Llanes, J. M., Verbeke, G., and Finlayson, C. (2009). Reproductive benefits of high social status in male macaques (*Macaca*). *Anim. Behav.* 78, 643–649. doi: 10.1016/j.anbehav.2009.06.012

Rosvold, H. E., Mirsky, A. F., and Pribram, K. H. (1954). Influence of amygdalectomy on social behavior in monkeys. *J. Comp. Physiol. Psychol.* 47, 173–178. doi: 10.1037/h0058870

Roth, B. L. (2016). DREADDs for neuroscientists. *Neuron* 89, 683–694. doi: 10.1016/j.neuron.2016.01.040

Sadowski, J. H. L. P., Jones, M. W., and Mellor, J. R. (2016). Sharp-wave ripples orchestrate the induction of synaptic plasticity during reactivation of place cell firing patterns in the hippocampus. *Cell Rep.* 14, 1916–1929. doi: 10.1016/j.celrep.2016.01.061

Sallet, J., Mars, R. B., Noonan, M. P., Andersson, J. L., O'Reilly, J. X., Jbabdi, S., et al. (2011). Social network size affects neural circuits in macaques. *Science* 334, 697–700. doi: 10.1126/science.1210027

Samuels, A., Silk, J. B., and Rodman, P. S. (1984). Changes in the dominance rank and reproductive behaviour of male bonnet macaques (*Macaca radiata*). *Anim. Behav.* 32, 994–1003. doi: 10.1016/S0003-3472(84)80212-2

Sapolsky, R. M. (2004). Social status and health in humans and other animals. *Annu. Rev. Anthropol.* 33, 393–418. doi: 10.1146/annurev.anthro.33.070203.144000

Sapolsky, R. M. (2005). The influence of social hierarchy on primate health. *Science* 308, 648–652. doi: 10.1126/science.1106477

Sapolsky, R. M., Romero, L. M., and Munck, A. U. (2000). How do glucocorticoids influence stress responses? Integrating permissive, suppressive, stimulatory and preparative actions. *Endocr. Rev.* 21, 55–89. doi: 10.1210/edrv.21.1.0389

Schafer, M., and Schiller, D. (2018). Navigating social space. *Neuron* 100, 476–489. doi: 10.1016/j.neuron.2018.10.006

Schjelderup-Ebbe, T. (1922). Beiträge zur Sozialpsychologie des Haushuhns. [Observation on the social psychology of domestic fowls.]. *Z. Für Psychol. Physiol. Sinnesorgane Abt 1 Z. Für Psychol.* 88, 225–252.

Scoville, W. B., and Milner, B. (1957). Loss of recent memory after bilateral hippocampal lesions. *J. Neurol. Neurosurg. Psychiatry* 20, 11–21. doi: 10.1136/jnnp.20.1.11

Shaikh, M. B., Schubert, K., and Siegel, A. (1994). Basal amygdaloid facilitation of midbrain periaqueductal gray elicited defensive rage behavior in the cat is mediated through NMDA receptors. *Brain Res.* 635, 187–195. doi: 10.1016/0006-8993(94)91438-9

Shaikh, M. B., and Siegel, A. (1994). Neuroanatomical and neurochemical mechanisms underlying amygdaloid control of defensive rage behavior in the cat. *Braz. J. Med. Biol. Res.* 27, 2759–2779.

Siegel, A., Roeling, T. A., Gregg, T. R., and Kruk, M. R. (1999). Neuropharmacology of brain-stimulation-evoked aggression. *Neurosci. Biobehav. Rev.* 23, 359–389. doi: 10.1016/s0149-7634(98)00040-2

Silk, J. B. (1999). Male bonnet macaques use information about third-party rank relationships to recruit allies. *Anim. Behav.* 58, 45–51. doi: 10.1006/anbe.1999.1129

Singleton, G. R., and Krebs, C. J. (2007). "Chapter 3 - The secret world of wild mice," in *The Mouse in Biomedical Research (Second Edition)*, eds J. G. Fox, M. T. FDavisson, F. W. Quimby, S. W. Barthold, C. E. Newcomer and A. L. Smith (Burlington: Academic Press), 25–51. Available online at: https://www.sciencedirect.com/science/article/pii/B9780123694546500157.

Smith, Y., Wichmann, T., and DeLong, M. R. (2014). Corticostriatal and mesocortical dopamine systems: do species differences matter? *Nat. Rev. Neurosci.* 15:63. doi: 10.1038/nrn3469-c1

So, N., Franks, B., Lim, S., and Curley, J. P. (2015). A social network approach reveals associations between mouse social dominance and brain gene expression. *PLoS One* 10:e0134509. doi: 10.1371/journal.pone.0134509

Squire, L. R. (2009). The legacy of patient H.M. for neuroscience. *Neuron* 61, 6–9. doi: 10.1016/j.neuron.2008.12.023

Stevenson, P. A., and Schildberger, K. (2013). Mechanisms of experience dependent control of aggression in crickets. *Curr. Opin. Neurobiol.* 23, 318–323. doi: 10.1016/j.conb.2013.03.002

Sun, Q., Li, X., Li, A., Zhang, J., Ding, Z., Gong, H., et al. (2020). Ventral hippocampal-prefrontal interaction affects social behavior via parvalbumin positive neurons in the medial prefrontal cortex. *iScience* 23:100894. doi: 10.1016/j.isci.2020.100894

Takahashi, A., Nagayasu, K., Nishitani, N., Kaneko, S., and Koide, T. (2014). Control of intermale aggression by medial prefrontal cortex activation in the mouse. *PLoS One* 9:e94657. doi: 10.1371/journal.pone.0094657

Tanaka, K. Z., He, H., Tomar, A., Niisato, K., Huang, A. J. Y., and McHugh, T. J. (2018). The hippocampal engram maps experience but not place. *Science* 361, 392–397. doi: 10.1126/science.aat5397

Tavares, R. M., Mendelsohn, A., Grossman, Y., Williams, C. H., Shapiro, M., Trope, Y., et al. (2015). A map for social navigation in the human brain. *Neuron* 87, 231–243. doi: 10.1016/j.neuron.2015.06.011

Terranova, J. I., Song, Z., Larkin, T. E., Hardcastle, N., Norvelle, A., Riaz, A., et al. (2016). Serotonin and arginine-vasopressin mediate sex differences in the regulation of dominance and aggression by the social brain. *Proc. Natl. Acad. Sci. U S A* 113, 13233–13238. doi: 10.1073/pnas.1610446113

Tolman, E. C. (1948). Cognitive maps in rats and men. *Psychol. Rev.* 55, 189–208. doi: 10.1037/h0061626

Tovote, P., Fadok, J. P., and Lüthi, A. (2015). Neuronal circuits for fear and anxiety. *Nat. Rev. Neurosci.* 16, 317–331. doi: 10.1038/nrn3945

Van de Poll, N. E., De Jonge, F., Van Oyen, H. G., and Van Pelt, J. (1982). Aggressive behaviour in rats: effects of winning or losing on subsequent aggressive interactions. *Behav. Processes* 7, 143–155. doi: 10.1016/0376-6357(82)90023-7

van der Kooij, M. A., Hollis, F., Lozano, L., Zalachoras, I., Abad, S., Zanoletti, O., et al. (2018). Diazepam actions in the VTA enhance social dominance and mitochondrial function in the nucleus accumbens by activation of dopamine D1 receptors. *Mol. Psychiatry* 23, 569–578. doi: 10.1038/mp.2017.135

Van Wilgenburg, E., Clémencet, J., and Tsutsui, N. D. (2010). Experience influences aggressive behaviour in the Argentine ant. *Biol. Lett.* 6, 152–155. doi: 10.1098/rsbl.2009.0616

Veening, J. G., Coolen, L. M., de Jong, T. R., Joosten, H. W., de Boer, S. F., Koolhaas, J. M., et al. (2005). Do similar neural systems subserve aggressive and sexual behaviour in male rats? Insights from c-Fos and pharmacological studies. *Eur. J. Pharmacol.* 526, 226–239. doi: 10.1016/j.ejphar.2005.09.041

Victora, C. G., Wagstaff, A., Schellenberg, J. A., Gwatkin, D., Claeson, M., and Habicht, J.-P. (2003). Applying an equity lens to child health and mortality: more of the same is not enough. *Lancet* 362, 233–241. doi: 10.1016/S0140-6736(03)13917-7

Wang, L., Chen, I. Z., and Lin, D. (2015). Collateral pathways from the ventromedial hypothalamus mediate defensive behaviors. *Neuron* 85, 1344–1358. doi: 10.1016/j.neuron.2014.12.025

Wang, F., Kessels, H. W., and Hu, H. (2014). The mouse that roared: neural mechanisms of social hierarchy. *Trends Neurosci.* 37, 674–682. doi: 10.1016/j.tins.2014.07.005

Wang, F., Zhu, J., Zhu, H., Zhang, Q., Lin, Z., and Hu, H. (2011). Bidirectional control of social hierarchy by synaptic efficacy in medial prefrontal cortex. *Science* 334, 693–697. doi: 10.1126/science.1209951

Warden, M. R., Selimbeyoglu, A., Mirzabekov, J. J., Lo, M., Thompson, K. R., Kim, S.-Y., et al. (2012). A prefrontal cortex-brainstem neuronal projection that controls response to behavioural challenge. *Nature* 492, 428–432. doi: 10.1038/nature11617

Watanabe, N., and Yamamoto, M. (2015). Neural mechanisms of social dominance. *Front. Neurosci.* 9:154. doi: 10.3389/fnins.2015.00154

Whitten, P. L. (1983). Diet and dominance among female vervet monkeys (*Cercopithecus aethiops*). *Am. J. Primatol.* 5, 139–159. doi: 10.1002/ajp.1350050205

Wilkinson, R. G., Marmot, M., and World Health Organization Regional office for Europe. (1998). *The Solid Facts: Social Determinants of Health*. Copenhagen: WHO Regional Office for Europe. Available online at: https://apps.who.int/iris/handle/10665/108082.

Wilson, C. J. (1987). Morphology and synaptic connections of crossed corticostriatal neurons in the rat. *J. Comp. Neurol.* 263, 567–580. doi: 10.1002/cne.902630408

Wilson, E. O. (1975). *Sociobiology: the New Synthesis*. Cambridge, MA: Belknap Press of Harvard University Press. Available online at: https://search.library.wisc.edu/catalog/999469896202121.

Winberg, S., and Nilsson, G. E. (1993). Roles of brain monoamine neurotransmitters in agonistic behaviour and stress reactions, with particular reference to fish. *Comp. Biochem. Physiol. C. Pharmacol. Toxicol. Endocrinol.* 106, 597–614. doi: 10.1016/0742-8413(93)90216-8

Zayan, R. C. (1974). Le role de la reconnaissance individuelle dans la stabilite des relations hierarchiques chez *Xiphophorus* (Pisces, Poeciliidae). *Behaviour* 49, 268–312.

Zayan, R. C. (1975a). Modification des effets liés à la priorité de résidence chez *Xiphophorus* (Pisces, Poeciliidae): le rôle des manipulations expérimentales. *Z. Für Tierpsychol.* 39, 463–491.

Zayan, R. C. (1975b). Défense du territoire et reconnaissance individuelle chez *Xiphophorus* (Pisces, Poeciliidae). *Behaviour* 52, 266–312.

Zhang, C., Zhu, H., Ni, Z., Xin, Q., Zhou, T., Wu, R., et al. (2022). Dynamics of a disinhibitory prefrontal microcircuit in controlling social competition. *Neuron* 110, 516–531.e6. doi: 10.1016/j.neuron.2021.10.034

Zhou, T., Zhu, H., Fan, Z., Wang, F., Chen, Y., Liang, H., et al. (2017). History of winning remodels thalamo-PFC circuit to reinforce social dominance. *Science* 357, 162–168. doi: 10.1126/science.aak9726

Zink, C. F., Tong, Y., Chen, Q., Bassett, D. S., Stein, J. L., and Meyer-Lindenberg, A. (2008). Know your place: neural processing of social hierarchy in humans. *Neuron* 58, 273–283. doi: 10.1016/j.neuron.2008.01.025

Conflict of Interest: The authors declare that the research was conducted in the absence of any commercial or financial relationships that could be construed as a potential conflict of interest.

frontiers | Frontiers in Cellular Neuroscience

ORIGINAL RESEARCH
published: 06 June 2022
doi: 10.3389/fncel.2022.891912

Potassium Channel Conductance Is Involved in Phenylephrine-Induced Spontaneous Firing of Serotonergic Neurons in the Dorsal Raphe Nucleus

Jing Wang[1,2†], Yingzi Wang[1†], Xiaona Du[1] and Hailin Zhang[1]*

[1] Department of Pharmacology, The Key Laboratory of Neural and Vascular Biology, Ministry of Education, The Key Laboratory of New Drug Pharmacology and Toxicology, Hebei Medical University, Shijiazhuang, China, [2] Department of Pharmacochemistry, Hebei University of Chinese Medicine, Shijiazhuang, China

The serotonergic (5-HT) network from the dorsal raphe nucleus (DRN) of the brain has been demonstrated to regulate cognition, emotion, and behaviors, including learning and the sleep-wake cycle. Dysregulation of the activity of 5-HT neurons in the DRN is thought to play an important role in emotional disorders. The activity of 5-HT neurons is regulated by norepinephrine (NE) released from the projection terminals of noradrenergic input from the locus coeruleus (LC) *via* activation of the α1-adrenoceptor. However, insight into the molecular mechanism underlying this NE-induced regulation of 5-HT neuron activity is not clear. In this study, using the agonist of α1-adrenoceptor phenylephrine (PE), brain slices, and patch clamp, we found that A-type, Kv7/KCNQ, and calcium-activated low-conductance K^+ channels (SK) underlie PE-induced spontaneous firing in DRN 5-HT neurons. Using single-cell PCR and immunofluorescence, we also identified the isoforms of these K^+ channel families that might contribute to the NE/PE-induced spontaneous firing of DRN 5-HT neurons.

Keywords: serotonergic neuron, phenylephrine, dorsal raphe nucleus, activity, A-type K^+ channels, Kv7/KCNQ K^+ channels, calcium-activated small-conductance K^+ (SK) channels

OPEN ACCESS

Edited by:
Grzegorz Hess,
Jagiellonian University, Poland

Reviewed by:
Marcin Siwiec,
Maj Institute of Pharmacology (IF PAS), Poland
Samir Haj-Dahmane,
University at Buffalo, United States
Joanna Urban-Ciećko,
Nencki Institute of Experimental Biology (PAS), Poland

***Correspondence:**
Hailin Zhang
zhanghl@hebmu.edu.cn

† These authors have contributed equally to this work

Specialty section:
This article was submitted to Cellular Neurophysiology, a section of the journal Frontiers in Cellular Neuroscience

Received: *08 March 2022*
Accepted: *22 April 2022*
Published: *06 June 2022*

Citation:
Wang J, Wang Y, Du X and Zhang H (2022) Potassium Channel Conductance Is Involved in Phenylephrine-Induced Spontaneous Firing of Serotonergic Neurons in the Dorsal Raphe Nucleus. Front. Cell. Neurosci. 16:891912. doi: 10.3389/fncel.2022.891912

INTRODUCTION

The serotonergic (5-HT) system originating in the dorsal raphe nucleus (DRN) plays a central role in multiple important brain functions, including learning, cognition, emotion, and the sleep-wake cycle (Lucki, 1998; Monti, 2010; Kawashima, 2018). There is ample evidence that the activity of DRN 5-HT neurons is correlated with reward levels (Nakamura et al., 2008; Bromberg-Martin et al., 2010; Hayashi et al., 2015), aversive stimuli (Schweimer and Ungless, 2010; Hayashi et al., 2015), and the absence of rewards (Li et al., 2013). Moreover, altered activity of these DRN 5-HT neurons is associated with the response to stress and the onset of psychiatric disorders such as major depressive disorder (MDD) and anxiety (Ohmura et al., 2020; Prakash et al., 2020; Zou et al., 2020). For a better understanding of the activity-dependent role of DRN 5-HT neurons in the above physiological and pathological processes, it is essential to understand the molecular/ionic mechanisms underlying the electrical discharge activity of these neurons.

Abbreviations: ACSF, artificial cerebrospinal fluid; DRN, dorsal raphe nucleus; HEPES, *N*-2-hydroxyethylpiperazine-*N*′-2-ethanesulfonic acid; I_A, A-type currents; I_M, M-type current; LC, locus coeruleus; MDD, major depressive disorder; NE, norepinephrine; PE, phenylephrine; PFA, paraformaldehyde; RTN, retrotrapezoid nucleus; SK, calcium-activated small-conductance K^+ channels; TEA, tetraethylammonium; TPH, tryptophan hydroxylase; 4-AP, 4-aminopyridine.

In most species, the 5-HT neurons of the DRN fire electrical discharges when recorded *in vivo*, with a slow, tonic firing pattern at typical frequency of about 0.5–3 Hz (Aghajanian et al., 1968; Aghajanian and Vandermaelen, 1982; Allers and Sharp, 2003). However, when recorded *in vitro* in brain slices, the 5-HT neurons are silent and do not fire spontaneously unless triggered by norepinephrine (NE), the transmitter released in the DRN mainly from the projection terminals of the noradrenergic input from the locus coeruleus (LC). In this case, the 5-HT neurons fire spontaneously after either NE or the α_1-adrenoceptor agonist phenylephrine (PE) is applied to the brain slices (Vandermaelen and Aghajanian, 1983; Pan et al., 1990; Judge and Gartside, 2006). These results suggest that noradrenergic modulation is critical for the firing activity of DRN 5-HT neurons. However, the molecules/ion channels responsible for this NE-induced modulation have not been elucidated.

Early studies suggest that NE or PE-induced firing initiation of DRN 5-HT neurons appears to depend in large part on the closure of membrane K^+ conductance (Aghajanian, 1985; Leonard, 2002), with the involvement of A-type K^+ currents (I_A) (Aghajanian, 1985). However, this mechanism has not been clearly elucidated. Subthreshold K^+ conductance is the most important determinant for triggering neuron firing. An example of this is the Kv7/KCNQ/M current (I_M). KCNQ/M-type currents have been shown to be involved in the regulation of spontaneous firing of central neurons, including DRN 5-HT neurons (Zhao et al., 2017; Su et al., 2019). In addition, KCNQ channels in chemosensitive neurons of the retrotrapezoid nucleus (RTN) have been reported to be the downstream effectors of NE modulation of RTN activity (Kuo et al., 2016). However, it is not known if KCNQ/M-type currents are also involved in NE-induced spontaneous firing of DRN 5-HT neurons. Another potential candidate for the K^+ conductance relevant here is the calcium-activated low-conductance K^+ channel (SK channel). Several conflicting reports on the effect of NE on SK channels through activation of the α_1-adrenoceptor have been published for neurons in both central and peripheral nervous systems, including the DRN 5-HT neurons (Pan et al., 1994; Wagner et al., 2001; Maingret et al., 2008). However, there is no direct evidence for NE inhibition of SK channel currents in DRN 5-HT neurons.

In this study, we sought to find the K^+ channels underlying the NE/PE-induced spontaneous firing of DRN 5-HT neurons, focusing on the A-type, KCNQ/M, and SK K^+ channels. Using brain slice preparations and patch clamp, we demonstrate that PE triggers the activity of DRN 5-HT neurons through the α_1-adrenoceptor and inhibition of the A-type, KCNQ/M, and SK K^+ channels. Using single-cell PCR and immunofluorescence, we also identified the isoforms of these K^+ channel families that might contribute to the NE/PE-induced spontaneous firing of DRN 5-HT neurons.

MATERIALS AND METHODS

Animal Preparation

Male 6- to 8-week-old C57BL/6 mice (Vital River, China) were used for the studies. All experiments were performed in accordance with the guidelines of the Animal Care and Use Committee of Hebei Medical University and approved by the Animal Ethics Committee of Hebei Medical University.

Ethics Statement

All experiments were performed in accordance with the guidelines of Animal Care and Use Committee of Hebei Medical University.

Brain Slice Preparation

The details for preparation of coronal brain sections containing DRN were the same as described in our previous work (Zhao et al., 2017). Briefly, mice were anesthetized with chloral hydrate [200 mg/kg, intraperitoneally (i.p.)]. After intracardial perfusion with an ice-cold sucrose solution (260 mM sucrose, 25 mM $NaHCO_3$, 2.5 mM KCl, 1.25 mM NaH_2PO_4, 2 mM $CaCl_2$, 2 mM $MgCl_2$, and 10 mM D-glucose; osmolarity, 295–305 mOsm; saturated with 95% O_2 and 5% CO_2), the brains of the mice were removed quickly and placed into the slicing solution. Coronal midbrain slices (200 μm thick) containing DRN (AP −3.8 to −4.8 mm; LM 0 mm; and DV −2.8 to −3.8 mm) were sectioned with a vibratome (VT1200S; Leica, Germany). The sections were incubated for 30 min at 36°C in oxygenated artificial cerebrospinal fluid (ACSF) (in mM: 124 NaCl, 3 KCl, 1.25 NaH_2PO_4, 2 $CaCl_2$, 2 $MgCl_2$, 25 $NaHCO_3$, 10 D-glucose; osmolarity, 280–300 mOsm), and stored at room temperature for 90 min (23–25°C) before use.

Identification of 5-HT Neurons and Electrophysiological Recordings

5-HT neurons located in the midline of the ventromedial subdivisions of the DRN were used. DRN 5-HT neurons were identified by single-cell PCR for the presence of tryptophan hydroxylase (TPH). Recordings in the slices were performed in whole-cell voltage-clamp configurations on a Multiclamp 700B amplifier coupled with a Digidata 1440A AD converter (Molecular Devices, United States) using borosilicate patch electrodes (1–3 MΩ) wrapped with parafilm to reduce pipette capacitance. Pipette series resistance (typically 4–8 MΩ) was compensated by 70–85% during voltage-clamp experiments and was checked frequently throughout the experiment; data were not used if series resistance changed by >15%. Voltage signals were filtered at 10 kHz and sampled at 20 μs using a Digidata 1440A data acquisition interface (Molecular Devices) and pClamp 9 software (Molecular Devices). For recording K^+ currents, glass electrodes (3–5 MΩ) were filled with the following internal solutions, namely, 115 mM K-methylsulfate, 20 mM KCl, 1 mM $MgCl_2$, 10 mM *N*-2-hydroxyethylpiperazine-*N*′-2-ethanesulfonic acid (HEPES), 0.1 mM EGTA, 2 mM MgATP, and 0.3 mM Na_2GTP, pH adjusted to 7.4 with KOH. For recording I_M and SK currents, ACSF was used as extracellular solution. For recording I_A current, HEPES-buffered ACSF (130 mM NaCl, 4 mM KCl, 2 mM $CaCl_2$, 2 mM $MgCl_2$, 10 mM HEPES, 10 mM D-glucose; 280–300 mOsm) was used as extracellular solution. To optimally isolate the outward SK currents from other K^+ currents and the Na^+ currents, 5 mM tetraethylammonium (TEA) and

1 μM tetrodotoxin were added to the extracellular solution in voltage-clamp experiments (Sailer et al., 2002; Pedarzani et al., 2005). For isolating A-type currents (I_A), 1 μM tetrodotoxin was used to block fast voltage-activated Na^+ channels, and 0.3 μM $CdCl_2$ was used to block voltage-activated Ca^{2+} channels (Itri et al., 2010; Hu et al., 2019).

For recording spontaneous firing of the neurons, cell-attached "loose-patch" (100–300 MΩ) recordings were used (Burlet et al., 2002). In this case, patch pipettes (2–4 MΩ) were filled with ACSF, and the spontaneous activity was recorded in the current-clamp mode (I = 0). All of the experiments were performed at room temperature (25 ± 2°C). In our recordings, the majority of the recorded neurons, ∼90%, were silent without added PE, and indeed a small number of recorded cells (∼10%, 10 out of 100) had activity of spontaneous firing. However, these neurons with spontaneous firing were found mostly to be either dopaminergic neurons or glutamatergic neurons as verified by the single-cell PCR post the electrophysiological recordings (n = 8, 80% dopaminergic neurons; n = 1, 10% glutamatergic neurons). The dopamine and glutamatergic neurons in DRN were also reported in the literature (Soiza-Reilly and Commons, 2011; Matthews et al., 2016; Commons, 2020). Therefore, neurons exhibiting spontaneous activity were not included for data analysis.

Immunofluorescence

After intracardial perfusion with 4% paraformaldehyde (PFA) in 0.01 M phosphate-buffered saline (PBS) (pH 7.4), followed by 0.01 M PBS, mice brains were post-fixed in 4% PFA at 4°C for 48 h and coronal midbrain slices were prepared. Sections (50 μm thick) were blocked with 0.3% Triton X-100 and 10% donkey serum (Biological Industries, Israel) in PBS and incubated overnight at 4°C with a mixture of primary antibodies. Sections were then washed with PBS three times (5 min) and then incubated in a mixture of secondary antibodies at room temperature for 2 h. Sections were then washed three times (7 min) with PBS. Finally, slices were mounted with Prolong Gold antifade reagent (Life Technologies, United States). Images were obtained on a Leica TCS SP5 confocal laser microscope (Leica, Germany) equipped with laser lines for FITC (Argon 488) and cy3 (HeNe 543). Images were analyzed with LAS-AF-Lite software (Leica, Germany).

Single-Cell PCR

PrimeScript™ II 1st Strand cDNA Synthesis Kit (Takara-Clontech, Japan) was used to perform reverse transcription. At the end of electrophysiological recordings, the recorded cell was aspirated into a pipette and then expelled into a sterile PCR tube containing 1 μl oligo-dT primer and 1 μl dNTP mixture. The mixture was heated to 65°C for 5 min and then cooled on ice for 2 min. Synthesis of the first single-strand cDNA from the cellular mRNA was performed with PrimeScript II reverse transcriptase (Takara) at 50°C for 50 min and then 85°C for 5 min. cDNA was stored at −20°C. Then, single-strand cDNA was amplified using GoTaq Green Master Mix (Promega, United States). Two rounds of conventional PCR with pairs of gene-specific outer (first round) and inner primers (second round) for GAPDH (positive control), TPH, Kv4.1–4.3, 3.3, 3.4, Kv1.4, SK1–3, and KCNQ1–5 were performed. After adding the specific outer primer pairs into each PCR tube (final volume 25 μl), first-round synthesis was performed as follows, namely, 95°C (5 min); 30 cycles of 95°C (50 s), 60°C (50 s), 72°C (50 s); 72°C (5 min). Then, 2 μl of the first PCR product were used for the second amplification with specific inner primers (final volume 25 μl). The second-round amplification was performed as follows, namely, 95°C (5 min); 35 cycles of 95°C (50 s), 58–63°C (45 s), 72°C (50 s) and 5 min elongation at 72°C. The final PCR products were separated by electrophoresis on 2% agarose gels. Negative control reactions with no added template were included in each experiment.

The "outer" primers (from 5′ to 3′) were as follows:

GAPDH	AAATGGTGAAGGTCGGTGTGAACG (sense)	AGTGATGGCATGGACTGTGGTCAT (antisense)
TPH	GAGTCCTCATGTACGGCACC	AGGCCGAACTCGATTGTGAA
Kv1.4	CTCTGGGCTCCACTAACGAG	CTTCTCAGAGACTCGGCGTT
Kv3.3	TGCTCAACTACTACCGCACC	AAGAATAGGGAGGCGAAGGC
Kv3.4	ACGTGACGGAGATTCATCGG	TCTTGAAGTCGGTGTGGTCG
Kv4.1	ACCACACTTGGGTATGGAG	TGAACTCGTGACACGTAGTCTTCT
Kv4.2	CGCTCTGATAGTGCTGAACG	CCTGCGGTCCTTGTACTCCT
Kv4.3	ATGCATCTCTGCCTACGACG	CTGCGGATGAAGCGGTATCT
KCNQ1	CCCAGTGCTGAAAGGAAGCG	ACGAAACACTTCCAACCCGT
KCNQ2	TCATCCCACCTCTGAACCAG	TGGGCGCAGACTCTCTTTG
KCNQ3	AGACGTGGAGCAAGTCACCTT	CCAGCCTTTGTATCGACAGC
KCNQ4	CCCGGGTGGACCAAATTGT	AGCCCTTCAGTCCATGTTGG
KCNQ5	GAAGCCGCTCTCCTACACC	TTCTGTCCATGCGCACCATA
SK1	GTCTCCTCCTGGATCGTTGC	CTTGGTGAGCTGTGTGTCCAT
SK2	ACCCTAGTGGATCTGGCAAAG	GAGCGCTCAGCATTGTAGGA
SK3	GGCGGATAGCCATGACCTAC	AAAGGTCCACCAGGGTGTTG

The "inner" primers (from 5′ to 3′) were as follows:

GAPDH	GCAAATTCAACGGCACAGTCAAGG	TCTCGTGGTTCACACCCATCACAA
TPH	TGGCTACAGGGAAGACAACG	GTATCTGGTTCCGGGGTGTA
Kv1.4	GACAACCGAACTTGTTCCGT	GTCTTAGCACTTGCCTTCTC
Kv3.3	GGGCTTCTGGGGCATAGAC	GTCCTGAAAACACAGACGCTT
Kv3.4	TTGTGTGCTGCCCTGATACG	GACAAACCACTCAATCCCACC
Kv4.1	TTGGGTCCATCTGCTCACTT	GGCCCCCATTTTGCTTATAC
Kv4.2	CCTGGAACGATACCCAGACAC	CCCGTGCGGTAGAAGTTGA
Kv4.3	AGCTTCCGTCAGACCATGTG	GGCAAAAGAAAGCCACCGAAT
KCNQ1	GTGTCCCTTCTCACTGGAGC	CACTGTAGATGGAGACCCGC
KCNQ2	CATCACCAAGTCAGAAGGTCAG	ACAAACTCGCAGTTACAGCTC
KCNQ3	CAAGTACAGGCGCATCCAAAC	GGCCAGAATCAAGCATCCCA
KCNQ4	ATGGGGCGCGTAGTCAAGGT	GGGCTGTGGTAGTCCGAGGTG
KCNQ5	GTTCGTCTACCACGCGTTC	CGAGCAAACCTCAGTCTTCC
SK1	ATGGTGCCGCATACCTACTG	CACGTGTTTCTCAGCCTTGG
SK2	GGATCTGGCAAAGACCCAGAAT	AGGGAGGGCATGAATGCTAC
SK3	CCCCATCCCTGGAGAGTACA	TTCACAGACTCGCACAGTCC

Drugs

All drugs were bath applied at the following concentrations, namely, PE (10 μM; Tocris), prazosin (5 μM; Sigma), apamin (500 nM; Sigma), 4-aminopyridine (4-AP; 4 mM; Sigma), XE991 (3 μM; Tocris), 6-cyano-7-nitroquinoxaline-2,3-dione (CNQX; 10 μM; Sigma), DL-2-amino-5-phosphonopentanoic acid (APV; 50 μM; Sigma), strychnine (2 μM; Sigma), and gabazine (10 μM; Sigma).

Commercial antibodies used were anti-TPH (1:400, mouse, sigma, T0678, RRID:AB_261587), anti-Kv4.2 (1:400, rabbit, AlomoneLabs, APC-023, RRID:AB_2040176), anti-Kv4.3 (1:400, rabbit, AlomoneLabs, APC-017, RRID:AB_2040178), anti-SK2 (1:200, rabbit, Bioss, DF13499, RRID:AB_2846518), anti-SK3 (1:200, rabbit, Proteintech, 17188-1-AP), anti-KCNQ2 (1:200, goat, Santa Cruz, sc-7793, RRID:AB_2296585), anti-KCNQ3 (1:200, goat, Santa Cruz, sc-7794, RRID:AB_2131714), and anti-KCNQ4 (1:200, rabbit, AlomoneLabs, APC-164, RRID:AB_2341042). Secondary antibodies used were donkey anti-mouse IgG (H + L) highly cross-adsorbed secondary antibody (Alexa Fluor 568, Thermo Fisher Scientific, A10037, RRID:AB_2534013, 1:1,000), donkey anti-rabbit IgG (H + L) highly cross-adsorbed secondary antibody (Alexa Fluor 488, Thermo Fisher Scientific, A-21206, RRID:AB_2535792, 1:1,000), and donkey anti-goat IgG (H + L) cross-adsorbed secondary antibody (Alexa Fluor 488, Thermo Fisher Scientific, A-11055, RRID:AB_2534102, 1:1,000).

Statistics

All data are expressed as mean ± SEM. Group size (n) indicates the number of independent, non-technical replicates. For electrophysiological data, the discharge rate and the current amplitudes were compared using the paired t-test, when data were normally distributed and there was no significant variance inhomogeneity. When normality or equal variance of samples was not present, the Wilcoxon matched-pairs signed-rank test was used. p-Values ≤ 0.05 were accepted as statistically significant. Data analysis was carried out using GraphPad Prism 6.0 (RRID:SCR_002798).

RESULTS

Previous studies have shown that activation of the α_1-adrenoceptor (by NE or PE) in DRN 5-HT neurons is associated with a depolarization of resting membrane potential and an increase in input resistance, likely due to reduced K^+ conductance (Aghajanian, 1985). However, the identity of this K^+ conductance is not known. After reviewing the experimental evidence in the literature described in the introduction, we aimed to study three families of K^+ channels, namely, the A-type, the KCNQ/M, and the SK channels. We first verified that PE, the selective α1-adrenoceptor agonist, elicits spontaneous firing of DRN 5-HT neurons that were otherwise silent. Firings of the neurons were recorded in DRN brain slices using a "loose cell-attached patch" method (Burlet et al., 2002), and the recorded neurons were located in the midline in the ventromedial subdivision of the DRN (**Figure 1A**), as 5-HT neurons are reported to be most densely located in this region (Gocho et al., 2013). 5-HT neurons were identified by the presence of TPH in single-cell PCR analysis after electrophysiological recordings (**Figure 1B**). PE (10 μM) significantly induced a slow (<5 Hz), clock-like discharge of action potentials in DRN 5-HT neurons, which was inhibited by the α_1-adrenoceptor antagonist prazosin (5 μM) (**Figure 1C**).

Role of the A-Type K^+ Current in Phenylephrine-Induced Spontaneous Firing of Dorsal Raphe Nucleus 5-HT Neurons

In a previous study, A-type currents (I_A) were found to be inhibited by PE in DRN 5-HT neurons. However, it was not tested whether this inhibition contributes to the PE-induced firing of these neurons (Aghajanian, 1985). Moreover, the expression profiles of A-type channel in DRN 5-HT neurons have not been investigated. Therefore, we first examined the subtypes of A-type K^+ channels expressed in DRN 5-HT neurons using single-cell PCR and immunofluorescence analysis. Single-cell PCR results revealed a strong expression of Kv4.2 and 4.3, a weak expression of Kv4.1, and no detectable expression of Kv1.4, Kv3.3, and Kv3.4 (**Figures 2Ai,ii**). Expression of Kv4.2 and Kv4.3 proteins in DRN 5-HT neurons was also confirmed by immunofluorescence, which showed strong signals for these channel proteins (**Figure 2B**), consistent with the results of single-cell PCR. These results suggest that Kv4.2 and 4.3 are the dominant A-type K^+ channels in DRN 5-HT neurons and mediate the majority of I_A. Next, we investigated the role of these A-type K^+ channels in PE-induced firing of 5-HT neurons. Synaptic blockers (CNQX, APV, and gabazine) were added to isolate the intrinsic firing properties and I_A were recorded using the protocol shown in **Figure 2Ci**; the cells were voltage-clamped at −70 mV, followed by a hyperpolarizing step to −100 mV (200 ms), and then a step depolarization to −20 mV (300 ms). I_A were isolated as characteristic transient currents with rapid activation and inactivation, measured as instantaneous currents at the beginning of the −20 mV step. Bath application of PE (10 μM) significantly reduced peak I_A currents (from 0.77 ± 0.05 to 0.37 ± 0.04 nA, $n = 6$, $p < 0.0001$, paired t-test), and this reduction was significantly reversed by prazosin (5 μM; **Figure 2C**), the antagonist of α_1-adrenoceptors. This result, in combination with the results shown in **Figure 1**, suggests that inhibition of I_A currents contributes to the PE-induced spontaneous firing of DRN 5-HT neurons. To confirm this, we tested the effect of A-type channel blocker, 4-AP. 4-AP at maximal I_A inhibiting concentration (4 mM) (Yao and Tseng, 1994; Serôdio et al., 1996; Song et al., 1998) also induced spontaneous firing in DRN 5-HT neurons, suggesting that inhibition of I_A indeed triggers spontaneous firing. However, in the continued presence of 4-AP, PE (10 μM) further increased the firing frequency from 0.51 ± 0.06 to 1.23 ± 0.07 Hz ($n = 13$, $p < 0.0001$, paired t-test, **Figure 2D**) in a statistically significant manner, indicating that another mechanism besides I_A inhibition was involved in the PE-induced spontaneous firing of DRN 5-HT neurons.

Role of KCNQ/M-Type Current in Phenylephrine-Induced Spontaneous Firing of Dorsal Raphe Nucleus 5-HT Neurons

Our previous studies have shown that the KCNQ4 channel is the predominant Kv7/KCNQ isoform expressed in DRN 5-HT

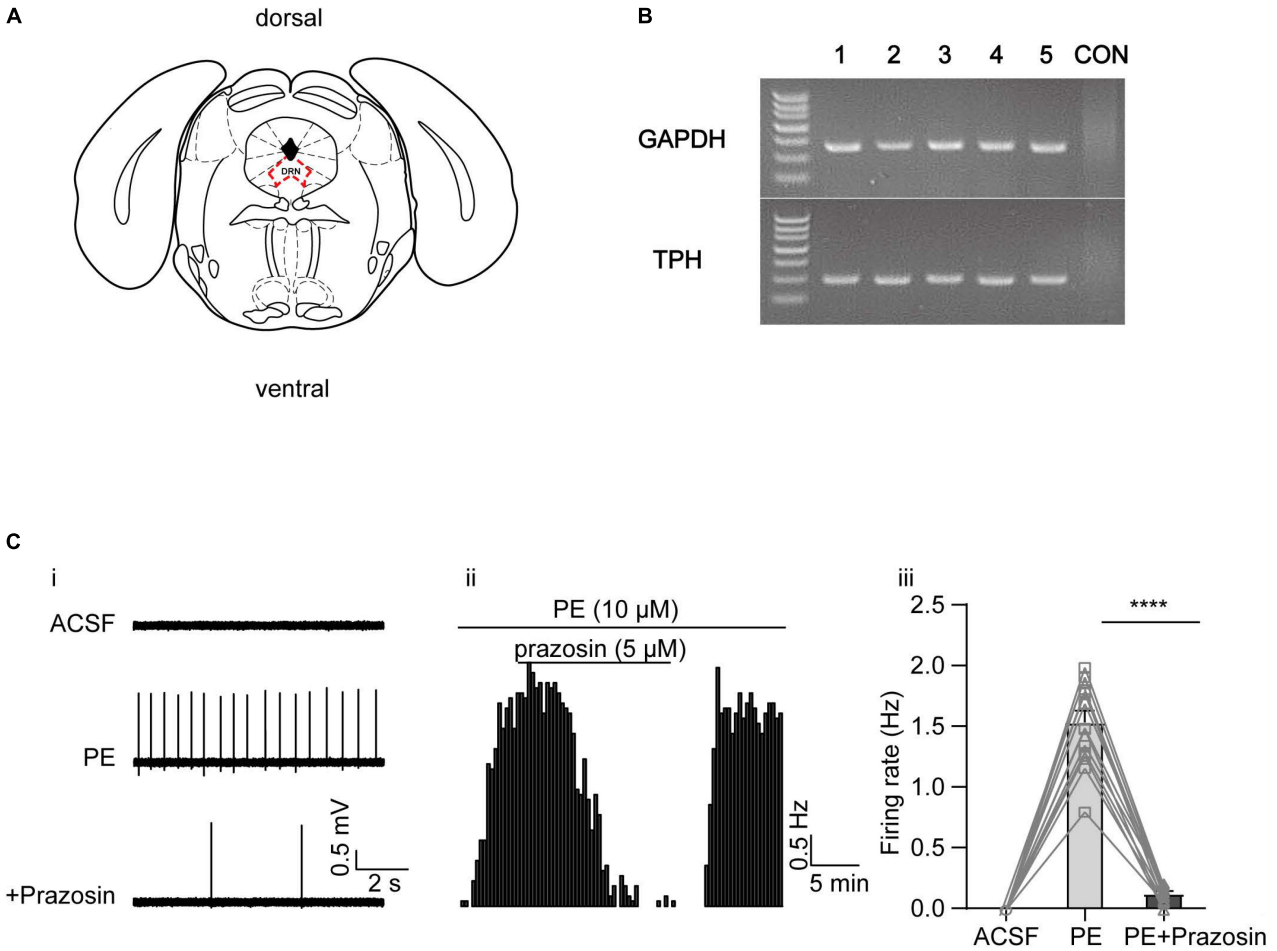

FIGURE 1 | Phenylephrine induces spontaneous firing in the DRN 5-HT neurons by activating α1 adrenergic receptor. **(A)** Schematic illustration of the dorsal raphe nucleus (DRN) on a coronal plane. **(B)** Representative image of single-cell PCR products displayed on a gel, from five DRN neurons (lanes 1–5), and a negative control ("CON") in which no DNA template from neurons was added. TPH, tryptophan hydroxylase, marker of 5-HT neurons. **(C)** PE induced the spontaneous firing activity in the DRN 5-HT neurons, which was inhibited by α1 adrenergic receptor blocker prazosin. **(i)** Representative traces of action potential spikes recorded using "loose patch" under current-clamp configuration performed on a DRN 5-HT neuron; the effects of PE (10 μM) and prazosin (5 μM) are shown. **(ii)** Example time course of the spontaneous firing frequency in a 5-HT neuron, under the influence of PE and prazosin. **(iii)** Summarized effects of PE and prazosin on the spontaneous firing frequency (paired *t*-test, $^{****}p < 0.0001$, $n = 13$).

neurons (Zhao et al., 2017), although other neuronal KCNQ members (KCNQ2, KCNQ3, and KCNQ5) in these neurons have not been studied. In this study, the results of single-cell PCR analysis revealed robust expression of KCNQ2, KCNQ3, and KCNQ4 mRNA in DRN 5-HT neurons (**Figures 3Ai,ii**). Consistently, the result of immunofluorescence analysis showed high expression levels of the KCNQ2, KCNQ3, and KCNQ4 proteins in DRN 5-HT neurons (**Figure 3B**). To correlate the PE-induced spontaneous firing with its modulation of KCNQ/M-type currents, we first examined whether PE could inhibit KCNQ/M-type currents in DRN 5-HT neurons. M-type currents were measured using the protocol shown in **Figure 3Ci** as characteristic slow deactivating tail currents at a −50 mV step from a depolarized potential of −20 mV (Zhao et al., 2017). As shown in **Figure 3C**, PE (10 μM) significantly inhibited the M-type currents from 74.67 ± 9.46 to 40.63 ± 5.69 pA ($n = 7$, $p < 0.01$, paired *t*-test). Subsequently, it was found that XE991, a selective KCNQ blocker, failed to further inhibit the M-type currents, indicating complete inhibition of this K^+ conductance by PE. Moreover, inhibition of M-type currents by XE991 resulted in depolarization of the resting membrane potential (from −63.91 ± 2.21 to −57.87 ± 1.83 mV, $n = 6$, $p < 0.05$, paired *t*-test, **Figure 3E**). With continued presence of XE991, PE (10 μM) further depolarized in a significant manner the resting membrane potential to −52.27 ± 2.47 mV. These results suggest that PE-induced inhibition of M-type current might trigger the neuronal firing. Next, we showed that blocking M-type current by addition of XE991 (3 μM) produced spontaneous firing of DRN 5-HT neurons (0.42 ± 0.06 Hz, $n = 14$, $p < 0.001$, Wilcoxon matched-pairs signed-rank test, **Figure 3D**). These results indicate that inhibition of KCNQ/M-type currents contributes to the PE-induced spontaneous firing

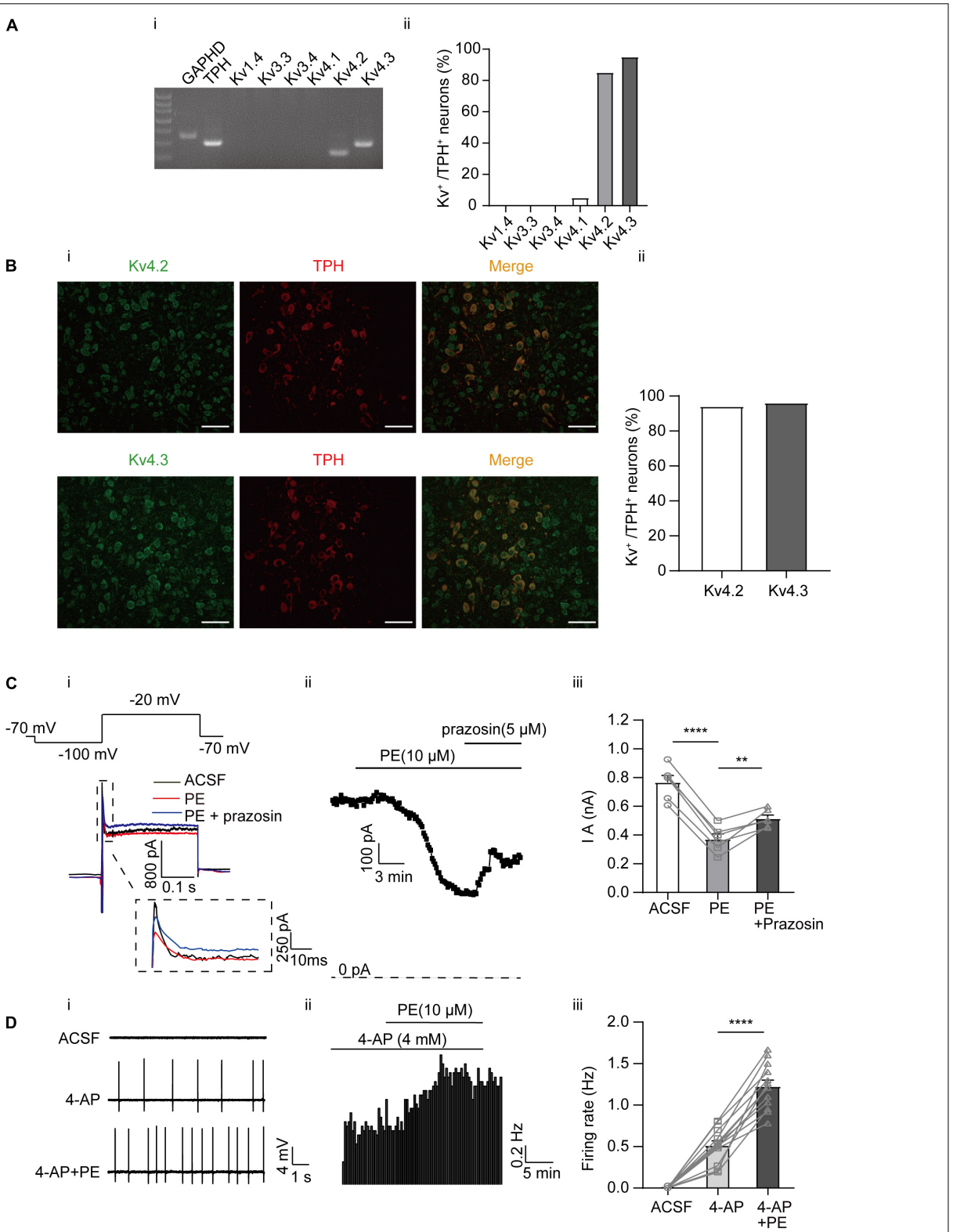

FIGURE 2 | Expression of A-type K^+ channels and their contribution to the PE-induced spontaneous firing of the DRN 5-HT neurons. **(A)** Expression of A-type K^+ channel-related subfamily members assessed using single-cell PCR analysis in the DRN neurons. **(i)** Representative image of single-cell PCR products showing the presence of different Kv subunits. **(ii)** Proportion of Kv1.4, 3.3, 3.4, and Kv4s-positive neurons in the TPH-positive neurons (n = 20). **(B) (i)** Confocal images of Kv4.2 and 4.3 protein expression in slice of the DRN, assessed using immunofluorescence methods. Scale bar = 50 μm. **(ii)** Proportion of Kv4.2 and 4.3-positive neurons

(Continued)

FIGURE 2 | in the TPH-positive neurons (n = 200). **(C)** PE potently inhibited A-type currents recorded using whole-cell patch clamp in the DRN 5-HT neurons. **(i)** Recording protocol used and the typical current traces recorded; the latter were from –20 mV. The current amplitude at the beginning of the –20 mV step was measured (dotted square, enlarged in inset). **(ii)** Time course for current amplitudes measured in **(i)**. **(iii)** Summarized data for experiments shown in **(i,ii)**. Paired t-test, $^{**}p < 0.01$, $^{****}p < 0.0001$, n = 6. **(D)** A-type K^+ channel blocker 4-AP (4 mM) induced spontaneous firing of the DRN 5-HT neurons. **(i)** Representative traces of action potential spikes recorded using "loose patch" under current-clamp configuration. **(ii)** Example time course of the spontaneous firing frequency in a 5-HT neuron, under the influence of 4-AP and PE. **(iii)** Summarized data for the effects of 4-AP and PE on the spontaneous firing frequency (paired t-test, $^{****}p < 0.0001$, n = 13).

of the DRN 5-HT neurons. Consistent with the involvement of multiple K^+ channels in the PE-induced spontaneous firing of the DRN 5-HT neurons, the XE991-induced firing rate was further increased when PE was applied (1.30 ± 0.12 Hz, n = 14, $p < 0.0001$, Wilcoxon matched-pairs signed-rank test, **Figure 3D**).

Role of Low-Conductance Ca^{2+}-Activated K^+ Current in Phenylephrine-Induced Spontaneous Firing of Dorsal Raphe Nucleus 5-HT Neurons

Ca^{2+}-activated K^+ (SK) channels have been shown to regulate the firing pattern of central neurons, including DRN 5-HT neurons (Pan et al., 1994; Wagner et al., 2001; Adelman et al., 2012; Gocho et al., 2013; Matschke et al., 2018). However, conflicting results have been reported regarding the role of SK channels in PE-induced firing of DRN 5-HT neurons (Pan et al., 1994; Maingret et al., 2008). Moreover, the molecular identities of the SK currents in DRN 5-HT neurons are not clear. Three isoforms of SK channels (SK1, SK2, and SK3) have been described (Adelman et al., 2012). We first examined the expression profiles of these SK channels in DRN 5-HT neurons using single-cell PCR (**Figure 4A**) and immunofluorescence approaches (**Figure 4B**). We observed strong expression of SK2 and SK3 channels in DRN 5-HT neurons at both mRNA and protein levels, suggesting that SK currents in DRN 5-HT neurons are mediated by these SK channels. It has been suggested that SK currents are primarily involved in slow afterhyperpolarization (sAHP) during action potential firing (Pan et al., 1994; Wagner et al., 2001; Adelman et al., 2012; Gocho et al., 2013; Matschke et al., 2018). We isolated the AHP outward currents (I_{AHP}) encoded by SK channels using a one-step voltage-clamp protocol (Matschke et al., 2018), the tail currents measured at the beginning of −60 mV following a depolarizing potential of 0 mV (**Figure 4Ci**). PE (10 μM) significantly inhibited the I_{AHP} in DRN 5-HT neurons, from initial current amplitudes of 44.04 ± 6.64 to 25.18 ± 6.28 pA (n = 6, $p < 0.01$, paired t-test, **Figure 4C**). It appears that PE only partially inhibited SK currents because apamin, a selective SK channel blocker, had a stronger inhibition on SK currents when applied either after (**Figures 4Ci,ii,iii**) or before (**Figures 4Di,ii,iii**) of PE. However, even with maximal inhibition of SK currents, apamin did not induce significant, sustained spontaneous firing of DRN 5-HT neurons (only a transient increase was occasionally observed, e.g., **Figure 4Eii**), although subsequent application of PE elicited firing of these neurons (**Figure 4E**). These results suggest that inhibition of SK channels does not trigger spontaneous firing of DRN 5-HT neurons.

Multiple K^+ Conductances Are Involved in the Phenylephrine-Induced Spontaneous Firing of the Dorsal Raphe Nucleus 5-HT Neurons

While blocking SK channels with apamin did not elicit as strong firing activity as blocking A-type and KCNQ/M channels, apamin triggered transient, sparse firing activity in some DRN 5-HT neurons (see, e.g., **Figure 4Eii**). This prompted us to further test the effect of apamin. We first induced firing of DRN 5-HT neurons using both XE991 and 4-AP to block A-type and KCNQ/M K^+ currents, and then additionally applied apamin. As shown in **Figure 5A**, the firing rate was further increased after apamin addition (from 0.87 ± 0.05 to 1.30 ± 0.07 Hz, n = 12, $p < 0.0001$, paired t-test, **Figure 5A**). Interestingly, PE also induced further firing activity when administered in addition to XE991 and 4-AP (from 0.96 ± 0.13 to 1.54 ± 0.20 Hz, n = 12, $p < 0.001$, paired t-test, **Figure 5B**), likely due to inhibition of SK channels. Taken together, these results imply that inhibition of SK currents, although not directly triggering spontaneous firing of DRN 5-HT neurons, contributed to the PE-induced firing activity of DRN 5-HT neurons.

Finally, to prove that the K^+ conductance of A-type, KCNQ/M, and SK channels are sufficient components for the PE-induced spontaneous firing of DRN 5-HT neurons, a cocktail of the blockers for these K^+ channels (4-AP, XE991, and apamin) was tested. The blocker cocktail evoked spontaneous firing of DRN 5-HT neurons (1.34 ± 0.39 Hz, n = 9, **Figure 5C**), which was not further enhanced by subsequent addition of PE (1.47 ± 0.32 Hz, n = 9, $p > 0.05$, paired t-test). These results suggest that blocking K^+ channels (A-type, KCNQ/M, and SK currents) is a sufficient mechanism to trigger PE-induced spontaneous firing of DRN 5-HT neurons.

DISCUSSION

In this study, we investigated the mechanism for PE-induced spontaneous firing activity in DRN 5-HT neurons. The results show that inhibition of K^+ currents from three K^+ channel families, A-type, KCNQ/M, and SK channels, likely underlies PE-induced firing of DRN 5-HT neurons.

Phenylephrine induced spontaneous firing of DRN 5-HT neurons through α1-adrenoceptor because this excitatory effect was blocked by prazosin (a specific α1-adrenoceptor antagonist). Furthermore, this excitatory effect was maintained in the

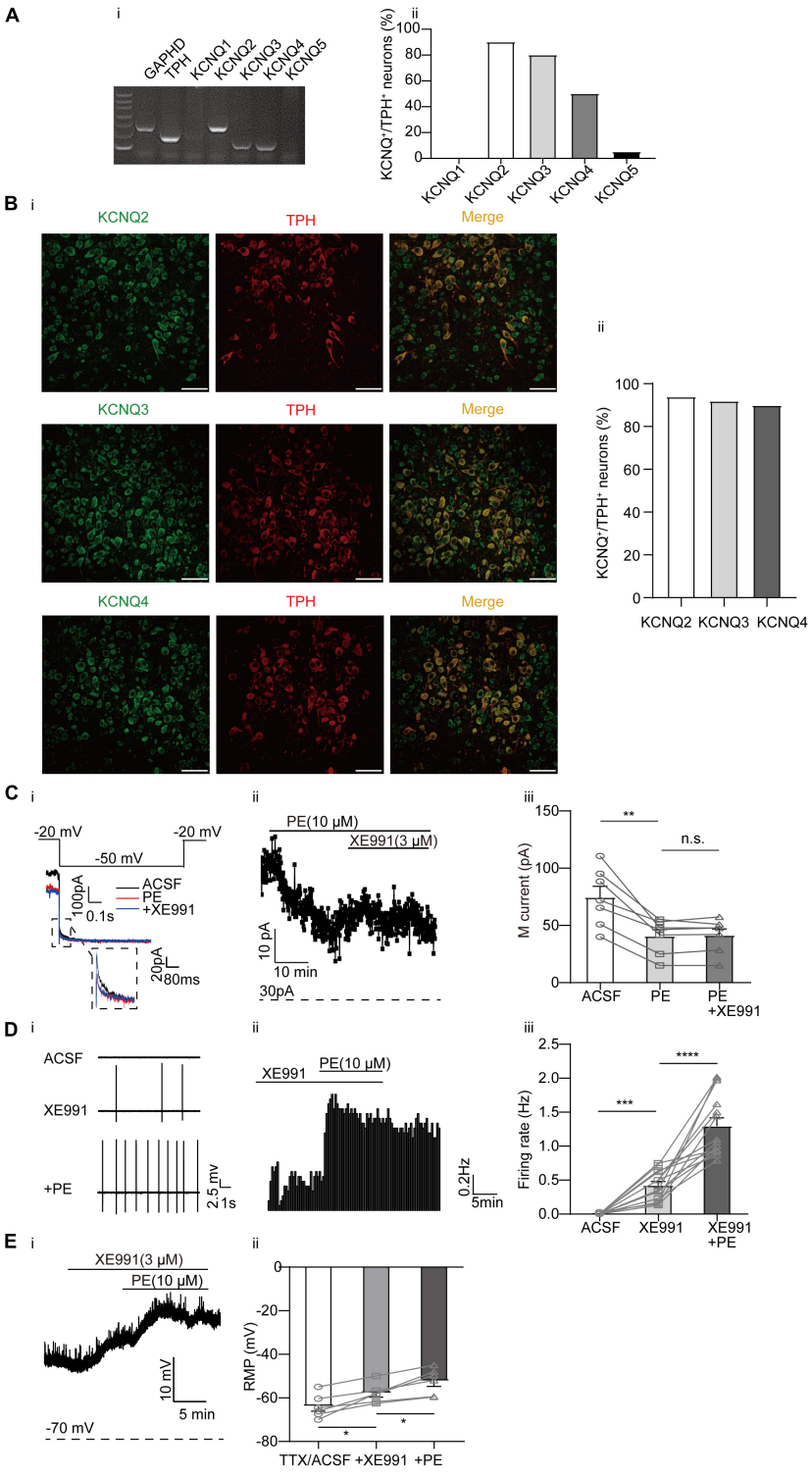

FIGURE 3 | Expression of M-type K^+ channels and their contribution to the PE-induced spontaneous firing of the DRN 5-HT neurons. **(A)** Expression of M-type K^+ channel-related subfamily members assessed using single-cell PCR analysis in the DRN neurons. **(i)** Representative image of single-cell PCR products showing the presence of different KCNQ subunits. **(ii)** Proportion of KCNQ1–5 positive neurons in the TPH-positive neurons (n = 20). **(B) (i)** Confocal images of KCNQ2, KCNQ3, and KCNQ4 expression in slice of the DRN, assessed using immunofluorescence methods. Scale bar = 50 μm. **(ii)** Proportion of KCNQ2, KCNQ3, and KCNQ4 positive neurons in the TPH-positive neurons (n = 200). **(C)** PE potently inhibited M-type currents recorded using whole-cell patch clamp in the DRN 5-HT neurons. **(i)** Recording protocol used and the typical current traces recorded; the latter were from –20 mV. The current amplitude at the beginning of the –50 mV step was

(Continued)

FIGURE 3 | measured (dotted square, enlarged in inset). The effects of PE and M-type K^+ channel blocker (XE991, 3 μM) are shown. **(ii)** Time course for current amplitudes measured in **(i)**. **(iii)** Summarized data for experiments shown in **(i,ii)**. Paired *t*-test, $^{n.s.}p > 0.05$, $^{**}p < 0.01$, $n = 7$. **(D)** M-type K^+ channel blocker XE991 (3 μM) induced spontaneous firing of the DRN 5-HT neurons. **(i)** Representative traces of action potential spikes recorded using "loose patch" under current-clamp configuration. **(ii)** Example time course of the spontaneous firing frequency in a 5-HT neuron, under the influence of 4-AP and PE. **(iii)** Summarized data for the effects of XE991 and PE on the spontaneous firing frequency (Wilcoxon matched-pairs signed-rank test, $^{***}p < 0.001$, $^{****}p < 0.0001$, $n = 14$). **(E)** M-type K^+ channel blocker XE991 (3 μM) induced depolarization of resting membrane potential of the DRN 5-HT neurons. **(i)** Example time course of the resting membrane potential in a 5-HT neuron, under the influence of 4-AP and PE. **(ii)** Summarized data for the effects of XE991 and PE on the resting membrane potential (Paired *t*-test, $^{*}p < 0.05$, $n = 6$).

presence of a cocktail of ionotropic receptor blockers that inhibit NMDA receptors AMPA/kainite receptors, $GABA_A$ receptors, and glycine receptors, suggesting that PE directly activates α1-adrenoceptor on DRN 5-HT neurons.

Although PE inhibition of A-type currents (I_A) through α1-adrenoceptor in DRN 5-HT neurons was described long ago (Aghajanian, 1985), the contribution of this modulation to the firing activity of DRN 5-HT neurons has not been established. Moreover, the identity of the I_A-correlated subtype channels in these neurons is unknown. In this regard, the results presented in this study provide a clear conclusion that PE-induced inhibition of I_A, carried by the Kv4.2 and 4.3 channel subfamily, contributes to the PE-induced spontaneous firing of DRN 5-HT neurons.

Several studies have shown a marked control of neuronal excitability by A-type currents (IA) (Carrasquillo et al., 2012; Zhao et al., 2016; Yu et al., 2019). At least six Kv channels, as pore-forming α subunits, can rapidly generate activating and inactivating K^+ currents with properties similar to neuronal I_A, including Kv1.4 (KCNA4), Kv3.3 (KCNC3), Kv3.4 (KCNC4), Kv4.1 (KCND1), Kv4.2 (KCND2), and Kv4.3 (KCND3) (Stuhmer et al., 1989; Baldwin et al., 1991; Pak et al., 1991; Vega-Saenz de Miera et al., 1992; Ritter et al., 2012). I_A encoded by these different Kv α subunits show unique properties, whereas I_A encoded by Kv1.4 and Kv4s is activated at low voltage, I_A encoded by Kv3.3 and 3.4 are activated at high-voltage (>-20 mV) (Vega-Saenz de Miera et al., 1992). Our results are partially in agreement with previous evidence that the Kv4.3 transcript is abundant in the rat raphe, whereas Kv4.1 and 4.2 signals are negligible (Serodio and Rudy, 1998). Our results suggest that both Kv4.2 and 4.3 are highly expressed in mouse DRN 5-HT neurons, whereas Kv1.4 and Kv4.1 are negligible. Thus, Kv4.2 and 4.3 channels are most likely the molecular correlates of sub-threshold A-type currents in 5-HT neurons, although Kv4.2 could play a more dominant role given the different properties of these two Kv4 channels in action potential firing (Carrasquillo et al., 2012).

However, the I_A blocker 4-AP did not induce spontaneous firing of DRN 5-HT neurons as efficiently as PE, even at a maximal concentration (4 mM), suggesting that mechanisms other than I_A inhibition are involved in the PE-induced spontaneous firing activity of 5-HT neurons. Inhibition of KCNQ/M currents (I_M) and low-conductance Ca^{2+}-activated K^+ (SK) currents (I_{SK}) are the main candidates for this. These two-channel families are widely expressed in the central nervous system and play a key role in the intrinsic excitability of neurons (Wang et al., 1998; Stocker and Pedarzani, 2000; Sailer et al., 2004; Adelman et al., 2012), and more importantly, they have a high propensity for Gq-coupled (like α1-Ars) neuromodulation (Marrion et al., 1989; Bernheim et al., 1992; Maingret et al., 2008; Adelman et al., 2012; Kuo et al., 2016).

Much evidence suggests that modulation of I_M has profound effects on neuronal excitability (Brown and Passmore, 2009; Zhao et al., 2017; Su et al., 2019), and the KCNQ/M channel is a target of modulation by Gq-coupled receptors, including α1-Ars (Suh et al., 2004; Delmas and Brown, 2005; Kuo et al., 2016). We have shown in this study that pharmacological inhibition of I_M by the specific blocker XE911 also induced spontaneous firing of DRN 5-HT neurons and that PE at the concentration that triggers spontaneous firing inhibited I_M in DRN 5-HT neurons. These results demonstrate that I_M is another mechanism for the PE-induced spontaneous firing in DRN 5-HT neurons. Since KCNQ2, Q3, and Q4 are abundantly expressed in DRN 5-HT neurons, and all of these KCNQ subfamily members are known to produce I_M (Brown and Passmore, 2009), the PE-induced inhibition of I_M should originate from these KCNQ channels, contributing to the initiation of spontaneous firing.

As discussed above for I_A and I_M, it could be similarly concluded that SK currents are also involved in the PE-induced spontaneous firing of DRN 5-HT neurons. However, the currents mediated by the SK channels are not involved in the initiation of the action potential like I_A and I_M, but are mainly thought to contribute to the hyperpolarization following action potential and therefore regulate firing frequency (Adelman et al., 2012). This is probably due to the fact that they are usually not active during resting membrane potential and require elevated cytosolic Ca^{2+} levels to become active. This is consistent with our findings that inhibition of SK currents *per se* did not trigger significant firing activity, but rather increased firing frequency once firing was initiated by, for example, inhibition of I_A and I_M. Our results suggest that of the three members of the SK channel family (SK1–SK3), SK2 and SK3 are the predominant types in DRN 5-HT neurons, consistent with previous findings (Stocker and Pedarzani, 2000; Sailer et al., 2004). Expression of mouse SK2 and SK3 was reported to produce functional, homomeric channels (Kohler et al., 1996; Shah and Haylett, 2000), whereas mouse SK1 cDNA did not produce functional plasma membrane channels (Benton et al., 2003). It should be noted that activation, rather than inhibition, of an apamin-sensitive late-AHP current by activation of α1-adrenoceptor in rat DRN 5-HT neurons has been reported (Pan et al., 1994), an observation that differs from our results. The different species used in this and our study

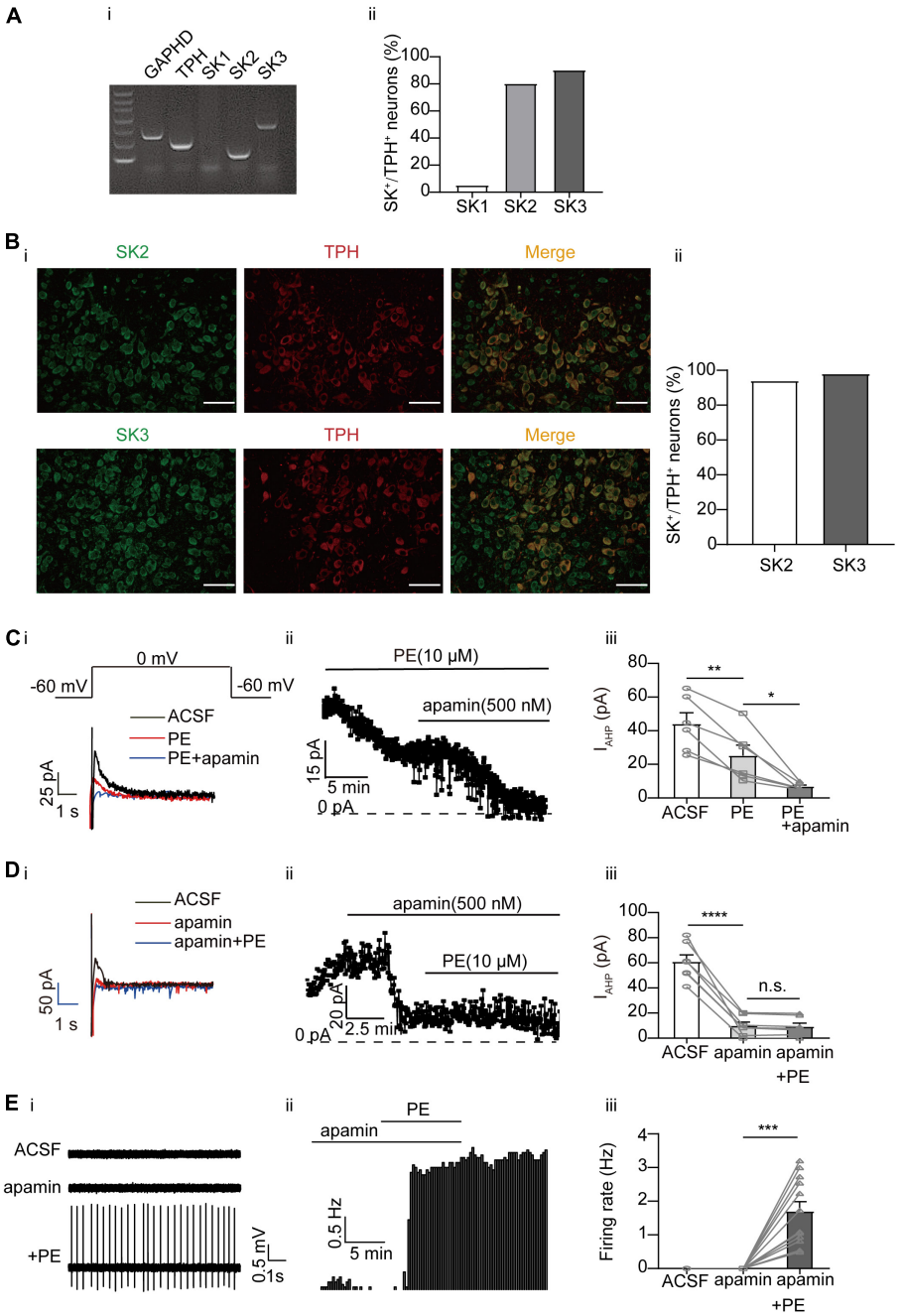

FIGURE 4 | Expression of SK channels and their contribution to the PE-induced spontaneous firing of the DRN 5-HT neurons. **(A)** Expression of SK channel-related subfamily members assessed using single-cell PCR analysis in the DRN neurons. **(i)** Representative image of single-cell PCR products showing the presence of different SK subunits. **(ii)** Proportion of SK1–SK3-positive neurons in the TPH-positive neurons ($n = 20$). **(B) (i)** Confocal images of SK2 and SK3 expression in slice of the DRN, assessed using immunofluorescence methods. Scale bar = 50 μm. **(ii)** Proportion of SK2 and SK3 positive neurons in the TPH-positive neurons ($n = 200$). **(C)** PE potently inhibited I_{AHP} currents, which was further inhibited by SK channel blocker apamin, recorded using whole-cell patch clamp in the DRN 5-HT neurons. **(i)** Recording protocol used and the typical current traces recorded; the latter were from 0 mV. The current amplitude at the beginning of the 0 mV step was measured; the effects of PE (10 μM) and apamin (500 nM) are shown. **(ii)** Time course for current amplitudes measured in **(i)**. **(iii)** Summarized data for experiments shown in **(i,ii)** (paired *t*-test, $^{**}p < 0.01$, $^{*}p < 0.05$, $n = 6$). **(D)** PE did not further inhibit I_{AHP} current in DRN 5-HT neurons, following the application of apamin (500 nM). **(i)** Recording protocol used and the typical current traces recorded. **(ii)** Time course for current amplitudes measured in **(i)**. **(iii)** Summarized data for experiments shown in **(i,ii)** (paired *t*-test, $^{****}p < 0.0001$, $^{n.s.}p > 0.05$, $n = 7$). **(E)** SK channel blocker apamin (500 nM) did not induce spontaneous firing of the DRN 5-HT neurons. **(i)** Representative traces of action potential spikes recorded using "loose patch" under current-clamp configuration. **(ii)** Example time course of the spontaneous firing frequency in a 5-HT neuron, under the influence of apamin and PE. **(iii)** Summarized data for the effects of apamin and PE on the spontaneous firing frequency (Wilcoxon matched-pairs signed-rank test, $^{***}p < 0.001$, $n = 12$).

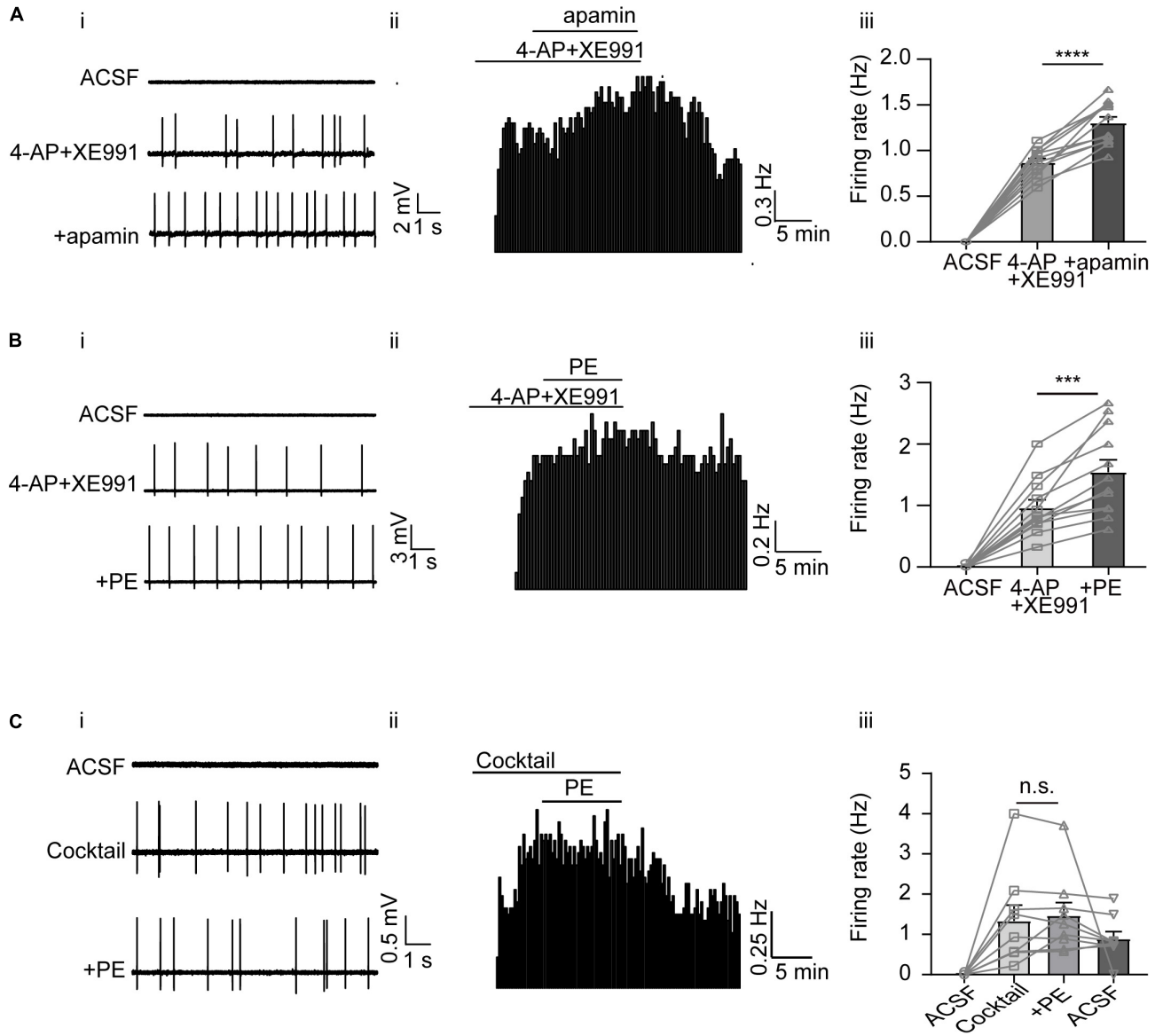

FIGURE 5 | The overall contribution of A-type, M-type, and SK channels to the PE-induced spontaneous firing of the DRN 5-HT neurons. **(A)** SK channel blocker apamin further increased the induced spontaneous firing of the DRN 5-HT neurons, following the application of 4AP and XE991. **(i)** Representative traces of action potential spikes recorded using "loose patch" under current-clamp configuration performed on a DRN 5-HT neuron; the effects of 4AP + XE991 and apamin are shown. **(ii)** Example time course of the spontaneous firing frequency in a 5-HT neuron, under the influence of 4AP + XE991 and apamin. **(iii)** Summarized effects of 4AP + XE991 and apamin on the spontaneous firing frequency (paired *t*-test, $^{****}p < 0.0001$, $n = 12$). **(B)** PE further increased the induced spontaneous firing of 5-HT neurons in the DRN, following the application of 4AP and XE991. **(i)** Representative traces of action potential spikes recorded using "loose patch" under current-clamp configuration performed on a DRN 5-HT neuron; the effects of 4AP + XE991 and PE are shown. **(ii)** Example time course of the spontaneous firing frequency in a 5-HT neuron, under the influence of 4AP + XE991 and PE. **(iii)** Summarized effects of 4AP + XE991 and PE on the spontaneous firing frequency (paired *t*-test, $^{***}p < 0.001$, $n = 12$). **(C)** Three K^+ channel blockers, 4AP, XE991, and apamin, together totally excluded further effect of PE on the spontaneous firing of the DRN 6-HT neurons. **(i)** Representative traces of action potential spikes recorded using "loose patch" under current-clamp configuration performed on a DRN 5-HT neuron; the effects of cocktail blockers (4-AP, XE991, and apamin) and PE are shown. **(ii)** Example time course of the spontaneous firing frequency in a 5-HT neuron, under the influence of cocktail blockers and PE. **(iii)** Summarized effects of cocktail blockers and PE on the spontaneous firing frequency (paired *t*-test, $^{n.s.}p > 0.05$, $n = 9$).

may be one explanation, but other unknown mechanisms could also play a role.

Finally, the fact that inhibition of K^+ conductance of the three channels discussed above completely excluded PE from further modulation of the firing activity clearly allows the conclusion that inhibition of K^+ conductance is a mechanism sufficient to trigger PE-induced spontaneous firing of DRN 5-HT neurons.

In summary, our results suggest that A-type, KCNQ/M, and SK channels are the K^+ channels that trigger PE-induced spontaneous firing in DRN 5-HT neurons. This mechanism is probably responsible for the neuronal modulation of DRN 5-HT neurons by the transmitter NE released from the terminals of the nerve fibers projecting from different brain regions. Whether this type of modulation is a unique mechanism for the DRN 5-HT neurons or a common mechanism for all central adrenergic neurons requires further investigation. Clarification of this question will help to understand the cellular mechanism of neuronal modulation and identify potential drug targets for therapeutic trials.

DATA AVAILABILITY STATEMENT

The original contributions presented in the study are included in the article/supplementary material, further inquiries can be directed to the corresponding author.

ETHICS STATEMENT

The animal study was reviewed and approved by Laboratory Animal Ethical and Welfare Committee, Hebei Medical University.

AUTHOR CONTRIBUTIONS

HZ conceived, designed, and supervised the experiments. JW performed the experiments, acquired and analyzed the data, and prepared the figures. YW performed immunofluorescence of the brain slices and performed the some preliminary electrophysiological experiments. HZ and XD prepared the final version of the manuscript. All authors contributed to the article and approved the submitted version.

FUNDING

This work was supported by the National Natural Science Foundation of China (nos. 81871075 and 82071533) grants to HZ, National Natural Science Foundation of China (no. 81870872) grants to XD, and Science Fund for Creative Research Groups of Natural Science Foundation of Hebei Province (no. H2020206474).

ACKNOWLEDGMENTS

We thank Lili for the advice with I_A pharmacology. We also thank Min Su for the technical assistance.

REFERENCES

Adelman, J. P., Maylie, J., and Sah, P. (2012). Small-conductance Ca2+-activated K+ channels: form and function. *Annu. Rev. Physiol.* 74, 245–269. doi: 10.1146/annurev-physiol-020911-153336

Aghajanian, G. K. (1985). Modulation of a transient outward current in serotonergic neurones by alpha 1-adrenoceptors. *Nature* 315, 501–503. doi: 10.1038/315501a0

Aghajanian, G. K., Foote, W. E., and Sheard, M. H. (1968). Lysergic acid diethylamide: sensitive neuronal units in the midbrain raphe. *Science* 161, 706–708. doi: 10.1126/science.161.3842.706

Aghajanian, G. K., and Vandermaelen, C. P. (1982). Intracellular recordings from serotonergic dorsal raphe neurons: pacemaker potentials and the effect of LSD. *Brain Res.* 238, 463–469. doi: 10.1016/0006-8993(82)90124-x

Allers, K. A., and Sharp, T. (2003). Neurochemical and anatomical identification of fast- and slow-firing neurones in the rat dorsal raphe nucleus using juxtacellular labelling methods in vivo. *Neuroscience* 122, 193–204. doi: 10.1016/s0306-4522(03)00518-9

Baldwin, T. J., Tsaur, M. L., Lopez, G. A., Jan, Y. N., and Jan, L. Y. (1991). Characterization of a mammalian cDNA for an inactivating voltage-sensitive K+ channel. *Neuron* 7, 471–483. doi: 10.1016/0896-6273(91)90299-f

Benton, D. C., Monaghan, A. S., Hosseini, R., Bahia, P. K., Haylett, D. G., and Moss, G. W. (2003). Small conductance Ca2+-activated K+ channels formed by the expression of rat SK1 and SK2 genes in HEK 293 cells. *J. Physiol.* 553, 13–19. doi: 10.1113/jphysiol.2003.054551

Bernheim, L., Mathie, A., and Hille, B. (1992). Characterization of muscarinic receptor subtypes inhibiting Ca2+ current and M current in rat sympathetic neurons. *Proc. Natl. Acad. Sci. U. S. A.* 89, 9544–9548. doi: 10.1073/pnas.89.20.9544

Bromberg-Martin, E. S., Hikosaka, O., and Nakamura, K. (2010). Coding of task reward value in the dorsal raphe nucleus. *J. Neurosci.* 30, 6262–6272. doi: 10.1523/JNEUROSCI.0015-10.2010

Brown, D. A., and Passmore, G. M. (2009). Neural KCNQ (Kv7) channels. *Br. J. Pharmacol.* 156, 1185–1195. doi: 10.1111/j.1476-5381.2009.00111.x

Burlet, S., Tyler, C. J., and Leonard, C. S. (2002). Direct and indirect excitation of laterodorsal tegmental neurons by Hypocretin/Orexin peptides: implications for wakefulness and narcolepsy. *J. Neurosci.* 22, 2862–2872. doi: 10.1523/JNEUROSCI.22-07-02862.2002

Carrasquillo, Y., Burkhalter, A., and Nerbonne, J. M. (2012). A-type K+ channels encoded by Kv4.2, Kv4.3 and Kv1.4 differentially regulate intrinsic excitability of cortical pyramidal neurons. *J. Physiol.* 590, 3877–3890. doi: 10.1113/jphysiol.2012.229013

Commons, K. G. (2020). Dorsal raphe organization. *J. Chem. Neuroanat.* 110:101868. doi: 10.1016/j.jchemneu.2020.101868

Delmas, P., and Brown, D. A. (2005). Pathways modulating neural KCNQ/M (Kv7) potassium channels. *Nat. Rev. Neurosci.* 6, 850–862. doi: 10.1038/nrn1785

Gocho, Y., Sakai, A., Yanagawa, Y., Suzuki, H., and Saitow, F. (2013). Electrophysiological and pharmacological properties of GABAergic cells in the dorsal raphe nucleus. *J. Physiol. Sci.* 63, 147–154. doi: 10.1007/s12576-012-0250-7

Hayashi, K., Nakao, K., and Nakamura, K. (2015). Appetitive and aversive information coding in the primate dorsal raphe nucleus. *J. Neurosci.* 35, 6195–6208. doi: 10.1523/JNEUROSCI.2860-14.2015

Hu, F., Zhou, J., Lu, Y., Guan, L., Wei, N. N., Tang, Y. Q., et al. (2019). Inhibition of Hsp70 Suppresses Neuronal Hyperexcitability and Attenuates Epilepsy by Enhancing A-Type Potassium Current. *Cell Rep.* 26, .168–181.

Itri, J. N., Vosko, A. M., Schroeder, A., Dragich, J. M., Michel, S., and Colwell, C. S. (2010). Circadian regulation of a-type potassium currents in the suprachiasmatic nucleus. *J. Neurophysiol.* 103, 632–640.

Judge, S. J., and Gartside, S. E. (2006). Firing of 5-HT neurones in the dorsal and median raphe nucleus in vitro shows differential alpha1-adrenoceptor and 5-HT1A receptor modulation. *Neurochem. Int.* 48, 100–107. doi: 10.1016/j.neuint.2005.09.003

Kawashima, T. (2018). The role of the serotonergic system in motor control. *Neurosci. Res.* 129, 32–39. doi: 10.1016/j.neures.2017.07.005

Kohler, M., Hirschberg, B., Bond, C. T., Kinzie, J. M., Marrion, N. V., Maylie, J., et al. (1996). Small-conductance, calcium-activated potassium channels from mammalian brain. *Science* 273, 1709–1714. doi: 10.1126/science.273.5282.1709

Kuo, F. S., Falquetto, B., Chen, D., Oliveira, L. M., Takakura, A. C., and Mulkey, D. K. (2016). In vitro characterization of noradrenergic modulation of chemosensitive neurons in the retrotrapezoid nucleus. *J. Neurophysiol.* 116, 1024–1035. doi: 10.1152/jn.00022.2016

Leonard, B. E. (2002). Neuropsychopharmacology—The fifth generation of progress. Edited by K. L. Davis, D. Charney, J. T. Coyle, C. Nemeroff. Lippincott, Williams and Wilkins: Philadelphia, 2002. ISBN: 0-7817-2837-1. Price: $189. Pages: 2080. *Hum. Psychol.* 17, 433–433.

Li, Y., Dalphin, N., and Hyland, B. I. (2013). Association with reward negatively modulates short latency phasic conditioned responses of dorsal raphe nucleus neurons in freely moving rats. *J. Neurosci.* 33, 5065–5078. doi: 10.1523/JNEUROSCI.5679-12.2013

Lucki, I. (1998). The spectrum of behaviors influenced by serotonin. *Biol. Psychiatry* 44, 151–162. doi: 10.1016/s0006-3223(98)00139-5

Maingret, F., Coste, B., Hao, J., Giamarchi, A., Allen, D., Crest, M., et al. (2008). Neurotransmitter modulation of small-conductance Ca2+-activated K+ channels by regulation of Ca2+ gating. *Neuron* 59, 439–449. doi: 10.1016/j.neuron.2008.05.026

Marrion, N. V., Smart, T. G., Marsh, S. J., and Brown, D. A. (1989). Muscarinic suppression of the M-current in the rat sympathetic ganglion is mediated by receptors of the M1-subtype. *Br. J. Pharmacol.* 98, 557–573. doi: 10.1111/j.1476-5381.1989.tb12630.x

Matschke, L. A., Rinne, S., Snutch, T. P., Oertel, W. H., Dolga, A. M., and Decher, N. (2018). Calcium-activated SK potassium channels are key modulators of the pacemaker frequency in locus coeruleus neurons. *Mol. Cell Neurosci.* 88, 330–341. doi: 10.1016/j.mcn.2018.03.002

Matthews, G. A., Nieh, E. H., Vander Weele, C. M., Halbert, S. A., Pradhan, R. V., Yosafat, A. S., et al. (2016). Dorsal Raphe Dopamine Neurons Represent the Experience of Social Isolation. *Cell* 164, 617–631. doi: 10.1016/j.cell.2015.12.040

Monti, J. M. (2010). The role of dorsal raphe nucleus serotonergic and non-serotonergic neurons, and of their receptors, in regulating waking and rapid eye movement (REM) sleep. *Sleep Med. Rev.* 14, 319–327. doi: 10.1016/j.smrv.2009.10.003

Nakamura, K., Matsumoto, M., and Hikosaka, O. (2008). Reward-dependent modulation of neuronal activity in the primate dorsal raphe nucleus. *J. Neurosci.* 28, 5331–5343. doi: 10.1523/JNEUROSCI.0021-08.2008

Ohmura, Y., Tsutsui-Kimura, I., Sasamori, H., Nebuka, M., Nishitani, N., Tanaka, K. F., et al. (2020). Different roles of distinct serotonergic pathways in anxiety-like behavior, antidepressant-like, and anti-impulsive effects. *Neuropharmacology* 167:107703. doi: 10.1016/j.neuropharm.2019.107703

Pak, M. D., Baker, K., Covarrubias, M., Butler, A., Ratcliffe, A., and Salkoff, L. (1991). mShal, a subfamily of A-type K+ channel cloned from mammalian brain. *Proc. Natl. Acad. Sci. U. S. A.* 88, 4386–4390. doi: 10.1073/pnas.88.10.4386

Pan, Z. Z., Grudt, T. J., and Williams, J. T. (1994). Alpha 1-adrenoceptors in rat dorsal raphe neurons: regulation of two potassium conductances. *J. Physiol.* 478, 437–447. doi: 10.1113/jphysiol.1994.sp020263

Pan, Z. Z., Williams, J. T., and Osborne, P. B. (1990). Opioid actions on single nucleus raphe magnus neurons from rat and guinea-pig in vitro. *J. Physiol.* 427, 519–532. doi: 10.1113/jphysiol.1990.sp018185

Pedarzani, P., McCutcheon, J. E., Rogge, G., Jensen, B. S., Christophersen, P., Hougaard, C., et al. (2005). Specific enhancement of SK channel activity selectively potentiates the afterhyperpolarizing current I(AHP) and modulates the firing properties of hippocampal pyramidal neurons. *J. Biol. Chem.* 280, 41404–41411. doi: 10.1074/jbc.M509610200

Prakash, N., Stark, C. J., Keisler, M. N., Luo, L., Der-Avakian, A., and Dulcis, D. (2020). Serotonergic Plasticity in the Dorsal Raphe Nucleus Characterizes Susceptibility and Resilience to Anhedonia. *J. Neurosci.* 40, 569–584. doi: 10.1523/JNEUROSCI.1802-19.2019

Ritter, D. M., Ho, C., O'Leary, M. E., and Covarrubias, M. (2012). Modulation of Kv3.4 channel N-type inactivation by protein kinase C shapes the action potential in dorsal root ganglion neurons. *J. Physiol.* 590, 145–161. doi: 10.1113/jphysiol.2011.218560

Sailer, C. A., Hu, H., Kaufmann, W. A., Trieb, M., Schwarzer, C., Storm, J. F., et al. (2002). Regional differences in distribution and functional expression of small-conductance Ca2+-activated K+ channels in rat brain. *J. Neurosci.* 22, 9698–9707. doi: 10.1523/JNEUROSCI.22-22-09698.2002

Sailer, C. A., Kaufmann, W. A., Marksteiner, J., and Knaus, H. G. (2004). Comparative immunohistochemical distribution of three small-conductance Ca2+-activated potassium channel subunits, SK1, SK2, and SK3 in mouse brain. *Mol. Cell Neurosci.* 26, 458–469. doi: 10.1016/j.mcn.2004.03.002

Schweimer, J. V., and Ungless, M. A. (2010). Phasic responses in dorsal raphe serotonin neurons to noxious stimuli. *Neuroscience* 171, 1209–1215. doi: 10.1016/j.neuroscience.2010.09.058

Serodio, P., and Rudy, B. (1998). Differential expression of Kv4 K+ channel subunits mediating subthreshold transient K+ (A-type) currents in rat brain. *J. Neurophysiol.* 79, 1081–1091. doi: 10.1152/jn.1998.79.2.1081

Serôdio, P., Vega-Saenz de Miera, E., and Rudy, B. (1996). Cloning of a novel component of A-type K+ channels operating at subthreshold potentials with unique expression in heart and brain. *J. Neurophysiol.* 75, 2174–2179. doi: 10.1152/jn.1996.75.5.2174

Shah, M., and Haylett, D. G. (2000). The pharmacology of hSK1 Ca2+-activated K+ channels expressed in mammalian cell lines. *Br. J. Pharmacol.* 129, 627–630. doi: 10.1038/sj.bjp.0703111

Soiza-Reilly, M., and Commons, K. G. (2011). Glutamatergic drive of the dorsal raphe nucleus. *J. Chem. Neuroanat.* 41, 247–255. doi: 10.1016/j.jchemneu.2011.04.004

Song, W. J., Tkatch, T., Baranauskas, G., Ichinohe, N., Kitai, S. T., and Surmeier, D. J. (1998). Somatodendritic depolarization-activated potassium currents in rat neostriatal cholinergic interneurons are predominantly of the A type and attributable to coexpression of Kv4.2 and Kv4.1 subunits. *J. Neurosci.* 18, 3124–3137. doi: 10.1523/JNEUROSCI.18-09-03124.1998

Stocker, M., and Pedarzani, P. (2000). Differential distribution of three Ca(2+)-activated K(+) channel subunits, SK1, SK2, and SK3, in the adult rat central nervous system. *Mol. Cell Neurosci.* 15, 476–493. doi: 10.1006/mcne.2000.0842

Stuhmer, W., Ruppersberg, J. P., Schroter, K. H., Sakmann, B., Stocker, M., Giese, K. P., et al. (1989). Molecular basis of functional diversity of voltage-gated potassium channels in mammalian brain. *EMBO J.* 8, 3235–3244. doi: 10.1002/j.1460-2075.1989.tb08483.x

Su, M., Li, L., Wang, J., Sun, H., Zhang, L., Zhao, C., et al. (2019). Kv7.4 Channel Contribute to Projection-Specific Auto-Inhibition of Dopamine Neurons in the Ventral Tegmental Area. *Front. Cell Neurosci.* 13:557. doi: 10.3389/fncel.2019.00557

Suh, B. C., Horowitz, L. F., Hirdes, W., Mackie, K., and Hille, B. (2004). Regulation of KCNQ2/KCNQ3 current by G protein cycling: the kinetics of receptor-mediated signaling by Gq. *J. Gen. Physiol.* 123, 663–683. doi: 10.1085/jgp.200409029

Vandermaelen, C. P., and Aghajanian, G. K. (1983). Electrophysiological and pharmacological characterization of serotonergic dorsal raphe neurons recorded extracellularly and intracellularly in rat brain slices. *Brain Res.* 289, 109–119. doi: 10.1016/0006-8993(83)90011-2

Vega-Saenz de Miera, E., Moreno, H., Fruhling, D., Kentros, C., and Rudy, B. (1992). Cloning of ShIII (Shaw-like) cDNAs encoding a novel high-voltage-activating, TEA-sensitive, type-A K+ channel. *Proc. Biol. Sci.* 248, 9–18. doi: 10.1098/rspb.1992.0036

Wagner, E. J., Ronnekleiv, O. K., and Kelly, M. J. (2001). The noradrenergic inhibition of an apamin-sensitive, small-conductance Ca2+-activated K+ channel in hypothalamic gamma-aminobutyric acid neurons: pharmacology, estrogen sensitivity, and relevance to the control of the reproductive axis. *J. Pharmacol. Exp. Ther.* 299, 21–30.

Wang, H. S., Pan, Z., Shi, W., Brown, B. S., Wymore, R. S., Cohen, I. S., et al. (1998). KCNQ2 and KCNQ3 potassium channel subunits: molecular correlates of the M-channel. *Science* 282, 1890–1893. doi: 10.1126/science.282.5395.1890

Yao, J. A., and Tseng, G. N. (1994). Modulation of 4-AP block of a mammalian A-type K channel clone by channel gating and membrane voltage. *Biophys. J.* 67, 130–142. doi: 10.1016/S0006-3495(94)80462-X

Yu, S., Zhang, Y., Zhao, X., Chang, Z., Wei, Y., Sun, Y., et al. (2019). Cholecystokinin type B receptor-mediated inhibition of A-type K(+) channels enhances sensory neuronal excitability through the phosphatidylinositol 3-kinase and c-Src-dependent JNK pathway. *Cell Commun. Signal.* 17:68. doi: 10.1186/s12964-019-0385-8

Zhao, C., Su, M., Wang, Y., Li, X., Zhang, Y., Du, X., et al. (2017). Selective Modulation of K(+) Channel Kv7.4 Significantly Affects the Excitability of DRN 5-HT Neurons. *Front. Cell Neurosci.* 11:405. doi: 10.3389/fncel.2017.00405

Zhao, X., Zhang, Y., Qin, W., Cao, J., Zhang, Y., Ni, J., et al. (2016). Serotonin type-1D receptor stimulation of A-type K(+) channel decreases membrane excitability through the protein kinase A- and B-Raf-dependent p38 MAPK pathways in mouse trigeminal ganglion neurons. *Cell Signal.* 28, 979–988. doi: 10.1016/j.cellsig.2016.05.004

Zou, W. J., Song, Y. L., Wu, M. Y., Chen, X. T., You, Q. L., Yang, Q., et al. (2020). A discrete serotonergic circuit regulates vulnerability to social stress. *Nat. Commun.* 11:4218. doi: 10.1038/s41467-020-18010-w

Conflict of Interest: The authors declare that the research was conducted in the absence of any commercial or financial relationships that could be construed as a potential conflict of interest.

Publisher's Note: All claims expressed in this article are solely those of the authors and do not necessarily represent those of their affiliated organizations, or those of the publisher, the editors and the reviewers. Any product that may be evaluated in this article, or claim that may be made by its manufacturer, is not guaranteed or endorsed by the publisher.

frontiers | Frontiers in Cellular Neuroscience

REVIEW
published: 09 June 2022
doi: 10.3389/fncel.2022.910015

On the Diverse Functions of Electrical Synapses

*Mitchell J. Vaughn and Julie S. Haas**

Department of Biological Sciences, Lehigh University, Bethlehem, PA, United States

Electrical synapses are the neurophysiological product of gap junctional pores between neurons that allow bidirectional flow of current between neurons. They are expressed throughout the mammalian nervous system, including cortex, hippocampus, thalamus, retina, cerebellum, and inferior olive. Classically, the function of electrical synapses has been associated with synchrony, logically following that continuous conductance provided by gap junctions facilitates the reduction of voltage differences between coupled neurons. Indeed, electrical synapses promote synchrony at many anatomical and frequency ranges across the brain. However, a growing body of literature shows there is greater complexity to the computational function of electrical synapses. The paired membranes that embed electrical synapses act as low-pass filters, and as such, electrical synapses can preferentially transfer spike after hyperpolarizations, effectively providing spike-dependent inhibition. Other functions include driving asynchronous firing, improving signal to noise ratio, aiding in discrimination of dissimilar inputs, or dampening signals by shunting current. The diverse ways by which electrical synapses contribute to neuronal integration merits furthers study. Here we review how functions of electrical synapses vary across circuits and brain regions and depend critically on the context of the neurons and brain circuits involved. Computational modeling of electrical synapses embedded in multi-cellular models and experiments utilizing optical control and measurement of cellular activity will be essential in determining the specific roles performed by electrical synapses in varying contexts.

Keywords: electrical synapse, gap junction, connexin, synchrony, integration

OPEN ACCESS

Edited by:
Arianna Maffei,
Stony Brook University, United States

Reviewed by:
Ernest Montbrio,
Pompeu Fabra University, Spain
Barry Connors,
Brown University, United States

***Correspondence:**
Julie S. Haas
julie.haas@lehigh.edu

Specialty section:
This article was submitted to Cellular Neurophysiology, a section of the journal Frontiers in Cellular Neuroscience

Received: *31 March 2022*
Accepted: *25 May 2022*
Published: *09 June 2022*

Citation:
Vaughn MJ and Haas JS (2022) On the Diverse Functions of Electrical Synapses. Front. Cell. Neurosci. 16:910015. doi: 10.3389/fncel.2022.910015

INTRODUCTION

Across the nervous system, neurons couple to other neurons at gap junctions formed by plaques of paired and docked hemichannel pores composed of connexin or innexin proteins (Phelan et al., 1996, 1998; Starich et al., 1996; Condorelli et al., 1998; Landesman et al., 1999; Rash et al., 2000, 2001a,b; Stebbings et al., 2000; Söhl and Willecke, 2003) that allow ions to pass between neurons. Gap junctions are the biophysical substrate for the neurophysiological component of electrical synapses (Furshpan and Potter, 1957, 1959; Watanabe, 1958; Bennett, 1966), which couple neurons in the mature mammalian brain. These unique structures enable current to flow directly between neurons without relying on energetically costly neurotransmitters or a presynaptic spike in order to initiate inter-neuronal communication. Similar to their more abundant counterpart, chemical synapses, the function of electrical synapses is of great interest in determining how neurons integrate inputs and information.

Much early work focused on the potential for electrical coupling to synchronize firing between neurons. Electrical synapses pass ions proportionally to the difference in membrane voltage between coupled neurons, and their most basic effect is to reduce that difference, resulting in minimization of differences in voltage or activity. This is thought to be the simplest, though not sole, mechanism that underlies synchrony between coupled neurons. Synchrony, generally considered, can be appreciated at the level of ongoing repetitive activity, or for individual spikes. Synchrony of spiking activity in broader heterogenous networks, while more complex in mechanisms, often relies on contributions from the inhibitory neurons that gap junctions frequently couple. Thus, electrical synapses contribute to synchrony both directly and indirectly. Because neuronal electrical synapses take diverse values of strength amongst brain areas, their effects only rarely approach the perfect synchronization that would occur between coupled neurons with infinitely strong electrical synapses. This opens the door to a variety of diverse effects mediated by electrical synapses within neural circuitry. Previous reviews have covered aspects of electrical synapses (Bennett and Zukin, 2004; Connors and Long, 2004; Haas et al., 2016; Connors, 2017; Nagy et al., 2018; Alcami and Pereda, 2019; Trenholm and Awatramani, 2019; Curti et al., 2022). Here, we detail the progress in understanding the functions of electrical synapses within, and as a result of, coupled circuits and networks. We organize our review by the different functions of electrical synapses, followed by comments on future directions for studying electrical synapses. Because so much work involves interrogating the role of electrical synapses in synchrony of rhythmic activity, that section is divided into subsections based on the source of the evidence.

Synchrony of Rhythmic Activity

Reports of synchrony are a hallmark of electrical synapse work across neural tissue (**Figure 1A**). Watanabe (1958) made the earliest inference, noting that the synchronous subthreshold fluctuations of lobster heart ganglion cells were a function of common presynaptic inputs and electrical coupling. This was followed by pioneering demonstrations of electrical coupling by Bennett (1966), who inferred that electrical synapses were likely to be associated with synchronization of activity, based on observations of electrical coupling in fish electromotor neurons and toad swim bladder motor neurons. Later, an early report of synchrony in feline inferior olive was associated with the presence of electrical synapses (Llinas et al., 1974). This was eventually followed by paired-patch recordings that identified electrical coupling between inhibitory interneurons in murine cortex and also found that coupled neurons were inclined to spike together when depolarized (Galarreta and Hestrin, 1999; Gibson et al., 1999; Beierlein et al., 2000). Electrical synapses have long been known to contribute to synchrony in crustacean neural networks (Eisen and Marder, 1982; Hooper and Marder, 1987; Gutierrez et al., 2013).

Neocortex

Cortical rhythms are diverse and include gamma-range oscillations, which are linked to higher-order function (Benchenane et al., 2011); beta oscillations, which are involved in sensorimotor processes (Kilavik et al., 2013); theta oscillations associated with learning, memory, spatial navigation, and speech (Benchenane et al., 2011; Giraud and Poeppel, 2012); delta oscillations that are related to speech processing and decision making (Giraud and Poeppel, 2012; Nácher et al., 2013); and alpha oscillations that are tied to attention (Buzsáki and Draguhn, 2004; Hanslmayr et al., 2011). In electrically coupled cortical interneurons, simultaneous depolarization drives coordinated spiking (Gibson et al., 1999, 2005; Beierlein et al., 2000; Blatow et al., 2003; Mancilla et al., 2007; Hu and Agmon, 2015). Carbachol-induced spiking is synchronous in coupled inhibitory neurons as well, and that synchrony is correlated with electrical synapse conductance, while uncoupled neurons displayed no correlation in spiking (Caputi et al., 2009). Similarly, correlated spiking induced by ACPD or carbachol is desynchronized by connexin36 knockout or pharmacological blockade of gap junctions (Deans et al., 2001; Blatow et al., 2003). For layers 2 and 3 basket cells, gamma frequency stimulation in one cell entrains gamma frequency spiking in coupled basket cells, albeit with a phase lag of about 10 ms; electrical coupling in addition to GABAergic connections shortened gap junction mediated postsynaptic potentials and promoted synchronous gamma activity (Tamás et al., 2000). Synchronization of cortical interneurons can entrain synchrony of rhythmic spiking in cortical pyramidal neurons (Whittington et al., 1995, 2000; Traub et al., 1996; Whittington and Traub, 2003; Cardin, 2016); synchronized network rhythms may be important for sensory processing, working memory, and attention (Buzsáki and Draguhn, 2004; Wang, 2010; Benchenane et al., 2011; Hanslmayr et al., 2011).

Thalamus

The thalamic reticular nucleus (TRN) receives excitatory input from ascending thalamic relay nuclei (Jones, 1975; Ohara and Lieberman, 1985; Fosse et al., 1986; Fitzpatrick et al., 1994; Liu and Jones, 1999), feedback excitation from layers 5 and 6 of cortex (Jones, 1975; Bromberg et al., 1981; Fonnum et al., 1981; Feig and Harting, 1998; Zhang and Jones, 2004), and a myriad of modulatory input (Wilson, 1985; Cornwall et al., 1990; Gandia et al., 1993; Reardon and Mitrofanis, 2000; Freeman et al., 2001; Prensa and Parent, 2001; Anaya-Martinez et al., 2006; Zikopoulos and Barbas, 2012; Leon-Dominguez et al., 2013); the exclusively GABAergic neurons of the TRN provide the main source of inhibitory drive onto thalamic nuclei (Scheibel and Scheibel, 1966; Jones, 1975; Houser et al., 1980), and thus control thalamocortical relay of sensory information. The TRN is integral in thalamocortical spindle oscillations during sleep and memory formation during sleep (Pinault, 2004; Steriade, 2005; Halassa et al., 2011; Latchoumane et al., 2017). Paired depolarization of coupled TRN neurons drives correlated spiking (Landisman et al., 2002; Haas and Landisman, 2011), and depolarization resulting from ACPD application also causes correlated spiking (Long et al., 2004). The cross-correlation of mGluR-induced subthreshold rhythms is positively correlated with the conductance of the electrical synapse within the pair.

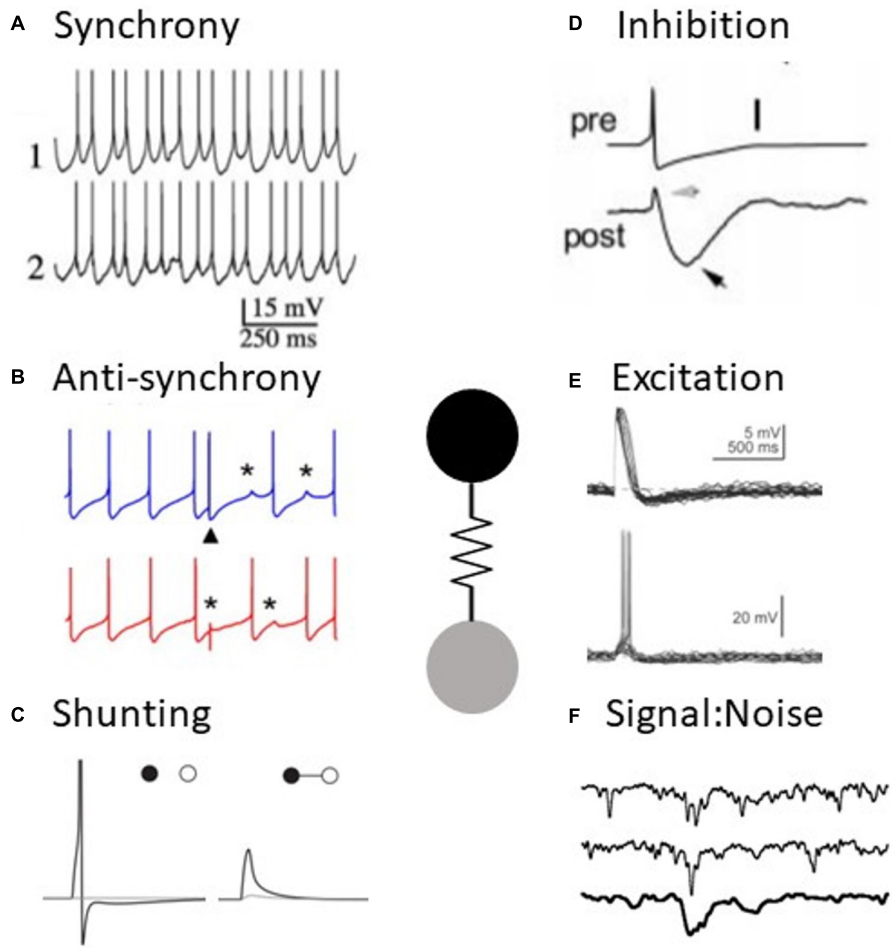

FIGURE 1 | Electrical synapses have diverse functions in neural processing. **(A)** Example of synchronous activity in coupled neurons (adapted from Long et al., 2004). **(B)** Example of anti-synchronous firing in coupled neurons (adapted from Vervaeke et al., 2010). **(C)** An electrical synapse (right) shunts an excitatory signal to one cell to subthreshold levels, compared to the uncoupled case (left) (adapted from Hjorth et al., 2009). **(D)** Slow spike afterhyperpolarizations appear as inhibition in a coupled neuron (adapted from Galarreta and Hestrin, 2001). **(E)** Spikes result in excitation in a coupled neuron (adapted from Apostolides and Trussell, 2014). **(F)** Example of a signal amidst noise in retinal neurons, impacted by the presence of electrical synapses (adapted from Dunn et al., 2006).

Hippocampus

The nested gamma and theta rhythms of the hippocampal formation are essential to its spatial and memory functions (Colgin and Moser, 2010), and hippocampal GABAergic neurons are connected *via* dendrodendritic gap junctions (Fukuda and Kosaka, 2000). Hippocampus basket cells initiate gamma oscillations when depolarized with potassium, glutamate, kainite, or carbachol; the measured power of those gamma oscillations through field potentials are reduced with gap junction blockers or connexin knockout (Hormuzdi et al., 2001; Traub et al., 2001). Furthermore, IPSCs onto pyramidal cells become more variable in connexin knock outs (Hormuzdi et al., 2001). The effect of gap junctions synchronizing gamma oscillations was reinforced by a following study recording field potentials of CA1 pyramidal neurons *in vivo*, where connexin36 knockout reduced the power of gamma oscillations (Buhl et al., 2003).

Synchronous high frequency (<150 hz) bursts of activity occur in hippocampal pyramidal neurons, and gap junctions are necessary for the high frequency bursts to occur *in vitro* (Draguhn et al., 1998), although this was not confirmed *in vivo* (Buhl et al., 2003). Seizing activity in hippocampal slices induced by Ca^{2+} free ACSF is reduced and desynchronized by weakening electrical coupling through acidification (Perez-Velazquez et al., 1994). Similarly, another hippocampal seizure model with no Mg^{2+} and 4-aminopyridine in the ACSF had its population bursts greatly reduced by gap junction blockers, suggesting that electrical synapses were partially responsible for simultaneous activity seen in the seizure model (Ross et al., 2000).

Cerebellum

The cerebellum is responsible for timing of motor control, and precise temporal precision of spiking is key to that function. Both low frequency (7–30 hz) oscillations and high frequency (>40 hz) oscillations have been observed in the cerebellum and may contribute to motor execution and learning (D'Angelo et al., 2009). *In vitro*, spontaneous spiking in coupled

Golgi inhibitory interneurons of the cerebellum is correlated. Further, coupled Golgi neurons oscillate synchronously or spike synchronously when depolarized with kainate (Dugué et al., 2009). Computational modeling of Golgi neurons suggests that transfer of the after hyperpolarization through the gap junction is critical for synchronized spiking. The afterhyperpolarization (AHP) is inhibitory to the coupled cell and determines the delay period after which a coupled neuron can next spike (Dugué et al., 2009). *In vivo* cell-attached recordings demonstrated that coupled Golgi interneuron spiking is correlated within a few ms (van Welie et al., 2016); knock-out of connexin36 results in uncorrelated spiking. Paired recordings showed that spiking in one neuron resulted in a depolarizing spikelet in the other, and in some instances, the spikelet was sufficient to drive a correlated spike within milliseconds. Altogether, these heroic *in vivo* experiments suggest that coupled Golgi interneurons spike together due to electrical synapses correlating subthreshold potentials and by driving a coupled neighbor past threshold through an excitatory spikelet.

Inferior Olive

The coupled neurons of the inferior olive provide error-signal input to cerebellar Purkinje cell dendrites and exhibit strong subthreshold and spiking oscillations in the 1–10 Hz range of frequency (Armstrong et al., 1968; De Zeeuw et al., 1998). Paired recordings of inferior olive (IO) neurons show that spontaneous spiking and subthreshold oscillations are highly correlated amongst coupled neurons. Knockout of connexin36 causes an increase in uncorrelated spiking and desynchronization of subthreshold oscillations, which still persist (Long et al., 2002; Leznik and Llinas, 2005). Long et al. (2002) suggest that coupled IO neurons spike synchronously in part due to coupled neurons faithfully spiking at the peak of membrane fluctuations, where decoupled neurons sometimes spike in the trough of their oscillation. Electrical synapses reduce excitability by shunting current, and therefore, they make IO neurons less likely to spike during the trough of a subthreshold membrane oscillation.

Synchronization of IO neurons *via* gap junctions affects the downstream synchrony of cerebellar neurons. *In vivo* injections of gap junction blockers into the IO or knockout of connexin36 reduces synchrony of complex spikes in postsynaptic Purkinje cells (Blenkinsop and Lang, 2006; Marshall et al., 2007) and interferes with motor learning (Van Der Giessen et al., 2008). This effect is presumably the result of desynchronized activity in the uncoupled IO.

Suprachiasmatic Nucleus

The suprachiasmatic nucleus (SCN) is a central regulator of circadian rhythms. Dye-coupling, which images the spread of gap junction-permeable dyes through coupled networks, is greatest during the sleep cycle, when there is more synchronous activity, than during the active cycle (Colwell, 2000). Coupling is positively correlated with synchronous spiking, while spiking was uncorrelated in uncoupled neurons (Long et al., 2005). The circadian rhythms of connexin36 knockout mice are irregular, so the synchronous firing during the wake cycle may be a component of circadian rhythm maintenance (Long et al., 2005). Long et al. (2005) also showed evidence that coupling between cells changes in strength over 24 h and that knockout rats lose rhythmicity of circadian activity in 24 h dark conditions.

Brainstem

Evidence for the synchronizing effects of gap junctions in brainstem is mixed. One study using adult rats found that gap junction blockers decreased synchrony of phrenic bursts (Solomon et al., 2003). In contrast, an earlier study found that gap junction blockers in neonatal brain stem slices showed that gap junctions reduce synchronized activity of the phrenic nerve in the short term (Bou-Flores and Berger, 2001). In the mesencephalic trigeminal nucleus, strong electrical synapses can drive a quiescent neighbor to spike within 2 ms of the spikes of coupled neurons. Further, subthreshold depolarizations of coupled neurons resulted in membrane potential oscillations that were correlated between coupled pairs (Curti et al., 2012). Synchronization of the mesencephalic trigeminal nucleus could be important for coordinated inputs to relax the jaw.

Spinal Cord

Electrical coupling is present between juvenile motor neurons in rats, but it does not persist with maturation (Walton and Navarrete, 1991; Chang et al., 1999). Juvenile motor neuron spiking is correlated, even the presence of TTX, but spiking becomes uncorrelated with pharmacological blockade of gap junctions (Tresch and Kiehn, 2000; Personius et al., 2001). Electrical synapses may have an important role in guiding development of motor neurons by promoting synchronous activity. Inhibition of acetylcholine release by motor neurons during development causes electrical synapses to persist into adolescence, suggesting that activity at the neuromuscular junction communicates the need to remove electrical synapses (Pastor et al., 2003).

Olfactory Bulb

Mitral cells in the olfactory bulb synchronously oscillate at 30–80 hz when stimulated with one or more odorants (Kashiwadani et al., 1999). Oscillations in the olfactory bulb have a role in odorant discrimination, and it is speculated that synchronous activity facilities the summation of EPSPs in piriform cortex (Schoppa and Urban, 2003; Rojas-Líbano and Kay, 2008). Electrical synapses contribute to synchrony in the olfactory bulb; depolarizing coupled mitral cells in the olfactory bulb drives correlated spiking that is absent when connexin36 is knocked out (Christie et al., 2005).

Retina

Retina is a major hub where electrical synapses exert influence on processing light signals. All layers of the retina express gap junctions, and their electrical synapse strength is regulated by brightness *via* dopamine, nitric oxide, and adenosine (Hampson et al., 1992; McMahon and Brown, 1994; Mills and Massey, 1995; Lee et al., 2002; Mills et al., 2007; Ribelayga et al., 2008; Bloomfield and Volgyi, 2009; Kothmann et al., 2009; Li et al., 2013; Jacoby et al., 2018; Trenholm and Awatramani, 2019). Electrical synapse regulation in retina is critical for adaptation to different light intensities.

The developing retina undergoes slow waves of activity that spread across ganglion cells with an interval on the order of minutes (Firth et al., 2005). Retinal waves require electrical synapses and L-type Ca^{2+} channels. It has been inferred that electrical synapses propagate the wave by transferring excitation driven by L-type Ca^{2+} channels (Singer et al., 2001; Firth et al., 2005). Further, electrical synapses contribute to the responsiveness of developing retina to light, and those electrical synapses are depressed by retinal waves and dopamine release (Arroyo and Feller, 2016).

Computational modeling of electrical synapses robustly supports the role of electrical synapses in synchronization (Mulloney et al., 1981; Sherman and Rinzel, 1992; Traub, 1995; Chow and Kopell, 2000; Moortgat et al., 2000; Velazquez and Carlen, 2000; Nomura et al., 2003; Pfeuty et al., 2003; Bem and Rinzel, 2004; Kopell and Ermentrout, 2004; Mancilla et al., 2007; Ostojic et al., 2009). Modeling suggests that electrical synapses can switch from promoting synchrony to anti-synchrony in different contexts (Mulloney et al., 1981; Sherman and Rinzel, 1992; Chow and Kopell, 2000; Lewis and Rinzel, 2003; Nomura et al., 2003; Pfeuty et al., 2003; Bem and Rinzel, 2004; Gibson et al., 2005; Mancilla et al., 2007). Some models point to voltage equalization as a key part of electrical synapse promotion of synchrony (Sherman and Rinzel, 1992; Montbrió and Pazó, 2020). In addition, models have shown that synchrony is promoted by strong electrical synapses, while asynchrony is promoted by weak electrical synapses (Chow and Kopell, 2000; Nomura et al., 2003; Bem and Rinzel, 2004).

Models also suggest that electrical synapses can promote anti-synchrony by preferentially passing the slower afterhyperpolarization that follows a spike. This causes electrical synapses to function as reciprocal inhibitory synapses, which optimizes firing when the neurons are 180° out of phase (Sherman and Rinzel, 1992; Bem and Rinzel, 2004; Ostojic et al., 2009; Vervaeke et al., 2010). Similarly, modeling by Ostojic et al. (2009) suggests that electrical synapses facilitate in-phase synchrony when they are primarily excitatory but facilitate bistable synchrony and asynchrony when they are primarily inhibitory; these models also suggest that electrical synapses are best able to promote synchrony when neurons are active at their resonant frequency. In addition, models by Pfeuty et al. (2003) demonstrate that electrical synapses promote anti-synchrony when there is a strong persistent sodium current and weak potassium current, but promote synchrony when there is a strong persistent potassium current. Other models suggest that generation of either synchronous or anti-synchronous activity require reciprocal GABAergic connections along with electrical synapses (Pfeuty et al., 2003; Bem et al., 2005; Gibson et al., 2005; Lau et al., 2010).

Although anti-synchronous firing between coupled neurons is a robust phenomenon across a wide spectrum of parameter space, experimental evidence for this phenomenon is notably lacking. One example of simulated electrical synapses and reciprocal GABAergic synapses, implemented using dynamic clamp in snail neurons, was able to produce anti-synchrony. Further, stimulation of sparse mossy fiber inputs to Golgi cells transiently switches coupled neurons from spiking synchronously to spiking asynchronously *in vitro* (Vervaeke et al., 2010; **Figure 1B**). However, anti-synchronous firing in coupled Golgi neurons was not observed *in vivo* (van Welie et al., 2016).

Contrary to the persistent thread of evidence connecting electrical synapses to synchronization, a few studies have suggested that electrical synapses fail to play a central role in synchronizing spiking in certain systems. In cortical inhibitory neurons, knockout of connexin36 did not impair synchrony of gamma activity, and synchrony of gamma activity was not correlated with electrical synapse strength (Salkoff et al., 2015; Neske and Connors, 2016).

Beyond Synchrony

Excitation

As mentioned above, by passing depolarizations between coupled neurons gap junctions can act as excitatory synapses (**Figure 1E**). Several studies have identified electrical synapses as actors in lateral excitation, resulting in enhanced sensitivity to stimuli or neural input. Retinal ganglion cells exhibit increased responses to low-contrast and moving stimuli due to lateral excitation from electrical synapses between bipolar, amacrine, or ganglion cells (Trenholm et al., 2013; Kuo et al., 2016). Moreover, excitatory electrical relay from AII amacrine cells to rod bipolar cells is critical for rod-mediated responses in ganglion cells (Güldenagel et al., 2001; Deans et al., 2002). For guinea pigs, the receptive fields of ON center medium retinal ganglion cells (RGCs) are effectively expanded by lateral excitation from electrically coupled ON center α-RGCs (Puller et al., 2020). Under scotopic conditions, electrically coupled directionally sensitive ganglion cells (DSCGs) broaden their tuning for their preferred direction, while uncoupled DSCGs tuning remain stable. Consequently, coupled DSCGs enhance their detection of movement at the cost of discrimination of movement direction through lateral excitation (Yao et al., 2018). It is suspected that coupled DSCGs could potentiate coupling under scotopic conditions to induce that effect, but it remains to be directly measured. In the olfactory bulb, mitral cells enhance reactions to odorants through electrical lateral excitation (Christie and Westbrook, 2006). In addition, depolarizing a Golgi cell in cerebellum increases firing rate in its neighbors. Glutamate uncaging experiments in conjunction with gap junction blockers revealed that gap junctions helped compensate for the decay of the many chemical synaptic inputs at distal dendrites (Vervaeke et al., 2012).

Direct excitatory drive by electrical synapses is a physiological certainty in several cases. Strong electrical synapses between TRN neurons enable bursts in one cell to drive a spike in its coupled neighbor (Parker et al., 2009; Haas et al., 2011). Similarly, Curti et al. (2012) demonstrated the excitatory power of strong electrical synapses in the mesencephalic trigeminal nucleus. In a pair with a coupling coefficient of 0.51, spiking in the presynaptic cell was sufficient to drive spiking in the postsynaptic cell. Interneurons in the stratum lacunosum moleculare of the hippocampus can generate large depolarizations, up to 10 mV, in their coupled neighbors when they burst, due to slower depolarizations passing the gap junction (Zsiros et al., 2007). Goldfish club endings excite Mauthner cells through a mixed

chemical and electrical synapse to trigger an escape reflex. The electrical synapses at the club ending experience a diverse array of plasticity mechanism, which may finely tune how the Mauthner cell responds to different auditory inputs (Pereda et al., 1992, 1994, 1998, 2004). M5 Intrinsically photosensitive retinal ganglion cells (ipRGCs) directly stimulate GABAergic amacrine cells through gap junctions (Pottackal et al., 2021). The amacrine cells then inhibit M5 and M4 ipRGCs; in this circuit, electrical synapses function as the excitatory component of feedback and feedforward inhibition. Striatal medium spiny neurons depolarize cholinergic interneurons through gap junctions, and electrical synapses contribute to the tonic activity observed in cholinergic interneurons (Ren et al., 2021). Electrical synapses also function to excite cortical parvalbumin neurons and cooperate with NMDAR inputs to drive bursts (Lee et al., 2021). In the TRN, spiking depolarizes coupled neighbors, and potentiation of an electrical synapse can transform a synapse from previously subthreshold to spike-driving (Fricker et al., 2021). Modeling of thalamocortical inhibitory feedback circuits revealed that excitation through electrical synapses in the TRN can affect the temporal separation of inputs relayed to cortex by thalamus (Pham and Haas, 2018). In this scenario, one TRN cell receiving earlier input from thalamus drives a coupled TRN cell to spike, which then delays spiking in its other thalamic cells. The degree of separation is directly tied to the strength of the electrical synapse, which can increase separation between spikes in thalamic relay cells by tens of ms. In a feed forward model circuit, powerful electrical synapses can drive coupled interneurons to spike and shorten the integration window for downstream cortical neurons (Pham and Haas, 2019).

Further, electrical synapses are capable of passing subthreshold chemical synaptic events. Subthreshold EPSPs in dorsal cochlear nucleus fusiform cells excite coupled stellate cells, and that excitation can be sufficient to drive spikes in the stellate cells (Apostolides and Trussell, 2014). Interneurons in the stratum lacunosum moleculare are excited by GABA due to HCO_3^- leaving the cell (Perkins and Wong, 1996); excitatory GABAergic postsynaptic potential are passed through the gap junction. Inhibitory Renshaw cells in the spinal cord also excite each other by passing cholinergic EPSPs through gap junctions (d'Incamps et al., 2012). Thus, subthreshold chemical synaptic inputs in one cell are computational relevant in its electrical coupled neighbor and may be an understudied feature of electrical synapses.

Inhibition

By passing hyperpolarizations such as AHPs or IPSPs between coupled neurons, gap junctions act as inhibitory synapses (**Figure 1D**). Due to the low-pass filtering that results from current flowing across two cell membranes, slower signals are preferentially transferred through electrical synapses compared to faster events such as action potentials. In the case of spikes, slow AHPs are passed more effectively than the spike itself, making the event as a whole net inhibitory to the coupled cell. This effect was noted in fast spiking cortical interneurons (Galarreta and Hestrin, 2001). Inhibition from electrical synapses can be compounded with an accompanying inhibitory chemical synapse between coupled neurons, enhancing the inhibitory effect after spiking (Galarreta and Hestrin, 2001). The spike waveform in the presynaptic cell is critical in determining whether electrical synapses will excite, inhibit, or both after a spike. Spikes with larger half widths or broad depolarizations underlying a burst are better at exciting the postsynaptic cells, while fast spikes and large AHPs are net inhibitory. Gibson et al. (2005) demonstrated that fast-spiking inhibitory neurons send effective inhibition after spiking, while low-threshold spiking neurons primarily depolarize the postsynaptic neurons after spiking. Membrane potential also affects the net valence of post synaptic potentials from electrical synapses *via* differences in postsynaptic membrane conductances. Fast-spiking neurons almost exclusively depolarize postsynaptic cells after spiking when the postsynaptic neuron is hyperpolarized, but they primarily inhibit depolarized postsynaptic cells (Otsuka and Kawaguchi, 2013).

Inhibition carried by gap junction-mediated AHPs was also described in Golgi interneurons (Vervaeke et al., 2010; Yaeger and Trussell, 2016; Hoehne et al., 2020). Interestingly, in this case electrical synapse inhibition was shown to function similar to feedforward inhibition. Stimulation of excitatory parallel fiber inputs to electrically coupled basket cells results in an EPSP followed by electrically mediated inhibitory postsynaptic potential. The inhibition delivered by electrical synapses in this case sharpens the EPSPs that precede them and reduces temporal summation, hallmarks of feedforward inhibition (Hoehne et al., 2020). In striatum, burst firing between 25 to 60 Hz of fast-spiking interneurons inhibits spiking in coupled neighbors by transferring AHPs (Russo et al., 2013). In the dorsal cochlear nucleus, fusiform cells are able to transfer subthreshold synaptic voltage fluctuations to stellate cells *via* electrical synapses (Apostolides and Trussell, 2014). EPSPs in fusiform cells drive depolarization followed by a hyperpolarization caused by closing HCN channels (Apostolides and Trussell, 2014). Both the depolarizing and hyperpolarizing aspects of the chemical postsynaptic potential in the fusiform cell is transferred to stellate cells through the gap junction. The ability for electrical synapses to hyperpolarize neurons and inhibit spiking is an important aspect of their function that should not be overlooked.

Shunting

Unlike chemical synapses, electrical synapses passively contribute to the excitability of neurons without requiring activation of the synapse for that effect. When one neuron in an electrically coupled pair is stimulated, the gap junction to the neighboring cell shunts current away and renders the first neurons less likely to spike (Llinas et al., 1974; Van Der Giessen et al., 2008; Hjorth et al., 2009; Chatzigeorgiou and Schafer, 2011; Kawano et al., 2011; Rabinowitch et al., 2013; **Figure 1C**). Consequently, each hyperpolarized neuron in a coupled network inhibits spike generation, and depolarization of those neurons lifts that opposition. Shunting by electrical synapses can be especially impactful when one neuron is coupled to many other neurons. In such a network, a central neuron is strongly inhibited from spiking until a threshold of neighbors are also depolarized (Chatzigeorgiou and Schafer, 2011; Rabinowitch et al., 2013),

effectively offering a mass-coincidence detection or insurance against erroneous responses.

Moreover, regulation of electrical synapse strength affects the overall excitability of a network. Coupled nNOS-1 amacrine cells in retina release nitric oxide in response to light, which consequently decouple the amacrine cells. Decoupling the amacrine cells increases their individual excitability by reducing the shunting of current to its neighbors (Jacoby et al., 2018).

Coincidence Detection

The same principles that enable electrical synapses to facilitate synchrony also allow them to act as coincident detectors. Typically, coincidence detection is conceptualized as the summation of near-simultaneous excitatory chemical inputs to one cell, driving spiking only when they are sufficiently coincident. Inputs arriving through electrical synapses can work in the same additive fashion. In addition, as mentioned earlier and in contrast to excitatory synapses, inactive electrically coupled neurons shunt current away from active neurons until they become depolarized themselves. As a result, electrical synapses can act as detectors of coincident depolarization between coupled neurons by effectively checking if both neurons in a pair are simultaneously depolarized before allowing spike generation. Furthermore, the spikelet generated by one neuron can drive spiking in a peri threshold neighbor, ensuring that coincident inputs are likely to result in both neurons spiking.

Galarreta and Hestrin (2001) injected current simulating subthreshold EPSPs into coupled cortical fast spiking interneurons, which drove spikes when they occurred within 1 ms, but failed to drive spikes when EPSPs were separated by 5 ms. Subthreshold current injections to each neuron of a pair that are mismatched in time fail to produce spiking in coupled amacrine cells, but generate spikes in both coupled cells when applied to both cells in a pair simultaneously (Veruki and Hartveit, 2002b). Similarly, Trenholm et al. (2013) stimulated one retinal ganglion cell with light and a coupled neighbor with current injection. Weaker light stimuli failed to drive spikes unless there was coincident stimulation of the coupled neighbor (Trenholm et al., 2013). In Golgi basket cells, simultaneous stimulation of both cells in a coupled pair has greater action potential probability compared to stimulation of one cell alone (Alcami, 2018). Computational modeling of striatal inhibitory neurons showed that electrical synapses reduce the overall firing of neurons in the circuit, but that effect was minimized when coupled neurons received coincident inputs (Hjorth et al., 2009). Experiments in *C. elegans* have found that RIH neurons act as a hub with electrical synaptic connections to multiple neural pathways; coincident stimulation from electrically connected partners were necessary to sufficiently stimulate RIH neurons and facilitate *C. elegans* escape response after a nose touch (Chatzigeorgiou and Schafer, 2011). Future modeling of the nose-touch-response circuit supports that electrical synapses from multiple pathways shunt current and make RIH neurons less responsive, while multiple simultaneous active neurons promote activation of RIH neurons and consequently the escape response (Rabinowitch et al., 2013). Taken together, the combined ability of electrical synapses to shunt current when a neuron is inactive, and promote activity when it is active, helps to cause synchronous activity and acts as detector of coincident activity across multiple neurons.

Signal to Noise Ratio

Neurons are subject to a variety of stochastic factors, including the random opening and closing of ionic channels and spontaneous synaptic activity. A fundamental task for the nervous system is to distinguish between signal and noise. Electrical synapses that shunt current and decrease excitability implement the functional effect of noise dampening (**Figure 1F**). Computational modeling supports the possibility of this mechanism for noise reduction *via* electrical synapses (Lamb and Simon, 1976; Vardi and Smith, 1996; Usher et al., 1999; DeVries et al., 2002; Medvedev, 2009).

Improvement of signal to noise ratio by electrical synapses has been investigated in multiple systems. Noise was measured in retinal preparations by recording membrane fluctuations of AII amacrine cells in complete darkness; noise was greater in amacrine cells with genetically knocked out connexin36 (Dunn et al., 2006). In the fish olfactory bulb, the variance of mitral cell response to an odorant increases with pharmacological blockade of gap junctions (Zhu et al., 2013). Electrical synapses suppress membrane oscillations entirely in drosophila lobula plate tangential cells, likely *via* shunting noisy intrinsic currents of in the cell (Ammer et al., 2022). It has also been inferred that electrical synapses improve signal to noise ratio in the fly olfactory bulb (Kazama and Wilson, 2009; Yaksi and Wilson, 2010) and monkey locus coeruleus (Usher et al., 1999). However, experiments comparing noise in the presence and absence of electrical synapses in those systems are still needed.

Asymmetry

Bidirectional flow of current is a notable distinguishing property of electrical synapses. Yet the magnitudes of signals relayed in each direction quite often show some degree of direction dependence. In the mammalian nervous system, asymmetry of synapses has been noted in neocortex (Galarreta and Hestrin, 2002), TRN (Haas et al., 2011; Sevetson and Haas, 2015; Zolnik and Connors, 2016), inferior olive (Devor and Yarom, 2002), cerebellum (Mann-Metzer and Yarom, 1999; Alcami and Marty, 2013; Szoboszlay et al., 2016), dorsal cochlear nucleus (Apostolides and Trussell, 2013), and mesencephalic trigeminal nucleus (Curti et al., 2012). Asymmetry could result from heterotypy of gap junction channels and plaques, where oligomerization or docking of different connexin or innexin proteins can asymmetrically pass current (Bukauskas et al., 1995; Phelan et al., 2008; Rash et al., 2013), and differences in hemichannel scaffolding (Marsh et al., 2017) could also contribute to the rectifying ability of electrical synapses. Even for homotypic gap junctions based on connexin36, which are largely voltage-independent (Srinivas et al., 1999), differences between cell properties, such as input resistance or cable properties, create functional asymmetry for signals sent across the gap junction (Mann-Metzer and Yarom, 1999; Veruki and Hartveit, 2002a; Nadim and Golowasch, 2006; Alcami and Marty, 2013; Amsalem et al., 2016; Mendoza and Haas, 2022). Furthermore,

those different sources of asymmetry can also compensate for or exacerbate genuine junctional asymmetry between electrical synapses (Mendoza and Haas, 2022). For example, at the Mauthner mixed synapse, heterotypic asymmetrical gap junctions composed of connexin34.7 and connexin35 preferentially pass current from the Mauthner cell to the club endings. At that synapse, rectification compensates for the large dendrite of the Mauthner cell, making the electrical synapse more functionally bidirectional (Rash et al., 2013).

Asymmetry of electrical synapses directly impacts their function. Full rectification can create nearly unidirectional communication, such as in the giant motor neuron of crayfish or pyloric circuit of the spiny lobster (Furshpan and Potter, 1957, 1959; Graubard and Hartline, 1987; Johnson et al., 1993). Voltage-dependent gating of gap junction channels allows crayfish presynaptic giant interneurons to unidirectionally excite the giant motor neuron and engage an escape reflex (Jaslove and Brink, 1986). For the pyloric circuit of the spiny lobster, the rectified synapse allows the lateral pyloric neuron to drive the pyloric neuron to burst, and then send a delayed chemical inhibitory signal to terminate the burst (Graubard and Hartline, 1987; Mamiya et al., 2003). In the dorsal cochlear nucleus (Apostolides and Trussell, 2014), near-complete asymmetry is a result of input resistance mismatch, and results in fusiform cells driving spikes in more-compact stellate cells. Asymmetry in this case ensures recruitment of local inhibition within the circuit even during subthreshold excitation of the fusiform cells.

For more moderate asymmetry, modeling results reveal an effect of asymmetry on detailed spike timing, even to the extent of reversing spike order in a coupled cells (Sevetson and Haas, 2015), and controls the phase of synchronous rhythmic activity (Mendoza and Haas, 2022). Modeling of larger networks shows that rectifying electrical synapses can improve the robustness of rhythmic activity (Gutierrez et al., 2013). Because electrical synapse plasticity has been shown to systematically alter the degree of asymmetry (Haas et al., 2011; Fricker et al., 2021), asymmetry may be actively regulated in order to tune spike timing and network activity. Collectively, our understanding of the function of asymmetry is still limited, but its potential impacts are worthy of additional investigation.

Future of Electrical Synapse Study

The study of electrical synapse function has a dense focus on the contribution of electrical synapses to synchronization of activity between coupled pairs. This attention is merited, and there is ample evidence to support this function, especially when neurons in a coupled network receive prolonged, simultaneous excitation. The next decade of research would greatly benefit from studies focusing on how electrical synapses in different systems affect transient inputs, and from studies that look at how temporal variation in the activity of multiple electrically coupled neurons in a network affect activity. In *C. elegans*, a hub and spoke model has been proposed, where a central neuron integrates the information from multiple electrical synapses to determine whether to fire. Such a computational process has not yet been explored in mammalian electrical networks.

One limitation to understanding the functions of electrical synapses within and beyond a network is that the gold standard for identification and measurement of coupling between neurons is dual whole-cell recordings, which is difficult and limited to two cells at a time. In this manner, the network is neglected. Extracellular methods, such as multi-electrode arrays, field recordings, and wide-scale imaging of fluorophores overcome this limitation, but do not reveal which neurons are coupled in a network or the strengths or spatial distributions of their coupling. One could hope that cell-specific optogenetics could mitigate the barrier (Dakin and Li, 2006; Qiao and Sanes, 2016), and some all-imaging approaches have identified GJ-mediated signals (Tian et al., 2021). In computational studies of neural networks, electrical synapses are most often neglected entirely, which we regard as a vast missed opportunity.

Improved imaging could bring new insight into the function of electrical synapses. Currently, we lack a dye that can pass through connexin36-based gap junctions and be imaged in live tissue, which limits our ability to identify and image specific gap junctions. A new GCaMP connexin36 hybrid gene has been created and used in HeLa cells (Moore et al., 2020). It is possible that replacement of the connexin36 gene with the GCaMP connexin36 hybrid would allow researchers to look at localized activity in the dendrites and near the gap junction. However, this is early speculation, and the viability of such a method needs to be vetted. Another major complication is differentiating connexin36 in the cytoplasm from connexin36 that forms gap junction pores.

A recent innovation has created novel connexin genes through an iterative mutation approach. Mutated perch connexin34.7 and connexin35 proteins form exclusively heterotypic gap junctions (Ransey et al., 2021a) resulting in asymmetrical electrical synapses (Ransey et al., 2021b), and expression of each protein can be directed toward specific cell types. This technique could be useful for interrogating how the addition or substitution of asymmetric electrical synapses modifies a circuit and behavior.

Electrical synapses have profound and complicated impacts on the processing of neural signals. The functional consequence of electrical synapses is collectively impacted by the membrane voltages of pre- and post-synaptic neurons, the waveform of spikes, the frequency of spiking, and their location on dendrites. Wherever electrical synapses are present, their function should be thoroughly interrogated. Moreover, it is important for connectome projects (Van Essen et al., 2013; Oh et al., 2014; Zhang et al., 2019) to include electrical connections in addition to chemical connections to achieve a whole picture of neural communication pathways.

AUTHOR CONTRIBUTIONS

JH and MV contributed equally to conceptualization and writing. Both authors contributed to the article and approved the submitted version.

FUNDING

This research was funded by the Whitehall Grant in Aid to JH.

REFERENCES

Alcami, P. (2018). Electrical synapses enhance and accelerate interneuron recruitment in response to coincident and sequential excitation. *Front. Cell. Neurosci.* 12:156. doi: 10.3389/fncel.2018.00156

Alcami, P., and Marty, A. (2013). Estimating functional connectivity in an electrically coupled interneuron network. *Proc. Natl. Acad. Sci.* 110, E4798–E4807. doi: 10.1073/pnas.1310983110

Alcami, P., and Pereda, A. E. (2019). Beyond plasticity: the dynamic impact of electrical synapses on neural circuits. *Nat. Rev. Neurosci.* 20, 253–271. doi: 10.1038/s41583-019-0133-5

Ammer, G., Vieira, R. M., Fendl, S., and Borst, A. (2022). Anatomical distribution and functional roles of electrical synapses in *Drosophila*. *Curr. Biol.* 32, 2022–2036.e4. doi: 10.1016/j.cub.2022.03.040

Amsalem, O., Van Geit, W., Muller, E., Markram, H., and Segev, I. (2016). From neuron biophysics to orientation selectivity in electrically coupled networks of neocortical L2/3 large basket cells. *Cereb. Cortex* 26, 3655–3668. doi: 10.1093/cercor/bhw166

Anaya-Martinez, V., Martinez-Marcos, A., Martinez-Fong, D., Aceves, J., and Erlij, D. (2006). Substantia nigra compacta neurons that innervate the reticular thalamic nucleus in the rat also project to striatum or globus pallidus: implications for abnormal motor behavior. *Neuroscience* 143, 477–486. doi: 10.1016/j.neuroscience.2006.08.033

Apostolides, P. F., and Trussell, L. O. (2013). Regulation of interneuron excitability by gap junction coupling with principal cells. *Nat. Neurosci.* 16, 1764–1772. doi: 10.1038/nn.3569

Apostolides, P. F., and Trussell, L. O. (2014). Control of interneuron firing by subthreshold synaptic potentials in principal cells of the dorsal cochlear nucleus. *Neuron* 83, 324–330. doi: 10.1016/j.neuron.2014.06.008

Armstrong, D., Eccles, J., Harvey, R., and Matthews, P. (1968). Responses in the dorsal accessory olive of the cat to stimulation of hind limb afferents. *J. Physiol.* 194, 125–145. doi: 10.1113/jphysiol.1968.sp008398

Arroyo, D. A., and Feller, M. B. (2016). Spatiotemporal features of retinal waves instruct the wiring of the visual circuitry. *Front. Neural Circuits* 10:54. doi: 10.3389/fncir.2016.00054

Beierlein, M., Gibson, J. R., and Connors, B. W. (2000). A network of electrically coupled interneurons drives synchronized inhibition in neocortex. *Nat. Neurosci.* 3, 904–910. doi: 10.1038/78809

Bem, T., Le Feuvre, Y., Rinzel, J., and Meyrand, P. (2005). Electrical coupling induces bistability of rhythms in networks of inhibitory spiking neurons. *Eur. J. Neurosci.* 22, 2661–2668. doi: 10.1111/j.1460-9568.2005.04405.x

Bem, T., and Rinzel, J. (2004). Short duty cycle destabilizes a half-center oscillator, but gap junctions can restabilize the anti-phase pattern. *Journal of neurophysiology* 91, 693–703. doi: 10.1152/jn.00783.2003

Benchenane, K., Tiesinga, P. H., and Battaglia, F. P. (2011). Oscillations in the prefrontal cortex: a gateway to memory and attention. *Curr. Opin. Neurobiol.* 21, 475–485. doi: 10.1016/j.conb.2011.01.004

Bennett, M. V. (1966). Physiology of electrotonic junctions. *Ann. N. Y. Acad. Sci.* 137, 509–539. doi: 10.1111/j.1749-6632.1966.tb50178.x

Bennett, M. V., and Zukin, R. S. (2004). Electrical coupling and neuronal synchronization in the Mammalian brain. *Neuron* 41, 495–511. doi: 10.1016/s0896-6273(04)00043-1

Blatow, M., Rozov, A., Katona, I., Hormuzdi, S. G., Meyer, A. H., Whittington, M. A., et al. (2003). A novel network of multipolar bursting interneurons generates theta frequency oscillations in neocortex. *Neuron* 38, 805–817. doi: 10.1016/s0896-6273(03)00300-3

Blenkinsop, T. A., and Lang, E. J. (2006). Block of inferior olive gap junctional coupling decreases Purkinje cell complex spike synchrony and rhythmicity. *J. Neurosci.* 26, 1739–1748. doi: 10.1523/JNEUROSCI.3677-05.2006

Bloomfield, S. A., and Volgyi, B. (2009). The diverse functional roles and regulation of neuronal gap junctions in the retina. *Nat. Rev. Neurosci.* 10, 495–506. doi: 10.1038/nrn2636

Bou-Flores, C., and Berger, A. J. (2001). Gap junctions and inhibitory synapses modulate inspiratory motoneuron synchronization. *J. Neurophysiol.* 85, 1543–1551. doi: 10.1152/jn.2001.85.4.1543

Bromberg, M. B., Penne, J. B. Jr., Stephenson, B. S., and Young, A. B. (1981). Evidence for glutamate as the neurotransmitter of corticothalamic and corticorubral pathways. *Brain Res.* 215, 369–374. doi: 10.1016/0006-8993(81)90519-9

Buhl, D. L., Harris, K. D., Hormuzdi, S. G., Monyer, H., and Buzsáki, G. (2003). Selective impairment of hippocampal gamma oscillations in connexin-36 knock-out mouse in vivo. *J. Neurosci.* 23, 1013–1018. doi: 10.1523/JNEUROSCI.23-03-01013.2003

Bukauskas, F. F., Elfgang, C., Willecke, K., and Weingart, R. (1995). Heterotypic gap junction channels (connexin26–connexin32) violate the paradigm of unitary conductance. *Pflügers Arch.* 429, 870–872. doi: 10.1007/BF00374812

Buzsáki, G., and Draguhn, A. (2004). Neuronal oscillations in cortical networks. *Science* 304, 1926–1929.

Caputi, A., Rozov, A., Blatow, M., and Monyer, H. (2009). Two calretinin-positive GABAergic cell types in layer 2/3 of the mouse neocortex provide different forms of inhibition. *Cereb. Cortex* 19, 1345–1359. doi: 10.1093/cercor/bhn175

Cardin, J. A. (2016). Snapshots of the brain in action: local circuit operations through the lens of γ oscillations. *J. Neurosci.* 36, 10496–10504. doi: 10.1523/JNEUROSCI.1021-16.2016

Chang, Q., Gonzalez, M., Pinter, M. J., and Balice-Gordon, R. J. (1999). Gap junctional coupling and patterns of connexin expression among neonatal rat lumbar spinal motor neurons. *J. Neurosci.* 19, 10813–10828. doi: 10.1523/JNEUROSCI.19-24-10813.1999

Chatzigeorgiou, M., and Schafer, W. R. (2011). Lateral facilitation between primary mechanosensory neurons controls nose touch perception in *C. elegans*. *Neuron* 70, 299–309. doi: 10.1016/j.neuron.2011.02.046

Chow, C. C., and Kopell, N. (2000). Dynamics of spiking neurons with electrical coupling. *Neural Comput.* 12, 1643–1678.

Christie, J. M., Bark, C., Hormuzdi, S. G., Helbig, I., Monyer, H., and Westbrook, G. L. (2005). Connexin36 mediates spike synchrony in olfactory bulb glomeruli. *Neuron* 46, 761–772. doi: 10.1016/j.neuron.2005.04.030

Christie, J. M., and Westbrook, G. L. (2006). Lateral excitation within the olfactory bulb. *J. Neurosci.* 26, 2269–2277.

Colgin, L. L., and Moser, E. I. (2010). Gamma oscillations in the hippocampus. *Physiology* 25, 319–329.

Colwell, C. S. (2000). Rhythmic coupling among cells in the suprachiasmatic nucleus. *J. Neurobiol.* 43, 379–388. doi: 10.1002/1097-4695(20000615)43:4<379::aid-neu6>3.0.co;2-0

Condorelli, D. F., Parenti, R., Spinella, F., Salinaro, A. T., Belluardo, N., Cardile, V., et al. (1998). Cloning of a new gap junction gene (Cx36) highly expressed in mammalian brain neurons. *Eur. J. Neurosci.* 10, 1202–1208. doi: 10.1046/j.1460-9568.1998.00163.x

Connors, B. W. (2017). Synchrony and so much more: diverse roles for electrical synapses in neural circuits. *Dev. Neurobiol.* 77, 610–624. doi: 10.1002/dneu.22493

Connors, B. W., and Long, M. A. (2004). Electrical synapses in the mammalian brain. *Annu. Rev. Neurosci.* 27, 393–418.

Cornwall, J., Cooper, J. D., and Phillipson, O. T. (1990). Projections to the rostral reticular thalamic nucleus in the rat. *Exp. Brain Res.* 80, 157–171. doi: 10.1007/BF00228857

Curti, S., Davoine, F., and Dapino, A. (2022). Function and plasticity of electrical synapses in the mammalian brain: role of non-junctional mechanisms. *Biology* 11:81. doi: 10.3390/biology11010081

Curti, S., Hoge, G., Nagy, J. I., and Pereda, A. E. (2012). Synergy between electrical coupling and membrane properties promotes strong synchronization of neurons of the mesencephalic trigeminal nucleus. *J. Neurosci.* 32, 4341–4359. doi: 10.1523/JNEUROSCI.6216-11.2012

Dakin, K., and Li, W.-H. (2006). Infrared-LAMP: two-photon uncaging and imaging of gap junctional communication in three dimensions. *Nat. Methods* 3, 959–959. doi: 10.1038/nmeth1206-959

D'Angelo, E., Koekkoek, S., Lombardo, P., Solinas, S., Ros, E., Garrido, J., et al. (2009). Timing in the cerebellum: oscillations and resonance in the granular layer. *Neuroscience* 162, 805–815. doi: 10.1016/j.neuroscience.2009.01.048

De Zeeuw, C. I., Hoogenraad, C. C., Koekkoek, S., Ruigrok, T. J., Galjart, N., and Simpson, J. I. (1998). Microcircuitry and function of the inferior olive. *Trends Neurosci.* 21, 391–400. doi: 10.1016/s0166-2236(98)01310-1

Deans, M. R., Gibson, J. R., Sellitto, C., Connors, B. W., and Paul, D. L. (2001). Synchronous activity of inhibitory networks in neocortex requires electrical

synapses containing connexin36. *Neuron* 31, 477–485. doi: 10.1016/s0896-6273(01)00373-7

Deans, M. R., Volgyi, B., Goodenough, D. A., Bloomfield, S. A., and Paul, D. L. (2002). Connexin36 is essential for transmission of rod-mediated visual signals in the mammalian retina. *Neuron* 36, 703–712. doi: 10.1016/s0896-6273(02)01046-2

Devor, A., and Yarom, Y. (2002). Electrotonic coupling in the inferior olivary nucleus revealed by simultaneous double patch recordings. *J. Neurophysiol.* 87, 3048–3058. doi: 10.1152/jn.2002.87.6.3048

DeVries, S. H., Qi, X., Smith, R., Makous, W., and Sterling, P. (2002). Electrical coupling between mammalian cones. *Curr. Biol.* 12, 1900–1907. doi: 10.1016/s0960-9822(02)01261-7

d'Incamps, B. L., Krejci, E., and Ascher, P. (2012). Mechanisms shaping the slow nicotinic synaptic current at the motoneuron–Renshaw cell synapse. *J. Neurosci.* 32, 8413–8423. doi: 10.1523/JNEUROSCI.0181-12.2012

Draguhn, A., Traub, R., Schmitz, D., and Jefferys, J. (1998). Electrical coupling underlies high-frequency oscillations in the hippocampus in vitro. *Nature* 394, 189–192. doi: 10.1038/28184

Dugué, G. P., Brunel, N., Hakim, V., Schwartz, E., Chat, M., Lévesque, M., et al. (2009). Electrical coupling mediates tunable low-frequency oscillations and resonance in the cerebellar Golgi cell network. *Neuron* 61, 126–139. doi: 10.1016/j.neuron.2008.11.028

Dunn, F. A., Doan, T., Sampath, A. P., and Rieke, F. (2006). Controlling the gain of rod-mediated signals in the mammalian retina. *J. Neurosci.* 26, 3959–3970. doi: 10.1523/JNEUROSCI.5148-05.2006

Eisen, J. S., and Marder, E. (1982). Mechanisms underlying pattern generation in lobster stomatogastric ganglion as determined by selective inactivation of identified neurons. III. Synaptic connections of electrically coupled pyloric neurons. *J. Neurophysiol.* 48, 1392–1415. doi: 10.1152/jn.1982.48.6.1392

Feig, S., and Harting, J. K. (1998). Corticocortical communication via the thalamus: ultrastructural studies of corticothalamic projections from area 17 to the lateral posterior nucleus of the cat and inferior pulvinar nucleus of the owl monkey. *J. Comp. Neurol.* 395, 281–295. doi: 10.1002/(sici)1096-9861(19980808)395:3<281::aid-cne2>3.0.co;2-z

Firth, S. I., Wang, C.-T., and Feller, M. B. (2005). Retinal waves: mechanisms and function in visual system development. *Cell Calcium* 37, 425–432. doi: 10.1016/j.ceca.2005.01.010

Fitzpatrick, D., Usrey, W. M., Schofield, B. R., and Einstein, G. (1994). The sublaminar organization of corticogeniculate neurons in layer 6 of macaque striate cortex. *Vis. Neurosci.* 11, 307–315. doi: 10.1017/s0952523800001656

Fonnum, F., Storm-Mathisen, J., and Divac, I. (1981). Biochemical evidence for glutamate as neurotransmitter in corticostriatal and corticothalamic fibres in rat brain. *Neuroscience* 6, 863–873. doi: 10.1016/0306-4522(81)90168-8

Fosse, V. M., Kolstad, J., and Fonnum, F. (1986). A bioluminescence method for the measurement of l-glutamate: applications to the study of changes in the release of l-glutamate from lateral geniculate nucleus and superior colliculus after visual cortex ablation in rats. *J. Neurochem.* 47, 340–349. doi: 10.1111/j.1471-4159.1986.tb04507.x

Freeman, A., Ciliax, B., Bakay, R., Daley, J., Miller, R. D., Keating, G., et al. (2001). Nigrostriatal collaterals to thalamus degenerate in parkinsonian animal models. *Ann. Neurol.* 50, 321–329. doi: 10.1002/ana.1119

Fricker, B., Heckman, E., Cunningham, P. C., Wang, H., and Haas, J. S. (2021). Activity-dependent long-term potentiation of electrical synapses in the mammalian thalamus. *J. Neurophysiol.* 125, 476–488. doi: 10.1152/jn.00471.2020

Fukuda, T., and Kosaka, T. (2000). Gap junctions linking the dendritic network of GABAergic interneurons in the hippocampus. *J. Neurosci.* 20, 1519–1528. doi: 10.1523/JNEUROSCI.20-04-01519.2000

Furshpan, E., and Potter, D. (1957). Mechanism of nerve-impulse transmission at a crayfish synapse. *Nature* 180, 342–343. doi: 10.1038/180342a0

Furshpan, E., and Potter, D. (1959). Transmission at the giant motor synapses of the crayfish. *J. Physiol.* 145:289. doi: 10.1113/jphysiol.1959.sp006143

Galarreta, M., and Hestrin, S. (1999). A network of fast-spiking cells in the neocortex connected by electrical synapses. *Nature* 402, 72–75. doi: 10.1038/47029

Galarreta, M., and Hestrin, S. (2001). Spike transmission and synchrony detection in networks of GABAergic interneurons. *Science* 292, 2295–2299. doi: 10.1126/science.1061395

Galarreta, M., and Hestrin, S. (2002). Electrical and chemical synapses among parvalbumin fast-spiking GABAergic interneurons in adult mouse neocortex. *Proc. Natl. Acad. Sci.* 99, 12438–12443. doi: 10.1073/pnas.192159599

Gandia, J. A., De Las Heras, S., Garcia, M., and Gimenez-Amaya, J. M. (1993). Afferent projections to the reticular thalamic nucleus from the globus pallidus and the substantia nigra in the rat. *Brain Res. Bull.* 32, 351–358. doi: 10.1016/0361-9230(93)90199-l

Gibson, J. R., Beierlein, M., and Connors, B. W. (1999). Two networks of electrically coupled inhibitory neurons in neocortex. *Nature* 402, 75–79. doi: 10.1038/47035

Gibson, J. R., Beierlein, M., and Connors, B. W. (2005). Functional properties of electrical synapses between inhibitory interneurons of neocortical layer 4. *J. Neurophysiol.* 93, 467–480. doi: 10.1152/jn.00520.2004

Giraud, A.-L., and Poeppel, D. (2012). Cortical oscillations and speech processing: emerging computational principles and operations. *Nat. Neurosci.* 15, 511–517. doi: 10.1038/nn.3063

Graubard, K., and Hartline, D. K. (1987). Full-wave rectification from a mixed electrical-chemical synapse. *Science* 237, 535–537. doi: 10.1126/science.2885921

Güldenagel, M., Ammermüller, J., Feigenspan, A., Teubner, B., Degen, J., Söhl, G., et al. (2001). Visual transmission deficits in mice with targeted disruption of the gap junction gene connexin36. *J. Neurosci.* 21, 6036–6044. doi: 10.1523/JNEUROSCI.21-16-06036.2001

Gutierrez, G. J., O'Leary, T., and Marder, E. (2013). Multiple mechanisms switch an electrically coupled, synaptically inhibited neuron between competing rhythmic oscillators. *Neuron* 77, 845–858. doi: 10.1016/j.neuron.2013.01.016

Haas, J. S., Greenwald, C. M., and Pereda, A. E. (2016). Activity-dependent plasticity of electrical synapses: increasing evidence for its presence and functional roles in the mammalian brain. *BMC Cell Biol.* 17 (Suppl. 1):14. doi: 10.1186/s12860-016-0090-z

Haas, J. S., and Landisman, C. E. (2011). State-dependent modulation of gap junction signaling by the persistent sodium current. *Front. Cell Neurosci.* 5:31. doi: 10.3389/fncel.2011.00031

Haas, J. S., Zavala, B., and Landisman, C. E. (2011). Activity-dependent long-term depression of electrical synapses. *Science* 334, 389–393. doi: 10.1126/science.1207502

Halassa, M. M., Siegle, J. H., Ritt, J. T., Ting, J. T., Feng, G., and Moore, C. I. (2011). Selective optical drive of thalamic reticular nucleus generates thalamic bursts and cortical spindles. *Nat. Neurosci.* 14, 1118–1120. doi: 10.1038/nn.2880

Hampson, E., Vaney, D. I., and Weiler, R. (1992). Dopaminergic modulation of gap junction permeability between amacrine cells in mammalian retina. *J. Neurosci.* 12, 4911–4922. doi: 10.1523/JNEUROSCI.12-12-04911.1992

Hanslmayr, S., Gross, J., Klimesch, W., and Shapiro, K. L. (2011). The role of alpha oscillations in temporal attention. *Brain Res. Rev.* 67, 331–343. doi: 10.1016/j.brainresrev.2011.04.002

Hjorth, J., Blackwell, K. T., and Kotaleski, J. H. (2009). Gap junctions between striatal fast-spiking interneurons regulate spiking activity and synchronization as a function of cortical activity. *J. Neurosci.* 29, 5276–5286. doi: 10.1523/JNEUROSCI.6031-08.2009

Hoehne, A., McFadden, M. H., and DiGregorio, D. A. (2020). Feed-forward recruitment of electrical synapses enhances synchronous spiking in the mouse cerebellar cortex. *Elife* 9:e57344. doi: 10.7554/eLife.57344

Hooper, S. L., and Marder, E. (1987). Modulation of the lobster pyloric rhythm by the peptide proctolin. *J. Neurosci.* 7, 2097–2112. doi: 10.1523/JNEUROSCI.07-07-02097.1987

Hormuzdi, S. G., Pais, I., LeBeau, F. E., Towers, S. K., Rozov, A., Buhl, E. H., et al. (2001). Impaired electrical signaling disrupts gamma frequency oscillations in connexin 36-deficient mice. *Neuron* 31, 487–495. doi: 10.1016/s0896-6273(01)00387-7

Houser, C. R., Vaughn, J. E., Barber, R. P., and Roberts, E. (1980). GABA neurons are the major cell type of the nucleus reticularis thalami. *Brain Res.* 200, 341–354. doi: 10.1016/0006-8993(80)90925-7

Hu, H., and Agmon, A. (2015). Properties of precise firing synchrony between synaptically coupled cortical interneurons depend on their mode of coupling. *J. Neurophysiol.* 114, 624–637. doi: 10.1152/jn.00304.2015

Jacoby, J., Nath, A., Jessen, Z. F., and Schwartz, G. W. (2018). A self-regulating gap junction network of amacrine cells controls nitric oxide release in the retina. *Neuron* 100, 1149–1162.e5. doi: 10.1016/j.neuron.2018.09.047

Jaslove, S. W., and Brink, P. R. (1986). The mechanism of rectification at the electrotonic motor giant synapse of the crayfish. *Nature* 323, 63–65. doi: 10.1038/323063a0

Johnson, B. R., Peck, J. H., and Harris-Warrick, R. M. (1993). Dopamine induces sign reversal at mixed chemical-electrical synapses. *Brain Res.* 625, 159–164. doi: 10.1016/0006-8993(93)90149-h

Jones, E. (1975). Some aspects of the organization of the thalamic reticular complex. *J. Comp. Neurol.* 162, 285–308. doi: 10.1002/cne.901620302

Kashiwadani, H., Sasaki, Y. F., Uchida, N., and Mori, K. (1999). Synchronized oscillatory discharges of mitral/tufted cells with different molecular receptive ranges in the rabbit olfactory bulb. *J. Neurophysiol.* 82, 1786–1792. doi: 10.1152/jn.1999.82.4.1786

Kawano, T., Po, M. D., Gao, S., Leung, G., Ryu, W. S., and Zhen, M. (2011). An imbalancing act: gap junctions reduce the backward motor circuit activity to bias *C. elegans* for forward locomotion. *Neuron* 72, 572–586. doi: 10.1016/j.neuron.2011.09.005

Kazama, H., and Wilson, R. I. (2009). Origins of correlated activity in an olfactory circuit. *Nat. Neurosci.* 12, 1136–1144. doi: 10.1038/nn.2376

Kilavik, B. E., Zaepffel, M., Brovelli, A., MacKay, W. A., and Riehle, A. (2013). The ups and downs of beta oscillations in sensorimotor cortex. *Exp. Neurol.* 245, 15–26. doi: 10.1016/j.expneurol.2012.09.014

Kopell, N., and Ermentrout, B. (2004). Chemical and electrical synapses perform complementary roles in the synchronization of interneuronal networks. *Proc. Natl. Acad. Sci.* 101, 15482–15487. doi: 10.1073/pnas.0406343101

Kothmann, W. W., Massey, S. C., and O'Brien, J. (2009). Dopamine-stimulated dephosphorylation of connexin 36 mediates AII amacrine cell uncoupling. *J. Neurosci.* 29, 14903–14911. doi: 10.1523/JNEUROSCI.3436-09.2009

Kuo, S. P., Schwartz, G. W., and Rieke, F. (2016). Nonlinear spatiotemporal integration by electrical and chemical synapses in the retina. *Neuron* 90, 320–332. doi: 10.1016/j.neuron.2016.03.012

Lamb, T., and Simon, E. (1976). The relation between intercellular coupling and electrical noise in turtle photoreceptors. *J. Physiol.* 263, 257–286. doi: 10.1113/jphysiol.1976.sp011631

Landesman, Y., White, T. W., Starich, T. A., Shaw, J. E., Goodenough, D. A., and Paul, D. L. (1999). Innexin-3 forms connexin-like intercellular channels. *J. Cell Sci.* 112, 2391–2396. doi: 10.1242/jcs.112.14.2391

Landisman, C. E., Long, M. A., Beierlein, M., Deans, M. R., Paul, D. L., and Connors, B. W. (2002). Electrical synapses in the thalamic reticular nucleus. *J. Neurosci.* 22, 1002–1009.

Latchoumane, C.-F. V., Ngo, H.-V. V., Born, J., and Shin, H.-S. (2017). Thalamic spindles promote memory formation during sleep through triple phase-locking of cortical, thalamic, and hippocampal rhythms. *Neuron* 95, 424–435.e6. doi: 10.1016/j.neuron.2017.06.025

Lau, T., Gage, G. J., Berke, J. D., and Zochowski, M. (2010). Local dynamics of gap-junction-coupled interneuron networks. *Phys. Biol.* 7:016015. doi: 10.1088/1478-3975/7/1/016015

Lee, E., Lee, S., Shin, J. J., Choi, W., Chung, C., Lee, S., et al. (2021). Excitatory synapses and gap junctions cooperate to improve Pv neuronal burst firing and cortical social cognition in Shank2-mutant mice. *Nat. Commun.* 12, 1–20. doi: 10.1038/s41467-021-25356-2

Lee, K. W., Hong, J. H., Choi, I. Y., Che, Y., Lee, J. K., Yang, S. D., et al. (2002). Impaired D2 dopamine receptor function in mice lacking type 5 adenylyl cyclase. *J. Neurosci.* 22, 7931–7940. doi: 10.1523/JNEUROSCI.22-18-07931.2002

Leon-Dominguez, U., Vela-Bueno, A., Froufe-Torres, M., and Leon-Carrion, J. (2013). A chronometric functional sub-network in the thalamo-cortical system regulates the flow of neural information necessary for conscious cognitive processes. *Neuropsychologia* 51, 1336–1349. doi: 10.1016/j.neuropsychologia.2013.03.012

Lewis, T. J., and Rinzel, J. (2003). Dynamics of spiking neurons connected by both inhibitory and electrical coupling. *J. Comput. Neurosci.* 14, 283–309. doi: 10.1023/a:1023265027714

Leznik, E., and Llinas, R. (2005). Role of gap junctions in synchronized neuronal oscillations in the inferior olive. *J. Neurophysiol.* 94, 2447–2456. doi: 10.1152/jn.00353.2005

Li, H., Zhang, Z., Blackburn, M. R., Wang, S. W., Ribelayga, C. P., and O'Brien, J. (2013). Adenosine and dopamine receptors coregulate photoreceptor coupling via gap junction phosphorylation in mouse retina. *J. Neurosci.* 33, 3135–3150. doi: 10.1523/JNEUROSCI.2807-12.2013

Liu, X. B., and Jones, E. G. (1999). Predominance of corticothalamic synaptic inputs to thalamic reticular nucleus neurons in the rat. *J. Comp. Neurol.* 414, 67–79.

Llinas, R., Baker, R., and Sotelo, C. (1974). Electrotonic coupling between neurons in cat inferior olive. *J. Neurophysiol.* 37, 560–571. doi: 10.1152/jn.1974.37.3.560

Long, M. A., Deans, M. R., Paul, D. L., and Connors, B. W. (2002). Rhythmicity without synchrony in the electrically uncoupled inferior olive. *J. Neurosci.* 22, 10898–10905. doi: 10.1523/JNEUROSCI.22-24-10898.2002

Long, M. A., Jutras, M. J., Connors, B. W., and Burwell, R. D. (2005). Electrical synapses coordinate activity in the suprachiasmatic nucleus. *Nat. Neurosci.* 8, 61–66. doi: 10.1038/nn1361

Long, M. A., Landisman, C. E., and Connors, B. W. (2004). Small clusters of electrically coupled neurons generate synchronous rhythms in the thalamic reticular nucleus. *J. Neurosci.* 24, 341–349. doi: 10.1523/JNEUROSCI.3358-03.2004

Mamiya, A., Manor, Y., and Nadim, F. (2003). Short-term dynamics of a mixed chemical and electrical synapse in a rhythmic network. *J. Neurosci.* 23, 9557–9564. doi: 10.1523/JNEUROSCI.23-29-09557.2003

Mancilla, J. G., Lewis, T. J., Pinto, D. J., Rinzel, J., and Connors, B. W. (2007). Synchronization of electrically coupled pairs of inhibitory interneurons in neocortex. *J. Neurosci.* 27, 2058–2073. doi: 10.1523/JNEUROSCI.2715-06.2007

Mann-Metzer, P., and Yarom, Y. (1999). Electrotonic coupling interacts with intrinsic properties to generate synchronized activity in cerebellar networks of inhibitory interneurons. *J. Neurosci.* 19, 3298–3306. doi: 10.1523/JNEUROSCI.19-09-03298.1999

Marsh, A. J., Michel, J. C., Adke, A. P., Heckman, E. L., and Miller, A. C. (2017). Asymmetry of an intracellular scaffold at vertebrate electrical synapses. *Curr. Biol.* 27, 3561–3567.e4. doi: 10.1016/j.cub.2017.10.011

Marshall, S. P., Van Der Giessen, R. S., De Zeeuw, C. I., and Lang, E. J. (2007). Altered olivocerebellar activity patterns in the connexin36 knockout mouse. *Cerebellum* 6, 287–299. doi: 10.1080/14734220601100801

McMahon, D. G., and Brown, D. R. (1994). Modulation of gap-junction channel gating at zebrafish retinal electrical synapses. *J. Neurophysiol.* 72, 2257–2268. doi: 10.1152/jn.1994.72.5.2257

Medvedev, G. S. (2009). Electrical coupling promotes fidelity of responses in the networks of model neurons. *Neural Comput.* 21, 3057–3078. doi: 10.1162/neco.2009.07-08-813

Mendoza, A. J., and Haas, J. S. (2022). Intrinsic sources and functional impacts of asymmetry at electrical synapses. *eNeuro* 9:ENEURO.0469-21.2022. doi: 10.1523/ENEURO.0469-21.2022

Mills, S. L., and Massey, S. C. (1995). Differential properties of two gap junctional pathways made by AII amacrine cells. *Nature* 377, 734–737. doi: 10.1038/377734a0

Mills, S. L., Xia, X. B., Hoshi, H., Firth, S. I., Rice, M. E., Frishman, L. J., et al. (2007). Dopaminergic modulation of tracer coupling in a ganglion-amacrine cell network. *Vis. Neurosci.* 24, 593–608. doi: 10.1017/S0952523807070575

Montbrió, E., and Pazó, D. (2020). Exact mean-field theory explains the dual role of electrical synapses in collective synchronization. *Phys. Rev. Lett.* 125:248101. doi: 10.1103/PhysRevLett.125.248101

Moore, K. B., Mitchell, C. K., Lin, Y.-P., Lee, Y.-H., Shihabeddin, E., and O'brien, J. (2020). Localized calcium signaling and the control of coupling at Cx36 gap junctions. *Eneuro* 7:ENEURO.0445-19.2020. doi: 10.1523/ENEURO.0445-19.2020

Moortgat, K. T., Bullock, T. H., and Sejnowski, T. J. (2000). Gap junction effects on precision and frequency of a model pacemaker network. *J. Neurophysiol.* 83, 984–997. doi: 10.1152/jn.2000.83.2.984

Mulloney, B., Perkel, D. H., and Budelli, R. W. (1981). Motor-pattern production: interaction of chemical and electrical synapses. *Brain Res.* 229, 25–33. doi: 10.1016/0006-8993(81)90742-3

Nácher, V., Ledberg, A., Deco, G., and Romo, R. (2013). Coherent delta-band oscillations between cortical areas correlate with decision making. *Proc. Natl. Acad. Sci.* 110, 15085–15090. doi: 10.1073/pnas.1314681110

Nadim, F., and Golowasch, J. (2006). Signal transmission between gap-junctionally coupled passive cables is most effective at an optimal diameter. *J. Neurophysiol.*95, 3831–3843. doi: 10.1152/jn.00033.2006

Nagy, J. I., Pereda, A. E., and Rash, J. E. (2018). Electrical synapses in mammalian CNS: past eras, present focus and future directions. *Biochim. Biophys. Acta Biomembr.* 1860, 102–123. doi: 10.1016/j.bbamem.2017.05.019

Neske, G. T., and Connors, B. W. (2016). Synchronized gamma-frequency inhibition in neocortex depends on excitatory-inhibitory interactions but not electrical synapses. *J. Neurophysiol.* 116, 351–368. doi: 10.1152/jn.00071.2016

Nomura, M., Fukai, T., and Aoyagi, T. (2003). Synchrony of fast-spiking interneurons interconnected by GABAergic and electrical synapses. *Neural Comput.* 15, 2179–2198. doi: 10.1162/089976603322297340

Oh, S. W., Harris, J. A., Ng, L., Winslow, B., Cain, N., Mihalas, S., et al. (2014). A mesoscale connectome of the mouse brain. *Nature* 508, 207–214.

Ohara, P. T., and Lieberman, A. (1985). The thalamic reticular nucleus of the adult rat: experimental anatomical studies. *J. Neurocytol.* 14, 365–411. doi: 10.1007/BF01217752

Ostojic, S., Brunel, N., and Hakim, V. (2009). Synchronization properties of networks of electrically coupled neurons in the presence of noise and heterogeneities. *J. Comput. Neurosci.* 26, 369–392. doi: 10.1007/s10827-008-0117-3

Otsuka, T., and Kawaguchi, Y. (2013). Common excitatory synaptic inputs to electrically connected cortical fast-spiking cell networks. *J. Neurophysiol.* 110, 795–806. doi: 10.1152/jn.00071.2013

Parker, P. R., Cruikshank, S. J., and Connors, B. W. (2009). Stability of electrical coupling despite massive developmental changes of intrinsic neuronal physiology. *J. Neurosci.* 29, 9761–9770. doi: 10.1523/JNEUROSCI.4568-08.2009

Pastor, A. M., Mentis, G. Z., De la Cruz, R. R., Díaz, E., and Navarrete, R. (2003). Increased electrotonic coupling in spinal motoneurons after transient botulinum neurotoxin paralysis in the neonatal rat. *J. Neurophysiol.* 89, 793–805. doi: 10.1152/jn.00498.2002

Pereda, A., Triller, A., Korn, H., and Faber, D. S. (1992). Dopamine enhances both electrotonic coupling and chemical excitatory postsynaptic potentials at mixed synapses. *Proc. Natl. Acad. Sci.* 89, 12088–12092. doi: 10.1073/pnas.89.24.12088

Pereda, A. E., Bell, T. D., Chang, B. H., Czernik, A. J., Nairn, A. C., Soderling, T. R., et al. (1998). Ca2+/calmodulin-dependent kinase II mediates simultaneous enhancement of gap-junctional conductance and glutamatergic transmission. *Proc. Natl. Acad. Sci. U. S. A.* 95, 13272–13277. doi: 10.1073/pnas.95.22.13272

Pereda, A. E., Nairn, A. C., Wolszon, L. R., and Faber, D. S. (1994). Postsynaptic modulation of synaptic efficacy at mixed synapses on the Mauthner cell. *J. Neurosci.* 14, 3704–3712. doi: 10.1523/JNEUROSCI.14-06-03704.1994

Pereda, A. E., Rash, J. E., Nagy, J. I., and Bennett, M. V. (2004). Dynamics of electrical transmission at club endings on the Mauthner cells. *Brain Res. Rev.* 47, 227–244. doi: 10.1016/j.brainresrev.2004.06.010

Perez-Velazquez, J., Valiante, T. A., and Carlen, P. L. (1994). Modulation of gap junctional mechanisms during calcium-free induced field burst activity: a possible role for electrotonic coupling in epileptogenesis. *J. Neurosci.* 14, 4308–4317. doi: 10.1523/JNEUROSCI.14-07-04308.1994

Perkins, K. L., and Wong, R. (1996). Ionic basis of the postsynaptic depolarizing GABA response in hippocampal pyramidal cells. *J. Neurophysiol.* 76, 3886–3894. doi: 10.1152/jn.1996.76.6.3886

Personius, K., Chang, Q., Bittman, K., Panzer, J., and Balice-Gordon, R. (2001). Gap junctional communication among motor and other neurons shapes patterns of neural activity and synaptic connectivity during development. *Cell Commun. Adhes.* 8, 329–333. doi: 10.3109/15419060109080748

Pfeuty, B., Mato, G., Golomb, D., and Hansel, D. (2003). Electrical synapses and synchrony: the role of intrinsic currents. *J. Neurosci.* 23, 6280–6294. doi: 10.1523/JNEUROSCI.23-15-06280.2003

Pham, T., and Haas, J. S. (2018). Electrical synapses between inhibitory neurons shape the responses of principal neurons to transient inputs in the thalamus: a modeling study. *Sci. Rep.* 8:7763. doi: 10.1038/s41598-018-25956-x

Pham, T., and Haas, J. S. (2019). Electrical synapses regulate both subthreshold integration and population activity of principal cells in response to transient inputs within canonical feedforward circuits. *PLoS Comput. Biol.* 15:e1006440. doi: 10.1371/journal.pcbi.1006440

Phelan, P., Goulding, L. A., Tam, J. L., Allen, M. J., Dawber, R. J., Davies, J. A., et al. (2008). Molecular mechanism of rectification at identified electrical synapses in the Drosophila giant fiber system. *Curr. Biol.* 18, 1955–1960. doi: 10.1016/j.cub.2008.10.067

Phelan, P., Nakagawa, M., Wilkin, M. B., Moffat, K. G., O'Kane, C. J., Davies, J. A., et al. (1996). Mutations in shaking-B prevent electrical synapse formation in the Drosophila giant fiber system. *J. Neurosci.* 16, 1101–1113. doi: 10.1523/JNEUROSCI.16-03-01101.1996

Phelan, P., Stebbings, L. A., Baines, R. A., Bacon, J. P., Davies, J. A., and Ford, C. (1998). *Drosophila* Shaking-B protein forms gap junctions in paired *Xenopus* oocytes. *Nature* 391, 181–184. doi: 10.1038/34426

Pinault, D. (2004). The thalamic reticular nucleus: structure, function and concept. *Brain Res. Brain Res. Rev.* 46, 1–31. doi: 10.1016/j.brainresrev.2004.04.008

Pottackal, J., Walsh, H. L., Rahmani, P., Zhang, K., Justice, N. J., and Demb, J. B. (2021). Photoreceptive ganglion cells drive circuits for local inhibition in the mouse retina. *J. Neurosci.* 41, 1489–1504. doi: 10.1523/JNEUROSCI.0674-20.2020

Prensa, L., and Parent, A. (2001). The nigrostriatal pathway in the rat: a single-axon study of the relationship between dorsal and ventral tier nigral neurons and the striosome/matrix striatal compartments. *J. Neurosci.* 21, 7247–7260. doi: 10.1523/JNEUROSCI.21-18-07247.2001

Puller, C., Duda, S., Lotfi, E., Arzhangnia, Y., Block, C. T., Ahlers, M. T., et al. (2020). Electrical coupling of heterotypic ganglion cells in the mammalian retina. *J. Neurosci.* 40, 1302–1310. doi: 10.1523/JNEUROSCI.1374-19.2019

Qiao, M., and Sanes, J. R. (2016). Genetic method for labeling electrically coupled cells: application to retina. *Front. Mol. Neurosci.* 8:81. doi: 10.3389/fnmol.2015.00081

Rabinowitch, I., Chatzigeorgiou, M., and Schafer, W. R. (2013). A gap junction circuit enhances processing of coincident mechanosensory inputs. *Current Biology* 23, 963–967. doi: 10.1016/j.cub.2013.04.030

Ransey, E., Chesnov, K., Bursac, N., and Dzirasa, K. (2021a). FETCH: a platform for high-throughput quantification of gap junction hemichannel docking. *bioRxiv[Preprint]* doi: 10.1101/2021.06.07.447352

Ransey, E., Chesnov, K., Wisdom, E., Bowman, R., Rodriguez, T., Adamson, E., et al. (2021b). Long-term precision editing of neural circuits using engineered gap junction hemichannels. *bioRxiv [Preprint]* doi: 10.1101/2021.08.24.457429

Rash, J., Staines, W., Yasumura, T., Patel, D., Furman, C., Stelmack, G., et al. (2000). Immunogold evidence that neuronal gap junctions in adult rat brain and spinal cord contain connexin-36 but not connexin-32 or connexin-43. *Proc. Natl. Acad. Sci.* 97, 7573–7578. doi: 10.1073/pnas.97.13.7573

Rash, J. E., Yasumura, T., Davidson, K., Furman, C., Dudek, F., and Nagy, J. (2001a). Identification of cells expressing Cx43, Cx30, Cx26, Cx32 and Cx36 in gap junctions of rat brain and spinal cord. *Cell Commun. Adhes.* 8, 315–320. doi: 10.3109/15419060109080745

Rash, J. E., Curti, S., Vanderpool, K. G., Kamasawa, N., Nannapaneni, S., Palacios-Prado, N., et al. (2013). Molecular and functional asymmetry at a vertebrate electrical synapse. *Neuron* 79, 957–969. doi: 10.1016/j.neuron.2013.06.037

Rash, J. E., Yasumura, T., Dudek, F. E., and Nagy, J. I. (2001b). Cell-specific expression of connexins and evidence of restricted gap junctional coupling between glial cells and between neurons. *J. Neurosci.* 21, 1983–2000. doi: 10.1523/JNEUROSCI.21-06-01983.2001

Reardon, F., and Mitrofanis, J. (2000). Organisation of the amygdalo-thalamic pathways in rats. *Anat. Embryol.* 201, 75–84. doi: 10.1007/pl00008229

Ren, Y., Liu, Y., and Luo, M. (2021). Gap junctions between striatal d1 neurons and cholinergic interneurons. *Front. Cell. Neurosci.* 15:674399. doi: 10.3389/fncel.2021.674399

Ribelayga, C., Cao, Y., and Mangel, S. C. (2008). The circadian clock in the retina controls rod-cone coupling. *Neuron* 59, 790–801. doi: 10.1016/j.neuron.2008.07.017

Rojas-Líbano, D., and Kay, L. M. (2008). Olfactory system gamma oscillations: the physiological dissection of a cognitive neural system. *Cogn. Neurodyn.* 2, 179–194. doi: 10.1007/s11571-008-9053-1

Ross, F., Gwyn, P., Spanswick, D., and Davies, S. (2000). Carbenoxolone depresses spontaneous epileptiform activity in the CA1 region of rat hippocampal slices. *Neuroscience* 100, 789–796. doi: 10.1016/s0306-4522(00)00346-8

Russo, G., Nieus, T. R., Maggi, S., and Taverna, S. (2013). Dynamics of action potential firing in electrically connected striatal fast-spiking interneurons. *Front. Cell. Neurosci.* 7:209. doi: 10.3389/fncel.2013.00209

Salkoff, D. B., Zagha, E., Yüzgeç, Ö, and McCormick, D. A. (2015). Synaptic mechanisms of tight spike synchrony at gamma frequency in cerebral cortex. *J. Neurosci.* 35, 10236–10251. doi: 10.1523/JNEUROSCI.0828-15.2015

Scheibel, M. E., and Scheibel, A. B. (1966). The organization of the nucleus reticularis thalami: a Golgi study. *Brain Res.* 1, 43–62. doi: 10.1016/0006-8993(66)90104-1

Schoppa, N. E., and Urban, N. N. (2003). Dendritic processing within olfactory bulb circuits. *Trends Neurosci.* 26, 501–506. doi: 10.1016/S0166-2236(03)00228-5

Sevetson, J., and Haas, J. S. (2015). Asymmetry and modulation of spike timing in electrically coupled neurons. *J. Neurophysiol.* 113, 1743–1751. doi: 10.1152/jn.00843.2014

Sherman, A., and Rinzel, J. (1992). Rhythmogenic effects of weak electrotonic coupling in neuronal models. *Proc. Natl. Acad. Sci.* 89, 2471–2474. doi: 10.1073/pnas.89.6.2471

Singer, J. H., Mirotznik, R., and Feller, M. (2001). Potentiation of L-type calcium channels reveals nonsynaptic mechanisms that correlate spontaneous activity in the developing mammalian retina. *J. Neurosci.* 21, 8514–8522. doi: 10.1523/JNEUROSCI.21-21-08514.2001

Söhl, G., and Willecke, K. (2003). An update on connexin genes and their nomenclature in mouse and man. *Cell Commun. Adhes.* 10, 173–180. doi: 10.1080/cac.10.4-6.173.180

Solomon, I. C., Chon, K. H., and Rodriguez, M. N. (2003). Blockade of brain stem gap junctions increases phrenic burst frequency and reduces phrenic burst synchronization in adult rat. *J. Neurophysiol.* 89, 135–149. doi: 10.1152/jn.00697.2002

Srinivas, M., Rozental, R., Kojima, T., Dermietzel, R., Mehler, M., Condorelli, D. F., et al. (1999). Functional properties of channels formed by the neuronal gap junction protein connexin36. *J. Neurosci.* 19, 9848–9855. doi: 10.1523/JNEUROSCI.19-22-09848.1999

Starich, T. A., Lee, R., Panzarella, C., Avery, L., and Shaw, J. E. (1996). eat-5 and unc-7 represent a multigene family in *Caenorhabditis elegans* involved in cell-cell coupling. *J. Cell Biol.* 134, 537–548. doi: 10.1083/jcb.134.2.537

Stebbings, L. A., Todman, M. G., Phelan, P., Bacon, J. P., and Davies, J. A. (2000). Two Drosophila innexins are expressed in overlapping domains and cooperate to form gap-junction channels. *Mol. Biol. Cell* 11, 2459–2470. doi: 10.1091/mbc.11.7.2459

Steriade, M. (2005). Sleep, epilepsy and thalamic reticular inhibitory neurons. *Trends Neurosci.* 28, 317–324. doi: 10.1016/j.tins.2005.03.007

Szoboszlay, M., Lőrincz, A., Lanore, F., Vervaeke, K., Silver, R. A., and Nusser, Z. (2016). Functional properties of dendritic gap junctions in cerebellar Golgi cells. *Neuron* 90, 1043–1056. doi: 10.1016/j.neuron.2016.03.029

Tamás, G., Buhl, E. H., Lörincz, A., and Somogyi, P. (2000). Proximally targeted GABAergic synapses and gap junctions synchronize cortical interneurons. *Nat. Neurosci.* 3, 366–371. doi: 10.1038/73936

Tian, H., Davis, H. C., Wong-Campos, J. D., Fan, L. Z., Gmeiner, B., Begum, S., et al. (2021). All-optical electrophysiology with improved genetically encoded voltage indicators reveals interneuron network dynamics in vivo. *bioRxiv[Preprint]* doi: 10.1101/2021.11.22.469481

Traub, R. D. (1995). Model of synchronized population bursts in electrically coupled interneurons containing active dendritic conductances. *J. Comput. Neurosci.* 2, 283–289. doi: 10.1007/BF00961440

Traub, R. D., Kopell, N., Bibbig, A., Buhl, E. H., LeBeau, F. E., and Whittington, M. A. (2001). Gap junctions between interneuron dendrites can enhance synchrony of gamma oscillations in distributed networks. *J. Neurosci.* 21, 9478–9486. doi: 10.1523/JNEUROSCI.21-23-09478.2001

Traub, R. D., Whittington, M. A., Stanford, I. M., and Jefferys, J. G. (1996). A mechanism for generation of long-range synchronous fast oscillations in the cortex. *Nature* 383, 621–624. doi: 10.1038/383621a0

Trenholm, S., and Awatramani, G. B. (2019). "Myriad roles for gap junctions in retinal circuits," in *Webvision: The Organization of the Retina and Visual System*, eds H. Kolb., E. Fernandez and R. Nelson (Salt Lake City (UT): University of Utah Health Sciences Center)doi: <PMID<PMID:NOPMID</PMID<

Trenholm, S., McLaughlin, A. J., Schwab, D. J., and Awatramani, G. B. (2013). Dynamic tuning of electrical and chemical synaptic transmission in a network of motion coding retinal neurons. *J. Neurosci.* 33, 14927–14938. doi: 10.1523/JNEUROSCI.0808-13.2013

Tresch, M. C., and Kiehn, O. (2000). Motor coordination without action potentials in the mammalian spinal cord. *Nat. Neurosci.* 3, 593–599. doi: 10.1038/75768

Usher, M., Cohen, J. D., Servan-Schreiber, D., Rajkowski, J., and Aston-Jones, G. (1999). The role of locus coeruleus in the regulation of cognitive performance. *Science* 283, 549–554. doi: 10.1126/science.283.5401.549

Van Der Giessen, R. S., Koekkoek, S. K., van Dorp, S., De Gruijl, J. R., Cupido, A., Khosrovani, S., et al. (2008). Role of olivary electrical coupling in cerebellar motor learning. *Neuron* 58, 599–612. doi: 10.1016/j.neuron.2008.03.016

Van Essen, D. C., Smith, S. M., Barch, D. M., Behrens, T. E., Yacoub, E., Ugurbil, K., et al. (2013). The WU-Minn human connectome project: an overview. *Neuroimage* 80, 62–79. doi: 10.1016/j.neuroimage.2013.05.041

van Welie, I., Roth, A., Ho, S. S., Komai, S., and Häusser, M. (2016). Conditional spike transmission mediated by electrical coupling ensures millisecond precision-correlated activity among interneurons in vivo. *Neuron* 90, 810–823. doi: 10.1016/j.neuron.2016.04.013

Vardi, N., and Smith, R. G. (1996). The AII amacrine network: coupling can increase correlated activity. *Vis. Res.* 36, 3743–3757. doi: 10.1016/0042-6989(96)00098-3

Velazquez, J. L. P., and Carlen, P. L. (2000). Gap junctions, synchrony and seizures. *Trends Neurosci.* 23, 68–74. doi: 10.1016/s0166-2236(99)01497-6

Veruki, M. L., and Hartveit, E. (2002b). Electrical synapses mediate signal transmission in the rod pathway of the mammalian retina. *J. Neurosci.* 22, 10558–10566. doi: 10.1523/JNEUROSCI.22-24-10558.2002

Veruki, M. L., and Hartveit, E. (2002a). AII (Rod) amacrine cells form a network of electrically coupled interneurons in the mammalian retina. *Neuron* 33, 935–946. doi: 10.1016/s0896-6273(02)00609-8

Vervaeke, K., Lőrincz, A., Gleeson, P., Farinella, M., Nusser, Z., and Silver, R. A. (2010). Rapid desynchronization of an electrically coupled interneuron network with sparse excitatory synaptic input. *Neuron* 67, 435–451. doi: 10.1016/j.neuron.2010.06.028

Vervaeke, K., Lőrincz, A., Nusser, Z., and Silver, R. A. (2012). Gap junctions compensate for sublinear dendritic integration in an inhibitory network. *Science* 335, 1624–1628. doi: 10.1126/science.1215101

Walton, K. D., and Navarrete, R. (1991). Postnatal changes in motoneurone electrotonic coupling studied in the in vitro rat lumbar spinal cord. *J. Physiol.* 433, 283–305. doi: 10.1113/jphysiol.1991.sp018426

Wang, X.-J. (2010). Neurophysiological and computational principles of cortical rhythms in cognition. *Physiol. Rev.* 90, 1195–1268. doi: 10.1152/physrev.00035.2008

Watanabe, A. (1958). The interaction of electrical activity among neurons of lobster cardiac ganglion. *Jpn. J. Physiol.* 8, 305–318. doi: 10.2170/jjphysiol.8.305

Whittington, M. A., and Traub, R. D. (2003). Interneuron diversity series: inhibitory interneurons and network oscillations in vitro. *Trends Neurosci.* 26, 676–682. doi: 10.1016/j.tins.2003.09.016

Whittington, M. A., Traub, R. D., and Jefferys, J. G. (1995). Synchronized oscillations in interneuron networks driven by metabotropic glutamate receptor activation. *Nature* 373, 612–615. doi: 10.1038/373612a0

Whittington, M. A., Traub, R. D., Kopell, N., Ermentrout, B., and Buhl, E. H. (2000). Inhibition-based rhythms: experimental and mathematical observations on network dynamics. *Int. J. Psychophysiol.* 38, 315–336. doi: 10.1016/s0167-8760(00)00173-2

Wilson, P. M. (1985). A photographic perspective on the origins, form, course and relations of the acetylcholinesterase-containing fibres of the dorsal tegmental pathway in the rat brain. *Brain Res.* 357, 85–118. doi: 10.1016/0165-0173(85)90001-3

Yaeger, D. B., and Trussell, L. O. (2016). Auditory Golgi cells are interconnected predominantly by electrical synapses. *J. Neurophysiol.* 116, 540–551. doi: 10.1152/jn.01108.2015

Yaksi, E., and Wilson, R. I. (2010). Electrical coupling between olfactory glomeruli. *Neuron* 67, 1034–1047. doi: 10.1016/j.neuron.2010.08.041

Yao, X., Cafaro, J., McLaughlin, A. J., Postma, F. R., Paul, D. L., Awatramani, G., et al. (2018). Gap junctions contribute to differential light adaptation across direction-selective retinal ganglion cells. *Neuron* 100, 216–228.e6. doi: 10.1016/j.neuron.2018.08.021

Zhang, L., and Jones, E. G. (2004). Corticothalamic inhibition in the thalamic reticular nucleus. *J. Neurophysiol.* 91, 759–766. doi: 10.1152/jn.00624.2003

Zhang, Z., Allen, G. I., Zhu, H., and Dunson, D. (2019). Tensor network factorizations: Relationships between brain structural connectomes and traits. *Neuroimage* 197, 330–343. doi: 10.1016/j.neuroimage.2019.04.027

Zhu, P., Frank, T., and Friedrich, R. W. (2013). Equalization of odor representations by a network of electrically coupled inhibitory interneurons. *Nat. Neurosci.* 16, 1678–1686. doi: 10.1038/nn.3528

Zikopoulos, B., and Barbas, H. (2012). Pathways for emotions and attention converge on the thalamic reticular nucleus in primates. *J. Neurosci.* 32, 5338–5350. doi: 10.1523/JNEUROSCI.4793-11.2012

Zolnik, T. A., and Connors, B. W. (2016). Electrical synapses and the development of inhibitory circuits in the thalamus. *J. Physiol.* 594, 2579–2592. doi: 10.1113/JP271880

Zsiros, V., Aradi, I., and Maccaferri, G. (2007). Propagation of postsynaptic currents and potentials via gap junctions in GABAergic networks of the rat hippocampus. *J. Physiol.* 578, 527–544. doi: 10.1113/jphysiol.2006.123463

Conflict of Interest: The authors declare that the research was conducted in the absence of any commercial or financial relationships that could be construed as a potential conflict of interest.

frontiers | Frontiers in Cellular Neuroscience

ORIGINAL RESEARCH
published: 15 June 2022
doi: 10.3389/fncel.2022.860823

Enhancement of Phosphorylation and Transport Activity of the Neuronal Glutamate Transporter Excitatory Amino Acid Transporter 3 by C3bot and a 26mer C3bot Peptide

*Johannes Piepgras[1], Astrid Rohrbeck[2], Ingo Just[2], Stefan Bittner[1], Gudrun Ahnert-Hilger[3] and Markus Höltje[4]**

[1] Department of Neurology, Focus Program Translational Neuroscience and Immunotherapy, Rhine-Main Neuroscience Network, University Medical Center of the Johannes Gutenberg University Mainz, Mainz, Germany, [2] Institute of Toxicology, Hannover Medical School, Hanover, Germany, [3] Department of Neurobiology, Max Planck Institute for Biophysical Chemistry, University of Göttingen, Göttingen, Germany, [4] Institut für Integrative Neuroanatomie, Charité – Universitätsmedizin Berlin, Corporate Member of Freie Universität Berlin and Humboldt-Universität zu Berlin, Berlin, Germany

OPEN ACCESS

Edited by:
James Foster,
University of North Dakota,
United States

Reviewed by:
Mariana Cooke,
University of Pennsylvania,
United States
Binglin Zhu,
University at Buffalo, United States
Jae-Won Yang,
Medical University of Vienna, Austria

***Correspondence:**
Markus Höltje
markus.hoeltje@charite.de

Specialty section:
This article was submitted to Cellular Neurophysiology, a section of the journal Frontiers in Cellular Neuroscience

Received: 23 January 2022
Accepted: 16 May 2022
Published: 15 June 2022

Citation:
Piepgras J, Rohrbeck A, Just I, Bittner S, Ahnert-Hilger G and Höltje M (2022) Enhancement of Phosphorylation and Transport Activity of the Neuronal Glutamate Transporter Excitatory Amino Acid Transporter 3 by C3bot and a 26mer C3bot Peptide. Front. Cell. Neurosci. 16:860823. doi: 10.3389/fncel.2022.860823

In primary murine hippocampal neurons we investigated the regulation of EAAT3-mediated glutamate transport by the *Clostridium botulinum* C3 transferase C3bot and a 26mer peptide derived from full length protein. Incubation with either enzyme-competent C3bot or enzyme-deficient C3bot$^{156-181}$ peptide resulted in the upregulation of glutamate uptake by up to 22% compared to untreated cells. A similar enhancement of glutamate transport was also achieved by the classical phorbol-ester-mediated activation of protein kinase C subtypes. Yet comparable, effects elicited by C3 preparations seemed not to rely on PKCα, γ, ε, or ζ activation. Blocking of tyrosine phosphorylation by tyrosine kinase inhibitors prevented the observed effect mediated by C3bot and C3bot 26mer. By using biochemical and molecular biological assays we could rule out that the observed C3bot and C3bot 26mer-mediated effects solely resulted from enhanced transporter expression or translocation to the neuronal surface but was rather mediated by transporter phosphorylation at tyrosine residues that was found to be significantly enhanced following incubation with either full length protein or the 26mer C3 peptide.

Keywords: C3 transferase, glutamate transporter, EAAT3, phosphorylation, uptake

INTRODUCTION

The prototypical *Clostridium botulinum* C3 transferase (C3bot) is an exoenzyme that represents a family of bacterial ADP-ribosyltransferases that, when taken up into target cells, effectively block Rho-signaling in an enzymatic manner (Aktories and Frevert, 1987; Aktories and Just, 2005). Small GTPases of the Rho family, especially RhoA, serve key functions as molecular switches in the regulation of the cytoskeleton in general and also in neuronal cells, and C3 protein has been extensively used as tool to investigate growth- and regeneration-associated morphological processes in different types of neurons. Activated RhoA signaling executed by downstream effector kinases

like ROCK leads to phosphorylation of myosin light chain thereby inducing growth cone collapse and axon retraction as observed after ischemic or traumatic brain injuries (Mulherkar et al., 2017; Sladojevic et al., 2017; Takase and Regenhardt, 2021). In this context, by using full length C3bot or C3-derived peptides (that lack the specific enzymatic activity of full length protein), our group and others have demonstrated the beneficial outcome of a treatment with C3bot for neuronal re-growth following damage of the CNS. This includes experimental lesion models both *in vitro* and *in vivo* (Dubreuil et al., 2003; Höltje et al., 2009; Boato et al., 2010; Loske et al., 2012) as well as clinical trials in patients with spinal cord injuries (McKerracher and Anderson, 2013; Watzlawick et al., 2014; Fehlings et al., 2018). For a long time unknown, recent work from our group has identified the intermediate filament protein vimentin as well as β1-integrin as cellular receptors for C3bot (Rohrbeck et al., 2014, 2017; Adolf et al., 2019). As mentioned, growth-promoting effects are also caused by enzyme-deficient C3bot-derived peptides like the 29mer C3bot$^{154-182}$ or 26mer C3bot$^{156-181}$, both including the catalytic amino acid glutamate at position 174 of full length C3bot, but in this case, the exact cellular enzyme-independent mechanisms remain to be unraveled.

However, besides exhibiting morphological effects C3bot also affects cellular transmitter transport mechanisms. Incubation of astrocytes with C3bot results in a NFκB-dependent upregulation of glial high-affinity glutamate transporter EAAT2 (GLT-1) accompanied by increased glutamate uptake. At the same time astrocytes treated with C3bot released higher amounts of glutamate by vesicular release (Höltje et al., 2008). Prompted by these findings we investigated putative effects of C3bot and enzyme-deficient C3bot$^{156-181}$ (C3bot 26mer) on glutamate uptake of hippocampal neurons.

As long known, glutamate not only represents the major excitatory neurotransmitter of the CNS but can also cause neuronal excitotoxicity at higher extracellular levels (Choi and Rothman, 1990; Lipton and Rosenberg, 1994). Therefore, maintenance of physiological extracellular glutamate levels is pivotal for fidelity of synaptic transmission and even to prevent neuronal cell death. Clearance from the synaptic cleft is mediated by high affinity glutamate transporters. Though not exclusively expressed at the cell surface, the neuronal excitatory amino acid transporter 3 (EAAT3) belongs to a family of five potassium-dependent glutamate transporters located at the plasma membrane (Arriza et al., 1997). Generally, glutamate transport is coupled with sodium-dependent H^+ inward-transport and counter-transport of K^+ (Owe et al., 2006). Besides their role in transporting amino acids, EAATs also function as chloride channels (Wadiche et al., 1995).

While the majority of glutamate clearance in the CNS is mediated by the mainly astroglial EAAT2, postsynaptic EAAT3 activity rather affects local glutamate concentrations and neighboring receptors (Lehre and Danbolt, 1998; Holmseth et al., 2012; Bjørn-Yoshimoto and Underhill, 2016). Moreover, EAAT3 provides the source of glutamate as precursor for GABA synthesis in inhibitory neurons (Mathews and Diamond, 2003) and therefore is involved in controlling inhibitory signaling in the brain. Neuronal EAAT3 plays another crucial role in preventing vulnerability to oxidative stress and to maintain redox homeostasis. Cysteine is an alternative transport substrate for EAAT3 and represents the rate-limiting factor for glutathione synthesis needed to reduce reactive oxygen species such as H_2O_2 (Griffith, 1999). In line with this, perturbation of EAAT3 surface transport activity is associated with various neuronal pathologies, including Parkinson's disease, epilepsy, or Huntington's disease (for review, see Malik and Willnow, 2019).

C3 proteins have proven to foster axon re-growth and to provide neuroprotection under pathological conditions that typically involve a disturbed glutamate balance in the CNS. Therefore, the current study was undertaken with the following aims: By using primary hippocampal neuronal cultures we investigated the effects of C3bot on neuronal glutamate uptake. Furthermore, we determine whether the effects strictly rely on enzyme-activity of C3 (as already shown for morphological and functional effects on astrocytes) or can also be elicited by enzyme-deficient C3bot 26mer.

Last but not least we analyzed the regulatory mechanisms underlying functional regulations of EAAT3 mediated by C3bot and C3bot 26mer.

MATERIALS AND METHODS

C3 Proteins

Development of C3bot-derived peptide and full length protein:

C3bot$^{156-181}$ (C3bot 26mer), was synthesized at Pharis Biotec GmbH (Hannover, Germany). C3bot was expressed as recombinant GST-fusion protein in *E. coli* TG1 harboring the respective DNA fragment in the plasmid pGEX-2T (Höltje et al., 2009).

Antibodies

Immunofluorescence

A polyclonal antibody against the excitatory amino acid transporter 3 (EAAT3) was purchased from Santa Cruz Biotechnology (#sc-25658, Santa Cruz, TX, United States). Polyclonal antisera obtained from Chemicon (Temecula, CA, United States) were used for detection of glutamate-aspartate transporter EAAT1 (GLAST, #AB1782) and glial glutamate transporter EAAT2 (GLT-1, #AB1783). Protein kinase C-alpha (PKCα) was detected by a monoclonal antibody obtained from BD Biosciences (#610107, Heidelberg, Germany). A polyclonal antibody against actin was purchased from SIGMA (#A5060 St. Louis, MO, United States). Morphology of hippocampal neurons was visualized by a polyclonal antiserum against microtubule associated protein 2 (MAP2, #AB5622) and neurofilament protein of 200 kDa (#AB5256) from Chemicon International (Hofheim, Germany). An affinity purified polyclonal rabbit IgG against full length C3bot developed by our group was applied (Rohrbeck et al., 2014). To detect the phosphorylation levels of EAAT3 a polyclonal antibody directed against phosphotyrosine was purchased from Santa Cruz Biotechnology (#sc-7020). Antibodies against protein kinase C isoforms γ (monoclonal #ab71558), ε (polyclonal #ab63638), and ζ (polyclonal #ab108970) were obtained from Abcam (Cambridge, United Kingdom).

Immunoblotting

Excitatory amino acid transporter 3 as well as actin antibodies were the same as used for immunofluorescence. Polyclonal anti EAAT1/GLAST (agc-021) was purchased from Alomone Labs (Jerusalem, Israel) and polyclonal anti EAAT2/GLT-1 was purchased from Abcam (Waltham, MA, United States). Monoclonal anti RhoA was purchased from Santa Cruz Biotechnology (#26C4). For detection of phosphorylated serine a polyclonal antibody from Abcam was used (#ab9332, Cambridge, United Kingdom). Detection of phosphotyrosine was achieved by using the same antibody as used for immunofluorescence.

Cell Culture

Hippocampal Cell Culture

Neuronal cultures from hippocampi of NMRI or SWISS mice were prepared from fetal animals at embryonic day 16 (E16). Dissected tissue pieces were rinsed with PBS, then with dissociation medium (MEM supplemented with 10% fetal calf serum, 100 IE insuline/l, 0.5 mM glutamine, 100 U/ml penicillin/streptomycin, 44 mM glucose and 10 mM HEPES buffer) and dissociated mechanically. Spun-down cells were resuspended in starter medium (serum-free neurobasal medium supplemented with B27, 0.5 mM glutamine, and 25 μM glutamate) and plated at a density of 8×10^4 cells/well on glass cover slips pre-coated with poly-L-lysine/collagen. All ingredients were obtained from Gibco/BRL. After 12–14 days in culture C3 preparations were added to the culture medium for another 72 h.

Astrocyte Culture

Primary astrocyte cultures were prepared from NMRI mice brains between postnatal days 2 and 3. Meninges were removed from whole brains and mechanically dissociated in Hank's buffered salt solution (HBSS) by fire polished Pasteur pipettes and centrifuged at $300 \times g$ for 3 min. Astrocytes were redissociated in HBSS and the procedure was repeated two times using smaller pipette tip diameters. Cells were first seeded onto 6-well plates (3.5 cm diameter/well) pretreated with poly-L-lysine (100 μg/ml in PBS). Astrocytes were incubated at 5% CO_2 in Dulbecco's Modified Eagle Medium (DMEM), supplemented with 10% fetal calf serum, 100 U/ml penicillin/streptomycin and 2 mM L-glutamine. Microglial cells were repeatedly detached from the astrocyte monolayer by shaking off. After 7 days in culture with a change of medium for two times cells were harvested and recultured in 24-well plates at a density of 4×10^4 cells/well with glass coverslips pretreated with poly-L-lysine if used for immunofluorescence methods.

Brain Homogenates

Brains of adult mice were homogenized using a glass/Teflon homogenizer (Wheaton, Potter-Elvehjem, clearance 0.1–0.15 μm) in ice-cold buffer containing 320 mM sucrose, 4 mM HEPES/KOH, pH 7.4, 1 mM PMSF, and 1 μl/ml protease inhibitor cocktail (Pi, Sigma-Aldrich) and centrifuged for 10 min at 4°C and $1300 \times g$ (Beckman rotor TLA-100.4). The resulting supernatant was used for detection of EAAT3 by Western blotting.

Immunohistochemistry and -Cytochemistry

Perfusion-fixed brains from adult NMRI-mice were dissected, cryoprotected and frozen at −80°C prior to cutting into 20 μm coronar sections. The sections were washed with PBS and incubated in blocking solution (10% NGS in PBS; 0.3% Triton-X-100) for 30 min at room temperature. Primary antibodies were applied overnight at 4°C. After incubating the sections, they were washed with PBS and incubated with secondary antibodies for 1 h at room temperature in the dark. Immunoreactivity was visualized using Alexa Fluor 488 or Alexa Fluor 594 goat anti-mouse and goat anti-rabbit secondary antibodies (Molecular Probes, Eugene, OR, United States). Again, sections were washed with PBS, stained with DAPI (4′,6-diamidino-2-phenylindole) for 10 min and mounted with Immu-Mount (Thermo Fisher Scientific, Waltham, MA, United States).

Cultured cells were fixed with 4% formaline for 15 min and subsequently permeabilized for 30 min at room temperature (RT) using 0.3% Triton X-100 dissolved in PBS. Staining with primary antibodies was performed overnight at 4°C. After washing in PBS secondary antibodies were applied for 1 h at room temperature (RT). Immunoreactivity was visualized using secondary antibodies as given above. Fluorescence was either visualized using an upright Leica DMLB epifluorescence equipment or by using confocal laser scanning microscopy (see below).

Confocal Laser Scanning Microscopy

Images were acquired using a Leica TCS SL confocal laser scanning microscope using a x40 oil immersion objective. Fluorescent dyes were excited at a wavelength of 488 nm (green fluorescence) and 543 nm (red fluorescence), respectively. Fluorescence from green and red channels was sequentially collected using two filters at 498–535 nm and 587–666 nm, respectively. Images were captured at a resolution of 1024×1024 pixels.

Glutamate Uptake Assay

Radiolabeled Glutamate

[^{3}H]radiolabeled L-glutamate (specific activity: 20 Ci/mmol) was obtained from Hartmann Analytic GmbH (Braunschweig, Germany). Usually, for glutamate uptake hippocampal neurons grown in 24-well plates were incubated with 50 μM of glutamate (applied as a combination of both tritiated and unlabeled glutamic acid) for 1 h with or without additives as indicated at 37°C in serum-free culture medium. For kinetic analysis of transport activity the uptake time was shortened to 10 min. GraphPad Prism software (San Diego, CA, United States) was used for non-linear regression and transformation of data. After removal of the medium and repeated washing (3x) with ice-cold Krebs-Hepes buffer containing 140 mM NaCl, 4.7 mM KCl, 2.5 mM $CaCl_2$, 15 mM Hepes, and 1.2 mM $MgSO_4$ adjusted to pH 7.4 cells were lysed with 0.4% Triton X-100 for 10 min at 42°C. Neuron lysates were subjected to liquid scintillation counting for determination of radioactivity. Values were adjusted to protein content.

Fluorometric Glutamate Measurements

For fluorometric glutamate detection the glutamate assay kit #ab138883 from Abcam was used according to the manufacturer. In brief, cells were incubated for 1 h with 50 μM of glutamate in serum-free culture medium. Following two washing steps, cells were lysed in 0.4% Trion-X100 as above. Neuron lysates were subjected to fluorometric reading using Ex/Em = 540/590 nm for determination of intracellular glutamate concentrations calculated from standards. Values were adjusted to protein content. The tyrosine kinase inhibitors Dasatinib (ab142050) and Genistein (ab120112) were purchased from Abcam (Waltham, MA, United States).

Biotinylation Assay

All work steps except for centrifugation in the cell culture centrifuge were carried out in the cold at 4°C or on ice according to manufacturers instructions (Thermo Fisher Scientific, Waltham, MA, United States). Hippocampal neurons cultured in 6-well plates were washed three times with PBS and then incubated with Sulfo-NHS-Biotin solution (1 mg/ml) for 30 min. Thereafter, the cells were washed twice with quenching buffer and then incubated with quenching buffer for 30 min with agitation. Following washing, cells were spun down and pellets obtained were lysed. Avidin agarose beads were added to the lysate and incubated overnight with agitation. The next day, part of the supernatant was saved and spun down avidin beads were washed three times with PBS. The supernatant and avidin beads were taken up in Laemmli buffer and processed for Western blot analysis.

Immunoisolation and Phosphorylation of Excitatory Amino Acid Transporter 3

Dynabeads® Protein G (Invitrogen) were incubated in antibody binding and washing buffer (PBS with 0.1% Tween-20) containing the antibody of interest. A polyclonal anti-EAAT3 antibody (Santa Cruz Biotechnology) and normal rabbit IgG for control were used in a concentration of 80 ng/ml antibody for binding to the beads (1–2 μg antibody per 200–500 μg of protein in cell lysate, see below). Binding was performed for 1 h at room temperature. Afterward, the antibody-beads complex was washed once in antibody binding and washing buffer and kept on ice. Cells were washed twice in ice cold PBS, scraped off the culture dish and collected in a vessel on ice. After centrifugation at 3000 rpm for 4 min the cell pellet was resuspended in ice cold PBS. After a final centrifugation at 20000 × *g* for 3 min the cell pellet was kept on ice for lysis and protein determination. Cells were lysed in an extraction buffer (KCl 140 mM, Hepes 2 mM and EDTA 20 mM at pH 7.4 together with 1% Triton X-100, 1 mM PMSF, 1 μl/ml protease and phosphatase inhibitors) for 1 h at 4°C. After, the insoluble fraction was separated by centrifugation at 2700 × *g* for 5 min. The supernatant was incubated with the Dynabeads®-antibody-complexes over night at 4°C. A part of the supernatant was boiled in Laemmli buffer. The Dynabeads-antibody-antigen-complex was washed three times in extraction buffer without Triton and resuspended in washing buffer before boiling in Laemmli buffer. Phosphorylation status was probed by using anti-phosphotyrosine and anti-phosphoserine antibody after protein separation by gel electrophoresis.

Imaging Analysis

To quantify the phosphorylation status of EAAT3 by immunofluorescence methods double stainings against EAAT3 and phosphotyrosine (pTyr) were applied to hippocampus cultures grown for 12–14 days *in vitro* and incubated for further 72 h with C3 preparations. Randomly chosen images of individual neurons were acquired at 100x magnification and mean brightness values within a circular region of interest (50 μm in diameter) centered on the soma of the respective neurons were calculated for red and green fluorescence by the histogram tool of Adobe Photoshop CS6. Both channels were superimposed and remaining brightness and saturation values for red and green fluorescence were set to zero (black). Then again, mean brightness values for the remaining yellow fluorescence representing the co-localized signal between EAAT3 and pTyr were calculated.

Experimental Design and Statistics

Typically, experiments were run at least three times if not stated otherwise. Uptake assays were determined in triplicates or quadruplicates for a single condition. In general, values are expressed as means ± SEM from one representative experiment or pooled experiments. Statistical significance or absence from that was calculated in **Figures 3–6** using Student's *t*-test and *p* values below 0.05 were considered significant.

RESULTS

To investigate C3 protein-mediated effects on neuronal plasma membrane glutamate transporter activity we used primary neuronal cultures from the hippocampus of embryonic mice representing a mixed culture of different neuronal subpopulations. Albeit not exclusively expressed at the plasma membrane, EAAT3 is the main neuronal surface glutamate transporter in the brain (Bjørn-Yoshimoto and Underhill, 2016). It is abundantly expressed *in vivo* in neuronal somata and neuropilar regions of various brain areas including cortex, basal ganglia and the hippocampus formation as shown for the adult mouse brain (**Figures 1A–C**). The observed distribution corresponded very well with early pioneering studies on its location (Rothstein et al., 1994). To test for suitability of our model system we aimed to evaluate the expression of EAAT3 in the neuronal cell culture used. Following cultivation for 14 days cells were stained for EAAT3 and glial fibrillary acidic protein (GFAP) to confirm neuronal expression of EAAT3. Indeed, transporter expression was clearly attributable to cells morphologically identifiable as neurons (**Figure 1D**). Further immunofluorescence analysis revealed a strong punctuate distribution of the transporter at the somatodendritic compartment (**Figure 1E**, microtubule-associated protein 2 was used as marker protein) and axonal processes (**Figure 1F**, neurofilament protein of 200 kDa was used as marker protein).

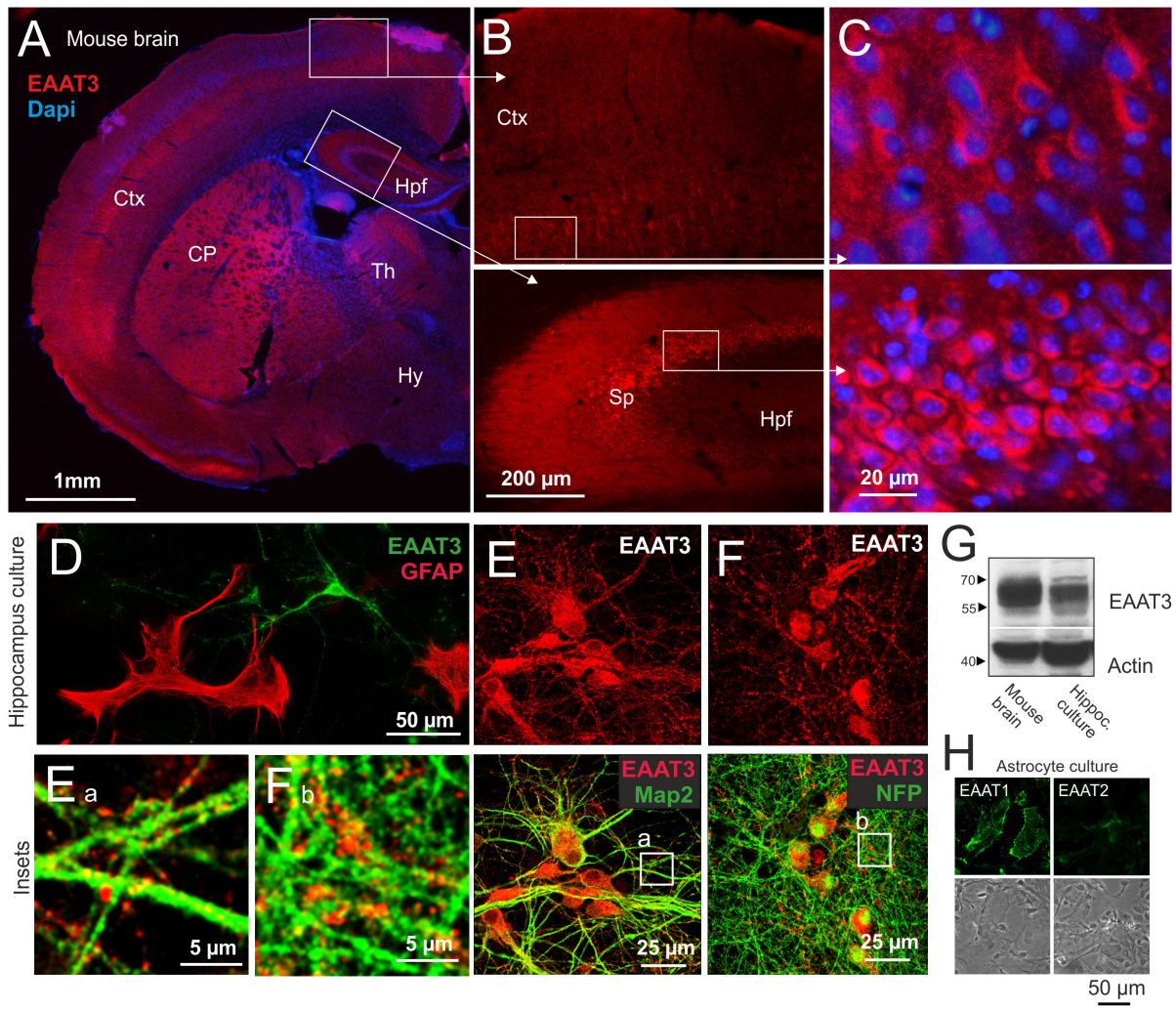

FIGURE 1 | Expression of the excitatory amino acid transporter 3 (EAAT3) in mouse brain and primary hippocampal neurons. **(A–C)** Expression pattern of EAAT3 in the adult mouse brain. Coronar cryosections of adult mouse brains were incubated with a polyclonal antibody directed against EAAT3. Protein expression was detected in neuronal perikarya and the neuropil of various brain areas, including caudate putamen, cortex and the hippocampus formation. Insets show enlargements of depicted areas. CP, Caudate putamen; Ctx, Cortex; Hpf, Hippocampus formation; Hy, Hypothalamus; Sp, Stratum pyramidale; Th, Thalamus. **(D)** Mouse hippocampal neurons were prepared at embryonic day 16, cells were grown on glass cover slips for 14 days, fixed and stained for EAAT3 and GFAP as marker for astrocytes present to some extent in culture. EAAT3 expression was restricted to neurons. **(E,F)** Mouse hippocampal neurons were prepared and cultured as described, fixed and stained for EAAT3, Map2 as dendritic **(E)** and NFP as axonal marker **(F)** by immunofluorescence methods and confocal imaging. EAAT3 staining was observed in a punctuate fashion throughout the cell body as well as dendritic and axonal processes [lower panels, see also insets **(E_a,F_b)**]. **(G)** Homogenates of whole mouse brains and cultured hippocampal neurons were subjected to Western blot procedure and probed for the expression of neuronal EAAT3. Actin was used as loading control. The antiserum detected a major band between the 55 and 70 kDa markers in both samples. Overall, the signals corresponded well with the expected molecular weight. **(H)** Murine astrocytes were cultured close to confluency, fixed and stained for the main glial glutamate transporter EAAT1 (GLAST) and EAAT2 (GLT-1) by immunofluorescence and confocal imaging. Astrocytes predominantly expressed EAAT1 at the plasma membrane. EAAT2 expression was observed at comparably low levels.

Transporter signals localized both at surface and cytoplasm which corresponds well with the different functions of EAAT3 served depending on its cellular localization (Bjørn-Yoshimoto and Underhill, 2016). Western blot studies detected a strong major and few weaker bands between 55 and 70 kDa in mouse brain homogenate and hippocampus culture yielding biochemical evidence for the presence of EAAT3 in both preparations (**Figure 1G**). Presence of astrocytes in neuronal cultures is unavoidable and therefore a glial contribution to observed glutamate uptake must taken into account and should be blocked pharmacologically to analyze pure neuronal transport activity. The basic possibility of glial glutamate transporter expression *in vitro* was confirmed by immunofluorescence microscopic analysis detecting mainly EAAT1 and low EAAT2 expression in purified astrocyte culture (**Figure 1H**).

Prior to the investigation of putative effects of C3bot preparations on glutamate uptake we tested the capacity of hippocampal neurons to take up glutamate in a specific manner.

To this end, cultivated cells were incubated with radiolabeled glutamate. Following incubation with [^{3}H]glutamate (total glutamate concentration 50 μM) for 60 min, cells were lysed and taken up glutamate was determined by liquid scintillation counting. Uptake of glutamate by hippocampal neurons was calculated to 2.6 nmol/mg protein (**Figure 2A**). Incubation with the potent glutamate uptake inhibitor L-*trans*-pyrrolidine-2,4-dicarboxylate (PDC, 1 mM) reduced the uptake by around 75%, confirming specificity of a large proportion of the transport. In a kinetic analysis of uptake we applied glutamate concentrations between 40 and 400 μM (**Figure 2B**). The maximal transport velocity V_{max} was calculated to 1.05 nmol/mg/min and K_m was at 78.36 μM. To visualize the extent of astrocytes present in culture and to estimate the proportion of glial EAAT1 and EAAT2 to the observed uptake we identified astrocytes by GFAP labeling and immunofluorescence imaging. At 14 days *in vitro*, only a minor proportion of GFAP-positive astrocytes was detected compared to the vast majority of EAAT3-positive neurons (**Figure 2C**). In addition, transporter expression was quantified biochemically. As expected, Western blot analysis revealed a predominant expression of EAAT3, whereas EAAT2 and especially EAAT1 were detected at noticeably lower levels

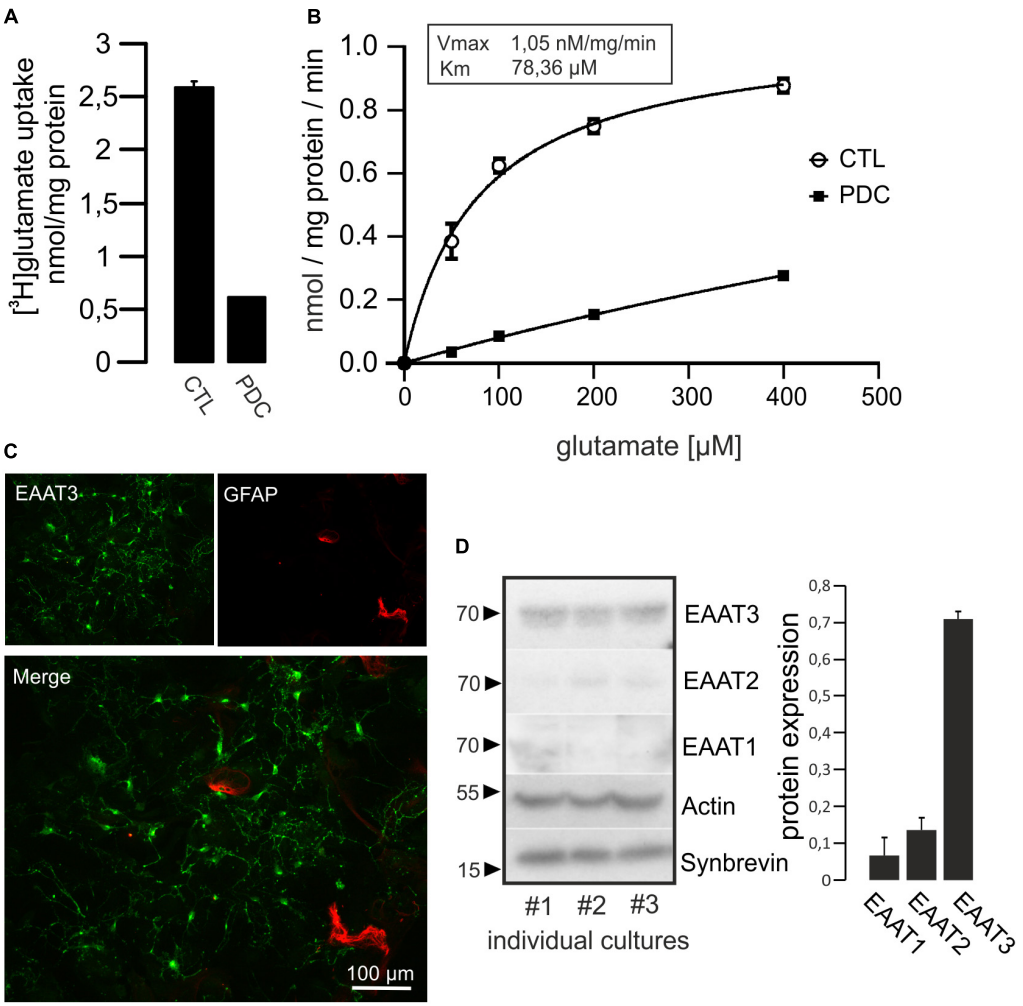

FIGURE 2 | Hippocampal neurons take up [^{3}H]glutamate in a specific manner. **(A)** Cultured hippocampal neurons were grown in 24-multiwell dishes for 14 days and incubated for 1 h with radiolabeled glutamate (50 μM). After removal of medium, cells were washed intensively, lysed and radioactivity taken up was calculated by liquid scintillation counting. Values were adjusted to protein content. Specific uptake was evaluated by the addition of 1 mM of the glutamate uptake inhibitor L-*trans*-pyrrolidine-2,4-dicarboxylate (PDC). Uptake of [^{3}H]glutamate was strongly inhibited by PDC and therefore regarded as specific. **(B)** Kinetic analysis of glutamate uptake (uptake time 10 min) revealed saturable concentration-dependent transport kinetics (V_{max} and K_m values are indicated). Values in **(A,B)** are expressed as means ± SEM from triplicate samples within a single representative experiment repeated two times. **(C)** Neurons were grown on glass cover slips for 14 days, fixed and stained for EAAT3 and GFAP as marker for astrocytes. Staining against EAAT3 and GFAP revealed that the vast majority of cells represented neurons at that culture time. **(D)** Homogenates of cultured hippocampal neurons were subjected to Western blot procedure and probed for the expression of neuronal EAAT3, as well as glial EAAT2 and EAAT1. Actin was used as loading control, Synaptobrevin was used as synaptic neuronal marker. Quantification from three individual cultures revealed that EAAT3 represented the predominant glutamate transporter. Values in **(D)** are expressed as means ± SEM adjusted to Actin from three individual cultures.

(**Figure 2D**). Taken together, hippocampal neurons seemed an adequate model to investigate effects of C3 preparations on specific glutamate transport activity in hippocampal cultures predominantly driven by EAAT3.

Full-length C3bot has already been shown to increase glutamate uptake in astrocytes (Höltje et al., 2008). These effects turned out to be a specific gene regulatory mechanism and did not result from the strong morphological alterations (stellation) astrocytes undergo in response to inhibition of RhoA by C3bot. C3bot 26mer covers the amino acids 156-181 of the full length sequence (**Figure 3A**) and has proven to be effective in increasing neuronal process outgrowth *in vitro* as well as to foster functional recovery and regenerative axon regrowth following experimental spinal cord injury in mice (Loske et al., 2012). These previous findings were qualitatively confirmed (**Supplementary Figure 1**). Hitherto, its effects on neuronal glutamate handling have not been studied. Although full length C3bot neuronal membrane binding and internalization have not completely understood so far intracellularly enriched C3bot can be easily visualized by a specific antibody not available for the peptide (**Figure 3B**). Transport activity of EAAT3 is known to be highly regulated. Amongst these regulatory factors a main

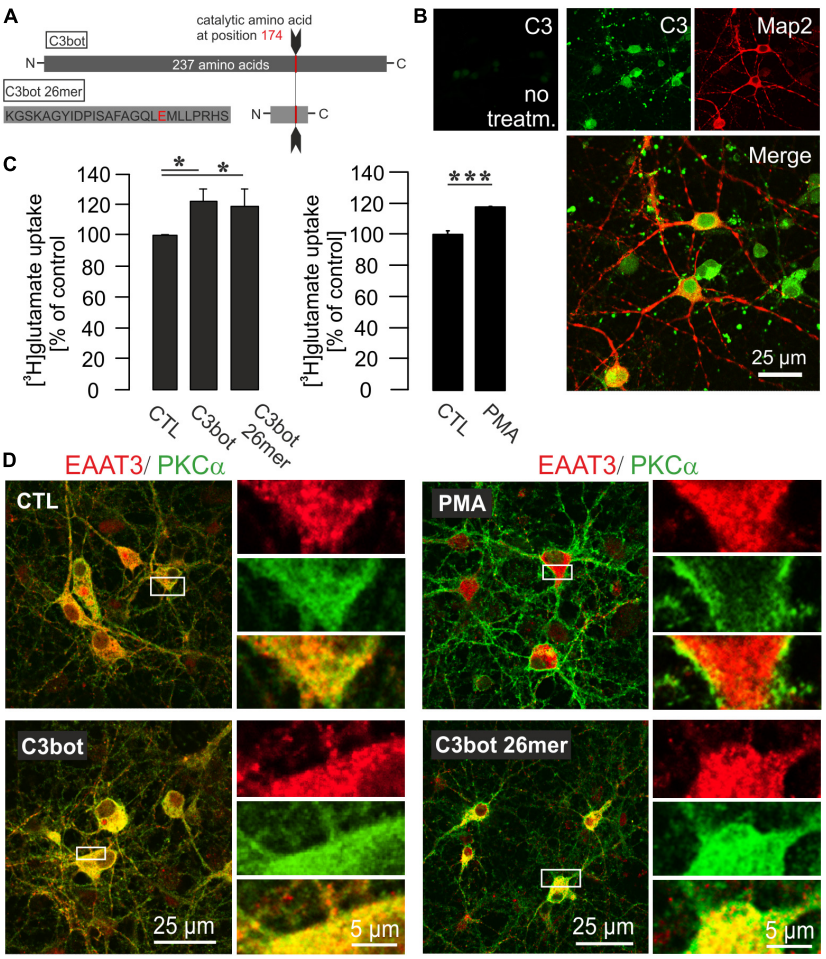

FIGURE 3 | Influence of C3bot, C3bot 26mer, or PKC activation on enhancement of glutamate uptake in hippocampal neurons. **(A)** C3bot 26mer covers the amino acids 156-181 of C3bot full length. Glutamate at position 174 *is* the catalytic amino acid that renders full length C3bot enzymatically active. **(B)** In cultures treated with C3bot full length protein presence of the C3 transferase was visualized after 72 h by a specific antibody directed against C3 protein. The C3bot signal was mainly detected at the somata and Map2-negative processes probably representing axons in a mixture of internalized and surface bound protein. Confocal imaging. **(C)** Hippocampal neurons were incubated with 50 µM [^{3}H]glutamate and uptake was measured as described before. Incubation with 300 nM of C3bot or C3bot 26mer for 3 days showed similar effects on uptake regulation. Following incubation with C3bot full length or C3bot 26mer transport activity was increased by C3bot (22%) and, slightly less, by the 26mer (19%). Prior to the uptake procedure, part of the cells were incubated for 30 min with 200 nM of the activator of PKC isoforms PMA. Preincubation with PMA increased the uptake by 19%. In addition, cells were preincubated with dihydrokainate (DHK, 1 mM for 30 min) prior to the uptake procedure to selectively block EAAT2 transport activity. Values therefore represent PDC- and DHK-sensitive counts (analyzed in triplicates) expressed as means ± SEM from 4 to 5 independent experiments. $^*p \leq 0.05$; $^{***}p \leq 0.005$. **(D)** Confocal imaging of PKCα and EAAT3 distribution in hippocampal neurons after treatment with C3bot, C3bot 26mer, or PMA. In control cells, PKCα showed a marked cytoplasmatic localization, indicative of inactive PKCα. Expression of EAAT3 was also detected throughout the whole cell. Addition of PMA resulted in a shift of PKCα to the plasma membrane characteristic for activation. Conversely, incubation with C3bot or C3bot 26mer did not result in activation of PKCα. Distribution of EAAT3 remained unchanged after either treatment.

signaling molecule is protein kinase C-alpha (PKCα) which is capable to change transport velocity and plasma membrane localization of EAAT3 (Huang et al., 2006). In this context, it has been demonstrated a convergence between Rho-regulated (and therefore C3bot-sensitive) and PKC signaling pathways (Peng et al., 2011). Moreover, a close association between PKCα and Rho GTPases has been shown (Pang and Bitar, 2005). To investigate C3-mediated alterations in glutamate uptake by hippocampal neurons we incubated cells with 300 nM of C3bot or C3bot 26mer for 72 h and analyzed the amount of glutamate uptake. C3bot increased the specific uptake by around 22% whereas transport activity was enhanced by 19% following incubation with the peptide (**Figure 3C**, left panel). To take into account that mainly EAAT2 might contribute to some extent to the uptake and therefore to minimize glial transport activity dihydrokainate (DHK) was used in all experimental conditions to specifically block glial EAAT2 activity. In addition, part of the cells under any given condition were also incubated with PDC as shown before to subtract non-specific uptake.

To test for the influence of PKCα on EAAT3-mediated transport activity in our neuronal systems, PKCα was activated by the phorbol ester phorbol 12-myristate 13-acetate (PMA, 200 nM, 20 min). Similar to the effects detected after treatment with C3bot preparations, preincubation of neurons with PMA enhanced glutamate uptake by 19% (**Figure 3C**, right panel). Confocal imaging confirmed PMA-mediated activation of PKCα by the shift from a cytoplasmatic distribution to a plasma membrane associated form (**Figure 3D**, right upper panel). Translocation of PKCα to the plasma membrane, on the other hand, could not be evoked by either C3bot or the 26mer, indicating a PKCα-insensitive mode of action (**Figure 3D**). Under either condition, no obvious redistribution of EAAT3 was detected. So, despite similar effects on glutamate uptake in neurons, effects mediated by C3bot preparations did not seem to base on PKCα activation. In addition to PKCα, activation of other classical PKC isoforms such as PKCγ or novel PKCε as well as unconventional PKCζ was analyzed by immunocytochemistry. However, neither treatment with C3bot nor C3bot 26mer showed an effect on these PKC isoforms as judged by lack of translocation to the plasma membrane (**Supplementary Figure 2**). Treatment with PMA, on the other hand, had a strong effect on the redistribution of PKCγ and, to a lesser extent, on PKCε, but as expected was ineffective in changing the expression of unconventional PKCζ. Taken together, uptake effects elicited by C3bot and C3bot 26mer do not seem to rely on activation of PKC. To address the cellular mechanisms involved in enhanced glutamate transport, we investigated the expression of EAAT3 after treatment with C3bot full length and peptide. Western blot analysis of whole cell lysates from hippocampal neurons, however, failed to detect changes in overall protein levels of EAAT3 (**Figure 4A**). To investigate effects of treatment on RhoA expression and ADP-ribosylation, cell lysates were probed for RhoA by Western blotting. Following incubation with C3bot, a complete shift of the RhoA signal to a higher molecular weight form became observable after 72 h of incubation, clearly indicative of C3bot-mediated ADP-ribosylation of RhoA (**Figure 4B**). Along with this, the RhoA signal was strongly reduced, indicative of the expected proteasomal degradation of RhoA following ADP-ribosylation and inactivation. Due to the lack of enzymatic activity of the 26mer, the RhoA signal remained at the same molecular weight and was largely unchanged. To address putative changes in transporter surface localization that might underlie the enhanced uptake activity, biotinylation experiments were performed. Again, following biotinylation of surface proteins and subsequent subcellular fractionation of hippocampal neurons, no significant alterations in the amount of biotinylated, therefore surface located, EAAT3 were detectable after either treatment regime (**Figure 4C**).

Since we were unable to detect major changes in total protein expression or transporter localization following incubation with either C3bot or C3 26mer, we aimed to investigate whether direct alterations such as the phosphorylation status of EAAT3 might account for the observed effects on transport activity. Therefore, we performed immunoprecipitation studies to isolate EAAT3 from cell lysates obtained from primary neurons, and incubated the isolated fraction with phospho-specific antibodies. To test for proper assay function, hippocampal cell lysates were incubated with magnetic beads coupled to the polyclonal EAAT3 antibody as well as rabbit IgG for negative control. In the EAAT3-immunoisolates a strong transporter signal could be detected that was absent in the IgG fraction (**Figure 5A**). Quantitative precipitation of EAAT3 from lysates was confirmed by lack of EAAT3 staining of the remaining supernatant (**Figure 5A**). We probed EAAT3 immunoprecipitates with phosphotyrosine (pTyr) and phospho-serine (pSer) antibodies to visualize putative changes in transporter phosphorylation. Phosphorylation of tyrosine was upregulated by about 40% in hippocampal neurons, whereas the phospho-serine signal remained largely unchanged (**Figure 5B**). To quantify the phosphorylation status of EAAT3 on the level of individual neurons we performed co-stainings for EAAT3 and phosphorylated amino acids by immunofluorescence. Due to the fact that both antibodies against EAAT3 and pSer were generated in the same species (rabbit) and the initial IP experiments yielded no effects of treatment on the pSer status of EAAT3 we performed the experiments with respect to phosphorylation at tyrosine residues only. At first, immunohistochemistry on mouse brain sections was performed to show that phosphorylation of EAAT3 at tyrosine residues occurs *in vivo*. Indeed, pTyr signals were found to co-localize with EAAT3 signals in neurons of various brain areas, including the cortex (**Figure 5C**). To quantify the amount of pTyr co-localizing with the EAAT3 signal following treatment of hippocampal neurons with C3bot and C3bot 26mer, cultures were treated as above and the amount of co-localization was quantified. We chose to perform this analysis at the level of individual neurons to ensure attribution of both signals to cells morphologically identifiable as neurons (**Figure 5D**). Analysis was restricted to a soma-centered circular region of interest (ROI) with a diameter of 50 μm to exclude putative unspecific effects on protein abundance by the enhanced branching pattern of the more distal neuronal processes mediated by C3bot or C3bot 26mer. Quantification revealed that incubation with C3bot had no effect on EAAT3 transporter expression, whereas C3bot 26mer slightly increased EAAT3 expression by 16% (**Figure 5E**). Both

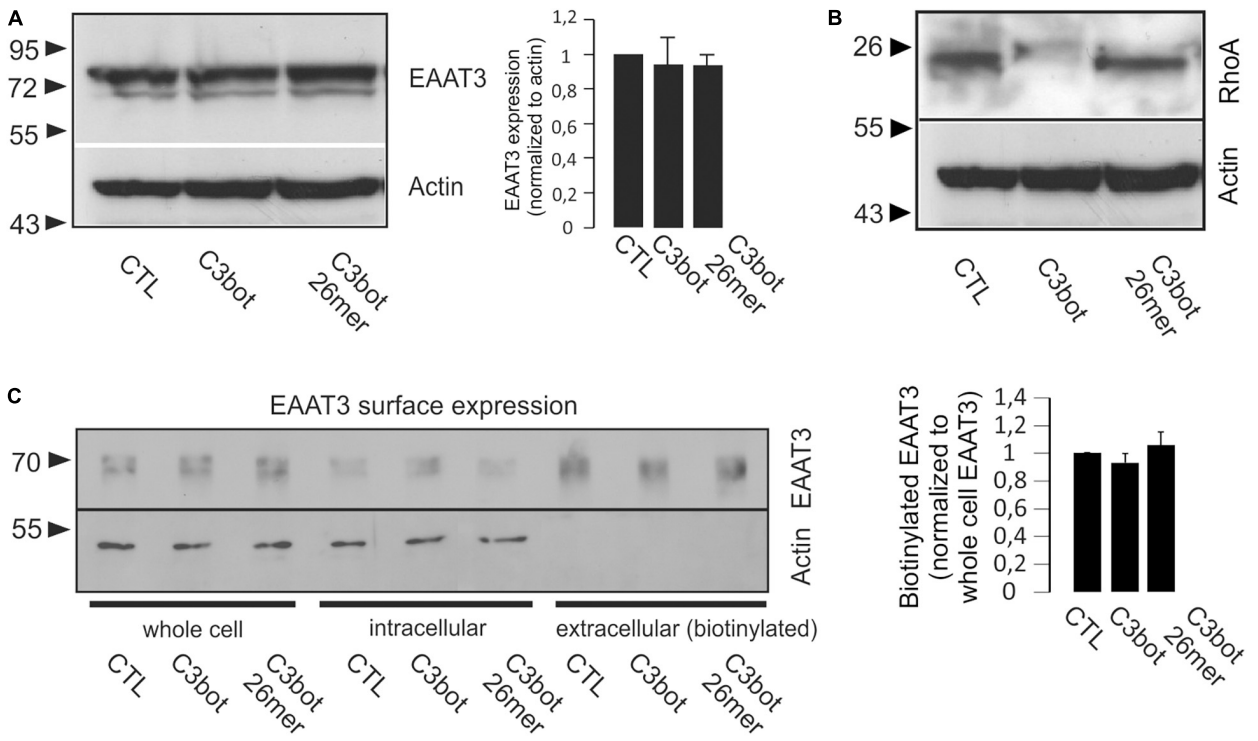

FIGURE 4 | Treatment with C3bot or C3bot 26mer does not alter protein expression and surface location of EAAT3. **(A)** Western blot analysis of EAAT3 expression following treatment of hippocampal neurons for 3 days with 300 nM of C3bot or C3bot 26mer. Quantification revealed that following either treatment, protein levels of EAAT3 remained unchanged after incubation with the C3 preparations. Values are expressed as means ± SEM from three independent experiments. **(B)** ADP-ribosylation of RhoA by C3bot. Homogenates of hippocampal neurons treated as above were subjected to Western blotting analysis and stained for RhoA. Actin served as loading control. Cells treated with C3bot exhibited a complete shift of RhoA to higher molecular weight form indicative of quantitative ADP-ribosylation by enzyme competent C3bot. Also, degradation of inactivate RhoA was observed. **(C)** Surface expression of EAAT3 was analyzed by biotinylation assays. Hippocampal neurons treated with C3bot or C3bot 26mer as above were subjected to biotinylation and subsequent subcellular fractionation into intracellular and extracellular (biotinylated) compartments. Quantification of EAAT3 in the pelleted extracellular fraction revealed no significant changes in surface expression of the transporter. Values are expressed as means ± SEM from three independent experiments.

full length protein and peptide enhanced overall pTyr signals by 40 and 48%, respectively. Co-localization of EAAT3 and pTyr were increased by 50.1% (full length C3bot) and 63% (peptide). More importantly, when normalized to EAAT3 expression the amount of co-localized signals between transporter and pTyr was increased by 39% following C3bot incubation and by 45% following treatment with 26mer.

In order to address directly whether the observed enhanced glutamate uptake following incubation with C3bot full length and peptide resulted from tyrosine phosphorylation we investigated the effect of blocking this process. During incubation with C3bot or C3bot 26mer, neurons were treated with a combination of the established tyrosine kinase inhibitors Dasatinib (200 nM) and Genistein (20 μM). We used a fluorometric assay to determine total intracellular glutamate levels from lysed cells after the uptake assay (glutamate was presented for 1 h at 50 μM in the medium). Incubation with C3bot or C3bot 26mer alone significantly increased intracellular glutamate concentrations by 53 and 46%, respectively (**Figure 6**). Addition of tyrosine kinase inhibitors completely blocked this effect. These findings add to the previous observation of an increased uptake of (labeled) glutamate into hippocampal neurons following incubation with C3 proteins by also demonstrating higher total intracellular glutamate levels. The sensitivity of this effect to tyrosine phosphorylation further underlines the contribution of this mechanism to an increased neuronal glutamate uptake mediated by C3bot and C3bot 26mer.

In summary, incubation of hippocampal neurons with full length C3bot and C3bot 26mer increased glutamate uptake activity mediated by EAAT3. The effect is very likely duo to an enhanced phosphorylation of EAAT3 at tyrosine residues.

DISCUSSION

Phosphorylation of Excitatory Amino Acid Transporter 3 Mediated by C3bot and C3bot 26mer

The current study addresses a novel regulatory mechanism of the neuronal glutamate transporter EAAT3 mediated by C3 proteins. Both full length C3bot and peptidic C3bot$^{156-181}$ (C3bot 26mer) exhibited moderate yet significant effects on glutamate transport in hippocampal neurons by increasing

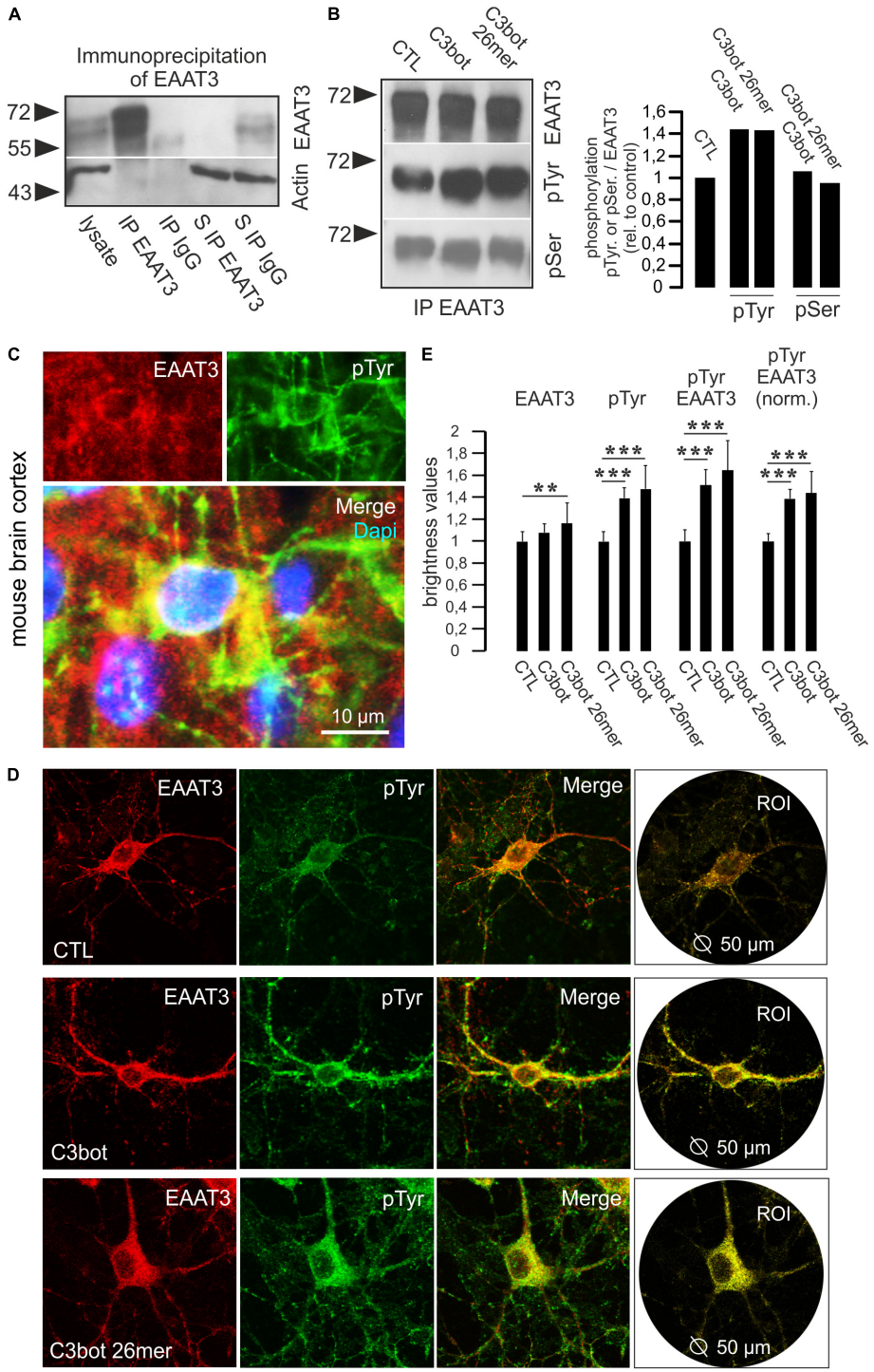

FIGURE 5 | Phosphorylation at tyrosine residues of EAAT3 is mediated by C3bot and 26mer. **(A)** Immunoprecipitation of EAAT3 from hippocampal cell lysates. Hippocampal neurons were lysed and subjected to immunoisolation of EAAT3. Lysates, precipitated fractions and remaining supernatants were probed for EAAT3 expression. Beads coated with rabbit IgG were used for negative control. Actin staining was used for loading control. For detection, light chain-specific secondary antibodies were applied to prevent unwanted detection of heavy chains of the precipitating polyclonal EAAT3 antibody. In the EAAT3 immunoprecipitates (IP) a strong transporter signal was detectable confirming precipitation of transporter by the antibody. In the rabbit IgG fraction no transporter signal was detectable. Clearance of the lysate from the EAAT3 signal following immunoisolation of EAAT3 (supernatant S IP EAAT3) confirmed proper assay function. **(B)** Hippocampal neurons were treated with 300 nM of C3bot or C3bot 26mer for 3 days. Immunoisolates were probed for EAAT3 and phosphorylation of the transporter at tyrosine and serine residues (pTyr, pSer) by phosphor-specific antibodies. Signals were quantified by calculating the ratio of phosphorylation signals to transporter expression and

(Continued)

FIGURE 5 | normalized to control conditions. Incubation with C3bot and C3bot 26mer resulted in an increased phosphorylation of tyrosine residues by 40%, phospho-serine signals were largely unchanged. **(C)** Phosphorylation of EAAT3 at tyrosine residues occurs *in vivo*. Cryosections from adult mouse brains were incubated with antibodies against EAAT3 and pTyr. Images depict co-localization of both signals in cortical neurons. **(D)** Phosphorylation of EAAT3 at tyrosine residues. Hippocampal neurons were incubated for 72 h with 300 nM of C3bot or C3bot 26mer. Fixed neurons were stained for EAAT3 and phosphorylated tyrosine. Co-localized signals were quantified by brightness analysis. Red and green fluorescence signals were subtracted and the remaining yellow fluorescence was analyzed within a circular region of interest (ROI) with a diameter of 50 μm centered on the soma of individual neurons. **(E)** Quantification of confocal imaging data. Incubation with both C3bot or C3bot 26mer increased the pTyr signal, peptidic C3bot also had a moderate positive effect on EAAT3 expression. Both treatment regimes resulted in an increased phosphorylation of EAAT3, shown both as total transporter phosphorylation and as values normalized to transporter expression. Values are expressed as means ± SEM from three (CTL and C3bot) or two (C3bot 26mer) independent experiments. CTL: n = 110 neurons; C3bot n = 102 neurons, C3bot 26mer, n = 69 neurons. $^{**}p \leq 0.01$; $^{***}p \leq 0.005$.

the uptake. In this context, total intracellular glutamate levels were increased. Biochemical and immunocytochemical evidence showed that alterations in the phosphorylation state of EAAT3 might be the underlying mechanism for the increased uptake. Pharmacological interference with tyrosine phosphorylation was able to block the effects of increased uptake. Furthermore, immunofluorescence methods revealed a slight increase in transporter expression following incubation with the C3 peptide. The exact mechanisms of action, however, remain elusive since the classical downstream-pathway of enzymatic inhibition of Rho-dependent signaling cascades can be excluded due to the lack of enzymatic activity. In this context, enzymatic full length protein and enzyme-deficient C3bot peptide must either serve different neuronal pathways that trigger tyrosine phosphorylation at EAAT3 or full length C3bot exhibits a so far unknown enzyme-independent mode of action shared by the peptide. However, a comparable neuronal response in the context of axon outgrowth, synapse formation, regeneration and neuronal plasticity following CNS lesion, as well as functional recovery *in vivo* was already observed after treatment with full length C3bot and C3bot peptides despite the lack enzymatic activity of C3bot peptides (Höltje et al., 2009; Boato et al., 2010; Loske et al., 2012). On the other hand, trophic effects on glial morphology and also glutamate handling by astrocytes seem to strictly rely on the enzymatic inhibition of Rho proteins and cannot be elicited by enzyme deficient C3 preparations (Höltje et al., 2005, 2008). The observed alterations in total intracellular glutamate levels mediated by C3bot and the peptide appeared to be larger than the pure uptake effects. Therefore, it can not be excluded that C3 proteins exert additional effects on neuronal glutamate turnover like reverse transport or degradation mechanisms. Part of the differences, however, between the effects on the uptake of labeled glutamate and the more pronounced increase in total glutamate might also arise from the different experimental paradigms using either radiolabeled glutamate or fluorometric (enzymatic) detection of unlabeled glutamate.

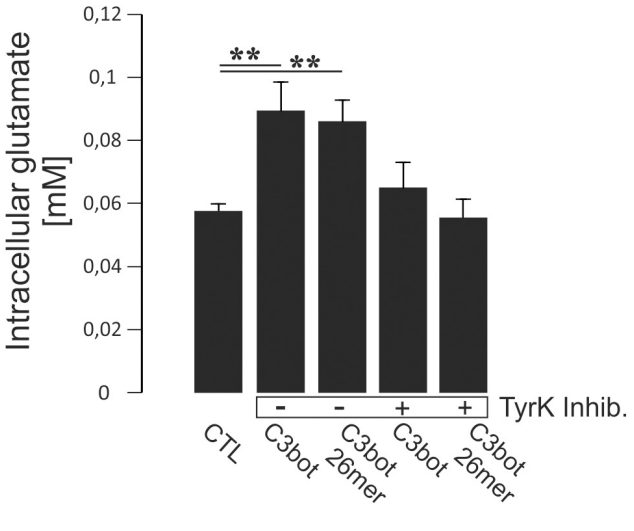

FIGURE 6 | Hippocampal neurons grown for 14 days in culture were incubated with 300 nM of C3bot or C3bot 26mer for additional 3 days with or without the addition of the tyrosine kinase inhibitors Dasatinib (200 nM) and Genistein (20 μM). Cells were then incubated with 50 μM of unlabeled glutamate for 1 h. Prior to the uptake, cells were preincubated with dihydrokainate (DHK, 1 mM for 30 min) to selectively block EAAT2 transport activity. After washing, cells were lysed and intracellular glutamate concentrations were analyzed fluorometrically and adjusted to protein content of each individual well. Neurons incubated with C3bot or C3bot 26mer showed intracellular glutamate concentrations enhanced by 53 and 46%, respectively. These effects were blocked in the presence of tyrosine kinase inhibitors. Values (analyzed in quadruplicates) are PDC- and DHK-sensitive and were calculated from fluorescence units and glutamate standards expressed as means ± SEM from 2 independent experiments. $^{**}p \leq 0.01$.

What regulatory mechanisms mediated by C3 proteins might be involved in the increased phosphorylation of EAAT3? A recent study showed that activation of the C3bot target RhoA by amphetamine in cultured noradrenergic neurons that also carry EAAT3 resulted in a decreased glutamate uptake that was, however, due to an enhanced endocytosis of EAAT3 (Underhill et al., 2020). Since C3bot and C3bot 26mer obviously do not interact with regulatory modulations controlling trafficking of EAAT3 to the neuronal surface as described for constitutive Rab11- or adapter protein-2-dependent endocytosis and recycling (González et al., 2007; Saha et al., 2021) or stimulated trafficking by PKCα (this paper, González et al., 2003), a direct functional regulation seems to occur. In earlier studies it was shown that PKCα-dependent phosphorylation of serine 465 enhanced isoflurane-induced activity of EAAT3, but again required EAAT3 redistribution to the plasma membrane (Huang et al., 2006, 2011). In our experiments incubation with C3bot preparations did neither result in PKCα activation and subsequent EAAT3 redistribution nor seemed serine phosphorylation to be involved. As observed, incubation with C3 proteins (followed by inactivation of Rho proteins at least in the case of enzyme-competent full length protein) results in an increased phosphorylation of EAAT3,

therefore inactivation of phosphatases or activation of kinases represent putative signaling pathways. Blockage of Rho-signaling by C3 proteins or downstream effectors like ROCK or mDia would result in decreased kinase activity and therefore represent an unlikely mechanism. Besides the well-characterized Rho protein downstream effector kinases that are mainly involved in phosphorylation of cytoskeletal proteins knowledge about interaction of Rho proteins with phosphatases is sparse. An interaction of activated RhoA with the inositol 5-phosphatase SHIP2 has been described that is involved in cell polarity and migration (Kato et al., 2012). To our knowledge, no phosphorylation pathway has been described so far that regulates EAAT3 activity without affecting its localization. Future work has to elucidate these pathways mediated by full length as well as peptidic C3bot. In case of C3bot 26mer, neuronal EAAT3 expression was slightly enhanced as observed by immunofluorescence. This was not reflected by the biochemical experiments carried out on whole cells and biotinylation experiments. We can only speculate that this discrepancy resulted from the different methods used (immunofluorescence on individual neurons versus Western blot of whole cultures). In line with this, undetectable changes in total protein by Western blotting might reflect the fact that EAAT3 expression in all cell types, including glial cells that might express smaller transporter amounts, was looked at.

Functional Implications

Generally, an increased glutamate clearance (stimulated by C3 preparations) from the extracellular space might be favorable under certain pathophysiological circumstances, e.g., spinal cord injury (SCI) in order to prevent further neuronal damage by excessive extracellular glutamate concentrations (Park et al., 2004). Given the fact that glutamate clearance mediated by EAAT3 serves various functions under both physiological and pathophysiological circumstances (Bianchi et al., 2014) interference with its function might, however, result in different outcomes. Generally, surface EAAT3 localizes rather perisynaptically than in the synaptic cleft of excitatory synapses and one of its function is considered to limit NMDAR activation by glutamate spillover between synapses (Diamond, 2002). Further evidence for the physiological function of EAAT3 in controlling synaptic strength and plasticity by modulating long-term potentiation (LTP) in the hippocampus stems from CA1 pyramidal cells lacking EAAT3 transport activity. Experiments showed that EAAT3 buffers glutamate release during synaptic events and reduces the recruitment of NMDAR subunits thereby facilitating LTP (Scimemi et al., 2009). Also, GABAergic neurotransmission and neuronal glutathione synthesis depend on EAAT3 activity (Sepkuty et al., 2002; Aoyama et al., 2006).

More recently, accumulating evidence has shown that altered EAAT3 function is associated with several neurological or psychiatry spectrum disorders. Many of these studies focus on genetic findings that document interference with transporter expression or localization. Amongst them are the obsessive-compulsive disorder state (Zike et al., 2017; Delgado-Acevedo et al., 2019; Underhill et al., 2019) and schizophrenia (Afshari et al., 2015). Hitherto, despite the accumulating evidence for the contribution of EAAT3 to the described physiological mechanisms and pathophysiological conditions the lack of a specific pharmacological inhibitor of EAAT3 has prevented a deeper understanding of its exact role in these processes. However, the advent of newly discovered imidazo[1,2-*a*]pyridine-3-amine compounds to selectively inhibit EAAT3 activity might improve future research (Wu et al., 2019). It is tempting to speculate that the observed neuroprotective effect (early onset of functional recovery and reduced lesion size) of treatment with C3bot 29mer and 26mer peptides following spinal cord injury in mice (Boato et al., 2010; Loske et al., 2012) might at least partially result from an increased glutamate uptake by neuronal EAAT3 to prevent excessive glutamate excitotoxicity often observed after injury. This might, however, include the glial transport systems following treatment with enzyme-competent full length C3bot (mainly GLT-1/EAAT2) that have been shown to be upregulated *in vitro* by C3bot (Höltje et al., 2008).

Taken together, we demonstrate a novel C3bot/C3bot 26mer-dependent tyrosine phosphorylation of the neuronal glutamate transporter EAAT3 by a so far unknown pathway that is very likely to result in an enhanced uptake activity.

DATA AVAILABILITY STATEMENT

The original contributions presented in this study are included in the article/**Supplementary Material**, further inquiries can be directed to the corresponding author/s.

ETHICS STATEMENT

Animal housing as well as all experiments using animal-derived tissue/cells were performed in accordance with institutional (Charité–Universitätsmedizin Berlin, Germany), local (LaGeSo, Berlin) and national guidelines (German Animal Welfare Act).

AUTHOR CONTRIBUTIONS

JP and MH performed the experiments and designed the study. AR, IJ, SB, and GA-H contributed to the conception and design of the study. MH wrote the first draft of the manuscript. All authors contributed to manuscript revision, read, and approved the submitted version.

FUNDING

This work was supported by grants of the Deutsche Forschungsgemeinschaft (DFG) to MH (HO 3249/5-1), GA-H (GAH 67/10-1), AR (RO 5129/2-1), and IJ (JU 231/7-1).

ACKNOWLEDGMENTS

We thank Birgit Metze, Marion Möbes, and Antje Dräger for their skillful technical assistance.

SUPPLEMENTARY MATERIAL

The Supplementary Material for this article can be found online at: https://www.frontiersin.org/articles/10.3389/fncel.2022.860823/full#supplementary-material

Supplementary Figure 1 | Increased neuronal outgrowth of hippocampal neurons following incubation with C3bot or C3 26mer. Hippocampal neurons were treated for 3 days with 300 nM of full length C3bot or peptidic C3bot 26mer, fixed and stained for Map2 as dendritic marker protein. Both C3bot and C3bot 26mer enhanced neuronal process outgrowth as visualized by immunofluorescence.

Supplementary Figure 2 | Hippocampal neurons grown for 14 days in culture were incubated with either 300 nM of C3bot or C3bot 26mer (3 days) or 200 nM of PMA for 20 min. Cells were fixed and stained against classic protein kinase C gamma (PKCγ), novel protein kinase C epsilon (PKCε), and unconventional protein kinase C zeta (PKCζ). Readout of activation of PKCs was a shift to the plasma membrane. Under control conditions, neurons showed a mainly cytoplasmatic PKC expression, being most prominent for PKCγ, followed by PKCζ and only very weak for PKCε. Incubation with C3bot full length or peptide had no effects on PKC localization, irrespective of the isoform. PMA, on the other hand, strongly activated PKCγ and, to some extent, PKCε in some cell somata. As expected for unconventional PKC isoforms, PKCζ was unaffected by PMA.

REFERENCES

Adolf, A., Rohrbeck, A., Münster-Wandowski, A., Johansson, M., Kuhn, H. G., Kopp, M. A., et al. (2019). Release of astroglial vimentin by extracellular vesicles: modulation of binding and internalization of C3 transferase in astrocytes and neurons. *Glia* 67, 703–717. doi: 10.1002/glia.23566

Afshari, P., Myles-Worsley, M., Cohen, O. S., Tiobech, J., Faraone, S. V., Byerley, W., et al. (2015). Characterization of a novel mutation in SLC1A1 associated with schizophrenia. *Mol. Neuropsychiat.* 1, 125–144. doi: 10.1159/000433599

Aktories, K., and Frevert, J. (1987). ADP-ribosylation of a 21-24 kDa eukaryotic protein(s) by C3, a novel botulinum ADP-ribosyltransferase, is regulated by guanine nucleotide. *Biochem. J.* 247, 363–368. doi: 10.1042/bj2470363

Aktories, K., and Just, I. (2005). Clostridial Rho-inhibiting protein toxins. *Curr. Top. Microbiol. Immunol.* 291, 113–145. doi: 10.1007/3-540-27511-8_7

Aoyama, K., Suh, S. W., Hamby, A. M., Liu, J., Chan, W. Y., Chen, Y., et al. (2006). Neuronal glutathione deficiency and age-dependent neurodegeneration in the EAAC1 deficient mouse. *Nat. Neurosci.* 9, 119–126. doi: 10.1038/nn1609

Arriza, J. L., Eliasof, S., Kavanaugh, M. P., and Amara, S. G. (1997). Excitatory amino acid transporter 5, a retinal glutamate transporter coupled to a chloride conductance. *Proc. Natl. Acad. Sci. U S A.* 94, 4155–4160. doi: 10.1073/pnas.94.8.4155

Bianchi, M. G., Bardelli, D., Chiu, M., and Bussolati, O. (2014). Changes in the expression of the glutamate transporter EAAT3/EAAC1 in health and disease. *Cell Mol. Life Sci.* 71, 2001–2015. doi: 10.1007/s00018-013-1484-0

Bjørn-Yoshimoto, W. E., and Underhill, S. M. (2016). The importance of the excitatory amino acid transporter 3 (EAAT3). *Neurochem. Int.* 98, 4–18. doi: 10.1016/j.neuint.2016.05.007

Boato, F., Hendrix, S., Huelsenbeck, S. C., Hofmann, F., Grosse, G., Djalali, S., et al. (2010). C3 peptide enhances recovery from spinal cord injury by improved regenerative growth of descending fiber tracts. *J. Cell Sci.* 123, 1652–1662. doi: 10.1242/jcs.066050

Choi, D. W., and Rothman, S. M. (1990). The role of glutamate neurotoxicity in hypoxic-ischemic neuronal death. *Annu. Rev. Neurosci.* 13, 171–182. doi: 10.1146/annurev.ne.13.030190.001131

Delgado-Acevedo, C., Estay, S. F., Radke, A. K., Sengupta, A., Escobar, A. P., Henriquez-Belmar, F., et al. (2019). Behavioral and synaptic alterations relevant to obsessive-compulsive disorder in mice with increased EAAT3 expression. *Neuropsychopharmacology* 44:1163. doi: 10.1038/s41386-018-0302-7

Diamond, J. S. (2002). A broad view of glutamate spillover. *Nat. Neurosci.* 5, 291–292. doi: 10.1038/nn0402-291

Dubreuil, C. I., Winton, M. J., and McKerracher, L. (2003). Rho activation patterns after spinal cord injury and the role of activated Rho in apoptosis in the central nervous system. *J. Cell Biol.* 162, 233–243. doi: 10.1083/jcb.200301080

Fehlings, M. G., Kim, K. D., Aarabi, B., Rizzo, M., Bond, L. M., McKerracher, L., et al. (2018). Rho inhibitor VX-210 in acute traumatic subaxial cervical spinal cord injury: design of the spinal cord injury Rho inhibition investigation (SPRING) clinical trial. *J. Neurotrauma* 35, 1049–1056. doi: 10.1089/neu.2017.5434

González, M. I., Bannerman, P. G., and Robinson, M. B. (2003). Phorbol myristate acetate-dependent interaction of protein kinase Calpha and the neuronal glutamate transporter EAAC1. *J. Neurosci.* 23, 5589–5593. doi: 10.1523/JNEUROSCI.23-13-05589.2003

González, M. I., Susarla, B. T. S., Fournier, K. M., Sheldon, A. L., and Robinson, M. B. (2007). Constitutive endocytosis and recycling of the neuronal glutamate transporter, excitatory amino acid carrier 1. *J. Neurochem.* 103, 1917–1931. doi: 10.1111/j.1471-4159.2007.04881.x

Griffith, O. W. (1999). Biologic and pharmacologic regulation of mammalian glutathione synthesis. *Free Radic. Biol. Med.* 27, 922–935. doi: 10.1016/s0891-5849(99)00176-8

Holmseth, S., Dehnes, Y., Huang, Y. H., Follin-Arbelet, V. V., Grutle, N. J., Mylonakou, M. N., et al. (2012). The density of EAAC1 (EAAT3) glutamate transporters expressed by neurons in the mammalian CNS. *J. Neurosci.* 32, 6000–6013. doi: 10.1523/JNEUROSCI.5347-11.2012

Höltje, M., Djalali, S., Hofmann, F., Münster-Wandowski, A., Hendrix, S., Boato, F., et al. (2009). A 29-amino acid fragment of Clostridium botulinum C3 protein enhances neuronal outgrowth, connectivity, and reinnervation. *FASEB J.* 23, 1115–1126. doi: 10.1096/fj.08-116855

Höltje, M., Hoffmann, A., Hofmann, F., Mucke, C., Grosse, G., Van Rooijen, N., et al. (2005). Role of Rho GTPase in astrocyte morphology and migratory response during in vitro wound healing. *J. Neurochem.* 95, 1237–1248. doi: 10.1111/j.1471-4159.2005.03443.x

Höltje, M., Hofmann, F., Lux, R., Veh, R. W., Just, I., and Ahnert-Hilger, G. (2008). Glutamate uptake and release by astrocytes are enhanced by *Clostridium botulinum* C3 protein. *J. Biol. Chem.* 283, 9289–9299. doi: 10.1074/jbc.M706499200

Huang, Y., Feng, X., Sando, J. J., and Zuo, Z. (2006). Critical role of serine 465 in isoflurane-induced increase of cell-surface redistribution and activity of glutamate transporter type 3. *J. Biol. Chem.* 281, 38133–38138. doi: 10.1074/jbc.M603885200

Huang, Y., Li, L., Washington, J. M., Xu, X., Sando, J. J., Lin, D., et al. (2011). Inhibition of isoflurane-induced increase of cell-surface redistribution and activity of glutamate transporter type 3 by serine 465 sequence-specific peptides. *Eur. J. Pharmacol.* 655, 16–22. doi: 10.1016/j.ejphar.2011.01.014

Kato, K., Yazawa, T., Taki, K., Mori, K., Wang, S., Nishioka, T., et al. (2012). The inositol 5 phosphatase SHIP2 is an effector of RhoA and is involved in cell polarity and migration. *Mol. Biol. Cell.* 23, 2593–2604. doi: 10.1091/mbc.E11-11-0958

Lehre, K. P., and Danbolt, N. C. (1998). The number of glutamate transporter subtype molecules at glutamatergic synapses: chemical and stereological quantification in young adult rat brain. *J. Neurosci.* 18, 8751–8757. doi: 10.1523/JNEUROSCI.18-21-08751.1998

Lipton, S. A., and Rosenberg, P. A. (1994). Excitatory amino acids as a final common pathway for neurologic disorders. *N. Engl. J. Med.* 330, 613–622. doi: 10.1056/NEJM199403033300907

Loske, P., Boato, F., Hendrix, S., Piepgras, J., Just, I., Ahnert-Hilger, G., et al. (2012). Minimal essential length of clostridium botulinum C3 peptides to enhance neuronal regenerative growth and connectivity in a non-enzymatic mode. *J. Neurochem.* 120, 1084–1096. doi: 10.1111/j.1471-4159.2012.07657.x

Malik, A. R., and Willnow, T. E. (2019). Excitatory amino acid transporters in physiology and disorders of the central nervous system. *Int. J. Mol. Sci.* 20:5671. doi: 10.3390/ijms20225671

Mathews, G. C., and Diamond, J. S. (2003). Neuronal glutamate uptake Contributes to GABA synthesis and inhibitory synaptic strength. *J. Neurosci.* 23, 2040–2048. doi: 10.1523/JNEUROSCI.23-06-02040.2003

McKerracher, L., and Anderson, K. D. (2013). Analysis of recruitment and outcomes in the phase I/IIa Cethrin clinical trial for acute spinal

cordinjury. *J. Neurotrauma* 30, 1795–1804. doi: 10.1089/neu.2013.2909

Mulherkar, S., Firozi, K., Huang, W., Uddin, M. D., Grill, R. J., Costa-Mattioli, M., et al. (2017). RhoA-ROCK inhibition reverses synaptic remodeling and motor and cognitive deficits caused by traumatic brain injury. *Sci. Rep.* 7:10689. doi: 10.1038/s41598-017-11113-3

Owe, S. G., Marcaggi, P., and Attwell, D. (2006). The ionic stoichiometry of the GLAST glutamate transporter in salamander retinal glia. *J. Physiol.* 577, 591–599. doi: 10.1113/jphysiol.2006.116830

Pang, H., and Bitar, K. N. (2005). Direct association of RhoA with specific domains of PKC-alpha. *Am. J. Physiol. Cell Physiol.* 289, C982–C993. doi: 10.1152/ajpcell.00364.2004

Park, E., Velumian, A. A., and Fehlings, M. G. (2004). The role of excitotoxicity in secondary mechanisms of spinal cord injury: a review with an emphasis on the implications for white matter degeneration. *J. Neurotrauma* 21, 754–774. doi: 10.1089/0897715041269641

Peng, J., He, F., Zhang, C., Deng, X., and Yin, F. (2011). Protein kinase C-α signals P115RhoGEF phosphorylation and RhoA activation in TNF-α-induced mouse brain microvascular endothelial cell barrier dysfunction. *J. Neuroinflamm.* 8:28. doi: 10.1186/1742-2094-8-28

Rohrbeck, A., Höltje, M., Adolf, A., Oms, E., Hagemann, S., Ahnert-Hilger, G., et al. (2017). The Rho ADP ribosylating C3 exoenzyme binds cells via an Arg-Gly-Asp motif. *J. Biol. Chem.* 292, 17668–17680. doi: 10.1074/jbc.M117.798231

Rohrbeck, A., Schröder, A., Hagemann, S., Pich, A., Höltje, M., Ahnert-Hilger, G., et al. (2014). vimentin mediates uptake of C3 exoenzyme. *PLoS One* 9:e101071. doi: 10.1371/journal.pone.0101071

Rothstein, J. D., Martin, L., Levey, A. I., Dykes-Hoberg, M., Jin, L., Wu, D., et al. (1994). Localization of neuronal and glial glutamate transporters. *Neuron* 13, 713–25. doi: 10.1016/0896-6273(94)90038-8

Saha, K., Yang, J. W., Hofmaier, T., Venkatesan, S., Steinkellner, T., Kudlacek, O., et al. (2021). Constitutive endocytosis of the neuronal glutamate transporter excitatory amino acid transporter-3 requires ARFGAP1. *Front. Physiol.* 12:671034. doi: 10.3389/fphys.2021.671034

Scimemi, A., Tian, H., and Diamond, J. S. (2009). Neuronal transporters regulate glutamate clearance, NMDA receptor activation, and synaptic plasticity in the hippocampus. *J. Neurosci.* 29, 14581–14595. doi: 10.1523/JNEUROSCI.4845-09.2009

Sepkuty, J. P., Cohen, A. S., Eccles, C., Rafiq, A., Behar, K., Ganel, R., et al. (2002). A neuronal glutamate transporter contributes to neurotransmitter GABA synthesis and epilepsy. *J. Neurosci.* 22, 6372–6379. doi: 10.1523/JNEUROSCI.22-15-06372.2002

Sladojevic, N., Yu, B., and Liao, J. K. (2017). ROCK as a therapeutic target for ischemic stroke. *Expert Rev. Neurother.* 17, 1167–1177. doi: 10.1080/14737175.2017.1395700

Takase, H., and Regenhardt, R. W. (2021). Motor tract reorganization after acute central nervous system injury: a translational perspective. *Neural Regen. Res.* 16, 1144–1149. doi: 10.4103/1673-5374.300330

Underhill, S. M., Colt, M. S., and Amara, S. G. (2020). Amphetamine stimulates endocytosis of the norepinephrine and neuronal glutamate transporters in cultured locus coeruleus neurons. *Neurochem. Res.* 45, 1410–1419. doi: 10.1007/s11064-019-02939-6

Underhill, S. M., Ingram, S. L., Ahmari, S. E., VeenstraVanderWeele, J., and Amara, S. G. (2019). Neuronal excitatory amino acid transporter EAAT3: emerging functions in health and disease. *Neurochem. Int.* 123, 69–76. doi: 10.1016/j.neuint.2018.05.012

Wadiche, J. I., Amara, S. G., and Kavanaugh, M. P. (1995). Ion fluxes associated with excitatory amino acid transport. *Neuron* 15, 721–728. doi: 10.1016/0896-6273(95)90159-0

Watzlawick, R., Sena, E. S., Dirnagl, U., Brommer, B., Kopp, M. A., Macleod, M. R., et al. (2014). Effect and reporting bias of RhoA/ROCK-blockade intervention on locomotor recovery after spinal cord injury: a systematic review and meta-analysis. *JAMA Neurol.* 71, 91–99. doi: 10.1001/jamaneurol.2013.4684

Wu, P., Bjørn-Yoshimoto, W. E., Staudt, M., Jensen, A. A., and Bunch, L. (2019). Identification and Structure-Activity Relationship Study of Imidazo[1,2-*a*]pyridine-3-amines as First Selective Inhibitors of Excitatory Amino Acid Transporter Subtype 3 (EAAT3). *ACS Chem. Neurosci.* 10, 4414–4429. doi: 10.1021/acschemneuro.9b00447

Zike, I., Xu, T., Hong, N., and Veenstra-VanderWeele, J. (2017). Rodent models of obsessive compulsive disorder: evaluating validity to interpret emerging neurobiology. *Neuroscience* 2017, 256–273. doi: 10.1016/j.neuroscience.2016.09.012

Conflict of Interest: The authors declare that the research was conducted in the absence of any commercial or financial relationships that could be construed as a potential conflict of interest.

Publisher's Note: All claims expressed in this article are solely those of the authors and do not necessarily represent those of their affiliated organizations, or those of the publisher, the editors and the reviewers. Any product that may be evaluated in this article, or claim that may be made by its manufacturer, is not guaranteed or endorsed by the publisher.

frontiers | Frontiers in Cellular Neuroscience

ORIGINAL RESEARCH
published: 23 June 2022
doi: 10.3389/fncel.2022.907308

Modulation of Cellular Circadian Rhythms by Secondary Metabolites of Lichens

*Soumi Srimani[1,2], Cosima Xenia Schmidt[1], Maria Pilar Gómez-Serranillos[2], Henrik Oster[1] and Pradeep K. Divakar[2]**

[1]*Institute of Neurobiology, Center of Brain, Behavior & Metabolism (CBBM), University of Lübeck, Lübeck, Germany,*
[2]*Department of Pharmacology, Pharmacognosy and Botany, Faculty of Pharmacy, Complutense University of Madrid, Madrid, Spain*

Background: Most mammalian cells harbor molecular circadian clocks that synchronize physiological functions with the 24-h day-night cycle. Disruption of circadian rhythms, through genetic or environmental changes, promotes the development of disorders like obesity, cardiovascular diseases, and cancer. At the cellular level, circadian, mitotic, and redox cycles are functionally coupled. Evernic (EA) and usnic acid (UA), two lichen secondary metabolites, show various pharmacological activities including anti-oxidative, anti-inflammatory, and neuroprotective action. All these effects have likewise been associated with a functional circadian clock.

Hypothesis/Purpose: To test, if the lichen compounds EA and UA modulate circadian clock function at the cellular level.

Methods: We used three different cell lines and two circadian luminescence reporter systems for evaluating dose- and time-dependent effects of EA/UA treatment on cellular clock regulation at high temporal resolution. Output parameters studied were circadian luminescence rhythm period, amplitude, phase, and dampening rate.

Results: Both compounds had marked effects on clock rhythm amplitudes and dampening independent of cell type, with UA generally showing a higher efficiency than EA. Only in fibroblast cells, significant effects on clock period were observed for UA treated cells showing shorter and EA treated cells showing longer period lengths. Transient treatment of mouse embryonic fibroblasts at different phases had only minor clock resetting effects for both compounds.

Conclusion: Secondary metabolites of lichen alter cellular circadian clocks through amplitude reduction and increased rhythm dampening.

Keywords: evernic acid, usnic acid, circadian clocks, amplitude, dampening, *in vitro* models

Abbreviations: EA, evernic acid; UA, usnic acid; BL, *Bmal1:luciferase*; P2L, *Per2:luciferase*; N44, hypothalamus-derived mouse N44; U2OS, human bone osteosarcoma epithelial; MEF, mouse embryonic fibroblast; Dex, dexamethasone; PRC, phase response curve.

OPEN ACCESS

Edited by:
Frédéric Gachon, The University of Queensland, Australia

Reviewed by:
Stephen Beesley, Florida State University, United States
Marian Henryk Lewandowski, Jagiellonian University, Poland

****Correspondence:***
Pradeep K. Divakar
pdivakar@farm.ucm.es

Specialty section:
This article was submitted to Cellular Neurophysiology, a section of the journal Frontiers in Cellular Neuroscience

Received: *08 April 2022*
Accepted: *20 May 2022*
Published: *23 June 2022*

Citation:
Srimani S, Schmidt CX, Gómez-Serranillos MP, Oster H and Divakar PK (2022) Modulation of Cellular Circadian Rhythms by Secondary Metabolites of Lichens. Front. Cell. Neurosci. 16:907308. doi: 10.3389/fncel.2022.907308

INTRODUCTION

The circadian clock system helps to maintain the adaptation of physiological and psychological functions to the changing environmental conditions induced by the Earth's rotation around its axis (Neumann et al., 2019). Studies reported that most cells and tissues of our body harbor molecular clocks which are in synchronization with day-night rhythms and coordinated by the suprachiasmatic nucleus (SCN) of the hypothalamus (Stephan and Zucker, 1972; Balsalobre et al., 1998; Yamazaki et al., 2000). At the cellular level, clock genes *Clock* (*Circadian Locomotor Output Cycles Kaput*), *Bmal1* (*Brain and Muscle ARNT-Like 1*), *Per1* (*Period 1*), *Per2* (*Period 2*), *Cry1* (*Cryptochrome 1*), *Cry*2 (*Cryptochrome 2*), and *Rev-Erbα* regulate these circadian rhythms (Hastings and Herzog, 2004). Interlocked transcriptional-translational feedback loops control these clock genes (Reppert and Weaver, 2002; Bell-Pedersen et al., 2005; Rosbash et al., 2007). Factors like sedentary lifestyle, prolonged stress or consumption of processed foods or high-sugar or high-fat diets alter circadian rhythms of cells and tissues and promote the development of a range of cardio-metabolic disorders and cancers (Tahara et al., 2015; Panda, 2016; Husse et al., 2017; Kiehn et al., 2017; Neumann et al., 2019). Many of these factors also result in the cellular accumulation of pro-oxidants and induce oxidative stress (OS), an imbalance between intracellular production of reactive oxygen species (ROS) and antioxidant defense mechanism (Charradi et al., 2013; Sharifi-Rad et al., 2020). OS activates a series of transcription factors including NF-κβ (nuclear factor kappa-light-chain-enhancer of activated B cells), AP-1 (Activator protein 1), p53 (Tumor Protein p53), HIF-1α (Hypoxia-inducible factor 1-alpha), PPAR-γ (Peroxisome proliferator-activated receptor gamma), β-catenin/Wnt, and *Nrf2* (nuclear factor erythroid 2-related factor 2; Reuter et al., 2010). Activation of these transcription factors results in the expression of more than 500 different genes encoding for growth factors, inflammatory cytokines, chemokines, cell cycle regulators, and anti-inflammatory molecules, and hence OS results in cytotoxic effects in many mammalian organs and tissues (Behl et al., 1994; Uttara et al., 2009; Reuter et al., 2010). Increased ROS generation and decreased antioxidative enzyme activity (like CAT, SOD, GPx, and GST) have been reported in animals deficient in clock proteins, supporting the evidence that the activity and expression of these genes in different brain regions follow the diurnal rhythm and thus they are under the control of the endogenous circadian system (Pablos et al., 1998; Baydas et al., 2002; Kondratov et al., 2006; Krishnan et al., 2008; Yuan et al., 2017). Hence, along with altered circadian rhythms, prolonged OS also leads to sustained inflammation and chronic diseases including obesity, cancer, diabetes, cardiovascular, neurodegenerative, and pulmonary disorders (Lu and Zee, 2006; Perwez Hussain and Harris, 2007; Reuter et al., 2010; Tahara et al., 2015; Panda, 2016; Sharifi-Rad et al., 2020).

Lichens are symbiotic organisms between a fungal (the mycobiont) and an algal and/or cyanobacterial (the photobiont) partner (Calcott et al., 2018). In addition to the predominant myco- and photobionts, additional fungi, and non-photosynthetic bacteria are often associated with a lichen thallus (Grube et al., 2015; Spribille et al., 2016; Smith et al., 2020). Primary metabolites (such as simple sugars, ribitol, or glucose) produced by the photobiont partner of lichens are used for the mycobiont's nutrition (Brodo et al., 2001; Calcott et al., 2018; Spribille et al., 2022). Lichens are well known to produce a large number of secondary metabolites with almost 1,000 known substances, the large majority of which are exclusively found in lichen forming fungi (Gómez-Serranillos et al., 2014; Calcott et al., 2018). These are deposited extracellularly, mainly in the medullary layer of lichen thallus or in the cortical layer. Phenolic compounds that originate from polyketide pathways, such as depsides, depsidones, and usnic acids are found almost exclusively in lichens. Atranorin and usnic acid are the most common and abundant cortical substances in lichens. They help in protecting the organism from UV radiation, environmental toxicity, pathogens, herbivores, and from other physical hazards (Ranković and Kosanić, 2015). Evernic acid (EA; molecular weight: 332.308 g), a depside, is produced in the medullary layer mainly by a common lichen species, *Evernia prunastri*, usually found in oak trees (Ter Heide et al., 1975; Joulain and Tabacchi, 2009). Other than *Evernia prunastri*, lichen genera such as *Ramalina* and *Hypogymnia* also produce EA (Olivier-Jimenez et al., 2019). Usnic acid (UA; molecular weight: 344.315 g), a dibenzofuran derivative, occurs in two enantiomers and is most commonly found in the cortex of *Usnea* species (Shukla et al., 2010). Other than in *Usnea*, it is also found in several lichen genera as *Cladonia, Lecanora, Ramalina, Xanthoparmelia, Flavoparmelia* and *Alectoria* (Cocchietto et al., 2002).

The production of primary metabolites by the photobionts is highly regulated by external cues like light, temperature, moisture, and gaseous concentrations in the atmosphere (Kallio and Heinonen, 1971; Kershaw and Smith, 1978; Okada et al., 1978; Korhonen and Kallio, 1987; Carré and Edmunds, 1993; Ott and Schieleit, 1994; Mittag, 2001; Segovia et al., 2003; Dodd et al., 2005; Eymann et al., 2017; Cano-Ramirez et al., 2018). *kaiA*, *kaiB*, and *kaiC* are the core clock genes in cyanobacteria as the circadian rhythms of it have been studied vigorously (Kondo and Ishiura, 2000; Dvornyk et al., 2003). Whereas the circadian clock genes have not been largely studied in fungi, this has only been well documented in a model organism like *Neurospora crassa* (Collett et al., 2002; Froehlich et al., 2002; Dunlap and Loros, 2005, 2006). Highly conserved circadian clock homologs are present in most plants and algae, while white collar-1 (WC-1), the circadian core clock component in fungi shows greater similarity in the sequences with the animal core clock component BMAL1/CLOCK (Tauber et al., 2004; Linde et al., 2017; Brody, 2019). More recently, the presence of core circadian clock genes frequency (*frq*), *wc-1*, white collar-2 (*wc-2*), and Frequency Interacting RNA Helicase (*frh*) have been reported in a lichenized fungus (Valim et al., 2022). They have also reported that the *frq* gene was activated in a light-dependent manner, similar to *Neurospora crassa*. Though it remains unclear whether lichens as a holobiont have any circadian rhythms, and thus the biosynthesis of the secondary metabolites is probably controlled by the circadian rhythms of the lichens.

Lichenized secondary metabolites impart a wide range of pharmacological activities like antioxidant, neuroprotective, cytotoxic, antimicrobial, anti-inflammatory, analgesic, and enzyme inhibitory action (Gómez-Serranillos et al., 2014; Fernández-Moriano et al., 2015a; Ranković and Kosanić, 2015; Yamamoto et al., 2015; Solárová et al., 2020). Anti-proliferative and anti-tumoral effect of UA (10 μg/ml and 50 μg/ml concentrations) on human lung cancer tumoral cells by stimulating APOPT1, CYCS, APAF1, CASP3, and CASP9 genes expression, has also been reported (Çoban et al., 2017). Fernández-Moriano et al. (2017) reported the neuroprotective potential of UA and EA with strong radical scavenging properties (ORAC and DPPH tests) and improved cellular redox status (by inhibiting H_2O_2 induced intracellular ROS overproduction, by restoring GSH/GSSG ratio and by lowering lipid peroxidation level through MDA) for the first time on 2017 in two models of central nervous system-like cells (U373-MG and SH-SY5Y cell lines). They have also reported that EA pre-treatment also improved the enzymatic and non-enzymatic antioxidant defense through the activation of the Nrf2 signaling pathway. UA exerts significant but more moderate effects (Fernández-Moriano et al., 2017). Further, they could be used in the therapy of oxidative stress–related diseases (Sahin et al., 2019).

Oxidative stress, mitochondrial impairment, neuroinflammation, and impaired protein degradation are the most important pathophysiologies behind the onset of neurodegenerative diseases like Parkinson's disease, Alzheimer's disease, etc. (Mandel et al., 2003). The brain has higher uptake of glucose and oxygen, which causes neurodegeneration *via* OS-related dysregulation of Nrf2-ARE defense system (Cui et al., 2016). *Nrf2* is activated in response to OS which also regulates the gene expression of antioxidant enzymes, GSH-related genes, and antioxidant proteins *via* the antioxidant responsive element (ARE) in a cell-type dependent manner (Itoh et al., 1997; Ishii et al., 2000; Mann and Forman, 2015). Previous studies reported that astrocytes play a major role in GSH synthesis and thus protect neurons from oxidative stress induced degeneration (Sagara et al., 1993; Fernandez-Checa et al., 1997; Ishii and Mann, 2014). Moreover, circadian rhythms of antioxidative gene expression were altered by 6-hydroxydopamine, a neurotoxin *via* downregulating the expression of *Bmal1*, *Per2*, and other clock genes in both the *in vitro* and *in vivo* PD animal models (Wang et al., 2018). As disruption of the circadian rhythm may be associated with the inadequate inactivation of *Nrf2* and dysregulation of astrocyte-neuron interactions, control of the circadian clock is particularly important for the normalization of brain functions and neuronal protections. Previous studies show that EA and UA are highly lipophilic in nature and, thus, cross lipid bilayers to reach the cytosol and mitochondria (Joseph et al., 2009; Shcherbakova et al., 2021). Hence, we can speculate that lichenized substances impart radical scavenging activities by altering the core clock gene expressions which also activates *Nrf2* and prevents neurodegenerations. However, until now it remains unclear whether these varieties of pharmacological activities imparted by lichenized secondary metabolites take place by altering the circadian clocks of the organism. Thus, in this present study, we aimed to find out whether two lichen metabolites, EA and UA, modulate circadian clock function at the cellular level.

MATERIALS AND METHODS

Reagents

DMEM (1×) Glutamax-I, DPBS, penicillin-streptomycin (P/S), fetal bovine serum (FBS), 1× 0.05% trypsin-EDTA (T/E), B-27, HEPES (1 M), and sodium bicarbonate 7.5% solution were purchased from Gibco, Thermo Fisher Scientific (Waltham, USA). EA and D-luciferin were purchased from Cayman Chemical, Ann Arbor, USA, and PanReac AppliChem, Darmstadt, Germany, respectively. DMEM low-glucose powder, D-(+)-glucose, UA, dexamethasone (Dex), and dimethyl-sulfoxide (DMSO) were purchased from Sigma Aldrich, St. Louis, USA. Acridine Orange Propidium Iodide (AO-PI) was purchased from Logos Biosystems, Gyeonggi-do, South Korea.

Cell Culture

Human bone osteosarcoma epithelial cells (U2OS), originally known as 2T cells, were derived from the bone tissue of a female teenager suffering from osteosarcoma. U2OS cells exhibit epithelial adherent morphology (Ponten and Saksela, 1967). An embryonic mouse hypothalamic cell line (N44) was isolated and immortalized from mouse embryonic (days 15–18 *post coitum*) hypothalamic primary cultures by retroviral transfer of SV40-T antigen (Cedarlane, Burlington, Canada). An embryonic mouse fibroblast (MEF) cell line was created and immortalized from PER2::LUCIFERASE reporter mice (Yoo et al., 2005) following standard protocols. N44-BL (Tsang et al., 2020), U2OS-BL (Maier et al., 2009), and MEF-P2L circadian reporter cells were authenticated by short tandem repeat (STR) profiling and tested negative for mycoplasma by PCR. Cells were maintained in DMEM with 4.5 g/L of D-glucose, supplemented with 10% (FBS) and 10,000 U P/S at 37°C with 5% CO_2. Cells stably expressing *Bmal1:luc* reporter *via* lentiviral transduction were generated polyclonally by puromycin selection (Brown et al., 2005; Lin et al., 2019; Tsang et al., 2020).

Bioluminescence Assay

The setup of the bioluminescence experiment is illustrated in **Figure 1A**. In brief, $2*10^5$ cells/ml of mouse hypothalamic (N44-BL), human osteosarcoma (U2OS-BL), and mouse embryonic fibroblast (MEF-P2L) cells stably expressing circadian clock reporter constructs (*Bmal1::luciferase*—BL or *Per2::luciferase*—P2L) were seeded in either 96-well plates (200 μl cell suspension/well) or 35-mm Petri dishes (2 ml cell suspension per dish) and grown to about 90% confluency (ca. 24 h at 37°C with 5% CO_2). On the next day, cells were synchronized by adding 100 nM Dex for 2 h at 37°C with 5% CO_2. To remove the phenol red from the DMEM, cells were washed with DPBS after the synchronization. After that, the medium was replaced with the same volume of recording medium (1 g/L DMEM low-glucose powder, 10 mM D-glucose, 3 mM 7.5% sodium bicarbonate, 10 mM HEPES, 1% 10,000 U penicillin/streptomycin, 2% B-27 supplement and

0.1 mM D-luciferin; Pilorz et al., 2020) in the dark. Plates were sealed with transparent film and luminescence was recorded for 3–5 days at 34°C using either Berthold TriStar LB 941 (Berthold Technologies, Wildbach, DE; N-44 and U2OS cells) or SpectraMax L 1-channel luminescence plate readers (Molecular Devices, San Jose, USA; MEF cells; Tsang et al., 2012). For the phase response experiment, cells were seeded in 35-mm Petri dishes. After 24 h incubation at 37°C with 5% CO_2, cells were synchronized for 2 h with Dex followed by washing with DPBS and a change to the recording medium. Dishes were covered with glass coverslips and sealed with vacuum grease. Bioluminescence was measured at 32.5°C in LumiCycle 32 luminometer (Actimetrics, Evanston, USA; Tsang et al., 2012).

Cell Treatment and Viability Assay

Usnic acid (UA; 2,6-Diacetyl-7,9-dihydroxy-8,9*b*-dimethyldibenzofuran-1,3(2*H*,9*bH*)-dione) and Evernic acid (EA; 2-hydroxy-4-[(2-hydroxy-4-methoxy-6-methylbenzoyl)oxy]-6-methyl-benzoic acid) were dissolved in dimethyl-sulfoxide (DMSO) followed by dilution in phosphate-buffered saline (PBS) to the desired concentrations (final concentration of DMSO lower than 0.1%). Cell viability assay was conducted after 24 h pre-treatment with different doses of secondary metabolites of lichens using AO-PI staining. Cells were seeded in 35-mm Petri dishes (2 ml cell suspension per dish) and grown to about 90% confluency (ca. 24 h at 37°C with 5% CO_2). On the next day, cell suspension was discarded, followed by a wash with DPBS. Cells were pre-treated with different concentrations of secondary metabolites and control (PBS/DMSO), added with 2 ml of cell culture medium, and incubated for approximately 24 h at 37°C + 5% CO_2. On the following day cells were washed with 1 ml of DPBS/ 35 mm dish. After that, 500 μl of T/E per 35 mm dish were added and incubated for approximately 2–3 min at 37°C + 5% CO_2. 2 ml cell culture medium was added to every 35 mm Petri dish and the cell suspension was centrifuged at 200× g for 5 min followed by the removal of the supernatant and resuspension in 1 ml of cell culture medium per sample. Eighteen microliters of this cell suspension was mixed with 2 μl of AO-PI stain. Ten microliters of this mixture was transferred to a channel in the Ultra-low Fluorescence counting slide for the estimation of viable cells (in the percentage of the total cells) were recorded in the LUNA-FL Dual Fluorescence Cell Counter by Logos Biosystems, Gyeonggi-do, South Korea. 94.35%, 96.35%, 96.2%, 96.3%, and 71.8% (n = 2) N44-BL cells were viable upon 24 h pre-treatment with control along with 10 μg/ml, 25 μg/ml, 50 μg/ml, and 100 μg/ml of UA, respectively. Whereas, 98.9%, 97.8%, and 96.5% (n = 2) U2OS-BL cells were viable after 24 h pre-treatment with control along with 10 μg/ml and 50 μg/ml of UA, respectively. Moreover, significant differences in the rhythm parameters were absent in cells treated with <10 μg/ml and concentrations between 10 μg/ml to 50 μg/ml of EA or UA against control. We then proceeded with our final data analysis and representation with a lower, i.e., 10 μg/ml and a higher, i.e., 50 μg/ml concentrations treatment of the studied secondary metabolites of lichens as these concentrations were not lethal to the cells. For the dose-response experiments, cells were kept in a recording medium containing different concentrations (10 μg/ml and 50 μg/ml) of UE or EA. Bioluminescence was recorded for 3–5 days. Control cells were exposed to recording medium containing the same volume of PBS/DMSO. Same doses of UA, EA or Control were added to the cells after 5 days of recording for resynchronization and bioluminescence was recorded for another 2–3 days. For phase response experiments, bioluminescence recordings were started after the addition of recording medium to the cells. At the indicated time points, equal volumes of PBS/DMSO, UA, or EA were added individually to the designated dishes without wash-out.

Data Transformation and Statistical Analysis

Circadian parameters of luminescence recordings were determined by individually adjusting for long-term trends in raw luminescence readouts by 24-h moving average baseline subtraction as described (Tsang et al., 2020). A damped sine wave $[y(t) = amplitude * e^{-dampening\ rate*t} * \sin(\frac{2\pi}{period}t + phase\ angle)]$ was fitted to baseline-adjusted data after testing for rhythmicity using the Cosinor algorithm (Nelson et al., 1979; Refinetti, 2004). Phase shifts were determined by comparing the fit peak times of substance and PBS/DMSO treated cells (Tsang et al., 2012). Amplitude effects were calculated after normalizing to starting values to account for differences in cell density or reporter signal. Treatment times for phase response profiles were determined *post hoc* using the intersection of the ascending cross-section of the sine fit with the x-axis as a reference and converted into degrees. Dampening rate constants of peak magnitudes were calculated from damped sine wave regressions using GraphPad Prism 9.1.2 software (GraphPad, La Jolla, USA). All statistical analyses were performed using GraphPad Prism. Two-tailed unpaired Student's *t*-tests were used for pairwise comparisons. Multi-group analyses were performed by 1-way ANOVA and Dunnett's *post-hoc* test. To compare changes in rhythm parameters in dose response experiments, 2-way ANOVAs with Tukey's *post-hoc* test was used. A p-value of < 0.05 was used as cut-off for significance (Tsang et al., 2012, 2020).

RESULTS

Quantitative Characterization of Circadian Luminescence Rhythms in Three Different Cell Lines

Figure 1B depicts the representative raw bioluminescence recordings of all three cell lines. **Figure 1C** represents the curve-fitted and detrended rhythm of the same data set. For the determination of circadian rhythm parameters (period, phase, and dampening rate) damped sine curves were fitted to the normalized data. The mean period lengths of MEF-P2L, N44-BL, and U2OS-BL cells were 22.2 ± 0.3 h, 23.9 ± 0.1 h, and 24.8 ± 0.06 h, respectively (**Figure 1D**). Significant differences in period length between all three cell lines were found. Phase shifts (**Figure 1E**) were determined by comparing the fit peak times in these cells. The mean phases of MEF-P2L, N44-BL,

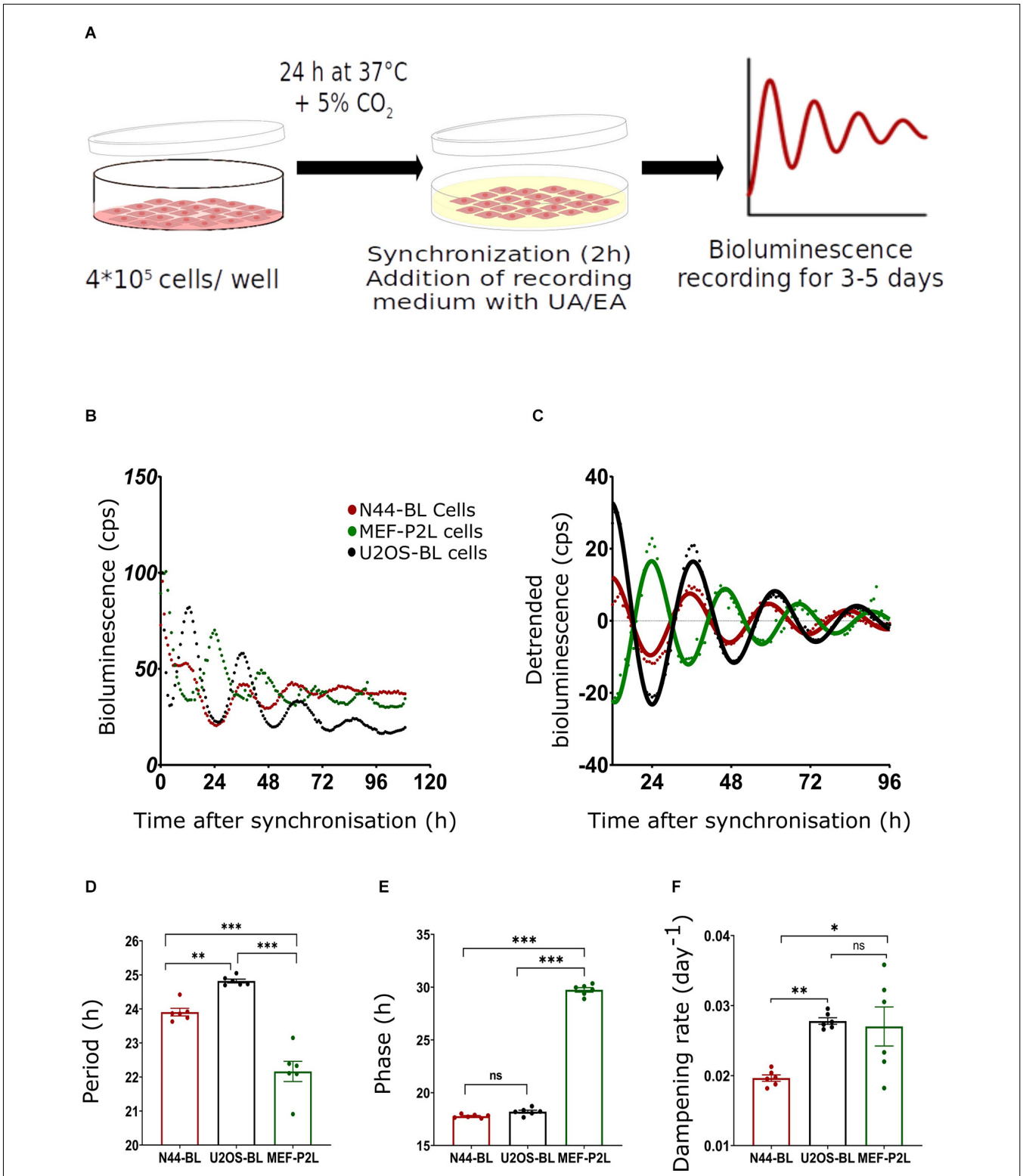

FIGURE 1 | Characterization of circadian luminescence rhythms in N44, U2OS, and MEF cells. **(A)** Experimental setup; for more details, see text. **(B)** Representative raw and **(C)** representative normalized data and sine curve fittings of *Bmal1:luc* (BL) and *Per2:luc* (P2L) luminescence recordings of hypothalamus-derived mouse N44 (N44-BL), human bone osteosarcoma epithelial (U2OS-BL), and mouse embryonic fibroblast (MEF-P2L) cells after synchronization with dexamethasone (Dex). **(D–F)** Luminescence period lengths **(D)**, rhythm phases **(E)**, and dampening rates **(F)** of the same data set. Single measures are shown; error bars indicate means ± SEM (*$p < 0.05$, **$p < 0.01$, ***$p < 0.001$; 1-way ANOVA with Dunnett's *post*-test; $n = 6$). ns, non-significant.

and U2OS-BL cells were 29.74 ± 0.21 h, 17.72 ± 0.07 h, and 18.34 ± 0.14 h, respectively. Dampening rate constants of peak magnitudes (**Figure 1F**) were calculated from damped sine wave regressions. Mean dampening rates of MEF-P2L, N44-BL, and U2OS-BL cells were 0.027 ± 0.003 h^{-1}, 0.020 ± 0.001 h^{-1}, and 0.028 ± 0.001 h^{-1}, respectively. Significant phase differences were observed between MEF-P2L cells and the other two cell lines. Significant differences in dampening rates were observed between N44-BL cells and the other two cell lines. In summary, irrespective of the type of cell line and the luciferase reporter among untreated cells, significantly different period length and dampening rates were observed. As expected from the feedback nature of the circadian molecular clockwork (**Figure 1E**), phasing was significantly different between P2L and BL rhythms.

Lichen Metabolite-Induced Dose- and Cell Type-Dependent Changes in Circadian Luminescence Rhythms

We conducted dose-response bioluminescence experiments in all the three cell lines to compare the extents to which different concentrations of UA or EA affect cellular P2L and BL rhythms. **Supplementary Figures S1A,C** depict the representative raw bioluminescence recording in N44-BL cells treated with different doses of UA (2.5 μg/ml, 5 μg/ml, 10 μg/ml and 50 μg/ml; **Supplementary Figure S1A**) and EA (5 μg/ml, 10 μg/ml, 25 μg/ml, 50 μg/ml and 100 μg/ml; **Supplementary Figure S1C**). Curve-fitted and detrended rhythms of the same data sets are presented under **Supplementary Figure S1B** (UA) and **Supplementary Figure S1D** (EA). For resynchronization, after 5 days of recording, the same doses of UA, EA, or Control were added to the cells with the pre-treatment and bioluminescence was recorded for another 2–3 days. In our exploratory analyses, significant resynchronization effect by the lichenized substances was not seen in any of the experiment (data are not shown here). **Supplementary Figures S1A,B** shows the representative raw (**Supplementary Figure S1A**) and curve-fitted detrended (**Supplementary Figure S1B**) bioluminescence *Bmal1:luc* rhythm of the N44 cells treated with different doses of UA against PBS/DMSO control. A significant difference in the rhythm parameters was absent in cells treated with <10 μg/ml and concentrations between 10 μg/ml to 50 μg/ml of EA or UA against control (data are not shown here). Whereas, cells became arrhythmic upon treatment with 100 μg/ml of EA (**Supplementary Figures S1C,D**). We speculated that the dampening in the rhythm at 50 μg/ml and arrhythmicity upon 100 μg/ml of UA or EA could be due to the cell death in such higher concentrations. We then conducted a cell viability assay using AO-PI stain in the N44 and U2OS cells after 24 h pre-treatment with different concentrations of UA against PBS/DMSO control. 94.35%, 96.35%, 96.2%, 96.3%, and 71.8% ($n = 2$) N44-BL cells were viable upon 24 h pre-treatment with control along with 10 μg/ml, 25 μg/ml, 50 μg/ml and 100 μg/ml of UA, respectively. Whereas, 98.9%, 97.8%, and 96.5% ($n = 2$) U2OS-BL cells were viable after 24 h pre-treatment with control along with 10 μg/ml and 50 μg/ml of UA, respectively. We then proceeded with our final data analysis and representation with a lower, i.e., 10 μg/ml and a higher, i.e., 50 μg/ml concentrations treatment of the studied secondary metabolites of lichens as these concentrations were not lethal to the cells. **Figures 2A**, **3A**, **4A** show representative BL and P2L rhythms of the respective N44-BL (**Figure 2A**), U2OS-BL (**Figure 3A**), and MEF-P2L cells (**Figure 4A**) treated with 10 and 50 μg/ml of UA against solvent control. On the other hand, **Figures 2B**, **3B**, **4B** depict representative BL and P2L curve-fitted normalized luminescence rhythms upon treatment with 10 and 50 μg/ml of EA against solvent control in N44-BL (**Figure 2B**), U2OS-BL (**Figure 3B**), and MEF-P2L cells (**Figure 4B**), respectively. Irrespective of reporter and cell type, 50 μg/ml of UA and EA yielded robust dampening of the luminescence rhythm. UA at 50 μg/ml dampened the BL rhythm more strongly than that of P2L. In general, BL rhythms in U2OS cells showed greater sensitivity towards any concentrations of both secondary lichen metabolites compared to solvent controls.

Comparison of Rhythm Parameter Changes After Treatment With Lichen Secondary Metabolites

Normalized amplitude, period, phase, and dampening rate in different reporter cell models are depicted in **Figures 2–4** in panels **C,D,E,F**, respectively. **Figures 2C–F** shows the rhythm parameters of N44-BL cells whereas **Figures 3C–F** and **4C–F** represent the rhythm parameters of U2OS-BL and MEF-P2L cells, respectively. Irrespective of the reporter cell line, a dampening of the amplitude was observed in all cells treated with either UA or EA (**Figures 2C**, **3C**, **4C**). In all the three cell lines, significantly lowered amplitudes were observed upon treatment with 50 μg/ml of UA or EA compared to solvent controls. U2OS-BL (**Figure 3C**) and MEF-P2L (**Figure 4C**) cells treated with 10 μg/ml of UA had significantly dampened amplitudes. UA treated cells showed lower amplitudes than solvent controls and EA treated cells. An exception was observed only in the case of N44-BL cells treated with 10 μg/ml of UA and EA (**Figure 2C**). At 10 μg/ml EA treated cells showed lower amplitudes than UA cells treated at the same concentration. Subtle differences in period length were observed only in MEF-P2L cells treated with 10 μg/ml (shortened) of UA and 50 μg/ml of EA (lengthened; **Figure 4D**). EA 10 μg/ml treated MEF-P2L cells had a significantly longer period than 10 μg/ml of UA treated cells. Irrespective of the reporter cell line, in cells treated with 50 μg/ml of UA and EA significant phase differences were observed, though directional effects on phase differed between cell types (**Figures 2E**, **3E**, **4E**). 50 μg/ml of UA or EA treated MEF-P2L (**Figure 4E**) and N44-BL (**Figure 2E**) cells showed significantly advanced phase compared to solvent controls whereas U2OS-BL (**Figure 3E**) showed significantly delayed phases upon treatment. N44-BL cells treated with 50 μg/ml of UA showed stronger phase delays than cells treated with EA at 50 μg/ml (**Figure 2E**). In contrast, among cells treated with 10 μg/ml of secondary metabolites, MEF-P2L cells showed significant phase advance upon treatment with 10 μg/ml of UA against solvent control (**Figure 4E**). Increased dampening was observed in BL reporter cells upon treatment with 50 μg/ml of UA in N44 cells and with

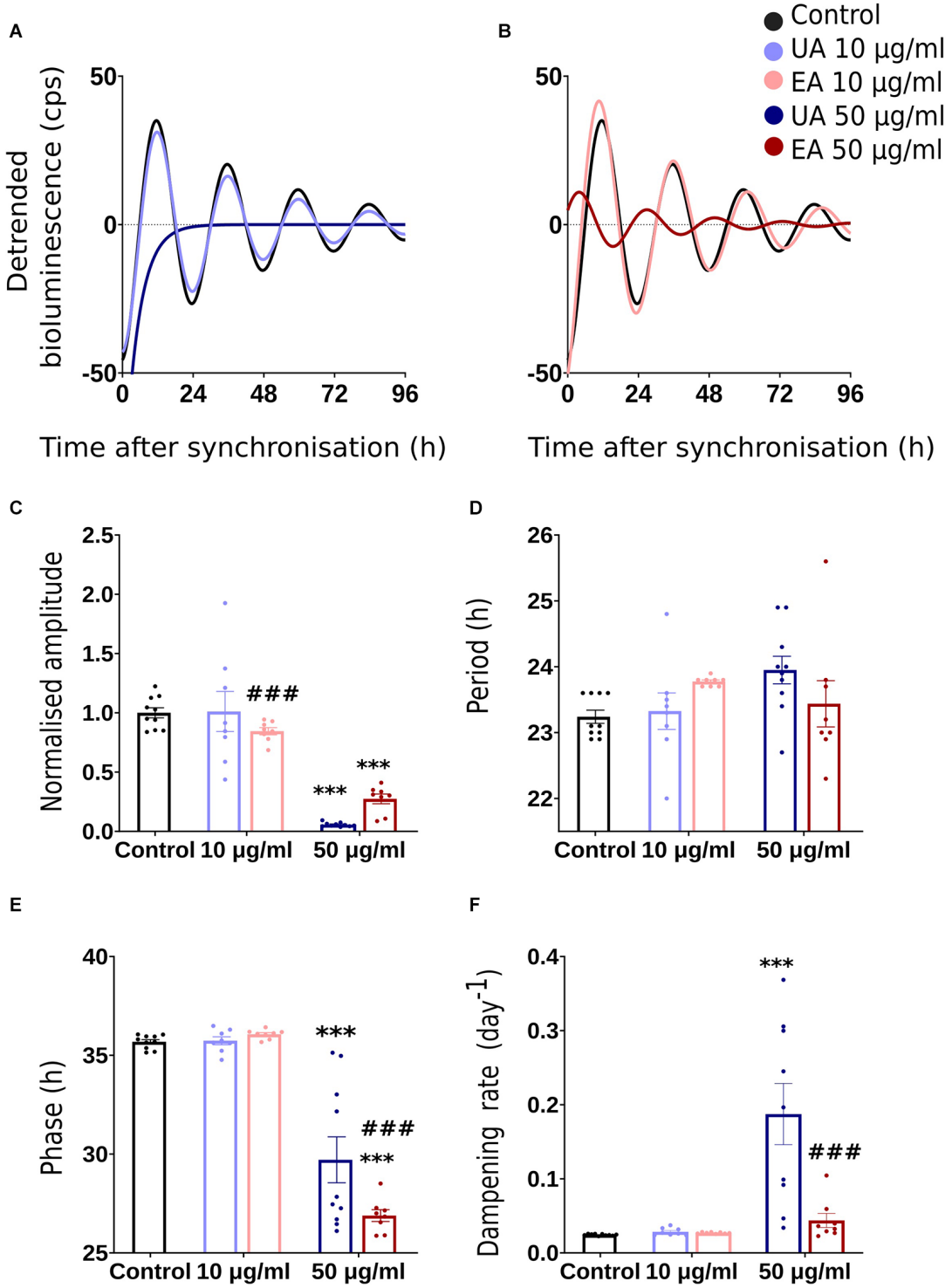

FIGURE 2 | Effects of lichenized secondary metabolites on circadian luminescence rhythms of N44-BL cells. Representative curve fits of *Bmal1:luc* luminescence rhythms in N44 cells after treatment with different doses of usnic acid (**A**, UA/Blue) or evernic acid (**B**, EA/Red). Amplitude **(C)**, Period **(D)**, Phase **(E)**, and Dampening effects **(F)** on bioluminescence rhythms in N44 cells after treatment with EA (10 or 50 µg/ml; red) or UA (10 or 50 µg/ml; blue) vs. solvent control (PBS/ DMSO; black). Single measures are shown; error bars indicate means ± SEM (***$p < 0.001$; 2-way ANOVA with Tukey's post-test). ###$p < 0.001$ between UA 10 vs. EA 10 or UA 50 vs. EA 50.

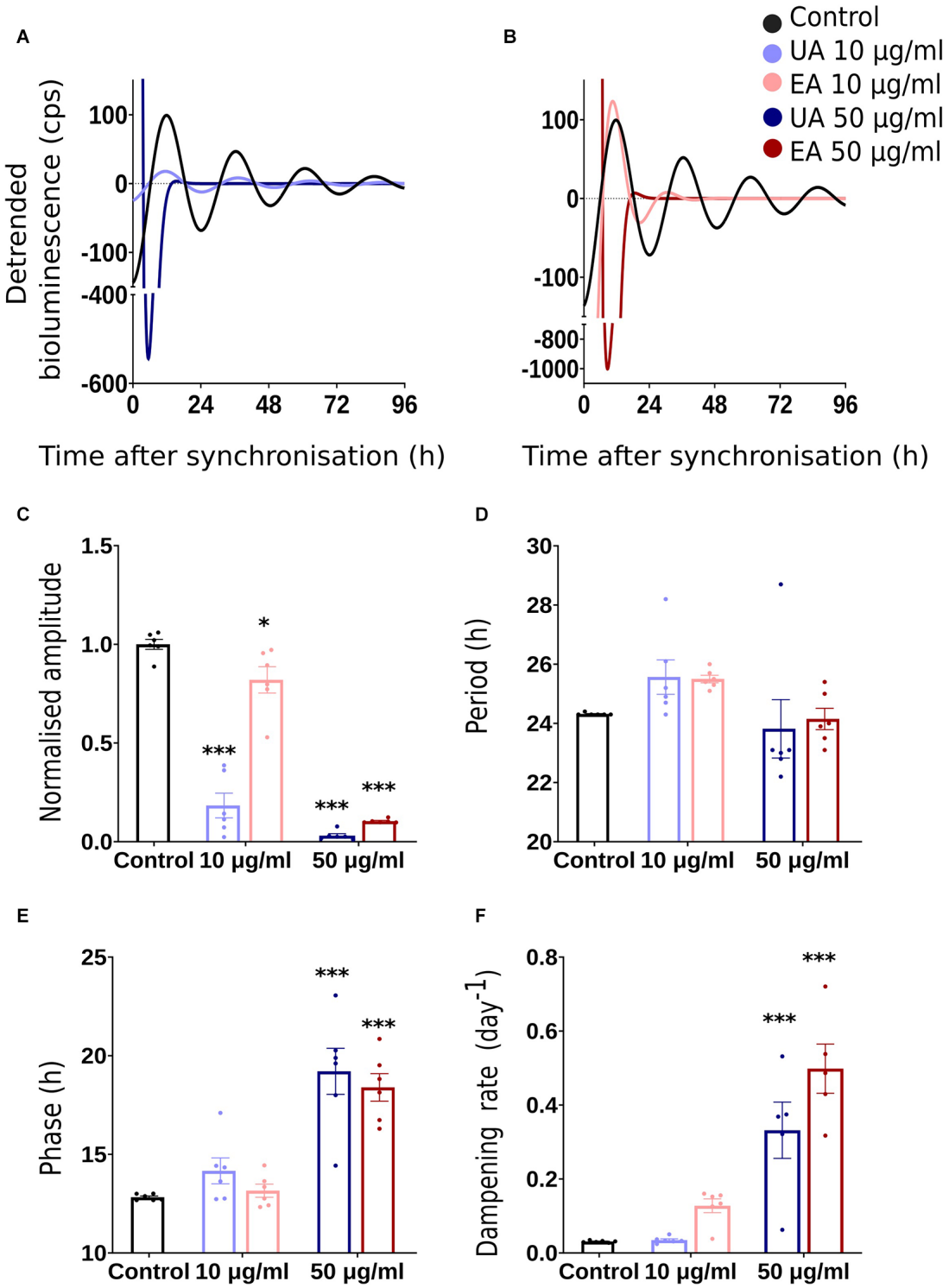

FIGURE 3 | Effects of lichenized secondary metabolites on circadian luminescence rhythms of U2OS-BL cells. Representative curve fits of *Bmal1:luc* luminescence rhythms in U2OS cells after treatment with different doses of usnic acid (**A**, UA/Blue) or evernic acid (**B**, EA/Red). Amplitude **(C)**, Period **(D)**, Phase **(E)**, and Dampening effects **(F)** on bioluminescence rhythms in U2OS cells after treatment with EA (10 or 50 µg/ml; red) or UA (10 or 50 µg/ml; blue) vs. solvent control (PBS/DMSO; black). Single measures are shown; error bars indicate means ± SEM (*$p < 0.05$, ***$p < 0.001$; 2-way ANOVA with Tukey's post-test).

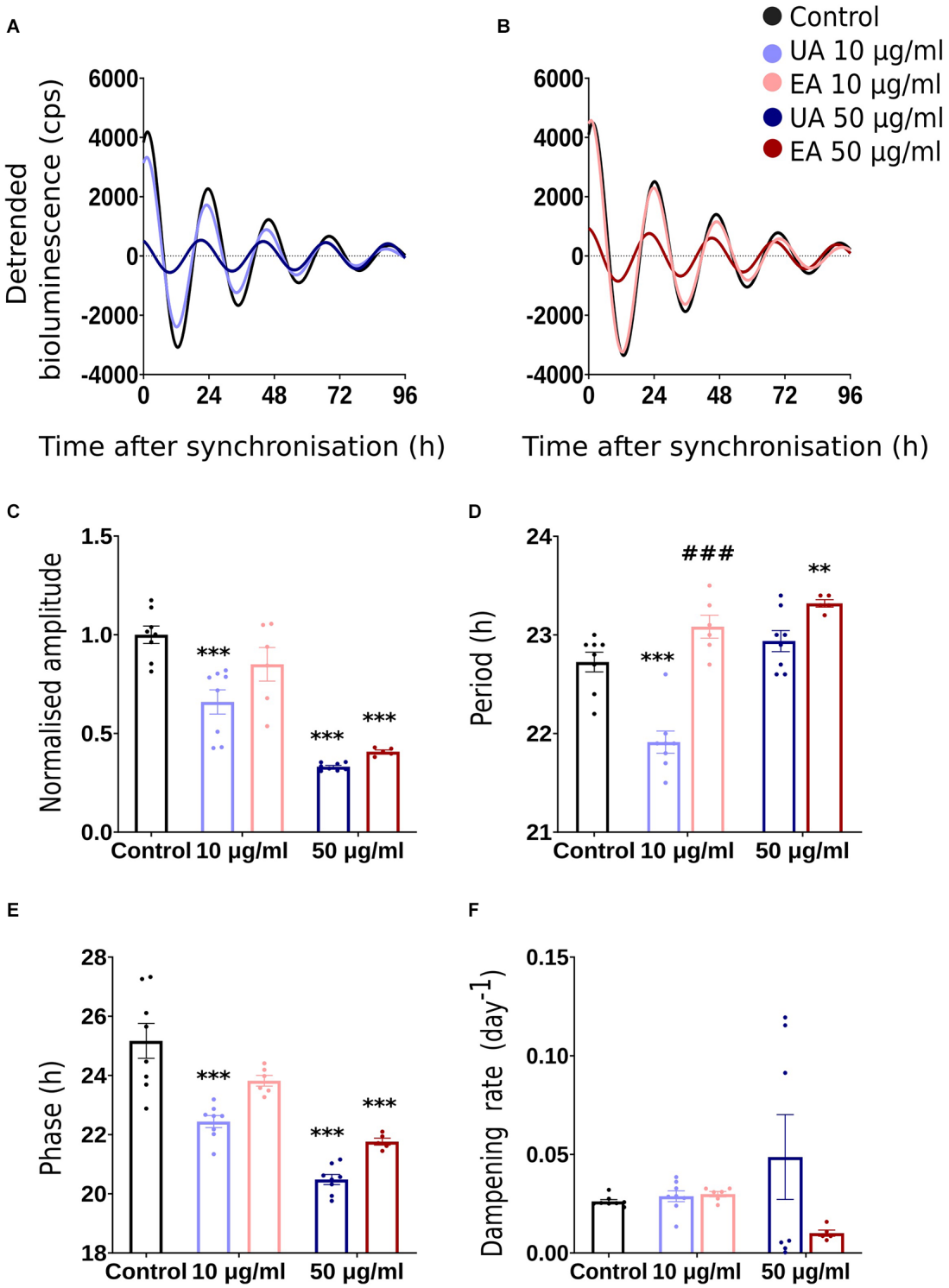

FIGURE 4 | Effects of lichenized secondary metabolites on circadian luminescence rhythms of MEF-P2L cells. Representative curve fits of *Per2:luc* luminescence rhythms in MEF cells after treatment with different doses of usnic acid (**A**, UA/Blue) or evernic acid (**B**, EA/Red). Amplitude **(C)**, Period **(D)**, Phase **(E)**, and Dampening effects **(F)** on bioluminescence rhythms in MEF cells after treatment with EA (10 or 50 µg/ml; red) or UA (10 or 50 µg/ml; blue) vs. solvent control (PBS/DMSO; black). Single measures are shown; error bars indicate means ± SEM (**$p < 0.01$, ***$p < 0.001$; 2-way ANOVA with Tukey's post-test). ###$p < 0.001$ between UA 10 vs. EA 10 or UA 50 vs. EA 50.

both UA and EA in U2OS cells (**Figures 2F**, **3F**, **4F**). N44-BL cells treated with 50 μg/ml of UA had significantly higher dampening rates than EA treated cells (**Figure 2F**). In summary, we have found that higher concentrations of secondary metabolites of lichens had marked effects on amplitude and dampening, while period and phase showed only modest responses.

Phase Responses of MEF *Per2:luc* Rhythms After Acute Treatment With Lichen Secondary Metabolites

A phase response curve (PRC) is the graphical illustration of phase shifts as a function of the circadian treatment phase induced by stimuli like light, food, temperature, or chemicals. As 50 μg/ml of UA and EA had profound dampening effects in all the cell models and significant differences in amplitude, period, and phase were observed from dose-dependent experiments on MEF-P2L cells treated with 10 μg/ml of UA or EA (**Figure 4E**), we wanted to investigate if these changes of circadian parameters are dependent on the phase of the treatment. We treated MEF-P2L cells with 10 μg/ml of UA or EA (or solvent) at different phases of the *Per2:luc* luminescence rhythm. **Figure 5A** shows representative data of treatments before the peak of luminescence (at ca. 70°) whereas treatment after the peak of luminescence (i.e., at ca. 160°), before the trough (at ca. 255°), and after the trough (at ca. 355°) are shown in **Figures 5B–D**, respectively. Panels on the left show raw data, middle panels the respective curve-fitted detrended data. Pink arrows indicate the approximate treatment times. Except the treatment at ca. 355°, PRCs reveal that UA treated cells showed advanced phase compared to EA treated cells (**Figure 5E**), though overall phase effects were rather small and differences in phase shifts were not significant at any time point. While PRCs on *Bmal1:luc* rhythm report that EA treated cells showed an advanced phase compared UA treated cells, the overall phase effects were inconclusive (**Supplementary Figure S2**). **Supplementary Figure S2** depicts the representative PRC of N44-BL (**Supplementary Figure S2A**) and U2OS-BL (**Supplementary Figure S2B**) cells.

DISCUSSION

To test our hypothesis, we chose three different commonly used cellular circadian models, i.e., mouse embryonic fibroblasts (MEF) and hypothalamic neurons (N44) along with human osteosarcoma (U2OS) cell lines with two different circadian luciferase reporters (*Bmal1* and *Per2*). In this way, changes in circadian clock rhythms upon treatment consistently observed in all models would likely also be applicable to other tissues and cell types. Along this line, previous studies reported a broad range of pharmacological activities of UA and EA like neuroprotective, cytoprotective, and antioxidant actions in healthy neuronal, cardiac, gastric cell lines, and cytotoxic, antiproliferative and anticarcinogenic effects in different cancer cell lines (MCF-7, HeLa, HCT-116, FemX, U937, LS174, SH-SY5Y, HL-60, A2780, SK-BR-3, HT29, and U373 MG; Marante et al., 2003; de Paz et al., 2010; Bačkorová et al., 2011; Bessadottir et al., 2012; Rabelo et al., 2012; Ranković et al., 2012; Brisdelli et al., 2013; Kosanić et al., 2013; Geng et al., 2018). In a previous study, Fernández-Moriano et al. (2017) had reported the neuroprotective potential of UA and EA with strong radical scavenging properties (ORAC and DPPH tests) for the first time in 2017 in two models of central nervous system-like cells (U373-MG and SH-SY5Y cell lines). They first measured approximately 55%–60% cell viability against control after inducing oxidative stress by the exogenous H_2O_2. Twenty-four hours of pre-treatment with 5 μg/ml EA showed the most promising and effective cytoprotection against the oxidative damage in both of the cell models tested. Whereas, that of UA in astrocytes and neurons were 2.5 μg/ml and 1 μg/ml, respectively (Fernández-Moriano et al., 2017). In our cellular models, except U2OS cells other two cells were from mouse embryonic hypothalamic neurons and fibroblasts. Moreover, exogenous oxidative stress was not induced in any of these cells.

We observed that irrespective of the cell model and luciferase reporter type, 50 μg/ml of UA or EA significantly lowered amplitudes and accelerated the dampening of cellular circadian rhythms (**Figures 2C**, **3C**, **4C**). The lowered dampening could result from cell death by the action of higher concentrations of secondary metabolites of lichens. To find out whether lichenized substances cause cell death, we conducted a cell viability assay using AO-PI stain in the N44 and U2OS cells after 24 h pre-treatment with different concentrations of UA against PBS/DMSO control. Our results showed that the 94.35%, 96.35%, 96.2%, 96.3%, and 71.8% (n = 2) N44-BL cells were viable upon 24 h pre-treatment with control along with 10 μg/ml, 25 μg/ml, 50 μg/ml, and 100 μg/ml of UA, respectively. Whereas, after 24 h pre-treatment with control along with 10 μg/ml and 50 μg/ml of UA the 98.9%, 97.8%, and 96.5% (n = 2) U2OS-BL cells were viable, respectively. We have observed that UA had stronger dampening effects on BL rhythms than on P2L (**Figures 2A**, **3A**, **4A**). Dose response experiments showed that BL rhythms in U2OS cells were more sensitive upon treatment with any concentration of both compounds (**Figures 3A,B**). At this point, the mechanism behind these effects remains unclear. Reduced amplitudes—but not stronger dampening of rhythms could result from lowered cellular levels of adenosine tri-phosphate (ATP) as ATP is required for the bioluminescence signal (Gould and Subramani, 1988). Usnic acid (10 μg/ml) treatment of the breast cancer cell line T47D and EA pre-treatment of primary neurons have been shown to reduce cellular levels of ATP by inducing the phosphorylation of adenosine monophosphate kinase (AMPK; Bessadottir et al., 2012) and proton leakage through the mitochondrial membrane (Lee et al., 2021).

Circadian rhythm alterations like disrupted sleep and dysregulated circadian gene expression patterns are early markers of neurodegenerative disease progression (Hatfield et al., 2004; Breen et al., 2014; Song et al., 2015; Musiek and Holtzman, 2016; Cronin et al., 2017; Musiek et al., 2018). Fernández-Moriano et al. (2017) reported the neuroprotective potential of UA and EA with strong radical scavenging properties in U373-MG astrocytoma and SH-SY5Y neuroblastoma cell lines. Dysfunctional astrocytes cause neurodegeneration by inducing OS, followed by downregulating *Nrf2* gene expression

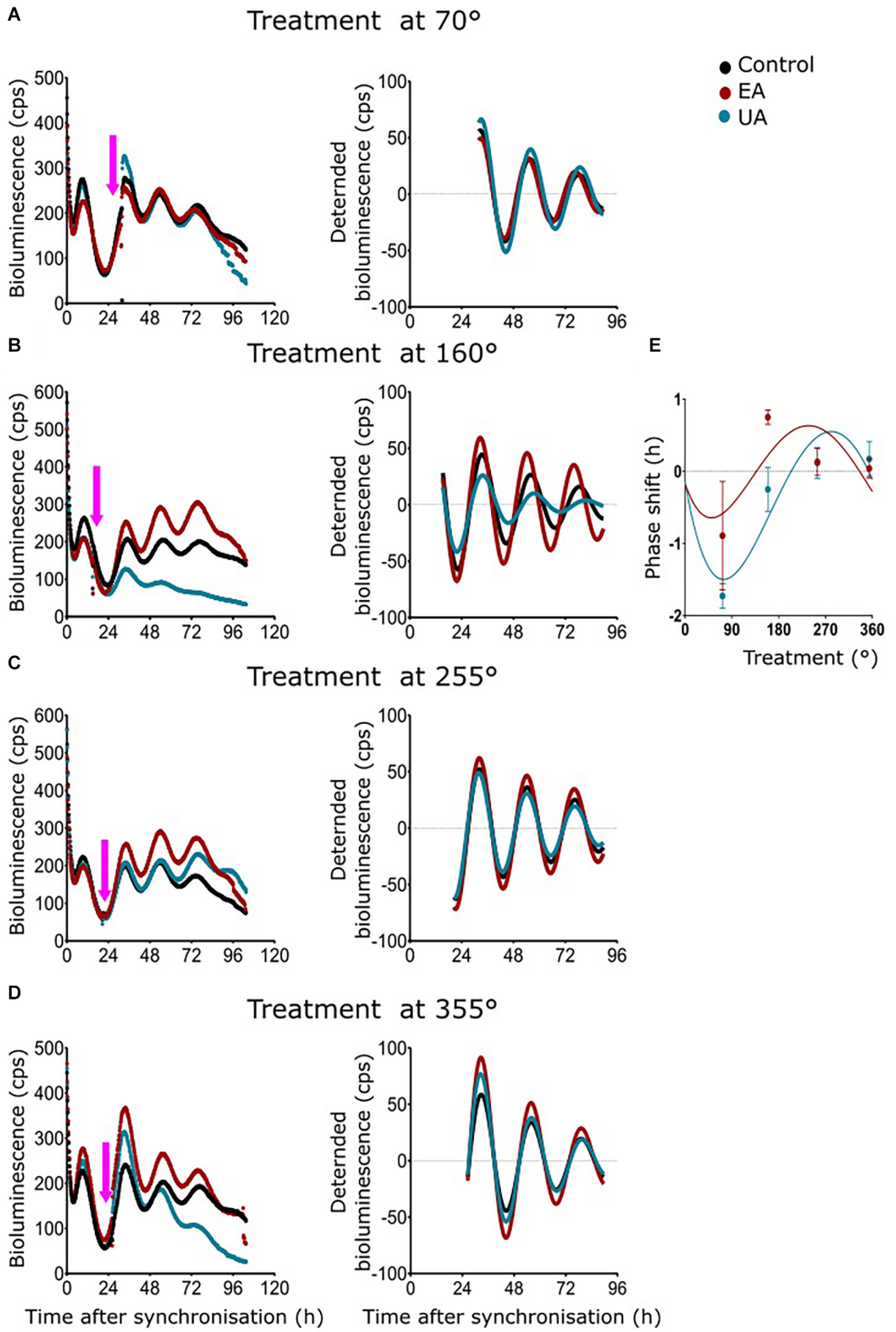

FIGURE 5 | Phase response curves (PRCs) of MEF *Per2:luc* rhythms after timed treatment with secondary lichen metabolites. **(A–D)** Raw bioluminescence data (left) and normalized curve fits (right) of luminescence in MEF-P2L cells treated with 10 μg/ml of UA (blue) or EA (red) vs. solvent control (PBS/DMSO; black) at 70° **(A)**, 160° **(B)**, 255° **(C)**, or 355° **(D)** of the pre-treatment *Per2:luc* rhythm. Pink arrows depict treatment time points. **(E)** PRC of the same data set (n = 3 per time point; data are averages ± SEM).

(Sagara et al., 1993; Fernandez-Checa et al., 1997; Itoh et al., 1997; Ishii et al., 2000; Ishii and Mann, 2014; Mann and Forman, 2015). Thus, it plays a critical role in brain health (Yamanaka et al., 2008; Macauley et al., 2011; Lian et al., 2015). Lananna et al. (2018)

reported that BMAL1 protein regulates astrocyte activation *via* a cell-autonomous mechanism.

Pre-treatment of primary astrocytes with EA counteracts MPP^+ induced COX2 (Cyclooxygenase 2) upregulation and glial activation by blocking the NF-κβ signaling pathway (Lee et al., 2021). It has been suggested that the regulation of NF-κβ activity in macrophages is negatively associated with *Bmal1* expression (Oishi et al., 2017). Besides, in U2OS cells, like CRY1, a core clock repressor, NF-κβ activation shortens the period length and represses BMAL1-mediated E-box transcription as its subunit RELA repressed the transcriptional activity of the BMAL1/CLOCK at the circadian E-box cis-element and it also altered the diurnal locomotor behavior by modifying the rhythms in the SCN (longer period; Shen et al., 2021). They have also reported that gene expression of BMAL1, IL-6, and TNF-α were upregulated by RELA. EA also imparts neuroprotective effects as its pre-treatment significantly reduces MPP^+ induced neurite shortening in the primary neurons through reduction of ROS and reduced ATP production (Lee et al., 2021). In line with this, motor function recovery is significantly accelerated in murine Parkinson's disease models when mice are treated with EA (Lee et al., 2021).

Usnic and evernic acids prevent ROS-induced oxidative damage in various cell types *via* activating the NRF2 signaling pathway, inhibiting caspase-3 activity, upregulating protein levels of Bcl-2, and downregulating protein level of BAX (Fernández-Moriano et al., 2015b, 2017; Krajka-Kuźniak and Baer-Dubowska, 2021). In line with their role in clock regulation, the loss of NRF2 function in mouse fibroblasts and hepatocytes alters circadian rhythms through increased Cry2 expression and repressed CLOCK/BMAL1 regulated E-box transcription in a time-dependent manner (Wible et al., 2018). Evernic acid pre-treatment restores MPP^+ induced cell viability by inducing BCL-2 and suppressing BAX protein levels in primary murine neurons (Lee et al., 2021). In the mouse central clock, p53 acts as a transcription factor that blocks BMAL1/CLOCK binding to the Per2 promoter (Miki et al., 2013), and other mechanisms of p53-clock interaction have been described (Gotoh et al., 2014; Jiang et al., 2016). Many of these pathways offer plausible mechanisms mediating the phase alterations and changes in amplitude and dampening of circadian clock rhythms after EA/UA treatment in the tested cell models. Further experiments are necessary to test this hypothesis.

In conclusion, cellular circadian clock functions in human osteosarcoma and embryonic mouse hypothalamic neurons and fibroblasts are altered by treatment with UA and EA, suggesting that lichen secondary metabolites may provide interesting novel therapeutic options for the treatment of chronodisruption-associated diseases. Our study sets a baseline for further exploration of potential natural products for therapeutic applications of chronodisruption-associated diseases.

LIMITATIONS

Serum shock or medium change synchronization effect against synchronization with Dex was not studied with any of the cellular models. Though we cannot exclude the interaction of the synchronization method and EA/UA treatment because of the simultaneous application.

Bioluminescence of all the dose-response and resynchronization experiments were recorded at 34°C in the plate readers, whereas bioluminescence for all the phase response experiments was recorded at 32.5°C due to the existing setup of the Lumicycle at this temperature.

DATA AVAILABILITY STATEMENT

The raw data supporting the conclusions of this article will be made available by the authors, without undue reservation.

AUTHOR CONTRIBUTIONS

SS: conceptualization, methodology, formal analysis, investigation, writing—original draft. CS: supervision, validation, writing—review and editing. HO: conceptualization, methodology, formal analysis, supervision, resources, software, funding acquisition, project administration, validation, visualization, writing—review and editing. MG-S and PKD: conceptualization, supervision, resources, funding acquisition, project administration, writing—review and editing. All authors contributed to the article and approved the submitted version.

FUNDING

This work was supported by an Erasmus+ fellowship (SS). HO was supported by the German Research Foundation (DFG; RTG-1957). PKD was supported by the Spanish Ministerio de Ciencia e Innovación (grant number PID2019-105312GB-I00).

ACKNOWLEDGMENTS

We would like to thank Prof. Dr. Achim Kramer for donating U2OS cells, Dr. Brid Bode for the MEF cells preparation from PER2::LUCIFERASE mice, and Dr. A. M. Neumann for help with cell culture experiments.

SUPPLEMENTARY MATERIAL

The Supplementary Material for this article can be found online at: https://www.frontiersin.org/articles/10.3389/fncel.2022.907308/full#supplementary-material.

Supplementary Figure 1 | Lichenized secondary metabolite's dose effects and resynchronization changes in N44-BL cells. **(A,B)** Representative raw **(A)** and representative curve fits **(B)** of *Bmal1:luc* luminescence rhythms and resynchronization effects of different concentrations of UA treatment on N44 cells. **(C,D)** Representative raw **(C)** and representative curve fits **(D)** of *Bmal1:luc* luminescence rhythms upon treatment with different concentrations of EA on N44 cells.

Supplementary Figure 2 | Phase response curves (PRCs) of N44 and U2OS *Bmal1:luc* rhythms after timed treatment with secondary lichen metabolites. PRC of the N44 cells **(A)** and the U2OS cells **(B)** treated with UA (blue) or EA (red) against solvent control (PBS/ DMSO; black) at different degrees of the *Bmal1:luc* rhythm (n = 3 per time point; data are averages ± SEM).

REFERENCES

Bačkorová, M., Bačkor, M., Mikeš, J., Jendželovský, R., and Fedoročko, P. (2011). Variable responses of different human cancer cells to the lichen compounds parietin, atranorin, usnic acid and gyrophoric acid. *Toxicol. In vitro* 25, 37–44. doi: 10.1016/j.tiv.2010.09.004

Balsalobre, A., Damiola, F., and Schibler, U. (1998). A serum shock induces circadian gene expression in mammalian tissue culture cells. *Cell* 93, 929–937. doi: 10.1016/s0092-8674(00)81199-x

Baydas, G., Gursu, M. F., Yilmaz, S., Canpolat, S., Yasar, A., Cikim, G., et al. (2002). Daily rhythm of glutathione peroxidase activity, lipid peroxidation and glutathione levels in tissues of pinealectomized rats. *Neurosci. Lett.* 323, 195–198. doi: 10.1016/s0304-3940(02)00144-1

Behl, C., Davis, J. B., Lesley, R., and Schubert, D. (1994). Hydrogen peroxide mediates amyloid β protein toxicity. *Cell* 77, 817–827. doi: 10.1016/0092-8674(94)90131-7

Bell-Pedersen, D., Cassone, V. M., Earnest, D. J., Golden, S. S., Hardin, P. E., Thomas, T. L., et al. (2005). Circadian rhythms from multiple oscillators: lessons from diverse organisms. *Nat. Rev. Genet.* 6, 544–556. doi: 10.1038/nrg1633

Bessadottir, M., Egilsson, M., Einarsdottir, E., Magnusdottir, I. H., Ogmundsdottir, M. H., Omarsdottir, S., et al. (2012). Proton-shuttling lichen compound usnic acid affects mitochondrial and lysosomal function in cancer cells. *PLoS One* 7:e51296. doi: 10.1371/journal.pone.0051296

Breen, D. P., Vuono, R., Nawarathna, U., Fisher, K., Shneerson, J. M., Reddy, A. B., et al. (2014). Sleep and circadian rhythm regulation in early Parkinson disease. *JAMA Neurol.* 71, 589–595. doi: 10.1001/jamaneurol.2014.65

Brisdelli, F., Perilli, M., Sellitri, D., Piovano, M., Garbarino, J. A., Nicoletti, M., et al. (2013). Cytotoxic activity and antioxidant capacity of purified lichen metabolites: an *in vitro* study. *Phytother. Res.* 27, 431–437. doi: 10.1002/ptr.4739

Brodo, I. M., Sharnoff, S. D., and Sharnoff, S. (2001). *Lichens of North America*. New Haven, CT: Yale University Press.

Brody, S. (2019). Circadian rhythms in fungi: structure/function/evolution of some clock components. *J. Biol. Rhythms* 34, 364–379. doi: 10.1177/0748730419852832

Brown, S. A., Fleury-Olela, F., Nagoshi, E., Hauser, C., Juge, C., Meier, C. A., et al. (2005). The period length of fibroblast circadian gene expression varies widely among human individuals. *PLoS Biol.* 3:e338. doi: 10.1371/journal.pbio.0030338

Calcott, M. J., Ackerley, D. F., Knight, A., Keyzers, R. A., and Owen, J. G. (2018). Secondary metabolism in the lichen symbiosis. *Chem. Soc. Rev.* 47, 1730–1760. doi: 10.1039/c7cs00431a

Cano-Ramirez, D. L., de Fraine, T. S., Griffiths, O. G., and Dodd, A. N. (2018). Photosynthesis and circadian rhythms regulate the buoyancy of marimo lake balls. *Curr. Biol.* 28, R869–R870. doi: 10.1016/j.cub.2018.07.027

Carré, I. A., and Edmunds, L. N. (1993). Oscillator control of cell division in Euglena: cyclic AMP oscillations mediate the phasing of the cell division cycle by the circadian clock. *J. Cell Sci.* 104, 1163–1173. doi: 10.1242/jcs.104.4.1163

Charradi, K., Elkahoui, S., Limam, F., and Aouani, E. (2013). High-fat diet induced an oxidative stress in white adipose tissue and disturbed plasma transition metals in rat: prevention by grape seed and skin extract. *J. Physiol. Sci.* 63, 445–455. doi: 10.1007/s12576-013-0283-6

Çoban, Z. D., Karaer, T., Atmaca, B., Demir, H. K., and Güran, Ş. (2017). Usnic acid uses mitochondrial apopitotic pathway in it's antitumoral role. *CMJ* 39, 539–545. doi: 10.7197/223.v39i31705.347452

Cocchietto, M., Skert, N., Nimis, P., and Sava, G. (2002). A review on usnic acid, an interesting natural compound. *Naturwissenschaften* 89, 137–146. doi: 10.1007/s00114-002-0305-3

Collett, M. A., Garceau, N., Dunlap, J. C., and Loros, J. J. (2002). Light and clock expression of the Neurospora clock gene frequency is differentially driven by but dependent on white collar-2. *Genetics* 160, 149–158. doi: 10.1093/genetics/160.1.149

Cronin, P., McCarthy, M. J., Lim, A. S., Salmon, D. P., Galasko, D., Masliah, E., et al. (2017). Circadian alterations during early stages of Alzheimer's disease are associated with aberrant cycles of DNA methylation in BMAL1. *Alzheimers Dement.* 13, 689–700. doi: 10.1016/j.jalz.2016.10.003

Cui, Z., Zhong, Z., Yang, Y., Wang, B., Sun, Y., Sun, Q., et al. (2016). Ferrous iron induces Nrf2 expression in mouse brain astrocytes to prevent neurotoxicity. *J. Biochem. Mol. Toxicol.* 30, 396–403. doi: 10.1002/jbt.21803

de Paz, G. A., Raggio, J., Gómez-Serranillos, M. P., Palomino, O. M., González-Burgos, E., Carretero, M. E., et al. (2010). HPLC isolation of antioxidant constituents from *Xanthoparmelia* spp. *J. Pharm. Biomed. Anal.* 53, 165–171. doi: 10.1016/j.jpba.2010.04.013

Dodd, A. N., Salathia, N., Hall, A., Kévei, E., Tóth, R., Nagy, F., et al. (2005). Plant circadian clocks increase photosynthesis, growth, survival and competitive advantage. *Science* 309, 630–633. doi: 10.1126/science.1115581

Dunlap, J. C., and Loros, J. J. (2005). Analysis of circadian rhythms in Neurospora: overview of assays and genetic and molecular biological manipulation. *Methods Enzymol.* 393, 3–22. doi: 10.1016/S0076-6879(05)93001-2

Dunlap, J. C., and Loros, J. J. (2006). How fungi keep time: circadian system in Neurospora and other fungi. *Curr. Opin. Microbiol.* 9, 579–587. doi: 10.1016/j.mib.2006.10.008

Dvornyk, V., Vinogradova, O., and Nevo, E. (2003). Origin and evolution of circadian clock genes in prokaryotes. *Proc. Natl. Acad. Sci. U S A* 100, 2495–2500. doi: 10.1073/pnas.0130099100

Eymann, C., Lassek, C., Wegner, U., Bernhardt, J., Fritsch, O. A., Fuchs, S., et al. (2017). Symbiotic interplay of fungi, algae and bacteria within the lung lichen *Lobaria pulmonaria* L. Hoffm. as assessed by state-of-the-art metaproteomics. *J. Proteome Res.* 16, 2160–2173. doi: 10.1021/acs.jproteome.6b00974

Fernandez-Checa, J. C., Kaplowitz, N., Garcia-Ruiz, C., Colell, A., Miranda, M., Mari, M., et al. (1997). GSH transport in mitochondria: defense against TNF-induced oxidative stress and alcohol-induced defect. *Am. J. Physiol. - Gastrointest. Liver Physiol.* 273, G7–G17. doi: 10.1152/ajpgi.1997.273.1.G7

Fernández-Moriano, C., Divakar, P. K., Crespo, A., and Gómez-Serranillos, M. P. (2015a). Neuroprotective activity and cytotoxic potential of two Parmeliaceae lichens: identification of active compounds. *Phytomedicine* 22, 847–855. doi: 10.1016/j.phymed.2015.06.005

Fernández-Moriano, C., González-Burgos, E., and Gómez-Serranillos, M. P. (2015b). Mitochondria-targeted protective compounds in Parkinson's and Alzheimer's diseases. *Oxidative Med. Cell. Longev.* 2015:408927. doi: 10.1155/2015/408927

Fernández-Moriano, C., Divakar, P. K., Crespo, A., and Gómez-Serranillos, M. P. (2017). Protective effects of lichen metabolites evernic and usnic acids against redox impairment-mediated cytotoxicity in central nervous system-like cells. *Food Chem. Toxicol.* 105, 262–277. doi: 10.1016/j.fct.2017.04.030

Froehlich, A. C., Liu, Y., Loros, J. J., and Dunlap, J. C. (2002). White Collar-1, a circadian blue light photoreceptor, binding to the frequency promoter. *Science* 297, 815–819.

Geng, X., Zhang, X., Zhou, B., Zhang, C., Tu, J., Chen, X., et al. (2018). Usnic acid induces cycle arrest, apoptosis and autophagy in gastric cancer cells *in vitro* and *in vivo*. *Med. Sci. Monit.* 24:556. doi: 10.12659/msm.908568

Gómez-Serranillos, M. P., Fernández-Moriano, C., González-Burgos, E., Divakar, P. K., and Crespo, A. (2014). Parmeliaceae family: phytochemistry, pharmacological potential and phylogenetic features. *RSC Adv.* 4, 59017–59047. doi: 10.1039/C4RA09104C

Gotoh, T., Vila-Caballer, M., Santos, C. S., Liu, J., Yang, J., and Finkielstein, C. V. (2014). The circadian factor period 2 modulates p53 stability and transcriptional activity in unstressed cells. *J. Mol. Cell Biol.* 25, 3081–3093. doi: 10.1091/mbc.E14-05-0993

Gould, S. J., and Subramani, S. (1988). Firefly luciferase as a tool in molecular and cell biology. *Anal. Biochem.* 175, 5–13. doi: 10.1016/0003-2697(88)90353-3

Grube, M., Cernava, T., Soh, J., Fuchs, S., Aschenbrenner, I., Lassek, C., et al. (2015). Exploring functional contexts of symbiotic sustain within lichen-associated bacteria by comparative omics. *ISME J.* 9, 412–424. doi: 10.1038/ismej.2014.138

Hastings, M. H., and Herzog, E. D. (2004). Clock genes, oscillators and cellular networks in the suprachiasmatic nuclei. *J. Biol. Rhythms* 19, 400–413. doi: 10.1177/0748730404268786

Hatfield, C. F., Herbert, J., Van Someren, E. J., Hodges, J. R., and Hastings, M. H. (2004). Disrupted daily activity/rest cycles in relation to daily cortisol rhythms of home dwelling patients with early Alzheimer's dementia. *Brain* 127, 1061–1074. doi: 10.1093/brain/awh129

Husse, J., Kiehn, J. T., Barclay, J. L., Naujokat, N., Meyer-Kovac, J., Lehnert, H., et al. (2017). Tissue-specific dissociation of diurnal transcriptome rhythms during sleep restriction in mice. *Sleep* 40:zsx068. doi: 10.1093/sleep/zsx068

Ishii, T., and Mann, G. E. (2014). Redox status in mammalian cells and stem cells during culture *in vitro*: critical roles of Nrf2 and cystine transporter activity in the maintenance of redox balance. *Redox Biol.* 2, 786–794. doi: 10.1016/j.redox.2014.04.008

Ishii, T., Itoh, K., Takahashi, S., Sato, H., Yanagawa, T., Katoh, Y., et al. (2000). Transcription factor Nrf2 coordinately regulates a group of oxidative stress-inducible genes in macrophages. *J. Biol. Chem.* 275, 16023–16029. doi: 10.1074/jbc.275.21.16023

Itoh, K., Chiba, T., Takahashi, S., Ishii, T., Igarashi, K., Katoh, Y., et al. (1997). An Nrf2/small Maf heterodimer mediates the induction of phase II detoxifying enzyme genes through antioxidant response elements. *Biochem. Biophys. Res. Commun.* 236, 313–322. doi: 10.1006/bbrc.1997.6943

Jiang, W., Zhao, S., Jiang, X., Zhang, E., Hu, G., Hu, B., et al. (2016). The circadian clock gene Bmal1 acts as a potential anti-oncogene in pancreatic cancer by activating the p53 tumor suppressor pathway. *Cancer Lett.* 371, 314–325. doi: 10.1016/j.canlet.2015.12.002

Joseph, A., Lee, T., Moland, C. L., Branham, W. S., Fuscoe, J. C., Leakey, J. E., et al. (2009). Effect of (+)-usnic acid on mitochondrial functions as measured by mitochondria-specific oligonucleotide microarray in liver of B6C3F1 mice. *Mitochondrion* 9, 149–158. doi: 10.1016/j.mito.2009.02.002

Joulain, D., and Tabacchi, R. (2009). Lichen extracts as raw materials in perfumery. Part 1: oakmoss. *Flavour Fragrance J.* 24, 49–61. doi: 10.1002/ffj.1916

Kallio, P., and Heinonen, S. (1971). Influence of short-term low temperature on net photosynthesis in some subarctic lichens. *Rep. Kevo. Subarctic Res. Stat.* 8, 63–72.

Kershaw, K. A., and Smith, M. M. (1978). Studies on lichen-dominated systems. XXI. The control of seasonal rates of net photosynthesis by moisture, light and temperature in *Stereocaulon paschale*. *Can. J. Bot.* 56, 2825–2830.

Kiehn, J. T., Koch, C. E., Walter, M., Brod, A., and Oster, H. (2017). Circadian rhythms and clocks in adipose tissues: current insights. *Chronophysiol. Ther.* 2017, 7–17. doi: 10.2147/CPT.S116242

Kondo, T., and Ishiura, M. (2000). The circadian clock of cyanobacteria. *BioEssays* 22, 10–15. doi: 10.1002/(SICI)1521-1878(200001)22:1<10::AID-BIES4>3.0.CO;2-A

Kondratov, R. V., Kondratova, A. A., Gorbacheva, V. Y., Vykhovanets, O. V., and Antoch, M. P. (2006). Early aging and age-related pathologies in mice deficient in BMAL1, the core component of the circadian clock. *Genes Dev.* 20, 1868–1873. doi: 10.1101/gad.1432206

Korhonen, P., and Kallio, P. (1987). The effect of different night conditions on the CO_2 fixation in a lichen *Xanthoria parietina*. *Photosynth. Res.* 12, 3–11. doi: 10.1007/BF00019146

Kosanić, M., Manojlović, N., Janković, S., Stanojković, T., and Ranković, B. (2013). *Evernia prunastri* and *Pseudoevernia furfuraceae* lichens and their major metabolites as antioxidant, antimicrobial and anticancer agents. *Food Chem. Toxicol.* 53, 112–118. doi: 10.1016/j.fct.2012.11.034

Krajka-Kuzniak, V., and Baer-Dubowska, W. (2021). Modulation of Nrf2 and NF-κB signaling pathways by naturally occurring compounds in relation to cancer prevention and therapy. Are combinations better than single compounds? *Int. J. Mol. Sci.* 22:8223. doi: 10.3390/ijms22158223

Krishnan, N., Davis, A. J., and Giebultowicz, J. M. (2008). Circadian regulation of response to oxidative stress in *Drosophila melanogaster*. *Biochem. Biophys. Res. Commun.* 374, 299–303. doi: 10.1016/j.bbrc.2008.07.011

Lananna, B. V., Nadarajah, C. J., Izumo, M., Cedeño, M. R., Xiong, D. D., Dimitry, J., et al. (2018). Cell-autonomous regulation of astrocyte activation by the circadian clock protein BMAL1. *Cell Rep.* 25, 1–9. doi: 10.1016/j.celrep.2018.09.015

Lee, S., Suh, Y. J., Yang, S., Hong, D. G., Ishigami, A., Kim, H., et al. (2021). Neuroprotective and anti-inflammatory effects of evernic acid in an MPTP-induced Parkinson's disease model. *Int. J. Mol. Sci.* 22:2098. doi: 10.3390/ijms22042098

Lian, H., Yang, L., Cole, A., Sun, L., Chiang, A. C. A., Fowler, S. W., et al. (2015). NFκB-activated astroglial release of complement C3 compromises neuronal morphology and function associated with Alzheimer's disease. *Neuron* 85, 101–115. doi: 10.1016/j.neuron.2014.11.018

Lin, H. H., Qraitem, M., Lian, Y., Taylor, S. R., and Farkas, M. E. (2019). Analyses of BMAL1 and PER2 oscillations in a model of breast cancer progression reveal changes with malignancy. *Integr. Cancer Ther.* 18:1534735419836494. doi: 10.1177/1534735419836494

Linde, A. M., Eklund, D. M., Kubota, A., Pederson, E. R., Holm, K., Gyllenstrand, N., et al. (2017). Early evolution of the land plant circadian clock. *New Phytol.* 216, 576–590. doi: 10.1111/nph.14487

Lu, B. S., and Zee, P. C. (2006). Circadian rhythm sleep disorders. *Chest* 130, 1915–1923. doi: 10.1378/chest.130.6.1915

Macauley, S. L., Pekny, M., and Sands, M. S. (2011). The role of attenuated astrocyte activation in infantile neuronal ceroid lipofuscinosis. *J. Neurosci.* 31, 15575–15585. doi: 10.1523/JNEUROSCI.3579-11.2011

Maier, B., Wendt, S., Vanselow, J. T., Wallach, T., Reischl, S., Oehmke, S., et al. (2009). A large-scale functional RNAi screen reveals a role for CK2 in the mammalian circadian clock. *Genes Dev.* 23, 708–718. doi: 10.1101/gad.512209

Mandel, S., Grünblatt, E., Riederer, P., Gerlach, M., Levites, Y., Youdim, M. B., et al. (2003). Neuroprotective strategies in Parkinson's disease. *CNS Drugs* 17, 729–762. doi: 10.2165/00023210-200317100-00004

Mann, G. E., and Forman, H. J. (2015). Introduction to special issue on 'Nrf2 regulated redox signaling and metabolism in physiology and medicine. *Free Radic. Biol. Med.* 88, 91–92. doi: 10.1016/j.freeradbiomed.2015.08.002

Marante, F. J., Castellano, A. G., Rosas, F. E., Aguiar, J. Q., and Barrera, J. B. (2003). Identification and quantitation of allelochemicals from the lichen Lethariella canariensis: phytotoxicity and antioxidative activity. *J. Chem. Ecol.* 29, 2049–2071. doi: 10.1023/a:1025682318001

Miki, T., Matsumoto, T., Zhao, Z., and Lee, C. C. (2013). p53 regulates Period2 expression and the circadian clock. *Nat. Commun.* 4, 1–11. doi: 10.1038/ncomms3444

Mittag, M. (2001). Circadian rhythms in microalgae. *Int. Rev. Cytol.* 206, 213–247. doi: 10.1016/s0074-7696(01)06023-5

Musiek, E. S., and Holtzman, D. M. (2016). Mechanisms linking circadian clocks, sleep and neurodegeneration. *Science* 354, 1004–1008. doi: 10.1126/science.aah4968

Musiek, E. S., Bhimasani, M., Zangrilli, M. A., Morris, J. C., Holtzman, D. M., Ju, Y. E. S., et al. (2018). Circadian rest-activity pattern changes in aging and preclinical Alzheimer disease. *JAMA Neurol.* 75, 582–590. doi: 10.1001/jamaneurol.2017.4719

Nelson, W., Tong, Y. L., Lee, J. K., and Halberg, F. (1979). Methods for cosinor-rhythmometry. *Chronobiologia* 6, 305–323.

Neumann, A. M., Schmidt, C. X., Brockmann, R. M., and Oster, H. (2019). Circadian regulation of endocrine systems. *Auton. Neurosci.* 216, 1–8. doi: 10.1016/j.autneu.2018.10.001

Oishi, Y., Hayashi, S., Isagawa, T., Oshima, M., Iwama, A., Shimba, S., et al. (2017). Bmal1 regulates inflammatory responses in macrophages by modulating enhancer RNA transcription. *Sci. Rep.* 7, 1–14. doi: 10.1038/s41598-017-07100-3

Okada, M., Inoue, M., and Ikeda, T. (1978). Circadian rhythm in photosynthesis of the green alga *Bryopsis maxima*. *Plant Cell Physiol.* 19, 197–202.

Olivier-Jimenez, D., Chollet-Krugler, M., Rondeau, D., Beniddir, M. A., Ferron, S., Delhaye, T., et al. (2019). A database of high-resolution MS/MS spectra for lichen metabolites. *Sci. Data* 6, 1–11. doi: 10.1038/s41597-019-0305-1

Ott, S., and Schieleit, P. (1994). Influence of exogenous factors on the ethylene production by lichens. I. Influence of water content and water status conditions on ethylene production. *Symbiosis* 16, 187–201.

Pablos, M. I., Reiter, R. J., Ortiz, G. G., Guerrero, J. M., Agapito, M. T., Chuang, J. I., et al. (1998). Rhythms of glutathione peroxidase and glutathione reductase in brain of chick and their inhibition by light. *Neurochem. Int.* 32, 69–75. doi: 10.1016/s0197-0186(97)00043-0

Panda, S. (2016). Circadian physiology of metabolism. *Science* 354, 1008–1015. doi: 10.1126/science.aah4967

Perwez Hussain, S., and Harris, C. C. (2007). Inflammation and cancer: an ancient link with novel potentials. *Int. J. Cancer* 121, 2373–2380. doi: 10.1002/ijc.23173

Pilorz, V., Kolms, B., and Oster, H. (2020). Rapid jetlag resetting of behavioral, physiological, and molecular rhythms in proestrous female mice. *J. Biol. Rhythms* 35, 612–627. doi: 10.1177/0748730420965291

Ponten, J., and Saksela, E. (1967). Two established *in vitro* cell lines from human mesenchymal tumours. *Int. J. Cancer* 2, 434–447. doi: 10.1002/ijc.2910020505

Rabelo, T. K., Zeidán-Chuliá, F., Vasques, L. M., dos Santos, J. P. A., da Rocha, R. F., de Bittencourt Pasquali, M. A., et al. (2012). Redox characterization of usnic acid and its cytotoxic effect on human neuron-like cells (SH-SY5Y). *Toxicol. In vitro* 26, 304–314. doi: 10.1016/j.tiv.2011.12.003

Ranković, B., and Kosanić, M. (2015). *Lichen Secondary Metabolites*. New York; Cham: Springer International Publishing.

Ranković, B., Kosanić, M., Stanojković, T., Vasiljević, P., and Manojlović, N. (2012). Biological activities of *Toninia candida* and *Usnea barbata* together with their norstictic acid and usnic acid constituents. *Int. J. Mol. Sci.* 13, 14707–14722. doi: 10.3390/ijms131114707

Refinetti, R. (2004). Non-stationary time series and the robustness of circadian rhythms. *J. Theor. Biol.* 227, 571–581. doi: 10.1016/j.jtbi.2003.11.032

Reppert, S. M., and Weaver, D. R. (2002). Coordination of circadian timing in mammals. *Nature* 418, 935–941. doi: 10.1038/nature00965

Reuter, S., Gupta, S. C., Chaturvedi, M. M., and Aggarwal, B. B. (2010). Oxidative stress, inflammation and cancer: how are they linked? *Free Radic. Biol. Med.* 49, 1603–1616. doi: 10.1016/j.freeradbiomed.2010.09.006

Rosbash, M., Bradley, S., Kadener, S., Li, Y., Luo, W., Menet, J. S., et al. (2007). Transcriptional feedback and definition of the circadian pacemaker in *Drosophila* and animals. *Cold Spring Harb. Symp. Quant. Biol.* 72, 75–83. doi: 10.1101/sqb.2007.72.062

Sagara, J. I., Miura, K., and Bannai, S. (1993). Maintenance of neuronal glutathione by glial cells. *J. Neurochem.* 61, 1672–1676. doi: 10.1111/j.1471-4159.1993.tb09802.x

Sahin, E., Dabagoglu Psav, S., Avan, I., Candan, M., Sahinturk, V., Koparal, A. T., et al. (2019). Vulpinic acid, a lichen metabolite, emerges as a potential drug candidate in the therapy of oxidative stress-related diseases, such as atherosclerosis. *Hum. Exp. Toxicol.* 38, 675–684. doi: 10.1177/0960327119833745

Segovia, M., Gordillo, F. J., and Figueroa, F. L. (2003). Cyclic-AMP levels in the lichen evernia prunastri are modulated by light quantity and quality. *J. Photochem. Photobiol. B: Biol.* 70, 145–151. doi: 10.1016/s1011-1344(03)00074-5

Sharifi-Rad, M., Anil Kumar, N. V., Zucca, P., Varoni, E. M., Dini, L., Panzarini, E., et al. (2020). Lifestyle, oxidative stress and antioxidants: back and forth in the pathophysiology of chronic diseases. *Front. Physiol.* 11:694. doi: 10.3389/fphys.2020.00694

Shcherbakova, A., Strömstedt, A. A., Göransson, U., Gnezdilov, O., Turanov, A., Boldbaatar, D., et al. (2021). Antimicrobial and antioxidant activity of *Evernia prunastri* extracts and their isolates. *World J. Microbiol. Biotechnol.* 37, 1–14. doi: 10.1007/s11274-021-03099-y

Shen, Y., Endale, M., Wang, W., Morris, A. R., Francey, L. J., Harold, R. L., et al. (2021). NF-κB modifies the mammalian circadian clock through interaction with the core clock protein BMAL1. *PLoS Genet.* 17:e1009933. doi: 10.1371/journal.pgen.1009933

Shukla, V., Joshi, G. P., and Rawat, M. S. M. (2010). Lichens as a potential natural source of bioactive compounds: a review. *Phytochem. Rev.* 9, 303–314. doi: 10.1007/s11101-010-9189-6

Smith, H. B., Dal Grande, F., Muggia, L., Keuler, R., Divakar, P. K., Grewe, F., et al. (2020). Metagenomic data reveal diverse fungal and algal communities associated with the lichen symbiosis. *Symbiosis* 82, 133–147. doi: 10.1007/s13199-020-00699-4

Solárová, Z., Liskova, A., Samec, M., Kubatka, P., Büsselberg, D., and Solár, P. (2020). Anticancer potential of lichens' secondary metabolites. *Biomolecules* 10:87. doi: 10.3390/biom10010087

Song, H., Moon, M., Choe, H. K., Han, D. H., Jang, C., Kim, A., et al. (2015). Aβ-induced degradation of BMAL1 and CBP leads to circadian rhythm disruption in Alzheimer's disease. *Mol. Neurodegener.* 10, 1–15. doi: 10.1186/s13024-015-0007-x

Spribille, T., Resl, P., Stanton, D. E., and Tagirdzhanova, G. (2022). Evolutionary biology of lichen symbioses. *New Phytol.* 234, 1566–1582. doi: 10.1111/nph.18048

Spribille, T., Tuovinen, V., Resl, P., Vanderpool, D., Wolinski, H., Aime, M. C., et al. (2016). Basidiomycete yeasts in the cortex of ascomycete macrolichens. *Science* 353, 488–492. doi: 10.1126/science.aaf8287

Stephan, F. K., and Zucker, I. (1972). Circadian rhythms in drinking behavior and locomotor activity of rats are eliminated by hypothalamic lesions. *Proc. Natl. Acad. Sci. USA* 69, 1583–1586. doi: 10.1073/pnas.69.6.1583

Tahara, Y., Shiraishi, T., Kikuchi, Y., Haraguchi, A., Kuriki, D., Sasaki, H., et al. (2015). Entrainment of the mouse circadian clock by sub-acute physical and psychological stress. *Sci. Rep.* 5, 1–11. doi: 10.1038/srep11417

Tauber, E., Last, K. S., Olive, P. J., and Kyriacou, C. P. (2004). Clock gene evolution and functional divergence. *J. Biol. Rhythms* 19, 445–458. doi: 10.1177/0748730404268775

Ter Heide, R., Provatoroff, N., Traas, P. C., De Valois, P. J., Van der Plasse, N., Wobben, H. J., et al. (1975). Qualitative analysis of the odoriferous fraction of oakmoss (*Evernia prunastri*). *J. Agric. Food Chem.* 23, 950–957.

Tsang, A. H., Koch, C. E., Kiehn, J. T., Schmidt, C. X., and Oster, H. (2020). An adipokine feedback regulating diurnal food intake rhythms in mice. *eLife* 9:e55388. doi: 10.7554/eLife.55388

Tsang, A. H., Sánchez-Moreno, C., Bode, B., Rossner, M. J., Garaulet, M., Oster, H., et al. (2012). Tissue-specific interaction of Per1/2 and Dec2 in the regulation of fibroblast circadian rhythms. *J. Biol. Rhythms* 27, 478–489. doi: 10.1177/0748730412462838

Uttara, B., Singh, A. V., Zamboni, P., and Mahajan, R. (2009). Oxidative stress and neurodegenerative diseases: a review of upstream and downstream antioxidant therapeutic options. *Curr. Neuropharmacol.* 7, 65–74. doi: 10.2174/157015909787602823

Valim, F. H., Dal Grande, F., Otte, J., Singh, G., Merges, D., Schmitt, I., et al. (2022). Identification and expression of functionally conserved circadian clock genes in lichen-forming fungi. *Res. Square* [Preprint]. doi: 10.21203/rs.3.rs-1499077/v1

Wang, Y., Lv, D., Liu, W., Li, S., Chen, J., Shen, Y., et al. (2018). Disruption of the circadian clock alters antioxidative defense via the SIRT1-BMAL1 pathway in 6-OHDA-induced models of Parkinson's disease. *Oxidative Med. Cell. Longev.* 2018:4854732. doi: 10.1155/2018/4854732

Wible, R. S., Ramanathan, C., Sutter, C. H., Olesen, K. M., Kensler, T. W., Liu, A. C., et al. (2018). NRF2 regulates core and stabilizing circadian clock loops, coupling redox and timekeeping in *Mus musculus*. *eLife* 7:e31656. doi: 10.7554/eLife.31656

Yamamoto, Y., Hara, K., Kawakami, H., and Komine, M. (2015). "Lichen substances and their biological activities," in *Recent Advances in Lichenology*, eds D. Upreti, P. Divakar, V. Shukla, and R. Bajpai (New Delhi: Springer), 181–199. doi: 10.1007/978-81-322-2235-4_10

Yamanaka, K., Chun, S. J., Boillee, S., Fujimori-Tonou, N., Yamashita, H., Gutmann, D. H., et al. (2008). Astrocytes as determinants of disease progression in inherited amyotrophic lateral sclerosis. *Nat. Neurosci.* 11, 251–253. doi: 10.1038/nn2047

Yamazaki, S., Numano, R., Abe, M., Hida, A., Takahashi, R. I., Ueda, M., et al. (2000). Resetting central and peripheral circadian oscillators in transgenic rats. *Science* 288, 682–685. doi: 10.1126/science.288.5466.682

Yoo, S. H., Ko, C. H., Lowrey, P. L., Buhr, E. D., Song, E. J., Chang, S., et al. (2005). A noncanonical E-box enhancer drives mouse Period2 circadian oscillations *in vivo*. *Proc. Natl. Acad. Sci. U S A* 102, 2608–2613. doi: 10.1073/pnas.0409763102

Yuan, G., Hua, B., Cai, T., Xu, L., Li, E., Huang, Y., et al. (2017). Clock mediates liver senescence by controlling ER stress. *Aging (Albany NY)* 9:2647. doi: 10.18632/aging.101353

Conflict of Interest: The authors declare that the research was conducted in the absence of any commercial or financial relationships that could be construed as a potential conflict of interest.

Publisher's Note: All claims expressed in this article are solely those of the authors and do not necessarily represent those of their affiliated organizations, or those of the publisher, the editors and the reviewers. Any product that may be evaluated in this article, or claim that may be made by its manufacturer, is not guaranteed or endorsed by the publisher.

frontiers | Frontiers in Cellular Neuroscience

ORIGINAL RESEARCH
published: 07 July 2022
doi: 10.3389/fncel.2022.936939

Fatty Acid-Binding Protein 5 Modulates Brain Endocannabinoid Tone and Retrograde Signaling in the Striatum

Mohammad Fauzan[1,2†], *Saida Oubraim*[3†], *Mei Yu*[1], *Sherrye T. Glaser*[1,4], *Martin Kaczocha*[1,2*] *and Samir Haj-Dahmane*[3,5*]

[1] Department of Anesthesiology, Renaissance School of Medicine, Stony Brook University, Stony Brook, NY, United States, [2] Department of Biochemistry and Cell Biology, Stony Brook University, Stony Brook, NY, United States, [3] Department of Pharmacology and Toxicology, Jacobs School of Medicine and Biomedical Sciences, University at Buffalo, State University of New York, Buffalo, NY, United States, [4] Department of Biological Sciences, Kingsborough Community College, Brooklyn, NY, United States, [5] University at Buffalo Neuroscience Program, Jacobs School of Medicine and Biomedical Sciences, University at Buffalo, State University of New York, Buffalo, NY, United States

OPEN ACCESS

Edited by:
Karima Chergui,
Karolinska Institutet (KI), Sweden

Reviewed by:
A. J. Baucum,
Indiana University, United States
Brian Burrell,
University of South Dakota,
United States

***Correspondence:**
Samir Haj-Dahmane
sh38@buffalo.edu
Martin Kaczocha
martin.kaczocha@stonybrook.edu

[†]These authors have contributed equally to this work

Specialty section:
This article was submitted to Cellular Neurophysiology, a section of the journal Frontiers in Cellular Neuroscience

Received: 06 May 2022
Accepted: 15 June 2022
Published: 07 July 2022

Citation:
Fauzan M, Oubraim S, Yu M, Glaser ST, Kaczocha M and Haj-Dahmane S (2022) Fatty Acid-Binding Protein 5 Modulates Brain Endocannabinoid Tone and Retrograde Signaling in the Striatum. Front. Cell. Neurosci. 16:936939. doi: 10.3389/fncel.2022.936939

The endocannabinoid (eCB) anandamide (AEA) and 2-arachidonoylglycerol (2-AG) are endogenous lipid neurotransmitters that regulate an array of physiological functions, including pain, stress homeostasis, and reward. Fatty acid-binding protein 5 (FABP5) is a key modulator of intracellular eCB transport and inactivation. Recent evidence suggests that FABP5 controls synaptic 2-AG signaling at excitatory synapses in the dorsal raphe nucleus. However, it is currently not known whether this function extends to other brain areas. To address this, we first profiled eCB levels across several brain areas in FABP5 knockout mice and wild-type controls and report that FABP5 deletion elevates AEA levels in the striatum, prefrontal cortex, midbrain, and thalamus, as well as midbrain 2-AG levels. The expression of eCB biosynthetic and catabolic enzymes was largely unaltered in these regions, although minor sex and region-specific changes in the expression of 2-AG catabolic enzymes were observed in female FABP5 KO mice. Robust FABP5 expression was observed in the striatum, a region where both AEA and 2-AG control synaptic transmission. Deletion of FABP5 impaired tonic 2-AG and AEA signaling at striatal GABA synapses of medium spiny neurons, and blunted phasic 2-AG mediated short-term synaptic plasticity without altering CB1R expression or function. Collectively, these results support the role of FABP5 as a key regulator of eCB signaling at excitatory and inhibitory synapses in the brain.

Keywords: endocannabinoid, FABP, fatty acid-binding protein, striatum, medium spiny neurons, anandamide, 2-arachidonoylglycerol, GABA synapses

INTRODUCTION

The endocannabinoids (eCBs) anandamide (AEA) and 2-arachidonoylglycerol (2-AG) are signaling lipids that activate cannabinoid type-1 (CB1R) and type-2 (CB2R) receptors in the central nervous system and peripheral tissues (Zou and Kumar, 2018). CB1R is widely expressed in the brain and regulates numerous physiological processes, including pain, neuroprotection,

cognitive functions, motor activity, and feeding behavior (Howlett et al., 2002; Kano et al., 2009; Di Marzo et al., 2015). In contrast, CB2R is primarily expressed in immune cells where it mediates the anti-inflammatory and immunosuppressive effects of eCBs (Ashton and Glass, 2007). In the central nervous system (CNS), the behavioral and physiological effects of eCBs and exogenous cannabinoids can be largely ascribed to CB1R activation, although a contribution of CB2R has been suggested (Van Sickle et al., 2005; Sadanandan et al., 2020).

In the CNS, 2-AG and AEA act as retrograde messengers and activate presynaptic CB1Rs to decrease neurotransmitter release, thereby inducing short- and long-term eCB-dependent synaptic plasticity (Wilson and Nicoll, 2002). In addition to "on demand" (phasic) signaling, eCBs are also synthesized and constitutively released to mediate tonic control of synaptic transmission (Alger, 2014; Oubraim et al., 2021). Retrograde eCB signaling is tightly regulated by the enzymes that mediate their biosynthesis and inactivation. Postsynaptic 2-AG biosynthesis is catalyzed by diacylglycerol lipase alpha (DAGLα) whereas its degradation in presynaptic neurons and surrounding astrocytes is mediated by monoacylglycerol lipase (MAGL) (Murataeva et al., 2014). N-acyl phosphatidylethanolamine-specific phospholipase D (NAPE-PLD) and fatty acid amide hydrolase (FAAH) are the main biosynthetic and catabolic enzymes for AEA, respectively (Maccarrone, 2017).

The inherent lipophilicity of eCBs limits their transport across aqueous compartments, including the cytosol and synaptic cleft. We previously identified fatty acid-binding proteins (FABPs) as chaperones that facilitate the intracellular trafficking of eCBs to their respective catabolic enzymes and nuclear receptors (Kaczocha et al., 2009, 2012). Among the FABPs expressed in the brain (FABP3, FABP5, and FABP7) (Furuhashi and Hotamisligil, 2008), FABP5 has been shown to play a key role in gating eCB signaling and metabolism (Kaczocha et al., 2009; Haj-Dahmane et al., 2018). Indeed, we have shown that FABP5 is indispensable for retrograde 2-AG signaling at glutamatergic synapses in the dorsal raphe nucleus (DRn) (Haj-Dahmane et al., 2018). Although these recent findings point to a potential role of FABP5 as a facilitator of retrograde 2-AG signaling, it remains to be determined whether this function extends to AEA and 2-AG transport at synapses in other brain areas. Here, we profiled regional eCB levels and the expression of their metabolizing enzymes in WT and FABP5 KO mice and demonstrate a critical role for FABP5 in controlling retrograde AEA and 2-AG signaling at striatal GABA synapses.

MATERIALS AND METHODS

Animals

All the procedures used in this study were approved by Stony Brook University (#1486041) and University at Buffalo (#RIA01023N) Animal Care and Use Committee in accordance with the National Institutes of Health Guide for the Care and Use of Laboratory Animals. Male and female wild-type (WT) C57BL/6 mice, as well as FABP5 KO mice on a C57BL/6 background (8–12 weeks), were group housed (3–4 per cage) with *ad libitum* access to food and water in temperature-controlled environment and 12-h light/dark cycle.

Real-Time PCR

Ribonucleic acid (RNA) was extracted using the RNeasy Mini Kit (Qiagen) followed by complementary DNA (cDNA) synthesis using the SuperScript III First-Strand Synthesis System (Thermo Fisher). Real-time polymerase chain reaction (qPCR) was performed with PowerUp SYBR green (Thermo Fisher) on a StepOnePlus instrument (Applied Biosystems). Quantification was performed using the $2^{-\Delta\Delta Ct}$ method with actin serving as the housekeeping gene. The following forward (F) and reverse (R) primers were used: FABP3: (F)CATCGAGAAGAACGGGGATA and (R)TCATCTGCTGTCACCTCGTC; FABP5: (F)TGGT CCAGCACCAGCAATG and (R)GACACACTCCACGAT CATCTTC; FABP7: (F)CCAGCTGGGAGAAGAGTTTG and (R)TTTCTTTGCCATCCCACTTC; CB1R: (F)AAG TCGATCTTAGACGGCCTT and (R)TCCTAATTTGGA TGCCATGTCTC; FAAH: (F)CCCTGCTCCAACTGGTACAG and (R)TCACAGTCAGTCAGATAGGAGG; MAGL: (F)CG GACTTCCAAGTTTTTGTCAGA and (R)GCAGCCACTAG GATGGAGATG; NAPE-PLD: (F)CTCCTGGACGAC AACAAGGTTC and (R)GCAAGGTCAAAAGGACCAAAC; ABHD4: (F)TTCCCCTACGACCAACTGAC and (R)CGAA GAACAGCCAGTGGATT; ABHD6: (F)ACACAAGGA CATGTGGCTCA and (R)ACTTGCCCCACTATGGACAG; DAGLα: (F)GTCCTGCCAGCTATCTTCCTC and (R)CGT GTGGGTTATAGACCAAGC; DAGLβ: (F)AGCGACGA CTTGGTGTTCC and (R)GCTGAGCAAGACTCCACCG; and actin: (F)GACGGCCAGGTCATCACTAT and (R)CGGATGTCAACGTCACACTT.

Lipid Quantification

Tissue eCB levels were quantified using mass spectrophotometry as previously described (Kaczocha et al., 2014). Brains were flash-frozen in liquid nitrogen followed by regional dissections on an ice block. The tissues were homogenized in 8 ml of 2:1:1 chloroform/ methanol/tris (50 mM, pH 8) containing deuterated standards, the phases were separated by centrifugation, and the chloroform phase was isolated and dried down under gentle argon stream. The samples were subsequently resuspended in 2:1 chloroform/methanol and injected into a Thermo TSQ Quantum Access Triple Quadrupole Mass Spectrometer (Thermo Fisher) and processed exactly as described previously (Kaczocha et al., 2014).

Immunohistochemistry

Immunofluorescence was performed as described previously (Peng et al., 2017). Briefly, striatal sections (30 μm) were incubated with the following primary antisera: goat anti-FABP5 (R&D Systems Inc, #AF1476), mouse anti-NeuN (Millipore, MAB377), and mouse anti-s100β (Sigma, #S2532). Secondary antibodies used were Alexa Fluor 594 donkey anti-goat (Jackson ImmunoResearch Labs, #711-585-152) and Alexa Fluor 488 donkey anti-mouse IgG (H+L) antibody (Jackson ImmunoResearch Labs). Fluorescent images were acquired on a Zeiss Axioplan 2 epifluorescent microscope. Images were

obtained using Zeiss AxioCam HRm monochrome digital camera and AxioVision Rel. 4.6 microscope software. Images were only adjusted for brightness and contrast.

Brain Slice Preparation

Mice were deeply anesthetized with isoflurane and decapitated. Using a vibratome (Lancer series 1,000; Ted Pella, Reading, CA), coronal brain slices of 350 μm containing striatum were cut in ice-cold chlorine-based ACSF (110 mM choline-Cl, 2.5 mM KCl, 0.5 mM $CaCl_2$, 7 mM $MgSO_4$, 1.25 mM NaH_2PO_4, 26.2 mM $NaHCO_3$, 11.6 mM sodium L-ascorbate, 3.1 mM sodium pyruvate, and 25 mM glucose, and equilibrated with 95% O_2 and 5% CO_2). Slices were first transferred to a chamber with the same cutting solution at 35°C for 15 min and then to a regular ACSF (119 mM NaCl, 2.5 mM $CaCl_2$, 1.3 mM $MgSO_4$, 1 mM NaH_2PO_4, 26.2 mM $NaHCO_3$, and 11 mM glucose continuously bubbled with a mixture of 95% O_2 and 5% CO_2) for additional 45 min at 35°C. Slices were allowed to recover at room temperature (≥ 1 h), before being transferred to a recording chamber, continuously perfused with standard ACSF saturated with 95% O_2 and 5% CO_2, and warmed at 30°C.

Whole-Cell Recordings

Whole-cell recordings were obtained from striatal medium spiny neurons (MSNs) and were visualized using an upright microscope (BX 51 WI; Olympus, Tokyo, Japan). Glass pipette electrodes with 3–5 MΩ resistance filled with an internal solution with the following composition: 110 mM cesium gluconate, 10 mM CsCl, 10 mM Na_2-phosphocreatine, 10 mM HEPES, 1 mM $MgCl_2$, 1 mM EGTA, 2 mM Na_2-ATP, 0.25 mM Na-GTP, and 5 mM QX-314 chloride, pH 7.3 (adjusted with CsOH; osmolarity, 280–290 mOsmol/l), were used. All recordings were performed in the presence of NMDA and AMPA receptors antagonist D-AP5 (50 μM) and DNQX (10 μM).

Inhibitory postsynaptic currents (IPSCs) were evoked with a single square-pulse with a stimulation intensity of 5–20 V and duration of 100–200 μs, delivered at 0.1 Hz, and voltage-clamped at −80 mV. To induce depolarization-induced suppression of inhibition (DSI), IPSCs at 3-s intervals were evoked before (4 IPSCs) and after (20 IPSCs) 5-s depolarization from −80 to 0 mV. All recorded currents were amplified with an Axoclamp 2B amplifier (Molecular Devices, Sunnyvale, CA), filtered at 3 kHz, digitized at 20 kHz with Digidata 1200 (Molecular Devices), and acquired using the pClamp 9 software (Molecular Devices).

Electrophysiology Data Analysis

The amplitude of evoked IPSCs (eIPSC) was determined by measuring the average current during a 2-ms period at the peak of each eIPSC and subtracted from the average baseline current determined during a 5-ms window taken before the stimulus artifact. All eIPSC amplitudes were normalized to the mean baseline amplitude recorded for at least 10 min before drug application. The magnitude of DSI was measured using the mean amplitude of three eIPSCs immediately after membrane depolarization, relative to the mean of four before depolarization.

Statistical Analysis

Real-time PCR and lipidomic results were analyzed using unpaired *t*-tests. Electrophysiology data were analyzed using paired *t*-tests within group comparisons and unpaired *t*-tests

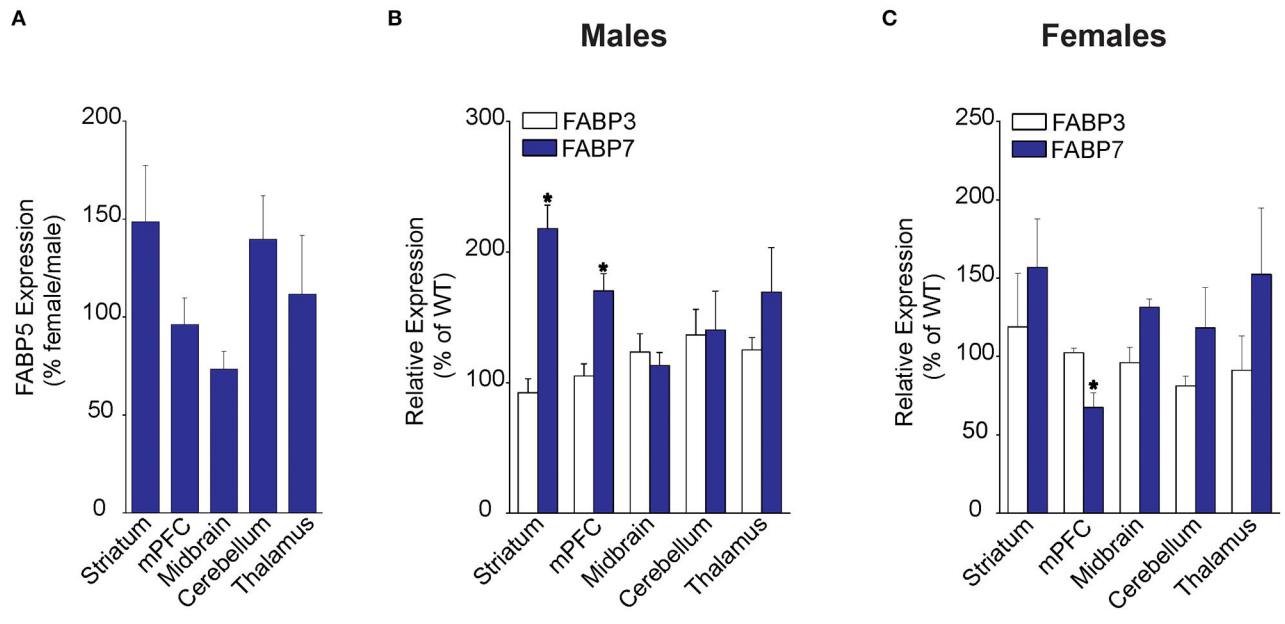

FIGURE 1 | Regional FABP expression in male and female WT and FABP5 KO mouse brains. **(A)** Comparative FABP5 expression in WT male and female mice in various brain areas was assessed by qPCR ($n = 5$). Data are presented as percent expression in female/male mice. **(B,C)** Relative expression of FABP3 and FABP7 in male and female FABP5 KO mice compared to WT controls ($n = 5$). *, $p < 0.05$; KO vs. WT.

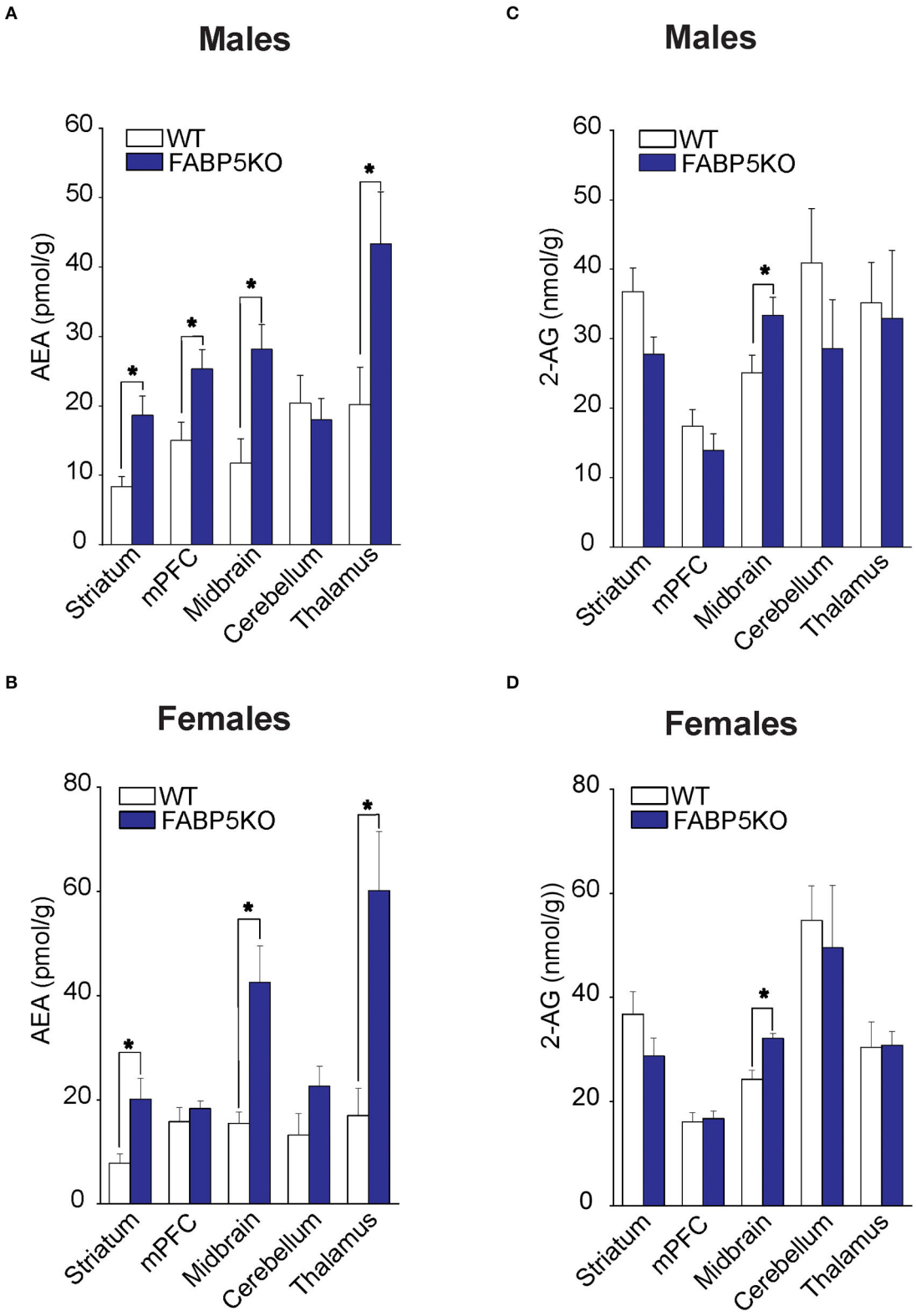

FIGURE 2 | 2-AG and AEA levels in brain regions of WT vs. FABP5 KO mice. Levels of AEA **(A,B)** and 2-AG **(C,D)** in the striatum, mPFC, midbrain, cerebellum, and thalamus of male and female WT and FABP5 KO mice ($n = 5$). *, $p < 0.05$; KO vs. WT.

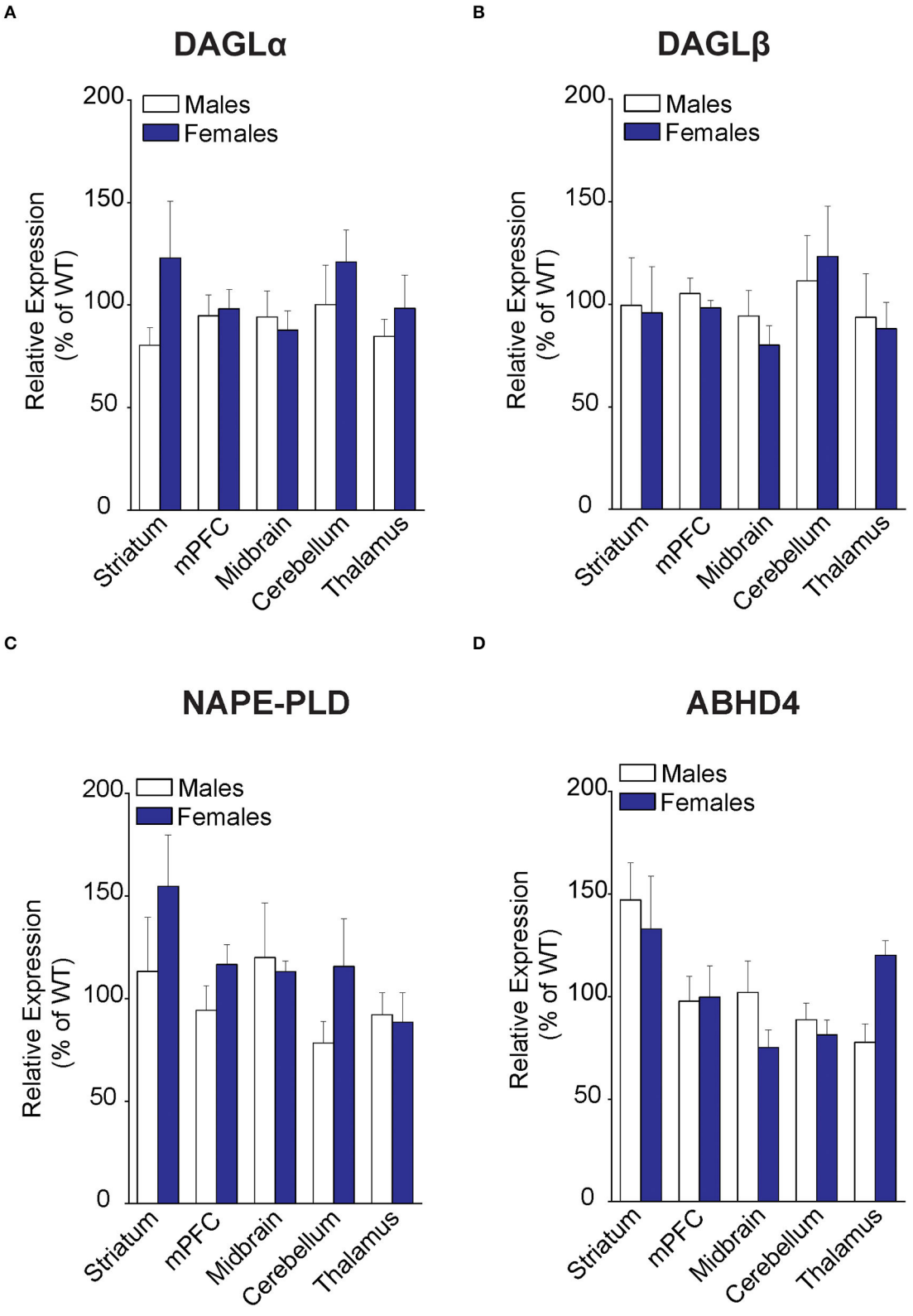

FIGURE 3 | Expression of 2-AG and AEA biosynthetic enzymes in brain regions of WT and FABP5 KO mice. **(A–D)** Relative expression of DAGLα, DAGLβ, NAPE-PLD, and ABHD4 in male and female FABP5 KO mice compared to WT controls ($n = 5$). Note that FABP5 deletion did not significantly alter the expression of these biosynthetic enzymes.

between groups with a significance threshold set at $p < 0.05$. Statistical analyses were performed using GraphPad Prism (version 9.3.1) and Origin software (version 9.0).

RESULTS

Comparative FABP5 Expression Across Brain Regions in Male and Female Mice

We first examined FABP5 expression in WT male and female mice across several brain regions, including striatum, medial prefrontal cortex (mPFC), midbrain, cerebellum, and the thalamus. Our results did not reveal the sex differences in relative FABP5 expression in the regions examined (**Figure 1A**). Next, we examined whether FABP5 deletion alters the expression of FABP3 and FABP7 and found comparable expression of FABP3 in male and female WT and FABP5 KO mice (**Figures 1B,C**). In contrast, an upregulation of FABP7 was observed in the striatum and mPFC of male FABP5 KO mice and downregulation in the mPFC of female FABP5 KO mice (**Figures 1B,C**). Collectively, our findings indicate comparable FABP5 expression between the sexes and reveal region-specific, as well as sexually dimorphic, compensatory changes in FABP7 levels.

FABP5 Deletion Elevates AEA and 2-AG Levels in Distinct Brain Regions

Fatty acid-binding protein 5 inhibition globally increases AEA levels in the mouse brain (Kaczocha et al., 2014). To explore whether elevations in AEA exhibit regional heterogeneity, we quantified AEA levels in the same brain areas as mentioned above. Compared to WT mice, elevated AEA levels were observed in the striatum, midbrain, and thalamus of male and female FABP5 KO mice (**Figures 2A,B**). Interestingly, AEA levels were elevated in the mPFC of male mice, but not in female FABP5 KO mice (**Figures 2A,B**). Previous work revealed increased 2-AG levels in the DRn of FABP5 KO mice (Haj-Dahmane et al., 2018). Similarly, we found that 2-AG levels were elevated in the midbrain of male and female FABP5 KO mice whereas no differences were observed in the other regions profiled (**Figures 2C,D**).

FABP5 Deletion Does Not Alter the Expression of Biosynthetic Enzymes for 2-AG and AEA

To determine whether the changes in eCB levels in FABP5 KO mice can be attributed to differential expression of their metabolizing enzymes, we first profiled eCB biosynthetic enzymes in the same regions as above. Comparable expression of DAGLα and DAGLβ was observed in the striatum, mPFC, midbrain, cerebellum, and thalamus of WT and FABP5 KO mice of both sexes (**Figures 3A,B**). Similarly, there was no change in the expression of NAPE-PLD and alpha-beta hydrolase domain containing 4 (ABHD4), which mediate the canonical and alternative AEA biosynthetic pathways, respectively (**Figures 3C,D**).

FABP5 Deletion Results in Sex- and Region-Specific Alterations in the Expression of CB1R and 2-AG Catabolic Enzymes

Examination of CB1R expression revealed comparable levels across the brain regions, with the sole exception of CB1R upregulation in the cerebellum of male FABP5 KO mice (**Figure 4A**). Next, an analysis of 2-AG catabolic enzymes demonstrated MAGL upregulation in the midbrain and downregulation of both MAGL and ABHD6, a minor brain 2-AG hydrolase, in the cerebellum of female FABP5 KO mice (**Figures 4B,C**). In contrast, the expression of the AEA catabolic enzyme FAAH was not altered in any of the regions examined (**Figure 4D**).

Effect of FABP5 Deletion on Tonic and Phasic eCB Signaling

We previously demonstrated that FABP5 controls retrograde 2-AG signaling at glutamate synapses in the DRn (Haj-Dahmane et al., 2018). However, it is currently not known whether FABP5 regulates retrograde eCB signaling in other brain areas, and notably at inhibitory synapses. The finding that FABP5 deletion elevated striatal AEA levels coupled with previous reports demonstrating retrograde AEA, as well as 2-AG signaling in this region (Adermark and Lovinger, 2007; Hashimotodani et al., 2007, 2008, 2013; Adermark et al., 2009), prompted us to examine FABP5 distribution and its influence upon eCB signaling within this area. Robust FABP5 expression was observed in this region and was largely restricted to astrocytes as indicated by colocalization with the astrocyte marker s100β (**Figure 5**). In contrast, FABP5 rarely colocalized with the neuronal marker NeuN (**Figure 5**).

Next, we examined tonic retrograde eCB signaling by assessing the depression of GABA synapses induced by MAGL or FAAH inhibition in WT and FABP5 KO mice. Pharmacological inhibition of MAGL using MJN110 (**Figures 6A,B**) or FAAH using PF3845 (**Figures 6C,D**) induced significant depression of evoked inhibitory postsynaptic currents (eIPSCs) in WT mice, indicating that both 2-AG and AEA mediate tonic control of striatal GABA synapses. Remarkably, FABP5 deletion blunted MJN110-induced depression of eIPSCs (**Figures 6A,B**) and markedly reduced the effect of PF3845 on eIPSCs amplitude (**Figures 6C,D**). These results indicate that FABP5 deletion impairs tonic AEA and 2-AG signaling at striatal GABA synapses.

We also examined the impact of FABP5 deletion on phasic eCB signaling as measured by depolarization-induced suppression of inhibition (DSI) (Narushima et al., 2006, 2007; Uchigashima et al., 2007). As expected, we observed DSI in GABA striatal MSNs (**Figures 7A,B**). Examination of which eCB mediates DSI revealed that inhibition of DAGLα with DO34 (1 μM) significantly reduced the magnitude of DSI (**Figure 7**). Furthermore, inhibition of MAGL with MJN110, which reduced the baseline amplitude of GABA eIPSCs (**Figure 6**), largely occluded DSI (**Figures 7A,B**), confirming that it is mediated by 2-AG. In contrast, inhibition of FAAH using PF3845 did not alter the magnitude of the DSI (**Figures 7A,B**). Importantly, genetic

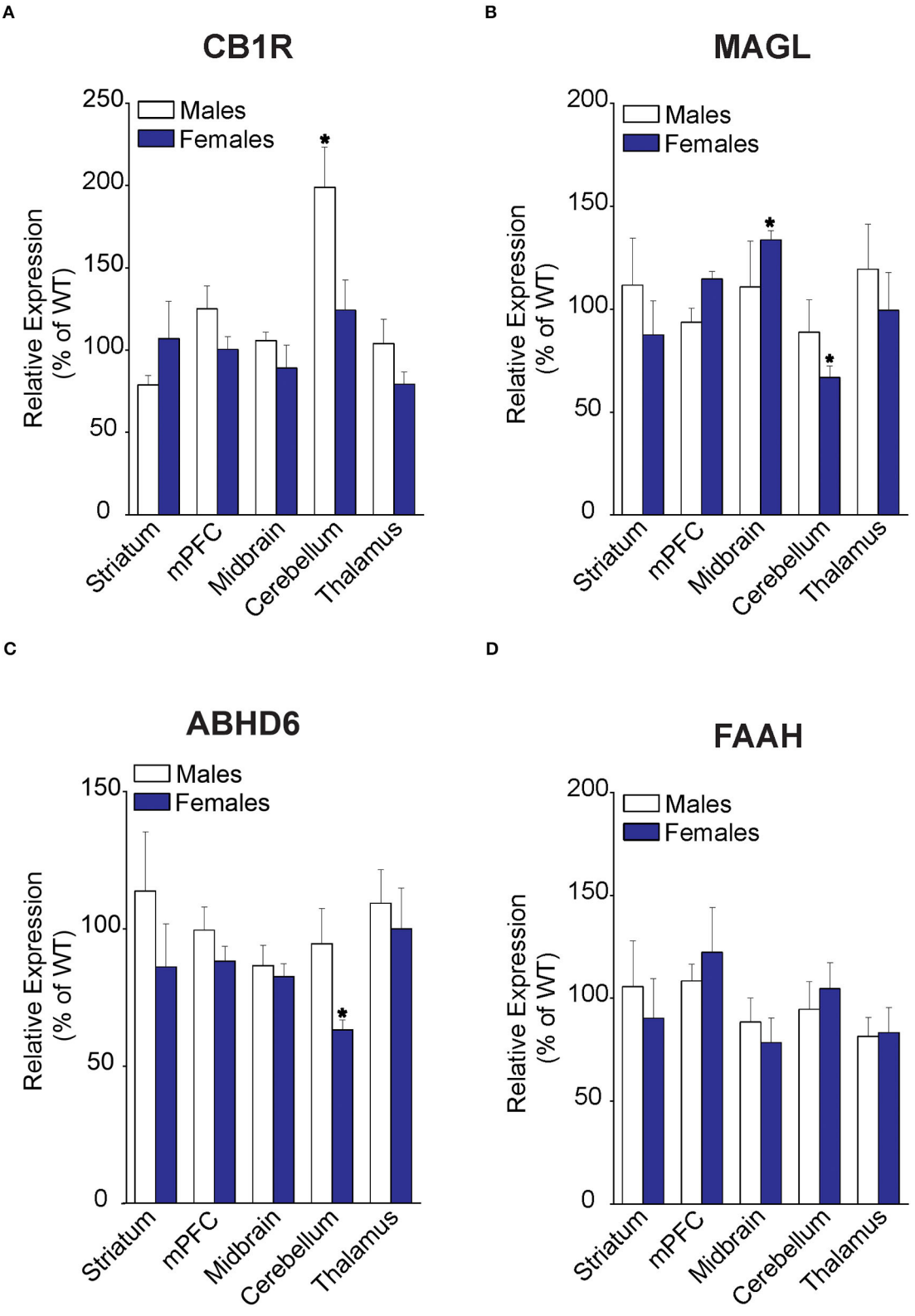

FIGURE 4 | Relative expression of 2-AG and AEA catabolic enzymes in brain regions of WT and FABP5 KO mice. **(A–D)** Relative expression of CB1R, MAGL, ABHD6, and FAAH in male and female FABP5 KO mice compared to WT controls ($n = 5$). *, $p < 0.05$; KO vs. WT.

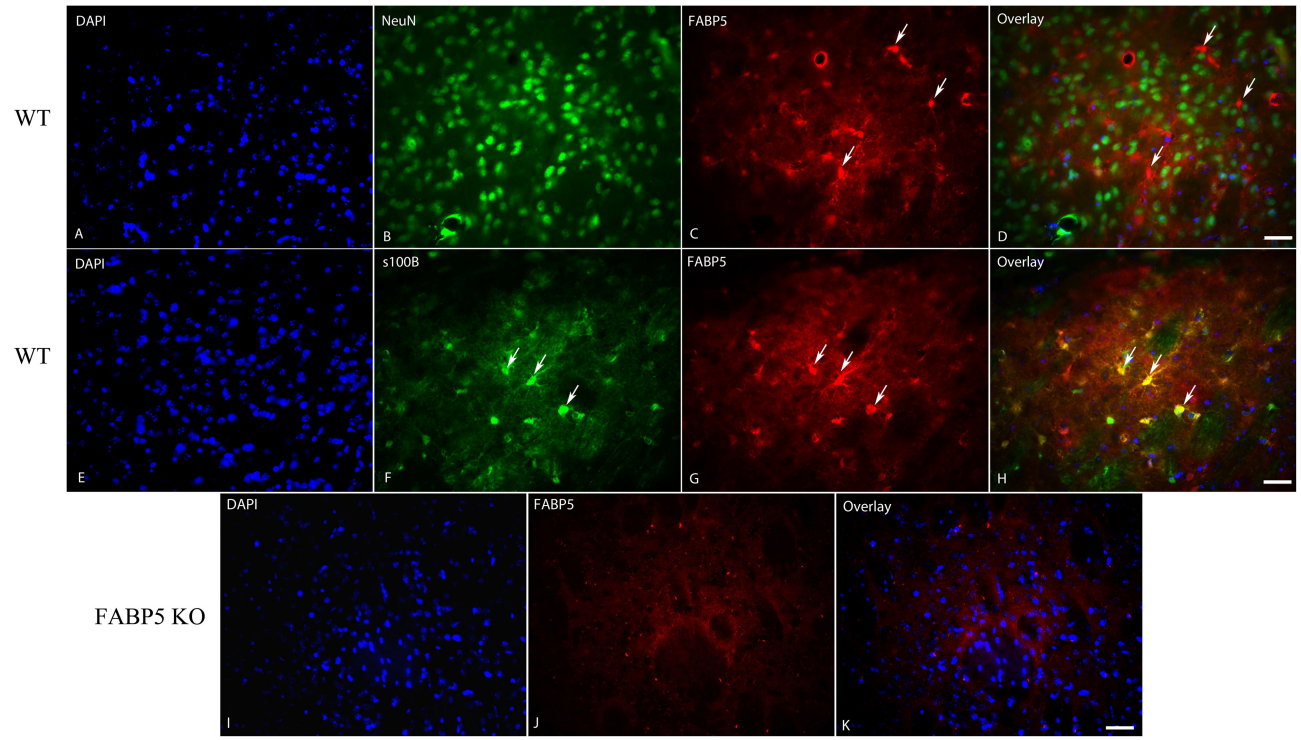

FIGURE 5 | Cellular distribution of FABP5 in the dorsal striatum. Immunolocalization of FABP5 in the striatum of WT mice. Staining for DAPI **(A)**, the neuronal marker NeuN **(B)**, FABP5 **(C)**, and overlay **(D)**. Note the minimal colocalization of FABP5 in NeuN labeled neurons (arrows). Staining for DAPI **(E)**, the astrocyte marker S100β **(F)**, FABP5 **(G)**, and overlay **(H)**. Note that there is robust colocalization between FABP5 and S100β (arrows), indicating that FABP5 is expressed in astrocytes. Immunostaining was conducted on striatal sections from three WT mice and representative images are shown. **(I–K)** The lack of FABP5 immunoreactivity in the striatum of FABP5 KO mice. Scale bar = 20 μm.

deletion of FABP5 abolished DSI in MSNs (**Figures 7A,B**), which was not further altered by MJN110 or PF3845. Collectively, these results reveal that FABP5 is essential for both tonic and phasic eCB signaling in the striatum.

To test whether the blockade of tonic and phasic eCB signaling observed in FABP5 KO mice can be attributed to altered CB1R function, we measured the inhibition of GABA eIPSCs induced by the exogenous CB1R agonist WIN55,212-2 (10 μM) in WT and FABP5 KO mice. The magnitude of CB1R-induced inhibition of eIPSCs was comparable in WT and FABP5 KO mice, thereby indicating no change in CB1R function between the genotypes (**Figures 7C,D**). Similarly, inhibition of DAGLα with DO34 did not affect the function of CB1R (**Figures 7C,D**). Taken together, these results indicate that the blockade of retrograde eCB signaling in FABP5 KO mice cannot be attributed to impaired CB1R function, but rather to impaired eCB trafficking.

DISCUSSION

The eCBs are essential messengers that fine-tune synaptic transmission and plasticity in the CNS. The lipophilic nature of eCBs necessitates a mechanism(s) that enables their translocation across the synaptic cleft from their site of synthesis to CB1Rs. Several mechanisms have been proposed to account for synaptic eCB transport, including FABP5 and extracellular vesicles (Kaczocha and Haj-Dahmane, 2021). We have previously shown that FABP5 is necessary for retrograde 2-AG signaling at glutamate synapses of DRn neurons (Haj-Dahmane et al., 2018). Here, we extend these findings and show that FABP5 is also indispensable for tonic and phasic 2-AG signaling at striatal GABA synapses, and for the first time reveal that FABP5 governs tonic AEA signaling.

Fatty acid-binding protein 5 has an established role in mediating intracellular AEA transport, thereby gating its subsequent metabolism by FAAH (Kaczocha et al., 2009). Accordingly, FABP5 inhibition elevates AEA levels in the whole brain (Kaczocha et al., 2014; Yu et al., 2014). Consistent with this function, our results revealed that AEA levels were elevated in the midbrain, striatum, and thalamus of both male and female KOs. Interestingly, AEA levels were increased in the mPFC of male mice, but not in female FABP5 KO mice. Since FAAH, NAPE-PLD, and ABHD4 expression is comparable between the sexes and genotypes, these sex-specific differences in AEA levels are unlikely to arise from altered expression of its biosynthetic or catabolic enzymes. We also observed that deletion of FABP5 resulted in a compensatory increase in FABP7 expression within the mPFC of male mice and a corresponding decrease in female FABP5 KO mice, suggesting compensatory adaptations in response to the loss of FABP5. Moreover, although upregulation

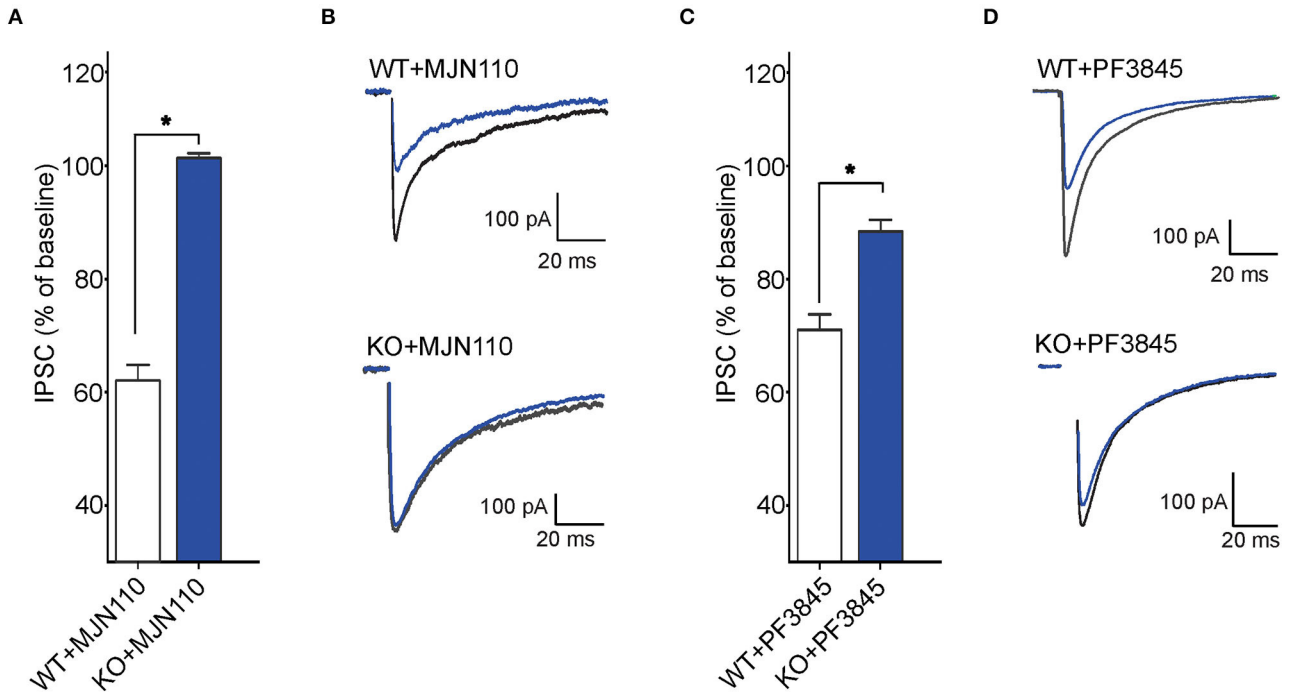

FIGURE 6 | FABP5 deletion impairs tonic 2-AG and AEA signaling at striatal GABA synapses. **(A)** The average depression of eIPSC induced by the MAGL inhibitor MJN110 (10 μM) in WT and FABP5 KO mice. Average reduction in the amplitude of eIPSCs to baseline, in WT (WT+MJN110: 62.01 ± 1.10%, $n = 5$ cells from 5 mice, t4 = 17.83, $p < 0.05$, vs. baseline) and FABP5 KO (KO+MJN110: 101.36 ± 0.32 %, $n = 5$ cells from 5 mice, t4 = −0.52, $p > 0.05$, vs. baseline) slices during bath application of MAGL inhibitor. **(B)** Sample eIPSC traces taken before and during MJN110 application in WT (top) and FABP5 KO mice (bottom). Note that FABP5 deletion prevents the depression of eIPSCs induced by MJN110. **(C)** Average reduction of eIPSC induced by the FAAH inhibitor PF3845 (3 μM) in WT (WT+PF3845: 71.14 ± 1.16%, n = 5 cells from five mice, t4 = 18.49, $p < 0.05$ vs. baseline) and FABP5 KO (KO+PF3845: 88.52 ± 0.74 %, n = 5 cells from 5 mice, t4 = 5.10, $p <$ 0.05, vs. baseline) slices. **(D)** Representative eIPSC traces before and during PF3845 application in WT and FABP5 KO mice. *, $p < 0.05$.

of FABP7 was observed in the striatum of male FABP5 KO mice, we observed no differences in 2-AG levels between male and female FABP5 KO mice, arguing against a role for this protein in 2-AG metabolism. However, we cannot rule out the possibility that the observed changes in mRNA expression may not translate to altered protein levels. One interesting finding of our study is that cerebellar AEA levels were unaltered in FABP5 KO mice of both sexes, consistent with a previous study reporting low levels of FABP5 expression in this region (Owada et al., 1996).

The results from previous studies indicate that retrograde AEA and 2-AG gate synaptic transmission in the striatum (Adermark and Lovinger, 2007; Hashimotodani et al., 2007, 2008, 2013; Adermark et al., 2009). As expected, we found that striatal GABA synapses are tonically modulated by AEA and 2-AG in WT mice as revealed by FAAH and MAGL inhibitor-induced depression of eIPSC amplitude. Genetic deletion of FABP5, which elevated striatal AEA levels, profoundly reduced AEA-mediated tonic signaling. This finding may reflect impaired intracellular AEA trafficking to FAAH for inactivation and synaptic transport to CB1R. In addition, whereas FABP5 deletion did not alter striatal 2-AG levels, it completely blocked tonic 2-AG mediated control of GABA synapses. This indicates that synaptic changes in 2-AG transport and signaling following FABP5 deletion may not be consistently reflected when quantifying bulk tissue 2-AG levels.

Employing selective DAGL, MAGL, and FAAH inhibitors, we further showed that striatal DSI is mainly attributable to retrograde 2-AG signaling. Genetic deletion of FABP5 blocked 2-AG-mediated DSI, an effect that was not a consequence of a reduction in 2-AG levels, altered expression of its biosynthetic or catabolic enzymes, or downregulation of CB1R. These findings are consistent with our previous results showing that pharmacological and genetic FABP5 inhibition abolishes 2-AG mediated tonic and phasic signaling at glutamate synapses in the DRn (Haj-Dahmane et al., 2018). Taken together, these studies establish FABP5 as a key regulator of synaptic eCB trafficking at both excitatory and inhibitory synapses in multiple brain areas.

Finally, we observed that FABP5 is mainly expressed in striatal astrocytes, which is distinct from other brain areas where neuronal FABP5 expression was reported (Owada et al., 1996; Haj-Dahmane et al., 2018). However, it is possible that FABP5 is expressed in presynaptic terminals, and additional high-resolution imaging studies will be required to test this possibility. Importantly, we previously demonstrated that primary astrocytes in culture secrete FABP5 whereas neurons do not (Haj-Dahmane et al., 2018), raising the intriguing possibility that FABP5 released from astrocytes may mediate synaptic AEA and 2-AG signaling in the striatum. Future studies addressing the contributions of astrocytic and neuronal FABP5 in controlling retrograde eCB signaling are required to test this notion.

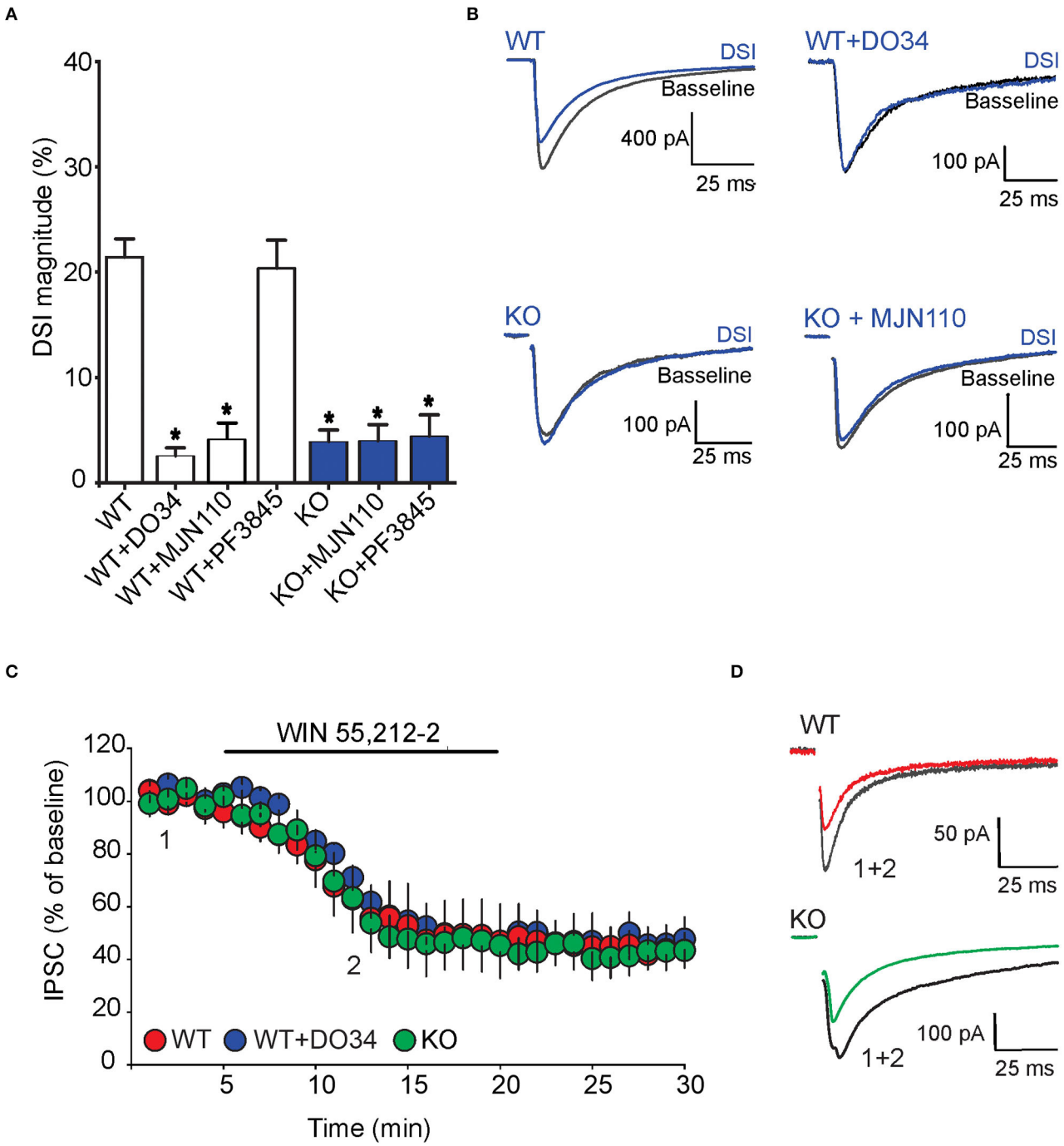

FIGURE 7 | FABP5 deletion blunts 2-AG mediated DSI without altering CB1R function in striatal MSNs. **(A)** DSI magnitude obtained in striatal slices from WT (white bars) and FABP5 KO mice (blue bars), incubated with vehicle (WT: 21.43 ± 1.70%, $n = 12$ cells from 10 mice; KO: 3.90 ± 1.08%, $n = 12$ cells from 10 mice), DO34 (1 μM) (WT + DO34: 2.53 ± 0.75%, $n = 8$ cells from 6 mice, $p < 0.05$ vs. WT), MJN110 (10 μm) (WT+MJN110: 4.14 ± 1.45%, $n = 7$ cells from 6 mice, $p < 0.05$ vs. WT), or PF3845 (3 μM) (WT+PF3845: 20.35 ± 2.66%, $n = 7$ cells from 6 mice, $p > 0.05$ vs. WT, $^*p < 0.05$ vs WT). **(B)** Sample eIPSC traces before and during DSI in WT, WT + D034, FABP5 KO, FABP5 KO + MJN110. **(C)** The depression of eIPSCs induced by the CB1R agonist WIN55,212-2 (10 μM) in striatal slices from WT (red) (WT: 47.81 ± 11.80% of baseline, $n = 9$ cells from 5 mice, $t_8 = 4.28$, $p < 0.01$, vs. baseline), WT + DO34 (blue) (WT+DO34: 49.75 ± 6.06% baseline, $n = 8$ cells from 5 mice, $t_7 = 9.84$, $p < 0.001$, vs. baseline), or FABP5 KO mice (green) (FABP5 KO: 45.18 ± 10.61% baseline, $n = 8$ cells from 5 mice, $t_7 = 5.11$, $p < 0.01$, vs. baseline). Note that FABP5 deletion or inhibition of DAGL did not alter CB1R function. **(D)** Sample eIPSC traces taken before (1) and during (2) WIN55,212-2 application in WT and FABP5 KO striatal slices.

DATA AVAILABILITY STATEMENT

The original contributions presented in the study are included in the article/supplementary materials, further inquiries can be directed to the corresponding authors.

ETHICS STATEMENT

The animal study was reviewed and approved by Animal Care and Use Committee in accordance with the National Institutes of Health Guide for the Care and Use of Laboratory Animals.

AUTHOR CONTRIBUTIONS

MF conducted biochemical and histological experiments. SO conducted the *in vitro* slice electrophysiology studies. MY and SG performed qPCR experiments. MF, SO, MK, and SH-D designed the study, analyzed the data, and wrote the manuscript. All authors contributed to the article and approved the submitted version.

FUNDING

This study was supported by the NIH grants: MH122461 (to SH-D and MK) and DA035949 (to MK).

ACKNOWLEDGMENTS

The authors wish to thank Rob Rieger at the Stony Brook University Biological Mass Spectrometry Core for help with eCB quantification. We also wish to thank Lizemarie Cirone for help with slice preparation and Keith Studholme for help with immunohistochemistry.

REFERENCES

Adermark, L., and Lovinger, D. M. (2007). Retrograde endocannabinoid signaling at striatal synapses requires a regulated postsynaptic release step. *Proc. Natl. Acad. Sci. U. S. A*. 104, 20564–20569. doi: 10.1073/pnas.0706873104

Adermark, L., Talani, G., and Lovinger, D. M. (2009). Endocannabinoid-dependent plasticity at GABAergic and glutamatergic synapses in the striatum is regulated by synaptic activity. *Eur. J. Neurosci*. 29, 32–41. doi: 10.1111/j.1460-9568.2008.06551.x

Alger, B. E. (2014). Seizing an opportunity for the endocannabinoid system. *Epilepsy Curr*. 14, 272–276. doi: 10.5698/1535-7597-14.5.272

Ashton, J. C., and Glass, M. (2007). The cannabinoid CB2 receptor as a target for inflammation-dependent neurodegeneration. *Curr. Neuropharmacol*. 5, 73–80. doi: 10.2174/157015907780866884

Di Marzo, V., Stella, N., and Zimmer, A. (2015). Endocannabinoid signalling and the deteriorating brain. *Nat. Rev. Neurosci*. 16, 30–42. doi: 10.1038/nrn3876

Furuhashi, M., and Hotamisligil, G. S. (2008). Fatty acid-binding proteins: role in metabolic diseases and potential as drug targets. *Nat. Rev. Drug Discov*. 7, 489–503. doi: 10.1038/nrd2589

Haj-Dahmane, S., Shen, R. Y., Elmes, M. W., Studholme, K., Kanjiya, M. P., and Bogdan, D., et al. (2018). Fatty-acid-binding protein 5 controls retrograde endocannabinoid signaling at central glutamate synapses. *Proc. Natl. Acad. Sci. U. S. A*. 115, 3482–3487. doi: 10.1073/pnas.1721339115

Hashimotodani, Y., Ohno-Shosaku, T., and Kano, M. (2007). Endocannabinoids and synaptic function in the CNS. *Neuroscientist* 13, 127–137. doi: 10.1177/1073858406296716

Hashimotodani, Y., Ohno-Shosaku, T., Maejima, T., Fukami, K., and Kano, M. (2008). Pharmacological evidence for the involvement of diacylglycerol lipase in depolarization-induced endocanabinoid release. *Neuropharmacology* 54, 58–67. doi: 10.1016/j.neuropharm.2007.06.002

Hashimotodani, Y., Ohno-Shosaku, T., Tanimura, A., Kita, Y., Sano, Y., Shimizu, T., et al. (2013). Acute inhibition of diacylglycerol lipase blocks endocannabinoid-mediated retrograde signalling: evidence for on-demand biosynthesis of 2-arachidonoylglycerol. *J. Physiol*. 591, 4765–4776. doi: 10.1113/jphysiol.2013.254474

Howlett, A. C., Barth, F., Bonner, T. I., Cabral, G., Casellas, P., Devane, W. A., et al. (2002). International union of pharmacology. XXVII. Classification of cannabinoid receptors. *Pharmacol. Rev*. 54, 161–202. doi: 10.1124/pr.54.2.161

Kaczocha, M., and Haj-Dahmane, S. (2021). Mechanisms of endocannabinoid transport in the brain. *Br. J. Pharmacol*. doi: 10.1111/bph.15469

Kaczocha, M., Rebecchi, M. J., Ralph, B. P., Teng, Y. H., Berger, W. T., Galbavy, W., et al. (2014). Inhibition of fatty acid binding proteins elevates brain anandamide levels and produces analgesia. *PLoS ONE* 9, e94200. doi: 10.1371/journal.pone.0094200

Kaczocha, M., Vivieca, S., Sun, J., Glaser, S. T., and Deutsch, D. G. (2012). Fatty acid-binding proteins transport N-acylethanolamines to nuclear receptors and are targets of endocannabinoid transport inhibitors. *J. Biol. Chem*. 287, 3415–3424. doi: 10.1074/jbc.M111.304907

Kaczocha, M.,, Glaser, S. T., and Deutsch, D. G. (2009). Identification of intracellular carriers for the endocannabinoid anandamide. *Proc. Natl. Acad. Sci. U. S. A*. 106, 6375–6380. doi: 10.1073/pnas.0901515106

Kano, M., Ohno-Shosaku, T., Hashimotodani, Y., Uchigashima, M., and Watanabe, M. (2009). Endocannabinoid-mediated control of synaptic transmission. *Physiol. Rev*. 89, 309–380. doi: 10.1152/physrev.00019.2008

Maccarrone, M. (2017). Metabolism of the endocannabinoid anandamide: open questions after 25 years. *Front. Mol. Neurosci*. 10, 166. doi: 10.3389/fnmol.2017.00166

Murataeva, N., Straiker, A., and Mackie, K. (2014). Parsing the players: 2-arachidonoylglycerol synthesis and degradation in the CNS. *Br. J. Pharmacol*. 171, 1379–1391. doi: 10.1111/bph.12411

Narushima, M., Uchigashima, M., Fukaya, M., Matsui, M., Manabe, T., et al. (2007). Tonic enhancement of endocannabinoid-mediated retrograde suppression of inhibition by cholinergic interneuron activity in the striatum. *J. Neurosci*. 27, 496–506. doi: 10.1523/JNEUROSCI.4644-06.2007

Narushima, M., Uchigashima, M., Hashimoto, K., Watanabe, M., and Kano, M. (2006). Depolarization-induced suppression of inhibition mediated by endocannabinoids at synapses from fast-spiking interneurons to medium spiny neurons in the striatum. *Eur. J. Neurosci*. 24, 2246–2252. doi: 10.1111/j.1460-9568.2006.05119.x

Oubraim, S., Wang, R., Hausknecht, K. A., Shen, R. Y., and Haj-Dahmane, S. (2021). Tonic endocannabinoid signaling gates synaptic plasticity in dorsal raphe nucleus serotonin neurons through peroxisome proliferator-activated receptors. *Front. Pharmacol*. 12, 691219. doi: 10.3389/fphar.2021.691219

Owada, Y., Yoshimoto, T., and Kondo, H. (1996). Spatio-temporally differential expression of genes for three members of fatty acid binding proteins in developing and mature rat brains. *J. Chem. Neuroanat*. 12, 113–122. doi: 10.1016/S0891-0618(96)00192-5

Peng, X., Studholme, K., Kanjiya, M. P., Luk, J., Bogdan, D., Elmes, M. W., et al. (2017). Fatty-acid-binding protein inhibition produces analgesic effects through peripheral and central mechanisms. *Mol. Pain*. doi: 10.1177/1744806917697007

Sadanandan, S. M., Kreko-Pierce, T., Khatri, S. N., and Pugh, J. R. (2020). Cannabinoid type 2 receptors inhibit GABAA receptor-mediated currents in cerebellar Purkinje cells of juvenile mice. *PLoS ONE* 15, e0233020. doi: 10.1371/journal.pone.0233020

Uchigashima, M., Narushima, M., Fukaya, M., Katona, I., Kano, M., and Watanabe, M. (2007). Subcellular arrangement of molecules for 2-arachidonoyl-glycerol-mediated retrograde signaling and its physiological contribution to synaptic modulation in the striatum. *J. Neurosci.* 2, 3663–3676. doi: 10.1523/JNEUROSCI.0448-07.2007

Van Sickle, M. D., Duncan, M., Kingsley, P. J., Mouihate, A., Urbani, P., Mackie, K., et al. (2005). Identification and functional characterization of brainstem cannabinoid CB2 receptors. *Science* 310, 329–332. doi: 10.1126/science.1115740

Wilson, R. I., and Nicoll, R. A. (2002). Endocannabinoid signaling in the brain. *Science* 296, 678–682. doi: 10.1126/science.1063545

Yu, S., Levi, L., Casadesus, G., Kunos, G., and Noy, N. (2014). Fatty acid-binding protein 5 (FABP5) regulates cognitive function both by decreasing anandamide levels and by activating the nuclear receptor peroxisome proliferator-activated receptor beta/delta (PPARbeta/delta) in the brain. *J. Biol. Chem.* 289, 12748–12758. doi: 10.1074/jbc.M114.559062

Zou, S., and Kumar, U. (2018). Cannabinoid receptors and the endocannabinoid system: signaling and function in the central nervous system. *Int. J. Mol. Sci.* 19, 833. doi: 10.3390/ijms19030833

Conflict of Interest: The authors declare that the research was conducted in the absence of any commercial or financial relationships that could be construed as a potential conflict of interest.

Publisher's Note: All claims expressed in this article are solely those of the authors and do not necessarily represent those of their affiliated organizations, or those of the publisher, the editors and the reviewers. Any product that may be evaluated in this article, or claim that may be made by its manufacturer, is not guaranteed or endorsed by the publisher.

frontiers | Frontiers in Cellular Neuroscience

TYPE Review
PUBLISHED 02 August 2022
DOI 10.3389/fncel.2022.917273

OPEN ACCESS

EDITED BY
Arianna Maffei,
Stony Brook University, United States

REVIEWED BY
Markus Rothermel,
University of Veterinary Medicine Hannover, Germany
Ricardo C. Araneda,
University of Maryland, College Park, United States

*CORRESPONDENCE
Mark Bolding
mark.bolding@gmail.com

SPECIALTY SECTION
This article was submitted to Cellular Neurophysiology, a section of the journal Frontiers in Cellular Neuroscience

RECEIVED 11 April 2022
ACCEPTED 11 July 2022
PUBLISHED 02 August 2022

CITATION
Mantraratnam V, Bonnet J, Rowe C, Janko D and Bolding M (2022) X-ray perception: Animal studies of sensory and behavioral responses to X-rays. *Front. Cell. Neurosci.* 16:917273. doi: 10.3389/fncel.2022.917273

X-ray perception: Animal studies of sensory and behavioral responses to X-rays

Vaishnavi Mantraratnam[1], Jorge Bonnet[1], Caleb Rowe[1], Daniel Janko[2] and Mark Bolding[1]*

[1]Department of Radiology, University of Alabama at Birmingham, Birmingham, AL, United States, [2]Department of Neurology, University of Alabama at Birmingham, Birmingham, AL, United States

Since their discovery in 1895, many studies have been conducted to understand the effect of X-rays on neural function and behavior in animals. These studies examined a range of acute and chronic effects, and a subset of studies has attempted to determine if X-rays can produce any sensory responses. Here we review literature on animal behavioral responses to X-rays from 1895 until 2021 to assess the evidence for detection of X-rays by sensory receptors in animals. We focus on the changes in appetitive and consummatory behavior, radiotaxis, behavioral arousal, and olfactory responses to X-rays that have been reported in the literature. Taken together, the reviewed literature provides a large body of evidence that X-rays can induce sensory responses in a wide variety of animals and also suggests that these responses are mediated by known sensory receptors. Furthermore, we postulate the role of reactive oxygen species (ROS), the most biologically active byproduct of X-rays, as a key mediator of sensory receptor responses to X-rays.

KEYWORDS

X-rays, optogenetics, ionizing radiation, sensory, vision

Introduction

X-rays have inspired fascination and curiosity since their discovery in 1895 by Wilhelm Conrad Röntgen and the effects of X-rays on animals and humans have been the focus of many investigations. The reaction to Röntgen's initial discovery was sensational and led to a veritable explosion of research on the mysterious rays and as early as 1897 when Freund had begun investigations into their biological effects (Widder, 2014).

X-rays are a form of high energy electromagnetic radiation that can penetrate matter more readily than visible light. At kilovolt energies (typical clinical values) the attenuation of X-rays per unit mass is approximately proportional to Z^3/E^3, where Z is the atomic number and E is the energy of the incident photon. As a result, X-rays are less attenuated by soft tissues and more attenuated by hard tissues and so X-rays can be used to produce the projections of tissue density known as radiographs. This property has led to the wide use of X-rays for clinical imaging. For higher Z materials (e.g., iodine, $Z = 53$), sharp increases in attenuation can be seen at energies near the binding energy of the inner shell electrons. These are known as k-edges and this property has led to the use of iodine and barium as clinical contrast agents. Abundant elements in tissue (i.e., carbon, hydrogen, oxygen, and nitrogen) have k-edges that are so low they are difficult to detect.

X-rays' impact on biology is principally by radiolysis of water. This is principally due to the ubiquity of water in biological systems. Essentially, a high energy photon can kick an electron out of a water molecule and into solution. This leads to a rapid cascade of events and the generation of reactive oxygen species (ROS) which have a wide range of reactivities. Importantly, at low concentrations ROS can act as a cellular signal and ROS plays a vital role in signal transduction, metabolic regulation, and homeostatic regulation in processes like apoptosis, autophagy, the cell cycle, and immunity (Moloney and Cotter, 2018; Unable to find information for 178238; Holmström and Finkel, 2014). At high concentrations ROS can damage a wide array of cellular components including DNA making ROS mutagenic at higher levels. Thus, X-rays could have significant modulatory effects on ROS-mediated signaling cascades and cellular function and these effects could vary dramatically with the dose delivered.

In current medical practice, X-ray dose is controlled and generally minimized to mitigate harmful effects while maintaining diagnostic utility (Tafti and Maani, 2022). As a result, much literature on X-ray perception derives from the earliest days of X-ray research when there was little awareness of their harmful effects. As awareness of these harmful effects has increased, research on the perceptual effects of X-rays has become rare. Investigations of the dose dependence of biological effects of X-rays is in some ways still not nuanced (Widder, 2014). Presently, a linear dose dependent harmful effect model is generally accepted though other models such as hormesis (i.e., low doses of ionizing radiation are beneficial) have good experimental support but limited acceptance (Baldwin and Grantham, 2015).

The objective of this review paper is to provide an overview of the many studies conducted to examine sensory effects or perception of X-rays by animals. In the current review we are concerned with the immediate sensory effects of X-rays rather than longer term biological effects of X-rays such as dermatitis, radiation sickness, or mutagenesis. This review does not include studies of the effects of X-rays on the production of lethal DNA mutations, or the directed evolution of X-rays resistance in bacteria or other prokaryotes. In particular, this review does not look at studies of the mutagenic and harmful effects of ionizing radiation in humans which have been the subject of other recent reviews (Rödel et al., 2017; Maqsudur Rashid et al., 2019; Shin et al., 2020). Finally, this review does not focus on studies of human perception of X-rays. While we may include studies on the perception of X-rays by humans in the chronology for context, they will not be discussed in depth. Human studies are the subject of a forthcoming review in preparation.

We are principally concerned with the questions of whether or not animals can have a sensory response to X-rays that is not simply due to tissue damage and, if so, what are the potential mechanisms driving this phenomenon. We discuss reports of specific sensory effects and suggest a common mechanism by which the sensory effects might arise. To facilitate discussion, we define specific meanings for several key concepts used in this paper. X-rays designate a penetrating form of high-energy electromagnetic radiation with wavelengths shorter than UV and longer than gamma rays. Here we define X-rays to have a wavelength ranging from 10 pm to 10 nm, corresponding to energies in the range 145 eV to 124 keV. As is consistent with most of the literature reviewed, we do not always make a clear distinction between X-rays and gamma rays. In this review "sensing," "sensation," and "perception" are inferred from behavioral or electrophysiological responses and can be considered synonymous unless otherwise noted. By "sensory receptor" we mean to indicate a membrane bound protein receptor such as a photo-, chemo-, or mechanoreceptor that is part of a sensory signaling pathway. At times "sensory receptor" may more broadly indicate the cell or organ that the protein receptor is a part of, and this should be clear from context. When the word "light" is used without qualification it indicates visible light and not ionizing radiation, UV, or infrared.

Prior to this paper, the most recent published review addressing questions in this area was Lipetz's review "The X-ray and radium phosphenes," which concluded that the visual system can be stimulated by X-rays mediated by the photoreceptors of the retina, and that fluorescence of the ocular media is negligible and does not constitute a viable mechanism, except at very high intensities of X-rays (Lipetz, 1955). Since 1955, a body of X-ray perception literature has accumulated that has not yet been reviewed.

Chronology

Röntgen is credited with the discovery of X-rays at the end of 1895. X-rays were initially described as invisible. By 1896, Brandes and Dorn reported that X-rays could produce phosphenes.[1] This claim was initially met with some resistance by other investigators including Röntgen. However, by the end of 1897 there were numerous reports that X-rays could produce visual effects. There were investigations into the nature of X-ray phosphenes over the next few years and the site of action was determined to be the retina. However, by 1906 the interest in the phenomena seems to have been lost and eventually X-rays were again generally considered to be invisible.

In 1932 two investigators, Taft and Pirne independently rediscovered the visual effects of X-rays. This led to the use of X-rays for ophthalmology and for basic research into human vision. The visual effects of X-rays began to be used as clinical tools for the evaluation of visual perception and for research purposes over the next two decades. In 1955 Lipetz began the first of a two-part report on investigations into the mechanism of X-ray visual phenomena with the following paragraph.

1 A phosphene is generally defined to be a sensation of light in the visual system that is produced by something other than light. So, strictly speaking, "X-ray phosphene" is an oxymoron.

> "OPHTHALMOLOGISTS, as well as radiologists, are aware that radium radiations and X-rays can produce a sensation of light on striking a person's eye. This phenomenon is being used clinically to locate foreign bodies within the eye and to test the retinae of cataractous eyes. It has recently been used to measure the diameters and refractive power of living human eyes. But the mechanism by which these radiations arouse a visual sensation is still unknown."

Around the time these two papers were published, several groups began investigations into the sensory effects of X-rays using a variety of animal models including monkeys, rats, insects, and crustaceans, which continued into the late 1970s. Kimeldorf was particularly active in this area and published papers over several decades and his book with Hunt entitled "Ionizing Radiation: Neural Function and Behavior" was published in 1965.

There were several particularly notable experiments over the era from the early 30s to the early 70s. Edward Baylor Frederick Smith conducted experiments on the perception of X-rays in Daphnia magnia (water fleas) and demonstrated phototaxis-like behavior in response to X-rays in 1958. Hunt, Garcia, and Kimmeldorf demonstrated radiation-induced conditioned avoidance and direct stimulation of the mammalian nervous system with X-rays in rats, mice, and cats in the early 1960s. These experiments were influenced by the first findings of sensory responses to X-rays shortly after the discovery of X-rays. In humans, multiple groups compared the properties of X-ray visual effects to the properties of light perception and deduced common properties and interactions between the perception of light and X-rays (Lipetz, 1955). X-rays perception was also used to measure the diameter of the globe by passing beams across the eye and having subjects report the percepts. Concurrently, X-ray perception was used clinically to look for foreign bodies in the eye by having patients report the location of the X-ray shadows (Godfrey et al., 1945).

As humans began to enter space, astronauts reported flashes of light during space travel. This led to space and terrestrial experiments on the visual effects of ionizing radiation in the 1970s and later in the 2010s. These experiments alongside the general interest in the effects of radiation prompted animal studies that sought to uncover the mechanisms of X-ray phosphenes throughout the 1950s into the 1970s (Doly et al., 1980a,b). Since the 1970s, there have been more sporadic but nonetheless highly informative experiments into the X-ray phosphene mechanism. In particular, Doly et al. (1980a,b) and Savchenko (1993) present convincing evidence that X-ray phosphenes in mammals are mediated by the rod cells of the retina. Since then, there have been multiple reports of human sensory perception of ionizing radiation during radiation therapies with cranial targets (Rödel et al., 2017; Maqsudur Rashid et al., 2019; Shin et al., 2020).

The history of reports of X-ray perception and significant developments is outlined in Table 1.

Observations and experiments in animals

In this section, we discuss specific studies that were conducted to examine animal responses to X-ray. Animals and insects have been observed to exhibit behavioral responses to X-rays. Vertebrates tested include Mammalian models with rat, mouse, and monkey models. Invertebrates include ant, moth, cockroach, sea anemone, and crustacean models. Plants, fungi, and humans have also been studied and have been reported to have prompt electrophysiological, perceptual, and behavioral responses to low doses of X-rays. In this paper we are principally concerned with studies in animals. Though, for context, we have included human studies in the above chronology, in the sections below we limit our discussion to animal studies. Studies of human perception of X-rays will be reviewed in a forthcoming paper currently in preparation. Table 2 outlines studies over the most active period of research in this area.

A variety of sources can be used to produce X-rays. The most commonly used source is an X-ray tube which consists of an anode and a cathode with a high potential difference (voltage) inside of an evacuated envelope that is usually made of glass. X-rays are produced when electrons strike the anode. The spectrum of X-ray emission is a function of the anode material and the voltage. A tube was used as the source in each of the experiments reviewed here. To a first approximation, the output of any X-ray tube is determined by the current, voltage, anode material, and spot size. The spot is the area of the anode from which the X-rays are emitted. X-ray intensity varies linearly with current. The radiation arriving at the irradiated sample is additionally affected by distance (intensity) and any intervening material such as the metal plates that are used to attenuate low energy X-rays (changes spectrum). The spectrum is determined by the voltage, anode material, and filtering. Intensity is determined by current but can vary in a non-trivial way with geometry. Knowing how these parameters vary over time should, in general, allow an approximation of the exposure of a sample on an axis with the beam to be made even if other details about the source are unknown. So, X-ray tubes are in some sense generic, though accurate estimates of intensity require measurements with calibrated detectors, because, for instance, intensity can vary with angle with respect to the beam axis in a way that differs from tube to tube. However, in the papers reviewed, there is wide variability in how the sources are described. Often key parameters or how they varied over time are not reported. Generally, an estimate of exposure or absorbed dose was reported along with some of the key parameters, but there is wide variability in the units used, how they were measured, and assumptions about absorption.

TABLE 1 A chronology of significant reports of X-ray perception.

Year	Model	Notable report or time period
1895	Human	Discovery of X-rays by Röntgen who states that X-rays are invisible.
1895–1906		The initial discoveries that X-rays can produce visual effects in humans and those animals exhibit phototaxis. The perception of X-rays by humans is found to require a dark-adapted vision—something that is found by all following investigators.
1896	Human and invertebrate	Brandes and Dorn report X-ray phosphenes, Axenfeld reports that insects and crustaceans exhibit phototaxis in response to X-rays and that this effect goes away if the animals are blinded (Lipetz, 1955).
1897	Human	Röntgen capitulates and reports that X-rays can produce visual responses (Lipetz, 1955).
1903	Human and vertebrate	Hardy and Anderson (1903) conclude that the site of X-ray phosphene production is the retina.
1906	Human	Except for reviews in 1910, 1912, and 1925, there are no more reports on X-ray phosphenes for many years. Lipetz (1955) speculates that this is because of increasing awareness of the harmful effects of X-rays.
Early 1930s to late 1950s		Visual effects of X-rays were used in clinical ophthalmology. "Seeing" lead letters and other targets with closed eyes is demonstrated. The psychophysics of X-ray "vision" investigated.
1932	Human	"Taft and Pirie independently rediscover the visibility of X-rays (Pirie, 1932; Taft, 1932). Pirie reports on identifying lead targets with closed eyes using X-rays (Pirie, 1932, 1934). Further reports were published about every 2 years until 1955 (Lipetz, 1955).
1941	Human	Newell and Borley (1941) measure the threshold X-ray intensity required to produce the phosphene in humans. The threshold varied from 0.5 to 1.4 r/min in three normal subjects for an area of 1 mm^2. They found the time course of dark adaptation for X-rays and light to be similar.
1945	Human	Based on the method described by Pirie in 1934, Godfrey et al. (1945) describe a refined technique to locate foreign bodies in the eye or orbit by the X-ray shadows cast on the retina of a patient. Like Newell and Borley, they reported that the dark adaptation curves for light and X-rays were similar.
1951	Human	Lipetz (1955) reports that in several experiments Belluci found that the pupillary response to X-rays was consensual and that X-ray phosphenes exhibit persistence of vision. Belluci also found that phosphene brightness increased with tube voltage and current and the phosphene changed from blue to yellow green to yellow as current increases.
1953	Human	Bornschein et al. (1953) found the threshold of X-ray vision to vary from 1.6 to 8.7 mr/s and that the threshold dose was nearly constant for durations of stimulus <20 ms. For greater durations the threshold dose increased with stimulus duration
Mid 1950s to Mid 1970s		Multiple investigators experiment with the sensory effects of X-rays using a variety of animal models including monkeys, rats, insects, and crustaceans. Kimeldorf and his collaborators are particularly active in this area.
1955	Human	Lipetz reports that X-rays were being used clinically in 1955 to locate foreign bodies in the eye and to test the retinas of cataractous eyes, but the mechanism of X-ray perception was unknown (Lipetz, 1955)
1958	Invertebrate	Baylor and Smith (1958) report that water fleas demonstrate phototaxis in response to X-rays as they would to blue light.
1960	Vertebrate	Kimeldorf et al. (1960) report the demonstration of an avoidance behavior conditioned by radiation exposure. They state, "The stimulus tends to be unique in that a specific receptor system is not known."
1960	Vertebrate	Garcia and Kimeldorf (1960) report that localized X-ray exposure of the head, thorax, abdomen, or pelvis served as a motivating stimulus to condition a saccharin aversion in rats.
1960s to 2000s	Human	Reports of light flashes from astronauts and other potential cosmic ray effects lead to ALFMED experiments during Apollo 16 and 17 transits in 1972 and the SilEye-Alteino and ALTEA projects aboard the MIR and ISS are performed in space 3 decades later. In both experiments astronauts wore helmets designed to capture the tracks of cosmic ray particles to determine if they coincided with the visual observation. It was concluded that the visual phenomena were caused by cosmic rays (Pinsky et al., 1975; Casolino et al., 2003a).
1960s	Vertebrate and invertebrate	In a series of papers, Bachofer and Wittry measure the Electroretinogram in response to X-ray stimulation in frogs and find that rhodopsin is sensitive to X-rays (Bachofer and Wittry, 1961, 1962; Bachofer and Esperance Wittry, 1963).
1962, 1963	Vertebrate	Hunt and Kimeldorf (1962) and Baldwin et al. (1963) report that rats can be aroused from sleep using X-rays and that this effect is not dependent on vision.
1962	Vertebrate	Barnes (1962) reports that behavioral avoidance of X-rays by rats can be eliminated by splanchnicectomy, but not ophthalmectomy.
1963	Vertebrate	Smith and Morris (1963) report conditioned avoidance to saccharine to low doses of X-rays and the response is minimally dulled with age.

(Continued)

TABLE 1 Continued

Year	Model	Notable report or time period
1963	Vertebrate	Garcia and Buchwald (1963) report on successful use of X-rays as a conditioned stimulus in an operant conditioning experiment.
1963	Invertebrate	Smith et al. (1963) report that moths in a darkened room respond behaviorally to brief pulses of low dose X-rays.
1963	Invertebrate	Baldwin et al. (1963) find a light-like on-response to X-ray stimulation in cockroaches.
1964	Invertebrate	Smith and Kimeldorf (1964) report the electrophysiological responses of moth eyes to beta radiation and compare it to light stimulation. They conclude that the X-ray response elicits an ERG like that of a light response.
1964	Vertebrate	Garcia et al. (1964) report that rats can be trained to respond behaviorally to very low doses of X-rays and that the site of action is in or near the olfactory bulbs.
1965	Vertebrate	Feder (1965) and Feder et al. (1966) reports on perception of X-rays by rats and concludes that the response to low doses is due to olfactory bulbs and the avoidance response to high doses is abdominal.
1966	Vertebrate	Cooper and Kimeldorf (1966) report that rat olfactory bulb neurons respond to X-rays electrophysiologically by transiently and promptly increasing firing rate.
1970	Invertebrate	Kimmeldorf's student Jordan reports that ERG responses to X-rays in Purple shore crabs are similar to responses to light (Jordan, 1970). He obtains quantum efficiencies of about 1% which is in line with reports of Lipetz.
1970s	Human	In several experiments observers view neutron beams and other high energy radiation sources to try and determine the mechanism of cosmic ray induced light flashes. Two of the principal hypotheses are Cherenkov radiation and direct photoreceptor stimulation (Charman et al., 1971; Tobias et al., 1971).
1971	Invertebrate	Kimeldorf and Fortner (1971) report that sea anemone responds to X-ray stimulation with immediate tentacle withdrawal and oral disc closure.
1972	Vertebrate	Chaddock (1972) reports that X-ray stimulation varies as a function of different monochromatic background illumination in monkeys.
1972	Invertebrate	Martinsen and Kimeldorf (1972) report that carpenter ants can sense X-rays with antennal flagella.
1974	Invertebrate	Dedrick and Kimeldorf (1974) report that sea urchins can sense X-rays and it resembles phototaxis.
1975	Invertebrate	Kernek and Kimeldorf (1975) report that shrimp can sense X-rays. "Prompt arousal responses were characterized by vigorous motions of appendages and by advancing, rolling and re- treating movements"
1980	Vertebrate	In two papers Doly et al. (1980a,b) report on the use of electrophysiology and photochemistry approaches in a rodent model to investigate the mechanism of formation of X-ray phosphenes.
1993	Vertebrate	Savchenko (1993) shows evidence that X-ray phosphenes occur as a result of the excitation of the rod apparatus.
2003 to 2009	Human	Casolino et al. (2003b), Fuglesang et al. (2006), Sannita et al. (2006), Narici et al. (2009) review reports of visual phenomena in space and propose mechanisms.
2010 to now		The term X-genetics was coined by Rachel Barry and Ge Wang. Many reports of phosphenes and other sensory effects in humans during proton and X-ray therapy with cranial targets.
2015	Human	Wilhelm-Buchstab et al. (2015) report that phosphenes can be generated extra retinally by proton therapy.
2020	Human	Narici et al. (2020) report that many sensory illusions are invoked by proton therapy and that the sensations track the irradiation closely in time and the visual sensations are extra retinal.
2021	Vertebrate	Matsubara et al. (2021) report successful demonstrations of scintillator mediated X-genetics using macroscopic scintillators and light sensitive optogenetic receptors and Chen et al. (2021) demonstrate X-genetics using scintillating nanoparticles and light sensitive optogenetic receptors.

Behavioral responses to various dosages of ionizing radiation

Behavioral responses have been observed from experiments with ionizing radiation and can be separated into three groups: (1) changes in food and water consumption, (2) radiotaxis (including flight in insects), attraction or avoidance of ionizing radiation and behavioral arousal (including measuring the heart rate, eye activity, wakefulness, oral dilation and tentacle retraction, movement of antennae), and (3) olfactory responses. This review focuses only on acute and immediate sensory or learning-related responses. We do not examine delayed responses other than avoidance or conditioning. Sensory responses are especially linked to the visual system in humans,

TABLE 2 Significant findings from animal studies of X-ray perception from 1956 to 1993 by Period.

Year	Overarching significant finding	Common name of animal model	Key papers
1956	Rats exhibit decreased sugar water consumption despite being in a food and water deprived state when conditioned to associate drinking sugar water with X-ray exposure. Furthermore, X-rays are shown to disrupt gastrointestinal function.	Sprague-Dawley Rats	Garcia et al., 1956a,b
1958	Water fleas or Daphnia magna exhibit unique downward swimming patterns in aversion to X-rays through a process likely mediated by the nauplius eye.	Water fleas	Baylor and Smith, 1958
1960	X-ray conditioning behavior found to be mediated by the abdomen. The eyes, vagus nerve, adrenal glands, and pituitary glands are not involved in sensations seemingly triggered by gastric dysfunction. Association of a distinctive taste is generated by conditioning animals to associate X-rays with particular fluids. Cats, mice, and rats all exhibit this taste sensation, and no evidence indicates the sensation is painful. Rats exhibit X-ray avoidance by preferring shielded chambers over non-shielded chambered in presence of X-rays.	Sprague- Dawley Rats, mice, cats	Garcia and Kimeldorf, 1960; Kimeldorf et al., 1960
1962	The entire gastrointestinal tract is highly radiosensitive with mucosa in the duodenum being the first tissue to show effects to ionizing radiation. The damaging effects of X-rays are sensed by the breakdown of the mucosa of the duodenum, small intestines, and stomach, which later progresses to the mouth, esophagus, and rectum. Acute X-ray perception is mediated by reactions in the gastrointestinal tract that signal *via* the splanchnic nerves. Sensory mechanisms outside the abdomen cavity mediate avoidance behavior after the first 15 min of irradiation. Acute responses to X-rays can be abrogated by intraperitoneal injection of procaine or surgical excision of one or more splanchnic nerves that innervate the thoracic trunk in the abdomen abrogates X-ray avoidance.	Sprague-Dawley Rats	Barnes, 1962
1963	Age of rats does not impact X-ray perception. Moths respond to low-intensity X-rays. Threshold intensity to promptly awaken rats from sleep within seconds is 0.25 r/s, with EEG responses within 1 s at 0.2 r/s, and rats can be conditioned with stimuli as low as 0.001 r/s. Changes in X-ray intensity caused "on-off" responses in the eye of cockroaches. Mammalian neurons respond perceptually and adaptively to extremely low levels of X-rays *via* two separate X-ray perception phenomena. Firstly, EEG recordings across various mammal models support the "hit" theory whereby a fast-acting mechanism is mediated by the reticular activating system in response to higher X-ray intensities. Secondly, conditioning experiments in rats support a "hangover effect" theory whereby extremely low doses of X-rays cause avoidance behavior as a result of the accumulation of breakdown products stimulating gastric dysfunction as signaled by a peripheral afferent effect.	Sprague-Dawley Rats, Wistar rats, Cockroach	Baldwin et al., 1963; Garcia and Buchwald, 1963; Smith and Morris, 1963
1964	X-rays are believed to stimulate neurons *via* biochemical interactions with afferent signaling cascades in the brain and secondary effects are ruled out by citing how X-rays must directly be aligned with the olfactory bulb and its primary neurons. It is posited that X-rays disrupt a biochemical signaling cascade in the olfactory bulbs after experiments using a precise X-ray machine directed toward specific regions of the brain delivered from various angles reveal the olfactory bulbs to be extremely radiosensitive. Moths respond on ERG to beta-radiation and X-rays at 0.25 mr elicit flight activity.	Sprague-Dawley Rats, Moths	Hunt and Kimeldorf, 1964; Smith and Kimeldorf, 1964
1965	Rats' ability to sense 0.1 s 0.2 r/s burst of X-rays to avoid shock is abrogated by the removal of olfactory bulbs. Phosphenes are noted as requiring higher X-ray dosages (10 r/min) and X-ray stimulation enhances retinal sensitivity to light and lowers thresholds where phosphenes occur although no irreversible damage is noted. Cockroaches respond to 0.09 mr delivered at 5.2 r/min in a 1 ms pulse in a dark-adapted state and the migration of eye pigments related to dark adaptation is shown to enhance radiosensitivity. Cockroaches may respond to even smaller X-ray doses given better X-ray technologies.	Sprague-Dawley Rats	Baldwin and Sutherland, 1965; Feder, 1965
1966	"Ions produced by radiation… in the mucus surrounding the cilia of olfactory receptors… stimulate receptors." X-rays cause activation and desynchronization of neurons in the olfactory bulb. Ablation of the olfactory bulb greatly diminished the impact of X-rays on sleeping rats. X-rays' impact on the olfactory bulb is dependent on normal sensory input. Alcohol washing of the nasal cavities in	Sprague-Dawley Rats	Cooper and Kimeldorf, 1966; Feder et al., 1966

(Continued)

TABLE 2 Continued

Year	Overarching significant finding	Common name of animal model	Key papers
	tracheostomized animals abrogated any influence of X-rays on neural activity, while saline washing temporarily abolished responses. Cooper recorded secondary olfactory neurons for these experiments. If Cooper used primary olfactory neurons, it could have refuted Kimdelorf's experiments using ozone, which reportedly ruled out that rats could "smell" X-rays. Rats respond to irradiation of the whole animal, head only, or olfactory bulbs and do not respond to the irradiation of the air surrounding the rats' nose, the body behind the head, or specifically the head posterior to the olfactory bulb.		
1970-1971	Sea anemones detect X-rays precisely and quickly with immediate tentacle withdrawal and oral disc closure responses. ERG responses to X-rays in Purple shore crabs are similar to responses to light. Fluorescence may play a role.	Sea anemones	Jordan, 1970; Kimeldorf and Fortner, 1971
1972	Visual detection of X-rays by Rhesus monkey changes as a function of varied background illumination. Carpenter ants have rapid and precise behavioral responses. Antennal flagella's sensory receptors (olfactory or ocular) were important for X-ray detection.	Rhesus monkeys, carpenter ants	Chaddock, 1972; Martinsen and Kimeldorf, 1972
1974	Sea urchins can detect X-rays *via* a dermal light sense that involves photostimulation of dermal nerve cells.	Sea urchins	Dedrick and Kimeldorf, 1974
1975	Red Ghost shrimp have rapid arousal to X-rays characterized by fervent advancing, rolling, and retreating.	Red ghost shrimp	Kernek and Kimeldorf, 1975
1980	Rod cells of the retina underlie X-ray phosphenes rather than any other biologic component of the eye. X-rays efficiently bleach isolated rhodopsin, which induces action potentials as recorded by ERG. The irradiation of proteins, including rhodopsin, disrupts weaker bonds in proteins causing partial disorganization of conformations. Unlike visual light which is absorbed by the chromophoric 11-cis retinal of rhodopsin, the energy from X-rays is absorbed by the opsin disorganizing its spatial conformation to facilitate an energy transfer that frees retinal.	Albino Rats	Doly et al., 1980a,b
1993	X-ray phosphenes have two distinct component reactions that can be altered by sodium azide, sodium nitrate, monoiodoacetate and other substances as measured by ERG in frogs. ERG of X-ray phosphenes is declared an essential tool to parcellate the radiational excitability of the central nervous system, but no further publications investigate the phenomena.	Rana temporaria frogs	Savchenko, 1993

however human visual perception of X-rays will be treated in a future review.

Changes in food and water consumption in response to radiation

Acute changes in food and water consumption as a behavioral response were noted in at least six studies. Across these studies, ionizing radiation was used as a conditioning stimulus to manipulate various food and fluid preferences and intake. Animals learned to avoid behaviors associated with irradiation such as certain foods, rooms, and fluids.

In a 1965 article, a radiotherapy source was used with silent shutter devices according to the schematic shown in Figure 1.

Kimeldorf et al. (1960) conducted a study to see whether radiation induced a conditioned avoidance response in rats, mice, and cats, using a G.E. Maxitron deep-therapy unit to irradiate the three models of interest. The mean dose rate measured at the center of the exposure was around 0.66 R/min or ∼0.011 R/s. All three species demonstrated a conditioned aversion toward radiation exposure and showed a progressive decrease in the amount of flavored fluid they consumed during each successive exposure. Garcia et al. (1956a) tested food and water consumption of rats surrounding 8 h exposures to gamma-radiation with ∼7 curies of Co-60 contained in a brass capsule, which is equivalent to a radiation flux of ∼9.4 R/h for a total dose amounting to ∼75 R per exposure. In these studies, the rats' consumption of food and water decreased during each exposure to gamma-radiation for 8 h. There was a highly significant difference between the water consumption of sham-irradiated and irradiated animals ($p < 0.001$). Sham-irradiated animals gained weight; in contrast, irradiated animals lost several grams during each exposure to radiation. Water consumption was not significantly different after the first exposure, but after the eighth exposure, the water consumption of the rats increased for the entire period. Food intake of

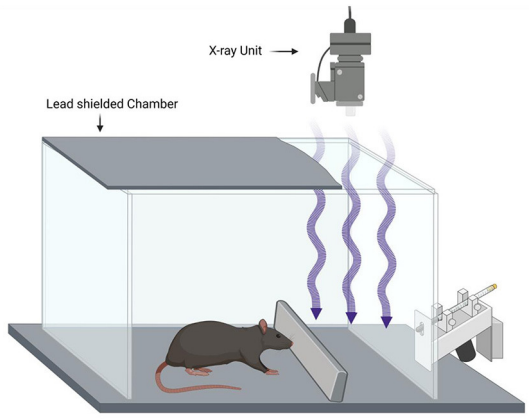

FIGURE 1
Example of a rodent X-ray conditioning experiment based on Feder (1965). Water restricted rats are conditioned to avoid a drinking tube by pairing X-ray exposure to a foot shock (unconditioned stimulus) providing evidence that the rats can make use of the X-ray exposure as a conditioned stimulus. Blocking the X-rays with lead prevents the effect showing that the X-rays are the conditioned stimulus and not some other cue.

irradiated rats was not different from that of sham-irradiated controls after either exposure.

Garcia et al. (1956b) used the same Cobalt-60 source mentioned previously and exposed the animals for 8 h in a radiation field of 9.4 R/h. This again resulted in a total dose of 75 R. Food and water consumption decreased in groups which had multiple exposures earlier; controls who were subjected to sham-irradiation maintained their level of consumption or had increased consumption with repeated confinement.

Garcia and Kimeldorf (1960) used a G.E Maxiton X-ray machine to irradiate Sprague-Dawley rats at four radiation dose levels: 54 R, 108 R, 252 R, and 360 R and each dose level had 70 animals in the subdivision. Another group of 14 animals were exposed to a single 54 R whole-body irradiation. The resultant dose rate was around 1 R/min. The total dose was around 60 R for this group. A second group of hypophysectomized animals were exposed for 3 h to make a total dose of 180 R. The results from this study showed that the abdomen is a significant, critical area in establishing conditioned avoidance responses to ionizing radiation. Exposures of 54 R or 108 R delivered to the abdominal region led to a decrease in consumption. Similar doses had no considerable effect when the beam was directed to other areas of the body excluding the abdominal region.

In Smith and Morris (1963), an X-ray machine was used to irradiate Wistar rats for 20 min per day. X-ray dosages of 350 R, 300 R, 200 R, 150 R, 100 R, and 50 R were administered at a rate of around 30 R per min. This study found that the rats that had been conditioned to associate saccharin enriched water with being irradiated kept avoiding the saccharin water, independent of dosages above 50 R after being deprived of water.

Overall, these studies measuring the changes in food and water consumption in response to radiation suggest neural mechanisms relating to disturbances in the enteric nervous system. These hypotheses will be further explored in the "Proposed Neural Mechanisms" section below.

Radiotaxis, avoidance, and behavioral arousal

Radiotaxis, a behavior analogous to phototaxis, and the more general behavior of avoidance of radiation is a response described in at least five studies from 1956 to 1993. Behavioral arousal is another reaction described in response to ionizing radiation. Responses that fall under this category include changes in heart rate, eye activity, wakefulness, oral dilation and tentacle retraction, as well as movement of antennae for specimens that do so. At least 12 studies between 1956 and 1993 described these reactions.

Baylor and Smith (1958) tested the perception of X-rays by daphnids with a type 200 B Kelley-Koet therapy unit. They exposed the animals to the X-ray for 30 min at a dose around 160–180 R/min. When irradiated by X-rays in the presence of red light, daphnids were found to swim downward as they do upon exposure to blue light, indicating a preferential stimulation of the nauplius eye.

Barnes (1962) tested peripheral neural paths mediating avoidance of radiation in rats using a Picker X-ray machine. A 40-min session of radiation of albino rats of the Sprague-Dawley strain was conducted. There were 1-min intervals applied during the first 15 min and then 5-min intervals for the remainder of the session. The unshielded compartment was irradiated around 32 R/min and the rate in a shielded compartment was around 0.75 R/min. The effect of this radiation was that the whole-body radiation led to avoidance behavior after 5–10 min of exposure in intact rats but not in rats with an intraperitoneal procaine injection or a splanchnicectomy, a surgical excision of a segment of one or more splanchnic nerves. The estimated dosage was around 16 R/min and until avoidance began, the rats spent only half of each in the compartment being irradiated at 32 R/min. They spent the remainder of each minute in the shielded compartment.

Hunt and Kimeldorf (1962) tested the stimulation of the nervous system with Sprague-Dawley rats using a Maxitron X-ray unit and exposed the rats to radiation for either 9 or 67 min. The dose rate for the rats in the high-intensity exposure group ranged between 1.5 and 2.5 R/s with a mean intensity around 1.9 R/s. The rate for the low-intensity exposure group ranged between 0.22 and 0.28 R/s with a mean intensity around 0.25 R/s. The high-intensity group displayed a significant peak in their heart rate at 30 s after exposure. The authors concluded that the threshold intensity of radiation to elicit clear neural activation and the diffusion of it (along with behavioral and heart

responses) is around the range of 0.25–1.9 R/s. They also found that the threshold intensity for activation for behavioral arousal only is <0.25 R/s.

Smith et al. (1963) tested motor responses in moths to low-intensity X-ray exposure using a Westinghouse Mexitron X-ray machine. They irradiate the moths for 1–15 s with rest times between exposures ranging from several seconds to 3 min. The delivered dose rate was between 0.01 and 1.5 R/s. Their results suggested that the threshold intensity for the visual activation is almost equal to the intensity required to initiate wing beat in the moth. The start of flight activity may be a result of visual stimulation with low intensity radiation.

Garcia and Buchwald (1963) used an HVL X-ray machine to irradiate Sprague-Dawley rats for 10 s at the rate of 1.0 R/s and for 15 s at the rate of 0.2 R/s. They found that the rats can sense the X-ray at dose rates as low as 0.050 R/s when the X-ray is used as a conditioned stimulus; behavioral arousal was measured when the dose rate was as low as 0.2 R/s in this study as well.

Baldwin et al. (1963) found that cockroaches reacted to changes in light intensity with a typical on-off response, after operating with an X-ray machine at a dose rate of 2,000 R/min. The cockroaches displayed recovery after 30 s after the end of X-ray exposure in duration of 5 min. The experiment had short rest periods of 5 min after irradiation and the cockroach electrical activity displayed an amplitude decrease with small doses of around 300 R. Essentially, the large doses of radiation used in this study led to a decreased amplitude and frequency in the electrical activity in the cockroach eye.

Smith and Kimeldorf (1964) experimented with moths using beta radiation with three sources of Tracerlab Medical Applicators with 22-, 50-, and 87-Me of Strontium-90 in equilibrium with yttrium-90. They alternated with 1–2 s duration of flickering light and 87-mc beta radiation that consisted of eight stimuli per second. They measured the amplitude and response at 1, 2, 5, 10, 30, and 45 min. They found that the best dose rate threshold to see a response to the flickering train of beta radiation was around the range of 0.02–0.06 R/s and that the maximum amplitude response occurred within 5 min.

Hunt and Kimeldorf (1964) when experimenting with Sprague-Dawley rats with a Maxitron X-ray unit found signs of behavioral arousal and neural activation. The experiment consisted of a 2-h test period with 5-min intervals for the first 30 and 10-min intervals for the remainder of the 2-h period. The total dose was around 1,000 R delivered at a rate of 1.9 R/s for the high-dose group and 0.25 R/s for the low-dose group. They noted arousal spikes during sleep, faster heart rate, and more wakefulness as measured by "active" ratings.

Baldwin and Sutherland (1965) experimented with the Cockroach Blaberus with an X-ray machine and found that in the eye, the smallest total dose that produced an electrical response was 0.09 mR delivered at a dose rate of 5.2 R/min for a pulse of 1-ms duration that created an actual dose rate below 1.5 R/s.

Jordan (1970) tested on the purple shore crab *Hemigrapsus nudus* with a General Electric model D-2 diagnostic X-ray machine and subjected the specimens to two flashes per second or constant exposure. The minimum beta dose that was created that led to a measurable visual "on" response was around 0.9 to 1.6 mR. The "on" responses consisted of visual responses and this study indicated that the structure of the eye and fluorescence may shape the "action spectrum."

Kimeldorf and Fortner (1971) tested the detection of ionizing radiations by a marine coelenterate, sea anemones, that were irradiated for 4 days at a maximum dosage of 20 R/s. The reaction time of the sea anemones ranged from 102 s at 20 R/s to 266 s at 1 R/s. At these times, tentacle withdrawal was observed. As the amount of exposure increased, the sea anemones further reacted, and the depressing of their peristome was observed with the dilation of the stomodeum. Furthermore, the oral disc was closed entirely as the extreme type of reaction, which is the strongest defensive reaction that the sea anemone can produce in response to noxious stimuli. For the tentacle retraction, reaction times ranged from 100 s at 20 R/s to 201 s at 2 R/s and other responses, including oral disk closure and mouth dilation, required much longer reaction times.

Martinsen and Kimeldorf (1972) tested the prompt detection of ionizing radiation by carpenter ants with a general electric Maxitron 300 therapy unit to irradiate the ants for 30 s at exposure rate below 0.7 R/s and up to 80 R/s. Fast behavioral responses were found to occur at rates around 0.05 R/s, including prompt, reflex-like responses such as head bobbing, brisk waving of the antennae, and rapid running behavior. This study also found that excitable tissues were stimulated by something inherent within them or accompanying exposure to X-rays. Carpenter ants also exhibited behavioral responses to radiation at 10 R/s within 1 s after the start of exposure. Overall, this study showed that in the range of 0.05–80 R/s, the strength and longevity of the responses was proportional to the exposure rate. The delay of the behavioral response was inversely related to the exposure rate.

Chaddock (1972) used a Universal X-ray machine with a rate of around 2–3 mR/s to irradiate Rhesus monkeys. The experiment used 15 s of targeted X-ray exposure to the head exposure to X-rays after which electric shocks were delivered for 0–3 s (Chaddock, 1972). The results of this experiment indicate that the sensitivity of the monkeys to detect X-ray stimulation depends on the monochromatic background illumination. The sensitivity of the monkey steadily decreased as the background illumination changed from red to blue at all exposure rates. Therefore, red was the most sensitive background illumination and blue was the least sensitive.

Dedrick and Kimeldorf (1974) tested the effects of ionizing radiation on sea urchins using a General Electric Maxitron-300 therapy unit. The duration of the exposure was 1–6 s and

the dose rates ranged between 1 and 15 R/s. Instantaneous behavioral effects to X-ray exposure were seen; the reaction times were "related inversely to the exposure rate in the manner of a neurogenic stimulus."

Kernek and Kimeldorf (1975) experimented with Red Ghost Shrimp, *Callianassa californiensis*, with GE Maxitron X-ray machine for an X-ray exposure for 150 s. This was a behavioral study in which five experiments were conducted using a 52 R/s dose rate and 1 using a 10 R/s dose rate. The responses measured from this study indicate that the X-ray serves as an excitatory stimulus and causes the shrimp to have fast arousal responses including the "motions of appendages" and grooming activity.

Doly et al. (1980a,b) conducted two studies on the retina of albino rats. In the first study, they used X-ray stimulation on the retina of albino rats. They used the X-ray Philips-11409 machine with a measured dose rate of 100 kV and 100 mA while delivering 80-ms pulses. The albino rats were under adaptation to darkness for 4–5 h, before the start of the experiment. The rats were killed and one of the eyes was removed to perform the isolation of the retina to then put it in a petri dish filled with a perfusion medium. The stimulation to the isolated retina was conducted in a dark room with a dim red light (wavelength > 610 nm). Under these conditions the isolated retina remained feasible for 4–6 h. Doly and the others postulated that it is possible to measure an electroretinogram from a "mammalian-isolated" retina that is exposed to X-rays. In addition, the electrophysiological response was due to the functionality and activity of the photoreceptors and the rods in rats because the light-adapted retina was not stimulated by radiation. With such conclusions, Doly and the others in the second study performed X-ray irradiation of rhodopsin extracts of the albino rats through the use of a RT-50 Massiot-Phillips X-ray tube for contact radiotherapy with a measured dose rate of 50 kV and 2 mA. They observed that the stimulation of photoreceptor tissue was caused by the X-rays using ERG (electroretinogram). They postulated that X-rays act on the rhodopsin and that ERG on isolated retinas demonstrated bleaching of the photopigments by X-rays. The retina's comparatively high radiosensitivity compared to isolated nerve fibers lead Doly and the others to believe that X rays act on the rhodopsin.

Savchenko (1993) worked on *Rana temporaria* frogs and used an X-ray diagnostic apparatus and subjected the frogs to stimuli at intervals of 2 min for 30–60 min. The dosage rates given were 3, 8, 16, and 53 R/s. This study concluded that the X-ray phosphene occurred due to the excitation of the rod cells, after oscillatory potentials were found in response to radiation and it was inferred that this excitement occurred in retinal cells, including the cell types horizontal, amacrine, or glial.

A recent study conducted by Lima and others in 2021 does not measure dose rate in R/s but instead in units of grays, which is equivalent to 100 rads. Lima et al. (2021) tested cortical electrical activity in water-deprived Wistar rats after exposure from a Clinac 600 C linear accelerator to visualize the effect of supplementation with omega-3. The rats were exposed for 5.02 min, and the dose applied was 2.4 Gy and in total 18 Gy of X-ray radiation was applied. 9 Gy was on the top of the head and another 9 Gy was applied on the bottom of the head of the rats. Radiation led to an increase in theta rhythm, regardless of omega-3 given or not.

Olfactory responses

Olfactory responses are another reaction observed as a response to ionizing radiation. Responses that fall under this category include olfactory bulb activation.

A study by Feder (1965) exposed Sprague-Dawley rats to X-ray radiation for 0.1s at a rate of 200 mR/s. The significant findings related to olfactory responses from this study were that there was a drastic decrease in the ability of the rat to detect radiation after its olfactory bulbs were destroyed or the nostril was flooded with alcohol. Cooper and Kimeldorf (1966) also used Sprague-Dawley rats and tested the effect of X-rays on the rat's olfactory bulb. In this experiment, a Westinghouse X-ray unit was used, and the animals were exposed to the radiation for 1–5 s. The dose rates ranged between 1.5 and 2.0 R/s, but in some cases were as low as 0.05 R/s. They found that olfactory bulb neurons do respond to X-rays but were not able to make any significant conclusions about the different types of olfactory responses. The strength of the olfactory response in this study indicated that the dose rates of 1.5–2.0 R/s are above the threshold for sensing X-rays. The conclusions from this study were that radiation on the posterior region of the head or body is limited and is inadequate in changing the activity of olfactory bulb neurons.

Proposed neural mechanisms

Neural mechanisms have been investigated in animal studies involving measuring the response of animal sensation and perception after the use of X-rays. From these studies, we deduce three main neural mechanisms by which animals may perceive X-rays: visual perception, signal cascade disruption, and olfactory perception. In vision, the retina mainly underlies this perception (Mathis et al., 2017). In olfaction, distinct reactive oxygen species (ROS) related modifications to the pre-existing environment are likely being sensed unless a sensory protein exists (Cooper and Kimeldorf, 1966). In signal cascade disruption, ROS likely modifies proteins or signaling molecules, acts as a signaling molecule, or perturbs redox balance. Past studies have concluded that radiolysis of water predominates X-rays impact on biological systems leading to the generation of ROS (Zaider). Specifically, pH-neutral aqueous solutions produce ~42 nM diatomic hydrogens, ~60 nM hydrogen atoms, ~71 nM hydrogen peroxide, ~222 nM hydroxyl radicals,

~230 nM solvated electrons per Gy of energy deposited (Spinks and Woods, 1990). ROS is a well-documented 2nd messenger signal, but a comparably vital component of radiosensitivity is tryptophan residues (Davies, 2003). Interestingly, tryptophan residues readily participate in redox chemistry when electron-rich; react rapidly with radiogenic hydroxyl radicals, hydrated electrons, and hydrogen atoms; act as an photosensitizers in UV photoabsorption to generate ROS; and are oxidized by UV (Ehrenshaft et al., 2015). Thus, tryptophan residue interactions likely mediate a biochemical mechanism of radiosensitivity. Across all these mechanisms, ROS and tryptophan residues play a pivotal role in the radiosensitivity of biological systems.

The potential that X-rays mediated behavior derives from direct interaction of X-ray photons with sensory receptors is almost impossible. X-ray absorption is primarily determined by atomic number and since specific tryptophan residues in radiosensitive proteins underlie avoidance behaviors in animals like *C. elegans,* the X-rays certainly operate *via* a chemical intermediate (Gong et al., 2016). Any specialized X-ray detection conformation is improbable. Our lab has calculated that for a "~50 kDa protein… only about one out of 50 million molecules… can be expected to absorb an X-ray photon per Gy of irradiation" (Cannon et al., 2019). In other words, it is highly unlikely that individual high-energy photons are interacting with specialized "X-ray sensitive" protein conformations to initiate a signal transduction mechanism. The anomalistic absorbed X-ray photon (the one out of 50 million for a ~50 kDa protein) would have to be absorbed at the proper region and orientation to cause a conformational change if this hypothesis were true. Such a conformation likely does not exist. Instead, X-ray perception is likely mediated by the most biochemically prevalent byproduct of X-rays passing through a system, ROS, which conveniently is a well-established regulator of various ubiquitous signal transduction pathways. Furthermore, from an evolutionary perspective, if an animal relied on any specialized protein conformation for sensing specific X-ray collisions as indicative to harmful radiation, why would biology evolve to select for highly unlikely collisions with source photons rather than the most ubiquitously active molecules emitting from those source photons? In other words, animals relying on a specialized protein conformation for sensing specific X-ray collisions would be vastly outperformed by animals able to sense the more ubiquitous chemical byproducts of harmful radiation. Biology favors the biochemical evolution of functional proteins and proteins that sense redox balance would have robust applications. Such proteins are known to exist across the animal kingdom despite our limited ability to measure radical chemistry in biological systems (Sies and Jones, 2020). Ultimately, direct photosensing proteins with specialized "single-collision-event" conformations are highly unlikely. A forthcoming paper will discuss mechanisms of X-ray perception more holistically by incorporating a broader range of biology.

Visual perception

Visual perception or sensation of X-rays is a common and well-documented phenomena in humans. Studies of visual perception in humans will be reviewed in a forthcoming paper. In animal studies, photoreceptors and retinas have been implicated in X-ray perception in both vertebrates and invertebrates. The following section is organized chronologically.

In a 1970 study by Jordan Nelmichael, *Hemigrapsus nudus*, or purple shore crabs, were exposed to ionizing and non-ionizing radiation to explore the detection of visual responses (Jordan, 1970). Such bioelectric responses from the compound eye of the purple shore crab have been measured using an electroretinogram with light stimulation. The peak sensitivities to the stimulation of light were a result of each of the light absorption traits of rhodopsin, and fluorescence of the eye systems of the crab when ultraviolet light was used. These effects were taken into consideration because of the direct stimulation of the photopigment and possible secondary stimulation produced by fluorescence. The X-irradiation produced the same electrophysiological responses seen with the visible light at the start and end of the stimulation. Due to the low photon efficiency of this radiation, a direct influence on the photoreceptor mechanism was deemed unlikely.

Surprisingly, Kimeldorf and Fortner (1971) recorded behavioral responses to X-rays in Anthopleura xanthogrammica, a sea anemone, as well. This discovery further implicates X-ray perception across the animal kingdom. When irradiated, the sea anemone showed responses such as oral disc closure and tentacle retraction. Increased exposure resulted in faster tentacle retraction and immediate oral disc closure as a defensive reaction. Kimeldorf and Fortner suggested that a photoreceptor stimulation initiated by a wide spectrum of photon energies (of which need to be classified) were being activated. Another study co-authored by Kimeldorf investigated the immediate behavioral responses of the echinoderms *Strongylocentrotus purpuratus,* or sea urchin, to ionizing radiation (Dedrick and Kimeldorf, 1974). The findings showed that the sensitivity and efficiency of invertebrate's radiation detection improves as sense organs grow, particularly vision and olfaction. Although sea urchins lack visual organs, they have light sensitivity meditated by a dermal light sense. The dermal light sense involves nerve discharges that come from photostimulation of dermal cells. A 1-min exposure to strong light significantly increased the time it took for spines to react to X-rays. Thus, X-rays do not directly affect the subdermal nerve net, but rather excite photoreceptors.

Savchenko (1993) conducted a study recording electroretinogram responses to X-rays in male *Rana temporaria* frogs. The radiation stimulated excitation in the rod cells and X-ray responses were recorded *via* this excitation. Savchenko reported that it was not necessary to isomerize the

photopigment. He found that any process that leads to the "piercing" of the membrane by a radical can set off events that change the cell's excitability, and this could be observed in the retina due to molecular amplification of the signal causing widespread excitation in the frog retina. He conjectured that these X-ray-specific retinal reactions could be used to test the responsiveness of the central nervous system through an X-ray phosphene mechanism. Savchenko concluded that there is a signaling cascade disruption caused by radiation resulting in a visual response.

Overall, photoreceptor systems are implicated in X-ray perception, but more studies are needed to identify mechanisms and receptors that underpin these reactions. Specifically, visual X-ray perception studies have lacked molecular interventions that would delineate whether disrupted phototransduction or direct photoactivation is occurring.

Signaling disruption

The amplifying mechanism suggested by Savchenko is another possible neural mechanism for X-ray perception. Several studies expand upon and conjecture how X-ray irradiation leads to the disruption or amplification of neural signaling. This section is organized chronologically.

Garcia et al. (1956b) noted how Sprague-Dawley rats could be conditioned to alter food and water consumption using various levels of gamma radiation. They suggested that radiation impacted cholinergic nerves in the intestine which induced "an emotional state… reflected by… decrease[d]... consummatory behavior." Years later, the same group discovered that the abdomen was most sensitive to irradiation aversion of all the body parts they irradiated individually (Kimeldorf et al., 1960; Hunt and Kimeldorf, 1962). Nevertheless, head, thorax, abdomen, or pelvis were all sensitive, but none as sensitive as full body irradiation leading them to hypothesize stomach dysfunction underlies radiation's control on behavior. Their hypothesis fails to account for radiosensitivity of organs beyond the stomach. Experiments irradiating the head of opthalmectomized rats would rule out a neural mechanism in the skull, while irradiating the extremities would rule out peripheral nerve responses. Furthermore, X-rays interaction with the phototransduction had not been explored at this point although they knew that the eyes did react. Kimeldorf et al. (1960) conducted a study on the radiation-induced conditioned avoidance behavior in rats, mice, and cats. From these studies, they deduced that the eyes respond to X-rays in a more sensitive dose-dependent manner, than the rest of the body—though they still had not identified any mediators or mechanistic factors for these phenomena. Kimeldorf and Hunt addressed neural responses in the mammalian nervous system, adding that the extent of this enteric neural response was determined by radiation intensity. Furthermore, they suggest that arousal was not dependent upon direct visual stimulation by X-rays noting arousal occurred and persisted after irradiation, implicating a reflex activation of the adrenal medulla. This adrenal response could be directly related to the effects of X-rays or caused by a fear response to the perception of X-rays. Irradiation localized specifically to the head and adrenal medulla separately while measuring adrenal stimulation would rule out whether a direct interaction is occurring or not. In the same year, Barnes (1962) published a study a month before Kimeldorf and Hunt and found that Albino rats of the Sprague-Dawley strain displayed avoidance after radiation. Barnes implicated an early enteric neural response caused by a disturbance of gastric and intestinal mucosa, beginning in duodenum eliciting avoidance behavior.

Garcia and Buchwald (1963) conducted a study using Sprague-Dawley rats to analyze the perception of ionizing radiation by studying behavioral and electrical responses to very low doses of X-rays. They emphasized that they didn't agree with Hunt and Kimeldorf that the behavioral arousal from X-rays is evidence for "direct central neural effects"; instead, they indicate a "peripheral afferent effect" is occurring. They bring up that EEG desynchronization and behavioral arousal does not "constitute evidence for direct effects upon the central nervous system." They instead indicate that (1) there may be a detection mechanism similar to other sensory modalities that leads to an arousal response through the activation of the brainstem reticular formation or (2) there may be another response system with a lower threshold needed that depends on the total dose of radiation and time in order to create an effect. This disagreement with the previous study from Hunt and Kimeldorf (1962) is fascinating; though their data agreed with Hunt and Kimeldorf, they indicate that their hypotheses are different and diverge into indications that there is a peripheral effect instead of a central nervous system effect in the adrenal medulla.

Furthermore, Hunt and Kimeldorf (1964) in another study analyzing behavioral arousal and neural activation as radiosensitive reactions argue that the heart rate and arousal reactions to X-ray exposure in Sprague-Dawley rats tends to reject the idea of stimulation *via* abscopal effects at sites that are away from nervous tissue but agrees with the concept that ionizing radiation can stimulate the nervous system. In this study, they argued that the sensory deprivation could be caused by cortical inhibition and that chemoreceptors are most likely stimulated by ionizing radiation, since they have radiosensitive biochemical systems at the transduction or early amplification stages of receptor function. They suggested future studies of the radiosensitivity of chemoreceptors. They also postulate that penetrating ionizing radiation acts as a stimulus by causing energy transfer with irradiation through large areas of nervous tissue. They state that the effectiveness of radiation as a "distributed stimulus" depends on the "differential density of sensitive structures, the functional organization of neural elements, and the momentary state of excitability of those portions of the nervous system that are exposed." Kimeldorf

then collaborated with Smith, testing the bioelectrical response of the moth eye to beta-radiation, and found in this study that it is not clear if the beta radiation, the stimulus, acts on the receptor or if the effects seen in the moth eye are a secondary effect from fluorescence caused by irradiation (Smith and Kimeldorf, 1964). These two studies use different animal models, and it may be hard to reconcile these two studies. Though receptors and the activity of them can be generalized due to shared receptor functions, contrasting different mechanisms for cascade signaling may be important between vertebrates and invertebrates.

The *Callianassa californiensis*, known as the red ghost shrimp, was used in a study by Kernek and Kimeldorf (1975) for the discovery of behavioral responses and neural mechanisms with the use of X-rays. The removal of the antennules and limitations to the abdomen's exposure to the X-rays did not depress the shrimp's avoidance behavioral response, which indicated the activation of a complex and well distributed chemoreceptor system. The responses from the antennule and swimmeret preparations were very similar and that indicated that there was a common type of chemoreceptor reacting in both sites. Such chemoreceptors were located in all of the macrurus decapod's appendages. Due to the distribution of these chemoreceptors in the red ghost shrimp being studied, the critical receptor was indeed a type of chemoreceptor and the reason for the behavioral responses behind its neural signaling pathway.

There is a clear pattern of non-photoreceptor neural signaling effects identified in these studies in response to ionizing radiation. Future studies are needed to identify specific affected neurons in the central or peripheral nervous system and test the radiosensitivity of receptor types—especially chemoreceptors—and identify how the radiation acts on the receptors themselves.

Olfactory perception

Olfactory perception of X-rays has been observed in animals with well-developed olfaction. In these studies, the neural mechanisms are specifically concerned with the olfactory bulb. This section is organized chronologically.

Cooper and Kimeldorf (1966) examined the activity of neurons in a rat's olfactory bulb in response to X-rays; they illustrated that olfactory bulb neurons do respond when exposed to irradiation through the use of the advancement of a microelectrode going through the olfactory bulb until a unit or response had been obtained with an amplitude that remained stable over a period of at least 5 min. The limitation in the study was that the rate and pattern of unit activity in the olfactory bulb varies greatly from unit to unit under resting conditions, as do the rat's responses to odors, even though several types of responses of olfactory bulb units to X-irradiation were described. Furthermore, the strength of the responses of many units to irradiation indicate that the dose rates that were used in this study are considerably above threshold. There were no "systematic threshold determinations" made in this study, but some units were studied which responded to the accumulated dosages of 20 mR or less delivered at a dose rate of 50 mR/s. The conclusion provided by the authors was that; "We can only conclude at present, therefore, that radiation impinging on the posterior part of the head or on the body only is of inappropriate quality of insufficient intensity [at the dose rates used in this study] to alter the activity of olfactory bulb neuron."

Feder et al. tested the detection of minute doses of ionizing radiation in Sprague-Dawley rats (Feder, 1965; Feder et al., 1966). In the experiments, the opthamlactomized rat learned that the presence of the radiation will come before an electric shock to the paw, indicating the radiation was a cue for the shock. The researchers concluded that a receptor-like mechanism for the detection of the X-rays in the rat is centered in or around the olfactory bulbs. One shortcoming of this study is that their conclusion is not adequately supported; they should have irradiated the olfactory bulb and based their conclusion from that. Another approach to address this shortcoming is to irradiate the olfactory receptors in the nasal area of Sprague-Dawley rats. Perhaps, there is a possibility of detecting X-rays at the peripheral level of the nervous system, at the nose where olfactory receptor neurons are located.

Martinsen and Kimeldorf (1972) used carpenter ants to analyze their prompt detection of ionizing radiation. They suggested that sensory receptors at the antennal flagella had been often answerable for detection and were the cause of the onset of "off" responses, as ants with shellacked antennae did show detection after exposure, suggesting that the effect of the X-rays was centered around or on the antennal receptor.

There is clearly a pattern of signaling cascades within olfactory perception that become impacted by ionizing radiation. In the future, it will be important to identify the regions implicated in signaling cascades in the olfactory bulb area and receptors involved in olfaction.

Discussion and future experiments

Based on reports over several decades, it is evident that animals can sense or perceive X-rays. X-rays were shown to induce neural activity changes, conditioned behavioral responses, and prompt behavioral responses in animals. This is supported by a large number of studies showing rapid behavioral responses that are neuronally mediated and have sensory-like properties involved with the activation of radiation and by studies showing conditioned responses and learned avoidance behavior. It is also evident that these responses vary in type and depend on a variety of mechanisms. The major responses reported in the literature are changes in food and

water consumption, radiotaxis, avoidance of ionizing radiation, behavioral arousal, and neural responses in the olfactory and visual receptors.

We found no linear pattern for changes in food and water consumption, radiotaxis, behavioral arousal, or olfactory responses to increasing doses of ionizing radiation. The search for a pattern was greatly complicated by the fact that these studies were spread over many decades. Over this time, there have been advances in technology and large changes in the way that radiation doses are reported, resulting in a large non-uniformity in how experiments were conducted, and results were reported. Furthermore, there were a large variety of animal models used in the studies. These inconsistencies make generalizations of dose-response relationships difficult.

Broadly speaking, photoreceptors, and to a lesser extent chemoreceptors, are implicated in many of the sensory effects of low dose radiation. However, future research will need to more closely examine whether there is a phosphene effect of some kind in the visual system or whether there truly are receptors within the visual system that respond very specifically to radiation *via* increased excitation or increased amount of generated action potentials. With high radiation doses delivered to the whole body, there is a pattern of avoidance identified in response to ionizing radiation and in rats this response can be mitigated by surgical excision of a segment of one or more splanchnic nerves.

It is clear that the retina and photoreceptors mediate the visual response of X-ray energies, while extraretinal processes may be important in other forms of ionizing radiation generated phosphenes. Fluorescence has often been suggested as a mechanism for visual stimulation, but there is little evidence for this at X-ray energies. The response to low dose X-rays has been shown to have properties much like light perception in many species including the production of light ERGs and neural spiking behavior. There have also been interactions observed between light reception and X-ray reception. Notably, detection often, but not always, requires a dark-adapted photoreceptor and in mammals the rod photoreceptor is implicated. Paradoxically, it has been reported that X-rays do not cause photobleaching of rhodopsin or "visual purple."

In olfactory and chemosensory responses much evidence suggests that the olfactory bulb is the site of action in rats and antennae, or other chemosensory organs are the site of action in invertebrates. Removal of these organs eliminates these sensory responses, and it is possible to observe the neural response electrophysiologically.

Taken together the evidence suggests that brief pulses of low dose X-rays in the range of 0.01–1 Gy per s can activate several classes of sensory receptors through some still poorly understood mechanism. As discussed above, our group believes that ROS production by X-rays and activation of receptor proteins are the most likely mechanism of visual and olfactory response. Past studies have concluded that radiolysis of water predominates X-rays impact on biological systems leading to the generation of ROS (Zaider, 1988). Specifically, pH-neutral aqueous solutions produce ∼42 nM diatomic hydrogens, ∼60 nM hydrogen atoms, ∼71 nM hydrogen peroxide, ∼222 nM hydroxyl radicals, ∼230 nM solvated electrons per Gy of energy deposited (Spinks and Woods, 1990). ROS are well-documented cellular messengers and at higher concentrations oxidative stressors that induce changes in cellular function.

With respect to the doses described in these experiments, one Gray is a substantial radiation dose, but is not significantly dangerous. For context, a human being, on average a 1 Gr whole-body dose would have about a 5% chance of inducing a lethal cancer. The LD50 level for a whole-body dose is about 3.5 Gy, but the risk of death below 3 Gy is effectively zero. For localized doses, 1 Gy to the skin would have no clinical effect, though at levels above about 2–5 Gy it is possible to have effects like transient erythema. However, the tolerance of radiation can vary by orders of magnitude between species. For example, nematodes exhibit a much higher tolerance for radiation than humans. Weidhaas studied the effect of irradiation on the vulva of *C. elegans*; the report found that there is no significant lethality for doses of up to 500 Gy, and with only a small change in the vulva phenotype at 100 Gy (Weidhaas et al., 2006). In 1960, Meyers reported that the dose required for complete sterilization of populations of various species of nematode varied from about 400 Gy to higher than 1,600 Gy. The paper "Oxidative stress pretreatment increases the X-radiation resistance of the nematode Caenorhabditis elegans" looked at the lethality of X-rays on c-elegans; their data shows an LD50 of between 300 and 400 Gy.

Based on these reports, we speculate that X-rays could be used in a way analogous to how visible light is used for optogenetics. Others have used the term "X-genetics" for the use of X-rays for neuromodulation, a nomenclature we will adopt here. As far as we are aware, Rachel Berry and Ge Wang were the first to use this term. The premise of X-genetics is to modulate neural activity by expressing receptor proteins in neurons to confer radiosensitivity to neurons. In other words, we propose that there is an array of metabotropic or ionotropic receptor proteins with neuromodulation potential similar to channelrhodopsin that could be activated by X-rays. The compelling evidence for direct activation of visual receptors by X-rays also suggests that scintillators or transduction of X-rays to light may be an unnecessary component for X-genetics. If ROS production is indeed the mediator for X-ray transduction, then particles or molecules that enhance ROS production may be a more suitable substrate for enhancing X-genetic efficiency.

Author contributions

VM, JB, CR, DJ, and MB conceived the initial ideas and wrote the manuscript. All authors contributed to the article and approved the submitted version.

Conflict of interest

The authors declare that the research was conducted in the absence of any commercial or financial relationships that could be construed as a potential conflict of interest.

Publisher's note

All claims expressed in this article are solely those of the authors and do not necessarily represent those of their affiliated organizations, or those of the publisher, the editors and the reviewers. Any product that may be evaluated in this article, or claim that may be made by its manufacturer, is not guaranteed or endorsed by the publisher.

References

Bachofer, C. S., and Esperance Wittry, S. (1963). Off-response of electroretinogram induced by X-ray stimulation. *Vis. Res.* 3, 51–59. doi: 10.1016/0042-6989(63)90067-1

Bachofer, C. S., and Wittry, S. E. (1961). Electroretinogram in response to X-ray stimulation. *Science* 133, 642–644. doi: 10.1126/science.133.3453.642

Bachofer, C. S., and Wittry, S. E. (1962). Comparison of stimulus energies required to elicit the ERG in response to X-rays and to light. *J. Gen. Physiol.* 46, 177–187. doi: 10.1085/jgp.46.2.177

Baldwin, J., and Grantham, V. (2015). Radiation hormesis: historical and current perspectives. *J. Nucl. Med. Technol.* 43, 242–246. doi: 10.2967/jnmt.115.166074

Baldwin, W. F., and Sutherland, J. B. (1965). Extreme sensitivity to low-level X-rays in the eye of the cockroach Blaberus. *Radiat. Res.* 24, 513. doi: 10.2307/3571642

Baldwin, W. F., Sutherland, J. B., and Habowsky, J. E. J. (1963). Effects of X-rays on electrical activity in the eye of the cockroach *Blaberus giganteus*. *Nature* 199, 616–616. doi: 10.1038/199616a0

Barnes, C. D. (1962). Peripheral neural paths mediating avoidance of radiation in rats. *Am. J. Physiol.* 203, 379–382. doi: 10.1152/ajplegacy.1962.203.2.379

Baylor, E. R., and Smith, F. E. (1958). Animal perception of X-rays. *Radiat. Res.* 8, 466–474. doi: 10.2307/3570438

Bornschein, H., Pape, R., and Zakovsky, J. (1953). Über die Röntgenstrahlenempfindlichkeit der menschlichen Netzhaut. *Naturwissenschaften* 40, 251–251. doi: 10.1007/BF00591563

Cannon, K. E., Ranasinghe, M., Do, A., Pierce, H. M., Millhouse, P. W., Roychowdhury, A., et al. (2019). LITE-1 mediates X-ray avoidance response in C. *elegans*. *BioRxiv*. doi: 10.1101/766568

Casolino, M., Bidoli, V., Di Fino, D., Furano, G., Minori, M., and Morselli, A. (2003a). "Light flashes observations on board Mir and ISS with Sileye experiments," in *International Cosmic Ray Conference*.

Casolino, M., Bidoli, V., Morselli, A., Narici, L., De Pascale, M. P., Picozza, P., et al. (2003b). Space travel: dual origins of light flashes seen in space. *Nature* 422, 680. doi: 10.1038/422680a

Chaddock, T. E. (1972). Visual detection of X-ray by the rhesus monkey. *J. Comp. Physiol. Psychol.* 78, 190–201. doi: 10.1037/h0032179

Charman, W. N., Dennis, J. A., Fazio, G. G., and Jelley, J. V. (1971). Visual sensations produced by single fast particles. *Nature* 230, 522–524. doi: 10.1038/230522a0

Chen, Z., Tsytsarev, V., Finfrock, Y. Z., Antipova, O. A., Cai, Z., Arakawa, H., et al. (2021). Wireless optogenetic modulation of cortical neurons enabled by radioluminescent nanoparticles. *ACS Nano* 15, 5201–5208. doi: 10.1021/acsnano.0c10436

Cooper, G. P., and Kimeldorf, D. J. (1966). The effect of X-rays on the activity of neurons in the rat olfactory bulb. *Radiat. Res.* 27, 75. doi: 10.2307/3571816

Davies, M. J. (2003). Singlet oxygen-mediated damage to proteins and its consequences. *Biochem. Biophys. Res. Commun.* 305, 761–770. doi: 10.1016/s0006-291x(03)00817-9

Dedrick, M. C., and Kimeldorf, D. J. (1974). Immediate behavioral responses of an echinoderm to ionizing radiations. *Physiol. Behav.* 12, 393–398. doi: 10.1016/0031-9384(74)90114-0

Doly, M., Isabelle, D. B., Vincent, P., Gaillard, G., and Meyniel, G. (1980a). Mechanism of the formation of X-ray-induced phosphenes. I. Electrophysiological investigations. *Radiat. Res.* 82, 93–105. doi: 10.2307/3575240

Doly, M., Isabelle, D. B., Vincent, P., Gaillard, G., and Meyniel, G. (1980b). Mechanism of the formation of X ray-induced phosphenes. II. Photochemical investigations. *Radiat. Res.* 82, 430–440. doi: 10.2307/3575310

Ehrenshaft, M., Deterding, L. J., and Mason, R. P. (2015). Tripping up Trp: modification of protein tryptophan residues by reactive oxygen species, modes of detection, and biological consequences. *Free Radic. Biol. Med.* 89, 220–228. doi: 10.1016/j.freeradbiomed.2015.08.003

Feder, B. H. (1965). Central-nervous-system reactions to ionizing radiation. *JAMA* 192, 297–298. doi: 10.1001/jama.1965.03080170025006

Feder, B. H., Garcia, J., Koelling, R. A., and Buchwald, N. A. (1966). Detection of minute doses of ionizing radiation. *Acta Radiol. Ther. Phys. Biol.* 5, 101–104. doi: 10.3109/02841856609139548

Fuglesang, C., Narici, L., Picozza, P., and Sannita, W. G. (2006). Phosphenes in low earth orbit: survey responses from 59 astronauts. *Aviat. Space Environ. Med.* 77, 449–452.

Garcia, J., and Buchwald, N. A. (1963). Perception of ionizing radiation. a study of behavioral and electrical responses to very low doses of X-ray. *Bol. Inst. Estud. Med. Biol. Univ. Nac. Auton. Mex.* 21, 391–405.

Garcia, J., Buchwald, N. A., Feder, B. H., Koelling, R. A., and Tedrow, L. (1964). Sensitivity of the head to X-ray. *Science* 144, 1470–1472. doi: 10.1126/science.144.3625.1470

Garcia, J., and Kimeldorf, D. J. (1960). Some factors which influence radiation-conditioned behavior of rats. *Radiat. Res.* 12, 719–727. doi: 10.2307/3571006

Garcia, J., Kimeldorf, D. J., and Hunt, E. L. (1956b). Conditioned responses to manipulative procedures resulting from exposure to gamma radiation. *Radiat. Res.* 5, 79–87. doi: 10.2307/3570285

Garcia, J., Kimeldorf, D. J., Hunt, E. L., and Davies, B. P. (1956a). Food and water consumption of rats during exposure to gamma-radiation. *Radiat. Res.* 4, 33–41. doi: 10.2307/3570389

Godfrey, E. W., Schenck, H. P., and Silcox, L. E. (1945). Response of the retina to the direct roentgen beam. *Radiology* 44, 229–236. doi: 10.1148/44.3.229

Gong, J., Yuan, Y., Ward, A., Kang, L., Zhang, B., Wu, Z., et al. (2016). The *C. elegans* taste receptor homolog LITE-1 is a photoreceptor. *Cell* 167, 1252–1263.e10. doi: 10.1016/j.cell.2016.10.053

Hardy, W. B., and Anderson, H. K. (1903). On the sensation of light produced by radium rays and its relation to the visual purple. *Proc. R. Soc. Lond.* 72, 393–398.

Holmström, K. M., and Finkel, T. (2014). Cellular mechanisms and physiological consequences of redox-dependent signalling. *Nat. Rev. Mol. Cell Biol.* 15, 411–421. doi: 10.1038/nrm3801

Hunt, E. L., and Kimeldorf, D. J. (1962). Evidence for direct stimulation of the mammalian nervous system with ionizing radiation. *Science* 137, 857–859. doi: 10.1126/science.137.3533.857

Hunt, E. L., and Kimeldorf, D. J. (1964). Behavioral arousal and neural activation as radiosensitive reactions. *Radiat. Res.* 21, 91–110. doi: 10.2307/3571517

Jordan, N. M. (1970). The visual response of the purple shore crab, *Hemigrapsus nudus*, to ionizing and non-ionizing radiations (Dissertation). Available online at: https://ir.library.oregonstate.edu/concern/graduate_thesis_or_dissertations/5t34sn29j

Kernek, S. P., and Kimeldorf, J. (1975). X-ray induced behavioral reactions and detection mechanisms in the shrimp. *Physiol. Behav.* 15, 1–5. doi: 10.1016/0031-9384(75)90269-3

Kimeldorf, D. J., and Fortner, R. W. (1971). The prompt detection of ionizing radiations by a marine coelenterate. *Radiat. Res.* 46, 52–63. doi: 10.2307/3573101

Kimeldorf, D. J., Garcia, J., and Rubadeau, D. O. (1960). Radiation-induced conditioned avoidance behavior in rats, mice, and cats. *Radiat. Res.* 12, 710–718. doi: 10.2307/3571005

Lima, H. G. I. F., Lopes, I. M. S. S., Oliveira, A. P. B., Costa, E. V. L., Aguiar, L. A. A., Lindoso, B. P. A., et al. (2021). Omega-3 effects on electrocorticographic patterns of adult Wistar rats exposed to ionizing radiation. *Biochem. Biophys. Rep.* 26, 100992. doi: 10.1016/j.bbrep.2021.100992

Lipetz, L. E. (1955). The X-ray and radium phosphenes. *Br. J. Ophthalmol.* 39, 577–598. doi: 10.1136/bjo.39.10.577

Maqsudur Rashid, A., Ramalingam, L., Al-Jawadi, A., Moustaid-Moussa, N., and Moussa, H. (2019). Low dose radiation, inflammation, cancer and chemoprevention. *Int. J. Radiat. Biol.* 95, 506–515. doi: 10.1080/09553002.2018.1484194

Martinsen, D. L., and Kimeldorf, D. J. (1972). The prompt detection of ionizing radiations by carpenter ants. *Biol. Bull.* 143, 403–419. doi: 10.2307/1540062

Mathis, T., Vignot, S., Leal, C., Caujolle, J.-P., Maschi, C., Mauget-Faÿsse, M., et al. (2017). Mechanisms of phosphenes in irradiated patients. *Oncotarget* 8, 64579–64590. doi: 10.18632/oncotarget.18719

Matsubara, T., Yanagida, T., Kawaguchi, N., Nakano, T., Yoshimoto, J., Sezaki, M., et al. (2021). Remote control of neural function by X-ray-induced scintillation. *Nat. Commun.* 12, 4478. doi: 10.1038/s41467-021-24717-1

Moloney, J. N., and Cotter, T. G. (2018). ROS signalling in the biology of cancer. *Semin. Cell Dev. Biol.* 80, 50–64. doi: 10.1016/j.semcdb.2017.05.023

Narici, L., De Martino, A., Brunetti, V., Rinaldi, A., Sannita, W. G., and Paci, M. (2009). Radicals excess in the retina: a model for light flashes in space. *Radiat. Meas.* 44, 203–205. doi: 10.1016/j.radmeas.2009.01.005

Narici, L., Titova, E., Obenaus, A., Wroe, A., Loredo, L., Schulte, R., et al. (2020). Multiple sensory illusions are evoked during the course of proton therapy. *Life Sci Space Res (Amst)* 26, 140–148. doi: 10.1016/j.lssr.2020.04.006

Newell, R. R., and Borley, W. E. (1941). Roentgen measurement of visual acuity in cataractous eyes. *Radiology* 37, 54–61. doi: 10.1148/37.1.54

Pinsky, L. S., Osborne, W. Z., and Bailey, J. V. (1975). "Correlation of individual cosmic ray nuclei with the observation of light flashes by Apollo astronauts," in: *International Cosmic Ray Conference*.

Pirie, A. H. (1932). Reading with closed eyes. *Can. Med. Assoc. J.* 27, 488–490.

Pirie, A. H. (1934). An apparatus for reading with closed eyes. *BJR* 7, 111–116. doi: 10.1259/0007-1285-7-74-111

Rödel, F., Fournier, C., Wiedemann, J., Merz, F., Gaipl, U. S., Frey, B., et al. (2017). Basics of radiation biology when treating hyperproliferative benign diseases. *Front. Immunol.* 8, 519. doi: 10.3389/fimmu.2017.00519

Sannita, W. G., Narici, L., and Picozza, P. (2006). Positive visual phenomena in space: a scientific case and a safety issue in space travel. *Vis. Res.* 46, 2159–2165. doi: 10.1016/j.visres.2005.12.002

Savchenko, B. N. (1993). Specific features of the electroretinogram of vertebrates induced by X-rays. *Neurosci. Behav. Physiol.* 23, 49–55. doi: 10.1007/BF01182638

Shin, E., Lee, S., Kang, H., Kim, J., Kim, K., Youn, H., et al. (2020). Organ-specific effects of low dose radiation exposure: a comprehensive review. *Front. Genet.* 11, 566244. doi: 10.3389/fgene.2020.566244

Sies, H., and Jones, D. P. (2020). Reactive oxygen species (ROS) as pleiotropic physiological signalling agents. *Nat. Rev. Mol. Cell Biol.* 21, 363–383. doi: 10.1038/s41580-020-0230-3

Smith, J. C., and Kimeldorf, D. J. (1964). The bioelectrical response of the insect eye to beta-radiation. *J. Insect Physiol.* 10, 839–847. doi: 10.1016/0022-1910(64)90064-2

Smith, J. C., Kimeldorf, D. J., and Hunt, E. L. (1963). Motor responses of moths to low-intensity X-ray exposure. *Science* 140, 805–806. doi: 10.1126/science.140.3568.805

Smith, J. C., and Morris, D. D. (1963). The use of X-rays as the unconditioned stimulus in five-hundred-day-old rats. *J. Comp. Physiol. Psychol.* 56, 746–747. doi: 10.1037/h0041235

Spinks, J. W. T., and Woods, R. J. (1990). "Water and inorganic aqueous systems," in *An Introduction Toradiation Chemistry*. 3rd ed. New York, NY (USA): Wiley-Interscience, 243–307.

Taft, R. B. (1932). Concerning the visibility of Roentgen rays. *Am. J. Roentgenol. Rad. Ther.* 28.

Tafti, D., and Maani, C. V. (2022). *X-ray Production*. Treasure Island, FL: StatPearls Publishing (StatPearls).

Tobias, C. A., Budinger, T. F., and Lyman, J. T. (1971). Radiation-induced light flashes observed by human subjects in fast neutron, X-ray and positive pion beams. *Nature* 230, 596–598. doi: 10.1038/230596a0

Weidhaas, J. B., Eisenmann, D. M., Holub, J. M., and Nallur, S. V. (2006). A *Caenorhabditis elegans* tissue model of radiation-induced reproductive cell death. *Proc. Natl. Acad. Sci. U. S. A.* 103, 9946–9951. doi: 10.1073/pnas.0603791103

Widder, J. (2014). The origins of radiotherapy: discovery of biological effects of X-rays by Freund in 1897, Kienböck's crucial experiments in 1900, and still, it is the dose. *Radiother. Oncol.* 112, 150–152. doi: 10.1016/j.radonc.2014.06.010

Wilhelm-Buchstab, T., Buchstab, B. M., Leitzen, C., Garbe, S., Müdder, T., Oberste-Beulmann, S., et al. (2015). Extraretinal induced visual sensations during IMRT of the brain. *PLoS ONE* 10, e0123440. doi: 10.1371/journal.pone.0123440

Zaider, M. (1988). The link between biology and physics. *Am. J. Clin. Oncol.* 11, 212–219. doi: 10.1097/00000421-198806000-00002

frontiers | Frontiers in Cellular Neuroscience

TYPE Original Research
PUBLISHED 10 August 2022
DOI 10.3389/fncel.2022.913299

OPEN ACCESS

EDITED BY
Maurizio Giustetto,
University of Turin, Italy

REVIEWED BY
Maria Amalia Di Castro,
Sapienza University of Rome, Italy
Andrea Marcantoni,
University of Turin, Italy

*CORRESPONDENCE
Ulf Strauss
ulf.strauss@charite.de

SPECIALTY SECTION
This article was submitted to Cellular Neurophysiology, a section of the journal Frontiers in Cellular Neuroscience

RECEIVED 05 April 2022
ACCEPTED 13 July 2022
PUBLISHED 10 August 2022

CITATION
Döhne N, Falck A, Janach GMS, Byvaltcev E and Strauss U (2022) Interferon-γ augments GABA release in the developing neocortex *via* nitric oxide synthase/soluble guanylate cyclase and constrains network activity.
Front. Cell. Neurosci. 16:913299.
doi: 10.3389/fncel.2022.913299

Interferon-γ augments GABA release in the developing neocortex *via* nitric oxide synthase/soluble guanylate cyclase and constrains network activity

Noah Döhne[1], Alice Falck[1], Gabriel M. S. Janach[1], Egor Byvaltcev[1,2] and Ulf Strauss[1]*

[1]Institute of Cell Biology and Neurobiology, Charité—Universitätsmedizin Berlin, Corporate Member of Freie Universität Berlin, Humboldt-Universität zu Berlin, Berlin, Germany, [2]Institute of Neuroscience, Lobachevsky State, University of Nizhny Novgorod, Nizhny Novgorod, Russia

Interferon-γ (IFN-γ), a cytokine with neuromodulatory properties, has been shown to enhance inhibitory transmission. Because early inhibitory neurotransmission sculpts functional neuronal circuits, its developmental alteration may have grave consequences. Here, we investigated the acute effects of IFN-γ on γ-amino-butyric acid (GABA)ergic currents in layer 5 pyramidal neurons of the somatosensory cortex of rats at the end of the first postnatal week, a period of GABA-dependent cortical maturation. IFN-γ acutely increased the frequency and amplitude of spontaneous/miniature inhibitory postsynaptic currents (s/mIPSC), and this could not be reversed within 30 min. Neither the increase in amplitude nor frequency of IPSCs was due to upregulated interneuron excitability as revealed by current clamp recordings of layer 5 interneurons labeled with VGAT-Venus in transgenic rats. As we previously reported in more mature animals, IPSC amplitude increase upon IFN-γ activity was dependent on postsynaptic protein kinase C (PKC), indicating a similar activating mechanism. Unlike augmented IPSC amplitude, however, we did not consistently observe an increased IPSC frequency in our previous studies on more mature animals. Focusing on increased IPSC frequency, we have now identified a different activating mechanism—one that is independent of postsynaptic PKC but is dependent on inducible nitric oxide synthase (iNOS) and soluble guanylate cyclase (sGC). In addition, IFN-γ shifted short-term synaptic plasticity toward facilitation as revealed by a paired-pulse paradigm. The latter change in presynaptic function was not reproduced by the application of a nitric oxide donor. Functionally, IFN-γ-mediated alterations in GABAergic transmission overall constrained early neocortical activity in a partly nitric oxide–dependent manner as revealed by microelectrode array field recordings in brain slices analyzed with a spike-sorting algorithm. In summary, with IFN-γ-induced,

NO-dependent augmentation of spontaneous GABA release, we have here identified a mechanism by which inflammation in the central nervous system (CNS) plausibly modulates neuronal development.

KEYWORDS

IFN-γ, type-II interferon, cerebral cortex, neuroimmunology, phasic inhibition, MEA, NO

Introduction

IFN-γ, the only type-II IFN, is a pleiotropic inflammatory cytokine and contributes to immune defense against viruses, bacteria, and tumors (Kak et al., 2018). As a part of the adaptive and innate immune response, IFN-γ is mainly secreted by lymphocytes and functionally acts by influencing gene expression, protein synthesis, and induction of an antiproliferative state on most cell types by activating IFN-γ receptor and subsequently the JAK-STAT1 (Janus kinase–signal transducer and activator of transcription 1) pathway (Ivashkiv, 2018). IFN-γ is present in central nervous system (CNS) at baseline levels and is elevated in conditions, such as viral infections, CNS trauma, and cerebral ischemia (Monteiro et al., 2017). In the CNS, IFN-γ serves an important neuron-specific function (Clark et al., 2022), notably by enabling non-cytolytic viral clearance (Patterson et al., 2002).

Beyond its canonical role in controlling intracellular pathogens, a growing body of evidence suggests a direct impact of IFN-γ on the CNS. The absence of IFN-γ leads to neurodevelopmental abnormalities (Monteiro et al., 2015) that differ in healthy vs. inflammatory conditions (Litteljohn et al., 2014). Notably, some neuropsychiatric diseases, such as autism spectrum disorder (ASD; Saghazadeh et al., 2019) and depression (Schmidt et al., 2014), are associated with increased IFN-γ levels. Developmental disturbances due to withdrawal of care (i.e., maternal deprivation) also cause elevated IFN-γ levels as shown in hippocampus and prefrontal cortex of newborn rats (Giridharan et al., 2019) and intrauterine inflammation leads to the accumulation of IFN-γ-producing γ/δ T cells in the brain of fetal mice (Lewis et al., 2021). However, T cells of patients with schizophrenia exhibit decreased production of IFN-γ (Arolt et al., 2000), and the IFN-γ inducer Anaferon improved outcomes in schizophrenia therapy (Vetlugina et al., 2016). As many neuropsychiatric conditions display altered IFN-γ levels, and IFN-γ knockout produces changes in behavior and cognitive performance (for review Monteiro et al., 2017), taken together extant evidence indicates a possible role for IFN-γ in maintaining healthy brain function.

Moreover, IFN-γ has been reported to have fast-acting neuromodulatory properties (Müller et al., 1993; Janach et al., 2022). IFN-γ attenuates I_h, but unlike type-I IFNs (Stadler et al., 2014), it leaves pyramidal neurons' excitability unchanged due to acutely augmented inhibition. In particular, IFN-γ augments GABA (γ-amino-butyric acid)ergic currents in the developed rat neocortex (Janach et al., 2020) by increasing synaptic $GABA_A$ channel number in a protein kinase C (PKC)-dependent manner (Janach et al., 2022). In line with this, IFN-γ augments GABAergic currents in the hippocampus (Brask et al., 2004; Flood et al., 2019).

Such alterations of electrical properties could particularly affect neuronal development that is tightly regulated by early neuronal activity in addition to genetic fate (Kirischuk et al., 2017). With regard to the latter, GABA (in particular) plays a key role (Le Magueresse and Monyer, 2013). For instance, on the one hand, GABA acts excitatory during early neurodevelopment due to elevated intracellular chloride (Ben-Ari, 2002), and during development (excitatory) GABA regulates glutamatergic synapse formation *via* *N*-methyl-D-aspartate receptor (NMDA) activation (Wang and Kriegstein, 2008). On the other hand, GABA may also inhibit neocortical neurons in the first postnatal week (Daw et al., 2007). However, GABAergic neurons also coordinate the development of local cortical networks during a narrow critical postnatal period (Modol et al., 2020). Given these few selected examples of findings concerning the established role of GABA in neuronal development, it does not come as a surprise that the disruption of developing GABAergic neocortical inhibitory network has been implicated in neurodevelopmental disorders, including schizophrenia (Lewis et al., 2005), epilepsy (Cobos et al., 2005), and autism (Pizzarelli and Cherubini, 2011). If IFN-γ altered GABAergic transmission in the developing brain, then this would have broad neurodevelopmental implications, including modulation of cortical maturation.

Taken together, it is clear that the developing brain is vulnerable to disruption of GABAergic transmission, IFN-γ can alter GABAergic currents, and IFN-γ is present at a baseline level or might be elevated by several conditions in the developing brain. Unraveling interactions of the immune system and developing neuronal circuits will foster a better understanding of the biology behind neurodevelopmental diseases. In the long run, such understanding might enable the treatment or even prevention of neurodevelopmental diseases. As a first step, we have here addressed on both, a single cell and a

network level, whether IFN-γ affects inhibitory transmission in neocortical neuronal development, and if so whether the effect is comparable to the one we have previously observed in more mature animals. We have focused on GABAergic synapses at a critical developmental stage (P6–7) during ongoing GABAergic synaptogenesis in rats (Luhmann and Prince, 1991). We mainly investigated spontaneous events because they play a crucial role in synaptic structure and function and act autonomously in regulating synaptic plasticity and homeostasis (Kavalali, 2015).

Materials and methods

Interferon-γ

Chinese hamster ovary or *E. coli*-derived recombinant IFN-γ (U-Cytech, Utrecht, Netherlands; Active Bioscience, Hamburg, Germany) was reconstituted in double distilled water, aliquoted to 1.0 e^5 IU, and stored at −20°C. Aliquots were thawed directly prior to usage. Final concentration for all experiments was 1,000 IU ml^{-1}.

Animals

For all experiments, Wistar pups of either sex were used on postnatal days 6 and 7 (P6–7). All experiments were carried out in agreement with the European Communities Council Directive of 22 September 2010 (2010/63/EU) under the licenses T 0212/14, T-CH 0034/20 for wild-type rats, and T0215/11 for transgenic rats. For some experiments, we used W-Tg(Slc32a1-YFP*)1Yyan vesicular GABA transporter (VGAT)-Venus transgenic rats that express the yellow fluorescent protein Venus in VGAT expressing neurons, developed by Uematsu et al. (2008) that enabled us to identify interneurons in the slice.

Acute slice preparation

As generally described in Zaqout et al. (2019), decapitation was followed by rapid removal of the brain, which then was transferred into carbogenated (95% O_2; 5% CO_2) 2°C sucrose artificial cerebrospinal fluid (sACSF) containing (in mM): 85 NaCl, 2.5 KCl, 1 NaH_2PO_4, 7 $MgCl_2$, 26 $NaHCO_3$, 50 sucrose, 10 D(+)-glucose (Carl Roth, Karlsruhe, Germany), and 0.5 $CaCl_2$ (Merck, Darmstadt, Germany). 300 μM thick coronary slice containing somatosensory cortex were cut using a VT1200S vibratome (Leica, Wetzlar, Germany). Slices were recovered for 30 min in 34°C sACSF and were subsequently held at room temperature in modified ACSF containing (in mM): 92 NaCl, 2.5 KCl, 1.2 NaH_2PO_4, 30 $NaHCO_3$, 25 D(+)-glucose (Carl Roth), 5 sodium ascorbate, 20 2-[4-(2-hydroxyethyl)piperazin-1-yl] ethanesulfonic acid (HEPES), 3 sodium pyruvate, 2 $MgSO_4$, 2 $CaCl_2$ (Merck), and 2 thiourea (VWR Chemicals, Radnor, PA, United States) until recording. All variations of ACSF were continuously carbogenated.

Ex vivo patch clamp recordings

Slices were transferred to a submerged type recording chamber continuously perfused with carbogenated ACSF containing (in mM): 119 NaCl, 2.5 KCl, 1 NaH_2PO_4, 1.3 $MgCl_2$, 26 $NaHCO_3$, 10 D(+)-glucose (Carl Roth), and 2.5 $CaCl_2$ (Merck) at 32 ± 2°C. Slices were visualized using infrared differential interference contrast (DIC) microscopy with a Zeiss Axioskop 2 FS plus (Carl Zeiss, Oberkochen, Germany). Glass micropipettes (2–5 MΩ) were pulled from lead (PG10165-4, WPI, Sarasota, FL, United States) or borosilicate (GB150-10P, Science Products, Hofheim, Germany) glass capillaries using a P-97 micropipette puller (Sutter Instrument, Novato, CA, United States). For IPSC recordings, 6-cyano-7-nitroquinoxaline-2,3-dione (CNQX, 20 μM) and D(-)-2-Amino-5-phosphonopentanoic acid (DAP-5, 25 μM) (Tocris, Bristol, United Kingdom) were added to the perfusate to block glutamatergic ion currents and pipettes were filled with a high chloride internal solution containing (in mM): 140 CsCl (Biomol, Hamburg, Germany), 4 NaCl, 1 $MgCl_2$ (Carl Roth), 10 HEPES, 0.1 ethylene glycol-bis(β-aminoethyl ether)-N,N,N',N'-tetraacetic acid (EGTA), 0.3 GTP, 2 Mg^{2+}−ATP (Merck), (305 mOsm, pH set to 7.25 with KOH), and 5 mM QX-314 (Merck) to improve the signal-to-noise ratio. Calphostin C (Enzo Life Sciences, NY, United States) was dissolved in DMSO at 1 mM and aliquoted to working sizes. Prior to respective experiments, Calphostin C was added to the pipette solution to a final concentration of 100 nM. When Calphostin C was used, slice and pipette were continuously exposed to full-spectrum white light (Bruns et al., 1991). Other drugs in this study included: Bicuculline methiodide (Tocris), *S*-Nitroso-*N*-acetylpenicillamine (SNAP) (cayman chemical, Ann Arbor, MI, United States), 1H-[1,2,4]oxadiazolo[4,3-a]quinoxalin-1-one (ODQ) (Tocris), tetrodotoxin (TTX) (Tocris), and *N*-[3(Aminomethyl)benzyl] acetamidine dihydrochloride (1400W) (Sigma-Aldrich, St. Louis, United States). ODQ was dissolved in dimethylsulfoxide (DMSO) at 100 mM and aliquoted to working sizes. Total DMSO in perfusate never exceeded 0.1%. All other reagents and drugs, unless specified otherwise, were dissolved and aliquoted in double distilled water.

For current-clamp recordings, internal solution contained (in mM) 120 K-Gluconate, 11 EGTA, 10 HEPES, 10 phosphocreatine, 1 $MgCl_2$, 2 Mg^{2+}-ATP, 0.3 GTP, 10 KCl (Merck), and 1 $CaCl_2$ (Carl Roth). After establishing whole-cell configuration, pipette solution was allowed to diffuse into the cell, and blockers were bath applied for at least 5 min before recording started. Spontaneous/miniature inhibitory

postsynaptic current (s/mIPSC) recordings were excluded from analysis when series resistance (R_s) changed by more than 25%, initial IPSC frequency was below 10 events min^{-1} (0.167 events s^{-1}), holding current (that was mainly due Cl^- enhanced tonic inhibition and Cs^+ mediated depolarization, **Supplementary Figure 1A**) changed abruptly or hyperpolarized beyond −800 pA, indicating the development of technical leak. If access resistance changed during experiments, efforts were made to reestablish access, and experiments were discontinued if unsuccessful. IFN-γ exposure time was aimed at 25 min. In some cases, a later time point (up to 30 min) or an earlier time point (minimum 15 min) was used. Reasons included changed series resistance that had to be corrected or sudden changes in holding current. An overview of exposure times is given in **Supplementary Figure 1B**, population data averages are stated in the respective figure legends. Electric activity was recorded using an EPC-10 double amplifier (HEKA Elektronik GmbH, Reutlingen, Germany), digitized at 6.25 kHz after Bessel filtering (2.5 kHz), and stored *via* PatchMaster 2.91 (HEKA). Spontaneous and miniature IPSCs were analyzed using Synaptosoft MiniAnalysis Software (Synaptosoft Inc., Fort Lee, NJ, United States). Negative deflections deviating from baseline by more than 3 RMS (root mean square) noise were counted as IPSCs. Upon manual review, erroneously detected events were removed and missed events were added. For every data point, events from two consecutive minutes of recordings were averaged. For washout experiments, slices were incubated in ACSF containing IFN-γ, CNQX (20 μM), and DAP-5 (25 μM) at 34°C for 30 min. IPSCs were recorded under continuous perfusion of the same solution until stable recording conditions were achieved. Then, IFN-γ was removed from the perfusion. Electrically evoked orthodromic IPSCs have been rarely demonstrated before P14 (Luhmann and Prince, 1991). In this study, stimulating currents (0.02–1 mA, applied for 100 μs, delivered through a 1 MΩ glass electrode filled with ACSF, positioned 150 μm apically and 200 μm laterally of the recorded neuron) reliably evoked delayed inward current responses that could be blocked by bicuculline, confirming their GABAergic identity (**Supplementary Figure 2E**). To avoid stimulus-induced long-term changes in synaptic transmission, paired stimuli were applied at 10 s intervals. For paired-pulse experiments, R_s changes up to 35% were tolerated. Paired-pulse recordings were analyzed using FitMaster v2 × 90.5 (HEKA). For every datapoint, 20 traces were analyzed by dividing the amplitude of the second-evoked IPSC through the amplitude of the first. Of 20 ratios, the mean ratio was calculated for comparison. Current-clamp recordings were analyzed using FitMaster software for spike detection and counting. Calculations requiring polynomial fitting were performed using OriginPro 2022 (OriginLab, Northhampton, MA, United States). Neurons recorded in voltage clamp had a mean capacitance of C_{before} = 118.0 ± 3.4 pF that slightly decreased to C_{after} = 112.0 ± 3.2 pF ($p < 0.0001$, $n = 111$, $N = 42$ paired t-test) over the course of voltage clamp recordings.

Post hoc visualization

For cell selection, pyramidal neurons were identified by their typical morphology in DIC microscopy, VGAT expressing interneurons could be identified *via* fluorescence. To validate correct cell selection, in a subset of recordings, $N_ε$ -(+)-Biotinyl-L-lysine (biocytin) (Invitrogen, Waltham, MA, Unites States) was added to the pipette solution to a final concentration of 1%. After recording, slices were fixed in cold phosphate-buffered saline with 4% paraformaldehyde for 1 h. Then, slices were washed in 0.1 M phosphate buffer and subsequently incubated in 4°C phosphate buffer with 0.3% Triton-X (Sigma-Aldrich), 0.05% NaN_3 (Merck), and fluorescent-conjugated streptavidin (Alexa Fluor 647, 1:1,000, Invitrogen) for 48 h. Following another washing step, slices were mounted and imaged using a laser scanning confocal microscope (FV1000, Olympus, Tokyo, Japan).

Multielectrode array recordings

Neuronal activity was recorded with a Multielectrode Array (MEA), consisting of 60 electrodes in an 8 × 8 layout with electrode diameters of 10 μM, and 200 μM spacing (60MEA200/10iR, Multi Channel Systems (MCS), Reutlingen, Germany). Slices, prepared as described above, were placed in the recording chamber, so that somatosensory cortex covered the electrodes. The recording chamber was briefly drained to ensure contact between slice surface and electrodes. Slices were secured by steel anchors (Warner Instruments, Holliston, United States) and were continually perfused with carbogenated ACSF (4–6 ml min^{-1}), maintained at 30°C by the Pt100 Temperature Controller System (MCS). In all recordings, the K^+-channel blocker 4-Aminopyridine (50 μM, 4-AP, Sigma-Aldrich) was used to enhance activity. Recordings were started after 5 min of stabilization and lasted 30 min, under control and test condition, respectively. Electrical activity was recorded by the MEA 2100-120 system (bandwidth = 1–3,000 Hz, gain = × 10, MCS) and sampled at 10 kHz using Multi Channel Experimenter software (MCS). Given the electrode distance of 200 μm, it is unlikely but possible that events cross the detection threshold on multiple channels. Event sorting was performed with the spyKing circus algorithm (Yger et al., 2018) to avoid repetitive counting. Event detection threshold was set to 8 MAD (mean absolute deviation) from baseline of a given channel. Data were high-pass filtered at 300 Hz (3rd-order Butterworth filter) and whitened using the spyKing circus software.[1] Event sorting was performed over the entire recording, including control and test conditions. Sorted data were reviewed with PHY graphical user interface.[2] For further analysis, we included the

1 https://github.com/spyking-circus/spyking-circus

2 https://github.com/cortex-lab/phy

last 20 min of each condition. Only event clusters with normally distributed amplitudes were considered for analysis.

Statistical analysis and data reporting

The study was designed to enable longitudinal pairwise comparison. Note that a direct comparison of IPSC frequencies between different neurons is hampered by the huge variance of the frequency of GABAergic inputs at this developmental stage that might be due to staggered maturation, and many other factors (for instance slicing angle, depth in the slice, quality of individual preparation, **Supplementary Figures 2A–C**). All statistical analyses were performed using OriginPro 2022 (OriginLab). Datasets were tested for normal distribution using the Shapiro–Wilk test. In case of rejection ($p \leq 0.05$), the Wilcoxon signed-rank test for paired data was used to test for statistical significance. Probability distributions were tested for equality using the Kolmogorov–Smirnov test. Due to low event counts, data for all recordings under a certain experimental condition were pooled for probability distributions. Total number of events analyzed, number of recordings, and number of animals are given in the respective figure legends. When normal distribution could not be rejected, Student's *t*-test or paired Student's *t*-test was used, respectively. The null hypothesis was rejected for $p \leq 0.05$. All data are given in $d_{variable}$ = mean ± standard error of the mean (*P*, statistical test, *n* = number of recordings, *N* = number of animals), unless otherwise specified.

Figures and images

Figures were plotted using OriginPro 2022 (OriginLab). Images of biocytin-filled neurons were adjusted (brightness inversion, contrast, scale bars, z-stack projection) with Fiji software (Schindelin et al., 2012). Final assembly was achieved using Corel Draw 2017 (Corel Corporation, Ottawa, ON, Canada).

Results

Interferon-γ acutely increased sIPSC frequency and amplitude

We have previously found an increased inhibition in the neocortex of late juvenile and adult rats under the influence of IFN-γ (Janach et al., 2020). Given the prominent role of GABAergic transmission in cortical development, herein, we have studied IFN-γ effects on developing neurons. In detail, we whole-cell recorded spontaneous inhibitory postsynaptic currents (sIPSCs) in somatosensory pyramidal layer 5 neurons

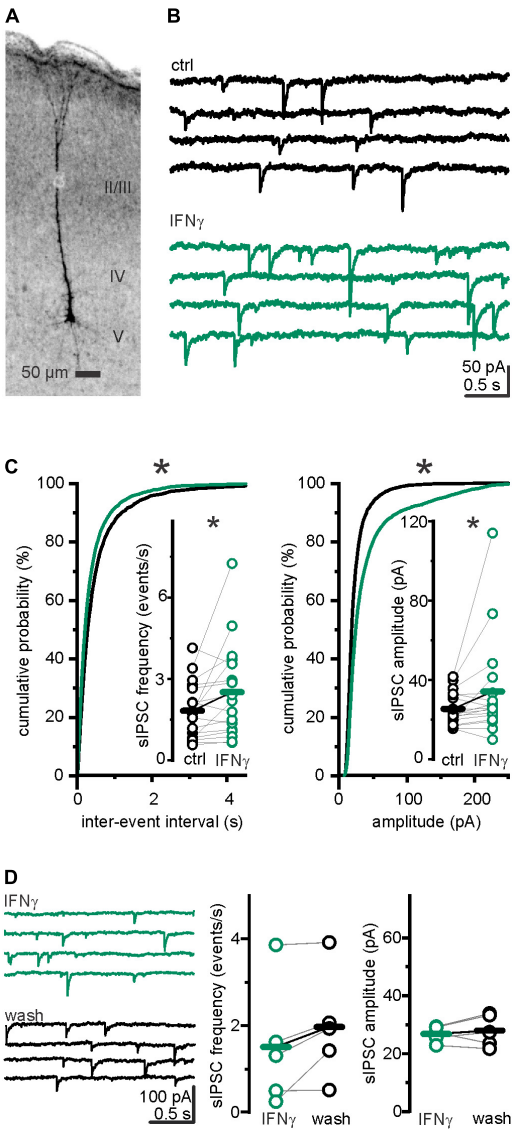

FIGURE 1
IFN-γ increased frequency and amplitude of spontaneous IPSCs in layer 5 pyramidal neurons of P6–7 rats. **(A)** Example image of a biocytin-filled neuron ensuring its layer 5 pyramidal identity. Brightness inverted, z-stack projection at average intensity. **(B)** Current traces with spontaneous IPSCs (sIPSCs) recorded before (control) and under IFN-γ (1,000 IU ml^{-1}). **(C)** Cumulative probability plots of all amplitudes and inter-event intervals (IEI) before (*black*) and under (*green*) IFN-γ application. IFN-γ application shifted the amplitude distribution curve to higher amplitudes ($p < 0.0001$; Kolmogorov–Smirnov test, ctrl = 3,671 events vs. IFN-γ = 5,108 events, *n* = 17 recordings, *N* = 8) and shorter IEIs ($p < 0.0001$; Kolmogorov–Smirnov test, ctrl = 3,637 IEIs vs. IFN-γ = 5,074 IEIs, *n* = 17 recordings, *N* = 8). Population data reveal increased sIPSC frequency and amplitude upon IFN-γ (23.1 ± 0.8 min) (*inset*). **(D)** sIPSC amplitude and frequency remained stable for at least 30 min after IFN-γ was removed from the perfusate, as example traces (*left*) and population data (*right*) show. Series resistance (R_s) slightly increased from $R_{s\ ctrl}$ = 11.1 ± 1.3 MΩ to $R_{s\ IFN\text{-}\gamma}$ = 11.9 ± 1.5 MΩ ($p = 0.02$, paired Wilcoxon signed-rank test, *n* = 17, *N* = 8). Holding current was reduced from I_{ctrl} = −243.2 ± 39.6 pA to $I_{IFN\text{-}\gamma}$ = −153.3 ± 26.6

(Continued)

FIGURE 1
pA (p = 0.02, paired Wilcoxon signed-rank test, n = 17, N = 8). Elevated R_s cannot cause IPSC amplitude or frequency increase. During washout experiments, series resistance slightly increased from $R_{s\ IFN\text{-}\gamma}$ = 14.6 ± 2.1 MΩ to $R_{s\ wash}$ = 16.4 ± 2.4 MΩ (p = 0.04, paired t-test, n = 5, N = 1). Holding current remained comparable ($I_{hold\ IFN\text{-}\gamma}$ = −144.0 ± 26.1 pA vs. $I_{hold\ wash}$ = −121.9 ± 20.0 pA; p = 0.3, paired t-test, n = 5, N = 1). *p < 0.05.

(Figure 1A) from P6 to 7 Wistar rats. As seen in more mature neurons, bath-applied IFN-γ (1,000 IU ml^{-1}) increased the mean amplitude of sIPSCs at P6–7 from I_{ctrl} = 25.6 ± 2.2 pA to $I_{IFN\text{-}\gamma}$ = 36.1 ± 6.7 pA (p = 0.005, Wilcoxon signed-rank test, n = 17, N = 8; Figures 1B,C). Surprisingly, the sIPSC frequency also increased markedly from f_{ctrl} = 1.96 ± 0.27 events s^{-1} to $f_{IFN\text{-}\gamma}$ = 2.73 ± 0.46 events s^{-1} (p = 0.039, Wilcoxon signed-rank test, n = 17, N = 8). We then addressed whether these relatively acute effects ceased upon removal of IFN-γ. We found that, when preincubated with IFN-γ for at least 30 min, sIPSC frequency and amplitude remained stable for at least 30 min during washout ($f_{IFN\text{-}\gamma}$ = 1.51 ± 0.64 events s^{-1} vs. f_{wash} = 1.97 ± 0.56 events s^{-1}, p = 0.09, paired t-test, n = 5, N = 1; $I_{IFN\text{-}\gamma}$ = 26.8 ± 1.2 pA vs. I_{wash} = 28.0 ± 2.5 pA, p = 0.5, paired t-test, n = 5, N = 1; Figure 1D). This indicates that IFN-γ induced changes in GABAergic transmission do not vanish within 30 min. Instead, the trend toward higher frequencies plausibly indicates an inductive effect of IFN-γ on sIPSC frequency. To test whether our intracellular solution produced changes in sIPSC frequency or amplitude during long-term experiments (i.e., if this is merely a time-dependent effect), we recorded sIPSCs for 15–20 min in plain ACSF and found that both, frequency (f_{before} = 2.4 ± 0.3 events s^{-1} vs. f_{after} = 2.5 ± 0.4 events s^{-1}; p = 0.62, paired t-test, n = 11, N = 3) and amplitude (I_{before} = 27.5 ± 3.1 pA vs. I_{after} = 24.3 ± 2.2 pA; p = 0.19, paired t-test, n = 11, N = 3), remained comparable (Supplementary Figure 1C). The considerable increase in sIPSC frequency may suggest a presynaptic action in addition to the previously described postsynaptic mechanism (Janach et al., 2022) behind the increased amplitude. Therewith, the observed augmentation of inhibition by IFN-γ is not only reproduced in the developing rat brain but exhibits a feature that is not consistently observed at later stages of brain development.

Interferon-γ left interneuron excitability unchanged and increased inhibitory postsynaptic currents frequency under voltage-dependent sodium channel blockage

One possible presynaptic mechanism underlying the observed IFN-γ-induced increase in sIPSC frequency in early postnatal development includes augmented interneuron excitability. As medial ganglionic eminence and preoptic area interneurons have completed migration by the end of the first postnatal week (Bortone and Polleux, 2009), we performed current-clamp recordings in layer 5 interneurons that we identified by VGAT-Venus expression. For *post hoc* verification, we filled the neurons with biocytin and visualized them following the recording (Figure 2A). Bath applied IFN-γ left averaged parameters for sub- and suprathreshold excitability comparable, including: Input resistance, determining voltage change upon current injection, $R_{in\ ctrl}$ = 302.0 ± 19.5 MΩ vs. $R_{in\ IFN\text{-}\gamma}$ = 315.2 ± 39.2 MΩ, (p = 0.67, paired t-test, n = 15, N = 7), rheobase, lowest current capable of eliciting a single action potential, $I_{rheobase\ ctrl}$ = 83.7 ± 4.9 pA vs. $I_{rheobase\ IFN\text{-}\gamma}$ = 86.3 ± 9.7 pA (p = 0.79, paired t-test, n = 15, N = 7), slope of the frequency–current relationship $FI\text{-}slope_{ctrl}$ = 358.0 ± 44.5 Hz nA^{-1} vs. $FI\text{-}slope_{IFN\text{-}\gamma}$ = 362.2 ± 40.9 Hz nA^{-1} (p = 0.9, paired t-test, n = 15, N = 7) and frequency at 2 × rheobase $f_{2xRB\ ctrl}$ = 28.8 ± 3.7 Hz vs. $f_{2xRB\ IFN\text{-}\gamma}$ = 31.1 ± 4.0 Hz (p = 0.5, paired t-test, n = 12, N = 5). Notably, FI-slope and firing frequency at 2 × rheobase are parameters that reflect a neuron's input–output relationship (Figures 2B,C).

Given the high variability and axonal divergence of GABAergic interneurons, we could not exclude subtype-specific IFN-γ action on interneuron excitability. We therefore next investigated whether the observed effect is dependent on presynaptic firing. Because IPSCs that might be elicited by presynaptic action potentials were not distinguishable from those resulting from spontaneous vesicle release by amplitude (Supplementary Figure 1D), we investigated the spontaneous vesicle release separately. We recorded miniature IPSCs (mIPSCs) from layer 5 pyramidal neurons in the presence of tetrodotoxin (TTX, 1 μM), a blocker of voltage-gated sodium channels. Despite continuously suppressed interneuronal firing, upon IFN-γ application mIPSC frequency increased from f_{ctrl} = 1.93 ± 0.27 events s^{-1} to $f_{IFN\text{-}\gamma}$ = 2.43 ± 0.34 events s^{-1} (p = 0.04, paired t-test, n = 18, N = 8) and amplitude increased from I_{ctrl} = 23.5 ± 2.8 pA to $I_{IFN\text{-}\gamma}$ = 25.7 ± 3.4 pA (p = 0.03, Wilcoxon signed-rank test, n = 18, N = 8) (Figures 2D,E). It remained possible that synapses of distinct interneuron groups (that connect to different parts of the neuron) are differentially affected by IFN-γ. Because the kinetics of synaptic currents, in particular the rise time (Xiang et al., 2002), give insights on synapse localization along the somatodendritic axis (e.g., perisomatic vs. dendritic site), we analyzed 10–90% rise times of mIPSCs before and after IFN-γ application and found that the mean rise time remained similar (rise $time_{ctrl}$ = 3.7 ± 0.4 ms vs. rise $time_{IFN\text{-}\gamma}$ = 3.9 ± 0.4 ms, p = 0.5, paired t-test, n = 18, N = 8). However, the cumulative probability distribution reveals a slight shift toward shorter rise times (Figures 2F,G). Because of the small yet significant difference between the probability distributions, we are not confident that this can

10.3389/fncel.2022.913299

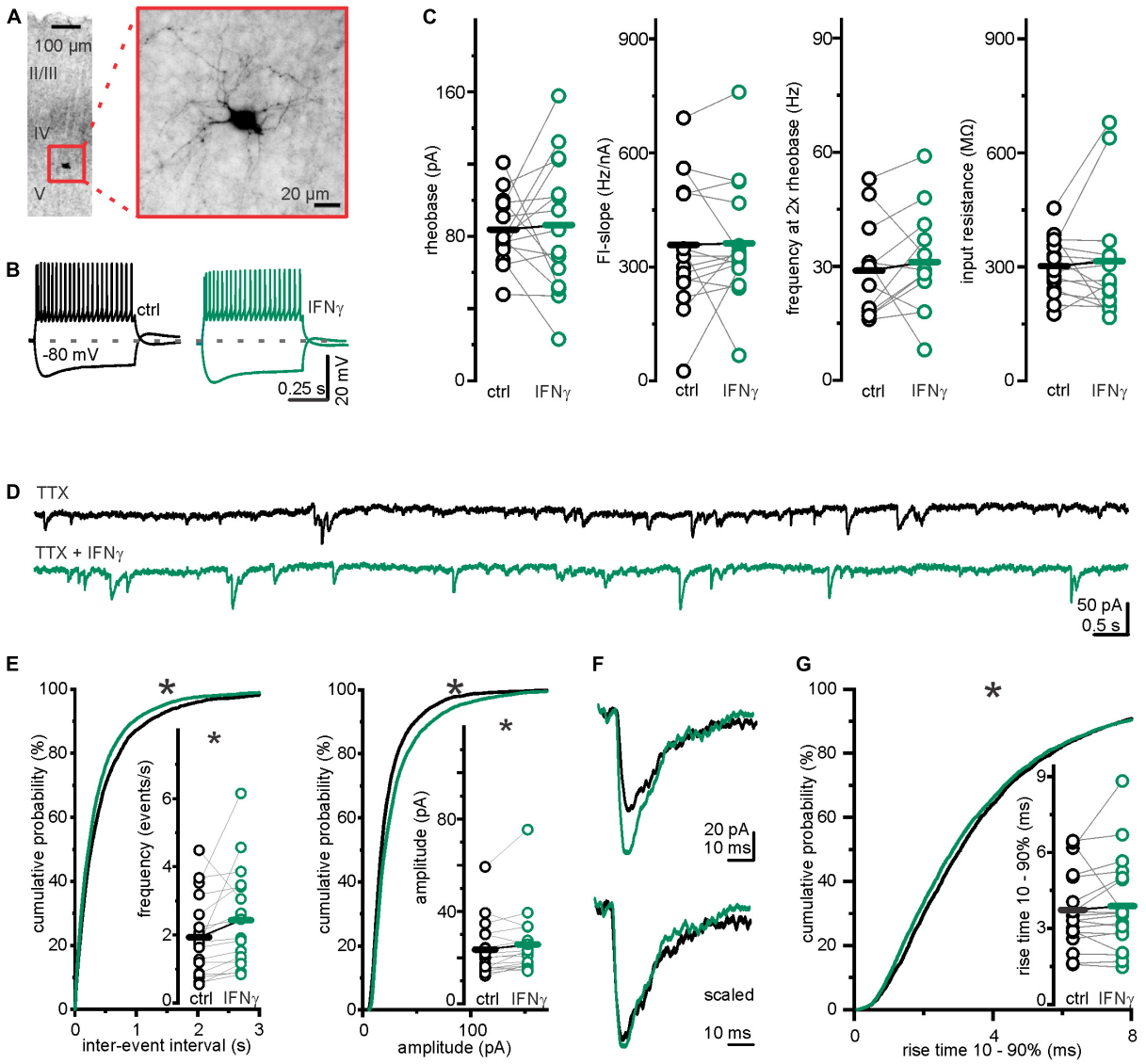

FIGURE 2

Changes in inhibitory transmission were not caused by interneuronal excitability alterations. **(A)** Example image of a *post hoc* biocytin staining, confirming layer 5 localization and interneuron morphology. **(B)** Example interneuronal voltage traces upon rectangular current injections before (*black*) and under (*green*) 25 min of continuous bath application of IFN-γ. **(C)** IFN-γ did not consistently affect interneuron excitability. Averages of excitability parameters: rheobase, FI-slope, firing frequency at 2 × rheobase, and input resistance remained comparable after 20–30 min of continuous application of IFN-γ. **(D)** Traces of miniature IPSCs (mIPSCs) recorded from layer 5 pyramidal neurons before (*black*) and with (*green*) 24.6 ± 1.0 min of continuous bath application of IFN-γ. Continuous bath application of tetrodotoxin (1 µM) suppressed action potential derived IPSCs. **(E)** Frequency and amplitude of mIPSCs were significantly increased following continuous bath application of IFN-γ for 24.6 ± 1.0 min. Interevent interval (IEI) probability plot is shifted to shorter IEIs upon IFN-γ ($p < 0.0001$, Kolmogorov–Smirnov test, ctrl = 4,139 IEIs vs. IFN-γ = 5,221 IEIs, 18 recordings, $N = 8$), amplitude probability is shifted to larger amplitudes ($p < 0.0001$, Kolmogorov–Smirnov test, ctrl = 4,175 events vs. IFN-γ = 5,257 events, 18 recordings, $N = 8$). **(F)** Exemplary mIPSCs recorded from the same neuron before (*black*) and under IFN-γ (*green*). The lower traces are peak-scaled for comparability. **(G)** IFN-γ shifted the rise time probability distribution of mIPSCs toward faster rise times (below 60%) ($p = 0.001$, Kolmogorov–Smirnov test, ctrl = 4,175 events vs. IFN-γ = 5,257 events, 18 recordings, $N = 8$). Mean rise time remained comparable (*inset*). For mIPSC recordings, R_s and I_{hold} remained comparable: $R_{s\ ctrl} = 13.7 \pm 1.7$ MΩ vs. $R_{s\ IFN\text{-}\gamma} = 13.8 \pm 1.5$ MΩ ($p = 0.9$, paired *t*-test, $n = 18$, $N = 8$); $I_{hold\ ctrl} = -298.0 \pm 36.0$ pA vs. $I_{hold\ IFN\text{-}\gamma} = -226.7 \pm 22.5$ pA ($p = 0.09$, paired Wilcoxon signed-rank test, $n = 18$, $N = 8$). *$p < 0.05$.

be interpreted solely as an increased portion of perisomatic inhibition upon IFN-γ addition. A better distinction/a greater gap might be stashed by the relative electrotonic compactness of developing neurons.

Taken together, we have found that the IFN-γ-induced increase in sIPSC frequency appears independent of and cannot be attributed to an increase in layer 5 interneuron excitability or presynaptic firing.

Protein kinase C inhibitor calphostin C, applied to the postsynaptic neuron, prevented interferon-γ mediated increase in mIPSC amplitude, but not frequency

We have previously reported that IFN-γ augments GABAergic currents by promoting postsynaptic membrane association of $GABA_A$ receptors *via* a PKC-dependent mechanism (Janach et al., 2022) in late juvenile rats. To test whether the observed increase in s/mIPSC frequency is caused by higher amplitudes (i.e., whether more amplitudes are elevated above baseline noise levels), we recorded mIPSCs under postsynaptic block of PKC by Calphostin C (100 nM). Calphostin C in the postsynaptic neuron prevented an increase in mIPSC amplitude upon IFN-γ application ($I_{CalC\ ctrl}$ = 24.1 ± 3.7 pA vs. $I_{CalC\ IFN_{-\gamma}}$ = 25.3 ± 4.2, p = 0.4, Wilcoxon signed-rank test, n = 8, N = 2, **Figure 3**). However, mIPSC frequency increased from $f_{CalC\ ctrl}$ = 2.36 ± 0.3 events s^{-1} to $f_{CalC\ IFN_{-\gamma}}$ = 3.52 ± 0.42 events s^{-1} (p = 0.02, paired t-test, n = 8, N = 2).

These findings suggest that the observed IFN-γ-induced IPSC amplitude increase at the end of the first postnatal week is both postsynaptic and PKC mediated, as previously described for older stages (Janach et al., 2022). In addition, they indicate separate mechanisms for IPSC amplitude and frequency increase upon IFN-γ application. Thus, the persistence of the IFN-γ-induced increase in frequency under block of the major known postsynaptic mediator renders a postsynaptic contribution to the frequency effect unlikely.

The interferon-γ-induced increase in sIPSC frequency was mimicked by nitric oxide and depended on inducible nitric oxide synthase and soluble guanylate cyclase

IFN-γ induces nitric oxide (NO) production (Blanchette et al., 2003). NO is also a known regulator of synaptic release (reviewed in Hardingham et al., 2013): NO donors increase (Li et al., 2004; Yang and Cox, 2007) and knockout of NO receptor soluble guanylate cyclase (sGC) decreases IPSC frequencies (Wang et al., 2017). Therefore, the IFN-γ induced elevation of IPSC frequency we observed in pyramidal neurons at P6–7 might be caused by elevated NO levels. Decreased IPSC frequencies upon NO, however, have been reported (Lee, 2009).

To test whether NO is sufficient to induce an increase in inhibitory release at P6–7, we recorded sIPSCs and added SNAP (300 μM), an NO releasing agent widely used to study the impact of NO on neurophysiology (Li et al., 2004). Within 5 min, sIPSC frequency increased from f_{ctrl} = 2.79 ± 0.36 events s^{-1} to f_{SNAP} 3.32 ± 0.43 events s^{-1} (p = 0.002, paired t-test, n = 11, N = 3), while sIPSC amplitude remained comparable (I_{ctrl} = 24.0 ± 2.8 vs. I_{SNAP} = 22.2 ± 1.6 pA; p = 0.5, Wilcoxon signed-rank test, n = 11, N = 3; **Figure 4A**). NO donors can activate leaky, Cs^+ sensitive, K^+-channels (Kang et al., 2007). In our experiments, however, the Cs^+ containing pipette solution should omit putative K^+ currents. Accordingly, holding currents remained similar upon SNAP application: $I_{hold\ ctrl}$ = −265.8 ± 44.3 pA vs. $I_{hold\ SNAP}$ = −262.9 ± 45.9 pA p = 0.73, paired t-test, n = 11, N = 3).

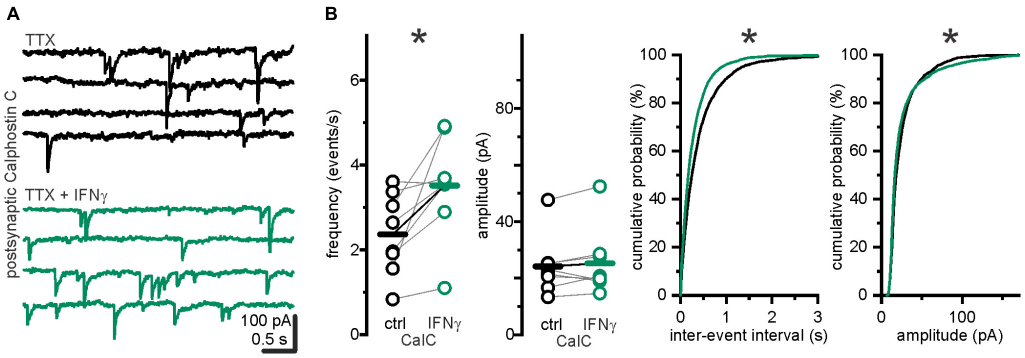

FIGURE 3
IFN-γ increased mIPSC frequencies when amplitude augmentation was suppressed by postsynaptic PKC inhibition *via* calphostin C. **(A)** Example traces of mIPSCs recorded under postsynaptic intracellular application of PKC inhibitor Calphostin C (100 nM) before (*black*) and with IFN-γ (*green*). **(B)** Under intracellular PKC inhibition, IFN-γ, bath applied for 25.0 ± 1.0 min, increased mIPSC frequency and shifted IEI probability distribution toward shorter IEIs (p < 0.0001, Kolmogorov–Smirnov test, ctrl = 2,254 IEIs vs. IFN-γ = 3,359 IEIs, 8 recordings, N = 2). Mean amplitudes remained comparable, however, amplitude probability distribution was slightly shifted toward lower amplitudes (below 80%), as well as higher amplitudes (above 90%) (p < 0.0001, Kolmogorov–Smirnov test, ctrl = 2,270 events vs. IFN-γ = 3,375 events, 8 recordings, N = 2). Series resistance slightly increased from $R_{s\ CalC\ ctrl}$ = 15.4 ± 1.9 MΩ to $R_{s\ CalC\ IFN_{-\gamma}}$ = 17.5 ± 2.2 MΩ (p = 0.001, paired t-test, n = 8, N = 2), holding current slightly decreased from −196.9 ± 27.1 pA to −121.1 ± 11.2 pA (p = 0.02, paired t-test, n = 8, N = 2). *p < 0.05.

10.3389/fncel.2022.913299

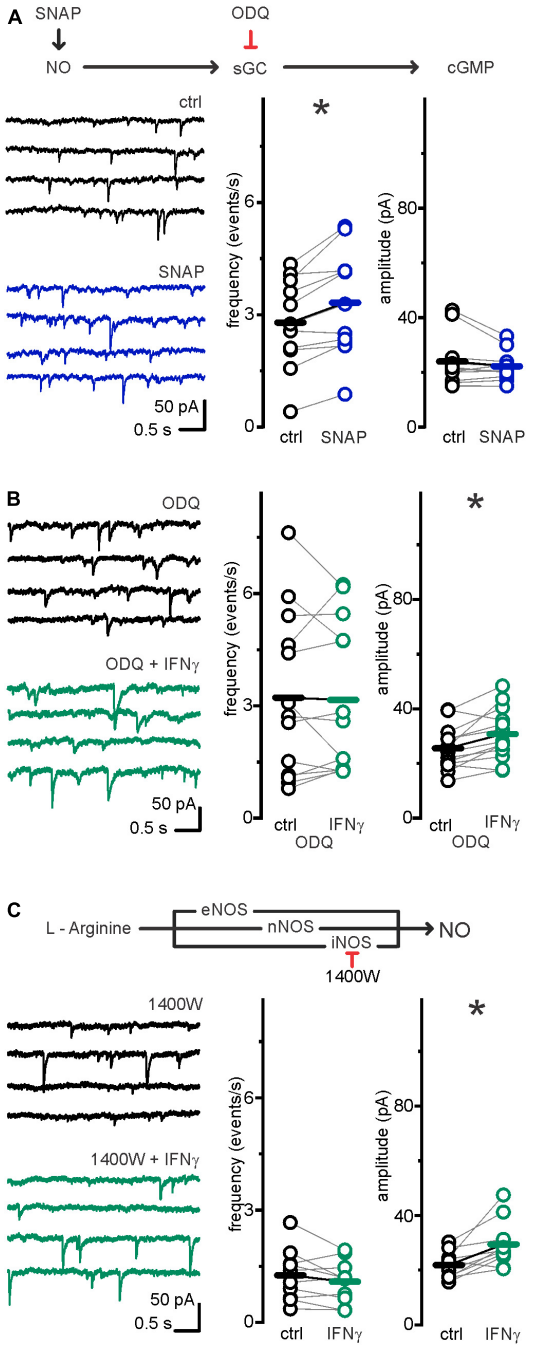

FIGURE 4
Increase in IPSC frequency, but not amplitude, depended on iNOS–NO–cGC–pathway. **(A)** *Upper row:* Drug interactions. SNAP spontaneously degrades, thereby releasing NO. ODQ selectively inhibits NO receptor soluble guanylate cyclase (sGC). *Lower row:* NO donor SNAP mimics IFN-γ effect on frequency but not amplitude: following continuous bath application of SNAP (300 μM) for 5 min, sIPSC frequency, but not amplitude, was significantly increased. Example traces left and grouped data right. Series resistance and holding current remained comparable: $R_{s\ ctrl}$ = 12.5 ± 1.2 MΩ vs. $R_{s\ SNAP}$ = 12.7 ± 1.2 MΩ (p = 0.65, paired t-test, n = 11, N = 3). $I_{hold\ ctrl}$ = −265.8 ± 44.3 pA vs. $I_{hold\ SNAP}$ = −262.9 ± 45.9 pA (p = 0.73, paired t-test, n = 11, N = 3). **(B)** sGC inhibitor ODQ (100 μM) inhibited sIPSC frequency, but not amplitude increase upon IFN-γ, bath applied for 23.1 ± 1.1 min. Example current traces left, grouped data right. Series resistance and holding current remained comparable: $R_{s\ ODQ\ ctrl}$ = 12.1 ± 1.8 MΩ vs. $R_{s\ ODQ\ IFN\text{-}\gamma}$ = 11.8 ± 1.5 MΩ (p = 0.6, paired t-test, n = 13, N = 7). $I_{hold\ ODQ\ ctrl}$ = −365.8 ± 45.1 pA vs. $I_{hold\ ODQ\ IFN\text{-}\gamma}$ = −306.3 ± 33.5 pA (p = 0.1, paired t-test, n = 13, N = 7). **(C)** NO is produced by three isoforms of nitric oxide synthase [inducible (iNOS), neuronal (nNOS), and endothelial (eNOS)]. In the presence of iNOS inhibitor 1400W (10 μM), IFN-γ, bath applied for 22.1 ± 0.8 min, increased sIPSC amplitude, but not frequency. Example current traces left, grouped data right. Series resistance and holding current remained comparable: $R_{s\ 1400W\ ctrl}$ = 14 ± 1.7 MΩ vs. $R_{s\ 1400W\ IFN\text{-}\gamma}$ = 13.6 ± 1.6 MΩ (p = 0.66, paired t-test, n = 10, N = 4). $I_{hold\ 1400W\ ctrl}$ = −319.9 ± 34.6 pA vs. $I_{hold\ 1400\ W\ IFN\text{-}\gamma}$ = −308.4 ± 43.6 pA (p = 0.13, paired t-test, n = 10, N = 4). *p < 0.05.

NO has been shown to impact GABAergic synaptic release *via* binding to its direct receptor sGC (Wang et al., 2017), and sGC is expressed in layer 5 neurons around P6–7 (Ding et al., 2005). If IFN-γ effects on presynaptic release are NO-mediated, blocking sGC should abolish them. Therefore, we tested this by utilizing ODQ (100 μM), a selective sGC blocker (Yang and Cox, 2007; Wang et al., 2017). Indeed, IFN-γ application failed to increase the sIPSC frequency in the presence of ODQ ($f_{ODQ\ ctrl}$ = 3.22 ± 0.61 vs. $f_{ODQ\ IFN\text{-}\gamma}$ = 3.16 ± 0.56 events s^{-1}; p = 0.67, Wilcoxon signed-rank test, n = 13, N = 7). The IFN-γ induced increase in sIPSC amplitudes from $I_{ODQ\ ctrl}$ = 25.5 ± 2.2 to $I_{ODQ\ IFN\text{-}\gamma}$ = 30.8 ± 2.6 pA (p = 0.005, paired sample t-test, n = 13, N = 7), however, persisted under ODQ application (**Figure 4B**). This suggests that NO binding to sGC specifically mediates the increase in sIPSC frequency.

IFN-γ may induce NO production *via* inducible nitric oxide synthase (iNOS) (Stuehr and Marletta, 1987). To assess whether iNOS is involved in presynaptic IFN-γ effects, we recorded sIPSCs in neocortical pyramidal neurons in the presence of the potent and irreversible iNOS inhibitor 1400W (Garvey et al., 1997). We observed that the addition of 1400W (10 μM) reliably prevented sIPSC frequency increase upon IFN-γ application: Under 1400W, IFN-γ increased sIPSC amplitude ($I_{1400W\ ctrl}$ = 21.8 ± 1.6 to $I_{1400W\ IFN\text{-}\gamma}$ = 29.4 ± 2.7 pA; p = 0.007, paired t-test, n = 10, N = 3), whereas sIPSC frequency remained comparable ($f_{1400W\ ctrl}$ = 1.26 ± 0.22 to $f_{1400W\ IFN\text{-}\gamma}$ = 1.09 ± 0.18 events s^{-1}, p = 0.16, paired t-test, n = 10, N = 3; **Figure 4C**). Of note, although 1400W may partly block neuronal (n)NOS (Garvey et al., 1997) with a nominal IC_{50} of 7.3 μM (Alderton et al., 2001), concentrations needed to effectively inhibit nNOS are ≥100 μM (Pigott et al., 2013).

In summary, these data indicate that IFN-γ increases presynaptic GABA release in an iNOS and sGC-dependent fashion.

10.3389/fncel.2022.913299

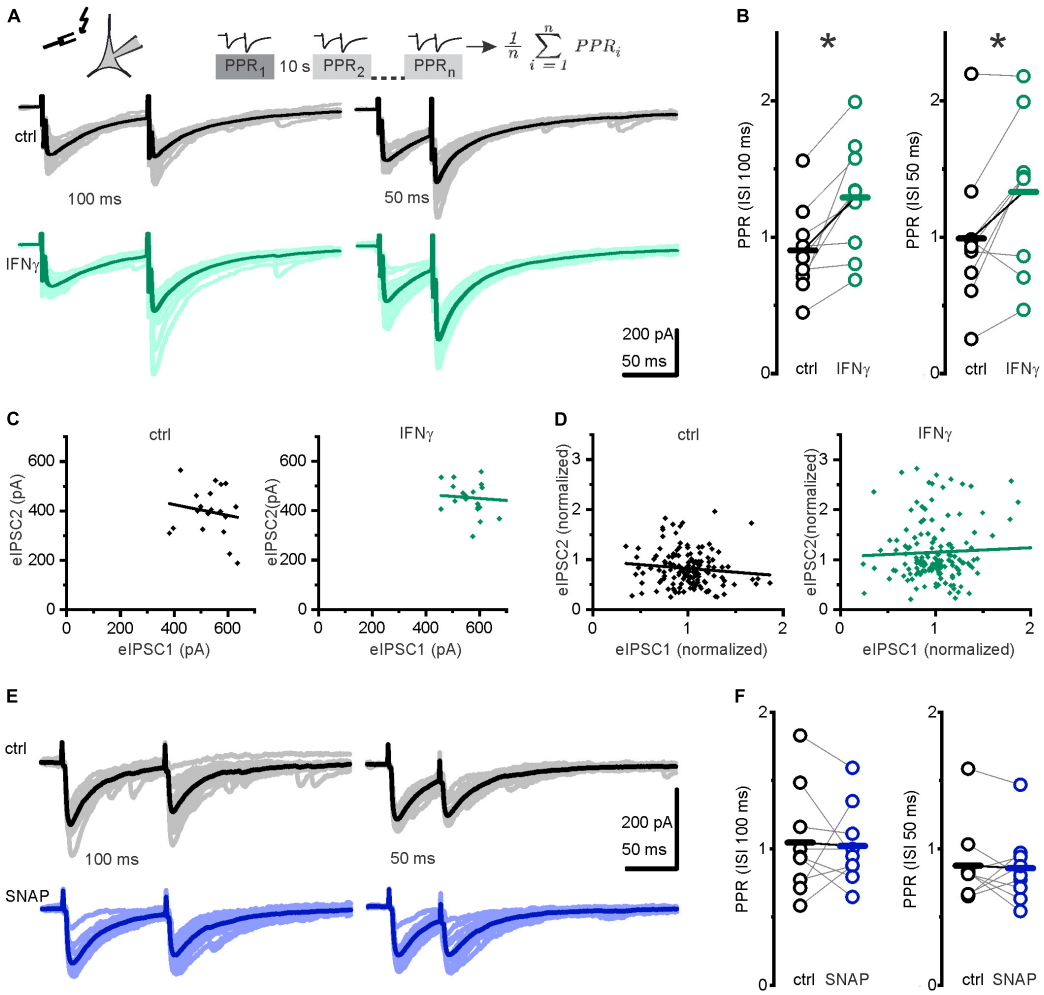

FIGURE 5
IFN-γ promoted paired-pulse facilitation. **(A)** *Upper row*: Paired-pulse paradigm: two consecutive IPSCs were evoked by electrical stimulation at 100 or 50 ms interstimulus interval (ISI). The paired-pulse ratio (PPR) was calculated by division of the second eIPSC amplitude by the first eIPSC amplitude. Twenty individual paired-pulse ratios were recorded and averaged for every data point. Stimulation was paused for 10 s between each pair. *Lower row:* Pairs of evoked IPSCs at 100 ms ISI (*left*) and 50 ms ISI (*right*), without (*black*) and with IFN-γ (*green*). Darker lines represent averages, stimulus artifacts truncated for clarity. Note comparable kinetics of evoked and spontaneous IPSCs of interfering sIPSCs during eIPSC decay. **(B)** IFN-γ, bath applied for 20 min, increased PPR (second amplitude divided by first amplitude). **(C,D)** PPR appears to be independent on previous release. **(C)** Plot of peak amplitudes of eIPSC2 vs. eIPSC1 for individual paired pulses from one neuron before (*ctrl, black*) and under 20 min of IFN-γ (*IFN-γ, green*). **(D)** Plot of normalized amplitude of eIPSC2 against eIPSC1 for all neurons investigated. Amplitudes were normalized to mean value of eIPSC1 for each pair. Lines represent linear regression [correlation coefficient −0.16 (p = 0.5) for ctrl and −0.08 (p = 0.7) for IFN-γ for one neuron **(C)** and −0.11 (p = 0.17) for ctrl and 0.04 (p = 0.6) for IFN-γ for all neurons **(D)**]. **(E)** Example traces of paired-pulse recordings before (*black*) and under (*blue*) application of the NO donor SNAP. Trace averages are shown in strong colors, and individual traces in light colors. **(F)** Paired-pulse ratios remained comparable after the application of SNAP (300 μM) for 5 min. Series resistance slightly increased from $R_{s\ ctrl}$ = 11.1 ± 0.8 MΩ to $R_{s\ IFN-\gamma}$ = 13.5 ± 1.0 MΩ (p = 0.01, paired t-test, n = 9, N = 6). Holding current remained grossly comparable $I_{hold\ ctrl}$ = −316.7 ± 34.6 pA vs. $I_{hold\ IFN-\gamma}$ = −252.4 ± 35.9 pA, p = 0.06, paired t-test, n = 9, N = 6). For SNAP experiments, series resistance and holding current remained comparable ($R_{s\ ctrl}$ = 18.4 ± 2.5 MΩ vs. $R_{s\ SNAP}$ = 19.8 ± 2.5 MΩ, p = 0.1, paired t-test, n = 9, N = 3; $I_{hold\ ctrl}$ = −185.7 ± 36.0 pA vs. $I_{hold\ SNAP}$ = −127.3 ± 13.6 pA). *p < 0.05.

Interferon-γ facilitated short-term synaptic plasticity in GABAergic presynapses

Spontaneous and evoked GABA release neither completely overlaps nor is entirely separable (Horvath et al., 2020). To differentiate between IFN-γ effects on evoked vs. spontaneous GABA release, we used a paired-pulse paradigm revealing a paired-pulse ratio (PPR) that is commonly seen as an index of release probability (Kravchenko et al., 2006). We recorded eIPSCs evoked by pairs of stimuli at interstimulus intervals (ISI) of 100 or 50 ms. IFN-γ, bath applied for 20 min, consistently increased the PPR (defined as amplitude of the second response divided by the amplitude of the first

response) at both intervals tested (from $PPR100ms_{ctrl}$ = 0.9 ± 0.1 to $PPR100ms_{IFN\text{-}\gamma}$ = 1.3 ± 0.1, p = 0.005, paired t-test, n = 9, N = 6 and from $PPR50ms_{ctrl}$ = 1.0 ± 0.2 to $PPR50ms_{IFN\text{-}\gamma}$ = 1.3 ± 0.2, p = 0.02, paired t-test, n = 9, N = 6; **Figures 5A,B**), i.e., it shifted the PPR toward facilitation. To estimate whether the PPR depends on the initial eIPSC amplitude, we used linear regression analysis in plots of second eIPSC amplitude vs. first eIPSC amplitude. Under control conditions, correlation coefficients (Pearson's r) ranged from −0.6 to 0.1, none of these were statistically significant. Under IFN-γ application, correlation coefficients ranged from −0.67 to 0.45, one point of which was statistically significant at r = −0.46, p = 0.04. Using normalized amplitudes, we then pooled all experiments in each group. Pooled analysis showed no correlation between first and second eIPSC amplitudes (r_{ctrl} = −0.11, p = 0.17; $r_{IFN\text{-}\gamma}$ = 0.04, p = 0.6, **Figures 5C,D**). This implies that PPR under control conditions and under the influence of IFN-γ does not depend on previous release as is seen in more mature rat neocortical pyramidal neurons (**Supplementary Figures 2F,G**; Xiang et al., 2002).

Because we have here investigated short-term plasticity (i.e., the ratio of consecutive eIPSC amplitudes at a given time point), we slightly released the restrictions on R_s for this particular series (see section "Materials and methods"). Subsequently, only four recordings matched our usual R_s constraints for absolute amplitude comparison in long-term recordings. Amplitudes remained comparable in a preliminary analysis of absolute amplitude values of evoked potentials in these (**Supplementary Figure 2D**). This is in contrast to the amplitude increase both in s/mIPSCs evinced in this study and in eIPSCs of more mature neurons studied previously (Janach et al., 2020). Moreover, while the release probability for s/mIPSC increased, the one for eIPSC probably decreased upon IFN-γ addition, thereby masking the (postsynaptic) IFN-γ effects. Given this, as well as the lack of PPD under control conditions, evoked release might be constrained in immature GABAergic synapses.

To test whether NO might contribute to IFN-γ-induced paired-pulse facilitation, we recorded another series using the paired-pulse paradigm and observed whether NO donor SNAP has an effect on PPR. SNAP (300 μM), applied for 5 min, did not alter the PPR at 100 or 50 ms ISI ($PPR100ms_{ctrl}$ = 1.0 ± 0.1 vs. $PPR100ms_{SNAP}$ = 1.0 ± 0.1, p = 0.8, paired t-test, n = 9, N = 3 and $PPR50ms_{ctrl}$ = 0.9 ± 0.1 vs. $PPR50ms_{SNAP}$ = 0.9 ± 0.1, p = 0.8, paired t-test, n = 9, N = 3; **Figures 5E,F**). As the PPR remained comparable under application of NO donor SNAP, we conclude that NO does not contribute to IFN-γ-mediated paired-pulse facilitation.

However, paired-pulse facilitation implies an increased capability of reliably transferring inhibition at higher frequencies (Luhmann et al., 2014). Following this, paired-pulse facilitation points to stronger inhibition at frequencies ≥10 Hz.

Interferon-γ constrained excitability in the developing cortex

There is an ongoing debate about whether GABA acts inhibitory or excitatory at the early stages of development. At least in mice of the first postnatal week, $GABA_AR$ openings in L5 neurons lead predominantly to depolarizing currents (Rheims et al., 2008). This may drive specific patterns of activity in developing neuronal networks (Ben-Ari, 2002; Ben-Ari et al., 2007). However, hyperpolarizing GABA actions in the neocortex have also been seen in the first postnatal week (Daw et al., 2007). In any case, the opening of $GABA_ARs$, in addition to its effect on membrane voltage, mediates a drop in membrane resistance that shunts excitatory inputs (Staley and Mody, 1992). Therefore, even "depolarizing" actions can (1) be considered as inhibitory, (2) inhibit neuronal output *in silico* (Morita et al., 2006), and (3) suppress network activity *in vivo* (Kirmse et al., 2015).

We here aimed at elucidating if and how the IFN-γ-induced increase in GABAergic transmission affects the developing cortical network. We therefore positioned brain slices on a microelectrode array (MEA, **Figure 6A**) and enhanced spontaneously occurring electrical events with 4-AP (50 μM). IFN-γ attenuated the frequency of these events on average by a factor of 0.45 ± 0.09 within 15 min (from f_{ctrl} = 22.6 ± 4.3 events min^{-1} to $f_{IFN\text{-}\gamma}$ = 9.4 ± 2.8 events min^{-1}, $p < 0.0001$, paired Wilcoxon signed-rank test, n = 49 distinguishable events, recorded in 8 slices from 6 animals, **Figures 6B,E**). This effect is GABA-mediated, as the frequency is not diminished upon IFN-γ when $GABA_A$ receptors are blocked with bicuculline (10 μM) (average factor 1.2 ± 0.2, f_{BMI} = 17.8 ± 4.8 events min^{-1} vs. $f_{BMI\ IFN\text{-}\gamma}$ = 10.9 ± 2.9 events min^{-1}, p = 0.5, paired Wilcoxon signed-rank test, n = 30 distinguishable events, recorded in 5 slices from 3 animals, **Figures 6D,E**). Because our patch clamp recordings imply that NO elevated spontaneous GABA release upon IFN-γ application, we next tested if IFN-γ attenuates network activity when NO production was inhibited. In the presence of 1400W (10 μM), IFN-γ attenuated the frequency of events on average by a factor of 0.84 ± 0.13 (f_{1400W} = 48.3 ± 10.6 events min^{-1} vs. $f_{1400W\ IFN\text{-}\gamma}$ = 31.1 ± 5.8 events min^{-1}, $p < 0.0001$, Wilcoxon signed-rank test, n = 77 distinguishable events, recorded in 8 slices from 3 animals **Figures 6C,E**). However, 1400W significantly reduces the effect size ($p < 0.0001$, Kruskal–Wallis ANOVA, performed on relative change factors **Figure 6E**). Note that the absolute event numbers largely depended on experimental conditions of each individual slice, thus enabling only longitudinal paired comparison. The Ca^{2+}-dependent stimulation of transmitter release by 4-AP applies to both glutamatergic and GABAergic synapses: however, the effect of 4-AP enhanced release of GABA might be countered by the inhibition of postsynaptic GABA currents (Gu et al., 2004), thereby enabling the overall pro-excitatory effect of 4-AP. Both effects theoretically could mask

10.3389/fncel.2022.913299

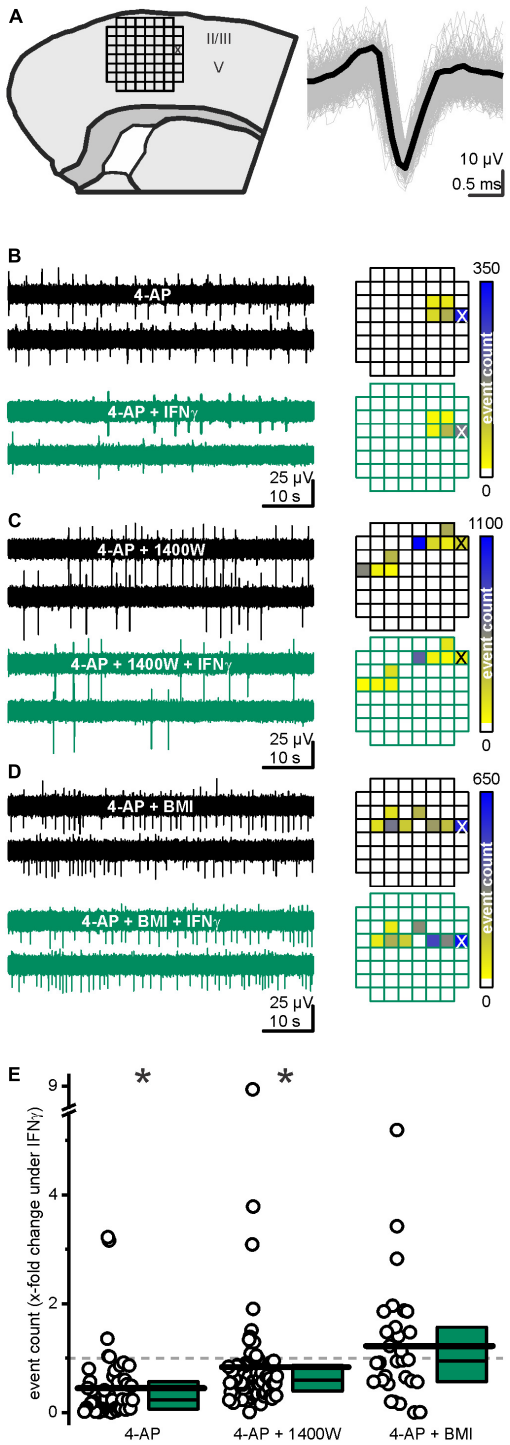

FIGURE 6
IFN-γ suppressed 4-aminopyridine (4-AP)-induced neuronal activity. **(A)** Experimental sketch: the grid represents the placement of the microelectrode array (MEA) (*left*). All accounts of one event, detected by a spike sorting algorithm, plotted on top of each other (*gray*) and the template they were matched to (*black, right*). All displayed events were recorded from the electrode marked with X in the figure on the left.
(B) IFN-γ-curbed network activity in acute neocortical slices.
(Continued)

FIGURE 6
Sample traces (*left*) recorded from the same electrode (marked with X in the heatmap below) before (*black*) and under (*green*) IFN-γ application. **(C)** Continuous iNOS inhibition *via* 1400W (10 μM) partly prevented IFN-γ-mediated network activity suppression. **(D)** IFN-γ required functioning $GABA_A$ receptors to curb network activity. Under continuous bicuculline methiodide (BMI, 10 μM) application, IFN-γ failed to significantly alter event count. Example traces on top and exemplary heatmap below. **(E)** Relative event count change upon IFN-γ application in the absence of blockers and with 1400W or BMI, respectively. Most events considerably decreased in frequency upon IFN-γ. This attenuation is partly prevented in presence of 1400W and absent in the presence of BMI. Top, middle, and bottom lines of boxes represent percentiles 75, 50, and 25, respectively, and long bars represent means. $*p < 0.05$.

the sIPSC enhancement by IFN-γ. However, this would lead to an underestimation of the effect.

In summary, IFN-γ attenuates neocortical activity, i.e., it exerts network inhibition by constraining the occurrence of spontaneous events in a partly NO-dependent manner.

Discussion

Combining measurements at the single cell and network level, we herein have found that, during a period of GABA-dependent cortical maturation, IFN-γ acutely increases the frequency and amplitude of GABAergic IPSCs on neocortical pyramidal neurons. This effect was not reversible within 30 min. The increase in IPSC frequency is not a result of enhanced interneuron excitability, since interneuronal sub- and suprathreshold excitability parameters remained stable, and elevated IPSC frequency was still present under action potential suppression. We have identified iNOS and sGC as mediators of increased IPSC frequency upon IFN-γ, plausibly acting through elevated levels of NO. Notably, manipulations of the iNOS–NO–sGC pathway revealed a differential effect on frequency and amplitude, i.e., a specificity of NO for the putatively pre-synaptically mediated frequency increase. Together with the apparent separation of the IFN-γ effects on the frequency and amplitude of IPSCs, the cessation of IPSC amplitude increases when PKC was blocked postsynaptically argues against an increased $GABA_AR$ sensitivity that might have uncovered subthreshold events from the noise. However, we cannot entirely exclude a contribution of synaptic modifications (i.e., an increased number of release sites) to the effect. Additionally, IFN-γ alters presynaptic function by shifting paired-pulse ratios toward facilitation. In contrast to the effect of IFN-γ on IPSCs, the effect on short-term synaptic plasticity was not dependent on NO. Functionally, IFN-γ constrains network activity in a GABA- and partially NO-dependent manner.

These new findings expand our existing knowledge of the neuromodulatory effects of IFN-γ on GABAergic transmission.

The increase in s/mIPSC amplitude that we observed here resembles the one that we have previously observed in adult and late juvenile rats (Janach et al., 2020). There we identified PKC-dependent increase in postsynaptic $GABA_A$ receptor number as an underlying mechanism mainly by peak-scaled non-stationary noise analysis (Janach et al., 2022). Non-stationary noise analysis, however, is difficult to apply in developing systems because it requires many low rise time IPSCs, but immature synaptic integration results in comparatively low IPSC frequencies. We have here found, however, that PKC inhibitor Calphostin C, when added to the postsynaptic neuron, prevented increased amplitudes upon IFN-γ addition. This, in addition to a comparable effect size, led us to conclude that the mechanism for amplitude increase resembles the one we found in more mature neurons. Therefore, we did not attempt to investigate whether NO-mediated postsynaptic mechanisms, such as PKG-dependent phosphorylation (McDonald and Moss, 1994; Robello et al., 1996), or whether the altered expression of GABA receptor subunits and Cl^- co-transporters that were reported in early life inflammation (Reid et al., 2013) contribute to, or counteract with, the s/mIPSC amplitude increases.

Instead, we have here focused on a developmental peculiarity in the neocortex of P6–7 rats, namely, the IFN-γ induced increase in IPSC frequency. Although, in retrospect, a trend toward an increase in IPSC frequency might become apparent in more mature animals (Janach et al., 2020, 2022), this was rather inconsistent. Why does IFN-γ cause a robust and reliable increase in IPSC frequency early postnatal but much less later? There are several plausible explanations. (1) Active heterodimers of the sGC (that we herein have recognized as necessary for the IPSC frequency increase) are more prevalent in young rats than in adult rats (Haase et al., 2010). (2) As microglia in early brain development are in an activated state and gradually inactivate by P10 (Hristova et al., 2010), they constitutively express iNOS (Crain et al., 2013) that enables mechanisms to rapidly increase NO other than *via de novo* iNOS synthesis (that takes 12 h; Jiang et al., 2022). Such mechanisms include both substrate and cofactor availability (for review, see Cinelli et al., 2020). This scenario is in line with the rather long IFN-γ exposure necessary for increased IPSC frequencies in hippocampal neurons of more mature animals (Brask et al., 2004). (3) Functional synapses on pyramidal cells in early development may originate from interneurons disparate to those seen at later stages. For instance, certain early generated somatostatin expressing interneurons are more likely to form functional synapses with pyramidal neurons around P5–7 in mice (Wang et al., 2019), and the presynaptic response to IFN-γ might be subtype-specific. However, our analysis of mIPSC rise times might suggest a slight preference for perisomatic synapses in the IFN-γ effect on spontaneous release probability.

In line with our pharmacological evidence that iNOS is involved in IFN-γ-induced frequency change, NOS blockage has been shown to prevent an IFN-γ-induced IPSC frequency increase (Brask et al., 2004) and IFN-γ slows γ-oscillations in an iNOS-dependent manner in organotypic hippocampal culture (Ta et al., 2019). In contrast to the tightly regulated, Ca^{2+}-dependent, precise, and short-ranged nNOS action (Hardingham et al., 2013), iNOS can produce large amounts of NO independent of Ca^{2+} (Cinelli et al., 2020), plausibly enabling widespread multisynaptic actions. Regardless of the actual source, NO has been shown to increase IPSC frequency not only in the cortex (Wang et al., 2017) but also in the thalamus (Yang and Cox, 2007) and in the paraventricular nucleus (Li et al., 2004). Our data indicate that sGC is a prerequisite for the IFN-γ effect, therefore favoring a scenario in which NO impacts GABA release *via* downstream sGC targets (for review Hardingham et al., 2013). One of these putative targets, the hyperpolarization-activated cyclic nucleotide-gated cation (HCN) channel is involved in enhancing GABA release (Kopp-Scheinpflug et al., 2015; Wang et al., 2017). HCN channels are present in cortical GABAergic boutons but their role may be more complex because blocking them also increases IPSC frequency (Cai et al., 2021). However, the PKC-mediated attenuation of HCN that we have previously seen upon type-I and II interferon application (Reetz et al., 2014; Janach et al., 2020), as well as direct activation of release machinery by PKC (Yawo, 1999; Xu et al., 2014), would be incompatible both with the lack of IPSC frequency increase when sGC was blocked (**Figure 4B**) and with findings in the central amygdala where PKCε suppressed GABA release (Bajo et al., 2008). Other feasible sGC targets that could influence GABA release include P/Q Ca^{2+} channels as identified in brainstem neurons (Tozer et al., 2012) and faster vesicle recycling (Micheva et al., 2003). Again, NO-related mechanisms upstream of sGC, such as directly influencing L-Type Ca^{2+} channels (Tozer et al., 2012) or nitrosylation of release machinery proteins (Palmer et al., 2008), are less likely involved here. Rather, sGC-independent mechanisms inhibited cortical P/Q Ca^{2+} channels (Petzold et al., 2008). Further, the block of α-amino-3-hydroxy-5-methyl-4-isoxazolepropionic acid (AMPA) and NMDA receptors throughout our experiments excluded a contribution of directly NO-modulated NMDA (Dawson et al., 1996) or IFN-γ-increased AMPA Ca^{2+} conductance (Mizuno et al., 2008). NO may still induce Ca^{2+} release from intracellular sources as seen in striatal neurons (Horn et al., 2002). Taken together, we cannot rule out NO-mediated increase in presynaptic Ca^{2+}, a classical modulator of transmitter release. Moreover, NO (donors) may elevate IPSC frequency Ca^{2+} independently (Li et al., 2004).

A parsimonious explanation of the obvious differences in the IFN-γ effect on s/mIPSCs and eIPSCs would be differential regulation of spontaneous and evoked GABA release by IFN-γ application indirectly implying segregation of the mechanisms underlying these two forms of vesicle release (Horvath et al., 2020). A plausible scenario for the peculiarities in evoked release would be that IFN-γ-mediated Ca^{2+} elevation might

meet a relative lack of slow-binding Ca^{2+} buffer parvalbumin (PV) in the boutons of early postnatal interneurons (del Rio et al., 1994). The latter may decelerate the decay of residual Ca^{2+} (Caillard et al., 2000). This hypothesis awaits further experimental examination.

The relative lack of PPD combined with a large variance of PPRs evinced in our sample when compared with PPD obtained under the same conditions in more mature animals (**Supplementary Figure 2F**; see also Xiang et al., 2002), is an incidental but interesting finding that is possibly linked to inhibitory synapse development.

IFN-γ-mediated changes certainly interfere with the complex role GABA is playing in neocortical development. Although the actual outcome is hard to predict, a transient alteration in GABAergic (or glutamatergic) signaling during cortical development can lead to persisting changes (Kaindl et al., 2008; Stefovska et al., 2008). Balanced GABA is crucial for adequate neuronal stem cell proliferation, cell migration, and synaptogenesis (for review, Wang and Kriegstein, 2009). Increased GABAergic signaling enhances interneuron apoptosis, curbs network synchrony (Duan et al., 2020), and causes GABA synapse elimination (Wu et al., 2012). GABAergic interneurons control critical periods of synaptic plasticity in functional circuits of the cortex (for review Hensch, 2005), i.e., enhanced GABAergic transmission prematurely induces such periods (Fagiolini et al., 2004), leading to a mismatch of sensory stimuli and synaptic plasticity. In line with this, transient disturbances of interneuron generation and integration cause long-term behavioral abnormalities—even after cell counts normalize (Magno et al., 2021). On one hand, excitation–inhibition balance is stabilized by GABAergic currents adapting to activity (Xue et al., 2014) but also sensory deprivation may increase GABAergic inhibition (Maffei et al., 2006). On the other hand, in our study, GABAergic transmission induced by IFN-γ led to an overall reduced spontaneous activity, which, in a period of incomplete synaptogenesis, may lead to decreased excitatory synaptic integration (Burrone et al., 2002).

The neuroimmune interaction we describe here might have clinical implications as altered GABAergic transmission is associated with neurodevelopmental disorders (Deidda et al., 2014). Even in the absence of disease, transient pharmacological increase in GABAergic transmission in juvenile mice not only leads to anxiety-related behavior in adults (Shen et al., 2012) but also normalizes disturbed social preferences in IFN-γ deficient mice (Filiano et al., 2016). In ASD, IFN-γ is notably the most pronounced among commonly elevated pro-inflammatory cytokines (reviewed in Saghazadeh et al., 2019) and children with ASD have elevated nitrate plasma levels that correlate with levels of IFN-γ but not with other cytokines (Sweeten et al., 2004). Alcohol dependence increases IFN-γ production in brain immune cells, as well as mIPSC frequency in the central amygdala that normalizes upon application of the anti-inflammatory cytokine interleukin 10 (Patel et al., 2021).

Our findings shed light on the acute effects of IFN-γ on early GABAergic transmission thus providing a mechanism for how early inflammation could interfere with cortical development. This might have far-reaching consequences because functional disturbances in early microcircuits lead to aberrant cortical wiring at later stages that may cause neurological or psychiatric conditions (Molnár et al., 2020).

Data availability statement

The original contributions presented in this study are included in the article/**Supplementary material**, further inquiries can be directed to the corresponding author.

Ethics statement

The animal study was reviewed and approved by the European Communities Council Directive of September 22nd, 2010 (2010/63/EU) under the licenses T 0212/14, T-CH 0034/20 for wildtype rats and T0215/11 for transgenic rats.

Author contributions

ND and US conceptualized the study and wrote the manuscript. ND performed and analyzed patch clamp recordings and *post hoc* stainings. AF supervised, analyzed, and contributed to MEA recordings. GJ, EB, and US contributed to patch clamp recordings. All authors contributed to the article and approved the submitted version.

Funding

We thank the Antje-Bürgel Stiftung and the Berlin Institute of Health for supporting ND and GJ with individual grants, respectively. EB was funded by the Ministry of Science and Higher Education of the Russian Federation Academic Excellence Program "priority-2030" of Lobachevsky University until February 2022.

Acknowledgments

We thank P. Lange and C.V. Braun for coding assistance, S. Grosser for microscopy instructions, A. Schädlich for

contributing to MEA recordings, J. König and R. Dannenberg for technical assistance. Special thanks go to Michael Depew for critical comments and language editing. VGAT-Venus transgenic rats were generated by Drs. Y. Yanagawa, M. Hirabayashi, and Y. Kawaguchi in National Institute for Physiological Sciences, Okazaki, Japan, using pCS2-Venus provided by A. Miyawaki.

Conflict of interest

The authors declare that the research was conducted in the absence of any commercial or financial relationships that could be construed as a potential conflict of interest.

Publisher's note

Supplementary material

The Supplementary Material for this article can be found online at: https://www.frontiersin.org/articles/10.3389/fncel.2022.913299/full#supplementary-material

References

Alderton, W. K., Cooper, C. E., and Knowles, R. G. (2001). Nitric oxide synthases: Structure, function and inhibition. *Biochem. J.* 357, 593–615. doi: 10.1042/0264-6021:3570593

Arolt, V., Rothermundt, M., Wandinger, K. P., and Kirchner, H. (2000). Decreased in vitro production of interferon-gamma and interleukin-2 in whole blood of patients with schizophrenia during treatment. *Mol. Psychiatry* 5, 150–158. doi: 10.1038/sj.mp.4000650

Bajo, M., Cruz, M. T., Siggins, G. R., Messing, R., and Roberto, M. (2008). Protein kinase C epsilon mediation of CRF- and ethanol-induced GABA release in central amygdala. *Proc. Natl. Acad. Sci. U.S.A.* 105, 8410–8415. doi: 10.1073/pnas.0802302105

Ben-Ari, Y. (2002). Excitatory actions of GABA during development: The nature of the nurture. *Nat. Rev. Neurosci.* 3, 728–739. doi: 10.1038/nrn920

Ben-Ari, Y., Gaiarsa, J. L., Tyzio, R., and Khazipov, R. (2007). GABA: A pioneer transmitter that excites immature neurons and generates primitive oscillations. *Physiol. Rev.* 87, 1215–1284. doi: 10.1152/physrev.00017.2006

Blanchette, J., Jaramillo, M., and Olivier, M. (2003). Signalling events involved in interferon-γ-inducible macrophage nitric oxide generation. *Immunology* 108, 513–522. doi: 10.1046/j.1365-2567.2003.01620.x

Bortone, D., and Polleux, F. (2009). KCC2 expression promotes the termination of cortical interneuron migration in a voltage-sensitive calcium-dependent manner. *Neuron* 62, 53–71. doi: 10.1016/j.neuron.2009.01.034

Brask, J., Kristensson, K., and Hill, R. H. (2004). Exposure to interferon-γ during synaptogenesis increases inhibitory activity after a latent period in cultured rat hippocampal neurons. *Eur. J. Neurosci.* 19, 3193–3201. doi: 10.1111/j.0953-816X.2004.03445.x

Bruns, R. F., Miller, F. D., Merriman, R. L., Howbert, J. J., Heath, W. F., Kobayashi, E., et al. (1991). Inhibition of protein kinase C by calphostin C is light-dependent. *Biochem. Biophys. Res. Commun.* 176, 288–293. doi: 10.1016/0006-291X(91)90922-T

Burrone, J., O'Byrne, M., and Murthy, V. N. (2002). Multiple forms of synaptic plasticity triggered by selective suppression of activity in individual neurons. *Nature* 420, 414–418. doi: 10.1038/nature01242

Cai, W., Liu, S.-S., Li, B.-M., and Zhang, X.-H. (2021). Presynaptic HCN channels constrain GABAergic synaptic transmission in pyramidal cells of the medial prefrontal cortex. *Biol. Open* 11:bio058840. doi: 10.1242/bio.058840

Caillard, O., Moreno, H., Schwaller, B., Llano, I., Celio, M. R., and Marty, A. (2000). Role of the calcium-binding protein parvalbumin in short-term synaptic plasticity. *Proc. Natl. Acad. Sci. U.S.A.* 97, 13372–13377. doi: 10.1073/pnas.230362997

Cinelli, M. A., Do, H. T., Miley, G. P., and Silverman, R. B. (2020). Inducible nitric oxide synthase: Regulation, structure, and inhibition. *Med. Res. Rev.* 40, 158–189. doi: 10.1002/med.21599

Clark, D. N., Begg, L. R., and Filiano, A. J. (2022). Unique aspects of IFN-γ/STAT1 signaling in neurons. *Immunol. Rev.* 2, 1–18. doi: 10.1111/imr.13092

Cobos, I., Calcagnotto, M. E., Vilaythong, A. J., Thwin, M. T., Noebels, J. L., Baraban, S. C., et al. (2005). Mice lacking Dlx1 show subtype-specific loss of interneurons, reduced inhibition and epilepsy. *Nat. Neurosci.* 8, 1059–1068. doi: 10.1038/nn1499

Crain, J. M., Nikodemova, M., and Watters, J. J. (2013). Microglia express distinct M1 and M2 phenotypic markers in the postnatal and adult central nervous system in male and female mice. *J. Neurosci. Res.* 91, 1143–1151. doi: 10.1002/jnr.23242

Daw, M. I., Ashby, M. C., and Isaac, J. T. R. (2007). Coordinated developmental recruitment of latent fast spiking interneurons in layer IV barrel cortex. *Nat. Neurosci.* 10, 453–461. doi: 10.1038/nn1866

Dawson, V. L., Kizushi, V. M., Huang, P. L., Snyder, S. H., and Dawson, T. M. (1996). Resistance to neurotoxicity in cortical cultures from neuronal nitric oxide synthase-deficient mice. *J. Neurosci.* 16, 2479–2487. doi: 10.1523/jneurosci.16-08-02479.1996

Deidda, G., Bozarth, I. F., and Cancedda, L. (2014). Modulation of GABAergic transmission in development and neurodevelopmental disorders: Investigating physiology and pathology to gain therapeutic perspectives. *Front. Cell. Neurosci.* 8:119. doi: 10.3389/fncel.2014.00119

del Rio, J., de Lecea, L., Ferrer, I., and Soriano, E. (1994). The development of parvalbumin-immunoreactivity in the neocortex of the mouse. *Dev. Brain Res.* 81, 247–259. doi: 10.1016/0165-3806(94)90311-5

Ding, J. D., Burette, A., and Weinberg, R. J. (2005). Expression of soluble guanylyl cyclase in rat cerebral cortex during postnatal development. *J. Comp. Neurol.* 485, 255–265. doi: 10.1002/cne.20494

Duan, Z. R. S., Che, A., Chu, P., Modol, L., Bollmann, Y., Babij, R., et al. (2020). GABAergic restriction of network dynamics regulates interneuron survival in the developing cortex. *Neuron* 105, 75.e–92.e. doi: 10.1016/j.neuron.2019.10.008

Fagiolini, M., Fritschy, J. M., Löw, K., Möhler, H., Rudolph, U., and Hensch, T. K. (2004). Specific GABAA circuits for visual cortical plasticity. *Science* 303, 1681–1683. doi: 10.1126/science.1091032

Filiano, A. J., Xu, Y., Tustison, N. J., Marsh, R. L., Baker, W., Smirnov, I., et al. (2016). Unexpected role of interferon-γ 3 in regulating neuronal connectivity and social behaviour. *Nature* 535, 425–429. doi: 10.1038/nature18626

Flood, L., Korol, S. V., Ekselius, L., Birnir, B., and Jin, Z. (2019). Interferon-γ potentiates GABAA receptor-mediated inhibitory currents in rat hippocampal CA1 pyramidal neurons. *J. Neuroimmunol.* 337:577050. doi: 10.1016/j.jneuroim.2019.577050

Garvey, E. P., Oplinger, J. A., Furfine, E. S., Kiff, R. J., Laszlo, F., Whittle, B. J. R., et al. (1997). 1400W is a slow, tight binding, and highly selective inhibitor of inducible nitric-oxide synthase in vitro and in vivo. *J. Biol. Chem.* 272, 4959–4963. doi: 10.1074/jbc.272.8.4959

Giridharan, V. V., Réus, G. Z., Selvaraj, S., Scaini, G., Barichello, T., and Quevedo, J. (2019). Maternal deprivation increases microglial activation and neuroinflammatory markers in the prefrontal cortex and hippocampus of infant rats. *J. Psychiatr. Res.* 115, 13–20. doi: 10.1016/j.jpsychires.2019.05.001

Gu, Y., Ge, S. Y., and Ruan, D. Y. (2004). Effect of 4-aminopyridine on synaptic transmission in rat hippocampal slices. *Brain Res.* 1006, 225–232. doi: 10.1016/j.brainres.2004.02.008

Haase, N., Haase, T., Seeanner, M., and Behrends, S. (2010). Nitric oxide sensitive guanylyl cyclase activity decreases during cerebral postnatal development because of a reduction in heterodimerization. *J. Neurochem.* 112, 542–551. doi: 10.1111/j.1471-4159.2009.06484.x

Hardingham, N., Dachtler, J., and Fox, K. (2013). The role of nitric oxide in pre-synaptic plasticity and homeostasis. *Front. Cell. Neurosci.* 7:190. doi: 10.3389/fncel.2013.00190

Hensch, T. K. (2005). Critical period plasticity in local cortical circuits. *Nat. Rev. Neurosci.* 6, 877–888. doi: 10.1038/nrn1787

Horn, T. F. W., Wolf, G., Duffy, S., Weiss, S., Keilhoff, G., and MacVicar, B. A. (2002). Nitric oxide promotes intracellular calcium release from mitochondria in striatal neurons. *FASEB J.* 16, 1611–1622. doi: 10.1096/fj.02-0126com

Horvath, P. M., Piazza, M. K., Monteggia, L. M., and Kavalali, E. T. (2020). Spontaneous and evoked neurotransmission are partially segregated at inhibitory synapses. *eLife* 9:e52852. doi: 10.7554/eLife.52852

Hristova, M., Cuthill, D., Zbarsky, V., Acosta-Saltos, A., Wallace, A., Blight, K., et al. (2010). Activation and deactivation of periventricular white matter phagocytes during postnatal mouse development. *Glia* 58, 11–28. doi: 10.1002/glia.20896

Ivashkiv, L. B. (2018). IFNγ: Signalling, epigenetics and roles in immunity, metabolism, disease and cancer immunotherapy. *Nat. Rev. Immunol.* 18, 545–558. doi: 10.1038/s41577-018-0029-z

Janach, G. M. S., Böhm, M., Döhne, N., Kim, H.-R., Rosário, M., and Strauss, U. (2022). Interferon-γ enhances neocortical synaptic inhibition by promoting membrane association and phosphorylation of GABAA receptors in a protein kinase C-dependent manner. *Brain. Behav. Immun.* 101, 153–164. doi: 10.1016/j.bbi.2022.01.001

Janach, G. M. S., Reetz, O., Döhne, N., Stadler, K., Grosser, S., Byvaltcev, E., et al. (2020). Interferon-γ acutely augments inhibition of neocortical layer 5 pyramidal neurons. *J. Neuroinflammation* 17:69. doi: 10.1186/s12974-020-1722-y

Jiang, X., He, H., Mo, L., Liu, Q., Yang, F., Zhou, Y., et al. (2022). Mapping the plasticity of morphology, molecular properties and function in mouse primary microglia. *Front. Cell. Neurosci.* 15:811061. doi: 10.3389/fncel.2021.811061

Kaindl, A. M., Koppelstaetter, A., Nebrich, G., Stuwe, J., Sifringer, M., Zabel, C., et al. (2008). Brief alteration of NMDA or GABAA receptor mediated neurotransmission has long term effects on the developing cerebral cortex. *Mol. Cell. Proteomics* 7, 2293–2310. doi: 10.1074/mcp.M800030-MCP200

Kak, G., Raza, M., and Tiwari, B. K. (2018). Interferon-gamma (IFN-γ): Exploring its implications in infectious diseases. *Biomol. Concepts* 9, 64–79. doi: 10.1515/bmc-2018-0007

Kang, Y., Dempo, Y., Ohashi, A., Saito, M., Toyoda, H., Sato, H., et al. (2007). Nitric oxide activates leak K+ currents in the presumed cholinergic neuron of basal forebrain. *J. Neurophysiol.* 98, 3397–3410. doi: 10.1152/jn.00536.2007

Kavalali, E. T. (2015). The mechanisms and functions of spontaneous neurotransmitter release. *Nat. Rev. Neurosci.* 16, 5–16. doi: 10.1038/nrn3875

Kirischuk, S., Sinning, A., Blanquie, O., Yang, J.-W., Luhmann, H. J., and Kilb, W. (2017). Modulation of neocortical development by early neuronal activity: Physiology and pathophysiology. *Front. Cell. Neurosci.* 11:379. doi: 10.3389/fncel.2017.00379

Kirmse, K., Kummer, M., Kovalchuk, Y., Witte, O. W., Garaschuk, O., and Holthoff, K. (2015). GABA depolarizes immature neurons and inhibits network activity in the neonatal neocortex in vivo. *Nat. Commun.* 6:7750. doi: 10.1038/ncomms8750

Kopp-Scheinpflug, C., Pigott, B. M., and Forsythe, I. D. (2015). Nitric oxide selectively suppresses IH currents mediated by HCN1-containing channels. *J. Physiol.* 593, 1685–1700. doi: 10.1113/jphysiol.2014.282194

Kravchenko, M. O., Moskalyuk, A. O., Fedulova, S. A., and Veselovsky, N. S. (2006). Calcium-dependent changes of paired-pulse modulation at single GABAergic synapses. *Neurosci. Lett.* 395, 133–137. doi: 10.1016/j.neulet.2005.10.070

Le Magueresse, C., and Monyer, H. (2013). GABAergic interneurons shape the functional maturation of the cortex. *Neuron* 77, 388–405. doi: 10.1016/j.neuron.2013.01.011

Lee, J. J. (2009). Nitric oxide modulation of GABAergic synaptic transmission in mechanically isolated rat auditory cortical neurons. *Korean J. Physiol. Pharmacol.* 13, 461–467. doi: 10.4196/kjpp.2009.13.6.461

Lewis, D. A., Hashimoto, T., and Volk, D. W. (2005). Cortical inhibitory neurons and schizophrenia. *Nat. Rev. Neurosci.* 6, 312–324. doi: 10.1038/nrn1648

Lewis, E. L., Tulina, N., Anton, L., Brown, A. G., Porrett, P. M., and Elovitz, M. A. (2021). IFNγ-Producing γ/δ T cells accumulate in the fetal brain following intrauterine inflammation. *Front. Immunol* 12:741518. doi: 10.3389/fimmu.2021.741518

Li, D. P., Chen, S. R., Finnegan, T. F., and Pan, H. L. (2004). Signalling pathway of nitric oxide in synaptic GABA release in the rat paraventricular nucleus. *J. Physiol.* 554, 100–110. doi: 10.1113/jphysiol.2003.053371

Litteljohn, D., Nelson, E., and Hayley, S. (2014). IFN-γ differentially modulates memory-related processes under basal and chronic stressor conditions. *Front. Cell. Neurosci.* 8:391. doi: 10.3389/fncel.2014.00391

Luhmann, H. J., Kirischuk, S., Sinning, A., and Kilb, W. (2014). Early GABAergic circuitry in the cerebral cortex. *Curr. Opin. Neurobiol.* 26, 72–78. doi: 10.1016/j.conb.2013.12.014

Luhmann, H. J., and Prince, D. A. (1991). Postnatal maturation of the GABAergic system in rat neocortex. *J. Neurophysiol.* 65, 247–263. doi: 10.1152/jn.1991.65.2.247

Maffei, A., Nataraj, K., Nelson, S. B., and Turrigiano, G. G. (2006). Potentiation of cortical inhibition by visual deprivation. *Nature* 443, 81–84. doi: 10.1038/nature05079

Magno, L., Asgarian, Z., Pendolino, V., Velona, T., Mackintosh, A., Lee, F., et al. (2021). Transient developmental imbalance of cortical interneuron subtypes presages long-term changes in behavior. *Cell Rep.* 35:109249. doi: 10.1016/j.celrep.2021.109249

McDonald, B. J., and Moss, S. J. (1994). Differential phosphorylation of intracellular domains of γ-aminobutyric acid type A receptor subunits by calcium/calmodulin type 2-dependent protein kinase and cGMP-dependent protein kinase. *J. Biol. Chem.* 269, 18111–18117. doi: 10.1016/s0021-9258(17)32424-9

Micheva, K. D., Buchanan, J. A., Holz, R. W., and Smith, S. J. (2003). Retrograde regulation of synaptic vesicle endocytosis and recycling. *Nat. Neurosci.* 6, 925–932. doi: 10.1038/nn1114

Mizuno, T., Zhang, G., Takeuchi, H., Kawanokuchi, J., Wang, J., Sonobe, Y., et al. (2008). Interferon-γ directly induces neurotoxicity through a neuron specific, calcium-permeable complex of IFN-γ receptor and AMPA GluR1 receptor. *FASEB J.* 22, 1797–1806. doi: 10.1096/fj.07-099499

Modol, L., Bollmann, Y., Tressard, T., Babij, R., Che, A., Duan, Z. R. S., et al. (2020). Assemblies of perisomatic GABAergic neurons in the developing barrel cortex. *Neuron* 105, 93–105. doi: 10.1016/j.neuron.2019.10.007

Molnár, Z., Luhmann, H. J., and Kanold, P. O. (2020). Transient cortical circuits match spontaneous and sensory-driven activity during development. *Science* 370:eabb2153. doi: 10.1126/science.abb2153

Monteiro, S., Ferreira, F. M., Pinto, V., Roque, S., Morais, M., De Sá-Calc?da, D., et al. (2015). Absence of IFNγ promotes hippocampal plasticity and enhances cognitive performance. *Transl. Psychiatry* 5:e707. doi: 10.1038/tp.2015.194

Monteiro, S., Roque, S., Marques, F., Correia-Neves, M., and Cerqueira, J. J. (2017). Brain interference: Revisiting the role of IFNγ in the central nervous system. *Prog. Neurobiol.* 156, 149–163. doi: 10.1016/j.pneurobio.2017.05.003

Morita, K., Tsumoto, K., and Aihara, K. (2006). Bidirectional modulation of neuronal responses by depolarizing GABAergic inputs. *Biophys. J.* 90, 1925–1938. doi: 10.1529/biophysj.105.063164

Müller, M., Fontana, A., Zbinden, G., and Gähwiler, B. H. (1993). Effects of interferons and hydrogen peroxide on CA3 pyramidal cells in rat hippocampal slice cultures. *Brain Res.* 619, 157–162. doi: 10.1016/0006-8993(93)91607-T

Palmer, Z. J., Duncan, R. R., Johnson, J. R., Lian, L. Y., Mello, L. V., Booth, D., et al. (2008). S-nitrosylation of syntaxin 1 at Cys145 is a regulatory switch controlling Munc18-1 binding. *Biochem. J.* 413, 479–491. doi: 10.1042/BJ20080069

Patel, R. R., Wolfe, S. A., Bajo, M., Abeynaike, S., Pahng, A., Borgonetti, V., et al. (2021). IL-10 normalizes aberrant amygdala GABA transmission and reverses anxiety-like behavior and dependence-induced escalation of alcohol intake. *Prog. Neurobiol.* 199:101952. doi: 10.1016/j.pneurobio.2020.101952

Patterson, C. E., Lawrence, D. M. P., Echols, L. A., and Rall, G. F. (2002). Immune-mediated protection from measles virus-induced central nervous system disease is noncytolytic and gamma interferon dependent. *J. Virol.* 76, 4497–4506. doi: 10.1128/jvi.76.9.4497-4506.2002

Petzold, G. C., Haack, S., Von Bohlen Und Halbach, O., Priller, J., Lehmann, T. N., Heinemann, U., et al. (2008). Nitric oxide modulates spreading

depolarization threshold in the human and rodent cortex. *Stroke* 39, 1292–1299. doi: 10.1161/STROKEAHA.107.500710

Pigott, B., Bartus, K., and Garthwaite, J. (2013). On the selectivity of neuronal NOS inhibitors. *Br. J. Pharmacol.* 168, 1255–1265. doi: 10.1111/bph.12016

Pizzarelli, R., and Cherubini, E. (2011). Alterations of GABAergic signaling in autism spectrum disorders. *Neural Plast.* 2011:297153. doi: 10.1155/2011/297153

Reetz, O., Stadler, K., and Strauss, U. (2014). Protein kinase C activation mediates interferon-β-induced neuronal excitability changes in neocortical pyramidal neurons. *J. Neuroinflammation* 11, 1–14. doi: 10.1186/s12974-014-0185-4

Reid, A. Y., Riazi, K., Campbell Teskey, G., and Pittman, Q. J. (2013). Increased excitability and molecular changes in adult rats after a febrile seizure. *Epilepsia* 54, 45–48. doi: 10.1111/epi.12061

Rheims, S., Minlebaev, M., Ivanov, A., Represa, A., Khazipov, R., Holmes, G. L., et al. (2008). Excitatory GABA in rodent developing neocortex in vitro. *J. Neurophysiol.* 100, 609–619. doi: 10.1152/jn.90402.2008

Robello, M., Amico, C., Bucossi, G., Cupello, A., Rapallino, M. V., and Thellung, S. (1996). Nitric oxide and GABAA receptor function in the rat cerebral cortex and cerebellar granule cells. *Neuroscience* 74, 99–105. doi: 10.1016/0306-4522(96)00110-8

Saghazadeh, A., Ataeinia, B., Keynejad, K., Abdolalizadeh, A., Hirbod-Mobarakeh, A., and Rezaei, N. (2019). A meta-analysis of pro-inflammatory cytokines in autism spectrum disorders: Effects of age, gender, and latitude. *J. Psychiatr. Res.* 115, 90–102. doi: 10.1016/j.jpsychires.2019.05.019

Schindelin, J., Arganda-Carreras, I., Frise, E., Kaynig, V., Longair, M., Pietzsch, T., et al. (2012). Fiji: An open-source platform for biological-image analysis. *Nat. Methods* 9, 676–682. doi: 10.1038/nmeth.2019

Schmidt, F. M., Lichtblau, N., Minkwitz, J., Chittka, T., Thormann, J., Kirkby, K. C., et al. (2014). Cytokine levels in depressed and non-depressed subjects, and masking effects of obesity. *J. Psychiatr. Res.* 55, 29–34. doi: 10.1016/j.jpsychires.2014.04.021

Shen, Q., Fuchs, T., Sahir, N., and Luscher, B. (2012). GABAergic control of critical developmental periods for anxiety- and depression-related behavior in mice. *PLoS One* 7:e47441. doi: 10.1371/journal.pone.0047441

Stadler, K., Bierwirth, C., Stoenica, L., Battefeld, A., Reetz, O., Mix, E., et al. (2014). Elevation in type i interferons inhibits HCN1 and slows cortical neuronal oscillations. *Cereb. Cortex* 24, 199–210. doi: 10.1093/cercor/bhs305

Staley, K. J., and Mody, I. (1992). Shunting of excitatory input to dentate gyrus granule cells by a depolarizing GABA(A) receptor-mediated postsynaptic conductance. *J. Neurophysiol.* 68, 197–212. doi: 10.1152/jn.1992.68.1.197

Stefovska, V. G., Uckermann, O., Czuczwar, M., Smitka, M., Czuczwar, P., Kis, J., et al. (2008). Sedative and anticonvulsant drugs suppress postnatal neurogenesis. *Ann. Neurol.* 64, 434–445. doi: 10.1002/ana.21463

Stuehr, D. J., and Marletta, M. A. (1987). Induction of nitrite/nitrate synthesis in murine macrophages by BCG infection, lymphokines, or interferon-gamma. *J. Immunol.* 139, 518–525.

Sweeten, T. L., Posey, D. J., Shankar, S., and McDougle, C. J. (2004). High nitric oxide production in autistic disorder: A possible role for interferon-γ. *Biol. Psychiatry* 55, 434–437. doi: 10.1016/j.biopsych.2003.09.001

Ta, T.-T., Dikmen, H. O., Schilling, S., Chausse, B., Lewen, A., Hollnagel, J.-O., et al. (2019). Priming of microglia with IFN-γ slows neuronal gamma oscillations in situ. *Proc. Natl. Acad. Sci.* 116, 4637–4642. doi: 10.1073/pnas.1813562116

Tozer, A. J. B., Forsythe, I. D., and Steinert, J. R. (2012). Nitric oxide signalling augments neuronal voltage-gated L-type (Ca v1) and P/Q-type (Ca v2.1) channels in the mouse medial nucleus of the trapezoid body. *PLoS One* 7:1–7. doi: 10.1371/journal.pone.0032256

Uematsu, M., Hirai, Y., Karube, F., Ebihara, S., Kato, M., Abe, K., et al. (2008). Quantitative chemical composition of cortical GABAergic neurons revealed in transgenic venus-expressing rats. *Cereb. Cortex* 18, 315–330. doi: 10.1093/cercor/bhm056

Vetlugina, T. P., Lobacheva, O. A., Sergeeva, S. A., Nikitina, V. B., Nevidimova, T. I., and Semke, A. V. (2016). Adjunctive use of interferon γ inducer for treatment of patients with schizophrenia. *Acta Neuropsychiatr.* 28, 149–156. doi: 10.1017/neu.2015.60

Wang, C. Z., Ma, J., Xu, Y. Q., Jiang, S. N., Chen, T. Q., Yuan, Z. L., et al. (2019). Early-generated interneurons regulate neuronal circuit formation during early postnatal development. *eLife* 8, 1–21. doi: 10.7554/eLife.44649

Wang, D. D., and Kriegstein, A. R. (2008). GABA regulates excitatory synapse formation in the neocortex via NMDA receptor activation. *J. Neurosci.* 28, 5547–5558. doi: 10.1523/JNEUROSCI.5599-07.2008

Wang, D. D., and Kriegstein, A. R. (2009). Defining the role of GABA in cortical development. *J. Physiol.* 587, 1873–1879. doi: 10.1113/jphysiol.2008.167635

Wang, Q., Mergia, E., Koesling, D., and Mittmann, T. (2017). Nitric oxide/cGMP signaling via guanylyl cyclase isoform 1 modulates glutamate and GABA release in somatosensory cortex of mice. *Neuroscience* 360, 180–189. doi: 10.1016/j.neuroscience.2017.07.063

Wu, X., Fu, Y., Knott, G., Lu, J., Di Cristo, G., and Josh Huang, Z. (2012). GABA signaling promotes synapse elimination and axon pruning in developing cortical inhibitory interneurons. *J. Neurosci.* 32, 331–343. doi: 10.1523/JNEUROSCI.3189-11.2012

Xiang, Z., Huguenard, J. R., and Prince, D. A. (2002). Synaptic inhibition of pyramidal cells evoked by different interneuronal subtypes in layer V of rat visual cortex. *J. Neurophysiol.* 88, 740–750. doi: 10.1152/jn.2002.88.2.740

Xu, C., Liu, Q. Y., and Alkon, D. L. (2014). PKC activators enhance GABAergic neurotransmission and paired-pulse facilitation in hippocampal CA1 pyramidal neurons. *Neuroscience* 268, 75–86. doi: 10.1016/j.neuroscience.2014.03.008

Xue, M., Atallah, B. V., and Scanziani, M. (2014). Equalizing excitation-inhibition ratios across visual cortical neurons. *Nature* 511, 596–600. doi: 10.1038/nature13321

Yang, S., and Cox, C. L. (2007). Modulation of inhibitory activity by nitric oxide in the thalamus. *J. Neurophysiol.* 97, 3386–3395. doi: 10.1152/jn.01270.2006

Yawo, H. (1999). Protein kinase C potentiates transmitter release from the chick ciliary presynaptic terminal by increasing the exocytotic fusion probability. *J. Physiol.* 515, 169–180. doi: 10.1111/j.1469-7793.1999.169ad.x

Yger, P., Spampinato, G. L. B., Esposito, E., Lefebvre, B., Deny, S., Gardella, C., et al. (2018). A spike sorting toolbox for up to thousands of electrodes validated with ground truth recordings in vitro and in vivo. *eLife* 7:e34518. doi: 10.7554/eLife.34518

Zaqout, S., Blaesius, K., Wu, Y. J., Ott, S., Kraemer, N., Becker, L. L., et al. (2019). Altered inhibition and excitation in neocortical circuits in congenital microcephaly. *Neurobiol. Dis.* 129, 130–143. doi: 10.1016/j.nbd.2019.05.008

frontiers | Frontiers in Cellular Neuroscience

TYPE Original Research
PUBLISHED 22 August 2022
DOI 10.3389/fncel.2022.966636

OPEN ACCESS

EDITED BY
Enrico Cherubini,
European Brain Research Institute, Italy

REVIEWED BY
Dominique Debanne,
INSERM U1072 Neurobiologie des canaux Ioniques et de la Synapse, France
Jonathan Mapelli,
University of Modena and Reggio Emilia, Italy

*CORRESPONDENCE
Haruyuki Kamiya
kamiya@med.hokudai.ac.jp

SPECIALTY SECTION
This article was submitted to Cellular Neurophysiology, a section of the journal Frontiers in Cellular Neuroscience

RECEIVED 11 June 2022
ACCEPTED 29 July 2022
PUBLISHED 22 August 2022

CITATION
Kamiya H (2022) Modeling analysis of subthreshold voltage signaling along hippocampal mossy fiber axons. *Front. Cell. Neurosci.* 16:966636. doi: 10.3389/fncel.2022.966636

Modeling analysis of subthreshold voltage signaling along hippocampal mossy fiber axons

Haruyuki Kamiya*

Department of Neurobiology, Hokkaido University Graduate School of Medicine, Sapporo, Japan

Axons are classically thought of as electrically well isolated from other parts of the neurons due to the shape of a long cable-like structure. In contrast to this classical view on axonal compartmentalization, recent studies revealed that subthreshold depolarization of soma and dendrite passively propagates to the axons for a substantial distance, as demonstrated in some experimentally accessible axons including hippocampal mossy fibers and cortical pyramidal cell axons. Passive propagation of subthreshold dendritic EPSPs to the axons, defined as EPreSPs (excitatory presynaptic potentials), has been demonstrated to affect transmitter release from the axon terminals. To further characterize and explore the functional significance of passive subthreshold voltage signaling along the axons, the model of EPreSPs along hippocampal mossy fibers, proposed by Alle and Geiger, was reconstructed on the NEURON simulator. To test the effect of EPreSPs on action potentials and transmitter release from the axon terminals, additional conductances were incorporated into the previous passive propagation model. These include the axonal sodium, potassium, and leak channels as well as presynaptic calcium channels composed of P/ Q-, N-, and R-types, which are reconstructed from the properties of those recorded from mossy fiber boutons experimentally. In this revised model, the preceding subthreshold EPreSPs slightly reduced the action potential-evoked presynaptic calcium currents by a decrease in the amplitude of action potentials due to the slow depolarization. It should be mentioned that EPreSPs by themselves elicited small calcium currents during subthreshold depolarization through these high-voltage activated calcium channels. Since the previous experimental study by simultaneous pre and postsynaptic recordings demonstrated that EPreSPs enhanced action potential-evoked transmitter release from the mossy fiber terminals, it has been suggested that different mechanisms from the enhancement of action potential-evoked presynaptic calcium entry may involve enhanced transmitter release by EPreSP. Small calcium entry by subthreshold EPreSPs may enhance transmitter release from the mossy fiber terminals by acting as high-affinity calcium sensors for enhancing transmitter release. Another form of axonal subthreshold voltage signaling, GABA-EPreSPs elicited by a spillover of GABA

from surrounding interneurons, was also explored. Functional consequences of the two modes of axonal subthreshold voltage signaling were discussed with the simulation results.

KEYWORDS

axon, simulation, voltage, calcium current, mossy fiber

Introduction

In most axons, action potentials are generated at the axon initial segment (AIS) and propagate reliably to the distal axon terminals (Bean, 2007; Schmidt-Hieber et al., 2008). In addition to this canonical mode of signaling in the axons, recent studies have revealed that somatodendritic depolarization distributes for a substantial distance by passive propagation due to the cable properties of the axon (Alle and Geiger, 2006; see also Shu et al., 2006), and referred to as excitatory presynaptic potentials (EPreSPs). This non-canonical mode of axonal signaling may add a new modality of analog information processing by axons (Debanne et al., 2011, 2013). Although the functional implication of this non-canonical axonal signaling remains elusive (Ohura and Kamiya, 2016; Trigo, 2019), this mechanism may substantially influence the information transfer through the neuronal network in an activity-dependent manner (Scott et al., 2008; Ohura and Kamiya, 2018a; Kamiya and Debanne, 2020).

The mathematical simulation has been widely used to describe the activities of the axon in the central nervous system, as supplementary to the experimental approach with direct recordings from the axons or the terminals (Engel and Jonas, 2005; Schmidt-Hieber et al., 2008; Diwakar et al., 2009; Ohura and Kamiya, 2018b). The mechanisms underlying the propagation of EPreSPs along the axons were also explored with computer simulations (Alle and Geiger, 2006). They adopted the simple multicompartmental model of the granule cell structure, and successfully reconstructed the passive propagation of EPreSPs quantitatively. However, it was not possible to evaluate the effects on the propagation of action potentials or the subsequent transmitter release from the axon terminals, since the model in their study was incorporated only with passive properties of axonal membranes and not with active conductances. In this study, it was attempted to incorporate the active conductances into the axonal membranes, namely axonal sodium and potassium channels (Engel and Jonas, 2005) as well as the presynaptic calcium channels (Bischofberger et al., 2002) composed of P/Q-type, N-type, and R type (Li et al., 2007) to get insights into the functional consequence of EPreSPs propagation. Using this revised model, action potentials propagating along axons as well as presynaptic calcium current elicited by action potentials were readily calculated, and the consequence of EPreSPs on the axonal propagation and transmitter release were explored.

Here, it was found that the subthreshold EPreSPs slightly reduce the amplitude of the propagating action potentials by the small preceding depolarization. The simulated presynaptic calcium currents during action potentials also reduced the amplitudes. EPreSPs themselves elicited a small calcium current through these calcium channels. Taken together, our simulation data suggested that the facilitated transmitter release observed in the experiments (Alle and Geiger, 2006) attributed to the small calcium entry acting on the high-affinity calcium sensor for synaptic facilitation such as synaptotagmin 7 (Jackman et al., 2016).

In addition, the roles of another form of subthreshold voltage signaling, namely GABA-EPreSPs due to spill-over transmission from the surrounding GABAergic interneurons (Alle and Geiger, 2007) were explored in the mossy fiber model. Since hippocampal mossy fiber axons expressed functional $GABA_A$-receptors whose activation leads to depolarization due to relatively high intracellular Cl^- concentrations in the axonal cytoplasm (Ruiz et al., 2003), activation of axonal $GABA_A$-receptors potentially modulate the propagating action potentials as well as the subsequent transmitter release. Although the existence of modulatory effects of GABA on the excitability of the mossy fiber axons is shown, the functional consequence of the heterosynaptic actions of GABA has not been explored in detail. In this study, the effects of GABA-EPreSPs were tested on the propagating action potentials as well as presynaptic Ca^{2+} entry during the action potentials reconstructed in the hippocampal mossy fiber model. The simulation demonstrated that GABA-EPreSPs show profound shunting inhibition which reduces the amplitude of axonal action potentials and the presynaptic Ca^{2+} currents evoked by the action potentials, which confirms the notions of the previous experimental study by optically monitoring Ca^{2+} transient at single mossy fiber terminals (Ruiz et al., 2003).

Materials and methods

Simulation

Simulations were performed using the NEURON simulation platform version 7.8 for Windows (Hines and Carnevale, 1997). In this study, we adopted the structural model of the granule cell for the reproduction of the simulation of EPreSP propagation

(Alle and Geiger, 2006). Briefly, the structure of the granule cell (Geiger et al., 2002) was approximated by dendrites (one main trunk attached with three primaries and nine secondary branches), a soma (diameter, 15 μm), 10 axonal cylinders (diameter, 0.4 μm; length, 150 μm), and 10 *en passant* boutons (diameter, 7 μm) attached with four filopodial extensions (length 20 μm, diameter 0.1 μm). The first axonal cylinder had a proximal diameter of 1 μm and a distal one of 0.4 μm. The hilar collaterals (length 200 μm, diameter 0.2 μm) originated at 50, 100, and 200 μm from the soma, and each carried one large MFB. **Figure 2A** illustrates the shape of the granule cell model used in this study. The passive electrical properties of the axon including MFBs and filopodial extensions were assumed to be uniform and were the same as for the somatodendritic domain. Specific membrane capacitance Cm 1 $\mu F/cm^2$, specific membrane resistance Rm 60 $k\Omega\ cm^2$, and specific intracellular resistivity Ri 70 Ω cm. The time step used in all simulations was 0.05 ms. The resting membrane potential was set to -80 mV.

The models of axonal Na^+ and K^+ channels suggested by Engel and Jonas (2005) are based on the data recorded from mossy fiber boutons and reconstructed in our previous study (Ohura and Kamiya, 2018b; Kamiya, 2019b). The model assumed a Hodgkin Huxley-type gating model adapted to channels recorded in mossy fiber terminals, and K^+ channel inactivation (Geiger and Jonas, 2000) was reconstructed by implementing multiplicatively with parameters of recombinant $K_V1.4$ channels (Wissmann et al., 2003). The reversal potential of the leak conductance was set to −81 mV to maintain stability. Voltage-gated Na^+ channels and K^+ channels were inserted into all compartments of the granule cell model, respectively. The Na^+ conductance density was set to 50 ms cm^{-2} for the axon and boutons and 10 ms cm^{-2} for the soma. The K^+ conductance density was set to 36 ms cm^{-2} throughout all parts of the neurons. Action potentials were evoked by injection of depolarizing current into the 9th bouton (0.2 ms, 0.1 or 0.2 nA) or the soma (2 ms, 0.2 nA). The equilibrium potentials for Na^+ and K^+ ions were assumed to be +50 and −85 mV, respectively.

The models of presynaptic Ca^{2+} channels of P/Q-type, N-type, and R-type are reconstructed using the kinetic parameters supplied in Table 2 of the paper by Li et al. (2007). The gating models of these presynaptic Ca^{2+} channels assumed six states gating model consisting of five closed states (C0–C4) and a single open state (O) for each subtype. Transitions from C0 to C4 are assumed to be voltage-dependent, while a transition from C4 to O is voltage-independent. To test for the efficacy of presynaptic Ca^{2+} channel activation by propagating action potentials, the Ca^{2+} current at the mossy fiber boutons was calculated.

In addition, spillover transmission from surrounding interneurons (Alle and Geiger, 2007), namely GABA-EPreSPs, was tested for the functional impact on the action potential propagation and the subsequent Ca^{2+} entry to the presynaptic terminals. For the simulation of this form of subthreshold axonal voltage signaling, $GABA_A$ receptor-mediated conductances were introduced into the axonal membrane in between MFBs at the same density (10 point sources of 0.01 ns distributed along 150 μm of the axon), because the surfaces of MFBs and interleaved in the model are of comparable size. The reversal potential of $GABA_A$ receptor-mediated currents of −65 mV is taken to be similar to that of somatodendritic $GABA_A$ receptors of granule cells (Misgeld and Frotscher, 1986). This would correspond to an intracellular chloride concentration of 12 mM for a receptor channel permeable exclusively to chloride ions (Bormann et al., 1987). The reversal potential of −78 mV was chosen to study isolated shunt effects (corresponding to intracellular chloride concentrations of 7 mM), and that of −52 mV (corresponding to 21 mM) was chosen to simulate relatively high presynaptic chloride concentrations as have been observed at the calyx of Held (Price and Trussell, 2006), and neocortical proximal axons (Szabadics et al., 2006). The time course of the simulated $GABA_A$ receptor-mediated conductance change was chosen such that the resulting current matched the observed spill-over currents.

Results

Implementing active conductances into the model of EPreSP propagation

In a previous study, it was reported that passive propagation of axonal subthreshold voltage signaling was quantitatively reconstructed in a multi-compartment model of hippocampal mossy fibers mimicking the structure of *en passant* axon and the passive properties of cell membranes (Alle and Geiger, 2006). To look for the functional impacts of axonal subthreshold voltage signaling on the spike propagation and the subsequent transmitter release, it was attempted to incorporate active conductances such as the voltage-dependent Na^+- and K^+-channels for reconstructing action potential propagation along axons, as well as voltage-dependent Ca^{2+}-channels for transmitter release from the axon terminals. For this purpose, we adopted the modified Hodgkin and Huxley-type model that incorporated the experimentally determined gating properties of presynaptic Na^+ channels (Engel and Jonas, 2005) as well as presynaptic K^+ channels which shows inactivation (Geiger and Jonas, 2000), reconstructed in Ohura and Kamiya (2018b). To verify that the model reconstitutes the axonal Na^+-channel properties, simulations of voltage-clamp conditions in the single compartment of a 10 μm sphere were performed (**Figure 1A**). The calculated Na^+ current (I_{Na}) represents similar kinetic properties and voltage-dependency to those reported in the direct recording experiments from the mossy fiber terminals (Engel and Jonas, 2005). For instance, the time constants (τ) of

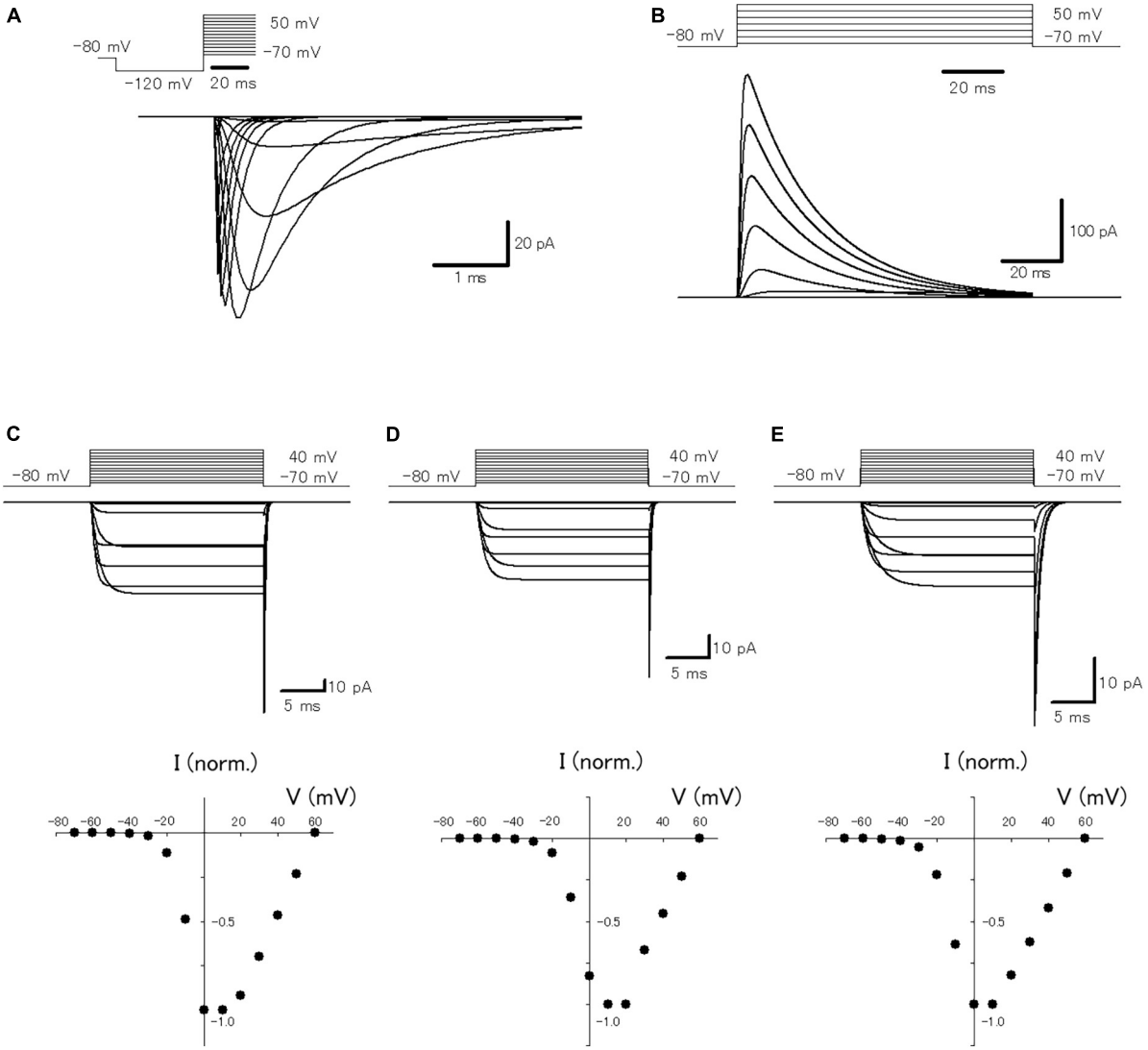

FIGURE 1
Reconstruction of axonal sodium and potassium current as well as presynaptic calcium current at the hippocampal mossy fiber boutons. **(A)** The voltage-dependency of activation of the simulated axonal sodium current. Traces of calculated sodium current at various test potentials: holding potential at −80 mV for 10 ms, pre-pulse at −120 mV for 30 ms, and test pulses between −70 and +70 mV with 10 mV increments. **(B)** The voltage-dependency of activation of the simulated axonal potassium current. Traces of calculated potassium current by test pulses between −70 and +50 mV with 20 mV increments. The voltage-dependency of activation of the reconstructed P/Q-type **(C)**, N-type **(D)**, and R-type **(E)** components of presynaptic calcium current. Traces of calculated calcium current at various test potentials: holding potential −80 mV, test pulses to between −70 and +40 mV with 10 mV increment, and step back to −80 mV. The lower graphs represent the I–V relationship of the reconstructed P/ Q-, N-, and R-type components of presynaptic calcium current.

activation and inactivation at −40 mV were 250 μs and 1.75 ms in this simulation, while that determined experimentally was 264 ± 77 μs and 0.95 ± 0.11 ms, respectively. The calculated K^+ current (I_K) also shows similar gating properties including inactivation during prolonged depolarization (**Figure 1B**) as experimentally observed by Geiger and Jonas (2000). The time constant of inactivation at 30 mV was 24.5 ms in this simulation, while that determined experimentally was 15.5 ± 0.6 ms. In addition, it was attempted to reconstruct the model of presynaptic Ca^{2+} channels at mossy fiber boutons composed of P/ Q-, N-, and R-types. The calculated P/Q-type, N-type, and R-type Ca^{2+} current (I_{Ca}) represent the kinetics of activation and deactivation as well as voltage-dependency (**Figures 1C–E**) similar to those observed experimentally (Li et al., 2007). The time constants of activation of P/Q-type, N-type, and R-type I_{Ca} at 0 mV were 1.04, 1.07, and 1.62 ms in this simulation, while that determined experimentally was 0.79 ± 0.09 ms, 0.93 ± 0.14 m, and 1.79 ± 0.28 ms, respectively. It should be noted that relatively slower activation, as well as slower deactivation observed as in a tail current, is reconstructed in

the model of R-type channels (Figure 1E). The time constants of deactivation of P/Q-type, N-type, and R-type ICa at −80 mV were 0.15, 0.16, and 0.60 ms in this simulation, while that determined experimentally was 0.09 ± 0.01 ms, 0.06 ± 0.01 m, and 0.55 ± 0.08 ms, respectively.

To test for the functional influence of subthreshold EPreSPs on the axonal spike propagation and subsequent transmitter release from the presynaptic terminals, the reconstructed models of voltage-dependent Na^+, K^+, and Ca^{2+} channels were implemented into the granule cell model with solely passive membrane properties for the simulation of EPreSPs propagation (Alle and Geiger, 2006) described previously. Consistent with the simulation in the passive model, the subthreshold somatodendritic EPSPs are distributed substantially also into the axon in an active granule cell model (Figure 2A). The calculated EPreSPs at each bouton spaced 150 μm inter-bouton distance gradually decrease the amplitude and the peak time was delayed with the distance from the soma. The peak amplitudes of EPreSPs are plotted against the distance from the soma, and the fitted curve with single exponential decay shows a distance constant λ_{EPreSP} = 448 μm (Figure 2B) similar to 430 μm those obtained in the previous experimental study (Alle and Geiger, 2007).

Introducing voltage-dependent Na^+- and K^+-channels to the model enabled reconstitute the action potentials propagating along the mossy fiber axons (Alle et al., 2009). Stimulation at the soma generated propagating action potentials reliably toward the distal axons (Figure 2C). In addition, the implementation of presynaptic Ca^{2+} channels enabled the calculation of Ca^{2+}-current (I_{Ca}) elicited by the propagating action potentials (Figure 2D). The time course of I_{Ca} nicely reproduced that of experimentally obtained waveforms (Li et al., 2007). Again, the component mediated by R-type showed slower kinetics as shown in the green trace.

Effect of EPreSPs on propagating action potential and the subsequent presynaptic Ca^{2+} entry

Introducing the active conductance to the granule cell model enabled the reconstruction of the propagation of action potentials in the presence and absence of EPreSPs, and passive propagation of dendritic EPSPs distributed to the axon (Alle and Geiger, 2006). Stimulation at the soma elicited action potentials propagating to the axon and I_{Ca} was elicited at the axon terminals in the model as described above (Figure 3A). Preceding synaptic input elicited prolonged depolarization of the proximal axon, and the amplitude of action potential decreased by depolarization of EPreSPs (Figure 3B). It should be noted that the peak height of the action potential also slightly decreased, possibly by the inactivation of Na^+ channels (Figures 3B–D). As expected from the decrease in both the amplitude and the peak height of action potentials, the calculated I_{Ca} reduced the peak without affecting the time course significantly (Figures 3B–D). It is also calculated EPreSPs without stimulating the soma, to see whether EPreSPs themselves elicited substantial I_{Ca}. Although EPreSP alone does not seem to evoke a substantial inward current with the same gain, magnification of the *Y*-axis visualizes the slow inward current through the presynaptic Ca^{2+} channels composed of P/Q-, N-, and R-types (Figure 3E), suggesting that subthreshold depolarization surely activate these high-voltage activated Ca^{2+} channels to some extent. Since the previous experimental studies revealed that EpreSPs enhance the action potential-evoked transmitter release (Alle and Geiger, 2006), reduced presynaptic I_{Ca} by preceding EpreSPs may not account for the enhancement of transmitter release. The peak amplitude of I_{Ca} was reduced by EPreSPs to 90.3% (from 113 to 102 pA). The charge transfer of I_{Ca} was also reduced to 89.4% (from 72.0 to 64.4 fC). Although the mechanisms remain to be elucidated, it was supposed that Ca^{2+} entry by the small I_{Ca} during EpreSPs may enhance the transmitter release in a Ca^{2+}-dependent manner.

As a molecular basis of the enhanced synaptic transmission by EPreSPs, high-affinity Ca^{2+}-sensor molecules are supposed to involve. Among them, synaptotagmin 7 (Jackman and Regehr, 2017) is the leading candidate, for the high affinity for Ca^{2+}, slow binding kinetics, and high abundance in many brain regions including hippocampal mossy fibers. It should be noted that the knockout mice of synaptotagmin 7 showed significantly reduced synaptic facilitation at the mossy fiber-CA3 synapses (Jackman et al., 2016).

Effect of GABA-EPreSPs on propagating action potential and the presynaptic Ca^{2+} entry

To further explore the roles of subthreshold voltage signaling in the modulation of axonal functions, then we examined the effect of GABA-EPreSPs (Alle and Geiger, 2007), a subthreshold depolarization of axonal membranes caused by the spill-over transmission from the surrounding GABAergic synapses. Mossy fibers express functional $GABA_A$ receptors on the axonal membrane and activation of the $GABA_A$ receptors enhances the excitability of the mossy fiber axons (Ruiz et al., 2003). The GABA-EPreSPs were calculated by injecting slow synaptic conductance on the assumption that the equilibrium potential of Cl^- as −52 mV assumes a higher Cl^- concentration in the axon terminals (Price and Trussell, 2006), and displayed depolarizing GABA-EPreSPs (Figure 4A) those similar to obtained experimentally (Alle and Geiger, 2007). Action potentials and the subsequent I_{Ca} (Figure 4B) were pronouncedly suppressed by the preceding GABA-EPreSPs (Figure 4C), as expected from

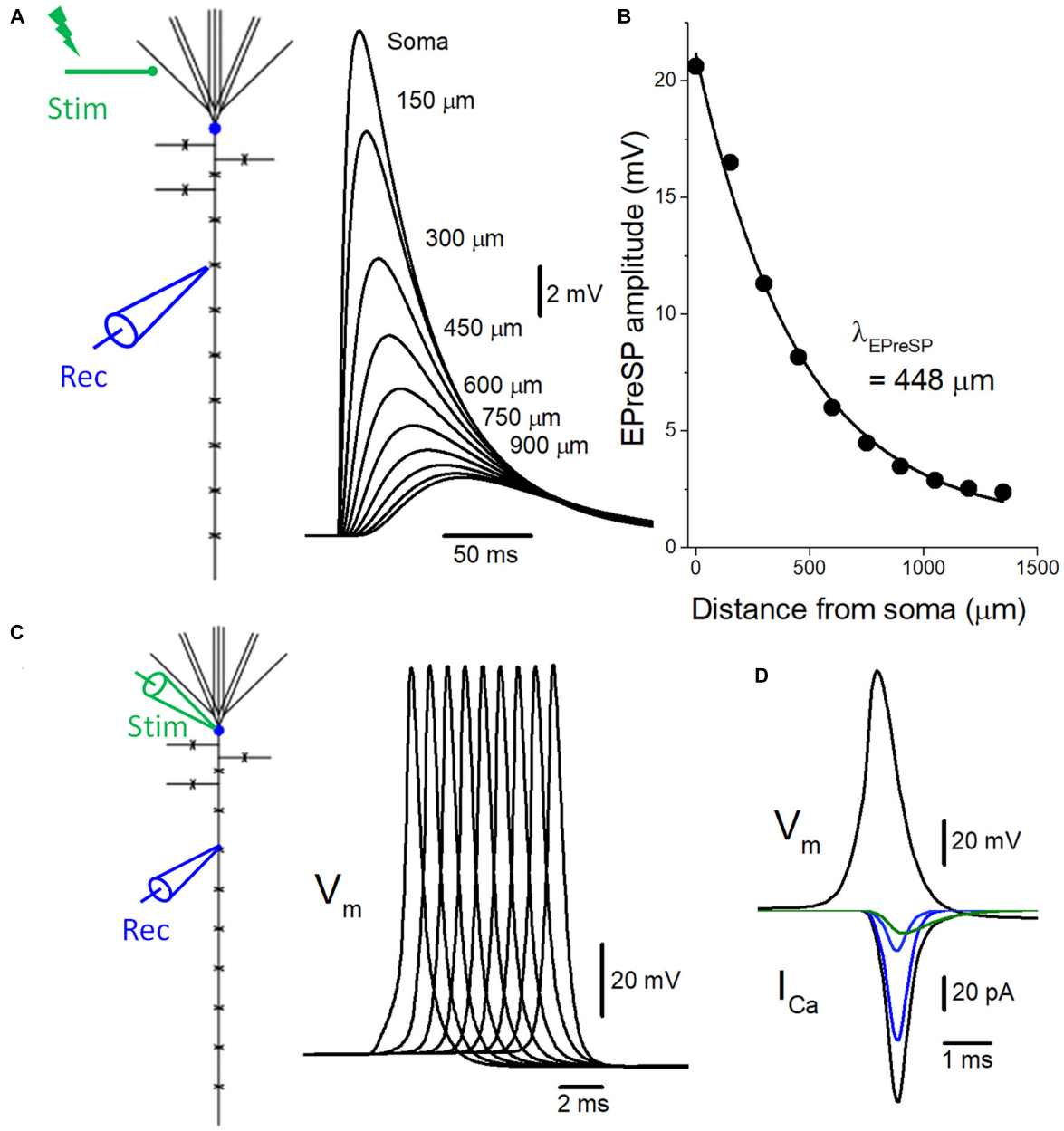

FIGURE 2
Introduction of active conductance to the passive model of voltage signaling along the mossy fiber axon. **(A)** The multi-compartment model of granule cell was reconstructed according to the previous study (Alle and Geiger, 2006). Somatic depolarization, as well as EPreSPs at the mossy fiber boutons evenly spaced every 150 μm along the main axons elicited by subthreshold dendritic synaptic input, are superimposed. **(B)** The peak amplitudes of EPreSPs are plotted against the distance from the soma. The fitted curve with single exponential decay shows a similar constant λ_{EPreSP} = 448 μm to those obtained in the previous experimental study. **(C)** Propagation of action potentials (V_m: upper) throughout *en passant* axon with 9 boutons evenly spaced every 150 μm following stimulation at the soma. **(D)** Simulated propagating action potentials at the mossy fiber bouton (V_m: upper) and presynaptic Ca^{2+} currents (I_{Ca}: lower) during the action potentials. Total presynaptic calcium current (I_{Ca}: black) consists of the components representing the sum of P/Q- (dark blue), N- (blue), and R-type (green) calcium channels.

shunting effects (Cattaert and El Manira, 1999) expected to influence GABAergic transmission more significantly. When the traces with or without GABA-EPreSPs were superimposed, the time course was not affected much but only the peak amplitudes were suppressed, consistent with the contribution of shunting inhibition (**Figure 4D**). The peak amplitude of I_{Ca} was reduced by GABA-EPreSPs to 51.7% (from 107 to 55.3 pA). The charge transfer of I_{Ca} was also reduced to 53.0% (from 69.0 to 36.6 fC). As in the case of EPreSPs, small presynaptic I_{Ca} can be visualized with higher

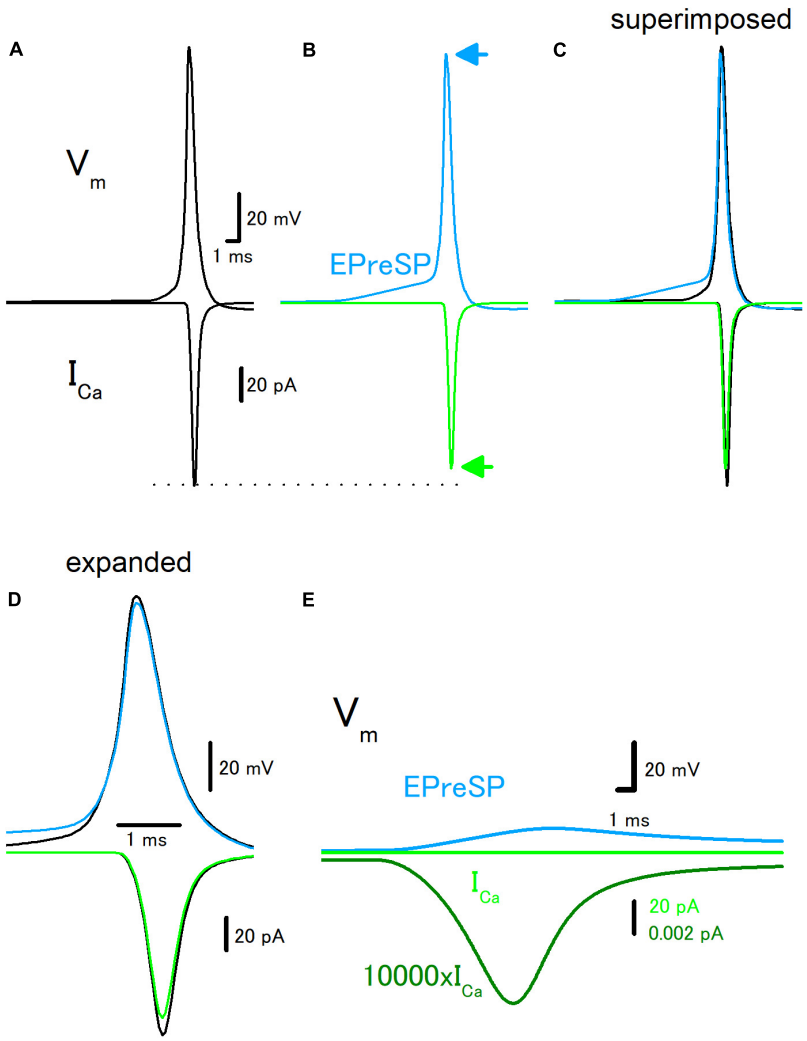

FIGURE 3
Effects of EPreSP on the propagating action potential and presynaptic calcium current. **(A)** Simulated propagating action potential (V_m: upper) and presynaptic calcium current (I_{Ca}: lower) of the first mossy fiber bouton of the main trunk in the control condition. **(B)** Propagating action potential (blue) and presynaptic calcium current (green) were calculated with the preceding EPreSPs elicited by stimulation of dendritic input. The synaptic conductance was set to evoke somatic EPSPs of approximately 20 mV. Superimposed **(C)** and time expanded **(D)** traces of propagating action potential and presynaptic calcium current. **(E)** Subthreshold EPreSP (blue)-induced presynaptic calcium current (green) and that of magnified 10,000 times (dark green). Note that the subthreshold EPreSP itself elicited substantial presynaptic calcium current.

magnification, although it is almost undetectable with the original magnification (Figure 4E).

Discussion

In this study, numerical simulations using a realistic model of hippocampal mossy fiber were performed to illustrate the roles of subthreshold voltage signaling on the propagating action potentials as well as transmitter release processes. EPreSPs, passively propagated dendritic EPSPs into the axon and reduced the amplitudes of action potentials presynaptic calcium current (I_{Ca}) by the slow depolarization. GABA-EPreSPs, another form of subthreshold depolarization of axons by spill-over transmission from surrounding inhibitory neurons, also reduced the amplitudes of action potentials presynaptic I_{Ca} by strong shunting of $GABA_A$ receptor activation.

Reconstruction of action potentials and presynaptic Ca^{2+} current in the granule cell model

In the previous study (Alle and Geiger, 2006), the authors experimentally demonstrated that dendritic EPSPs distribute to the axonal membranes for a substantial distance and were

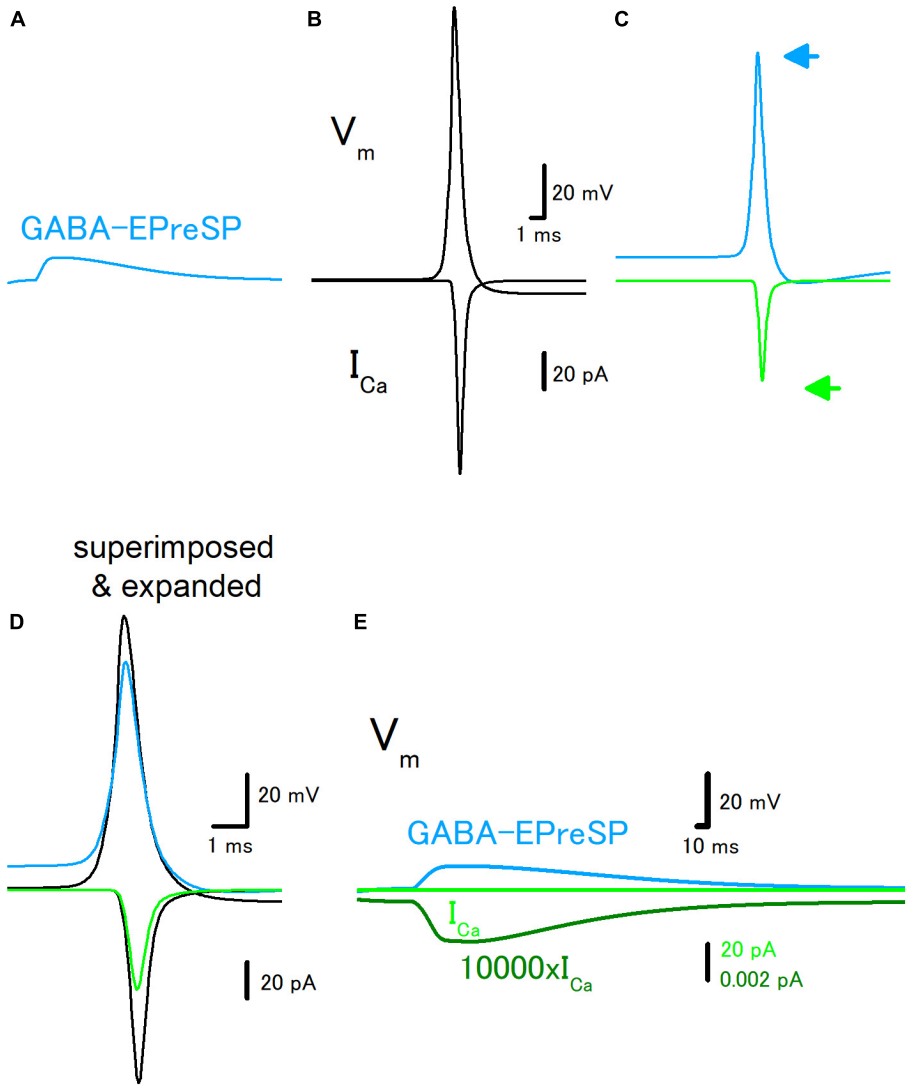

FIGURE 4
Effects of GABA-EPreSP on the propagating action potential and presynaptic calcium current. **(A)** Simulated depolarizing GABA-EPreSPs (blue) elicited by the activating presynaptic $GABA_A$ receptors assuming the reversal potentials of −52 mV positive than the resting membrane potentials. **(B)** Simulated propagating action potential (V_m: upper) and presynaptic calcium current (I_{Ca}: lower) of the first mossy fiber bouton of the main trunk in the control condition. **(C)** Propagating action potential (blue) and presynaptic calcium current (green) were calculated with the preceding GABA-EPreSPs elicited by stimulation of presynaptic $GABA_A$ receptors. The synaptic conductance was set to evoke somatic EPSPs of approximately 20 mV. **(D)** Superimposed and time expanded traces of propagating action potential and presynaptic calcium current. **(E)** Subthreshold GABA-EPreSP (blue)-induced presynaptic calcium current (green) that magnified 10,000 times (dark green).

termed as EPreSPs. They also demonstrated that numerical simulation in the reconstructed granule cell model with passive membrane properties reconstructs the EPreSPs distribution quantitatively. However, the model has not included the active conductance components, and therefore hardly evaluates the effects on the propagating action potentials and subsequent presynaptic Ca^{2+} entry. So far, the model of Na^+ and K^+ channels on the mossy fiber axons was reconstructed according to the paper by Engel and Jonas (2005). In addition, the realistic models of Ca^{2+} channels were reconstructed according to the kinetic parameters obtained by direct recordings from the mossy fiber terminals (Li et al., 2007). By introducing these models of voltage-dependent channels, simulations of EPreSPs, as well as propagating action potentials and subsequent presynaptic Ca^{2+} current, were enabled. It may offer a unique opportunity to evaluate the modulation of axonal functions by subthreshold voltage signaling. Taking advantage of the modeling approach, this study aims at determining the impacts of subthreshold voltage signaling, namely EPreSPs and GABA-EPreSPs, on the propagating action potentials and the presynaptic Ca^{2+} currents. It should be noted that a sufficiently realistic simulation enables extrapolation of the biophysical

mechanisms for modulation of the presynaptic Ca^{2+} dynamics underlying synaptic modulation and plasticity.

Reduction of presynaptic Ca^{2+} current by preceding EPreSPs

To illuminate the functional impacts of subthreshold voltage signaling on the axonal functions, the effects of preceding EPreSPs, passive propagated somatodendritic EPSPs into the axon, were explored with the model of mossy fibers incorporated with the active conductances. Our simulation demonstrated that EPreSPs slightly reduced the amplitudes of the propagating action potentials, possibly by reflecting the inactivation of voltage-dependent Na^+ channels. Due to this reduction of the amplitude of action potentials, the presynaptic Ca^{2+} current elicited by the propagating action potentials was suppressed by the preceding EPreSPs. Taking account of the steep non-linear dependency of Ca^{2+} entry on the transmitter release (Wu and Saggau, 1994; Zucker and Regehr, 2002), this may result in the substantial reduction of transmitter release from the mossy fiber terminals.

In the previous experimental study, it was found that the preceding EPreSPs enhanced synaptic transmission (Alle and Geiger, 2006). Although the exact mechanism underlying this synaptic enhancement by the preceding EPreSPs remains elusive, the results of the present simulation study suggested that the Ca^{2+} current elicited by the propagating action potentials is predicted to decrease due to the voltage dependency of the gating properties of the presynaptic Na^+, K^+, and Ca^{2+} channels. This indicates that some additional mechanisms are involved to counteract the predicted decrease in Ca^{2+} entry. One candidate mechanism would be the facilitation of presynaptic Ca^{2+} current observed in the Calyx of Held axon terminals (Cuttle et al., 1998) by Ca^{2+}-dependent mechanisms (Tsujimoto et al., 2002; Mochida et al., 2008; Leal et al., 2012). Since our Ca^{2+}-channel model on the hippocampal mossy fiber terminals does not undergo facilitation when tested with a paired-pulse protocol of 50 ms interval of the short depolarizing pulse to 0 mV for 1 ms (not shown), it is speculated that Ca^{2+}-dependent facilitation of presynaptic Ca^{2+} channels contributes to counteract suppression of Ca^{2+} entry during propagating action potentials by the preceding EPreSPs. Alternatively, slow depolarization by EPreSPs may inactivate axonal K^+-channels (Geiger and Jonas, 2000; Alle et al., 2011) and prolong the duration of action potentials to enhance the presynaptic Ca^{2+} entry. In this view, it should be noted that our previous experimental study demonstrated that presynaptic Ca^{2+} current during action potentials at hippocampal mossy fiber terminals facilitate by the afterdepolarization (ADP), a slow subthreshold depolarization following the action potentials lasting for tens of milliseconds, to a small extent (Ohura and Kamiya, 2018b; Kamiya, 2019a). The contribution of the subthreshold-active K_v7 potassium channels (Martinello et al., 2015) or the kainate-type glutamate receptors (Schmitz et al., 2001) on the mossy fibers was also supposed for regulation by subthreshold voltage signaling. Identification of ionic as well as biophysical mechanisms for this facilitation of presynaptic Ca^{2+} current would be the issue to be clarified in future investigations.

Reduction of presynaptic Ca^{2+} current by preceding GABA-EPreSPs

For a more comprehensive understanding of subthreshold voltage signaling in axons, a similar test has been adopted for the GABA-EPreSPs due to heterosynaptic activation of axonal $GABA_A$ receptors due to spill-over transmission from the surrounding inhibitory synapses (Alle and Geiger, 2007). Hippocampal mossy fiber express $GABA_A$ receptors (Bergersen et al., 2003), and activation of these receptors enhances the excitability of mossy fiber axons (Ruiz et al., 2003). Possible higher Cl^- concentration in axon than in somatodendritic compartment (Price and Trussell, 2006) resulting in depolarization by activation of presynaptic $GABA_A$ receptors (Szabadics et al., 2006). Simulation in this study revealed that the preceding GABA-EPreSPs suppressed the action potential amplitude and the Ca^{2+} current. It is worth noting that the effect is more prominent for GABA-EpreSPs than EPreSPs, as expected from shunting (Segev, 1990; Graham and Redman, 1994) due to the increased Cl^- conductance by activation of $GABA_A$ receptors (Staley and Mody, 1992). Although spill-over transmission by GABA enhances the excitability of the axons, it may suppress synaptic transmission at the mossy fiber-CA3 synapse at each synaptic contact by a prominent shunting effect by GABA. This notion was also supported by the measurement of presynaptic Ca^{2+} transients from a single mossy fiber terminal revealed that activation of presynaptic $GABA_A$ receptors suppressed the presynaptic Ca^{2+} transients (Ruiz et al., 2003). This form of modulation may be drawn as a close analogy of presynaptic inhibition at the primary afferent synapse (Nicoll and Alger, 1979) in that depolarizing action of presynaptic $GABA_A$ receptors leads to the suppression of transmitter release from the axon terminals.

In this study, a series of numerical simulations using a sufficiently realistic model of hippocampal mossy fiber was performed to illustrate the functional consequence of subthreshold voltage signaling along the axon. EPreSPs by passive propagation of dendritic EPSPs into the proximal portions of the axons are expected to reduce the presynaptic Ca^{2+} entry during action potentials, while the subthreshold depolarization may elicit a small Ca^{2+} current by itself. It was speculated that the enhanced synaptic transmission by EPreSPs observed in the previous experimental study (Alle and Geiger, 2006) may be explained by assuming Ca^{2+}-dependent facilitation of the transmitter release process. Since

it was demonstrated that the hippocampal mossy fibers express abundant synaptotagmin 7 which critically be involved in the facilitation of a wide dynamic range at this synapse (Jackman et al., 2016), the contribution of this high-affinity Ca^{2+}-sensor molecule, as well as facilitation of P/Q-type Ca^{2+} channels as well as action potential broadening of action potential by accumulated inactivation of K^+ channels (Geiger and Jonas, 2000) are supposed to be involved. Despite the unveiled detailed mechanisms, this non-canonical mode of voltage-signaling axon may add extreme complexity to the information transfer at the hippocampal mossy fiber synapse.

Data availability statement

All datasets generated for this study are included in the article.

Author contributions

HK performed the simulation, analyzed the data, and wrote the manuscript.

Funding

This study was supported by Grant-in-Aid for Scientific Research (KAKENHI) from the Japan Society for the Promotion of Science (21K06434 and 21H05166 to HK).

Conflict of interest

The author declares that the research was conducted in the absence of any commercial or financial relationships that could be construed as a potential conflict of interest.

Publisher's note

All claims expressed in this article are solely those of the authors and do not necessarily represent those of their affiliated organizations, or those of the publisher, the editors and the reviewers. Any product that may be evaluated in this article, or claim that may be made by its manufacturer, is not guaranteed or endorsed by the publisher.

References

Alle, H., and Geiger, J. R. (2006). Combined analog and action potential coding in hippocampal mossy fibers. *Science* 311, 1290–1293. doi: 10.1126/science.1119055

Alle, H., and Geiger, J. R. (2007). GABAergic spill-over transmission onto hippocampal mossy fiber boutons. *J. Neurosci.* 27, 942–950. doi: 10.1523/JNEUROSCI.4996-06.2007

Alle, H., Kubota, H., and Geiger, J. R. (2011). Sparse but highly efficient Kv3 outpace BKCa channels in action potential repolarization at hippocampal mossy fiber boutons. *J. Neurosci.* 31, 8001–8012. doi: 10.1523/JNEUROSCI.0972-11.2011

Alle, H., Roth, A., and Geiger, J. R. (2009). Energy-efficient action potentials in hippocampal mossy fibers. *Science* 325, 1405–1408. doi: 10.1126/science.1174331

Bean, B. P. (2007). The action potential in mammalian central neurons. *Nat. Rev. Neurosci.* 8, 451–465. doi: 10.1038/nrn2148

Bergersen, L., Ruiz, A., Bjaalie, J. G., Kullmann, D. M., and Gundersen, V. (2003). GABA and $GABA_A$ receptors at hippocampal mossy fibre synapses. *Eur. J. Neurosci.* 18, 931–941. doi: 10.1046/j.1460-9568.2003.02828.x

Bischofberger, J., Geiger, J. R., and Jonas, P. (2002). Timing and efficacy of Ca^{2+} channel activation in hippocampal mossy fiber boutons. *J. Neurosci.* 22, 10593–10602. doi: 10.1523/JNEUROSCI.22-24-10593.2002

Bormann, J., Hamill, O. P., and Sakmann, B. (1987). Mechanism of anion permeation through channels gated by glycine and gamma-aminobutyric acid in mouse cultured spinal neurones. *J. Physiol.* 385, 243–86. doi: 10.1113/jphysiol.1987.sp016493

Cattaert, D., and El Manira, A. (1999). Shunting versus inactivation: analysis of presynaptic inhibitory mechanisms in primary afferents of the crayfish. *J. Neurosci.* 19, 6079–6089. doi: 10.1523/JNEUROSCI.19-14-06079.1999

Cuttle, M. F., Tsujimoto, T., Forsythe, I. D., and Takahashi, T. (1998). Facilitation of the presynaptic calcium current at an auditory synapse in rat brainstem. *J. Physiol.* 512(Pt 3), 723–729. doi: 10.1111/j.1469-7793.1998.723bd.x

Debanne, D., Bialowas, A., and Rama, S. (2013). What are the mechanisms for analogue and digital signalling in the brain? *Nat. Rev. Neurosci.* 14, 63–69. doi: 10.1038/nrn3361

Debanne, D., Campanac, E., Bialowas, A., Carlier, E., and Alcaraz, G. (2011). Axon physiology. *Physiol. Rev.* 91, 555–602. doi: 10.1152/physrev.00048.2009

Diwakar, S., Magistretti, J., Goldfarb, M., Naldi, G., and D'Angelo, E. (2009). Axonal Na+ channels ensure fast spike activation and back-propagation in cerebellar granule cells. *J. Neurophysiol.* 101, 519–532. doi: 10.1152/jn.90382.2008

Engel, D., and Jonas, P. (2005). Presynaptic action potential amplification by voltage-gated Na^+ channels in hippocampal mossy fiber boutons. *Neuron* 45, 405–417. doi: 10.1016/j.neuron.2004.12.048

Geiger, J. R., Bischofberger, J., Vida, I., Fröbe, U., Pfitzinger, S., Weber, H. J., et al. (2002). Patch-clamp recording in brain slices with improved slicer technology. *Pflugers Arch.* 443, 491–501. doi: 10.1007/s00424-001-0735-3

Geiger, J. R., and Jonas, P. (2000). Dynamic control of presynaptic Ca^{2+} inflow by fast-inactivating K^+ channels in hippocampal mossy fiber boutons. *Neuron* 28, 927–939. doi: 10.1016/S0896-6273(00)00164-1

Graham, B., and Redman, S. (1994). A simulation of action potentials in synaptic boutons during presynaptic inhibition. *J. Neurophysiol.* 71, 538–549. doi: 10.1152/jn.1994.71.2.538

Hines, M. L., and Carnevale, N. T. (1997). The NEURON simulation environment. *Neural Comput.* 9, 1179–1209. doi: 10.1162/neco.1997.9.6.1179

Jackman, S. L., and Regehr, W. G. (2017). The mechanisms and functions of synaptic facilitation. *Neuron* 94, 447–464. doi: 10.1016/j.neuron.2017.02.047

Jackman, S. L., Turecek, J., Belinsky, J. E., and Regehr, W. G. (2016). The calcium sensor synaptotagmin 7 is required for synaptic facilitation. *Nature* 529, 88–91. doi: 10.1038/nature16507

Kamiya, H. (2019a). Excitability tuning of axons by afterdepolarization. *Front. Cell Neurosci.* 13:407. doi: 10.3389/fncel.2019.00407

Kamiya, H. (2019b). Modeling analysis of axonal after potential at hippocampal mossy fibers. *Front. Cell Neurosci.* 13:210. doi: 10.3389/fncel.2019.00210

Kamiya, H., and Debanne, D. (2020). Editorial: axon neurobiology: fine-scale dynamics of microstructure and function. *Front. Cell Neurosci.* 14:594361. doi: 10.3389/fncel.2020.594361

Leal, K., Mochida, S., Scheuer, T., and Catterall, W. A. (2012). Fine-tuning synaptic plasticity by modulation of CaV2.1 channels with Ca^{2+} sensor proteins. *Proc. Natl. Acad. Sci. U.S.A.* 109, 17069–17074. doi: 10.1073/pnas.1215172109

Li, L., Bischofberger, J., and Jonas, P. (2007). Differential gating and recruitment of P/ Q-, N-, and R-type Ca^{2+} channels in hippocampal mossy fiber boutons. *J. Neurosci.* 27, 13420–13429. doi: 10.1523/JNEUROSCI.1709-07.2007

Martinello, K., Huang, Z., Lujan, R., Tran, B., Watanabe, M., Cooper, E. C., et al. (2015). Cholinergic afferent stimulation induces axonal function plasticity in adult hippocampal granule cells. *Neuron* 85, 346–363. doi: 10.1016/j.neuron.2014.12.030

Misgeld, U., and Frotscher, M. (1986). Postsynaptic-GABAergic inhibition of non-pyramidal neurons in the guinea-pig hippocampus. *Neuroscience* 19, 193–206. doi: 10.1016/0306-4522(86)90015-1

Mochida, S., Few, A. P., Scheuer, T., and Catterall, W. A. (2008). Regulation of presynaptic CaV2.1 channels by Ca^{2+} sensor proteins mediates short-term synaptic plasticity. *Neuron* 57, 210–216. doi: 10.1016/j.neuron.2007.11.036

Nicoll, R. A., and Alger, B. E. (1979). Presynaptic inhibition: transmitter and ionic mechanisms. *Int. Rev. Neurobiol.* 21, 217–258. doi: 10.1016/S0074-7742(08)60639-X

Ohura, S., and Kamiya, H. (2016). Excitability tuning of axons in the central nervous system. *J. Physiol. Sci.* 66, 189–196. doi: 10.1007/s12576-015-0415-2

Ohura, S., and Kamiya, H. (2018a). Short-term depression of axonal spikes at the mouse hippocampal mossy fibers and sodium channel-dependent modulation. *eNeuro* 5: ENEURO.0415-17.2018. doi: 10.1523/ENEURO.0415-17.2018

Ohura, S., and Kamiya, H. (2018b). Sodium channel-dependent and -independent mechanisms underlying axonal afterdepolarization at mouse hippocampal mossy fibers. *eNeuro* 5. doi: 10.1523/ENEURO.0254-18.2018

Price, G. D., and Trussell, L. O. (2006). Estimate of the chloride concentration in a central glutamatergic terminal: a gramicidin perforated-patch study on the calyx of Held. *J. Neurosci.* 26, 11432–11436. doi: 10.1523/JNEUROSCI.1660-06.2006

Ruiz, A., Fabian-Fine, R., Scott, R., Walker, M. C., Rusakov, D. A., and Kullmann, D. M. (2003). $GABA_A$ receptors at hippocampal mossy fibers. *Neuron* 39, 961–973. doi: 10.1016/S0896-6273(03)00559-2

Schmidt-Hieber, C., Jonas, P., and Bischofberger, J. (2008). Action potential initiation and propagation in hippocampal mossy fibre axons. *J. Physiol.* 586, 1849–1857. doi: 10.1113/jphysiol.2007.150151

Schmitz, D., Mellor, J., and Nicoll, R. A. (2001). Presynaptic kainate receptor mediation of frequency facilitation at hippocampal mossy fiber synapses. *Science* 291, 1972–1976. doi: 10.1126/science.1057105

Scott, R., Lalic, T., Kullmann, D. M., Capogna, M., and Rusakov, D. A. (2008). Target-cell specificity of kainate autoreceptor and Ca^{2+}-store-dependent short-term plasticity at hippocampal mossy fiber synapses. *J. Neurosci.* 28, 13139–13149. doi: 10.1523/JNEUROSCI.2932-08.2008

Segev, I. (1990). Computer study of presynaptic inhibition controlling the spread of action potentials into axonal terminals. *J. Neurophysiol.* 63, 987–998. doi: 10.1152/jn.1990.63.5.987

Shu, Y., Hasenstaub, A., Duque, A., Yu, Y., and McCormick, D. A. (2006). Modulation of intracortical synaptic potentials by presynaptic somatic membrane potential. *Nature* 441, 761–765. doi: 10.1038/nature04720

Staley, K. J., and Mody, I. (1992). Shunting of excitatory input to dentate gyrus granule cells by a depolarizing GABAA receptor-mediated postsynaptic conductance. *J. Neurophysiol.* 68, 197–212. doi: 10.1152/jn.1992.68.1.197

Szabadics, J., Varga, C., Molnár, G., Oláh, S., Barzó, P., and Tamás, G. (2006). Excitatory effect of GABAergic axo-axonic cells in cortical microcircuits. *Science* 311, 233–235. doi: 10.1126/science.1121325

Trigo, F. F. (2019). Antidromic analog signaling. *Front. Cell Neurosci.* 13:354. doi: 10.3389/fncel.2019.00354

Tsujimoto, T., Jeromin, A., Saitoh, N., Roder, J. C., and Takahashi, T. (2002). Neuronal calcium sensor 1 and activity-dependent facilitation of P/Q-type calcium currents at presynaptic nerve terminals. *Science* 295, 2276–2279. doi: 10.1126/science.1068278

Wissmann, R., Bildl, W., Oliver, D., Beyermann, M., Kalbitzer, H. R., Bentrop, D., et al. (2003). Solution structure and function of the "tandem inactivation domain" of the neuronal A-type potassium channel Kv1.4. *J. Biol. Chem.* 278, 16142–16150. doi: 10.1074/jbc.M210191200

Wu, L. G., and Saggau, P. (1994). Presynaptic calcium is increased during normal synaptic transmission and paired-pulse facilitation, but not in long-term potentiation in area CA1 of hippocampus. *J. Neurosci.* 14, 645–654. doi: 10.1523/JNEUROSCI.14-02-00645.1994

Zucker, R. S., and Regehr, W. G. (2002). Short-term synaptic plasticity. *Annu. Rev. Physiol.* 64, 355–405. doi: 10.1146/annurev.physiol.64.092501.114547

frontiers | Frontiers in Cellular Neuroscience

TYPE Original Research
PUBLISHED 24 August 2022
DOI 10.3389/fncel.2022.920075

OPEN ACCESS

EDITED BY
Luigi Catacuzzeno,
University of Perugia, Italy

REVIEWED BY
Ilenio Servettini,
Università di Napoli Federico II, Italy
Antonio Michelucci,
University of Perugia, Italy

*CORRESPONDENCE
Raul E. Guzman
r.guzman@fz-juelich.de

SPECIALTY SECTION
This article was submitted to Cellular Neurophysiology, a section of the journal Frontiers in Cellular Neuroscience

RECEIVED 20 April 2022
ACCEPTED 28 July 2022
PUBLISHED 24 August 2022

CITATION
Sierra-Marquez J, Gehlen J, Schöneck M, Bungert-Plümke S, Willuweit A, Balduin C, Müller F, Lampert A, Fahlke C and Guzman RE (2022) ClC-3 regulates the excitability of nociceptive neurons and is involved in inflammatory processes within the spinal sensory pathway. *Front. Cell. Neurosci.* 16:920075. doi: 10.3389/fncel.2022.920075

ClC-3 regulates the excitability of nociceptive neurons and is involved in inflammatory processes within the spinal sensory pathway

Juan Sierra-Marquez[1], Jana Gehlen[1], Michael Schöneck[2], Stefanie Bungert-Plümke[1], Antje Willuweit[2], Carina Balduin[2], Frank Müller[1], Angelika Lampert[3], Christoph Fahlke[1] and Raul E. Guzman[1]*

[1]Institute of Biological Information Processing, Molecular and Cellular Physiology (IBI-1), Forschungszentrum Jülich, Jülich, Germany, [2]Medical Imaging Physics, Institute of Neuroscience and Medicine (INM-4), Forschungszentrum Jülich, Jülich, Germany, [3]Institute of Physiology, RWTH Aachen, Aachen, Germany

ClC-3 Cl^-/H^+ exchangers are expressed in multiple endosomal compartments and likely modify intra-endosomal pH and $[Cl^-]$ *via* the stoichiometrically coupled exchange of two Cl^- ions and one H^+. We studied pain perception in *Clcn3*$^{-/-}$ mice and found that ClC-3 not only modifies the electrical activity of peripheral nociceptors but is also involved in inflammatory processes in the spinal cord. We demonstrate that ClC-3 regulates the number of Na_V and K_V ion channels in the plasma membrane of dorsal root ganglion (DRG) neurons and that these changes impair the age-dependent decline in excitability of sensory neurons. To distinguish the role of ClC-3 in Cl^-/H^+ exchange from its other functions in pain perception, we used mice homozygous for the E281Q ClC-3 point mutation (*Clcn3*$^{E281Q/E281Q}$), which completely eliminates transport activity. Since ClC-3 forms heterodimers with ClC-4, we crossed these animals with *Clcn4*$^{-/-}$ to obtain mice completely lacking in ClC-3-associated endosomal chloride–proton transport. The electrical properties of *Clcn3*$^{E281Q/E281Q}$/*Clcn4*$^{-/-}$ DRG neurons were similar to those of wild-type cells, indicating that the age-dependent adjustment of neuronal excitability is independent of ClC-3 transport activity. Both *Clcn3*$^{-/-}$ and *Clcn3*$^{E281Q/E281Q}$/*Clcn4*$^{-/-}$ animals exhibited microglial activation in the spinal cord, demonstrating that competent ClC-3 transport is needed to maintain glial cell homeostasis. Our findings illustrate how reduced Cl^-/H^+ exchange contributes to inflammatory responses and demonstrate a role for ClC-3 in the homeostatic regulation of neuronal excitability beyond its function in endosomal ion balance.

KEYWORDS

ClC-3, chloride-proton exchanger, neuronal excitability, pain, microglia activation, action potential, DRG

Introduction

CLC-type Cl^-/H^+ exchangers are expressed in the endoplasmic reticulum, Golgi apparatus, and endosomes/lysosomes, with isoform-specific subcellular distributions (Jentsch and Pusch, 2018; Bose et al., 2021). Their physiological importance has been demonstrated by studies of knockout animal models and by naturally occurring mutations in patients with genetic diseases: genetic ablation or naturally occurring mutations in *CLCN3* or *CLCN7* causes neurodegeneration in the central nervous system (CNS; Kornak et al., 2001; Stobrawa et al., 2001; Dickerson et al., 2002; Kasper et al., 2005; Duncan et al., 2021). Mutations in the *CLCN4* gene are associated with intellectual disability and epilepsy (Veeramah et al., 2013; Hu et al., 2016; Palmer et al., 2018; He et al., 2021b; Guzman et al., 2022), and *CLCN6* mutations result in West syndrome and lysosomal storage disease (Poet et al., 2006; He et al., 2021a). Genetic ablation of ClC-6 or downregulation of ClC-3 alters pain sensitivity in mice (Poet et al., 2006; Pang et al., 2016), suggesting a role for Cl^-/H^+ exchangers in pain regulation. However, the functions of CLC transporters in the peripheral nervous system are insufficiently understood.

ClC-3 was suggested to contribute to endosomal acidification (which is initially set by the proton ATPase) by mediating shunting inward chloride currents (Stobrawa et al., 2001). However, the strong outward rectification of ClC-3 (Guzman et al., 2013; Rohrbough et al., 2018) argues against such a function and instead suggests that Cl^-/H^+ actively acidifies endosomal compartments by exchanging luminal chloride for protons. However, it is unclear how changes in Cl^-/H^+ exchange modify cell function and how the genetic ablation of individual transporters results in neurodegeneration of variable severity. Impaired pain sensitivity might be caused by a variety of cellular processes; therefore, studying the mechanisms underlying hyperalgesia in $Clcn3^{-/-}$ mice may provide new insight into the cellular functions of CLC-type Cl^-/H^+ exchangers.

We found that $Clcn3^{-/-}$ sensory dorsal root ganglion (DRG) cells are hyperexcitable, likely due to altered plasma membrane densities of Na^+ and K^+ channels (Pang et al., 2016). Moreover, we observed microglia activation within the $Clcn3^{-/-}$ dorsal horn of the spinal cord (DHSC). To distinguish whether these alterations are caused by loss of ClC-3-mediated Cl^-/H^+ exchange or ClC-3 chaperone function, we used a knock-in mouse model ($Clcn3^{E281Q/E281Q}$) that expresses transport-incompetent ClC-3 E281Q (Guzman et al., 2013). Since ClC-4 is targeted to recycling endosomes and lysosomes in the form of ClC-3/ClC-4 heterodimers, $Clcn3^{E281Q/E281Q}/Clcn4^{-/-}$ double-mutant (*DMut*) mice were generated to completely abolish ClC-3-associated Cl^-/H^+ exchange. In these double mutants, disruption of endosomal ClC-3-associated Cl^-/H^+ exchange did not change the excitability of DRG neurons, suggesting that ClC-3-mediated Cl^-/H^+ exchange does not regulate the excitability of nociceptive sensory neurons. However, enhanced microglia activation within the spinal tissue of $Clcn3^{-/-}$ and *DMut* mice indicates that ClC-3 transport is required to maintain neuroglia homeostasis. Our findings demonstrate how ClC-3 Cl^-/H^+ exchangers orchestrate two distinct processes within the sensory pathway.

Materials and methods

Animal handling and maintenance

ClC-3 knockout mice (Stobrawa et al., 2001) were kindly provided by Dr. T. Jentsch (Leibniz-Institut für Molekulare Pharmakologie and Max-Delbrück-Centrum für Molekulare Medizin, Berlin, Germany) and maintained in house by breeding heterozygous mice. Heterozygous $Clcn3^{+/E281Q}$ was generated by Cyagen Biosciences (Santa Clara, CA, United States) by site-directed mutagenesis in the C57BL/6 background. Homozygous animals were obtained by mating heterozygous mice and identified by PCR using the KAPA Mouse Genotyping Kit (Kapa Biosystems/Roche, KK-7302, Wilmington, MA, United States), according to the manufacturer's instruction. All $Clcn3^{-/-}$ mice used in this study showed the same phenotype and identical structural changes previously described by others (Stobrawa et al., 2001; Dickerson et al., 2002; Yoshikawa et al., 2002). The lack of commercially available antibodies (Comini et al., 2022) prevented validation of *ClC-3 knockout* at the protein level. $Clcn4^{-/-}$ mice were generated by Trans Genic Inc. (Kawasaki, Japan), obtained from Deltagen (San Mateo, USA), and maintained as homozygous animals. To generate double-mutant $Clcn3^{E281Q/E281Q}/Clcn4^{-/-}$ homozygous mice, homozygous $Clcn4^{-/-}$ were crossed with homozygous $Clcn3^{E281Q/E281Q}$; the subsequent crossing of heterozygous first-generation offspring was used to generate $Clcn3^{E281Q/E281Q}/Clcn4^{-/-}$ (**Supplementary Figure 1**). All animals were genotyped; PCR protocol and primers for genotyping of all mouse modes are provided in **Table 1**. All mice were housed with a maximum of five mice in the home cage, with food and water ad libitum under controlled conditions with a 12 h–12 h light–dark cycle, air humidity of 55 ± 10%, and a constant room temperature (RT) of 22°C.

Nociceptive testing

Animals of both sexes were used for all nociceptive behavior test experiments, without obvious sex differences. Homozygous

TABLE 1 List of primers used for genotyping.

Primer	Sequence	Product size (bp)
S for wild type (WT)	GATCTAATTCTGCCTTCCTC	550 WT
S for *Clcn3*$^{-/-}$	GGAAGACAATAGCAGGCATGC	650 Mut
AS for WT/*Clcn3*$^{-/-}$	ACTCTGCCCATGTTTTCCACT	WT/Mut
S for WT	TCTTGCGGCGTGGCCGTCCACCCGG	329 WT
S for *Clcn4*$^{-/-}$	GACGTTGTTTGTCTTCAAGAAGCTTC	628 Mut
AS for WT/*Clcn4*$^{-/-}$	CAAGGGGATGACCGCGAGTGACTGTC	WT/Mut
S for WT/ *Clcn3*^{E281Q}	CACGGGATCACAGTAGTGAAAGG	250 WT
AS for WT/ *Clcn3*^{E281Q}	CGCTGCAGTCCATTAAACAGTTTC	332 Mut

S, sense primer, or forward primer; AS, antisense primer, or reverse primer.

female and male mice were compared with their wild-type (WT) littermates at age 21 ± 2 days (P21) or 60 ± 5 days (P60). Before the start of the behavioral test, each mouse was habituated to the testing room for 30 min in a clean single cage. To prevent learning effects, animals were randomly exposed to different temperatures. Each temperature was measured once per day, with at least 1 h between measurements. Animals were rested in empty cages for at least 2 h at RT between the tail flick and hot plate tests.

All behavioral pain experiments were performed by experimenters blinded to the genotype, recorded, and analyzed afterward. For tail flick tests, tails were immersed in water baths (Julabo, Germany) at different temperatures of 46, 48, or 50°C, while the mouse was loosely restrained in the experimenter's hand. The time before the tail withdrawal was recorded, and each temperature was evaluated in triplicate with a one-day interval between tests. The hot plate test was performed by placing mice onto the metal surface of a heating plate (Ugo Basile S.R.L., Gemonio, Varese, Italy), which was surrounded by a 20-cm-high transparent Plexiglas cylinder and allowed free movement. For this set of experiments, temperatures of 46, 48, 50, and 52°C were used. We avoided higher temperatures, which are often used in this test (Marics et al., 2014), because of the hyperalgesia phenotype of *Clcn3*$^{-/-}$. The video-recorded experiments were carefully analyzed using slow-motion presentations. Since a hyperlocomotion phenotype has been described for *Clcn3*$^{-/-}$ mice (Stobrawa et al., 2001), the time period until the animals showed discomfort by licking or shaking the paw was manually analyzed rather than using an automated device. If the animals did not show any reaction within 30 s, they were immediately removed to avoid tissue damage (Marics et al., 2014). The response of each mouse to each temperature was evaluated once per day in triplicate, with 1 h between measurements and one-day interval between tests. After injection of 5 µl 0.5% (v/v) formalin solution into the right hind paw with a Hamilton microliter syringe (Merck KGaA, Darmstadt, Germany), individual mice were placed into a transparent box (19 cm × 19 cm × 11 cm) with three mirrored walls. The number of paw flinches per minute was recorded and analyzed afterward. The number of flinches was manually counted using slow-motion videos. Measurements were repeated every 5 min for a total of 40 min.

Dorsal root ganglion neuron culture

Dorsal root ganglion neurons were cultured according to a previous protocol with slight modifications (Bost et al., 2017). Dorsal roots were dissected from P21 or P60 animals and cleaned from connective tissue and fibers in ice-cold Locke's solution (in mM: 154 NaCl, 5.6 KCl, 3.6 $NaHCO_3$, 5 HEPES [4-(2-hydroxyethyl)-1-piperazineethanesulfonic acid), 6 glucose, adjusted to pH 7.3 with NaOH]. After treatment with 200 µl TrypLE Express Enzyme (Cat. 12604013, Gibco, Grand Island, NY, United States) for 5 min at RT, ganglia were immediately transferred into a tube containing 1 ml Neurobasal-A medium (Cat. 10888022, Gibco, Grand Island, NY, United States), 20 µl freshly thawed Liberase (DH Research Grade, Cat. 5401054001, Roche Diagnostics Deutschland GmbH, Mannheim, Germany), and collagenase to a final concentration of 2.3 units/ml and incubated in a water bath at 37°C. Neurons were dissociated using a three-step process: a 7-min incubation, followed by pipetting 10 times with a 1-ml pipette; a 5-min incubation, followed by pipetting 10 times; and a final 5-min incubation, followed by pipetting 15–17 times. After adding 200 µl fetal bovine serum (Cat. 10270-106, Gibco, Grand Island, NY, United States) and incubating at 37°C for 3 min with gentle agitation, cells were sedimented at 400 × *g* for 4 min. The cell pellet was then washed with 700 µl Dulbecco's phosphate-buffered saline (PBS; Cat. 14190094, Gibco, Grand Island, NY, United States). After re-pelleting (400 × *g* for 4 min), freshly prepared NBA-enriched culture medium containing 1% B-27 supplement (Cat. 17504044, Gibco, Grand Island, NY, United States), 1% GlutaMAX (Cat. 35050061, Gibco, Grand Island, NY, United States), 0.4% penicillin/streptomycin (Cat. 15070-063, Gibco, Grand

Island, NY, United States), and 5% fetal bovine serum in neurobasal-A medium was added to the cells. The neuronal cell suspension was diluted in 3.5-ml-enriched NBA medium, and approximately, 500 µl cell suspension was seeded onto poly-D-lysine-coated coverslips and cultured at 37°C with 5% CO_2 and 90% humidity for 1–5 days. At 24 h after plating, a cocktail of uridine and floxuridine thymidylate synthase inhibitors were added to a final concentration of 40 and 100 mM, respectively; 12 h later, the culture medium was replaced with an enriched NBA medium without inhibitors.

Electrophysiological experiments

Action potentials (APs) were measured using whole-cell recordings in the current-clamp mode under physiological saline solutions, adapted from a published method (Liu et al., 2010; Hoerauf et al., 2015): the bath solution (330 mOsm/kg, adjusted to pH 7.4 with NaOH) contained (in mM) 130 NaCl, 4 KCl, 1 $MgCl_2$, 2 $CaCl_2$, 10 HEPES, and 48 D-glucose. The pipette solution (310 mOsm/kg, adjusted to pH 7.4 with NaOH) contained (in mM) 135 K-gluconate, 7 NaCl, 2 $MgCl_2$, 2 Na-ATP, 0.3 Na_2-GTP, 10 HEPES, and 0.2 EGTA. The passive and active properties of the cells were obtained from the voltage responses to 1 s rectangular current pulse injections, with a pre- and post-pulse period of 500 ms. Resting membrane potentials (RMPs) were recorded a few minutes after establishing the whole-cell configuration. Neurons were visualized using an Andor's Neo 5.5 sCMOs camera attached to the microscope, which is regularly calibrated with a calibration slide. Only neurons with a diameter below 23 µm were used for electrophysiology. Only neurons with a stable RMP between –60 mV and –75 mV and with a series resistance of <12 MΩ were included in the analysis. Input resistance (R_{in}) was calculated as the slope of the relationship between the voltage response to a current injection within a range from –60 to 20 pA before the first AP. AP thresholds were obtained from the first derivative of the voltage response (Lazarus and Huang, 2011) and AP half-widths from the difference between the rising and decaying phase times at the half-maximum amplitude of the AP. The after-hyperpolarization amplitude (AHP) is defined as the difference between the AP threshold and the minimum voltage response after the peak maximum. All AP properties were analyzed from the first-ever AP using a custom-written Igor-based macro (Igor Pro 7.01 software, WaveMetrics; kindly provided by Dr. Karlijn van Aerde and Dr. Dirk Feldmeyer, INM-10, Forschungszentrum Jülich).

An index to evaluate the intrinsic excitability was used to estimate the excitability of the neuron, as previously described (Lazarus and Huang, 2011): a lower excitability index (EI) indicates a more excitable cell, and a higher EI a less excitable cell (Lazarus and Huang, 2011). The EI is calculated using properties, such as RMP, AP threshold, and R_{in}, as follows:

$$EI = \left(\frac{AP\ threshold - RMP}{R_{in}}\right)$$

Sodium and potassium currents were measured using whole-cell patch-clamp recordings in the voltage-clamp mode. To reduce space-clamp errors, healthy DRG neurons with no obvious processes were used within the first 24 h after plating. For sodium currents, the bath solution contained (in mM) 20 NaCl, 105 choline-Cl, 3 KCl, 1 $MgCl_2$, 1 $CaCl_2$, 10 HEPES, 10 D-glucose, 20 tetraethylammonium chloride, 0.1 $CdCl_2$, and 3 4-aminopyridine (4-AP) at 305 mOsm/kg and pH 7.4 (adjusted with choline-OH), and the pipette solution contained (in mM) 7 NaCl, 105 CsF, 10 EGTA, 10 HEPES, and 50 D-glucose at 300 mOsm/kg and pH 7.4 (adjusted with CsOH). To distinguish tetrodotoxin-sensitive (TTX-S) and TTX-resistant (TTX-R) sodium channels, TTX was applied to a final concentration of 300 nM *via* a perfusion pipette, and current recordings were compared before and after the application of TTX (Meents and Lampert, 2016; Fischer et al., 2017). For potassium currents, the bath solution contained (in mM) 150 choline-Cl, 5 KCl, 1 $MgCl_2$, 2 $CaCl_2$, 10 HEPES, 1 $CdCl_2$, and 10 D-glucose at 320 mOsm/kg and pH 7.4 (adjusted with choline-OH), and the pipette solution contained (in mM) 120 K-gluconate, 20 KCl, 2 $MgCl_2$, 1 $CaCl_2$, 10 EGTA, 10 HEPES, 5 Mg-ATP, and 0.3 Na_2-GTP at 315 mOsm/kg and pH 7.4 (adjusted with NaOH). To block fast-inactivating potassium currents, 5 mM 4-AP was added to the bath solution. In all cases, the osmolality was adjusted with D-glucose and measured with a freezing point osmometer (Osmomat 3000 basic, Gonotec).

Na^+ currents were elicited by applying 50-ms test pulses (–100 mV to +40 mV in 5 mV increment every 3 s) from a holding potential of –100 mV. Current inactivation was studied with 500-ms test pulses (–100 mV to +30 mV in 5 mV increment, followed by a 50 ms step at –10 mV) every 3 s from a holding potential of –100 mV. K^+ currents were elicited by applying 100 ms test pulses (–80 mV to +60 mV in 10 mV increment every 3 s) from a holding potential of –80 mV. Inward-rectifier K channels (IRK) currents were studied during 200-ms test pulses (0 mV to –160 mV in 10 mV decrement every 3 s) from a holding potential of –50 mV.

Recordings were filtered at 10 kHz and sampled at 100 kHz using an EPC10 double patch amplifier, controlled by PatchMaster (HEKA Elektronik). Borosilicate pipettes (GC150F-10, Harvard Apparatus, United States) were pulled with a resistance of 1.9–2.9 MΩ and coated with a thin layer of wax to reduce the capacitance. Cell capacitance (C_m) and series resistance (R_s) were compensated, and P/4 leak subtraction with a baseline of –80 mV (for K^+ currents) and −100 mV (for Na^+ currents) was used to correct linear current components. Peak currents for sodium and mean steady-state currents were plotted against the test voltage to obtain current–voltage relationships.

Activation curves for sodium currents were derived by plotting normalized G_{Na} as a function of test potential and fitted with the Boltzmann equation (Meents and Lampert, 2016).

Immunohistochemistry

Dissected spinal cord, dorsal roots, and hippocampus were fixed with 4% PFA for 45 min and retinal tissues for 20 min. All fixed tissues were immersed in a 10% sucrose solution for 1 h at RT and incubated overnight in 30% sucrose at 4°C. After cryoprotection, samples were embedded in optimal cutting temperature compound. Tissue sections (20 µm for the spinal cord, dorsal roots, and retina; 100 µm for the hippocampus) were cut using a cryostat, mounted onto single slides, dried for 5 min at RT, and stored at −20°C until use. To unmask antigens and epitopes (for all antibodies except anti-recoverin and anti-rhodopsin antibodies), sections were treated with sodium citrate buffer (10 mM sodium citrate containing 0.05% Tween 20, pH 6.0 adjusted with NaOH) at 80°C for 15 min and then blocked in PBS containing 0.5% Triton X-100, 10% fetal bovine serum, and 1% bovine serum albumin for 2 h at RT. Samples were incubated with primary antibody (**Table 2**) diluted in blocking solution for 72 h at 4°C (RT for retinal sections). Slides were then washed five times for 10 min each with 0.1 M phosphate buffer (PB; 100 mM Na_2HPO_4 and 100 mM NH_2PO_4, adjusted to pH 7.2 with NaOH) and incubated with secondary antibody (**Table 2**) diluted in blocking solution for 1.5 h at RT in a dark humidified chamber. Finally, slides were washed five times with PB and mounted with Aqua-Poly/Mount on a glass coverslip. Slides were stored overnight at RT until completely dry and stored at −20°C until analysis.

Confocal microscopy and image analysis

Optical images were acquired on a confocal microscope (TCS SP5 II, Leica Microsystems, Germany) using a 20 × /0.70 or 63 × /1.32–0.6 oil immersion objective and digitalized at a resolution of 1024 × 1024 pixels, 200 Hz velocity, and 6-line average in sequential scanning mode. For large tissue imaging, a tile-scan procedure was applied with a 10% stitching threshold. Identical laser intensities and digital gains were used when comparing samples from different phenotypes. Images were processed with FIJI Image J v.1.53c (Wayne Rasband, National Institutes of Health, United States; Schindelin et al., 2012; Rueden et al., 2017), and a self-made pipeline in CellProfiler™ v.3.1.9 cell image analysis software (Broad Institute, Cambridge, MA, United States; Lamprecht et al., 2007; McQuin et al., 2018) was used for automated analysis of cellular fluorescence, area, and shape and number of events. Confocal immunofluorescence images were exported in color and eight-bit grays, and region of interest (ROI) was defined in dorsal horn layers I to IV according to the Allen Brain Atlas of the Mouse Spinal Cord (Lein et al., 2007). Using the point-and-click graphical user interface (GUI), we created a sequential series of modules for image and object processing function. For neuronal counting, "Neurons" for the NeuN staining and "nuclei" for the To-Pro-3 were applied using a global or adaptive threshold strategy. Both objects were delimited using OTSU image processing with either two- or three-class thresholding with a threshold correction factor of 1.0 and a minimum lower bound of 0.2 (pixels below this number were not considered). Neurons and nuclei were identified using a shape method that used peak brightness to identify like-rounded objects. The same approach was used to identify the processes of the astrocytes, microglia, and chemokine ligand (CCL2) staining. The percentage of the area covered by each channel was obtained by dividing it by the area of the ROI. This protocol was standardized with pictures from all phenotypes, and then a high-throughput analysis was done for the whole data set. Although the pipeline was helpful for quantification in the dorsal horn of the spinal cord, counting the DRG neurons was only possible manually using ImageJ.

Western blotting

Tissue samples from at least two animals were homogenized in ice-cold homogenizing buffer containing 2 mM EDTA pH 8.0, 1 mM cOmplete™ (Cat. 5056489001, COEDTAF-RO, Roche, Mannheim, Germany), and protease inhibitor cocktail mPIC, 1:500 dilution (Cat. P8340, Sigma Aldrich-Merck KGaA, Darmstadt, Germany) and sedimented at 100,000 × *g* for 15 min at 4°C. Pellets were resuspended in solubilization buffer (1% SDS, 10 mM NaPOi (phosphate buffer composed of 92.2 mmol Na_2HPO_4 and 6.8 mmol NaH_2PO_4), and 1 mM cOmplete™) and sedimented at 15000 × *g* for 10 min. Samples were heated at 95°C for 5 min with a 4× loading buffer (200 mM Tris-Cl, pH 6.8, 8% SDS, 4% 2-mercaptoethanol, 50% glycerin, and 0.04% bromophenol blue), and proteins were resolved by polyacrylamide gel electrophoresis. After transfer to PVDF membrane using the semi-dry transfer technique, membranes were dried overnight, blocked for 2 h in 5% nonfat milk solution in PBS containing 0.05% Tween-20 (PBS-T) or in PBS-T containing 3% bovine serum albumin, and incubated overnight at 4°C with primary antibody (anti-rabbit $Na_v1.8$ sodium channel, or mouse anti-α-tubulin; **Table 2**). Membranes were washed with PBS-T and incubated for 1 h with goat-α-rabbit IgG-horseradish peroxidase (HRP) secondary antibody (**Table 2**). Membranes were exposed to an equal amount of enhanced chemiluminescent Super Signal™ West Pico PLUS (Cat. 34579, Thermo Scientific, Waltham, MA, United States)

TABLE 2 List of antibodies used in immunohistochemistry and Western blot experiments.

Primary antibodies	Catalog N°	Dilution	RRID
Goat-α-Rabbit IgG-Peroxidase, Merk	A6154	1:25000	AB_258284
Anti-mouse α-Tubulin	T9026	1:1000	AB_477593
Anti-rabbit $Na_v1.8$ (SCN10A), Alomone	ASC-016	1:500	AB_2040188
CGRP Anti-rabbit, Millipore	AB15360	1:4000	AB_672958
NeuN Anti-rabbit, Abcam	AB104225	1:1000	AB_10711153
NeuN Anti-mouse, Millipore	MAB377	1:500	AB_2298772
CD11b Anti-rabbit, Abcam	AB133357	1:500	AB_2650514
Glial fibrillary acidic protein (GFAP) anti chicken, Novus	NB110-58368	1:500	AB_921444
Isolectin GS-IB4 Biotin-XX, Invitrogen	I21414	1:500	AB_2314665
MCP-1 (CCL2) Anti-mouse, Merk	SRP4207	1:500	
TRPV1, Anti-rabbit, Synaptic Systems	444 003	1:1000	AB_2864791
Recoverin, Anti-rabbit, Chemicon	AB5585	1:2000	AB_2253622
Rhodopsin antibody, 1D4, Anti-mouse. R. Molday, University of British Columbia.	MA1-722	1:500	AB_325050 (Thermo Fischer)
Secondary antibodies and markers			
Donkey anti mouse Cy3 Dianova	715-165-150	1:200	AB_2340813
Donkey anti rabbit Cy2 Dianova	711-225-152	1:400	AB_2340612
Donkey anti rabbit Cy5 Dianova	711-175-152	1:400	AB_2340607
Donkey anti chicken Cy2 Dianova	703-545-155	1:500	AB_2340375
Streptavidin A488, Thermo Fisher	S11223	1:1000	
TO-PRO^{TM}-3 A642, Thermo Fisher	T3605	1:1000	

RRID, Research resource identifier.

substrate, and the exposure time was adjusted depending on protein abundance (1–10 min) to maximize band visibility and minimize background.

Real-time PCR

Total RNA was extracted from freshly dissected DRG neurons from two-month-old mice using the TRIzol^{TM} (Cat. 15596026, Invitrogen, Carlsbad, CA, United States)-chloroform method, and 1 μg total RNA was converted into cDNA using One-Step SuperScript^{TM} III® reverse transcriptase (Cat. 12574018, Invitrogen, Carlsbad, CA, United States) in a Gradient Thermocycler (Biometra, Göttingen, Germany). The master mix contained 12.5 μl 2× reaction mix (containing 0.4 mM each dNTP and 3.2 mM $MgSO_4$), 1 μl enzyme, 0.5 μl 10 mM sense/antisense primers (specific for each isoform), 1 μg template RNA, and RNA-free water to a final volume of 25 μl. cDNA was synthesized by incubation for 30 min at 55°C, followed by 2 min at 94°C. PCR conditions were 40 cycles of 15 s at 94°C (denaturation), 30 s at 55–65°C (annealing), and 5 min at 68°C for the extension, with a final step of 1 min at 68°C. The reference gene was 18S RNA. Primers to identify the ClC isoforms are listed in Table 3. PCR products were assessed by 1% agarose gel electrophoresis [with SYBR^{TM} safe (Cat. S33102, Invitrogen, Carlsbad, CA, United States) staining] at 120 V for 35 min. PCR band size was determined using a GeneRuler 100 bp DNA Ladder (Cat. SM0322, Thermo Scientific, Waltham, MA, United States).

Data analysis

Statistical analysis was performed using OriginPro version 2018b (OriginLab Corporation, Northampton, MA, United States) and Microsoft Excel (Microsoft 365). Data are presented as the mean ± standard error of the mean (SEM) and plotted as boxplots (with boxes indicating the upper and the lower quartiles and whiskers the upper and lower 90 percentiles). The non-paired two-tailed *t*-test or the Mann–Whitney test was used to compare two groups, depending on whether the data followed a normal distribution. For comparing more than two groups, one-way ANOVA was used for normally distributed data without significant variance inhomogeneity. For more than two factors or independent variables, and one dependent variable, two- or three-way ANOVA was used. If *F*-value was statistically significant ($p < 0.05$), a Tukey *post hoc* test was conducted.

Each data sample was collected randomly and considered independent. We used the Shapiro–Wilk test to evaluate if the data followed a normal distribution and Levene's test for assessing the homogeneity of variances. Data that did not follow a normal distribution were normalized. If normalization

TABLE 3 List of primers used to identify the ClC exchangers in dorsal root ganglion (DRG).

Isoform	Sequence	Type	Size (bp)
ClC-3a	5′-CGCCCAGCTTGCTATGCCTCTGAG-3′	Forward	324
	5′-AGCTAGTGCCCCTGATGCCAGTC-3′	Reverse	
ClC-3b	5′-CGCCCAGCTTGCTATGCCTCTGAG-3′	Forward	500
	5′-AGCTAGTGCCCCTGATGCCAGTC-3′	Reverse	
ClC-3c	5′-ATGGATGCTTCTTCTGATCC-3′	Forward	379
	5′-AGCTAGTGCCCCTGATGCCAGTC-3′	Reverse	
ClC-4	5′-GACGTGGGGACCTACGAGGACTTCC-3′	Forward	508
	5′-CACTCAAAATAGTCTTTATCTCGGGTATGCC-3′	Reverse	
18S	5′-CAGTATGACTCCACTCACGGCAAATTC-3′	Forward	530
	5′-CACAGTCTTCTGGGTGGCAGTGATG-3′	Reverse	

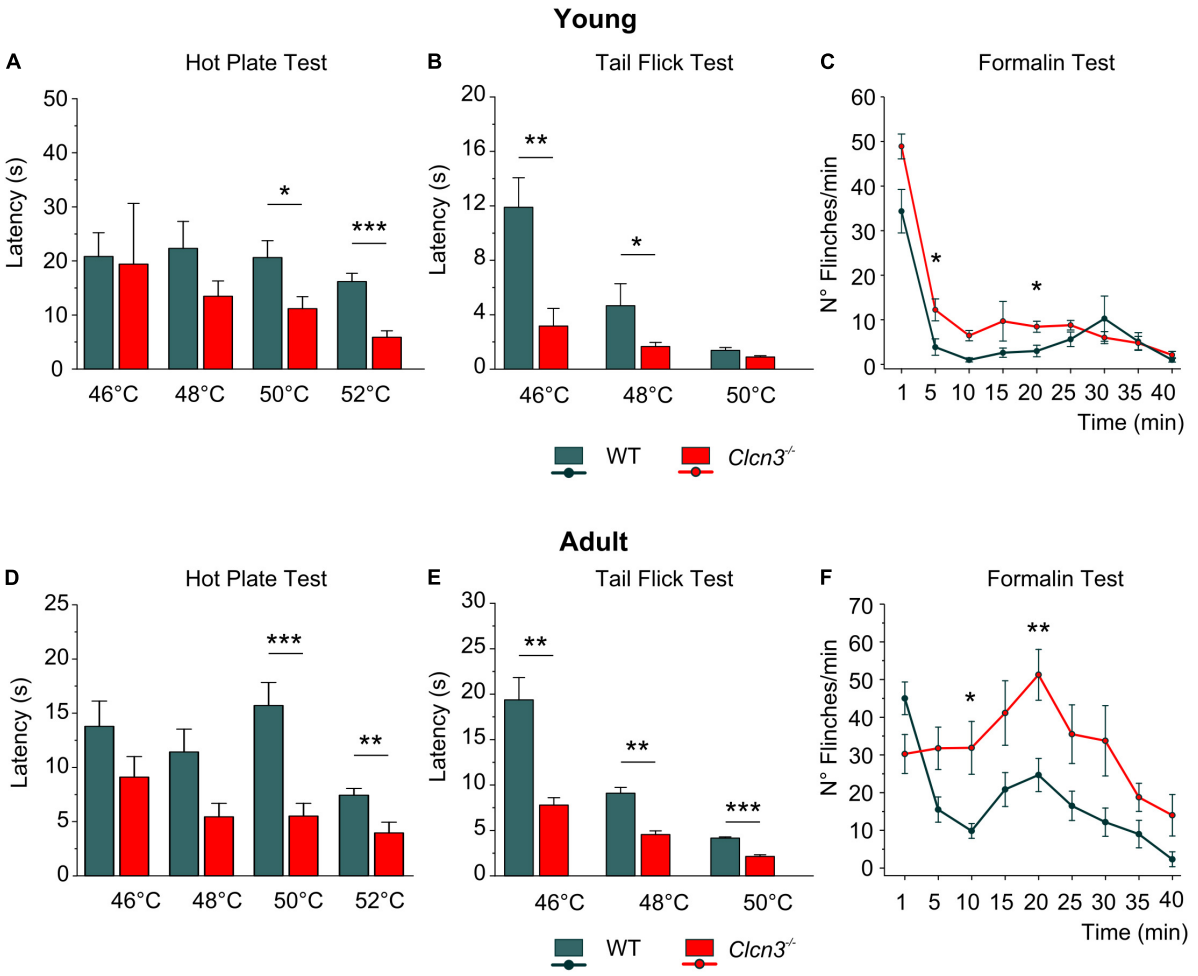

FIGURE 1
Acute pain experiments in young P21 **(A–C)** and adult P60 **(D–F)** mice show increased thermal sensitivity and lower latencies in mutants compared with wild type (WT) animals. **(A)** Hot plate test, P21; WT (n = 7); $Clcn3^{-/-}$ (n = 8). **(B)** Tail flick test, P21; WT (n = 8); $Clcn3^{-/-}$ (n = 9). **(C)** Formalin test, P21; WT (n = 8); $Clcn3^{-/-}$ (n = 9). **(D)** Hot plate test at different temperatures, P60; WT (n = 11); $Clcn3^{-/-}$ (n = 13). **(E)** Tail flick test, P60; WT (n = 8); $Clcn3^{-/-}$ (n = 9). **(F)** Formalin test, P60; WT (n = 6); $Clcn3^{-/-}$ (n = 8). Statistical significance levels are $^{*}p < 0.05$, $^{**}p < 0.01$, $^{***}p < 0.001$. $Clcn3^{-/-}$ versus WT; n represents the number of animals. Two-way ANOVA or three-way ANOVA analyses were used to detect interactions between variables, and Tukey *post hoc* test for pairwise comparisons. Data are presented as the mean ± SEM.

was not possible or variances were not homogenous, a non-parametric test (Mann–Whitney or Kruskal–Wallis ANOVA test) was chosen. Grubb's test was used to test for outliers. The *n* value provides the number of cells (or measurement), and N, the number of animals; both values are given in the figure legends. Differences with *p*-values < 0.05 were considered significant. Asterisk (*) was used to represent differences between groups and (‡) when also animals were compared ($^{*‡}p < 0.05$, $^{**‡‡}p < 0.01$; $^{***‡‡‡}p < 0.001$).

Results

Genetic ablation of ClC-3 leads to hyperalgesia

Clcn3$^{-/-}$ mice suffer from neurodegeneration in the hippocampus and the retina, with loss of neurons beginning at P21 and completed at P60 (Stobrawa et al., 2001). Since neurodegeneration might affect pain sensitivity, we evaluated pain sensitivity before and after neuronal loss at P21 (young) and P60 (adult). At both developmental stages, we found significantly shorter paw withdrawal latencies to heat stimuli in *Clcn3*$^{-/-}$ mice than in WT mice (**Figures 1A,D**). The tail flick test confirmed that *Clcn3*$^{-/-}$ mice are more sensitive to noxious thermal stimuli than the WT animals (**Figures 1B,E**). This phenotype was consistently observed for all temperatures evaluated (**Supplementary Table 1**). In contrast to our results, a previous report did not identify differences in thermal pain perception between *Clcn3*$^{-/-}$ and WT mice (Pang et al., 2016). Pang et al. (2016) used an automated hot plate device that measured the latency of paw licking, rearing, and jumping in triplicate at 15-min intervals. Repeated pain exposure may have modified reaction latencies in these experiments (Suaudeau et al., 2005) and may have masked the differences in response to noxious temperatures we observed between WT and *Clcn3*$^{-/-}$ (**Figure 1**). We, therefore, measured the effects of each temperature only once per day with at least 1 h between measurements.

Subcutaneous injections of formalin (0.5%) into the hind paw trigger a biphasic pain reaction, comprising an early phase (1–5 min post-injection; **Figures 1C,F**) due to direct activation of peripheral nociceptors and an inflammatory late-phase reaction (10 min post-injection) associated with persistent pain signals at the supraspinal level (Taylor et al., 1995; Abbadie et al., 1997). Young *Clcn3*$^{-/-}$ were more sensitive to noxious stimuli at both phases, with significantly more flinches per min in the mutant than in WT animals (**Figures 1C**; **Supplementary Table 2**). However, in the late inflammatory phase, only adult *Clcn3*$^{-/-}$ mice showed more severe reactions than WT (**Figure 1F**; **Supplementary Table 2**), suggesting that lack of ClC-3 alters behavioral pain perception at all ages.

Ablation of ClC-3 changes the excitability of sensory dorsal root ganglion neurons

We next examined the electrical properties of sensory neurons from young and adult WT and *Clcn3*$^{-/-}$ mice using current-clamp recordings. Similar numbers of APs were recorded in DRG neurons from young WT and *Clcn3*$^{-/-}$ upon injection of depolarizing currents (**Figures 2A,B**). However, although the firing rates decreased in older WT mice, this developmental change was not observed in mutant mice (**Figures 2A,B**). The rheobase current (i.e., the minimum current amplitude required to elicit an AP) was reduced in *Clcn3*$^{-/-}$ adult neurons (**Figure 2D**), with membrane input resistances significantly higher in both young and adult *Clcn3*$^{-/-}$ animals (**Figures 2C,E**). AP thresholds and after-hyperpolarization amplitudes (AHP) were slightly shifted toward more depolarizing potentials in *Clcn3*$^{-/-}$ mice compared with WT mice (**Figure 2F**; **Supplementary Figure 2**), but AP amplitudes and RMPs were unchanged (**Figures 2G,H**). We also compared the first, second, third, and fourth APs for WT and mutant adult cells and found that AP thresholds, amplitudes, and AHP were not different (**Table 4**).

We next compared the EI for WT and *Clcn3*$^{-/-}$ cells. The EI integrates multiple cellular properties (see the equation in the "Materials and methods" section), such as RMP, AP threshold, and the input resistance (R_{in}) to estimate the intrinsic excitability of a cell (Lazarus and Huang, 2011), with a lower EI indicating increased excitability. Consistent with the age-dependent reduction in neuronal excitability, we obtained lower EIs for DRG neurons from young WT mice compared with adults. However, in DRG neurons from *Clcn3*$^{-/-}$ mice, EI values did not change with age, resulting in significant differences between adult WT and mutant cells (young DRG, WT 58 ± 4.0 pA vs. *Clcn3*$^{-/-}$ 47 ± 3.0 pA, Student's *t*-test $p = 0.05$; adult DRG, WT 74 ± 9.0 pA vs. *Clcn3*$^{-/-}$, 42 ± 3.0 pA, Mann–Whitney test $p = 0.0017$). We conclude that ClC-3 transporters contribute to the age-dependent regulation of neuronal excitability in sensory DRG cells.

Clcn3 deletion alters ion channel density in the plasma membrane of dorsal root ganglion neurons

Voltage-gated sodium channels are necessary to initiate and propagate APs, and changes in the expression or function

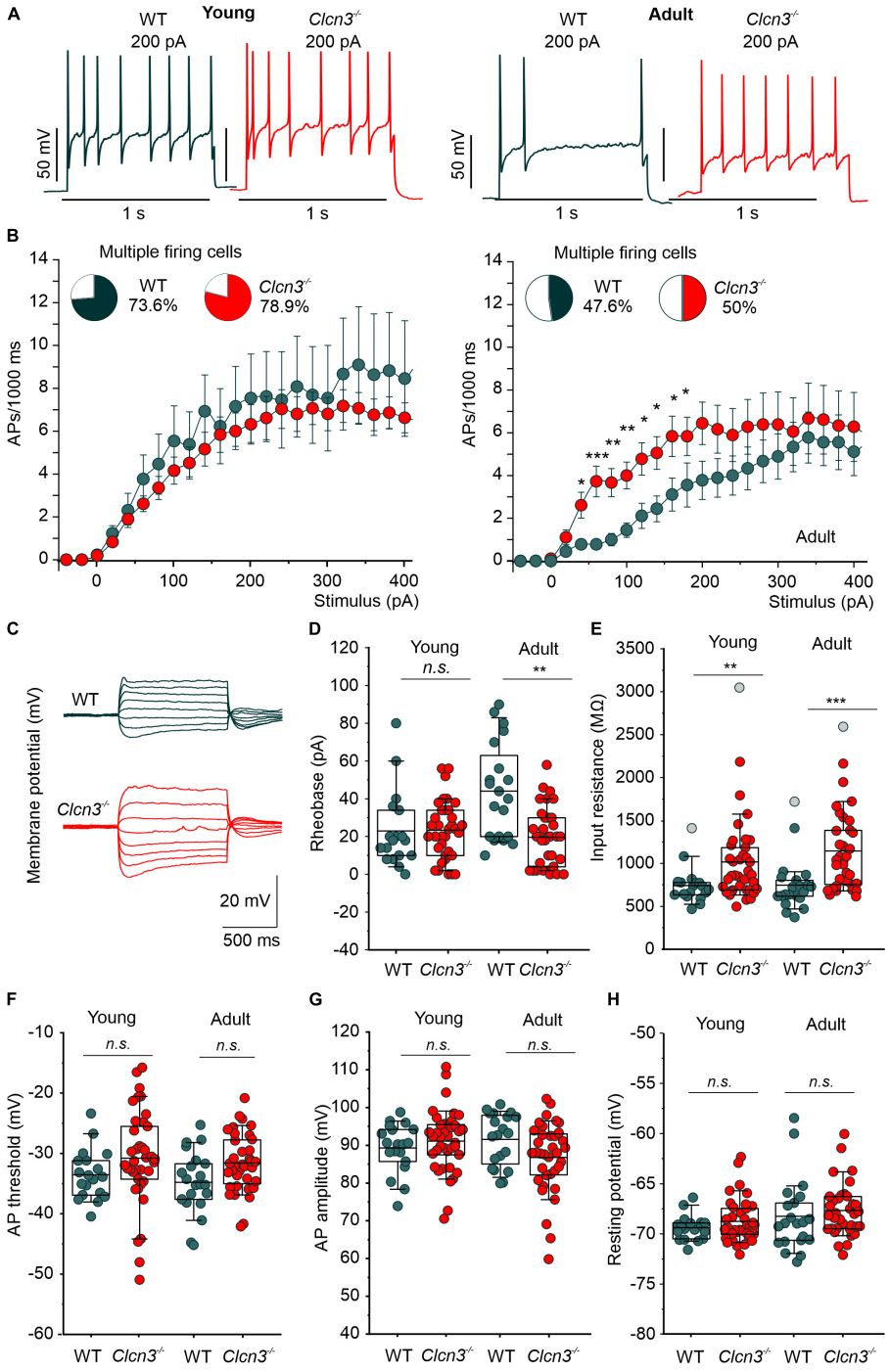

FIGURE 2
Change in excitability of dorsal root ganglion (DRG) neurons from young and adult *Clcn3*$^{-/-}$ animals. **(A)** Representative traces of action potentials (APs) elicited by a current injection of 200 pA in young (left) and adult (right) wild type (WT) (green) and *Clcn3*$^{-/-}$ (red) neurons. **(B)** Average firing frequencies from young and adult *Clcn3*$^{-/-}$ and WT dorsal root ganglion (DRG) neurons. Insets show the percentage of multiple firing neurons for each condition. **(C)** Representative current responses of control (green) and a *Clcn3*$^{-/-}$ (red) neuron to hyperpolarizing and depolarizing current pulses. **(D)** Current threshold necessary to elicit the first action potential (AP; rheobase) in young and adult *Clcn3*$^{-/-}$ and WT DRG neurons. **(E)** Average input resistances of DRG neurons from P21 and P60 mice. Symbols in gray are outliers values included in the analysis. **(F)** AP thresholds, **(G)** amplitudes, and **(H)** RMP for young and adult neurons. Data were collected from young WT (n = 19 cells from four animals) and *Clcn3*$^{-/-}$ (n = 38 cells from four animals) and adult WT (n = 21 cells from seven animals) and *Clcn3*$^{-/-}$ (n = 36 cells from six animals) cells. Statistical significance levels are *$p < 0.05$, **$p < 0.01$, ***$p < 0.001$, n.s., not significant. A two-way ANOVA or Kruskal–Wallis ANOVA was used to compare the age and phenotype of the two groups. The Tukey *post hoc* test was used for pairwise comparisons. Data are presented as the mean ± SEM. In boxplots, boxes indicate the upper and lower quartiles, and whiskers the upper and lower 90 percentiles.

TABLE 4 Properties of the action potentials (APs) generated in response to 200 pA current injection for 1 s were not different between wild type (WT) and *ClCn3*$^{-/-}$ adult dorsal root ganglion (DRG) neurons.

200 pA of current injection	Phenotype	V. Threshold (mV)	Amplitude (mV)	AHP (mV)
First Action potential (AP)	WT ($n = 9$)	−59.0 ± 4.7	118.1 ± 5.4	−11.8 ± 3.9
	***Clcn3*$^{-/-}$ ($n = 16$)**	−62.6 ± 2.1	123.6 ± 2.6	−16.4 ± 2.4
Second AP	WT ($n = 9$)	−17.0 ± 2.5	69.8 ± 4.3	27.0 ± 2.1
	***Clcn3*$^{-/-}$ ($n = 16$)**	−15.1 ± 1.3	66.8 ± 3.0	28.9 ± 1.7
Third AP	WT ($n = 9$)	−16.3 ± 2.2	67.8 ± 4.2	25.5 ± 1.9
	***Clcn3*$^{-/-}$ ($n = 16$)**	−14.0 ± 1.3	64.3 ± 3.3	28.9 ± 1.6
Fourth AP	WT ($n = 4$)	−11.7 ± 3.8	57.8 ± 6.6	26.6 ± 3.9
	***Clcn3*$^{-/-}$ ($n = 16$)**	−12.3 ± 1.4	61.0 ± 3.9	29.4 ± 1.7

No statistical differences were found. Significance levels $p > 0.05$ using Student's *t*-test. Data are presented as mean ± SEM.

of these channels are associated with various pain disorders (Cummins and Waxman, 1997; Berta et al., 2008; Dib-Hajj et al., 2010; Lampert et al., 2010; Bernal, 2018). Small-diameter DRG neurons express fast-inactivating TTX-sensitive (TTX-S) $Na_v1.1$, $Na_v1.6$, and $Na_v1.7$ and slow-inactivating TTX-resistant (TTX-R) $Na_v1.8$ and $Na_v1.9$ (Rush et al., 2007) channels. In patch-clamp experiments, we measured sodium currents in DRG neurons from *Clcn3*$^{-/-}$ and WT adults before and during the extracellular application of 300 nM TTX, using the same voltage protocol. Total Na^+ current densities were slightly increased in *Clcn3*$^{-/-}$ DRG neurons (**Figures 3A,B**), along with a significantly decreased TTX-R component (**Figures 3A,C**). To determine the TTX-S Na^+ current, the TTX-R component was subtracted from the total Na^+ current. The TTX-S current did not differ between *Clcn3*$^{-/-}$ and WT cells (**Figures 3A,D**). Western blotting showed that $Na_v1.8$ protein levels were not reduced in *Clcn3*$^{-/-}$ cells (**Supplementary Figure 3**), indicating that loss of ClC-3 does not affect the *de novo* synthesis of $Na_v1.8$ channels. We observed minor changes in the voltage dependence of sodium channel activation and inactivation in *Clcn3*$^{-/-}$ neurons compared with WT neurons (**Supplementary Figures 4A–F**), probably due to changes in the relative amplitudes of different sodium channels in DRG neurons. Taken together, these observations suggest that ClC-3 regulates the surface membrane insertion of the TTX-R $Na_v1.8$/$Na_v1.9$, but not of the $Na_v1.1$, $Na_v1.6$, or $Na_v1.7$ channels.

Altered nociception has also been associated with changes in the surface expression and biophysical properties of K^+ channels (Duan et al., 2012; Laumet et al., 2015; Conner et al., 2016). In whole-cell recordings, outward-rectifier potassium currents were larger in small-diameter DRG neurons from adult *Clcn3*$^{-/-}$ mice than in those from adult WT mice (**Figure 3E**). To identify which types of K^+ channels are affected by ClC-3 deletion, we recorded K^+ currents before and during the application of 5 mM 4-AP. 4-AP blocks A-type fast-inactivating voltage-gated K^+ currents (I_A), whereas both slow-inactivating voltage-gated K^+ currents (I_D) and delayed-rectifier voltage-gated K^+ currents (I_K) are 4-AP-insensitive (Vydyanathan et al., 2005). I_D and I_K currents were larger in neurons from adult *Clcn3*$^{-/-}$ mice compared with adult WT mice (**Figure 3F**), whereas I_A currents did not differ (**Figure 3G**). DRG neurons also express inward-rectifier potassium channels ($K_{ir}2.3$ and $K_{ir}2.4$) (Busserolles et al., 2020) or $K_{ir}3.1$ (Seitz et al., 2021). Electrophysiological recording of inward-rectifier potassium channels showed small currents of up to 300 pA at -160 mV (**Supplementary Figure 4G**), with no difference between WT and *Clcn3*$^{-/-}$ DRG neurons (**Supplementary Figure 4H**). We conclude that ClC-3 regulates the plasma membrane density of slow-inactivating and delayed-rectifier voltage-gated K^+ channels, but not of other K^+ channels.

ClC-3 Cl^-/H^+ transport is not required for the normal excitability of sensory dorsal root ganglion cells

ClC-3 exchanges Cl^- for H^+ at a fixed stoichiometry of 2:1 and, thus, might modify endosomal [Cl^-] or pH (Guzman et al., 2013; Rohrbough et al., 2018). To separate the function of ClC-3-associated Cl^-/H^+ exchange in regulating neuronal excitability from other ClC-3 functions, we used a knock-in animal model expressing mutant ClC-3 with a neutralizing point mutation in the proton glutamate: E281Q, E339Q, and E312Q in ClC-3a, ClC-3b, and ClC-3c, respectively (Accardi et al., 2005; Guzman et al., 2013; Rohrbough et al., 2018). In each isoform, this mutation abolishes Cl^-/H^+ exchange but does not affect the ability to heterodimerize with ClC-4 and to target ClC-4 to recycling endosomes or late endosome/lysosomes (Guzman et al., 2013, 2017). Since ClC-4 is also expressed in DRG neurons (**Supplementary Figure 5**), we generated the double-mutant *Clcn3*$^{E281Q/E281Q}$/*Clcn4*$^{-/-}$ to completely abolish ClC-3-associated Cl^-/H^+ exchange in all organelles. *Clcn4*$^{-/-}$ and *Clcn3*$^{E281Q/E281Q}$ pups are born at the Mendelian ratio, are fertile, and develop normally with no obvious phenotype. In contrast, *Clcn3*$^{E281Q/E281Q}$/*Clcn4*$^{-/-}$ are born at the Mendelian ratio; they show a stronger phenotype than the *Clcn3*$^{-/-}$, are smaller, and develop with delay in comparison to littermates.

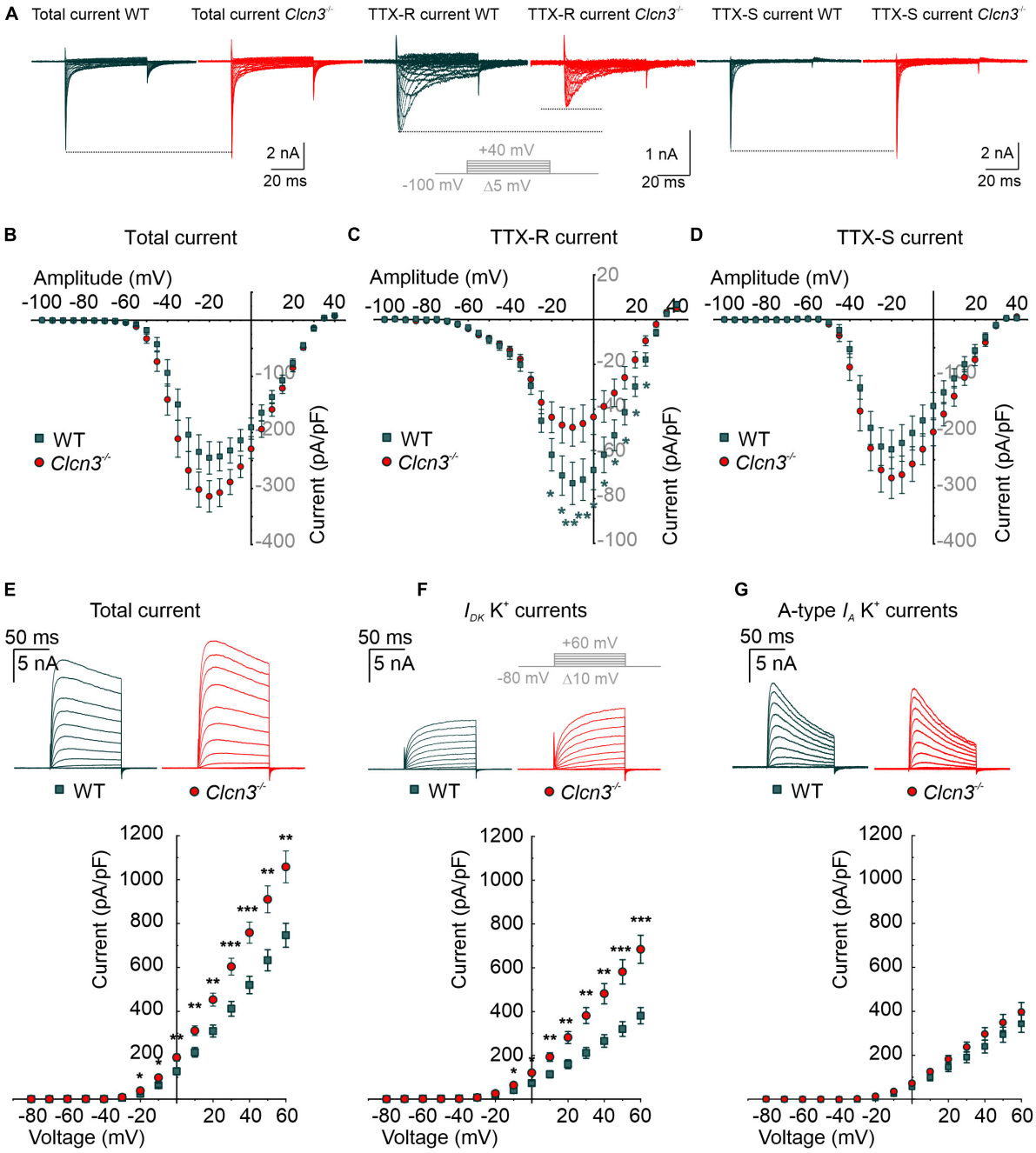

FIGURE 3
Whole-cell Na^+ and K^+ currents from cultured wild type (WT) and *Clcn3*$^{-/-}$ dorsal root ganglion (DRG) adult neurons. **(A)** Representative traces of Na^+ currents before (total Na^+ current) and during the application of 300 nM TTX (TTX-R current), and after digital subtraction of the TTX-R current from the total Na^+ current (TTX-S current) from WT (green) and *Clcn3*$^{-/-}$ (red) cells. The inset illustrates the voltage protocol used to elicit Na^+ currents during and after TTX application. **(B–D)** Current–voltage relationships of total **(B)**, TTX-R **(C)**, and TTX-S **(D)** Na^+ current densities from WT (green, n = 23 from five animals) and *Clcn3*$^{-/-}$ (red, n = 23 from eight animals) DRG neurons. Traces were aligned to the holding current at −100 mV, and dotted lines were set to the maximum pick current of the WT to illustrate changes in the *Clcn3*$^{-/-}$. **(E–G)** Representative recordings of the K^+ current (upper panel) and current–voltage relationship (lower panel) were obtained from WT (green, n = 16 from five animals) and *Clcn3*$^{-/-}$ (red, n = 20 from three animals) DRG neurons. Inset in gray depicts the voltage protocol used to elicit K^+ currents during and after 4-AP application. **(E)** Total K^+ current densities are significantly higher in the absence of ClC-3. **(F)** Slow-inactivating K^+ currents obtained from the same neuron showed in **E**, after the application of 5 mM 4-AP, a compound that blocks fast-inactivating K^+ channels, showed a similar phenotype as for the total K^+ current. **(G)** Fast-inactivating K^+ currents are obtained by subtracting the slow-inactivating (**F**) from the total **(E)** current. Statistical significance levels are $*p < 0.05$, $**p < 0.01$, and $***p < 0.001$; Student's t-test. Data are presented as mean ± SEM.

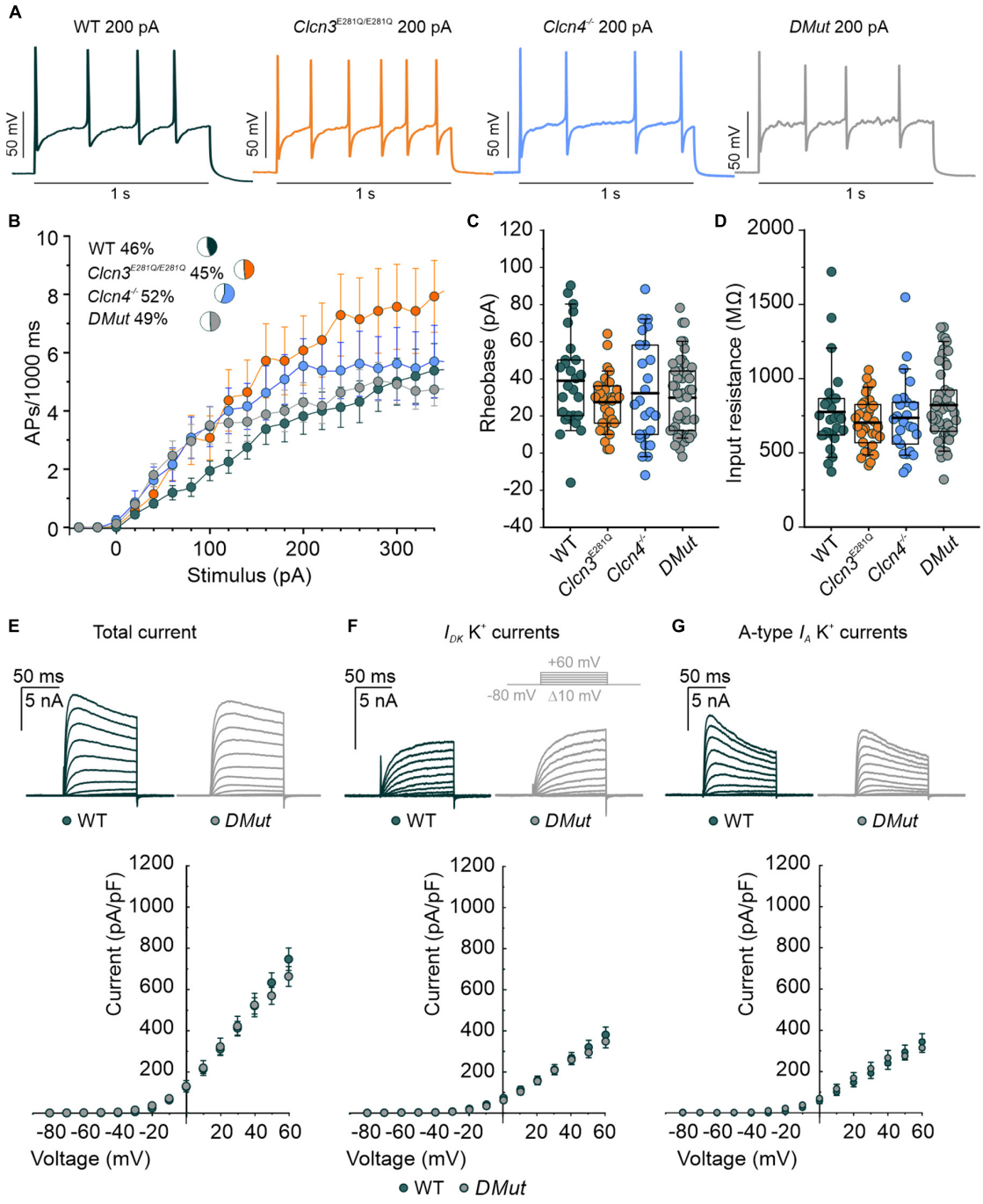

FIGURE 4
Comparison of the action potential (AP) properties of wild type (WT), *Clcn3*$^{E281Q/E281Q}$, *Clcn4*$^{-/-}$, and *Clcn3*$^{E281Q/E281Q}$/*Clcn4*$^{-/-}$ (*DMut*) dorsal root ganglion (DRG) neurons from adult mice. **(A)** Representative APs elicited by 200 pA current injection in adult WT (green), *Clcn3*$^{E281Q/E281Q}$ (orange), *Clcn4*$^{-/-}$ (blue), and *DMut* (gray) neurons. **(B)** AP frequencies for all conditions. Insets show the percentage of multiple firing neurons for each condition. **(C)** Rheobase and **(D)** input resistance. Data were collected from WT (green, *n* = 27 cells from three animals), *Clcn3*$^{E281Q/E281Q}$ (orange, *n* = 31 cells from three animals), *Clcn4*$^{-/-}$ (blue, *n* = 25 cells from three animals), or *Clcn3*$^{E281Q/E281Q}$/*Clcn4*$^{-/-}$ (gray, *n* = 49 from seven animals) neurons. **(E–G)** Representative recordings of the K^+ current (upper panel) and current–voltage relationship (lower panel) were obtained from WT (green, *n* = 16 from five animals) and *DMut* (gray, *n* = 10 from three animals) DRG neurons. The inset illustrates the voltage protocol used to elicit K^+ currents during and after 4-AP application. Total **(E)**, slow-inactivating **(F),** and fast-inactivating **(G)** K^+ currents densities are not different between phenotypes. One-way ANOVA or one-way Kruskal–Wallis ANOVA was used for statistical analysis. Data are presented as the mean ± SEM. In boxplots, boxes indicate the upper and lower quartiles, and whiskers the upper and lower 90 percentiles.

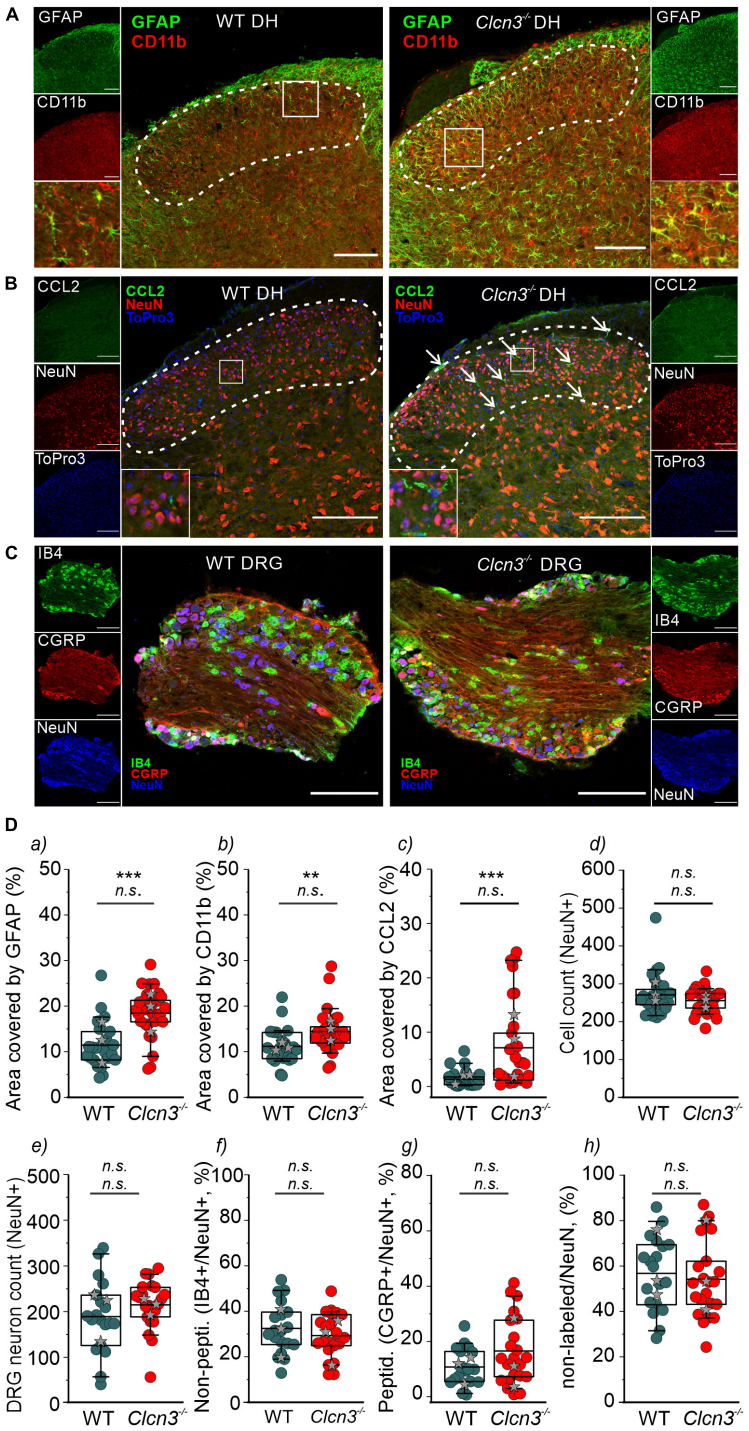

FIGURE 5

ClC-3 disruption leads to neuroinflammation within the DHSC. **(A)** glial fibrillary acidic protein (GFAP) and CD11b positivity in the dorsal horn (DH) layers I–IV of wild type (WT) and *Clcn3*$^{-/-}$ mice. **(B)** Section of the lumbar spinal cord from WT and *Clcn3*$^{-/-}$ mice stained for CCL2 (green), NeuN (red), and TO-PRO-3 (blue, nuclei). **(C)** Representative immunofluorescence confocal images of dorsal root ganglia from WT and *Clcn3*$^{-/-}$ mice stained for NeuN (blue), IB4 non-peptidergic small-diameter (green), and CGRP peptidergic (red) neurons. **(D)** (a) Area of glia expressing GFAP, (b) activated microglia expressing CD11b, (c) area of neuronal CCL2 expression, and (d) neuronal count in the dorsal horn from WT and mutant spinal cords. (e–h) Quantitative analysis of the total neuron count within the dorsal root ganglion (DRG). Each dot represents a single measurement, (a–d) WT (n = 29), *Clcn3*$^{-/-}$ (n = 33); (g, h) WT (n = 23), *Clcn3*$^{-/-}$ (n = 29). Three or four mice were used per genotype, with at least six slices from the lumbar section of each animal. Sections were 20-μm thick and collected every 100 μm apart. Scale bar: 200 μm. Statistical significance levels are $^{**}p < 0.01$, $^{***}p < 0.001$, n.s., not significant. *Clcn3*$^{-/-}$ differs from WT using the Student's t-test (upper symbol), and statistics per animal with the data displayed with gray stars (lower symbol). In boxplots, boxes indicate the upper and lower quartiles, and whiskers the upper and lower 90 percentiles.

For DRG neurons isolated from P60 animals, AP frequencies were similar for WT, *Clcn3*$^{E281Q/E281Q}$, *Clcn4*$^{-/-}$, and *Clcn3*$^{E281Q/E281Q}$/*Clcn4*$^{-/-}$ (**Figures 4A,B**). All AP parameters tested were indistinguishable between DRG neurons from P60 mutant and WT mice (**Figures 4C,D** and **Supplementary Figure 6**). Total potassium currents were similar between *Clcn3*$^{E281Q/E281Q}$/*Clcn4*$^{-/-}$ and WT cells. Furthermore, the separation of A-type fast-inactivating from slow-inactivating voltage-gated K^+ channels confirmed the WT-like phenotype of *Clcn3*$^{E281Q/E281Q}$/*Clcn4*$^{-/-}$ neurons, with I_A, I_D, and I_K currents similar to those of WT neurons (**Figures 4E–G**). These results suggest that ClC-3-associated Cl^-/H^+ exchange is not required for normal excitability in sensory DRG neurons.

Cl^-/H^+ transport activity regulates microglia activation

Microglia are a specialized population of macrophage-like cells in the CNS that modulate neuronal activity and neuronal excitability in nociceptive pathologies (Vallejo et al., 2010). Immunohistochemical analysis with antibodies against the microglial marker integrin alpha-M or also known as cluster of differentiation molecule 11B (CD11b) and the astrocyte marker glial fibrillary acidic protein (GFAP) (Lan et al., 2017) was conducted to evaluate glial activation in *Clcn3*$^{-/-}$ from adult mice (**Figure 5A**, dashed line, and **Figure 5Da,b** and **Supplementary Figure 7**). In layers I, II, III, and IV of the DHSC of P60 animals, GFAP levels were increased by about 89% and CD11b levels by 49% in *Clcn3*$^{-/-}$ compared with WT (**Figure 5Da,b**). In P21 *Clcn3*$^{-/-}$ mice, microglia and astrocyte proliferation were increased (**Supplementary Figure 8**). These results indicate that neuroinflammatory changes are associated with glial activation in the dorsal horn of the *Clcn3*$^{-/-}$ spinal cord.

Chemokine ligand 2 is a chemotactic factor that attracts immune cells, such as monocytes/macrophages and natural killer cells. Increased CCL2 expression in DRG neurons and the spinal cord has been associated with inflammatory pain and hypersensitivity (Menetski et al., 2007; Illias et al., 2018; Gschwandtner et al., 2019). At P60, fine cellular processes reactive to CCL2 were readily visible and more abundant within the DHSC region in *Clcn3*$^{-/-}$ than in WT mice (**Figure 5B**), resulting in larger CCL2-stained areas in the *Clcn3*$^{-/-}$ dorsal horn (**Figure 5Dc**). These observations are consistent with increased CCL2 secretion contributing to the development of hyperalgesia in *Clcn3*$^{-/-}$. To test for neurodegeneration, dorsal root ganglia or spinal cord sections were stained for the neuronal marker NeuN. This revealed no difference in the total number of neurons between the dorsal root ganglia of P60 WT and mutant animals (**Figures 5C,De**). Isolectin B4 (IB4) is a marker for non-peptidergic neurons, and calcitonin gene-related peptide (CGRP) is a marker for peptidergic neurons (Priestley, 2009). Staining for IB4 and CGRP revealed more non-peptidergic IB4-positive cells than peptidergic CGRP-positive cells (**Figure 5Df,g**) in both WT and *Clcn3*$^{-/-}$ mice, but no differences in the number of cells between WT and mutant tissues. Results were similar for large- and medium-diameter neurons, which are NeuN-positive, but negative for IB4 and CGRP (**Figure 5Dh**). The DHSC receives nociceptive inputs in layers I and II and non-nociceptive inputs in layers I, IV, and V from small-, medium-, and large-diameter DRG neurons (Stucky, 2007). Similar to the dorsal root ganglia, neuron numbers in layers I–IV of the DHSC were not reduced in *Clcn3*$^{-/-}$ compared with WT animals (**Figure 5Dd**). We conclude that genetic ablation of ClC-3 does not lead to neurodegeneration in the dorsal root ganglia or in the dorsal horn of the spinal cord.

To investigate the role of ClC-3-associated Cl^-/H^+ exchange in these inflammatory processes, we compared GFAP and CD11b levels in WT, *Clcn3*$^{E281Q/E281Q}$, *Clcn4*$^{-/-}$, and *Clcn3*$^{E281Q/E281Q}$/*Clcn4*$^{-/-}$ mice (**Figure 6**). Numbers of neuronal cells were similar (**Figure 6C**), and areas reactive to GFAP or positive for the microglia marker CD11b were significantly increased in all genotypes (**Figures 6A,D,E**). Moreover, glial cells had more and longer processes in mutants than in WT mice (**Figures 6A,B**, insets). The CCL2-positive area was ∼30-fold greater in *Clcn3*$^{E281Q/E281Q}$, *Clcn4*$^{-/-}$, and *Clcn3*$^{E281Q/E281Q}$/*Clcn4*$^{-/-}$ than in WT mice (**Figures 6B,F**). Overall, these findings demonstrate that fully functional ClC-3 and ClC-4 chloride transporters are required to prevent microglia and astrocyte proliferation.

Neurodegeneration in *Clcn3*$^{-/-}$, *Clcn3*$^{E281Q/E281Q}$, *Clcn4*$^{-/-}$, and *Clcn3*$^{E281Q/E281Q}$/*Clcn4*$^{-/-}$ animals

Hippocampal and retinal neurodegeneration is well established in *Clcn3*$^{-/-}$ animals (Stobrawa et al., 2001; Dickerson et al., 2002). The lack of neurodegeneration in the DRG or DHSC region (**Figure 5**) indicates that separate classes of neurons have distinct sensitivities to reduced levels of Cl^-/H^+ exchange. This finding prompted us to study neurodegeneration in the hippocampus and retina in various animal models with distinct levels of endosomal Cl^-/H^+ exchange (**Figure 7**). In agreement with previous studies, ClC-3 ablation resulted in severe neurodegeneration in the hippocampus and retina (**Figure 7**; Stobrawa et al., 2001; Dickerson et al., 2002). *Clcn4*$^{-/-}$ mice do not exhibit hippocampal or retinal degeneration (**Figure 7**). *Clcn3*$^{E281Q/E281Q}$ animals had normal hippocampal morphology but the reduced thickness of the photoreceptor layer (**Figure 7C**), indicating that the retina is

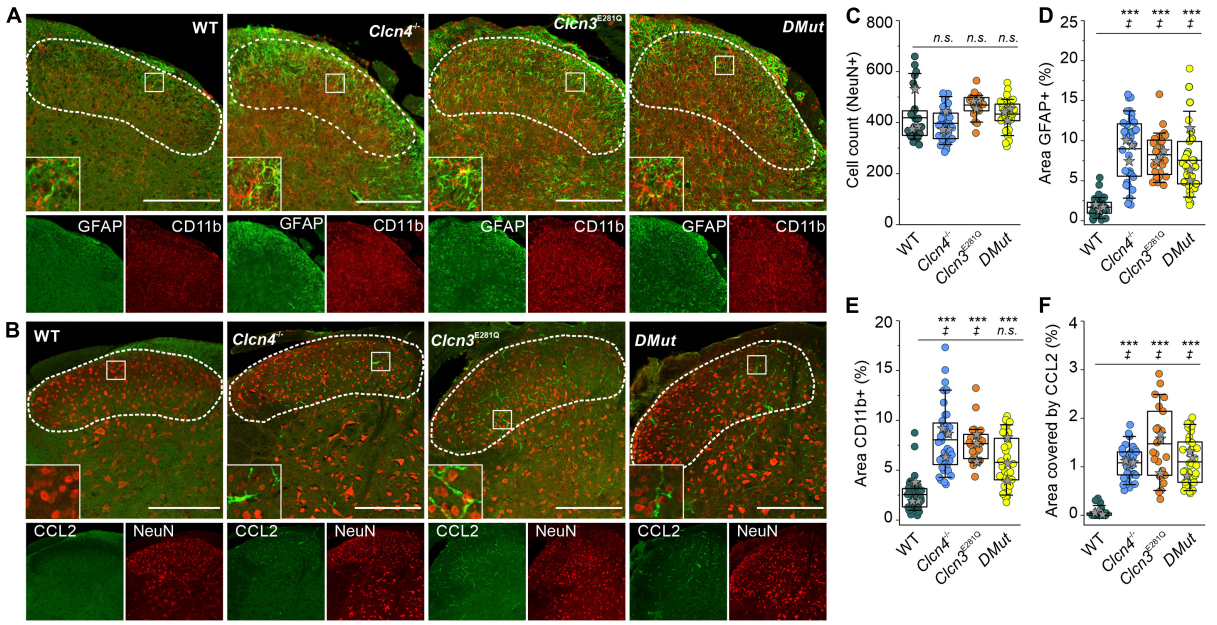

FIGURE 6
Reduced Cl^-/H^+ exchange triggers neuroglia activation in the spinal cord. **(A)** Representative immunofluorescence confocal images of lumbar spinal cord sections from WT, *Clcn3*$^{E281Q/E281Q}$, *Clcn4*$^{-/-}$, and *Clcn3*$^{E281Q/E281Q}$/*Clcn4*$^{-/-}$ (*DMut*) mice stained for glial fibrillary acidic protein (GFAP) (green) and CD11b (red). Layers I–IV of the dorsal horn are outlined with a dashed line. Insets show increased GFAP and CD11b reactivity in mutant mice. **(B)** Lumbar spinal cord sections from mice with the indicated genotypes were stained for CCL2 (green) and NeuN (red). **(C)** Total cell numbers in the dorsal horn of WT and mutant's spinal cords. **(D)** Areas of glia positive for GFAP or to CD11b in **E** for WT (n = 34), *Clcn3*$^{E281Q/E281Q}$ (n = *24*), *Clcn4*$^{-/-}$ (n = 36), and *Clcn3*$^{E281Q/E281Q}$/*Clcn4*$^{-/-}$ (*DMut*; n = 30). **(F)** Area of CCL2 immunofluorescence in WT (n = 30), *Clcn3*$^{E281Q/E281Q}$ (n = 23), *Clcn4*$^{-/-}$ (n = 34), and *Clcn3*$^{E281Q/E281Q}$/*Clcn4*$^{-/-}$ (n = 36). Each dot represents a single measurement. Three or four mice were used per genotype, with at least six slices from the lumbar section of each animal. Sections were 20-μm thick and collected every 100 μm apart. Scale bar: 200 μm. Asterisk (*) was used to represent differences between groups and (‡) when also animals were compared ($^‡p < 0.05$, $^{***}p < 0.001$). n.s., not significant; one-way ANOVA (Tukey's HSD *post hoc* test). In boxplots, boxes indicate the upper and lower quartiles, and whiskers the upper and lower 90 percentiles.

more sensitive than the hippocampus to reduced levels of ClC-3-associated Cl^-/H^+ exchange. CA1 and CA2 hippocampal regions and retinal tissue in *Clcn3*$^{E281Q/E281Q}$/*Clcn4*$^{-/-}$ mice were almost completely absent at the age of P21 (**Figures 7A,B**). These findings highlight the sensitivity of neuronal tissues to reduced Cl^-/H^+ exchange. Whereas the DHSC is viable in the complete absence of ClC-3-associated transport in *Clcn3*$^{-/-}$, the retina is degenerated by the absence of ClC-3-mediated Cl^-/H^+-exchange even in presence of ClC-4. The hippocampus tolerates reduced Cl^-/H^+-exchange in *Clcn3*$^{E281Q/E281Q}$, but is complete loss in *Clcn3*$^{E281Q/E281Q}$/*Clcn4*$^{-/-}$ and *Clcn3*$^{-/-}$.

Discussion

We have demonstrated that genetic ablation of the Cl^-/H^+ exchanger ClC-3 alters nociception in mice. In *Clcn3*$^{-/-}$ animals, we observed enhanced electrical activity of peripheral nociceptors and inflammatory processes at the spinal cord. We considered that ClC-3 might affect cellular processes either by changing chemical or electrical gradients at endosomes or by supporting the intracellular trafficking of other proteins *via* a chaperone-like function. To distinguish between these possibilities, we generated mutant mice (*Clcn3*$^{E281Q/E281Q}$) that express transport-incompetent ClC-3. Since E281Q ClC-3 can still heterodimerize with the related transporter ClC-4, the genetic ablation of ClC-4 was also necessary to abolish all ClC-3-associated Cl^-/H^+ exchanges in recycling endosomes and lysosomes. *Clcn3*$^{E281Q/E281Q}$/*Clcn4*$^{-/-}$ animals had an inflammatory response in the DHSC and early onset hippocampal and retinal degeneration, illustrating the importance of ClC-3 Cl^-/H^+ transport for neuroglia function and neuronal integrity in supraspinal brain regions. In contrast, the electrical properties of sensory DRG neurons were similar in *Clcn3*$^{E281Q/E281Q}$ and *Clcn3*$^{E281Q/E281Q}$/*Clcn4*$^{-/-}$ mice, indicating that ClC-3-dependent regulation of neuronal excitability is independent of Cl^-/H^+ exchange.

ClC-3 ablation impairs age-related adjustment in neuronal excitability, which is thought to result from developmental changes in the expression and/or function of ion channels, such as Na^+ and K^+ channels (Scott et al., 1988; Wang and Albers, 2009). Specifically, reduced K^+ conductances were proposed to reduce excitability in old neurons

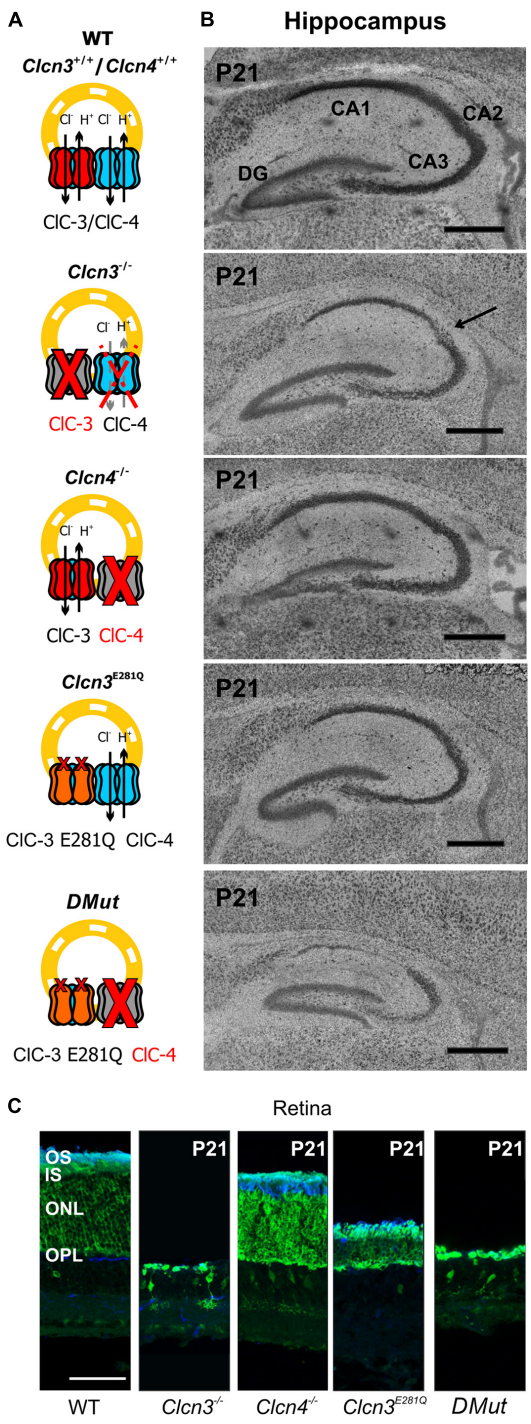

FIGURE 7
Hippocampal and retinal degeneration in different animal models of Cl^-/H^+ exchange. **(A)** Cartoons illustrating heterodimerization between ClC-3 and ClC-4 and the contribution of Cl^-/H^+ transport function in endosomes for each genotype and **(B)** representative confocal images of Nissl-stained sagittal (100 μm) section indicating hippocampal formation from 21-day-old WT, *Clcn3*$^{-/-}$, *Clcn3*$^{E281Q/E281Q}$, *Clcn4*$^{-/-}$, and *Clcn3*$^{E281Q/E281Q}$/*Clcn4*$^{-/-}$ (*DMut*) mice. The arrow indicates neurodegeneration in the CA2 region of the

(Continued)

FIGURE 7 (Continued)
Clcn3$^{-/-}$ hippocampus. **(C)** Representative immunofluorescence confocal images of retinal sections from different mouse genotypes at P21. Sections were immunostained using an anti-recoverin antibody to indicate the inner segments, somas, and terminals of photoreceptors (green; this antibody also occasionally labels type 2 bipolar cells) and anti-rhodopsin to identify the outer segment of rod cells (blue). OS, outer segment; IS, inner segment; ONL, outer nuclear layer; OPL, outer plexiform layer. Scale bar: 0.5 mm for hippocampal and 50 μm for retinal images.

(Scott et al., 1988). DRG neurons from adult *Clcn3*$^{-/-}$ (but not *Clcn3*$^{E281Q/E281Q}$/*Clcn4*$^{-/-}$ mice) had increased densities of slow-inactivating and delayed-rectifier voltage-gated K^+ currents (**Figure 3F**). Other current components, such as I_A and inward-rectifying voltage-gated K^+ currents, were unaffected by ClC-3 ablation. Two-pore domain K^+ (K_{2P}) channels help to set and stabilize the RMP (Rasband et al., 2001). Since the RMP was unchanged, we excluded the possibility that the expression or trafficking of K_{2P} channels is altered in *Clcn3*$^{-/-}$ mice. A greater number of voltage-dependent K^+ channels in knockout cells may facilitate AP repolarization and enhance excitability (Scott et al., 1988). We found a reduced density of TTX-R Na^+ currents mediated by $Na_v1.8$ and/or $Na_v1.9$ in DRG neurons from adult *Clcn3*$^{-/-}$ mice (**Figure 3C**), but no significant change in TTX-S currents (**Figure 3D**), which are predominately mediated by $Na_v1.7$ (Chen et al., 2018). Modeling studies have demonstrated that the excitability of peripheral neurons depends on the ratio of $Na_v1.7$ to $Na_v1.8$ (Petersson et al., 2014; Tigerholm et al., 2015); thus, the observed changes in sodium currents can explain the observed hyperexcitability of *Clcn3*$^{-/-}$ DRG. TTX-R currents play a dominant role in all phases of the AP (Blair and Bean, 2002) and are believed to adjust the AP voltage threshold in DRG neurons (Bennett et al., 2019). Our results indicate that ClC-3 contributes to the homeostatic regulation of neuronal excitability by controlling the number of ion channels, such as Na^+ and K^+ channels in the surface membrane. Since these changes were not found in *Clcn3*$^{E281Q/E281Q}$/*Clcn4*$^{-/-}$ mice, we conclude that the regulatory mechanism is not mediated by Cl^-/H^+ exchange activity but instead by a chaperone function of ClC-3.

Formalin injection induces a biphasic pain reaction (**Figure 1**). During the early phase, activation of C-type nociceptors and the release of mediators, such as ATP, glutamate, kinins, histamine, serotonin, cytokines, and tropic factors, promote peripheral sensitization (Hunskaar and Hole, 1987; Amaya et al., 2013). The second phase is dominated by inflammatory responses in the DHSC (Hunskaar and Hole, 1987; Tjølsen et al., 1992). Young and adult *Clcn3*$^{-/-}$ mice were more sensitive to formalin application. This enhanced behavioral pain response during the second phase suggests that a central sensitization within the dorsal horn changes the elicited sensory response and releases

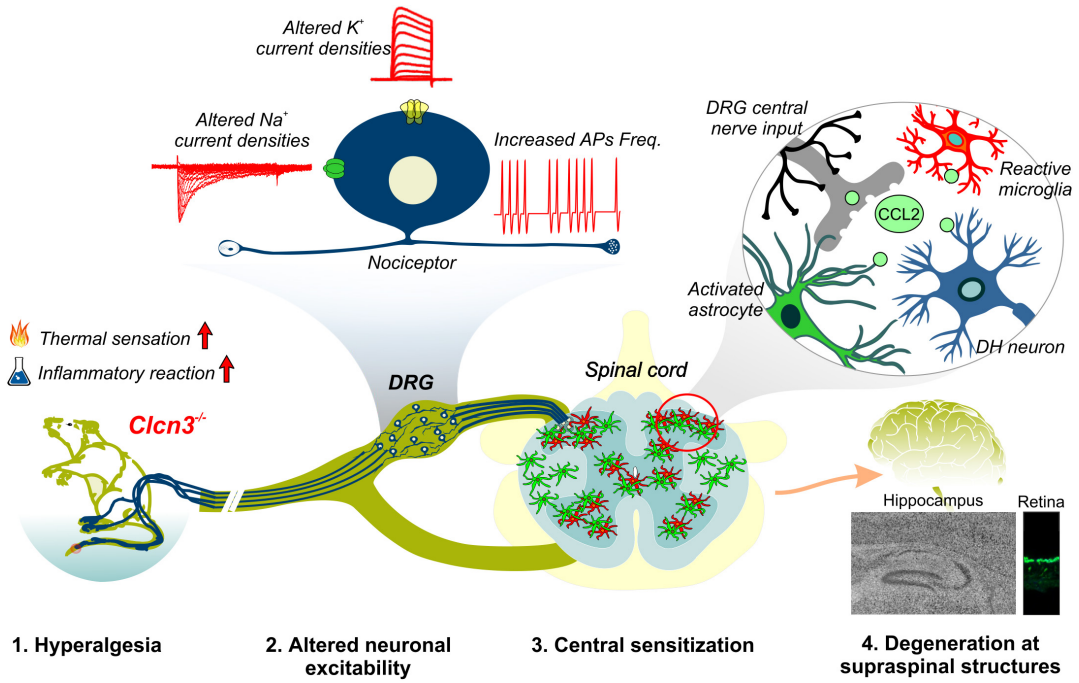

FIGURE 8
Summary of phenotypic alterations in *Clcn3*$^{-/-}$.

pro-inflammatory mediators to the spinal cord *in Clcn3*$^{-/-}$ (Ren and Dubner, 2008; Vallejo et al., 2010; Mika et al., 2013). We found increased numbers of activated astrocytes and microglia within the spinal cord of *Clcn3*$^{-/-}$ mice at P21 and P60 (**Supplementary Figure 8**; **Figure 5**). The identification of reactive microglia in young and adult *Clcn3*$^{-/-}$ and in adult *Clcn4*$^{-/-}$, *Clcn3*$^{E281Q/E281Q}$, and *Clcn3*$^{E281Q/E281Q}$/*Clcn4*$^{-/-}$ mice (**Figure 5**; and **Figure 6**) suggests that astrocytes and microglia homeostasis critically depend on the presence of fully competent, functional chloride transporters.

Chemokine ligand 2 is a chemotactic factor that attracts monocytes, CD4+ T cells, natural killer cells, and dendritic cells to sites of inflammation (Carr et al., 1994). Increased CCL2 expression following inflammation or injury attracts leukocytes to mediate defense, cytokine release, and repair (Gschwandtner et al., 2019). Higher CCL2 expression in DRG neurons, as well as in the spinal cord, is associated with inflammatory pain and hypersensitivity (Menetski et al., 2007; Illias et al., 2018). We studied the effect of ClC-3-associated Cl^-/H^+ exchange on CCL2 expression levels in dorsal horn layers I–IV and found that CCL2 levels were increased in *Clcn3*$^{-/-}$, *Clcn4*$^{-/-}$, *Clcn3*$^{E281Q/E281Q}$, and *Clcn3*$^{E281Q/E281Q}$/*Clcn4*$^{-/-}$ mice (**Figures 5B,Dc**, **6B,F**). A recent report demonstrated that CC12 is released *via* recycling endosomes and that changes in endo-lysosomal ion transport directly stimulate CCL2 release by promoting transfer through early and recycling endosomes (Plesch et al., 2018). ClC-3 isoforms are found in different organelles of the endo-lysosomal trafficking system, with ClC-3c present in recycling endosomes (Guzman et al., 2015; Comini et al., 2022). Taken together, our data suggest that impaired endosomal Cl^-/H^+ exchange causes neuroinflammation and pain in the *Clcn3*$^{-/-}$ mouse model *via* enhanced CCL2 release triggering an inflammatory reaction.

Many ion channels are sorted *via* the secretory pathway (Griffith, 2001; Swanwick et al., 2010; Capera et al., 2019) and recycled *via* clathrin-mediated endocytosis (Okuse et al., 2002; Liu et al., 2005; Swanwick et al., 2010; Conrad et al., 2018, 2021). ClC-3 has clathrin-binding motifs in its amino terminus (Zhao et al., 2007; Stauber and Jentsch, 2010) and, thus, might facilitate the endocytosis of membrane proteins and direct them to lysosomes (ClC-3b) or the recycling endosome (ClC-3c) (Guzman et al., 2015, 2017; Comini et al., 2022). In *Clcn3*$^{E281Q/E281Q}$/*Clcn4*$^{-/-}$ mice, ClC-3-associated endosomal Cl^-/H^+ exchange does not occur. In contrast, *Clcn3*$^{E281Q/E281Q}$ animals have no obvious phenotype, likely because E281Q ClC-3 can still interact with and direct ClC-4 to the recycling endosome and lysosome (Guzman et al., 2017; Weinert et al., 2020). There are no phenotypic alterations in *Clcn4*$^{-/-}$, but the lack of ClC-4 in the *Clcn3*$^{E281Q/E281Q}$/*Clcn4*$^{-/-}$ mouse caused a strong CNS phenotype (**Figure 7**), with degenerated hippocampal CA1 and CA2 regions at the age, at which neurodegeneration is starting in the *Clcn3*$^{-/-}$ mouse. Retinal tissue appears to be more sensitive to reduced levels of Cl^-/H^+ transporters than the hippocampus. Whereas hippocampal

regions are not affected in the *Clcn3*$^{E281Q/E281Q}$, the reduced thickness of retinal neuronal tissue in these animals already evidences the tight dependency between the viability of the neurons and Cl^-/H^+ transporters in this CNS region. Recently, the *Clcn3*$^{unc/unc}$ knock-in mouse model was generated, carrying the E224A mutation in the "gating glutamate" that uncouples Cl^- currents from H^+ counter transport. *Clcn3*$^{unc/unc}$ mice do not have a severe phenotype, but in *Clcn3*$^{unc/unc}$/*Clcn4*$^{-/-}$ animals hippocampal neurodegeneration can be seen in the third postnatal week (Weinert et al., 2020). Data from the *Clcn3*$^{E281Q/E281Q}$/*Clcn4*$^{-/-}$ and *Clcn3*$^{unc/unc}$/*Clcn4*$^{-/-}$ mouse models reinforce the importance of ClC-3 Cl^-/H^+ transport function for neuronal survival within the CNS in supraspinal brain regions, such as the hippocampus and retina.

Ablation or mutation of the genes encoding CLC-type Cl^-/H^+ exchangers has been linked to a variety of neurodevelopmental syndromes. Patients with these syndromes often have severe symptoms, thought to be caused by disturbed endosomal ion homeostasis. Here, we identified ClC-3-dependent cellular processes that are not coupled to its ion-exchange mechanism but are instead linked to a possible chaperone function. Our findings, summarized in **Figure 8**, identified ClC-3 as an integral part of the molecular machinery underlying age-related changes in neuronal sensitivity and excitability. We also demonstrated that altered Cl^-/H^+ transport may modify chemokine release and, thus, regulate inflammatory processes. Modulation of inflammatory responses by CLC-type transporter functions may be responsible for the severe phenotype of engineered animal models and may contribute to symptom severity in patients with CLC-linked neurological diseases.

Data availability statement

The original contributions presented in this study are included in the article/**Supplementary material**, further inquiries can be directed to the corresponding author.

Ethics statement

The animal study was reviewed and approved by German Animal Welfare Act (TierSchG § § 7–9) and State Agency for Nature, Environment and Consumer Protection, North Rhine Westphalia, and the local Animal Protection Committee, file numbers 84-02.04.2015.A108 and 84-02.04.2015.A307.

Author contributions

JS-M performed the experiments, analyzed the data, and drafted the manuscript. AW, CB, and MS performed the animal behavior test and analyzed the data. SB-P performed the Western blot experiments. JG and FM performed the retina and hippocampal immunostainings experiments. AL provided the macro for VGSC analyses. CF supervised the research and wrote the manuscript. RG conceived the idea, supervised the research, and wrote the manuscript. All authors contributed to the article and approved the submitted version.

Funding

This work was supported by the German Research Foundation (DFG) (GU 2042/2–1) to RG.

Acknowledgments

We thank Dr. T. Jentsch for providing the *ClCn3*$^{-/-}$ mouse model; Dr. Karlijn van Aerde and Dr. Dirk Feldmeyer for giving the Igor-based macro used to analyze AP data; Dr. Ute Becherer and Margaret Klose for providing the protocol used for extraction and culture of DRG neurons; and Verena Graf for assisting with the animal behavior experiments. We thank Dr. Juan Carlos Valdelamar-Villegas for helpful discussion. We are grateful to the staff of our animal facility and to Nicola Kornadt-Beck for her invaluable support in all aspects of animal work.

Conflict of interest

The authors declare that the research was conducted in the absence of any commercial or financial relationships that could be construed as a potential conflict of interest.

Publisher's note

Supplementary material

The Supplementary Material for this article can be found online at: https://www.frontiersin.org/articles/10.3389/fncel.2022.920075/full#supplementary-material

References

Abbadie, C., Taylor, B. K., Peterson, M. A., and Basbaum, A. I. (1997). Differential contribution of the two phases of the formalin test to the pattern of c-fos expression in the rat spinal cord: Studies with remifentanil and lidocaine. *Pain* 69, 101–110. doi: 10.1016/s0304–3959(96)03285x

Accardi, A., Walden, M., Nguitragool, W., Jayaram, H., Williams, C., and Miller, C. (2005). Separate ion pathways in a Cl-/H+ exchanger. *J. Gen. Physiol.* 126, 563–570. doi: 10.1085/jgp.200509417

Amaya, F., Izumi, Y., Matsuda, M., and Sasaki, M. (2013). Tissue injury and related mediators of pain exacerbation. *Curr. Neuropharmacol.* 11, 592–597. doi: 10.2174/1570159X11311060003

Bennett, D. L., Clark, A. J., Huang, J., Waxman, S. G., and Dib-Hajj, S. D. (2019). The role of voltage-gated sodium channels in pain signaling. *Physiol. Rev.* 99, 1079–1151. doi: 10.1152/physrev.00052.2017

Bernal, L. (2018). Insights into the contribution of voltage-gated sodium channel 1.7 to paclitaxel-induced neuropathy. *J. Neurosci.* 38, 6025–6027. doi: 10.1523/Jneurosci.0692–18.2018

Berta, T., Poirot, O., Pertin, M., Ji, R. R., Kellenberger, S., and Decosterd, I. (2008). Transcriptional and functional profiles of voltage-gated Na+ channels in injured and non-injured DRG neurons in the SNI model of neuropathic pain. *Mol. Cell. Neurosci.* 37, 196–208. doi: 10.1016/j.mcn.2007.09.007

Blair, N. T., and Bean, B. P. (2002). Roles of tetrodotoxin (TTX)-sensitive Na+ current, TTX-resistant Na+ current, and Ca2+ current in the action potentials of nociceptive sensory neurons. *J. Neurosci.* 22, 10277–10290. doi: 10.1523/JNEUROSCI.22-23-10277.2002

Bose, S., He, H., and Stauber, T. (2021). Neurodegeneration upon dysfunction of endosomal/lysosomal CLC chloride transporters. *Front. Cell Dev. Biol.* 9:639231. doi: 10.3389/fce11.2021.639231

Bost, A., Shaib, A. H., Schwarz, Y., Niemeyer, B. A., and Becherer, U. (2017). Large dense-core vesicle exocytosis from mouse dorsal root ganglion neurons is regulated by neuropeptide Y. *J. Neurosci.* 346, 1–13. doi: 10.1016/j.neuroscience.2017.01.006

Busserolles, J., Gasull, X., and Noël, J. (2020). "Potassium channels and pain," in *The Oxford Handbook of the Neurobiology of Pain*, ed. P. J. N. Wood (Oxford University Press).

Capera, J., Serrano-Novillo, C., Navarro-Perez, M., Cassinelli, S., and Felipe, A. (2019). The potassium channel odyssey: Mechanisms of traffic and membrane arrangement. *Int. J. Mol. Sci.* 20, 734. doi: 10.3390/ijms20030734

Carr, M. W., Roth, S. J., Luther, E., Rose, S. S., and Springer, T. A. (1994). Monocyte chemoattractant protein 1 acts as a T-lymphocyte chemoattractant. *Proc. Natl. Acad. Sci. U.S.A.* 91, 3652–3656. doi: 10.1073/pnas.91.9.3652

Chen, L., Huang, J., Zhao, P., Persson, A. K., Dib-Hajj, F. B., Cheng, X., et al. (2018). Conditional knockout of NaV1.6 in adult mice ameliorates neuropathic pain. *Sci. Rep.* 8:3845. doi: 10.1038/s41598-018-22216-w.

Comini, M., Sierra-Marquez, J., Guzman, G., Franzen, A., Willuweit, A., Katona, I., et al. (2022). CLC anion/proton exchangers regulate secretory vesicle filling and granule exocytosis in chromaffin cells. *J. Neurosci.* 42, 3080–3095. doi: 10.1523/JNEUROSCI.2439-21.2022.

Conner, L. B., Alvarez, P., Bogen, O., and Levine, J. D. (2016). Role of Kv4.3 in vibration-induced muscle pain in the rat. *J. Pain* 17, 444–450. doi: 10.1016/j.jpain.2015.12.007

Conrad, R., Kortzak, D., Guzman, G. A., Miranda-Laferte, E., and Hidalgo, P. (2021). Ca(V) β controls the endocytic turnover of Ca(V) 1.2 L-type calcium channel. *Traffic* 22, 180–193. doi: 10.1111/tra.12788

Conrad, R., Stolting, G., Hendriks, J., Ruello, G., Kortzak, D., Jordan, N., et al. (2018). Rapid turnover of the cardiac L-type CaV1.2 channel by endocytic recycling regulates its cell surface availability. *iScience* 7, 1–15. doi: 10.1016/j.isci.2018.08.012

Cummins, T. R., and Waxman, S. G. (1997). Downregulation of tetrodotoxin-resistant sodium currents and upregulation of a rapidly repriming tetrodotoxin-sensitive sodium current in small spinal sensory neurons after nerve injury. *J. Neurosci.* 17, 3503–3514. doi: 10.1523/JNEUROSCI.17-10-03503.1997

Dib-Hajj, S. D., Cummins, T. R., Black, J. A., and Waxman, S. G. (2010). Sodium channels in normal and pathological pain. *Annu. Rev. Neurosci.* 33, 325–347. doi: 10.1146/annurev-neuro-060909-153234

Dickerson, L. W., Bonthius, D. J., Schutte, B. C., Yang, B., Barna, T. J., Bailey, M. C., et al. (2002). Altered GABAergic function accompanies hippocampal degeneration in mice lacking ClC-3 voltage-gated chloride channels. *Brain Res.* 958, 227–250. doi: 10.1016/s0006-8993(02)03519-9

Duan, K.-Z., Xu, Q., Zhang, X.-M., Zhao, Z.-Q., Mei, Y.-A., and Zhang, Y.-Q. (2012). Targeting A-type K+ channels in primary sensory neurons for bone cancer pain in a rat model. *Pain* 153, 562–574. doi: 10.1016/j.pain.2011.11.020

Duncan, A. R., Polovitskaya, M. M., Gaitan-Penas, H., Bertelli, S., VanNoy, G. E., Grant, P. E., et al. (2021). Unique variants in CLCN3, encoding an endosomal anion/proton exchanger, underlie a spectrum of neurodevelopmental disorders. *Am. J. Hum. Genet.* 108, 1450–1465. doi: 10.1016/j.ajhg.2021.06.003

Fischer, B. D., Ho, C., Kuzin, I., Bottaro, A., and O'Leary, M. E. (2017). Chronic exposure to tumor necrosis factor *in vivo* induces hyperalgesia, upregulates sodium channel gene expression and alters the cellular electrophysiology of dorsal root ganglion neurons. *Neurosci. Lett.* 653, 195–201. doi: 10.1016/j.neulet.2017.05.004

Griffith, L. C. (2001). Potassium channels: The importance of transport signals. *Curr. Biol.* 11, R226–R228. doi: 10.1016/S0960–9822(01)00111–7

Gschwandtner, M., Derler, R., and Midwood, K. S. (2019). More than just attractive: How CCL2 influences myeloid cell behavior beyond chemotaxis. *Front. Immunol.* 10:2759. doi: 10.3389/fimmu.2019.02759

Guzman, R. E., Bungert-Plümke, S., Franzen, A., and Fahlke, C. (2017). Preferential association with ClC-3 permits sorting of ClC-4 into endosomal compartments. *J. Biol. Chem.* 292, 19055–19065. doi: 10.1074/jbc.M117.801951

Guzman, R. E., Grieschat, M., Fahlke, C., and Alekov, A. K. (2013). ClC-3 is an intracellular chloride/proton exchanger with large voltage-dependent nonlinear capacitance. *ACS Chem. Neurosci.* 4, 994–1003. doi: 10.1021/cn400032z

Guzman, R. E., Miranda-Laferte, E., Franzen, A., and Fahlke, C. (2015). Neuronal ClC-3 splice variants differ in subcellular localizations, but mediate identical transport functions. *J. Biol. Chem.* 290, 25851–25862. doi: 10.1074/jbc.M115.668186

Guzman, R. E., Sierra-Marquez, J., Bungert-Plumke, S., Franzen, A., and Fahlke, C. (2022). Functional characterization of CLCN4 variants associated with X-linked intellectual disability and epilepsy. *Front. Mol. Neurosci.* 15:872407. doi: 10.3389/fnmol.2022.872407

He, H., Cao, X., Yin, F., Wu, T., Stauber, T., and Peng, J. (2021a). West syndrome caused by a chloride/proton exchange-uncoupling CLCN6 mutation related to autophagic-lysosomal dysfunction. *Mol. Neurobiol.* 58, 2990–2999. doi: 10.1007/s12035–021–02291–3

He, H., Guzman, R. E., Cao, D., Sierra-Marquez, J., Yin, F., Fahlke, C., et al. (2021b). The molecular and phenotypic spectrum of CLCN4-related epilepsy. *Epilepsia* 6, 1401–1415. doi: 10.1111/epi.16906

Hoerauf, W. W., Cazares, V. A., Subramani, A., and Stuenkel, E. L. (2015). Efficient transfection of dissociated mouse chromaffin cells using small-volume electroporation. *Cytotechnology* 67, 573–583. doi: 10.1007/s10616-014-9699-y

Hu, H., Haas, S. A., Chelly, J., Van Esch, H., Raynaud, M., de Brouwer, A. P., et al. (2016). X-exome sequencing of 405 unresolved families identifies seven novel intellectual disability genes. *Mol. Psychiat.* 21, 133–148. doi: 10.1038/mp.2014.193

Hunskaar, S., and Hole, K. (1987). The formalin test in mice: dissociation between inflammatory and non-inflammatory pain. *Pain* 30, 103–114. doi: 10.1016/0304-3959(87)90088-1

Illias, A. M., Gist, A. C., Zhang, H., Kosturakis, A. K., and Dougherty, P. M. (2018). Chemokine CCL2 and its receptor CCR2 in the dorsal root ganglion contribute to oxaliplatin-induced mechanical hypersensitivity. *Pain* 159, 1308–1316. doi: 10.1097/j.pain.0000000000001212

Jentsch, T. J., and Pusch, M. (2018). CLC chloride channels and transporters: Structure, function, physiology, and disease. *Physiol. Rev.* 98, 1493–1590. doi: 10.1152/physrev.00047.2017

Kasper, D., Planells-Cases, R., Fuhrmann, J. C., Scheel, O., Zeitz, O., Ruether, K., et al. (2005). Loss of the chloride channel ClC-7 leads to lysosomal storage disease and neurodegeneration. *EMBO J.* 24, 1079–1091. doi: 10.1038/sj.emboj.7600576

Kornak, U., Kasper, D., Bosl, M. R., Kaiser, E., Schweizer, M., Schulz, A., et al. (2001). Loss of the ClC-7 chloride channel leads to osteopetrosis in mice and man. *Cell* 104, 205–215. doi: 10.1016/s0092-8674(01)00206-9

Lampert, A., O'Reilly, A. O., Reeh, P., and Leffler, A. (2010). Sodium channelopathies and pain. *Pflugers Arch.* 460, 249–263. doi: 10.1007/s00424-009-0779-3

Lamprecht, M. R., Sabatini, D. M., and Carpenter, A. E. (2007). CellProfiler: Free, versatile software for automated biological image analysis. *Biotechniques* 42, 71–75. doi: 10.2144/000112257

Lan, X., Han, X., Li, Q., Yang, Q.-W., and Wang, J. (2017). Modulators of microglial activation and polarization after intracerebral haemorrhage. *Nat. Rev. Neurol.* 13, 420–433. doi: 10.1038/nrneur01.2017.69

Laumet, G., Garriga, J., Chen, S.-R., Zhang, Y., Li, D.-P., Smith, T. M., et al. (2015). G9a is essential for epigenetic silencing of K+ channel genes in acute-to-chronic pain transition. *Nat. Neurosci.* 18, 1746–1755. doi: 10.1038/nn.4165

Lazarus, M. S., and Huang, Z. J. (2011). Distinct maturation profiles of perisomatic and dendritic targeting GABAergic interneurons in the mouse primary visual cortex during the critical period of ocular dominance plasticity. *J. Neurophysiol.* 106, 775–787. doi: 10.1152/jn.00729.2010

Lein, E. S., Hawrylycz, M. J., Ao, N., Ayres, M., Bensinger, A., Bernard, A., et al. (2007). Genome-wide atlas of gene expression in the adult mouse brain. *Nature* 445, 168–176. doi: 10.1038/nature05453

Liu, C., Cummins, T. R., Tyrrell, L., Black, J. A., Waxman, S. G., and Dib-Hajj, S. D. (2005). CAP-1A is a novel linker that binds clathrin and the voltage-gated sodium channel Na(v)1.8. *Mol. Cell. Neurosci.* 28, 636–649. doi: 10.1016/j.mcn.2004.11.007

Liu, Y., Schirra, C., Edelmann, L., Matti, U., Rhee, J., Hof, D., et al. (2010). Two distinct secretory vesicle-priming steps in adrenal chromaffin cells. *J. Cell Biol.* 190:1067. doi: 10.1083/jcb.201001164

Marics, I., Malapert, P., Reynders, A., Gaillard, S., and Moqrich, A. (2014). Acute heat-evoked temperature sensation is impaired but not abolished in mice lacking TRPV1 and TRPV3 channels. *PLoS One* 9:e99828. doi: 10.1371/journal.pone.0099828

McQuin, C., Goodman, A., Chernyshev, V., Kamentsky, L., Cimini, B. A., Karhohs, K. W., et al. (2018). CellProfiler 3.0: Next-generation image processing for biology. *PLoS Biol.* 16:e2005970. doi: 10.1371/journal.pbi0.2005970

Meents, J. E., and Lampert, A. (2016). "Studying sodium channel gating in heterologous expression systems," in *Advanced Patch-Clamp Analysis for Neuroscientists*, ed. A. Korngreen (New York, NY: Springer), 37–65.

Menetski, J., Mistry, S., Lu, M., Mudgett, J. S., Ransohoff, R. M., DeMartino, J. A., et al. (2007). Mice overexpressing chemokine ligand 2 (CCL2) in astrocytes display enhanced nociceptive responses. *J. Neurosci.* 149, 706–714. doi: 10.1016/j.neuroscience.2007.08.014

Mika, J., Zychowska, M., Popiolek-Barczyk, K., Rojewska, E., and Przewlocka, B. (2013). Importance of glial activation in neuropathic pain. *Eur. J. Pharmacol.* 716, 106–119. doi: 10.1016/j.ejphar.2013.01.072

Okuse, K., Malik-Hall, M., Baker, M. D., Poon, W. Y., Kong, H., Chao, M. V., et al. (2002). Annexin II light chain regulates sensory neuron-specific sodium channel expression. *Nature* 417, 653–656. doi: 10.1038/nature00781

Palmer, E. E., Stuhlmann, T., Weinert, S., Haan, E., Van Esch, H., Holvoet, M., et al. (2018). De novo and inherited mutations in the X-linked gene CLCN4 are associated with syndromic intellectual disability and behavior and seizure disorders in males and females. *Mol. Psychiat.* 23, 222–230. doi: 10.1038/mp.2016.135

Pang, R.-P., Xie, M.-X., Yang, J., Shen, K.-F., Chen, X., Su, Y.-X., et al. (2016). Downregulation of ClC-3 in dorsal root ganglia neurons contributes to mechanical hypersensitivity following peripheral nerve injury. *Neuropharmacology* 110, 181–189. doi: 10.1016/j.neuropharm.2016.07.023

Petersson, M. E., Obreja, O., Lampert, A., Carr, R. W., Schmelz, M., and Fransen, E. (2014). Differential axonal conduction patterns of mechano-sensitive and mechano-insensitive nociceptors–a combined experimental and modelling study. *PLoS One* 9:e103556. doi: 10.1371/journal.pone.0103556

Plesch, E., Chen, C. C., Butz, E., Scotto Rosato, A., Krogsaeter, E. K., Yinan, H., et al. (2018). Selective agonist of TRPML2 reveals direct role in chemokine release from innate immune cells. *Elife* 7:39720. doi: 10.7554/eLife.39720

Poet, M., Kornak, U., Schweizer, M., Zdebik, A. A., Scheel, O., Hoelter, S., et al. (2006). Lysosomal storage disease upon disruption of the neuronal chloride transport protein ClC-6. *Proc. Natl. Acad. Sci. U.S.A.* 103, 13854–13859. doi: 10.1073/pnas.0606137103

Priestley, J. V. (2009). "Neuropeptides: Sensory systems," in *Encyclopedia of Neuroscience*, ed. L. R. Squire (Oxford: Academic Press), 935–943.

Rasband, M. N., Park, E. W., Vanderah, T. W., Lai, J., Porreca, F., and Trimmer, J. S. (2001). Distinct potassium channels on pain-sensing neurons. *Proc. Natl. Acad. Sci. U.S.A.* 98, 13373–13378. doi: 10.1073/pnas.231376298

Ren, K., and Dubner, R. (2008). Neuron-glia crosstalk gets serious: Role in pain hypersensitivity. *Curr. Opin. Anaest.* 21, 570–579. doi: 10.1097/AC0.0b013e32830edbdf

Rohrbough, J., Nguyen, H. N., and Lamb, F. S. (2018). Modulation of ClC-3 gating and proton/anion exchange by internal and external protons and the anion selectivity filter. *J. Physiol.* 596, 4091–4119. doi: 10.1113/jp276332

Rueden, C. T., Schindelin, J., Hiner, M. C., DeZonia, B. E., Walter, A. E., Arena, E. T., et al. (2017). ImageJ2: ImageJ for the next generation of scientific image data. *BMC Bioinform.* 18:529. doi: 10.1186/s12859-017-1934-z

Rush, A. M., Cummins, T. R., and Waxman, S. G. (2007). Multiple sodium channels and their roles in electrogenesis within dorsal root ganglion neurons. *J. Physiol.* 579, 1–14. doi: 10.1113/jphysi01.2006.121483

Schindelin, J., Arganda-Carreras, I., Frise, E., Kaynig, V., Longair, M., Pietzsch, T., et al. (2012). Fiji: An open-source platform for biological-image analysis. *Nat. Meth.* 9, 676–682. doi: 10.1038/nmeth.2019

Scott, B., Leu, J., and Cinader, B. (1988). Effects of aging on neuronal electrical membrane properties. *Mech. Ageing Dev.* 44, 203–214. doi: 10.1016/0047-6374(88)90022-x

Seitz, V., Stötzner, P., Labuz, D., and Machelska, H. (2021). "Patch clamp analysis of opioid-induced Kir3 currents in mouse peripheral sensory neurons following nerve injury," in *Opioid Receptors: Methods and Protocols*, ed. S. M. Spampinato (New York, NY: Springer), 127–137. doi: 10.1007/978-1-0716-0884-5_12

Stauber, T., and Jentsch, T. J. (2010). Sorting motifs of the endosomal/lysosomal CLC chloride transporters*. *J. Biol. Chem.* 285, 34537–34548. doi: 10.1074/jbc.M110.162545

Stobrawa, S. M., Breiderhoff, T., Takamori, S., Engel, D., Schweizer, M., Zdebik, A. A., et al. (2001). Disruption of ClC-3, a chloride channel expressed on synaptic vesicles, leads to a loss of the hippocampus. *Neuron* 29, 185–196. doi: 10.1016/S0896-6273(01)00189-1

Stucky, C. L. (2007). "IB4-positive neurons, role in inflammatory pain," in *Encyclopedia of Pain*, eds R. F. Schmidt and W. D. Willis (Berlin, Heidelberg: Springer), 952–955.

Suaudeau, C., do-Rego, J.-C., and Costentin, J. (2005). Modifications in avoidance reactions of mice, on a second exposure to the hot plate, resist to various amnesia-inducing treatments. *Cogn. Brain Res.* 25, 339–347. doi: 1016/j.cogbrainres.2005.06.007

Swanwick, R. S., Pristerá, A., and Okuse, K. (2010). The trafficking of Na(V)1.8. *Neurosci. Lett.* 486, 78–83. doi: 10.1016/j.neulet.2010.08.074

Taylor, B. K., Peterson, M. A., and Basbaum, A. I. (1995). Persistent cardiovascular and behavioral nociceptive responses to subcutaneous formalin require peripheral nerve input. *J. Neurosci.* 15, 7575–7584. doi: 10.1523/JNEUROSCI.15-11-07575.1995

Tigerholm, J., Petersson, M. E., Obreja, O., Eberhardt, E., Namer, B., Weidner, C., et al. (2015). C-fiber recovery cycle supernormality depends on ion concentration and ion channel permeability. *Biophys. J.* 108, 1057–1071. doi: 10.1016/j.bpj.2014.12.034

Tjølsen, A., Berge, O.-G., Hunskaar, S., Rosland, J. H., and Hole, K. (1992). The formalin test: An evaluation of the method. *Pain* 51, 5–17. doi: 10.1016/0304-3959(92)90003-T

Vallejo, R., Tilley, D. M., Vogel, L., and Benyamin, R. (2010). The role of glia and the immune system in the development and maintenance of neuropathic pain. *Pain Pract.* 10, 167–184. doi: 10.1111/j.1533–2500.2010.00367.x

Veeramah, K. R., Johnstone, L., Karafet, T. M., Wolf, D., Sprissler, R., Salogiannis, J., et al. (2013). Exome sequencing reveals new causal mutations in children with epileptic encephalopathies. *Epilepsia* 54, 1270–1281. doi: 10.1111/epi.12201

Vydyanathan, A., Wu, Z. Z., Chen, S. R., and Pan, H. L. (2005). A-type voltage-gated K+ currents influence firing properties of isolectin B4-positive but not isolectin B4-negative primary sensory neurons. *J. Neurophysiol.* 93, 3401–3409. doi: 10.1152/jn.01267.2004

Wang, S., and Albers, K. M. (2009). Behavioral and cellular level changes in the aging somatosensory system. *Ann. N.Y Acad. Sci.* 1170, 745–749. doi: 10.1111/j.1749–6632.2009.04011.x

Weinert, S., Gimber, N., Deuschel, D., Stuhlmann, T., Puchkov, D., Farsi, Z., et al. (2020). Uncoupling endosomal CLC chloride/proton exchange causes severe neurodegeneration. *EMBO J.* 39:e103358. doi: 10.15252/embj.2019103358

Yoshikawa, M., Uchida, S., Ezaki, J., Rai, T., Hayama, A., Kobayashi, K., et al. (2002). CLC-3 deficiency leads to phenotypes similar to human neuronal ceroid lipofuscinosis. *Genes Cells* 7, 597–605. doi: 10.1046/j.1365-2443.2002.00539

Zhao, Z., Li, X., Hao, J., Winston, J. H., and Weinman, S. A. (2007). The ClC-3 chloride transport protein traffics through the plasma membrane *via* interaction of an N-terminal dileucine cluster with clathrin. *J. Biol. Chem.* 282, 29022–29031. doi: 10.1074/jbc.M703506200

Advantages of publishing in Frontiers

OPEN ACCESS
Articles are free to read for greatest visibility and readership

FAST PUBLICATION
Around 90 days from submission to decision

HIGH QUALITY PEER-REVIEW
Rigorous, collaborative, and constructive peer-review

TRANSPARENT PEER-REVIEW
Editors and reviewers acknowledged by name on published articles

Frontiers
Avenue du Tribunal-Fédéral 34
1005 Lausanne | Switzerland

Visit us: www.frontiersin.org
Contact us: frontiersin.org/about/contact

REPRODUCIBILITY OF RESEARCH
Support open data and methods to enhance research reproducibility

DIGITAL PUBLISHING
Articles designed for optimal readership across devices

FOLLOW US
@frontiersin

IMPACT METRICS
Advanced article metrics track visibility across digital media

EXTENSIVE PROMOTION
Marketing and promotion of impactful research

LOOP RESEARCH NETWORK
Our network increases your article's readership